

**PHOTOCATHODIC COMPOSITE CONDUCTIVE POLYMER-TITANIA FILMS  
FOR USE IN SOLAR HYDROGEN GENERATION**

by

David R. Bruce

B.A.Sc., The University of Waterloo, 2002

M.A.Sc., McMaster University, 2005

A THESIS SUBMITTED IN PARTIAL FULFILLMENT OF  
THE REQUIREMENTS FOR THE DEGREE OF

DOCTOR OF PHILOSOPHY

in

THE FACULTY OF GRADUATE STUDIES

(Chemical and Biological Engineering)

THE UNIVERSITY OF BRITISH COLUMBIA

(Vancouver)

October 2012

© David R. Bruce, 2012

## Abstract

Green hydrogen generation can serve as a solution to energy storage needs of the 21<sup>st</sup> century if coupled with a renewable energy source such as solar power. There is an advantage to performing in-situ hydrogen generation at a photocatalytic surface in order to reduce system efficiency losses. Investigation into the limitations and benefits of coupled electrolytic and solar process are investigated in this dissertation.

Of chief examination were polybithiophene-titania composite films used as a photocathode in a Nafion 117 membrane based H<sub>2</sub>SO<sub>4</sub> electrolytic system. Titania content inclusion up to 0.35 mg/cm<sup>2</sup> with a range of film thicknesses between 1-20 μm, were investigated in several architectural configurations. The placement of the composite films was directed either towards or away from the proton conducting membrane in a 2-D or 3-D configuration.

The results indicated that the electrochemical benefits to titania inclusion and film thickness increase were counter to photonic energy collection. With an increase in titania there was an increase in electrochemical performance, but it led to worse photonic efficiency as suspected due to an increase in recombination from defect trap states. With an increase in film thickness there was an increase in photonic efficiency with increased photon absorption, but this was accompanied by an increase in cell resistance leading to worse electrochemical performance. Electrochemical performance was also enhanced by placing the catalytic film directly against the membrane, although photonic stimulation in this configuration was impossible in our current cell configuration. Photonic stimulation was enhanced by the deposition of the composite films onto a distributed 3-D carbon fibre substrate.

Doping of the 3-D composite films loaded on carbon fibre substrates with a Nafion ionomer interconnect was tested in an effort to enhance the triple phase connectivity of the cell. It was found that the doping resulted in a deactivation of the substrate (both electrochemical and photonic) due to the deposition method used, but increases in photonic performance at higher current densities showed that with less catalyst encapsulation this strategy may be a viable method to enhance PEM based photoelectrochemical cells.

## **Preface**

A version of Chapter 3 has been published. D. R. Bruce and D. P. Wilkinson, “Conductive Polymer-Titania Photocathode Development for Hydrogen Production,” ECS Transactions, vol. 28, no. 26, pp. 119-132, 2010. I conducted all the testing and wrote the manuscript.

# Table of Contents

<b>Abstract.....</b>	<b>ii</b>
<b>Preface.....</b>	<b>iv</b>
<b>Table of Contents .....</b>	<b>v</b>
<b>List of Tables .....</b>	<b>xiv</b>
<b>List of Figures.....</b>	<b>xv</b>
<b>List of Symbols and Abbreviations .....</b>	<b>xxxiv</b>
<b>Acknowledgements .....</b>	<b>xxxviii</b>
<b>Dedication .....</b>	<b>xl</b>
<b>Chapter 1: Introduction .....</b>	<b>1</b>
<b>1.1 History of Energy Use.....</b>	<b>1</b>
<b>1.2 Solar Devices.....</b>	<b>3</b>
1.2.1 Thermal Devices .....	6
1.2.2 Quantum Mechanical Devices .....	8
<b>1.3 Green Hydrogen Generation .....</b>	<b>9</b>
1.3.1 Standard Electrolysis .....	10
1.3.2 Direct Solar Hydrogen Generation Systems .....	16
1.3.3 Hybrid Solar-assisted Hydrogen Generation Systems.....	26
1.3.4 Analytical Measures.....	27
1.3.4.1 Solar Performance – $V_{oc}$ , $I_{sc}$ , Fill Factor, and Efficiency .....	28
1.3.4.2 Electrochemical Performance – The Tafel Equation .....	31
1.3.4.3 EIS.....	32

1.3.4.4	Benchmark Devices .....	33
<b>1.4</b>	<b>Research Objectives and Thesis Layout .....</b>	<b>36</b>
<b>Chapter 2:</b>	<b>Materials and Methods .....</b>	<b>39</b>
<b>2.1</b>	<b>Film Loading Procedures .....</b>	<b>39</b>
2.1.1	Loading Cell Configuration .....	40
2.1.2	Electropolymerization Treatment .....	44
<b>2.2</b>	<b>Film Characterization Procedures .....</b>	<b>47</b>
2.2.1	Surface Analysis – Atomic Force Microscopy .....	48
2.2.2	Thickness Analysis – Profilometry .....	48
2.2.3	Spectral Analysis – UV-Vis Spectrophotometry .....	50
2.2.4	Morphological Analysis – Scanning Electron Microscopy .....	50
2.2.5	Nanoparticulate Inclusion Analysis – Inductively Coupled Plasma Mass Spectroscopy .....	51
2.2.6	Through-Plane Conductivity Analysis – Sandwiched Conductivity Cell.....	52
<b>2.3</b>	<b>Film Testing Procedures.....</b>	<b>54</b>
2.3.1	Spray Loading of Electrodes.....	54
2.3.2	Membrane Preparation and Conditioning.....	55
2.3.3	Membrane Electrode Assembly.....	55
2.3.4	Cell and Instrumentation Setup.....	58
2.3.5	Photoelectrochemical Experiment Control Systems.....	63
2.3.6	Error Analysis of Experimental Data.....	66
2.3.7	Solar Simulator Calibration .....	67
2.3.8	Reference Electrode Calibration .....	68

2.3.9	Platinization of Titania.....	68
<b>Chapter 3: Phase 1 – Benchmarking of Photocathode Function.....</b>		<b>70</b>
<b>3.1</b>	<b>Introduction.....</b>	<b>70</b>
<b>3.2</b>	<b>Experimental .....</b>	<b>74</b>
<b>3.3</b>	<b>Characterization Results .....</b>	<b>75</b>
3.3.1	SEM/EDX.....	75
3.3.2	AFM.....	80
3.3.3	Profilometry .....	82
3.3.4	UV-Vis.....	85
3.3.5	ICP-MS .....	90
<b>3.4</b>	<b>Photoelectrochemical Results .....</b>	<b>91</b>
3.4.1	Standard Cathode Function – Platinum and Blank TGP-H-030.....	93
3.4.2	PBT Cathode Function.....	96
3.4.3	PBT-TiO <sub>2</sub> Cathode Function.....	98
3.4.4	PBT-TiO <sub>2</sub> :Pt Cathode Function .....	106
<b>3.5</b>	<b>Conclusions.....</b>	<b>108</b>
<b>Chapter 4: Phase 2 – Tunable Inclusion Parameters .....</b>		<b>110</b>
<b>4.1</b>	<b>Introduction.....</b>	<b>110</b>
<b>4.2</b>	<b>Experimental .....</b>	<b>112</b>
<b>4.3</b>	<b>Characterization Results .....</b>	<b>113</b>
4.3.1	Profilometry .....	113
4.3.2	ICP-MS .....	115
4.3.3	UV-Vis.....	116

4.3.4	SEM .....	120
4.3.5	Ex-Situ Resistance .....	125
<b>4.4</b>	<b>Photoelectrochemical Results .....</b>	<b>127</b>
4.4.1	Dark Performance .....	128
4.4.1.1	3-D (CFP Loadings).....	130
4.4.1.1.1	3-D Films Facing In Electrochemical Results .....	131
4.4.1.1.2	3-D Films Facing Out Electrochemical Results.....	138
4.4.1.2	2-D (316 SS Loadings) .....	146
4.4.1.2.1	2-D Films Facing In Electrochemical Results .....	146
4.4.1.2.2	2-D Films Facing Out Electrochemical Results.....	151
4.4.2	Illuminated Performance.....	155
4.4.2.1	3-D PBT-TiO <sub>2</sub> Photocathode Function.....	155
4.4.2.2	2-D PBT-TiO <sub>2</sub> Photocathode Function.....	161
4.4.3	EIS Analysis.....	163
4.4.3.1	Cell Resistance.....	163
4.4.3.2	Capacitive Double Layer .....	165
<b>4.5</b>	<b>Conclusions.....</b>	<b>166</b>
<b>Chapter 5: Phase 3 – Tunable Substrate Parameters .....</b>		<b>169</b>
<b>5.1</b>	<b>Introduction.....</b>	<b>169</b>
<b>5.2</b>	<b>Experimental .....</b>	<b>170</b>
<b>5.3</b>	<b>Characterization Results .....</b>	<b>172</b>
5.3.1	MPL Layer Variation – Nafion Addition.....	172
5.3.2	SEM .....	174

5.3.2.1	Nafion Coated TGP-H-030.....	174
5.3.2.2	Nafion Coated 20 $\mu\text{m}$ PBT-TiO <sub>2</sub> TGP-H-030 .....	176
<b>5.4</b>	<b>Photoelectrochemical Results .....</b>	<b>178</b>
5.4.1	Dark Performance .....	178
5.4.1.1	Blank Nafion Coated CFP .....	178
5.4.1.2	Nafion Coated CFP Baseline Samples.....	180
5.4.1.3	Bi-layered Nafion Coated CFP Baseline Samples.....	183
5.4.2	Illuminated Performance.....	185
5.4.2.1	Nafion Coated CFP Baseline Samples.....	186
5.4.2.2	Bi-layered Nafion Coated CFP Baseline Samples.....	188
<b>5.5</b>	<b>Conclusions.....</b>	<b>190</b>
<b>Chapter 6:</b>	<b>Conclusions and Recommendations .....</b>	<b>192</b>
<b>6.1</b>	<b>Conclusions.....</b>	<b>192</b>
<b>6.2</b>	<b>Recommendations.....</b>	<b>194</b>
6.2.1	Reactor and Testing Apparatus Upgrades.....	194
6.2.1.1	Acid Dosing and pH Measurement.....	195
6.2.1.2	Gas Capture and Analysis.....	196
6.2.1.3	Optical Upgrades .....	197
6.2.2	Alternative Sample Preparation .....	197
6.2.2.1	Microfibre Carbon Supports and Decal Architecture .....	198
6.2.2.2	Pulse Current Density Deposition.....	199
6.2.2.3	Different Conductive Polymer/Nanoparticle Combinations.....	200
6.2.2.4	Temperature and Supporting Electrolyte Variation.....	200

6.2.2.5	Selective Titania Surface Loading and Enhanced Particulate Connection .....	201
6.2.3	Additional Photoelectrochemical Testing Protocol .....	202
6.2.3.1	Rotating Disc Electrode (RDE) Experiments .....	202
6.2.3.2	Single Surface Energy Studies.....	203
6.2.3.3	Electrochemical Impedance Spectroscopy .....	203
6.2.3.4	Solar, pH and Temperature Variation.....	204
6.2.3.5	Lifetime/Degradation.....	205
<b>References.....</b>		<b>206</b>
<b>Appendix A - Helio-thermal Hydrolysis .....</b>		<b>232</b>
<b>Appendix B - Metal-oxide Particle Thermochemical Cycles .....</b>		<b>234</b>
<b>Appendix C - Properties of Light .....</b>		<b>237</b>
C.1	Solar Emission and Optical Attenuation of Terrestrial Insolation.....	237
C.2	Maxwell Equations and Electromagnetic Wave Movement.....	239
C.3	Refraction.....	239
C.4	Reflection.....	240
C.5	Absorption.....	241
<b>Appendix D - Absorption Spectra .....</b>		<b>244</b>
D.1	Absorption Spectra of FTO/ITO.....	244
D.2	Absorption Spectra of Water/ Sulfuric Acid.....	246
D.3	Absorption of Nafion .....	247
D.4	Absorption Spectra of Conductive Polymers.....	248
D.5	Absorption Spectra of TiO <sub>2</sub> /Composite Films.....	250
<b>Appendix E - Type I Solar Cells .....</b>		<b>253</b>

<b>Appendix F - Type II Solar Cells.....</b>	<b>255</b>
F.1 CIGS and CdS/CdTe Cells.....	255
F.2 Multijunction a-Si/a-SiGe Cells.....	256
<b>Appendix G - Type III Solar Cells.....</b>	<b>257</b>
G.1 Type IIIa Solar Cells.....	257
G.2 Type IIIb Solar Cells.....	258
G.2.1 Organic Thin Film, Bulk Heterojunction, and Composite Cells .....	259
G.2.2 Redox-coupled Dye cells .....	267
<b>Appendix H - Semiconductor Properties.....</b>	<b>271</b>
H.1 Excitation .....	271
H.2 Electronic Promotion in a Bulk Material .....	272
H.3 Electronic Promotion in Junctions and Under Bias .....	274
H.4 Valence and Conduction Band Theory.....	278
H.5 Doping and Solid Solutions .....	280
H.6 Dislocations and Trap Site Effects.....	284
H.7 Junctions - Charge Separation and Mobility.....	287
H.8 Quantum Efficiency and Quantum Effects .....	292
<b>Appendix I - Electrolytic Options Mated with Non-Solar Renewable Energy Sources</b>	<b>294</b>
<b>Appendix J - PEM Systems Overview .....</b>	<b>295</b>
<b>Appendix K - Electrochemical Basis for Electron Transfer and Equilibrium .....</b>	<b>300</b>
<b>Appendix L - Activation Overpotential Losses .....</b>	<b>307</b>
<b>Appendix M - Ohmic Overpotential Losses .....</b>	<b>321</b>
<b>Appendix N - Mass Transport Overpotential Losses .....</b>	<b>328</b>

<b>Appendix O - Extended EIS Analysis .....</b>	<b>330</b>
<b>Appendix P - Capacitance .....</b>	<b>339</b>
P.1 Double-layer Capacitance.....	339
P.2 Pseudocapacitance .....	341
<b>Appendix Q - Photovoltaic Device Benchmarks .....</b>	<b>343</b>
<b>Appendix R - Photochemical Device Benchmarks.....</b>	<b>352</b>
<b>Appendix S - Photoelectrochemical Device Benchmarks.....</b>	<b>354</b>
<b>Appendix T - Calibration Curves.....</b>	<b>356</b>
T.1 Calibration Curve for Peristaltic Pump.....	356
T.2 Calibration Curve for Solar Simulator Output.....	357
T.3 Calibration Curve of ICP-MS .....	358
<b>Appendix U - Paired Statistical Analysis .....</b>	<b>359</b>
U.1 PBT Film Thicknesses .....	359
U.2 1292s PBT vs. PBT-TiO <sub>2</sub> .....	360
U.3 1292s PBT-TiO <sub>2</sub> vs. PBT-TiO <sub>2</sub> :Pt .....	361
U.4 Increased Titania Content by Film Thickness for 3-D Films Facing Out.....	362
U.5 Increased Film Thickness by Titania Content for 3-D Films Facing Out.....	364
U.6 Increased Titania Content by Film Thickness for 3-D Films Facing Out.....	366
U.7 Increased Film Thickness by Titania Content for 3-D Films Facing Out.....	368
U.8 Facing In vs. Facing Out 3-D performance .....	370
U.9 Increased Film Thickness by Titania Content for 2-D Films Facing In .....	374
U.10 Increased Titania Content by Film Thickness for 2-D Films Facing In .....	376
U.11 Facing In vs. Facing Out 2-D performance .....	378

<b>Appendix V - Through Membrane Irradiation.....</b>	<b>382</b>
<b>Appendix W - Higher Intensity Sun Studies .....</b>	<b>384</b>

## List of Tables

Table 1 - EDX Results for 1292s loadings of PBT and PBT composite films.....	78
Table 2 - Profilometry measured film thickness comparison of PBT, PBT-TiO <sub>2</sub> , and PBT-TiO <sub>2</sub> :Pt. ....	83
Table 3 – Pseudo-exchange current density and pseudo-Tafel slope of blank and Nafion loaded TGP-H-030 substrates .....	180
Table 4 – Pseudo-exchange current density and pseudo-Tafel slope of 1 mg/cm <sup>2</sup> Nafion doped, PBT-TiO <sub>2</sub> films loaded on TGP-H-030 substrates and in comparison with equivalent undoped PBT-TiO <sub>2</sub> films .....	182
Table 5 – Pseudo-exchange current density and Pseudo-Tafel slope of bi-layer 1.0 mg/cm <sup>2</sup> Nafion doped 20 μm, 0.02 mg/cm <sup>2</sup> titania loaded, PBT-TiO <sub>2</sub> composite films on TGP-H-030 substrates.....	184
Table 6 - Standard reduction potentials. [225].....	301
Table 7 - Values of exchange current densities ( $i_0$ in A/cm <sup>2</sup> of $S_{vis}$ ) at different pressures and temperatures for a 20 cm <sup>2</sup> MF4-SK membrane electrode assembly. [249].....	314
Table 8 - Physical properties of TGP-H carbon-fibre materials. [86] .....	321

## List of Figures

Figure 1 - World energy consumption projections organized by national participation in the Organization for Economic Cooperation and Development (OECD nations) [1]. Reprinted with permission from DOE/EIA. ....	2
Figure 2 - The increase in worldwide production of PV modules (MW) during the last 15 years. The market growth rate in the last decade has been over 30%. [4] Reprinted with permission from Philosophical Transactions of the Royal Society A. ....	4
Figure 3 - A history of best cell efficiencies. [10] Reprinted with permission from MRS Bulletin.....	5
Figure 4 - Cost-efficiency analysis for photovoltaic technologies. [10] Reprinted with permission from MRS Bulletin.....	8
Figure 5 - Dependence of the reversible potential on electrolyte temperature, under standard conditions, and for 30wt,% KOH electrolyte at 25 atm pressure. [34] Reprinted with permission from the Journal of the Electrochemical Society. ....	14
Figure 6 - Fujishima and Honda electrochemical setup. Elements are as marked: (1)TiO <sub>2</sub> electrode, (2) Platinized platinum foil, (3) Glass frit, (4) External load, (5) Voltmeter. [36] Reprinted with permission from Nature. ....	16
Figure 7 - History of the number of citations of the landmark 1972 Fujishima and Honda paper. [38] Reprinted with permission from Surface Science Reports.....	17
Figure 8 - Schematic of multilayer Ga-AlAs-Si-RuO <sub>2</sub> -Pt direct solar water splitting cell. [47] Reprinted with permission from the Journal of Physical Chemistry B.....	18

Figure 9 - Two-cell PEC setup with two CIGS2 thin-film PV cells, RuO <sub>2</sub> anode for oxygen evolution and platinum cathode for hydrogen evolution. [48] Reprinted with permission from Thin Solid Films. ....	19
Figure 10 - Schematic of dual layer TiO <sub>2</sub> coated Si photoelectrochemical cell. [52] Reprinted with permission from Applied Physics Letters. ....	21
Figure 11 - Variation in open-circuit voltage with increasing solar intensity. [71] Reprinted with permission from Applied Physics Letters. ....	29
Figure 12 - Multi-Venn diagram of benchmark devices.....	35
Figure 13 - Schematic of first generation plating cell.....	41
Figure 14 - Photograph of second generation plating cell cartridge illustrating plating shape control .....	42
Figure 15 - Photograph of Kapton masked PET-ITO film with 2 cm <sup>2</sup> exposed active area and aluminum foil contact .....	43
Figure 16 - a) Bare 316SS electrode, b) Composite coated 316SS electrode.....	44
Figure 17 - Partial model of interfacial reactions for polythiophene electrogeneration on a platinum electrode using LiClO <sub>4</sub> as electrolyte salt. [76] Reprinted with permission from Springer.....	45
Figure 18 - Photographs of baseline loaded PBT on TGP-H-030 a) as loaded, and b) with film characterization cutouts taken from sample .....	46
Figure 19 - Profile scan of PBT loaded on a 25mm x 75mm glass slide.....	49
Figure 20 - Sample profilometric scan covering a 40mm travel span .....	49

Figure 21 - Photographs of conductivity cell equipment, including: a) Kapton masked graphite plate with composite coated 1/8" TGP-H-030 sample placed for measurement, b) Graphite plate compressed between gold-coated contacts.....	53
Figure 22 - Schematic of membrane electrode assembly (MEA).....	56
Figure 23 - MEA hinge jig schematic.....	57
Figure 24 - Photograph of a) assembled reactor and optical cell, b) assembled reactor mounted in beam path with electrical connections .....	58
Figure 25 - Schematic of electrical connection and control of the photoelectrochemical cell	59
Figure 26 - Electrochemical cell response with illumination for galvanostatic electrolysis runs at different current densities.....	60
Figure 27 - Example CV sweep rate variation for capacitive double layer calculation .....	63
Figure 28 - Photograph of chiller unit and catholyte dewer setup.....	64
Figure 29 - Photograph of peristaltic pump setup.....	65
Figure 30 - Photograph of a) Sciencetech solar simulator with optical rail orthogonal to beam output, and b) optical control (shutter and aluminum plate) mounted on optical rail .....	66
Figure 31 - Morphology of blank TGP-H-030 measured at 3,000X magnification .....	76
Figure 32 - Morphology of 1292s PBT loaded TGP-H-030 measured at 3,000X magnification – Site A .....	77
Figure 33 - Morphology of 1292s PBT loaded TGP-H-030 measured at 3,000X magnification – Site B .....	77
Figure 34 - Morphology of 1292s PBT-TiO <sub>2</sub> loaded TGP-H-030 measured at 3,000X magnification .....	79

Figure 35 - Morphology of 1292s PBT-TiO <sub>2</sub> :Pt loaded TGP-H-030 measured at 3,000X magnification .....	79
Figure 36 - 2x2 μm <sup>2</sup> AFM image of the surface of PBT-TiO <sub>2</sub> film deposited on FTO .....	82
Figure 37 - UV-Vis Absorption of blank FTO substrate .....	86
Figure 38 - PBT UV-Vis Absorption of FTO substrate.....	87
Figure 39 - PBT-TiO <sub>2</sub> UV-Vis Absorption on FTO Substrate .....	87
Figure 40 - PBT-TiO <sub>2</sub> :Pt UV-Vis Absorption on FTO Substrate.....	89
Figure 41 - Titania content as determined by ICP-MS of various loading times for composite films of PBT-TiO <sub>2</sub> and PBT-TiO <sub>2</sub> :Pt films loaded on TGP-H-030. Line is added for illustrative purposes and indicates the average loading.....	90
Figure 42 - Average Anode Potential for Electrolysis. Logarithmic trendline added to indicate Tafel correspondence. ....	92
Figure 43 - Baseline and Platinum Cathode Performance. Logarithmic trendlines added to indicate Tafel correspondence. ....	93
Figure 44 - Spray deposited platinum (1.0 mg/cm <sup>2</sup> ) electrolysis results with temperature variation. Logarithmic trendlines added to indicate Tafel correspondence.....	95
Figure 45 - Cyclic voltammogram of platinized platinum in 0.5M H <sub>2</sub> SO <sub>4</sub> , $v = 10\text{mV/s}$ . [91] Reprinted with permission from <i>Electrochimica Acta</i> .....	96
Figure 46 - Cathode polarization and light on/off potential difference for 646 s and 1292 s loadings of PBT films coated on TGP-H-030. Benchmark plots indicated with lines added for illustrative purposes.....	98

Figure 47 - Cathode polarization and light on/off potential difference for 1292 s loadings of PBT and PBT-TiO<sub>2</sub> films coated on TGP-H-030. Benchmark plots are indicated with lines added for illustrative purposes. .... 99

Figure 48 - Variation in photoresponse of 1292s loaded PBT-TiO<sub>2</sub> with a variation in cell resistance. Lines are added for illustrative purposes. .... 101

Figure 49 - Dark and illuminated cell performance of a spray loaded Nafion-TiO<sub>2</sub> on TGP-H-030 anode with Pt mesh cathode, separated by N117 in 0.5 mM H<sub>2</sub>SO<sub>4</sub>. .... 103

Figure 50 – Cell potential change with solar irradiation for a spray loaded Nafion-TiO<sub>2</sub> on TGP-H-030 anode with Pt mesh cathode, separated by N117 in 0.5 mM H<sub>2</sub>SO<sub>4</sub>. .... 104

Figure 51 - Dark and illuminated performance of a spray loaded Nafion-TiO<sub>2</sub> cathode on TGP-H-030 with a 1.5 mg/cm<sup>2</sup> RuO<sub>2</sub> anode separated by N117 in 0.5 mM H<sub>2</sub>SO<sub>4</sub>. .... 105

Figure 52 - Cathode polarization and light on/off potential difference for 1292 s loadings of PBT-TiO<sub>2</sub> and PBT-TiO<sub>2</sub>:Pt films coated on TGP-H-030. Benchmark plots indicated with lines added for illustrative purposes. .... 107

Figure 53 - Variation of loaded film thickness by loading method and loading time. Lines are added for illustrative purposes. .... 114

Figure 54 - Variation of titania content by loading method with increasing loading time. Lines are added for illustrative purposes. .... 115

Figure 55 - UV-Vis Absorption of blank ITO substrate ..... 117

Figure 56 - High concentration sol PBT-TiO<sub>2</sub> UV-Vis absorption on ITO substrate ..... 118

Figure 57 - Sonicated high concentration sol PBT-TiO<sub>2</sub> UV-Vis absorption on ITO substrate ..... 119

Figure 58 - Cross-sectional morphology of 1  $\mu\text{m}$  high concentration sonicated sol PBT-TiO<sub>2</sub> loaded TGP-H-030 measured at a) 500X, b) 3,000X, c) 10,000X, and d) 30,000X. Arrows highlight areas of composite deposition. .... 121

Figure 59 - Cross-sectional morphology of 10  $\mu\text{m}$  high concentration sonicated sol PBT-TiO<sub>2</sub> loaded TGP-H-030 measured at a) 500X, b) 3,000X, c) 10,000X, and d) 30,000X. Arrows highlight areas of composite inclusion, dashed circle highlights area of titania concentration. .... 123

Figure 60 - Variation in ex-situ resistance for PBT-TiO<sub>2</sub> loaded TGP-H-030 ..... 126

Figure 61 - Variation of loaded film thickness with titania inclusion, sorted by loading method. Lines are added for illustrative purposes. .... 128

Figure 62 - Schematic of electrolysis using a 2-dimensional 316-SS substrate and a 3-dimensional TGP-H-030 substrate with the film facing the N117 membrane. Cathodic composite catalyst sites are denoted with red diamonds, while RuO<sub>2</sub> anode catalyst sites are denoted as yellow circles. .... 129

Figure 63 - Schematic of electrolysis using a 2-dimensional 316-SS substrate and a 3-dimensional TGP-H-030 substrate with the film facing away from the N117 membrane. Cathodic composite catalyst sites are denoted with red diamonds, while RuO<sub>2</sub> anode catalyst sites are denoted as yellow circles. .... 130

Figure 64 - Cathodic potential (dark performance) of 1  $\mu\text{m}$  thick PBT-TiO<sub>2</sub> films for increasing TiO<sub>2</sub> content facing the N117 membrane in 0.5 mM H<sub>2</sub>SO<sub>4</sub>. Data at 1280  $\mu\text{A cm}^{-2}$  not shown but included in logarithmic curve fit. .... 131

Figure 65 - Variation of pseudo-exchange current density and pseudo-Tafel slope with titania inclusion for 1  $\mu\text{m}$  films loaded on CFP when placed facing the N117 membrane. Filled

symbols represent pseudo-exchange current density and open symbols represent pseudo-Tafel slope with lines added for illustrative purposes. .... 133

Figure 66 - Cathodic potential (dark performance) of 10µm thick PBT-TiO<sub>2</sub> films for increasing TiO<sub>2</sub> content facing the N117 membrane in 0.5 mM H<sub>2</sub>SO<sub>4</sub>. Data at 1280 µA cm<sup>-2</sup> not shown but included in logarithmic curve fit. .... 136

Figure 67 - Variation of pseudo-exchange current density and pseudo-Tafel slope with titania inclusion for 10 µm films loaded on CFP when placed facing the N117 membrane. Filled symbols represent pseudo-exchange current density and open symbols represent pseudo-Tafel slope with lines added for illustrative purposes. .... 137

Figure 68 - Cathodic potential (dark performance) of 1 µm thick PBT-TiO<sub>2</sub> films for increasing TiO<sub>2</sub> content facing away from the N117 membrane in 0.5 mM H<sub>2</sub>SO<sub>4</sub>. Data at 1280 µA cm<sup>-2</sup> not shown but included in logarithmic curve fit. .... 139

Figure 69 - Cathodic potential (dark performance) of 5 µm thick PBT-TiO<sub>2</sub> films for increasing TiO<sub>2</sub> content facing away from the N117 membrane in 0.5 mM H<sub>2</sub>SO<sub>4</sub>. Higher current density data not shown due to titania degradation issues, and not included in logarithmic curve fit. .... 140

Figure 70 - Cathodic potential (dark performance) of 10 µm thick PBT-TiO<sub>2</sub> films for increasing TiO<sub>2</sub> content facing away from the N117 membrane in 0.5 mM H<sub>2</sub>SO<sub>4</sub>. Higher current density data not shown due to titania degradation issues and not included in logarithmic curve fit. .... 141

Figure 71 - Cathodic potential (dark performance) of 20 µm thick PBT-TiO<sub>2</sub> films for increasing TiO<sub>2</sub> content facing away from the N117 membrane in 0.5 mM H<sub>2</sub>SO<sub>4</sub>. Higher current density data not shown due to titania degradation issues. .... 142

Figure 72 - Variation of pseudo-exchange current density with titania inclusion for films loaded on TGP-H-030 substrates when placed facing away from the N117 membrane in 0.5mM H<sub>2</sub>SO<sub>4</sub>. Lines are shown for illustrative purposes. .... 143

Figure 73 - Variation of pseudo-Tafel slope with titania inclusion for films loaded on TGP-H-030 substrates when placed facing away from the N117 membrane in 0.5M H<sub>2</sub>SO<sub>4</sub>. Lines are shown for illustrative purposes. .... 145

Figure 74 - Cathodic potential (dark performance) of 1µm thick 2-D PBT-TiO<sub>2</sub> films for increasing TiO<sub>2</sub> content facing the N117 membrane in 1M H<sub>2</sub>SO<sub>4</sub>. Lines are added for illustrative purposes. .... 148

Figure 75 - Cathodic potential (dark performance) of 10 µm thick 2-D PBT-TiO<sub>2</sub> films for increasing TiO<sub>2</sub> content facing the N117 membrane in 1M H<sub>2</sub>SO<sub>4</sub>. Lines are added for illustrative purposes. .... 149

Figure 76 - Variation of pseudo-exchange current density and pseudo-Tafel slope with titania inclusion for 1 and 10 um films loaded on 316SS perforated substrates when placed facing the N117 membrane in 1M H<sub>2</sub>SO<sub>4</sub>. Filled symbols represent pseudo-exchange current density and open symbols represent pseudo-Tafel slope with lines added for illustrative purposes. .... 150

Figure 77 - Cathodic potential of various thicknesses of PBT-TiO<sub>2</sub> films with differing TiO<sub>2</sub> content loaded on 316SS perforated substrates when placed facing away from the N117 membrane in 0.5 mM H<sub>2</sub>SO<sub>4</sub>. Data at 1280 µA/cm<sup>2</sup> not shown but included in logarithmic curve fit. .... 151

Figure 78 - Variation of pseudo-exchange current density and pseudo-Tafel slope with titania inclusion for 1, 10, and 20 µm films loaded on 316SS substrates when placed facing away

from the N117 membrane in 0.5 mM H<sub>2</sub>SO<sub>4</sub>. Filled symbols represent pseudo-exchange current density and open symbols represent pseudo-Tafel slope with lines added for illustrative purposes. .... 152

Figure 79 - Energy harvested for 20 μm PBT-TiO<sub>2</sub> films with differing TiO<sub>2</sub> content. Films loaded on TGP-H-030 substrate, tested against 1.5 mg/cm<sup>2</sup> RuO<sub>2</sub> on TGP-H-030, N117 membrane separator, in 0.5 mM H<sub>2</sub>SO<sub>4</sub> recirculated at 1 mL/s at 20°C. Lines are added for illustrative purposes. .... 156

Figure 80 - Energy harvested for 10 μm PBT-TiO<sub>2</sub> films with differing TiO<sub>2</sub> content. Films loaded on TGP-H-030 substrate, tested against 1.5 mg/cm<sup>2</sup> RuO<sub>2</sub> on TGP-H-030, N117 membrane separator, in 0.5 mM H<sub>2</sub>SO<sub>4</sub> recirculated at 1 mL/s at 20°C. Lines are added for illustrative purposes. .... 157

Figure 81 - Energy harvested for 5 μm PBT-TiO<sub>2</sub> films with differing TiO<sub>2</sub> content. Films loaded on TGP-H-030 substrate, tested against 1.5 mg/cm<sup>2</sup> RuO<sub>2</sub> on TGP-H-030, N117 membrane separator, in 0.5 mM H<sub>2</sub>SO<sub>4</sub> recirculated at 1 mL/s at 20°C. Lines are added for illustrative purposes. .... 158

Figure 82 - Energy harvested for 1 μm PBT-TiO<sub>2</sub> films with differing TiO<sub>2</sub> content. Films loaded on TGP-H-030 substrate, tested against 1.5 mg/cm<sup>2</sup> RuO<sub>2</sub> on TGP-H-030, N117 membrane separator, in 0.5 mM H<sub>2</sub>SO<sub>4</sub> recirculated at 1 mL/s at 20°C. Lines are added for illustrative purposes. .... 159

Figure 83 - Energy harvested for 1, 10, and 20 μm PBT-TiO<sub>2</sub> films with differing TiO<sub>2</sub> content. Films loaded on 316SS perforated substrate, tested against 1.5 mg/cm<sup>2</sup> RuO<sub>2</sub> on TGP-H-030, N117 membrane separator, in 0.5 mM H<sub>2</sub>SO<sub>4</sub> recirculated at 1 mL/s at 20°C. Lines are added for illustrative purposes. .... 161

Figure 84 - Energy harvested for 1, 10, and 20  $\mu\text{m}$  PBT-TiO<sub>2</sub> films with differing TiO<sub>2</sub> content. Films loaded on graphitized 316SS perforated substrate, tested against 1.5 mg/cm<sup>2</sup> RuO<sub>2</sub> on TGP-H-030, N117 membrane separator, in 0.5 mM H<sub>2</sub>SO<sub>4</sub> recirculated at 1 mL/s at 20°C. Lines are added for illustrative purposes. .... 162

Figure 85 - Cell resistance of PBT-TiO<sub>2</sub> samples loaded on TGP-H-030 in 0.5 mM H<sub>2</sub>SO<sub>4</sub> facing away from the membrane. Filled symbols denote 3-D samples, and open symbols denote 2-D samples. Lines are added for illustrative purposes. .... 164

Figure 86 - Measured capacitive double layer of PBT-TiO<sub>2</sub> films loaded on TGP-H-030 facing the N117 membrane, in 0.5 mM and 1M H<sub>2</sub>SO<sub>4</sub> recirculated at 1 mL/s at 20°C. Lines are added for illustrative purposes. .... 166

Figure 87 - Amount of Nafion ionomer added per times drop cast for bare TGP-H-030 substrates. Fitted line is added for illustrative purposes. .... 173

Figure 88 - Morphology of Nafion-coated TGP-H-030 measured for a) cross-sectional sample at 500X magnification, b) planar sample at 500X magnification, c) cross-sectional sample at 3,000X, and d) cross-sectional sample at 10,000X. Arrows highlight areas of Nafion inclusion. .... 175

Figure 89 - Morphology of PBT-TiO<sub>2</sub> loaded, Nafion-coated TGP-H-030 measured for a cross-sectional sample at a) 500X c) 10,000X, and d) 3,000X magnification. A reproduction of Figure 35 is shown in section b) for comparison with the Nafion loaded sample d) below. Arrows highlight areas of Nafion inclusion. .... 177

Figure 90 - Cathodic potential of Nafion doped blank TGP-H-030 substrates. Logarithmic curve fit used to demonstrate Tafel correlation. .... 179

Figure 91 - Cathodic potential of Nafion doped PBT-TiO<sub>2</sub> (filled symbol) composite films compared to non-doped (open symbol) samples loaded on TGP-H-030 substrates tested against 1.5 mg/cm<sup>2</sup> RuO<sub>2</sub> on TGP-H-030, with N117 membrane separator, in 0.5 mM H<sub>2</sub>SO<sub>4</sub> recirculated at 1 mL/s at 20°C. Lines are added for illustrative purposes. .... 181

Figure 92 - Cathodic potential of bi-layer Nafion doped 20 μm, 0.02 mg/cm<sup>2</sup> titania loaded, PBT-TiO<sub>2</sub> composite films on TGP-H-030 substrates tested against 1.5 mg/cm<sup>2</sup> RuO<sub>2</sub> on TGP-H-030, with N117 membrane separator, in 0.5 mM H<sub>2</sub>SO<sub>4</sub> recirculated at 1 mL/s at 20°C. Lines are added for illustrative purposes. .... 183

Figure 93 - Energy harvested from 1 mg/cm<sup>2</sup> Nafion doped PBT-TiO<sub>2</sub> (filled symbols) composite films with differing film thickness and TiO<sub>2</sub> content compared to non-doped (open symbol) samples loaded on TGP-H-030 tested against 1.5 mg/cm<sup>2</sup> RuO<sub>2</sub> on TGP-H-030, with N117 membrane separator, in 0.5 mM H<sub>2</sub>SO<sub>4</sub> recirculated at 1 mL/s at 20°C. Lines are added for illustrative purposes. .... 186

Figure 94 - Energy harvested from single and bi-layer TGP-H-030 20 μm, 0.02 mg/cm<sup>2</sup> TiO<sub>2</sub> baseline PBT-TiO<sub>2</sub> films with selective Nafion doping. Films are tested against 1.5 mg/cm<sup>2</sup> RuO<sub>2</sub> on TGP-H-030, with N117 membrane separator, in 0.5 mM H<sub>2</sub>SO<sub>4</sub> recirculated at 1 mL/s at 20°C. Lines are added for illustrative purposes. .... 189

Figure 95 - Equilibrium H<sub>2</sub> yields for direct thermal splitting as a function of temperature and pressure. [12] Reprinted with permission from Progress in Energy and Combustion Science. .... 232

Figure 96 - Solar thermochemical water-splitting cycle using the redox pair Fe<sub>3</sub>O<sub>4</sub>/FeO. [111] Reprinted with permission from Solar Energy. .... 234

Figure 97 - Variation of $\Delta G^0$ for the thermal decomposition of metal oxide and reduced metal oxide pairs as a function of temperature at 1 bar. [12] Reprinted with permission from Progress in Energy and Combustion Science. ....	234
Figure 98 - Number of thermochemical publications by year [106] Reprinted with permission from the International Journal of Hydrogen Energy. ....	236
Figure 100 - Electromagnetic energy dW emitted per unit area and per second into a wavelength interval, $d\lambda$ =one angstrom, by a blackbody at various temperatures between 3,000 and 6,000 K as a function of wavelength. [114] Reprinted with permission from Encyclopedia Britannica Online. ....	238
Figure 101 - Snell's Law.....	240
Figure 102 - Example visible spectrum anti-reflective coating diagram. [118] Reprinted with permission from Optics Letters.....	241
Figure 103 - AM1.5G full absorption spectrum. [58] Reprinted with permission from the International Journal of Hydrogen Energy. ....	243
Figure 104 - Transmission spectrum variability in FTO substrates with a variation in Fluorine doping rate. [120] Reprinted with permission from the Journal of the Electrochemical Society.....	244
Figure 105 - Variation in optoelectronic properties of FTO films with a modulation in Fluorine doping. [121] Reprinted with permission from the Journal of Applied Physics....	245
Figure 106 - IR absorption spectrum of H <sub>2</sub> O [123] Reprinted with permission from the Journal of Molecular Structure. ....	246
Figure 107 - UV-Vis absorption of Nafion 117 membrane a) as received and b) hydrated. [124] Reprinted with permission from European Polymer Journal. ....	247

Figure 108 - IR absorption of Nafion 115 membrane (Line 2) [125] Reprinted with permission from the Journal of Membrane Science. ....	248
Figure 109 - Absorption spectra of undoped polybithiophene films with various thicknesses: a)150, b)136, c)128, d) 110, e) 98, f) 72, g) 62, h) 50, i) 17 nm. [127] Reprinted with permission from Synthetic Metals. ....	249
Figure 110 - UV-Vis Absorption spectrum of TiO <sub>2</sub> . [129] Reprinted with permission from Thin Solid Films. ....	251
Figure 111 - Diffuse reflectance spectra of pure anatase powder (ST-21), pure rutile powder (PT-101), a mixture of pure anatase and rutile powders (3:1), and P-25. [130] Reprinted with permission from the Journal of Catalysis.....	252
Figure 112 - Current-voltage response for of a FTO/polythiophene/Al device for dark conditions and under monochromatic illumination ( $\lambda = 620 \text{ nm}$ , $1 \text{ W/m}^2$ ) through the FTO. [137] Reprinted with permission from Solar Energy Materials and Solar Cells. ....	264
Figure 113 - Energy level diagram of Gratzel cell. [3] Reprinted with permission from Philosophical Transactions of the Royal Society A.....	267
Figure 114 - Energy diagram for an n-type semiconductor-metal ohmic junction a) before and b) after contact. [169] Reprinted with permission from Springer. ....	274
Figure 115 - Energy diagram for an n-type semiconductor-metal rectifying junction a) before and b) after contact. [169] Reprinted with permission from Springer. ....	275
Figure 116 - Energy diagram for band bending of an n-type semiconductor-metal rectifying junction under a) reverse bias and b) forward bias. [169] Reprinted with permission from Springer.....	275

Figure 117 - Energy diagram for a p-type semiconductor-metal rectifying junction a) before and b) after contact. [169] Reprinted with permission from Springer. ....	276
Figure 118 - Energy diagram for band bending of an p-type semiconductor-metal rectifying junction under a) no bias, b) reverse bias and c) forward bias. [169] Reprinted with permission from Springer. ....	276
Figure 119 - Energy diagram for a diode for a) unbiased, b) reverse bias, and c) forward bias operation. [169] Reprinted with permission from Springer. ....	277
Figure 120 - Band energy diagram for a Zener diode under a) no bias, b) reverse bias, c) small forward bias, d) medium forward bias, and e) normal forward bias. [169] Reprinted with permission from Springer. ....	278
Figure 121 - Band energy diagrams of TiO <sub>2</sub> /PT junction a) before forming junction, and when the Fermi levels lie b) above and c) below the valence band of the PT layer. [72] Reprinted with permission from the Japanese Journal of Applied Physics. ....	279
Figure 122 - Band energy diagram for different moieties of polythiophene [80] Reprinted with permission from the Journal of Physical Chemistry C. ....	280
Figure 123 - a) Theoretical and b) experimental validation of nitrogen doping shift in absorption spectra for TiO <sub>2</sub> . [172] Reprinted with permission from Science. ....	281
Figure 124 - Shift in Fermi level of composite semiconductor system with metal nanoparticle inclusion. [178] Reprinted with permission from the Journal of Physical Chemistry C. ....	283
Figure 125 - Schematic diagram correlating bulk crystal states with cluster states. [185] Reprinted with permission from Critical Reviews in Solid State and Material Sciences. ....	285
Figure 126 - Equivalent circuit of an impurity photovoltaic cell with impurities located a) along a single plane, b) distributed through the bulk (dotted line shows the connection	

required to convert to the 3-band case). [189] Reprinted with permission from Progress in Photovoltaics: Research and Applications.....	286
Figure 127 - Mechanism of the formation of the dipole at the ALq3/Mg interface; separate materials (left), chemical reaction and formation of gap states that pin the Fermi level (middle), and electron transfer from an organometallic complex to the metal to establish thermodynamic equilibrium. [195] Reprinted with permission from Polymer. ....	288
Figure 128 - The EQE spectra of devices from 90 wt.% 7nm by 60 nm CdSe nanorods in P3HT of various thicknesses a) before and b) after 120 <sup>0</sup> C heat treatment. [199] Reprinted with permission from Advanced Functional Materials.....	290
Figure 129 - Quantum efficiency increase with an increase in nanoparticle inclusion for a CdSe composite solid state solar device. [201] Reprinted with permission from Physical Review B, Condensed Matter. ....	291
Figure 130 - Schematic of proton transport mechanisms; the vehicle mechanism (top), the Grotthuss or hopping mechanism (bottom). [224] Reprinted with permission from Polymer. ....	296
Figure 131 - Electrical conductivity versus water content for various samples of Nafion. [225] Reprinted with permission from Macromolecules. ....	297
Figure 132 - SPEEK conductivity versus reciprocal temperature as compared to N117. [35] Reprinted with permission from the International Journal of Hydrogen Energy. ....	298
Figure 133 - Poisoning of Nafion membrane by increased concentration of contaminant ions. [227] Reprinted with permission from the Journal of Power Sources.....	299
Figure 134 - Variation in titania conduction band edge with a variation in pH. [233] Reprinted with permission from the International Journal of Hydrogen Energy. ....	302

Figure 135 - Oxidative degradation mechanism for polythiophene. [235] Reprinted with permission from the Journal of Electroanalytical Chemistry and Interfacial Electrochemistry. .... 303

Figure 136 - Solution polarization of semiconductor surfaces. [230] Reprinted with permission from Current. .... 304

Figure 137 - Band energy diagram of PBT on a) metal and b) TiO<sub>2</sub>. [240] Reprinted with permission from Electrochimica Acta. .... 305

Figure 138 - Variation in PEM electrolysis cell performance with platinum black cathode loading. [245] Reprinted with permission from the International Journal of Hydrogen Energy. .... 309

Figure 139 - Comparison of cathodic overpotential for hydrogen production using Co and Pt doped TiO<sub>2</sub> on MWCNT. [96] Reprinted with permission from the International Journal of Hydrogen Energy. .... 310

Figure 140 - Cyclic voltammogram of Gore-Tex/Poly-3,4-ethylenedioxythiophene(PEDOT)/Polyethylene-glycol(PEG) electrode (Blue line) versus Gore-Tex/Platinum electrode (Grey line) showing improved composite hydrogen catalysis. [97] Reprinted with permission from Advanced Materials. .... 311

Figure 141 - Change of cell voltage with electrolysis time for heat treated RuO<sub>2</sub> anodes at 1100 mAcm<sup>-2</sup> in a SPE cell. [247] Reprinted with permission from the Journal of Molecular Catalysis A: Chemical. .... 312

Figure 142 - Cell voltage of PEM electrolysis for a variation in Sn-filled Ir<sub>x</sub>Sn<sub>1-x</sub>O<sub>2</sub> anodes. [248] Reprinted with permission from Electrochimica Acta. .... 312

Figure 143 - Cell voltage of PEM electrolysis for a variation in Pt-Ir-RuO <sub>x</sub> anodes. [245] Reprinted with permission of the International Journal of Hydrogen Energy.....	313
Figure 144 - Conductivity as a function of oxygen pressure for a) 968 <sup>0</sup> C rutile, b) 820 <sup>0</sup> C rutile, c) 861 <sup>0</sup> C anatase, d) 755 <sup>0</sup> C rutile, e) 626 <sup>0</sup> C rutile. [262] Reprinted with permission of Physical Review.....	323
Figure 145 - Correlation between the number of monomer units and hole mobility in conductive polymers. [267] Reprinted with permission from the Journal of the American Chemical Society. ....	325
Figure 146 - Increase in hole transfer rate with an increase in temperature for conductive polymers. [267] Reprinted with permission from the Journal of the American Chemical Society.....	326
Figure 147 - Conductivity of sulfuric acid solutions. [270, 271] Reprinted with permission from the Journal of Chemical & Engineering Data, and Physics and Chemistry of Liquids. .....	326
Figure 148 – Complex EIS model for TiO <sub>2</sub> in a 0.1M NaOH system with Pt counter electrode. [275] Reprinted with permission of Electrochimica Acta.....	330
Figure 149 - The equivalent circuit of impedance for a polythiophene film on an electrode. [277] Reprinted with permission from the Journal of the Electrochemical Society. ....	331
Figure 150 – Equivalent circuit for PBT film deposited on a Pt electrode. [278] Reprinted with permission from Comptes Rendus Chimie. ....	331
Figure 151 - Nyquist plot for for PBT film deposited on a Pt electrode. [278] Reprinted with permission from Comptes Rendus Chimie. ....	332

Figure 152 – Equivalent circuit for layers of porous PBT polymer coated on solid PBT deposited on a TiO <sub>2</sub> electrode. [240] Reprinted with permission from Electrochimica Acta. .....	333
Figure 153 – Bode plot for layers of porous PBT polymer coated on solid PBT deposited on a TiO <sub>2</sub> electrode. [240] Reprinted with permission from Electrochimica Acta. ....	334
Figure 154 – Equivalent circuit for a TiO <sub>2</sub> -PT pressed composite electrode. [69] Reprinted with permission from Electrochimica Acta .....	334
Figure 155 – Bode plots for a TiO <sub>2</sub> -PT pressed composite electrode. [69] Reprinted with permission from Electrochimica Acta .....	335
Figure 156 – Nyquist plot for PEDOT on N117. [282] Reprinted with permission from the Journal of Solid State Electrochemistry.....	336
Figure 157 – Impedance analysis for porous PANi on ITO. [283] Reprinted with permission from the Journal of Physics: Conference Series. ....	337
Figure 158 – Representation of EIS measurements on porous electrodes. [284] Reprinted with permission from Electrochimica Acta. ....	337
Figure 159 – Equivalent circuit for a polymer deposited on a carbon fibre surface. [285] Reprinted with permission from Surface Engineering.....	338
Figure 160 - Double-layer capacitance for carbon fibres in 0.1M LiClO <sub>4</sub> /acetonitrile solution as a function of their heat-treatment temperature for a) unmodified CF's, b) oxidized CF's. [286] Reprinted with permission from Carbon. ....	339
Figure 161 - Scan rate dependence of MnO <sub>2</sub> /PPy composite electrode in 0.5 M Na <sub>2</sub> SO <sub>4</sub> at a) 5, b) 20, c)50 and d) 100 mVs <sup>-1</sup> . Figure on the right shows the calculated specific	

capacitance of MnO <sub>2</sub> /PPp, MnO <sub>2</sub> , and PPy electrodes in 0.5 M Na <sub>2</sub> SO <sub>4</sub> . [287] Reprinted with permission from Electrochimica Acta. ....	340
Figure 163 - Intercalation and capacitive energy storage in titania nanoparticles. [291] Reprinted with permission from ECS Transactions.....	342
Figure 164 - Peristaltic pump flowrate calibration curve. Line is added for illustrative purposes. ....	356
Figure 165 - Solar simulator calibration curve. Lines are added for illustrative purposes. ...	357
Figure 166 - Titanium Ion Calibration Curve for ICP-MS. Line is added for illustrative purposes. ....	358
Figure 167 - Cathode polarization for 1292 s baseline loadings of PBT-TiO <sub>2</sub> films coated on Nafion doped TGP-H-030. Filled symbols represent dark performance while open symbols represent 1 Sun performance. Lines are added for illustrative purposes. ....	382
Figure 168 - Cathode polarization for 3.33 μm film thickness, 0.09 mgcm <sup>-2</sup> TiO <sub>2</sub> loading of PBT-TiO <sub>2</sub> coated on TGP-H-030. Filled symbols represent dark performance while open symbols represent varied solar performance. Lines are added for illustrative purposes. ....	384

## List of Symbols and Abbreviations

Symbol	Definition	Units
A	Spectral absorption	
b	Beam path length	m
B	Magnetic induction	T
$c_j$	Concentration of absorptive compound in solution	mol/L
c	Speed of light	m/s
$C_j$	Concentration of ion j	mol/L
$D_c$	Diffusion coefficient of charge carriers	$m^2/s$
D	Electric displacement	$C/m^2$
$D_{Red}$	diffusion coefficient of protons	$m^2/s$
e	Elementary charge	$1.6 \times 10^{-19} C$
E	Electric field	V
$E^0$	Standard potential	V
$E_A$	Activation energy barrier to electron transfer	kJ/mol
$E_{bg}$	Bandgap energy	eV
$E_k$	Electron kinetic energy	eV
$E_{ref}$	Energy of the reference electrode versus the vacuum level	V
F	Faraday's constant	96486 C/mol
f	Frequency of incident photon	$s^{-1}$
h	Planck's constant	$6.63 \times 10^{-34} Js$
H	Magnetic field	T
I	Power of transmitted light	$W/m^2$
$I_0$	Power of incoming monochromatic light	$W/m^2$
$i_0$	Exchange current density	$A/cm^2$
$I_p$	Current at the maximum power point	A
J	Current density	$A/cm^2$
$J_{SC}$	Short circuit current	A
$J_0$	Reverse saturation current density	$A/cm^2$
k	Boltzmann constant	$1.38 \times 10^{-23} J/K$
L	Separation between sites	m
$m_0$	Free electron mass	
$m^*$	Effective mass	
$n_{Di}$	Diode ideality factor	

$n_r$	Index of refraction	
$n_{pop}$	Charge carrier population	$m^{-3}$
$n$	Number of moles of electrons transferred in the electrochemical reaction	
$P$	Bound polarization of charges in the dielectric	$C/m^2$
$q$	Charge	$C$
$\theta_1$	Angle of incidence	
$\theta_2$	Angle of refraction	
$R$	Universal gas constant	$8.31 J/molK$
$R^2$	Coefficient of determination	
$T$	Absolute temperature	$K$
$U_{redox}$	Redox potential vs NHE	$V$
$V$	Electronic coupling matrix element between two species	
$V_p$	Voltage at the maximum power point	$V$
$W$	Radiant energy	$W/m^2$
$z_j$	Charge number of ion $j$	
$\beta$	Electronic coupling term	
$\delta$	Length of the diffusion boundary layer	$m$
$\delta_d$	Average inter-particle distance	$m$
$\Delta_f G^0_{Ox}$	Gibbs free energy of formation of the oxidized species	$kJ/mol$
$\Delta_f G^0_{Red}$	Gibbs free energy of formation of the reduced species	$kJ/mol$
$\epsilon$	Dielectric permittivity	$F/m$
$\epsilon_v$	Volume fraction of the evolved gas	
$\epsilon_a$	Molar absorptivity	$L/molm$
$\epsilon_0$	Permittivity of free space	$8.854 \times 10^{-12} F/m$
$\kappa$	Electrolyte conductivity	$S/m$
$\kappa_0$	Conductivity of the electrolyte without any bubbles present	$S/m$
$\lambda_E$	Reorganization energy due to geometric relaxation accompanying charge transfer	$eV$
$\lambda$	Wavelength	$Nm$
$\lambda_j$	Ionic molar conductivity	$S/m$
$\mu_j$	Mobility of ion $j$	$m^2/sV$
$\mu$	Mobility of charge carrier	$m^2/sV$
$\mu_{eh}$	Chemical potential of the electron-hole pair	$eV$
$\rho$	Resistivity	$\Omega m$

$\rho_q$	Charge density	C/m <sup>2</sup>
$\sigma_{sb}$	Stefan-boltzmann constant	0.136 cal/m <sup>2</sup> s <sup>1</sup> K <sup>4</sup>
$\sigma$	Electrical conductivity	S/m
$\Phi$	Total irradiance	W/m <sup>2</sup>
$\varphi$	Work function of the material	eV
$\omega$	Angular frequency	rad/s
$\Omega$	Solid angle of absorbed solar radiation	W/m <sup>2</sup> sr
$\hbar$	Reduced Planck's constant	J s

Abbreviation	Definition
DFT	Density Functional Theory
DOS	Density of States
EQE	External Quantum Efficiency
FF	Fill Factor
FTO	Fluorine Doped Tin Oxide
ICP-MS	Inductively Coupled Plasma Mass Spectrophotography
IPCE	Incoming Photonic Conversion Efficiency
ITO	Indium Tin Oxide
MEH-PPV	Poly(2-methoxy-5-(2'-ethyl-hexyl-oxy)p-phenylenevinylene
MWCNT	Multiwalled Carbon Nanotube
P3HT	Poly(3-hexylthiophene)
P3MT	Poly(3-methylthiophene)
PAni	Polyaniline
PBT	Polybithiophene
PPy	Polypyrrole
PT	Polythiophene
PZC	Point of Zero Charge
SCLC	Space-Charge Limited Conduction
SEM	Scanning Electron Microscope

## Acknowledgements

*“If I have seen further it is by standing on the shoulders of giants”*

*-Sir Isaac Newton*

I would first like to thank my supervisor, Dr. David Wilkinson, for the opportunity and open direction in pursuing this project. His continuous advice and guidance provided insight in the electrochemical field, and his drive helped me to pursue this academic dream by leading as an example of accomplishment. I admire his dedication to the energy industry, and his thoughtfulness towards the natural environment and the future of our world.

My appreciation goes out to my committee members Dr. Dan Bizzotto, Dr. Madjid Mohseni, and Dr. Fariborz Taghipour for their time and assistance when needed. They were always available for discussing problems and helping my understanding of the natural sciences.

Many thanks go out to everyone at CHBE, but most especially my friends in my research group, sports teams, art club, and drinking team. Alf, Ross, Ryan, Jimmy, Mau, Omar, Jono, Iwan, thank you for all of your help, guidance and support in both academic as well as with personal experiences (continued sanity). I cherish your friendships and I look forward to seeing them grow. Big thanks also go out to my friends across the country for being there and never missing a beat. Scott, Geoff, Kev, Laufred, Sol, physically apart but close in my heart.

Special thanks are owed to my loving parents, whose have supported me throughout my years of education, both morally and financially. Thank you so much for being so wonderfully understanding and guiding me as I learn and grow. I would also like to thank my brothers, who continue to impress me with their successes, both personal and academic. I'm so very proud of them and I cherish their love and comradery.

I would like to recognize and thank NSERC Canada, the UBC University Graduate Fellowship, and the Pacific Century Graduate Scholarships for their financial support.

Finally I would like to thank my beautiful wife Tanis for her everlasting love and support. A chapter of my life with many lonesome nights and empty weekends while squirreled away in the lab are coming to an end, and I look forward to spending the next chapter by your side.

-{to my Family}-

## **Chapter 1: Introduction**

### **1.1 History of Energy Use**

Prehistoric man discovered fire. Ever since that momentous occasion, there has existed an ideology of utilizing the planet's natural resources for proliferation, sustenance, and personal comfort. The trouble being we seem to have, in large part, viewed this luxury as an infinite resource, especially in the modernized western world. World energy use has been increasing at approximately 8 Quadrillion BTU/year, as seen in Figure 1 [1], and is set to increase exponentially as the world population is ever increasing, along with modernization of the developing world. This modernization is driving the per capita consumption of energy skyward, as a large proportion of the developing nations hoping to emulate the 'American Dream' to achieve middle class status. Middle class luxuries, such as modern electric appliances, multiple household automobiles, and computers and other entertainment devices are an established way of life, but with increasing luxuries come increasing energy use. Decadent lifestyle seems to be punctuated by nonchalant waste.

Figure 1. World energy consumption, 1990-2035  
(quadrillion Btu)

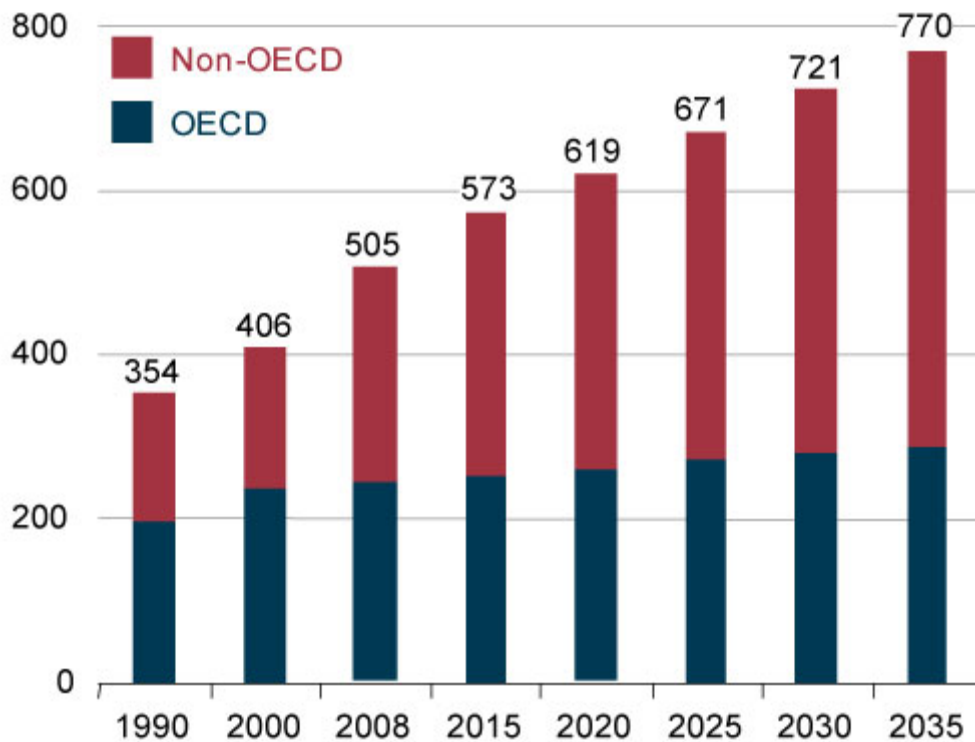


Figure 1 - World energy consumption projections organized by national participation in the Organization for Economic Cooperation and Development (OECD nations) [1]. Reprinted with permission from DOE/EIA.

Unfortunately with energy use from traditional and archaic technological sources there exist forms of pollution that have irreversibly altered the environment of our planetary ecosystem. Pollution from energy use, in the form of CO<sub>2</sub>, NO<sub>x</sub>, SO<sub>x</sub>, and other particulates from the burning of that first fire and from countless automobiles and industrial power technologies have contributed to environmental damage.

Our future does not have to be this way. It is everyone's responsibility on this planet to not only reduce the impact that they make, but to also ameliorate the damage that industrialization has caused thus far. Not all energy generation needs to produce effluent.

Emerging technology with the guise of realizing a clean future is under heavy investigation as the populous realizes the consequences of our actions. Alternative energy technologies exist that harness the natural powers of the world; wind turbines, tidal devices, and hydroelectric plants that spin generators to produce electricity, geothermal pumps and OTECS to utilize the geographical variation in temperature to produce energy, and solar powered devices to directly harness the heat and electromagnetic energy of the stars [2]. Care must be taken not to overlook the damage potential of these ‘clean’ technologies, with non-chemical environmental pollution in the form of noise and heat pollution coupled with potential ecosystem disturbance or destruction. Materials and methods of the final device production also weigh in on energy and toxic measures.

## **1.2 Solar Devices**

Solar energy, having a regular diurnal pattern has had much investment/attention in recent years (as detailed in Figure 2), and is perhaps the most attractive option for global rollout of an immediate green energy solution, and is expected to reach 300 GW in power generation by the year 2030 [3]. Solar radiation has a normal irradiance of only  $1 \text{ kW/m}^2$  in bright sunlight. If the average insolation over 24 h a day and 365 days per year is  $\sim 200 \text{ W/m}^2$ , the total annual terrestrial solar energy received is 6.31 GJ [4]. This amount would be typical of a location in the southwestern USA. If the conversion efficiency is  $\sim 10\%$ , then the converted energy would be 631 MJ or 175 kWh. If converted to a fuel, such as hydrogen, this is equivalent to 2660 moles of  $\text{H}_2$ , or  $\sim 66$  standard  $\text{m}^3$  of  $\text{H}_2$ . At  $\$0.25$  per  $\text{m}^3$ , the annual value of this hydrogen per  $\text{m}^2$  of collector area is only  $\$16.50$ . If a 10% return on investment is sought, the maximum capital cost is  $\$165$  per  $\text{m}^2$ . It is interesting that Biddle et al. [5] come to a very similar conclusion ( $\$162$  per  $\text{m}^2$ ) and note that only 36% of the capital cost is that

of the solar reactor and collector system. The other 64% of the overall cost is comprised of peripheral systems, including piping and reactor support, gas compression and control systems [4]. With the high balance of plant costs, any system built for solar generation of hydrogen from water will have to be very simple and fabricated from very cheap materials. Exotic and costly substances, such as Ru and Pt, are clearly too expensive for any practical system, unless used exceedingly sparingly. Bolton [4] also indicates that efficiency is the key to practical economic systems and that any system with an efficiency < 10% does not have much chance to succeed due to the above mentioned factors.

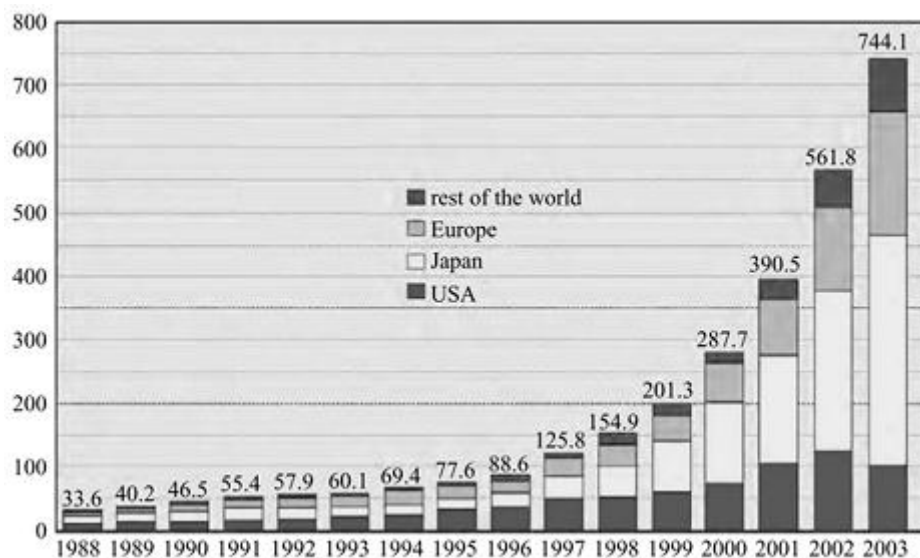


**Figure 2 - The increase in worldwide production of PV modules (MW) during the last 15 years. The market growth rate in the last decade has been over 30%. [4] Reprinted with permission from Philosophical Transactions of the Royal Society A.**

Commercial PV panels to date are typically made from purified silicon, but in principle the first solar devices were biological, in the form of chlorophyll based plants and algae. While it is possible to incorporate electrodes in a living system in which photosynthetic products are

electrochemically used as fuels, this approach is not very efficient ( $9\mu\text{W}/\text{cm}^2$  generated from 250W light source) due to complexities of *in vivo* electrochemical cell design [6]. The efficiency of other biological systems for solar energy capture can be higher, up to 5% efficient, through growth of specific strains of microscopic alga that produce bio-fuels from respiration [7]. Through the study of different biological systems, models have been constructed in order to mimic the natural chemical performance of cellular structure, using materials and devices based on inorganic sources which currently have more practical processability and ease of development [8]. Further still from biological systems, roll to roll processing of ultra-thin-film inorganic solar cells and improvements in multilayered devices continue to be investigated. The ongoing history of solar cell development is shown below in Figure 3 [9] and further reviewed by Ginley, Green and Collins [10].

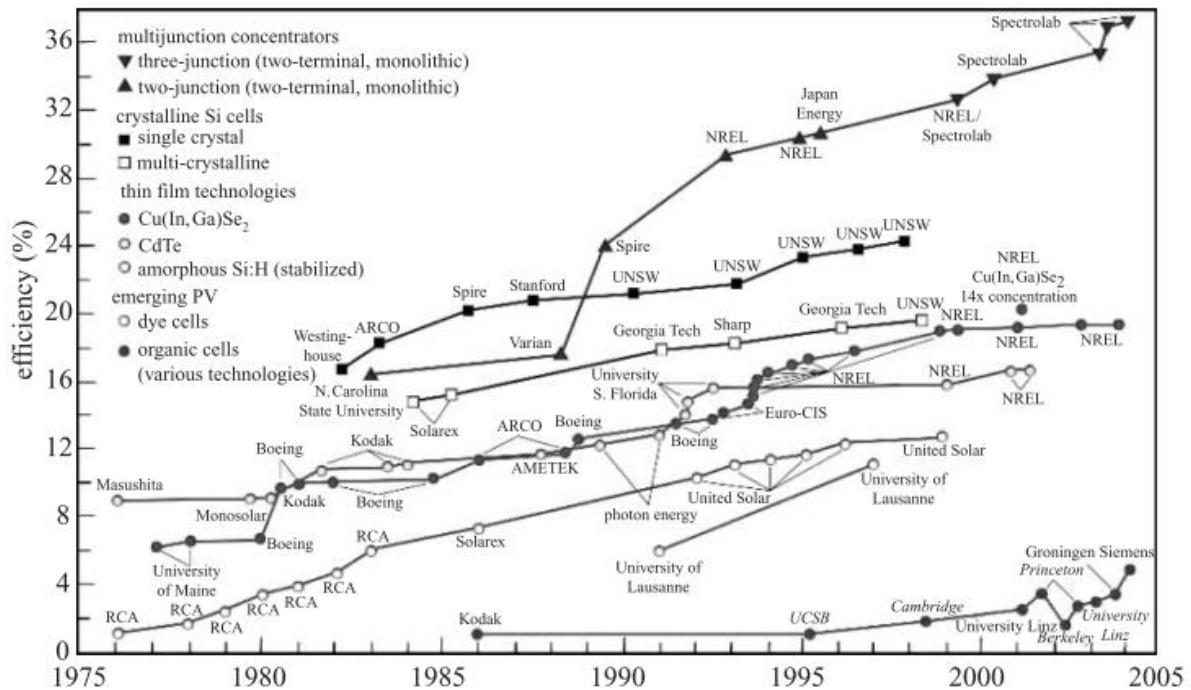


Figure 3 - A history of best cell efficiencies. [10] Reprinted with permission from MRS Bulletin.

Work has also been done to incorporate organic elements into non-biological devices, most notably with dye sensitized cells that use vegetable based dyes to improve the performance of inorganic semiconductor films [3], [11]. Solar energy conversion processes can also be generated by the use of focused solar power [12], rendering many of the above devices unstable or less efficient, but the focused power of concentrated systems also leads to different thermal energy capture strategies. Aside from biological processes, which will not be further addressed in this thesis, ultimately the breakdown of the types of solar devices can be attributed to their operation temperature, and if their electronic energy is used in a quantum mechanical electrical manner, or in a thermalized heat transfer manner.

### **1.2.1 Thermal Devices**

The variation in solar cell research has grown to encompass a large variety of approaches to transfer energy. Thermal heat cells have been developed to use low cost materials and store the energy as a high temperature heat sink, or to use the thermal gradient to drive steam turbines to generate electric potential. Usually these devices utilize mirrors to focus the light onto a central black body absorber, centered in a trough that circulates a high heat capacity transfer fluid, and operate in a temperature range of 200-600<sup>0</sup>C.

There also exists developing technology in the field of direct solar breakdown of water, or helio-thermal hydrolysis. In these devices the array of mirrors is much larger, and the focal point of the light beams is centered on a stable target high up on a tower.

More details regarding these technologies can be found in Appendix A.

A third type of photothermal process has been developed involving similarly intense solar heats, but in lieu of temperatures required to dissociate water they operate at temperatures

required to reduce metal oxide particles or operate other thermochemical cycles. More details regarding these technologies can be found in Appendix B.

All of these heliothermal systems take advantage of mostly the IR spectra, accounting for over 50% of the incoming photonic quanta (neglecting phononic-thermal generation). While achieving up to 47% energy conversion in a thermal application is attractive, the real power of the sun lies in the segregation and direct quantum mechanical capture of the incoming electromagnetic energy. In a recent review comparing the hybrid sulfuric acid Brayton cycle, the metal oxide cycle and electrolysis for hydrogen generation the results indicate that the hybrid cycle and electrolysis were most competitive, with the difference between them owing to the price of supplied electricity for electrolysis [13]. If the electricity were to be supplied by a solar array further examination of the costs would encompass a review of current quantum mechanical solar devices and their associated prices. The 1<sup>st</sup> direct bandgap silicon solar cells appeared in practical application over 50 years ago, developed by Bell Telephone Laboratories and formed from single crystal silicon. They were called 'solar batteries' and achieved an efficiency up to 11%. Cells developed previously to solar batteries by Bell labs were dubbed 'sun batteries' and had efficiencies an order of magnitude less [14]. Significant progress has been made since the inception of these devices, with current multicrystalline silicon based systems for the consumer ranging between 10 - 20% efficiency. Research has also been conducted into other thin film devices of Group II-V elements, layered to absorb a larger portion of the solar spectrum, with efficiencies greater than 30% [15]. A further investigation into the direction and history of quantum mechanical solar devices follows, to examine potential direction for further photoelectrochemical research.

### 1.2.2 Quantum Mechanical Devices

It has been estimated that an area 26,000 km<sup>2</sup> in size (the size of New Hampshire), covered with PV panels using current commercial technology, could produce enough energy to fulfill the current power needs of the United States [16]. Still, direct insolation has the limits of diurnal use, and can only achieve a max energy density of 0.1 W/cm<sup>2</sup> (1 kW/m<sup>2</sup>) without concentration. The solar emission and optical attenuation of terrestrial insolation is detailed in Appendix C.

In 1839 the photovoltaic effect was discovered by French physicist Edmond Becquerel, more than a century before the first crystalline silicon PV device developed in 1954 at Bell Laboratories [9]. Since then, quantum mechanical devices can be loosely broken down into three generations of research as shown in Figure 4: (I) Initial silicon based systems, (II) junctioned thin film technologies and amorphous silicon systems, and finally (III) advanced thin film multi-junctions and organic solar systems.

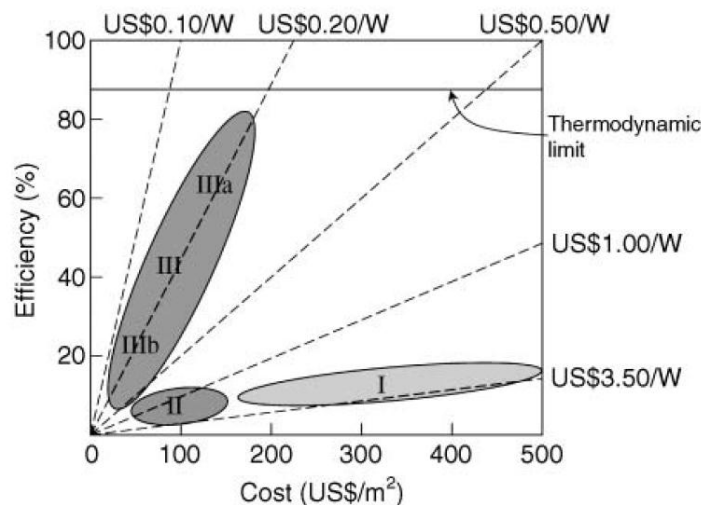


Figure 4 - Cost-efficiency analysis for photovoltaic technologies. [10] Reprinted with permission from MRS Bulletin.

These solar devices are reviewed in Appendices E,F, and G and highlight the advantages, disadvantages, and processability of each generation of devices.

After overviewing the technology development the following merits of composite organic solar devices were chosen for experimental analysis. The advantages of this technology include:

- Best performance from devices formed with polythiophene moieties
- Facile, high throughput, low temperature device fabrication routes
- Optimal energy capture performance in reduced semiconducting state
- Variation in charge transport can be determined by overlap of outer shell orbitals with adjacent materials
- Can be tailored with side groups to enhance electron transfer

The underlying principles regarding solar device design and operation can be found in Appendix H.

### **1.3 Green Hydrogen Generation**

With the increase in energy use, and standard diurnal solar cycling, energy storage is required. Electrical energy storage comes in two forms; storage of charge through segregation in a dielectric media, and storage of charge in chemical bonds separated from reactive components. Storage of charge through segregation in a dielectric media includes both capacitive and battery systems, and such charge storage will not be discussed here in detail. However, solar capacitive and battery devices of this type have been developed in a multitude of systems as seen by the works of Zach et al. [17], Huang et al. [18], Conway and Pell [19], Murakami et al.[20], Rousar et al. [21], Nomiyama et al.[22] and Zou [23].

Hydrogen has been evaluated as the premier energy carrier from solar fuel sources [24],

although currently 96% of hydrogen is derived from hydrocarbon sources [25]. It is through the use of electrolysis, that green hydrogen generation can be realized.

### **1.3.1 Standard Electrolysis**

Standard electrolysis can only be completely green if mated with clean energy technology for energy generation. Some places in the world have an abundance of renewable energy, so this is a viable option in those regions. These options are reviewed in Appendix I.

Commercial pressurized water electrolyzers, operate in concentrated (25-35 % w/w) alkaline solution at 70-90<sup>0</sup>C, and exhibit voltage efficiencies ranging from 65-75% at practical current densities of about 200 mA/cm<sup>2</sup> [26]. It has been demonstrated that a voltage efficiency close to 100% is attainable if the operating temperature of alkaline water electrolyzers is increased from 80<sup>0</sup>C to about 150<sup>0</sup>C [26]. Experimental work by Appleby and Crepy [27] and by Braun [28] has confirmed the hypothesis of LeRoy that an increase of the operating temperature to temperatures in the range of 120-150<sup>0</sup>C is advantageous for improving the energy efficiency, thus lowering hydrogen production costs [26]. The major drawback associated with increasing the operating temperature is again material related; finding stable materials for use as cell materials, such as separators, gaskets, sealants, and frames. Significant corrosion of cell construction materials in strong alkaline environments under the elevated temperatures is a concern, even if it appears most profitable to develop alkaline water electrolyzers which will operate at elevated temperatures.

The first proton exchange membrane (PEM) electrolyzers were created in 1966 by General Electric company [29]. The present costs of solid polymer electrolyte cells are considerably higher than those of conventional alkaline water electrolyzers. A large advantage of PEM systems is that PEM water electrolyzers are capable of operation at current densities of over

1 A/cm<sup>2</sup>, which is at least five times higher than the production rate of hydrogen in conventional alkaline water electrolyzers. An equivalent voltage input is required, with 1.9-2.0 V at 80<sup>0</sup>C and about 1.6 V at 150<sup>0</sup>C [26]. A recent result by Marshall et al. showed their best result was obtained with an Ir<sub>0.6</sub>Ru<sub>0.4</sub>O<sub>2</sub> anode and a 20 % w/w Pt/C cathode, with a cell voltage of 1.567 V at 1 A/cm<sup>2</sup> and 80<sup>0</sup>C when using Nafion 115 as the electrolyte membrane [30]. This represents a cell efficiency based on minimum chemical work of 76% ( $\epsilon_{\Delta G}$ ) and 94.4% based on the higher heating value ( $\epsilon_{\Delta H}$ ), equating to an energy consumption of 3.75kWhNm<sup>-3</sup> H<sub>2</sub> at 1 A/cm<sup>2</sup> [30]. The estimated capital cost of PEM water electrolyzers has been reduced from about \$260 to \$90 per square foot of active electrode area and continues to drop in price. At present, more than 90% of the capital cost of PEM water electrolyzers is for Nafion membranes, electrocatalysts, and current collectors [26]. Another advantage of PEM electrolysis is that operation at higher pressure is available. With increasing pressure, the size and number of ascending gas bubbles in the electrolyte decrease. Thus, ohmic losses in the solution are reduced. As a result of the reduction of ohmic losses, higher voltage efficiencies are obtained in pressure electrolyzers. Pressure electrolysis cells are also required to provide the capability to operate at a temperature in the range of 120-150<sup>0</sup>C, where a voltage efficiency (based on  $\Delta H$ ) close to 100% can be achieved at an operating current density of about 200mA/cm<sup>2</sup> [31]. Research is underway to improve the performance of the PEM membrane, as Nafion based membranes are limited in the 125-150<sup>0</sup>C range [32]. Alternatives to Nafion membranes have been evaluated for thermohydrolytic stability, with several families of polymers having been examined as viable candidates for replacement: polyether ketones, polyether sulfones, polybenzimidazoles, and polyphenyl quinoxalines. Representatives of each of the replacement polymer moieties were converted into ionomers

via sulfonation and fashioned into membranes for evaluation. In particular, the sulfonated polyetheretherketone (SPEEK) was examined by thermoconductimetric analysis and performance testing in an electrolytic system. Results were comparable to commercial perfluorocarbon sulfonated membranes, with the exception that they allowed for high temperature stability [32]. Sulfonated membrane based systems with a hydrated PEM are highly acidic, with a pH equivalent to that of a 10 % w/w H<sub>2</sub>SO<sub>4</sub> solution [26]. Further review of PEM manufacturers and membrane properties in PEM systems can be found in Appendix J.

LeRoy describes the approaches taken by the various groups as with respect to water electrolysis in terms of three electrochemical “windows”, related to the temperature [33]. The first of these is electrolysis operation at very high temperatures and pressures to reduce electrode overvoltages by improving the kinetics. The second alternative is to use intermediate electrolyte temperatures, in the range of 110-150<sup>0</sup>C with catalytic electrode activation to achieve acceptable overvoltages. At pressures above 25 atm, cell voltages in the range of 1.6-1.7V become possible. Operation at atmospheric pressure is possible for electrolyte temperatures below 90<sup>0</sup>C. This is the traditional operating regime of commercial water electrolyzers. It offers the most favorable conditions for the long life of electrocatalysts and of standard construction materials.

Thermodynamically it takes 237.2 kJ/mol at 298 K [4], or a 1.2291 V potential to split water into its constituent hydrogen and oxygen. This potential is further increased by system losses. LeRoy et al. [34] have performed a thorough examination of the thermodynamics of electrolytic systems, and the chemical phenomena and system losses will be further discussed below.

The transfer of energy into controlled ordered states is described by thermodynamics. The governance of regular energy exchange, or the spontaneity of a reaction is predicted by the free energy of the reaction, as explained by Gibbs:

$$\Delta G^0 = \sum_i \Delta_f G_{Red,i}^0 - \sum_j \Delta_f G_{Ox,j}^0 \quad \text{Eq. 1}$$

Where Gibbs free energy of formation of the oxidized ( $\Delta_f G_{Ox}^0$ ) and reduced species ( $\Delta_f G_{Red}^0$ ) define if a process will be spontaneous or not. At its basis, Gibbs describes how a summation of the 1<sup>st</sup> law of thermodynamics (enthalpy) and the 2<sup>nd</sup> law of thermodynamics (entropy) determines if a chemical reaction will proceed. It is noteworthy that while the enthalpy of states can be quantified at rest, the entropy is only defined when there is a chemical change, as it is a relative measure of disorder. Although reactions remain in their lowest energy conformation in a global system, there is a natural equilibrium constantly at play, and this equilibrium can be shifted with forces applied through applied chemical potential. Walter Nernst was the first to quantify the amount of chemical potential needed in terms of the flow of electrons with charge, q:

$$\Delta G^0 = -qE^0 = -nFE^0 \quad \text{Eq. 2}$$

Where n is the number of moles of electrons transferred in the electrochemical reaction, F is Faraday's constant (96486 C/mol) and  $E^0$  is the standard potential in V.

In terms of the reaction in question for our system, the thermodynamics of water splitting has been thoroughly detailed by LeRoy et al. [34] and has the following simple equation:



Graphically, LeRoy et al. [34] reported the following figure for hydrogen generation (Figure 5):

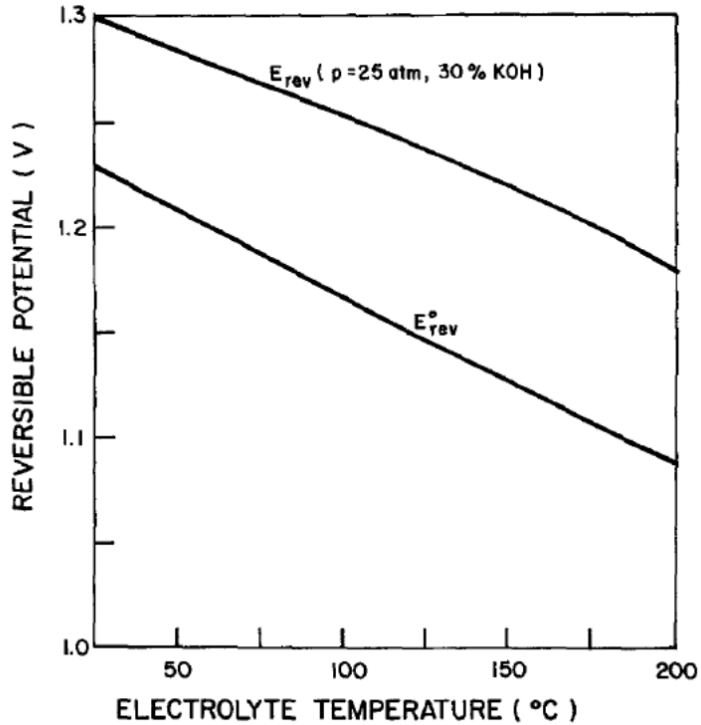


Figure 5 - Dependence of the reversible potential on electrolyte temperature, under standard conditions, and for 30wt,% KOH electrolyte at 25 atm pressure. [34] Reprinted with permission from the Journal of the Electrochemical Society.

As it can be seen, at STP it requires 1.2291 V to split water, and there is an advantage in increasing the temperature of the process, correctly displaying the isobaric partial derivative of the Gibbs free energy expression:

$$E_e = E^0 + \frac{\Delta S}{nF} (T - 298.15) \quad \text{Eq. 4}$$

Further discussion of the electrochemical basis for electron transfer and equilibrium in aqueous systems is described in Appendix K.

Of course this calculated potential is without accounting for any system losses. It has been shown that the columbic efficiency of PEM based electrolytic devices is above 90%,

decreasing only at higher current densities ( $> 100\text{mA}/\text{cm}^2$ ) [35]. In any electrochemical system, the losses can be divided into three ranges; Activation, Ohmic, and Mass Transfer. In each of these three system losses it is possible to breakdown typical benchmarks such as state of the art catalysts versus bare substrates. The overall cell voltage, expressed as a function of the various anodic and cathodic overpotentials, is shown below:

$$E_{Cell} = E_e + \eta_{s,a} - \eta_{s,c} + \eta_{iR} + \eta_{conc,a} - \eta_{conc,c} \quad \text{Eq. 5}$$

Examinations of losses governed by activation overpotential are detailed in Appendix L, losses governed by ohmic overpotential and conductivity related phenomena are detailed in Appendix M, and losses governed by mass transport detailed in Appendix N. After overviewing the losses from each aspect of electrochemical systems, the following areas were determined for potential experimental examination:

- (Activation) Replacement of platinum by a composite material on the cathode
  - Composites of conductive polymer-Pt have been used but degradation occurs
  - Composites of PEDOT-PSS have shown catalytic activity comparable to platinum for hydrogen production
- (Mass Transport) Utilization of carbon fibre material for dimensionally stable 3-D catalyst support
  - Inexpensive and easily manufacturable
  - Commonly used in existing PEM based devices mainly for mass transport
  - Membrane triple phase connectivity for enhanced device performance

### 1.3.2 Direct Solar Hydrogen Generation Systems

Fujishima and Honda 1<sup>st</sup> demonstrated direct (albeit chemically biased) photolysis of water on a single crystal as presented in their landmark paper in Nature in 1972 [36]. A schematic of their experimental setup is shown below in Figure 6:

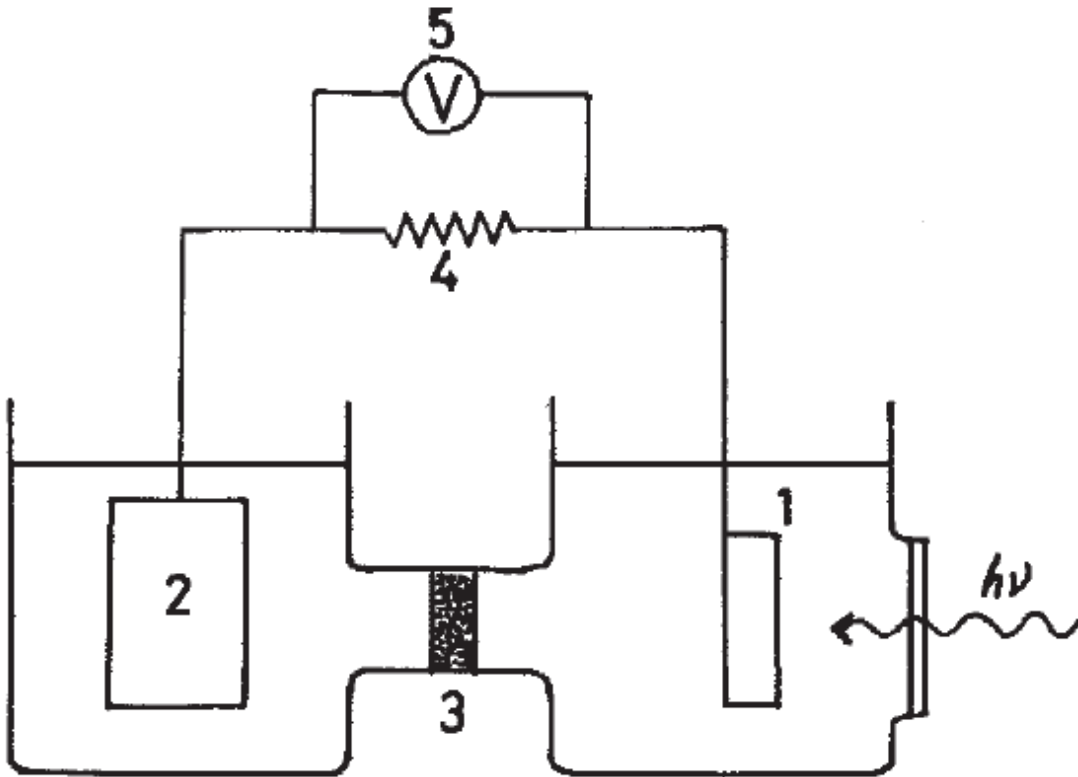


**Figure 6 - Fujishima and Honda electrochemical setup. Elements are as marked: (1)TiO<sub>2</sub> electrode, (2) Platinized platinum foil, (3) Glass frit, (4) External load, (5) Voltmeter. [36] Reprinted with permission from Nature.**

This experiment was repeated but with incorporating a membrane separator more recently by Selli et al. [37]. Since the report of the ability to spontaneously generate hydrogen gas from solar sources in 1972, the photoelectrochemical (PEC) field has started to receive much wider attention, due to its implications for solar energy conversion [38]. Smotkin et al.

connected several TiO<sub>2</sub> electrodes in series at a 45° angle and produced an array of bipolar electrodes for spontaneous photoelectrolysis, although using UV light and at efficiencies of ~0.06% [39]. Some attention to the parallel application of organic treatment with solar energy was demonstrated by some of the early work of Bard and co-workers at the University of Texas [40]. Frank and Bard were the first ones to propose that illuminated TiO<sub>2</sub> could be used for the purification of water via the photocatalytic decomposition of pollutants, but this aspect of photoelectrochemical device performance will not be discussed at this time [40]. Licht has identified that a tandem system of photoactive elements is needed to efficiently split water [41], although the potential needed to split water can be accomplished with one electrode while using an external bias voltage to overcome the system losses for a large bandgap semiconductor [42]. Overall, the emphasis on this technology continues to draw extensive attention, as illustrated in the chart below (Figure 7) by Fujishima et al. [38] tracking citations per year of the 1972 Nature paper:

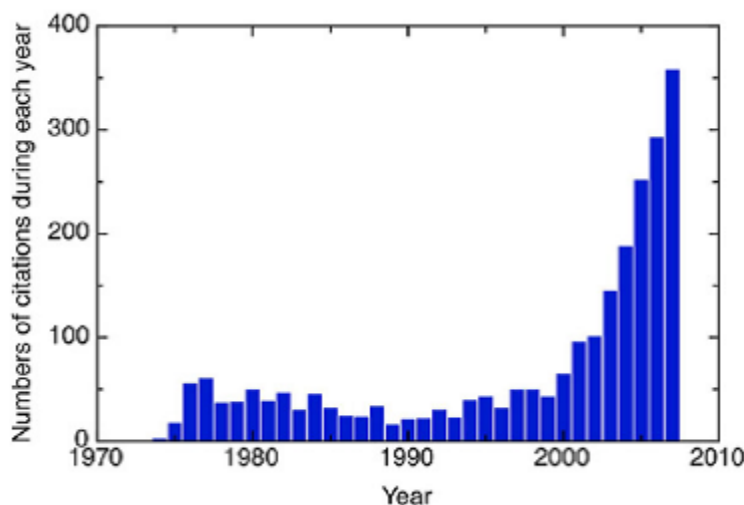


**Figure 7 - History of the number of citations of the landmark 1972 Fujishima and Honda paper. [38]**

**Reprinted with permission from Surface Science Reports.**

At present, the direct solar water splitting conversion efficiency for devices under conditions of AM1 (“one sun”) for one junction stable ceramic electrodes varies between to 1.5–1.9% for  $\text{TiO}_{2-x}$ , Rare Earth doped  $\text{TiO}_2$ ,  $\text{ZnO}_{1-x}$ , and Al doped ZnO, and approximately 1% for Ti or Ta doped  $\text{Fe}_2\text{O}_3$  and La doped  $\text{SrTiO}_3$  [43]. High hydrogen production efficiency was realized using monolithic tandem p-n-GaAs-p-n-GaInP<sub>2</sub>-Pt cells (12.4–16.5%) [44–46], multilayer GaAlAs–Si–CoS (or Pt) cells and multilayer Ga-AlAs–Si–RuO<sub>2</sub>-Pt cells (18.3%) [47], as well as triple-junction p-i-n a-Si (Pt) cells (7.8%) [46]. An example of such a multijunction device schematic is shown below in Figure 8 [47]:

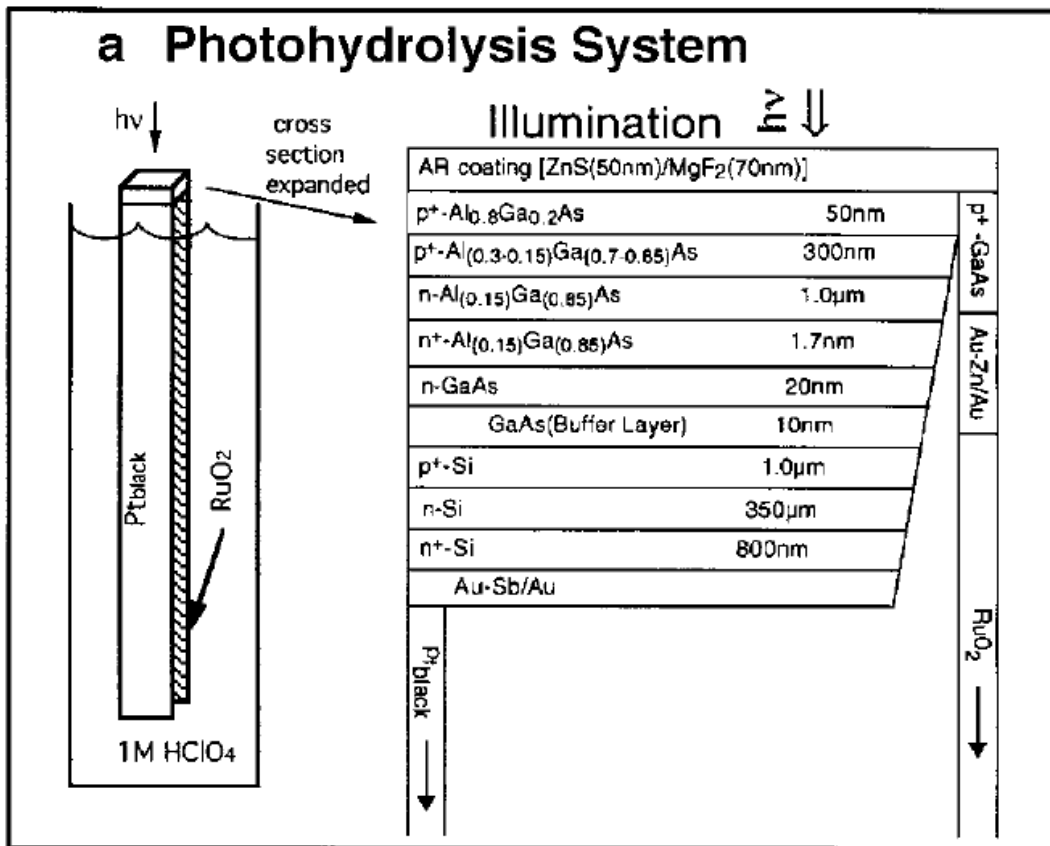
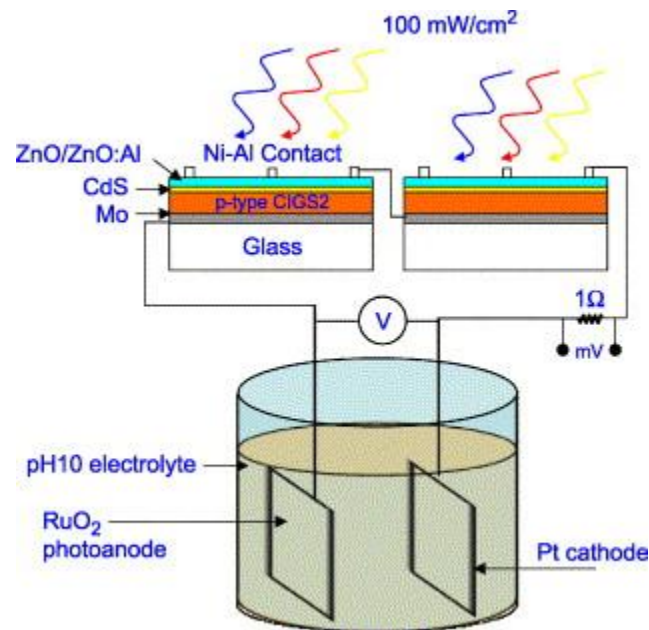


Figure 8 - Schematic of multilayer Ga-AlAs-Si-RuO<sub>2</sub>-Pt direct solar water splitting cell. [47] Reprinted with permission from the Journal of Physical Chemistry B.

Such outstanding results were realized with the use of rather expensive structures [43]. A cheaper alternative for a direct photoelectrochemical cell for water splitting was demonstrated using a multiple band gap combination of a  $\text{CuIn}_{1-x}\text{Ga}_x\text{S}_2$  (CIGS2) thin-film photovoltaic (PV) cell and a ruthenium oxide photoanodic catalyst and platinum cathode catalyst. The PEC setup consisting of two illuminated CIGS2 cells, a ruthenium oxide ( $\text{RuO}_2$ ) anode deposited on a titanium sheet for oxygen evolution and a platinum foil cathode for hydrogen evolution has been developed. This cell schematic is shown below, in Figure 9 [48]:



**Figure 9 - Two-cell PEC setup with two CIGS2 thin-film PV cells,  $\text{RuO}_2$  anode for oxygen evolution and platinum cathode for hydrogen evolution. [48] Reprinted with permission from Thin Solid Films.**

With this combination, a PEC efficiency of 4.29% has been achieved [48]. Membrane based direct systems from sulfite solutions have also been examined as a possible route to hydrogen production. A two-compartment photoelectrochemical cell configuration was proposed for photochemical generation of hydrogen from aqueous sulfide solutions. Optimized conditions

were found to be: 2.5 M sodium sulfide solution as the light-compartment electrolyte, 1 M sulfuric acid as the dark-compartment electrolyte, Nafion-coated Pt electrode further modified with electrodeposited Pt particles as hydrogen evolving cathode and Nafion membrane separating a CdS photoanode. Under these conditions, hydrogen can be photogenerated with quantum yield of 7–12% depending on the sunlight illumination power. Quantum yields tend to be higher for lower illumination intensities [49].

As mentioned above, considerable efficiencies for solar water splitting have been reported for the photovoltaic–photoelectrolytic device of Khaselev and Turner [44] and for the photovoltaic–electrolytic device of Licht [47]. The record efficiency of 18.3%, achieved on a AlGaAs/Si–RuO<sub>2</sub>/Pt system, is very encouraging although a few drawbacks still exist. Firstly, these systems are so expensive that the cost of the hydrogen fuel produced would not be competitive with other regenerative types of energy [38]. Electrochemical stability of photoelectrodes have been studied by Khaselev and Turner [45] by subjecting them to illuminated and dark environments in acidic and basic conditions. Corrosion was found in all cases with the best case (corrosion inhibition) being found for low cathodic potential conditions in an acid environment. The problem of photocorrosion of such systems has yet to be optimally solved, and exposed semiconductors should be modified to protect them from the solution [43]. Kelly and Gibson have found some solutions to the photocorrosion problem on triple-junction a-Si cells coated with indium-tin oxide, by designing a more durable ITO coating, protecting the ITO with fluorinated tin oxide (SnO<sub>2</sub>:F), and protecting the ITO with a glass layer. In particular, a PEC device made using the SnO<sub>2</sub>:F method had good solar to hydrogen efficiency (5–6%), and was still operative after one month [50]. Performance improvements in these cells can also be further realized through proper care

taken to match the thicker, top p-type layer of the photoelectrode with photoanodes of suitable thickness. The decrease in mismatch of electron-hole formation in the two-junction region appears to be the key for proper operation. [44]. It has also been shown that as a measure of overall modular design, an increase in reactor size can result in a significant decrease in performance of the photoelectrodes when scaled up [51] .

Other cells involving n-CdS, n-TiO<sub>2</sub>, or n-SrTiO<sub>3</sub>, as photoanodes have achieved efficiencies of ~10%. A group in Texas [39] coupled several photoelectrochemical cells, without wire connections, in a bipolar array and achieved water photolysis without any external bias. Overall, photoelectrochemical cells containing both n-type semiconductor photoanodes and p-type semiconductor photocathodes are the only device structure with the possibility of direct photolysis. Morisaki et al. [52] reported a hybrid photo-electrode, consisting of a combination PEC made of a TiO<sub>2</sub> layer, forming the photo-anode, and a Si photovoltaic cell underneath. This device diagram is shown in Figure 10:

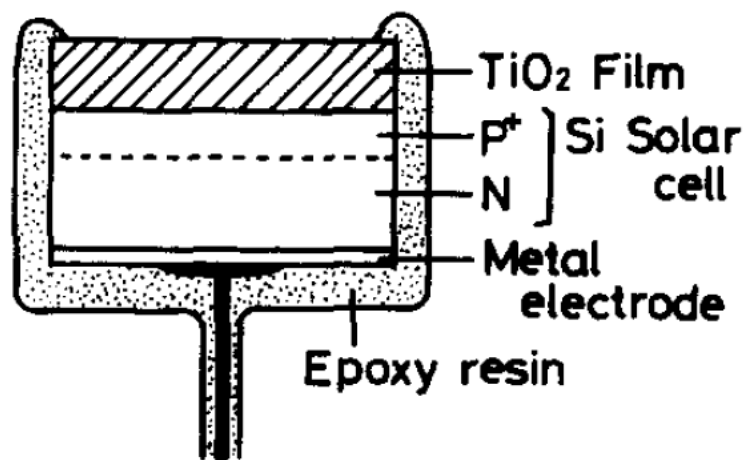


Figure 10 - Schematic of dual layer TiO<sub>2</sub> coated Si photoelectrochemical cell. [52] Reprinted with permission from Applied Physics Letters.

According to Morisaki et al., the anodic bias generated by the Si cell is  $\sim 0.7$  V. Since a PEC based solely on  $\text{TiO}_2$  exhibits  $\sim 0.8$  V, this gives a total output of  $\sim 1.5$  V, which is sufficient for the efficient performance of a hybrid photoelectrode [52]. Once again, sealing is a problem with these systems, because if it breaks down the underlying semiconductor is subject to photocorrosion. The use of Si as a p-type photocathode has also been investigated using cyclic voltammetry by Bookbinder et al. [53] and noted that when irradiated, ‘photocurrent is observed at electrode potentials that are significantly more positive than  $E^\circ(\text{H}_2\text{O}/\text{H}_2)$ , showing that light can be used to drive the uphill  $\text{H}_2$  evolution’. Experiments were conducted to improve the performance of the photocathode by the use of additional catalysis including platinum doping as well as a NN'-dialkyl-4,4'-bipyridinium redox reagent to facilitate charge transfer and reduce recombination. Although the coverage of the underlying silicon by the catalyst layers was free of pinholes, durability of the photocathodes was still a concern.

Alexander et al. [54] have briefly reviewed the principal n-type semiconductor materials which appear to be the most serious candidates for use as photoanodes for water cleavage. The choice of PEC system seems to be restricted to  $\text{WO}_3$ ,  $\alpha\text{-Fe}_2\text{O}_3$  and possibly  $\text{BiVO}_4$  photoanodes. The hematite phase of iron oxide has the smallest band gap, but tungsten oxide offers a significantly less positive photocurrent onset potential and better photoconversion efficiency as shown by the large IPCE values. A p- $\text{Fe}_2\text{O}_3$ /n- $\text{Fe}_2\text{O}_3$  tandem self-driven PEC was shown by Ingler and Khan [55] that showed solar-to-hydrogen photoconversion efficiency of 0.11%. The low efficiency was due to several factors, with the low net photocurrent density of the p/n- $\text{Fe}_2\text{O}_3$  PEC explained by the poor photoresponse of the p- $\text{Fe}_2\text{O}_3$  film compared to n- $\text{Fe}_2\text{O}_3$  films, low conductivity of iron(III) oxides, and the

consequent recombination of photogenerated electron hole pairs, generation of just enough photovoltage to have self-driven water splitting, and poor electrocatalytic activity of iron(III) oxides [55]. Using tungsten trioxide, initial multijunction prototypes formed by coating amorphous silicon tandem solar cells with sputter-deposited tungsten trioxide have been demonstrated operating at 0.6 % solar-to-hydrogen efficiency. Enhanced component films have been developed that will allow up to 2.2% solar to hydrogen conversion efficiency in similar devices. To achieve solar to hydrogen efficiencies over 10%, it is theorized that novel metal-oxide films need to be developed with bandgaps as low as 2.3 eV, and specialized solid-state junctions will need to be developed with correctly matched optical and electronic characteristics. Specific optimization pathways have been identified, including the development of reduced bandgap metal oxide films, such as doped  $\text{WO}_3$  or  $\text{TiO}_2$ , for higher-current photoelectrochemical junctions [56]. Further progress has been made on this device type including ternary and quaternary metal-oxide compounds, as well as non-oxide semiconductor materials, such as silicon-carbide and the copper-chalcopyrites [57]. Direct bandgaps in the copper-chalcopyrite alloy compositions result in strong absorption of solar irradiation, allow the bandgap to be engineered from 1.1 up to 2.5 eV, specifically with the inclusion of sulfur. Band edges can also be engineered to some extent by tailoring the alloy composition and excellent electronic transport properties can be maintained in chalcopyrite films, as demonstrated in the solar cells and in the PEC experiments. It has been shown that p-type chalcopyrite films can be operated with stability as photocathodes at high photocurrent levels [57]. Development of PEC systems has been substantially retarded by a lack of p-type semiconductor materials with a low band-gap and chemical stability. Again, it

is materials stability which continues to present one of the greatest challenges to PEC development [54].

Another way of improving solar absorption is the synthesis of new semiconductor phases made of solid solutions with wide band gap oxides (more than 3 eV) and rather small band gap oxides (corresponding to the maximum of the solar radiation spectrum, less than 1 eV).

The similarity of crystalline structures and electronic configurations of these oxides enables one to assume the existence of a wide range of solid solutions in the  $\text{TiO}_2\text{-MnO}_2$  system.

Investigations of solid solutions in the  $\text{TiO}_2\text{-MnO}_2$  system led to manufacturing semiconductor phases with a degree of dissolution of  $\text{MnO}_2$  up to 4 at.%. These photoelectrodes of the  $\text{TiO}_2\text{-MnO}_2$  systems are more sensitive in the visible range of the solar spectrum. However, the synthesis of solid solutions with large content of  $\text{MnO}_2$  was accompanied by the formation of non-photosensitive phases of  $\text{MnTiO}_3$  [43].

The manufacturing and investigations of more complicated, three and four-component compositions, is also very promising with the  $\text{Bi}_2\text{AlNbO}_7$  photocatalyst exhibiting the best photocatalytic activity with a rate of gas evolution  $\sim 710 \mu\text{mol/h}$  under UV irradiation [43].

Doping of indium-tantalum-oxide with nickel yields a series of photocatalysts,  $\text{In}_{1-x}\text{Ni}_x\text{TaO}_4$  ( $x = 0 - 0.2$ ), which induces direct splitting of water into stoichiometric amounts of oxygen and hydrogen under visible light irradiation with a quantum yield of about 0.66%, and with rates of  $\text{H}_2$  and  $\text{O}_2$  evolution that were about 16.6 and 8.3 mmol/h, respectively.

Investigation into more complex tailoring of surface gradients in materials is also being considered, as the formation of gradients may be used for the modification of the Schottky barrier in a controlled manner and can be used to adjust the mechanics of charge transfer to not require an external bias [58]. Efforts have also been underway to utilize quantum-dot

based devices, for tunable band gap tailoring through simple size quantization of decorated semiconductor monoliths [59] but care must be taken to ensure photostability of the nanoparticulate colloids.

Similar to the Gratzel system, another approach is through the work by Youngblood et al., showing the building blocks of artificial photosynthetic systems with wide band gap semiconductor particles, photosensitizer and electron relay molecules, and nanoparticle catalysts. Intercalated layered metal oxide semiconductors are junctioned with metal nanoparticles. These intercalation compounds, when sensitized with  $[\text{Ru}(\text{bpy})_3]^{2+}$  derivatives, catalyze the photoproduction of hydrogen from sacrificial electron donors ( $\text{EDTA}^{2-}$ ) or non-sacrificial donors (I). The devices are produced through exfoliation of layered metal oxide semiconductors, and multilayer electron donor-acceptor thin films or sensitized colloids in which individual nanosheets mediate light-driven electron transfer reactions are formed. When sensitizer molecules are “wired” to  $\text{IrO}_2 \cdot n\text{H}_2\text{O}$  nanoparticles, a dye-sensitized  $\text{TiO}_2$  electrode becomes the photoanode of a water-splitting photoelectrochemical cell. Although this system is an interesting proof-of-concept, the performance of these cells is still quite poor ( $\sim 1\%$  quantum yield) and the dye photodegrades rapidly. [60].

A complete summary of the history of monolithic semiconductor based photoelectrochemical water splitting is detailed by Bak et al. [58] and an abridged version of the analysis is also published [61]. An overview of particulate based water splitting systems and strategies can be found by Ni et al. [62]. A further update including more information on Tantalate based devices for visible light water splitting has been completed by Kudo [63] and in perhaps the most comprehensive analysis detailed by Kudo and Miseki [64].

### 1.3.3 Hybrid Solar-assisted Hydrogen Generation Systems

As previously discussed, many of the hydrogen generation schemes from a single photoreceptive element need a DC bias through conventional infrastructure until alternative sources can be established through gentrification of current energy distribution systems. The first demonstration of direct in situ hydrogen generation with  $\text{TiO}_2$  required additional bias [36]. As discussed previously, coupling with PV can facilitate this. This also leads to an advantage of being able to use these devices when solar activity is low.

A small amount of information has been published regarding field enhanced hydrogen generation. In  $\text{TiO}_2$  systems, a bias has been used to enhance the performance of photocatalytic degradation reactions as detailed by Vinodgopal et al. [65]. It was found that in a semiconductor particulate film the differing rates of electron or hole injection into the solution control the charge separation. If the photogenerated electrons can be driven away from the semiconductor particle (for example, with the application of an electric field), it should be possible to improve the efficiency of oxidation (i.e., reaction with holes) at the semiconductor electrolyte interface. It is evident from their measurements that the photocatalytic degradation occurs at a faster rate when the applied potential is maintained at +0.6 V [65], for  $\text{TiO}_2$ , a n-type material. This should also be true for the converse, a negative polarization on a p-type semiconductor on the cathode. Applied bias was also studied for the classic Fujishima and Honda system [36] by Shukla et al. [66]. It was shown that there was an increase in efficiency of 50% for the PV assisted PEC cell with a hydrogen production rate of  $37.4 \text{ l/h m}^2$ , while for the same PV (stand-alone) driven electrolysis the production rate is  $24.6 \text{ l/h m}^2$ . This was accomplished with a bias of only 0.3V. In the photoassisted

electrolysis mode, the operation of the cell showed oxygen gas evolving on the anode (i.e., n-TiO<sub>2</sub> surface) and hydrogen at the cathode (i.e., Pt electrode) in 1M NaOH.

Work has also been performed incorporating these device structures directly onto the membrane of PEM-PEC systems. Khare has loaded TiO<sub>2</sub> and conductive polymer into a membrane [67], and the incorporation of TiO<sub>2</sub> into the perfluoroionomer membrane was by treatment with TiCl<sub>4</sub> and methanol. Platinum was used as an electrocatalyst, and in order to make the system electronically as well as ionically conducting, the electrode was modified with polypyrrole (PPy). Previously, a similar system was reported for a hydrogen generating system consisting of TiO<sub>2</sub>, Pt and PPy [68] and this system was found to be more efficient than what was reported for a similar system without polypyrrole incorporation. However, these materials together had not been reported for the incorporation in a Nafion system. [67] The results of their tests have been very limited, with preliminary results showing 20 ml of H<sub>2</sub> gas evolution estimated over a 10 h duration. No follow up studies have been published to this work. Core-shell pressed electrodes of polythiophene and titania composites were formed and characterized [69]. The films were not tested for hydrogen production performance. Further studies on TiO<sub>2</sub> coated by poly (3-octylthiophene) (POT) molecules have been tested for solar photovoltaic performance, but not for hydrogen production [70]. The optical performance of the composite material is far superior to either POT or TiO<sub>2</sub> separately and shows excellent possibility for further solar device development.

#### **1.3.4 Analytical Measures**

Methods of comparison for performance of electrochemical systems and photovoltaic systems are outlined below to provide a comprehensive analysis of measured results.

#### 1.3.4.1 Solar Performance – $V_{oc}$ , $I_{sc}$ , Fill Factor, and Efficiency

The performance of solid state solar devices are commonly defined by four measurable variables: open circuit voltage ( $V_{oc}$ ), short circuit current ( $I_{sc}$ ), fill factor (FF), and external quantum efficiency (EQE, or IPCE - incoming photon conversion efficiency, if on a per wavelength basis).

The open circuit voltage is representative of the maximum potential the cell can generate when no current is being drawn through it.  $V_{oc}$  is controlled by the difference between the highest occupied molecular orbital (HOMO) of the donor and the lowest unoccupied molecular orbital (LUMO) of the acceptor in a junctioned device. As described above, the  $V_{oc}$  is only partly dependent on the difference in work functions of the electrodes [71], but they can create barriers which influence the performance of the device. In organic devices,  $V_{oc}$  varies linearly with the polymer oxidation potential, and the linear dependence of  $V_{oc}$  on the energy difference between the LUMO of the acceptor and the HOMO level of the donor. This result was explained by arguing that ohmic contacts are formed with the high anode work function and the low cathode work function electrodes, the quasi-Fermi levels of the electrodes will be pinned to the active materials. Variations in photovoltage are therefore dominated by variations in the photoactive materials only [71]. Also, the  $V_{oc}$  may be optimized through control of energy level alignment at the interface, and as previously discussed the matching of energy levels leads to the most efficient passage of energy. This may be accomplished by choice of an appropriate ionization potential of the polymer, or by modifying the position of the conduction band edge through surface treatments [69]. The  $V_{oc}$  of organic based devices increases logarithmically with light intensity in organic solar cells, reflecting the influence of photogenerated carrier density on the quasi-Fermi level position

(e.g.,  $V_{oc}$  for a P3HT based device). An example of this increase in  $V_{oc}$  with intensity is illustrated in Figure 11 [71]:

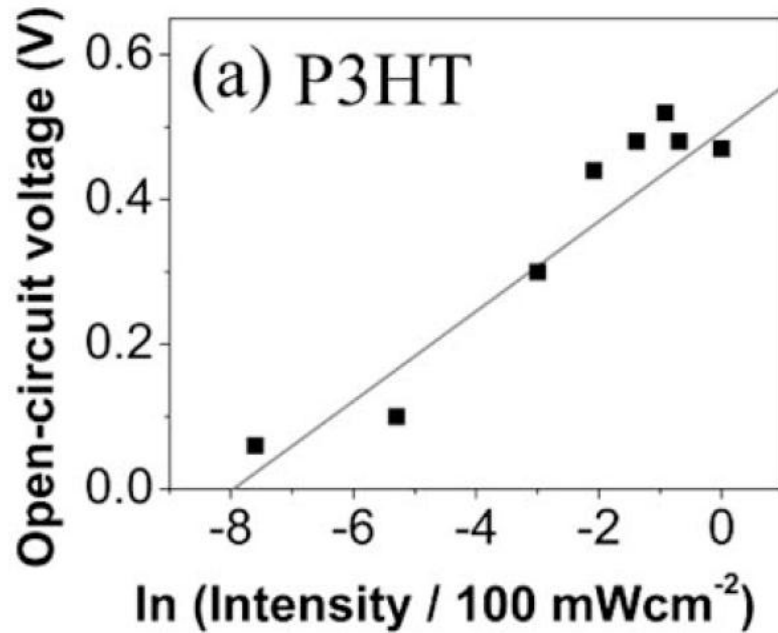


**Figure 11 - Variation in open-circuit voltage with increasing solar intensity. [71] Reprinted with permission from Applied Physics Letters.**

This dependence on light intensity can be described by the following diode ideality function:

$$V_{oc} = \frac{n_{DI}kT}{q} \ln\left(\frac{J_{sc}}{J_0} + 1\right) \quad \text{Eq. 6}$$

where  $n_{DI}$  is the diode ideality factor,  $k$  is the Boltzmann constant,  $T$  is the temperature,  $q$  is the elementary charge,  $J_{sc}$  is the short circuit current density and  $J_0$  is the reverse saturation current density [72]. For a  $\text{TiO}_2$ -PBT bilayer device  $n=2.4$  has been reported [72].

Leguenza et al. also have shown that there can be an increase in the  $V_{oc}$  with dipole alignment of the organic semiconductor layer [73]. This alignment of the dipoles allows a

distributed series and parallel charge distribution, with additive dipoles accounting for the very high  $V_{oc}$ .

For junctions between organic semiconductors and metal oxides,  $V_{oc}$  is expected to vary linearly with the difference between conduction band edge position of the metal oxide and the HOMO of the polymer, provided that the contacts are ohmic [71]. If the contacts between the electrodes are non-ohmic, or if the electrodes are insufficiently selective (donor or acceptor can exchange charges with both contacts) the  $V_{oc}$  may be reduced by shunting [71].

The short circuit current density is the limiting current that can be pulled through the solar device before the  $V_{oc}$  drops to zero due to energy losses. The short circuit current density depends on energy matching between phases, interfacial area, intimacy of surface contacts, and availability of mobile charge carriers [71].

The fill factor (FF) of a cell is a term created to illustrate how well the power absorbed decreases with increasing current. An ideal solar cell (FF = 1) would provide the same voltage indiscriminate of the power being drawn from it, up until its  $I_{sc}$ . In reality, there are many losses associated with devices, and the FF can be measured by [74]:

$$FF = \frac{V_p \cdot I_p}{V_{oc} \cdot I_{sc}} \quad \text{Eq. 7}$$

where the  $V_p$  and  $I_p$  correspond to the maximum power point of the device.

The solar conversion efficiency is the final comparative value, and essentially the best measure of a solar device's performance. The efficiency is given by [74]:

$$\eta = \frac{V_{oc} \cdot J_{sc} \cdot FF}{\Phi} \quad \text{Eq. 8}$$

where  $\Phi$  is the total irradiance. This same expression can be used to calculate the IPCE, as its integral is equivalent to the summed efficiencies.

### 1.3.4.2 Electrochemical Performance – The Tafel Equation

The electrochemical performance of an electrode can be further simplified into two performance indicators as defined by Julius Tafel [75]; the exchange current density, and the Tafel slope.

The total net current density is a sum of the anodic and cathodic reactions:

$$i = nFk^0 \left( C_{Ox}(0, t) \exp \frac{(1 - \alpha)F(E - E^0)}{RT} - C_{Red}(0, t) \exp \frac{-\alpha F(E - E^0)}{RT} \right) \quad \text{Eq. 9}$$

and the equilibrium potential of the reaction is:

$$E_e = E^0 - \frac{RT}{nF} \ln \left( \frac{C_{Ox}}{C_{Red}} \right) \quad \text{Eq. 10}$$

and the exchange current density,  $i_0$ :

$$i_0 = nFk^0 (C_{Ox})^{(1-\alpha)} (C_{Red})^\alpha \quad \text{Eq. 11}$$

The exchange current density represents a degree of general transition between equilibrium states. In our system on the cathode this is the equilibrium between hydrogen ion and hydrogen gas. The rate by which these two interchange is indicated by the exchange current density and is higher with higher catalytic activity. This expression allows the following relationship to be written for the overall 1<sup>st</sup> order chemical reaction:

$$\frac{i}{i_0} = \frac{C_{Ox}(0, t)}{C_{Ox}} \exp \frac{-\alpha F}{RT} \eta_c - \frac{C_{Red}(0, t)}{C_{Red}} \exp \frac{(1 - \alpha)F}{RT} \eta_a \quad \text{Eq. 12}$$

It is known as the Butler-Volmer Equation. A simplification of this equation, taking into account that the concentration of reactants is approximately equal to that of the bulk is given by the Butler-Erdey-Gruz-Volmer (BEV) equation:

$$\frac{i}{i_0} = \exp\left(\frac{-\alpha F}{RT} \eta_{s,c}\right) - \exp\left(\frac{(1-\alpha)F}{RT} \eta_{s,a}\right) \quad \text{Eq. 13}$$

where the total activation overpotential ( $\eta$ ) simplifies to the surface overpotential ( $\eta_s$ ).

Under a cathodic polarization, the anodic term in the BEV equation can be omitted, and the resultant reorganized Tafel equation is:

$$|\eta_s| = b \cdot \ln \left| \frac{i}{i_0} \right| \quad \text{Eq. 14}$$

where

$$b = -\frac{RT}{\alpha F} \quad \text{Eq. 15}$$

The term  $b$  is the Tafel slope, and is representative of losses that occur through the transition of electronic states. The Tafel slope applies to the kinetic loss area of the polarization curve, but before ohmic and mass transfer limitations occur. For good electrode performance, a high exchange current density and low Tafel slope are desirable, and can be used as performance indicators of an electrochemical reaction.

### 1.3.4.3 EIS

Electrochemical Impedance Spectroscopy analysis is used to describe system processes through the use of a time dependant frequency perturbation on the system. This analysis allows for the chemical reaction to be modeled as a complex electronic circuit, wherein the perturbation to the system can be used to deduce capacitive and resistive parameters using a known model. For our system using PBT-TiO<sub>2</sub> composites, several references have examined similar composites – but none for a distributed 3-D porous system with random particulate loading. For this reason a simplified contraction of this analytical procedure is

used, limiting the measurements to high frequency resistance. This resistance measurement is a measure of the overall cell resistance, and consists predominantly of the membrane ionic resistance, solution resistance, contact resistance and electronic resistances in a lumped term. Further EIS analytical procedures and literature results can be found in Appendix O, while analysis of double layer capacitance and pseudocapacitance are described in Appendix P.

#### **1.3.4.4 Benchmark Devices**

Specific examples of polythiophene composite materials have been used in three ways; for photocatalytic purposes (e.g., light induced dye degradation), for solid-state charge generation (photovoltaic devices), and for photoelectrochemical uses. These uses have been broken down and are illustrated in the Figure 12, alongside a Venn diagram analysis of the composite matrix used. The left division in the Venn diagram represents the type of conductive polymer, while the right represents the type of nanoparticulate inclusion or solid state junction. The union of the two represents devices or structures composed of polythiophene moieties with titania. Specific effects of the different constituent devices are highlighted in the subsequent tables, annotated with benchmark performance points and designated to the appropriate benchmark subdivision. The divisions in the figure are numbered and the numbered sections are referred to in the associated tables in the appendices.

For solid state photovoltaic devices, the table corresponding to composite polymer devices is shown in Appendix Q.

For photochemical processes, the table corresponding to composite polymer devices is shown in Appendix R.

Finally, for photoelectrochemical systems, the table corresponding to composite polymer devices is shown in Appendix S.

For photoelectrochemical devices, organics polymers have been used as the linkage for organic-based (thiol-derivatized phthalocyanines) catalytic production of hydrogen from water before [76], but not in conjunction with solar stimulation, although alluded to. In terms of semiconductor performance, as the polymeric elements are p-type materials, they are best employed as the cathodic electrode of a photoelectric chemical device for hydrogen generation.



but also due to reduced current generated in the active layer. Through modelling, it was also found that the power loss due to the distributed resistance is larger than the power loss from an equivalent lumped element resistance [77]. This is due to a distribution in the electric field across the device structure. This could be a difficulty in discerning the model for a distributed photovoltaic or photoelectrochemical device.

#### **1.4 Research Objectives and Thesis Layout**

Investigation of an idealized goal for solar technologies not only lies in their power conversion efficiencies, but also in their costs as well as ease of fabrication. The main focus of this investigation is thin film development of composite materials for use in solar assisted electrolysis. As identified in the literature this is usually accomplished at the photoanode due to the propensity of titania based devices to oxidize water. What has received almost no investigation, however, is light assisted electrolysis using a photocathodic element.

Investigation into photocathodic thin film polymer composite with nanoparticle inclusion is the first research objective of this dissertation. There are several potential advantages as previously illustrated for using a composite conducting polymer as the photoactive component on the cathode side, including resistance to oxidative degradation and potential inherent electrocatalytic improvement. The cathodic catalytic activity of organic composite films is a prospect for replacement of precious metal catalysts currently in use by electrolytic devices.

The investigation of utilizing composites of conductive polymer with titania inclusions is investigated in Chapter 3, and the results show that these materials can indeed be employed to reduce the amount of energy needed to drive the water splitting reaction on the cathode side. Incorporation of tunable nanoparticulate inclusions would also be an asset in order to

further tailor the films at a future time. This tailoring of the nanoparticle inclusion is briefly discussed in the recommendations.

The second research objective for investigation logically follows: how the structure of the catalytic layers affects both solar assisted and dark electrolysis. Parametric evaluation of both titania content and film thickness are evaluated on the basis of electrochemical and photonic benchmarks, and the results are presented in Chapter 4. It is found that an augmentation of photonic response with varied nanoparticulate inclusion can be described by modified surface energetics, charge separation and transfer, and charge trapping. The films are also influenced by film morphology. Films were investigated on the basis of 3-D or 2-D architecture in order to determine the mobility limitations (ionic and electronic) of the deposited films. Electrochemical performance without photonic stimulation is also affected by the composite film inclusions, and it is shown that there is a strong correlation suggesting catalytic enhancement can be controlled with simple augmentation of film loading procedures. This could prove to be a facile and effective way of tailoring a layered approach for photoelectrochemical device development.

The third and final research chapter, Chapter 5, stems from the discoveries made in the study of Chapter 4. Due to limitations in solution conductivity it was determined that ionic conductivity was limiting the performance of the photoactive device. The underlying architecture of the substrate was modified using a nafion ionomer to provide linkage between photoactive sites and the membrane to satisfy triple phase requirements. Several morphologies of Nafion coated on carbon substrates have been investigated to increase the linkage between ionic and electronic states in order to improve device performance.

A summary and recommended of future studies are presented in Chapter 6. Many interesting developments have been gleaned from this study, and time did not allow for a complete investigation of every phenomenon, but there exists potential for further significant improvements in device design. These design elements will be highlighted from the results, as well as from results reported in the theory section of this dissertation as shown for other solid state devices.

All of the apparatus and experimental methodology is explained in Chapter 2, and includes all procedural elements in order to replicate the conducted experiments. This includes the methodology for film creation and characterization techniques. Other characterization techniques attempted will be noted and the reasons why those results were not presented will be mentioned in an attempt to dissuade further researchers in this area from making the same time-consuming errors.

## Chapter 2: Materials and Methods

The materials and methods used in the dissertation investigation are described in this chapter.

The breakdown of the chapter starts with a description of the sourcing of chemicals and electrochemical build-up of the films. Characterization techniques and the equipment used follows, and highlights and difficulties or variability in the measurements. Finally, the photoelectrochemical reactor and system are described. Electrochemical techniques are presented in this subsection and the procedures used to determine our set hypothesis variables are described.

### 2.1 Film Loading Procedures

The PBT and PBT-TiO<sub>2</sub> films were prepared from a 0.5 M LiClO<sub>4</sub>, 0.1M 2-2' bithiophene solution in propylene carbonate replicating the work of Leguenza et al. [73]. All chemicals were obtained from Alfa Aesar and used without further purification. The purity of the 2-2' bithiophene was 98% monomer, while the purity of the LiClO<sub>4</sub> and propylene carbonate were 99%. Typically, the solutions were prepared batch-wise in a 100 mL volumetric flask, and stirred overnight to ensure complete dissolution of the lithium perchlorate. This batch wise preparation was done as aging of the loading sols due to contact with air was suspected due to a gradual color change from a bluish-grey to an orange-tea colored tint. Recycling of such a sol in an industrial application would constitute a large improvement in the loading process, and will be suggested in the Recommendations section of this dissertation.

For baseline sols with nanoparticle suspension, the TiO<sub>2</sub> content in the loading bath was set to 0.1% w/w, which is similar to the 0.05% w/w doses used by Ilieva et al. [78]. The TiO<sub>2</sub> was a standard P25 variant obtained from Degussa Huls AG that is widely used in industry and has a crystal structure of 75% anatase and 25% rutile mixed phase morphology and is

further discussed in Appendices D and H.6. The films were loaded in a Teflon loading cell after sonicating the mixture for 90 minutes.

### **2.1.1 Loading Cell Configuration**

Two iterations of loading cells were used to produce the electrodeposited films. The change in architecture of the loading cell was done to allow for flexibility in different sizes of exposed surface area to be loaded, different substrate architecture (TCO-glass, electrospun carbon, perforated stainless steel tabs), as well as to prevent leaking which was a problem in the first generation loading cell. The first generation plating cell, shown in Figure 13, was composed of platinum contacts for electronic contact with the substrate to be loaded, a titanium frame wrapped in platinum mesh as a counter electrode, and a 3M NaCl Ag/AgCl reference electrode, with the system controlled by a Solartron 1470E model multistat. The cell was machined from 3 solid blocks of Teflon, and silicone gaskets were used to seal the cell together in a “club sandwich” form. Compression of the cell was accomplished by a series of six 316L stainless steel bolts with wingnuts tightened in a cross pattern to reduce uneven pressure on the cell.

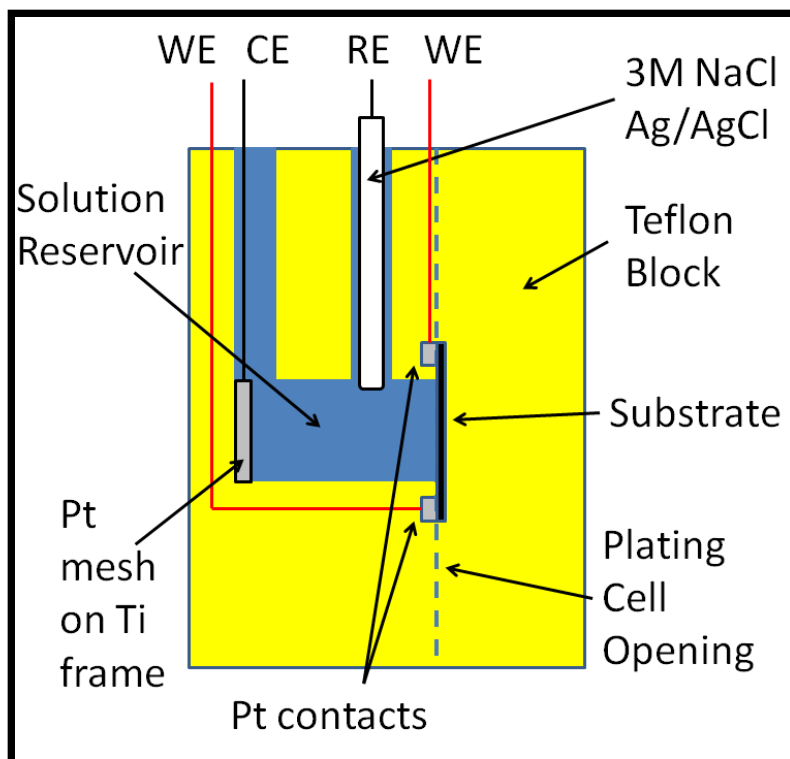


**Figure 13 - Schematic of first generation plating cell**

The second generation plating cell, shown in Figure 14, was composed of titanium frames for electronic contact with the substrate to be loaded, perforated titanium plate counter electrodes, and a 3M NaCl Ag/AgCl reference electrode. The system was once again controlled by a Solartron 1470E model multistat. In this variation of the loading cell, the substrates were sandwiched between two window-frame shaped titanium contacts to allow for unidirectional current distribution. The titanium contacts were sandwiched in a Teflon cartridge which was held together by Teflon screws tapped into the cartridge. The Teflon cartridge controlled the amount of substrate that is exposed to the loading solution, and several shapes (2 cm<sup>2</sup> circle, 1" square) were produced to allow for a variety of loading areas. A Teflon cartridge was also manufactured with a pocket in one half of the cell in order to hold and coat ITO slides, necessary for samples subject to several of the characterization

techniques. The counter electrodes, mesh-ported titanium plates, could be placed on either side of the cathode cartridge so that there could be a variation in the direction of loading if needed. For the experiments presented in this dissertation, bi-directional loading was not conducted, but will be recommended in order to vary the composition in further studies. This entire electrode assembly was then submerged in a double walled glass reactor which was filled with the loading sol. This “cartridge in pot” design allowed for an ease in substrate changeover between loadings, as the solution could be re-used for subsequent loadings after cleaning the electrodes. This modification accounted for a large savings in cost and environmental impact, as it allowed for more samples to be made per loading solution batch. As noted before, if an industrial scale-up is needed the re-use of this loading sol is essential.

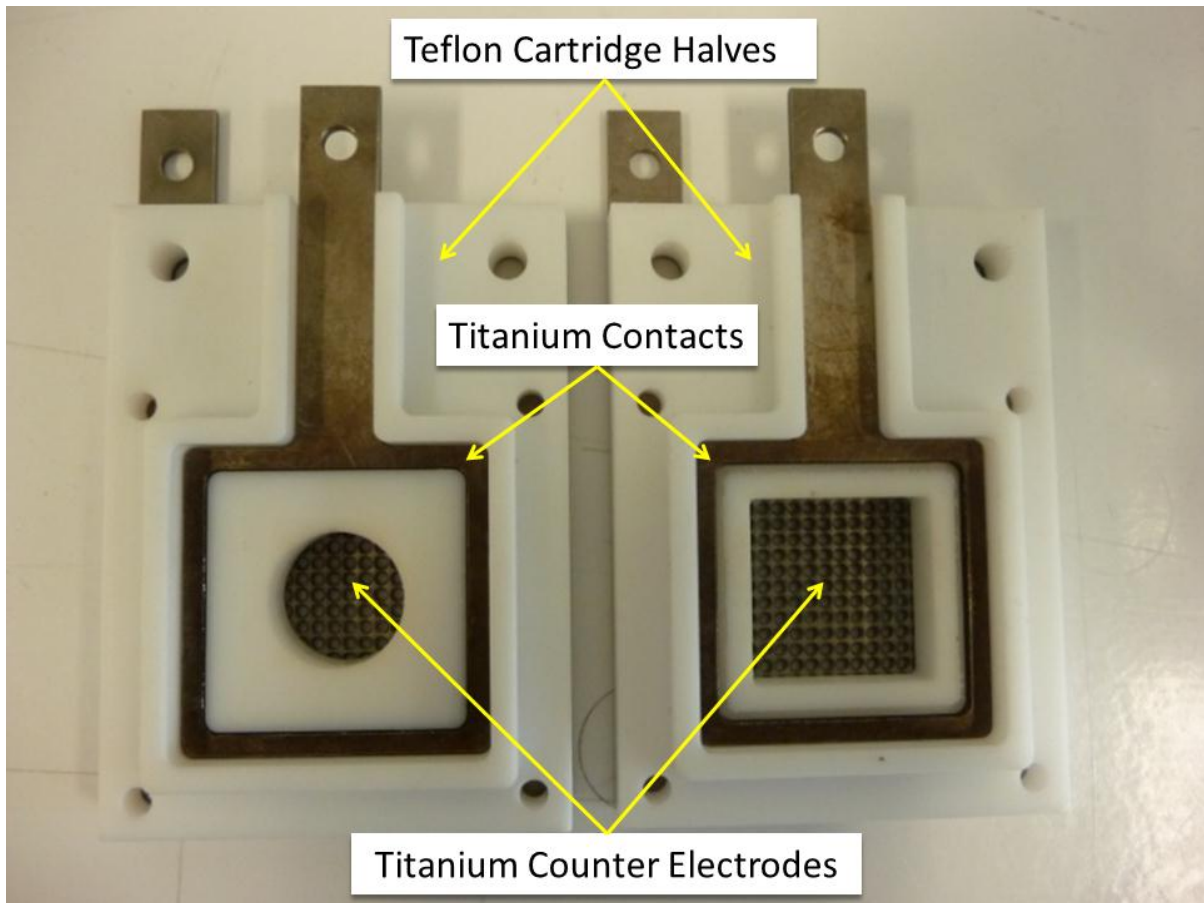


**Figure 14 - Photograph of second generation plating cell cartridge illustrating plating shape control**

Prior to use, the plating cell which was cleaned using isopropyl alcohol was thoroughly dried at 60°C and then rinsed with the loading solution. Films were deposited on the substrates at a current density of 0.5 mAcm<sup>-2</sup>, once again replicating the work of Leguenza et al. [73]. Care was taken to ensure the current density is accurately applied when samples of various active surface areas are loaded subsequently in one loading batch using different exposed areas, as the Solartron 1470E model multistat controls an absolute current and must be scaled to area. Samples were also loaded onto Kapton masked ITO on PET from Solaronix SA (Aubonne, Switzerland). Electrodes were composed from 1" squared PET-ITO, with a piece of aluminum foil connected to the ITO and similarly shielded from solution by Kapton film. A photograph of one of the prepared PET-ITO samples is shown below in Figure 15:

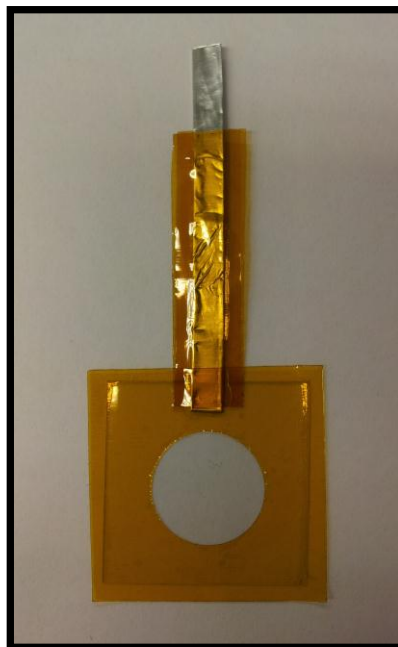


**Figure 15 - Photograph of Kapton masked PET-ITO film with 2 cm<sup>2</sup> exposed active area and aluminum foil contact**

These electrodes were used in place of the titanium frames but loaded in an identical manner to the other samples. A similar masking was used to load the 316SS electrodes used in

Chapter 4. A photograph of one of the bare electrodes is shown in Figure 16.a and a composite loaded substrate with masking removed shown in Figure 16.b.

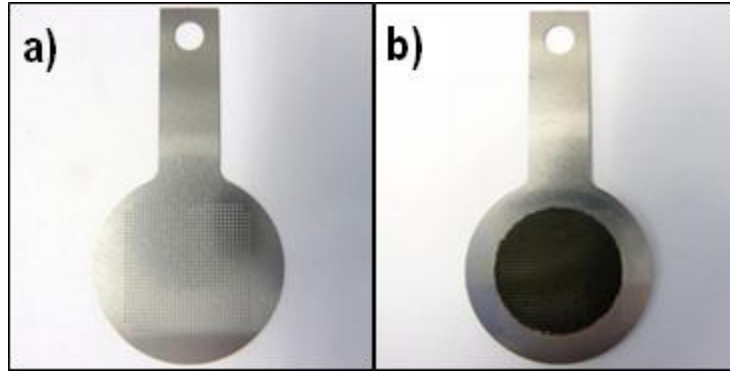


**Figure 16 - a) Bare 316SS electrode, b) Composite coated 316SS electrode**

### **2.1.2 Electropolymerization Treatment**

The electropolymerization of PBT is outlined in the diagram below, as reported by Schopf and Koßmehl (Figure 17) [79]:

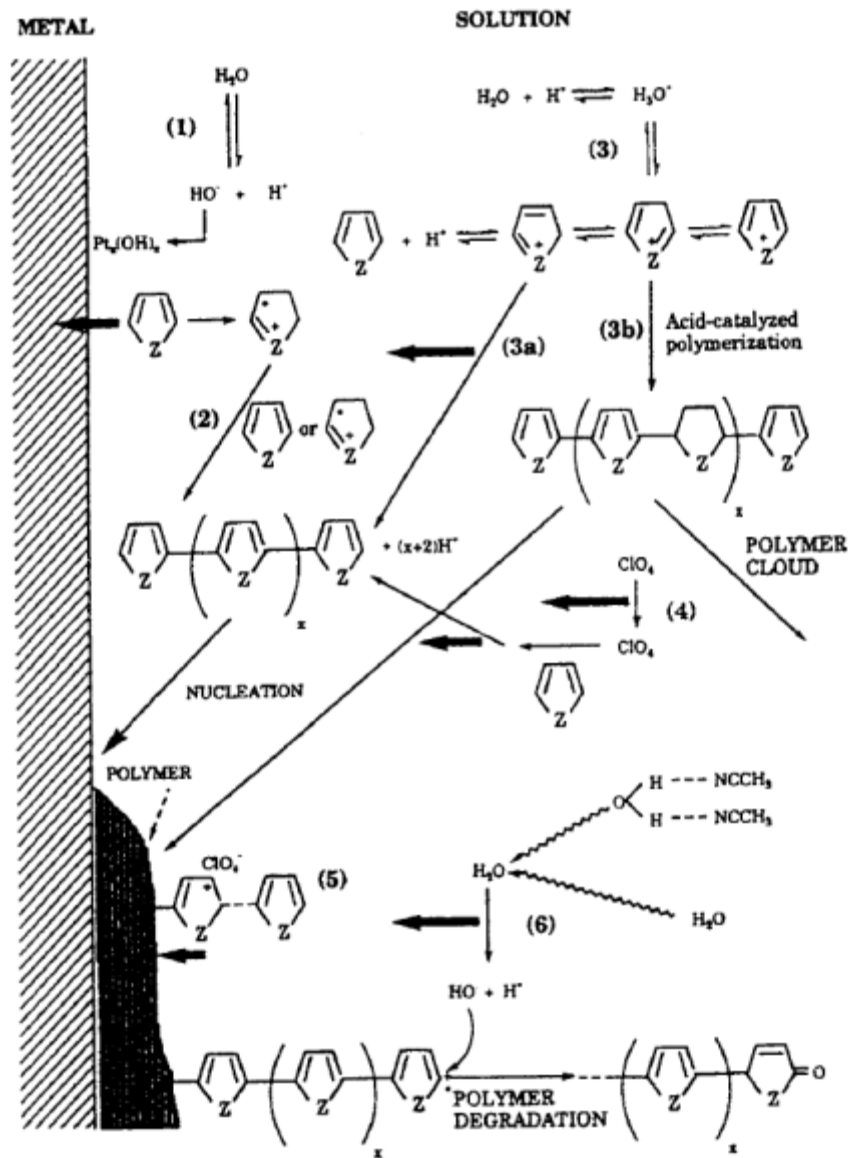
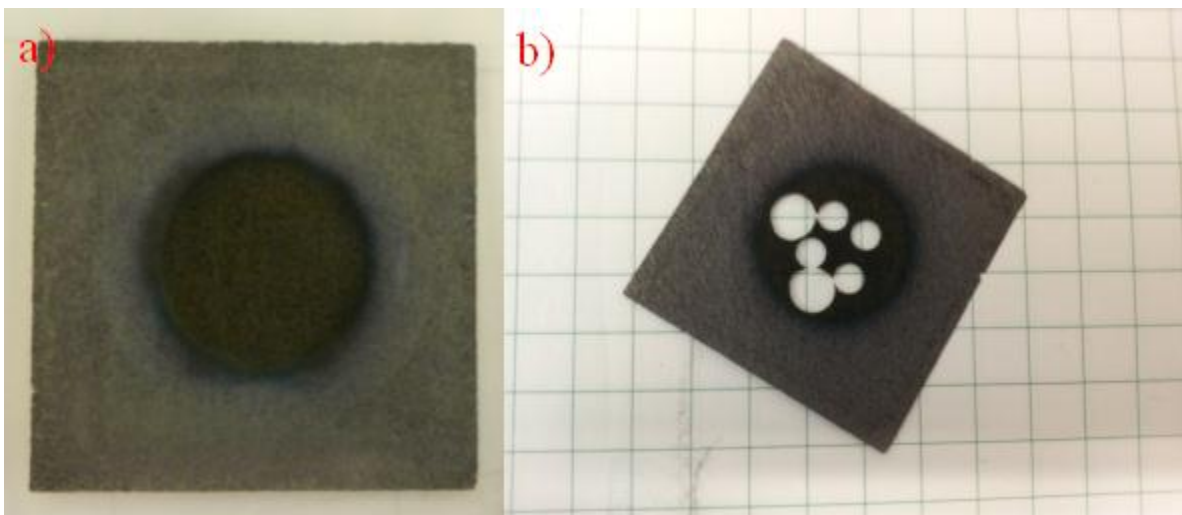


Figure 17 - Partial model of interfacial reactions for polythiophene electrogeneration on a platinum electrode using  $\text{LiClO}_4$  as electrolyte salt. [76] Reprinted with permission from Springer.

Variation in temperature and loading rate have a large effect on final polymer grain sizes, but in order to minimize the number of variables used in this study variation of these two aspects was not done and should be reserved for future work. The loading rate was fixed at 0.5  $\text{mA/cm}^2$  and the temperature was ambient ( $20^\circ\text{C}$ ).

The substrates with deposited films were removed from the plating cell and soaked in propylene carbonate for 24 hours to remove any ions and excess monomer loaded during the film polymerization. The soaked films were then dried at 60<sup>0</sup>C for 1 hour under a negative pressure of -25 in. Hg to evaporate off the propylene carbonate. For simplicity, no investigation in the effects of variation of the drying conditions (temperature or pressure) were conducted, but the samples have been previously shown to be temperature sensitive in solid state devices [73]. The device performance reported was worse when the samples were exposed to higher temperatures (>80<sup>0</sup>C) as a result of increased dipole disorganization caused by morphological changes from the drying step [73]. There also exists a large number of post-treatment annealing procedures that could be performed to tune the deposited films, but such treatments will also be left to future research direction.

A photograph of baseline loaded PBT on a TGP-H-030 sample is shown in Figure 18 below, alongside a photo of a sample with film characterization cut-outs (1/8” and 3/16” diameter holes) taken from the sample:



**Figure 18 - Photographs of baseline loaded PBT on TGP-H-030 a) as loaded, and b) with film characterization cutouts taken from sample**

For electrochemical testing, the films were further soaked in  $\text{H}_2\text{SO}_4$  (the catholyte used in our photoelectrochemical system) for 24 hours to remove any trace doping of  $\text{ClO}_4^-$  ions still remaining in the film. Films were stored in petri-dishes which were sealed with Parafilm wax to prevent air exchange and solution evaporation.

## **2.2 Film Characterization Procedures**

For ease of characterization, some films were deposited onto fluorine doped tin oxide (FTO) coated microscope slides ( $10 \Omega/\square$ ) as purchased from Solaronix SA (Aubonne, Switzerland) or indium tin oxide (ITO) coated microscope slides ( $8\text{-}10 \Omega/\square$ ) as purchased from Delta Technologies (Stillwater, MN, USA). The slides were cleaned with a mild detergent and  $18\text{M}\Omega$  de-ionized water rinses followed by a thorough rinse in isopropanol before being dried. The films were deposited on to the middle area ( $625 \text{ mm}^2$ ) of a  $75\text{mm} \times 25\text{mm}$  slide to allow for comparison of deposited film thicknesses, surface roughness and UV-Vis absorption spectroscopy. The amount of film deposited on a TCO substrate should be comparable to the film grown on TGP-H-030 as the nucleation and growth of the polymer should be consistent once the initial polymer grains have formed (14). In checking the polymerization deposition potentials on FTO versus the deposition potential on TGP-H-030 all of the film growth regardless of substrate occurs at approximately  $1.0 \text{ V}$  versus a  $3\text{M NaCl Ag/AgCl}$  reference electrode ( $\sim 0.791 \text{ vs. NHE}$ ). Some discrepancy can be seen in the initial charging of the surface when the potential is first applied for varying substrates. These differences in charge build up can be attributed to differences in the geometry and surface chemistry of the substrate being loaded.

### **2.2.1 Surface Analysis – Atomic Force Microscopy**

Atomic Force Microscopy (AFM) was conducted on samples of varying deposition time in order to ensure that the surface morphology of the samples remained consistent, independent of deposition time. It is known that PBT film growth follows a nucleation and growth mechanism and it is expected that the film will be deposited at a constant rate with constant galvanostatic loading density. These experiments were conducted on an Asylum Scanning Probe Microscope with an ORCA module. It was hoped that the ORCA module would be able to discern spatially resolved current measurements in the deposited film to identify between the nanoparticulate and polymeric nodes, but the surface roughness coupled with the softness of the sample limited our results to purely physical measurements. The samples were measured several times with a variety of scan areas (1x1, 2x2, 5x5, and 20x20  $\mu\text{m}^2$ ). It is difficult to compare the roughness of the film surface from a large scale perspective, as there is no way of knowing if the slide is sitting precisely flat on the AFM stage so tilt correction is not possible and would require a reference depth to the substrate surface. Even a small deviation in the angle of the substrate could allow for a large film-height variation in the magnitude of the larger scans, resulting in elevated roughness measurements, so the AFM data is limited to analysis on a sub-micrometer scale to limit this effect.

### **2.2.2 Thickness Analysis – Profilometry**

The film thicknesses were measured using a Dektak150 profilometer with the travel length set to 40-50 mm in order to fully traverse the breadth of the 25 mm x 25 mm deposited film. This was done to ensure that the height of the film was measured at both sides in order to correct for any unevenness or tilt of the underlying substrate. The scan traverse is shown below in Figure 19:

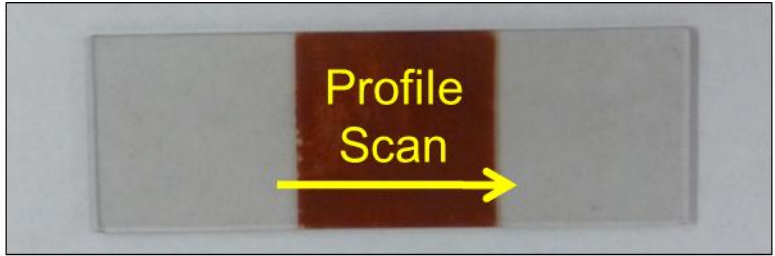


**Figure 19 - Profile scan of PBT loaded on a 25mm x 75mm glass slide**

The samples were measured at three points across the film and repeated at the first point three times, and at the second point two times to give a total of six perspectives as to the distribution of scan data. One such scan is shown in Figure 20, below:

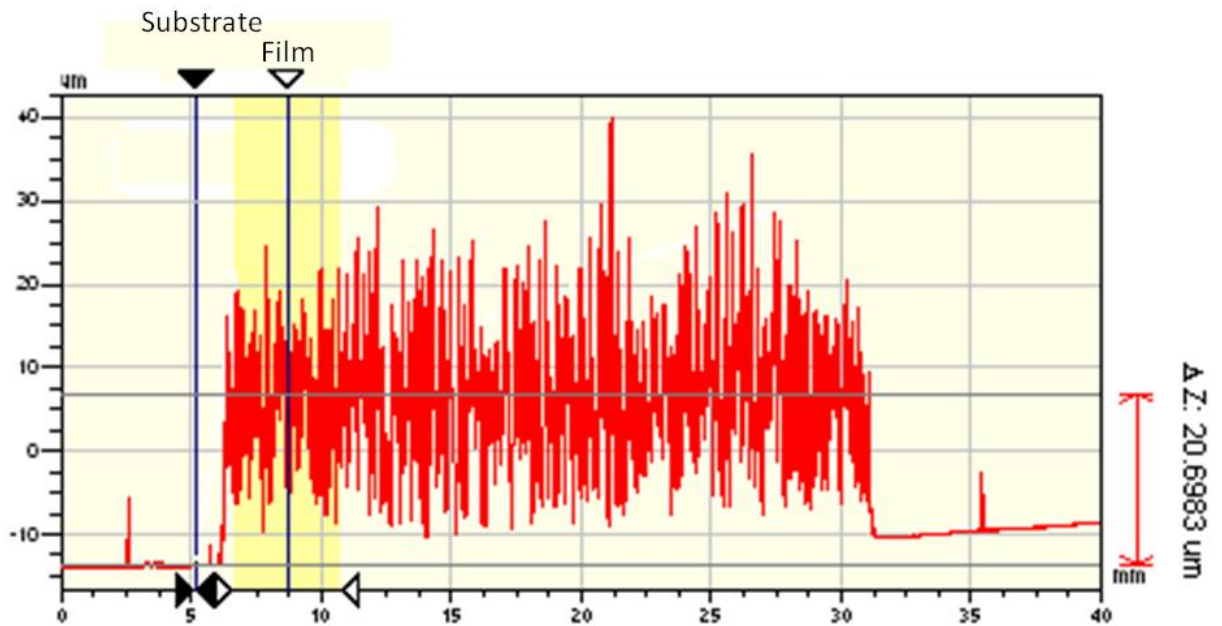


**Figure 20 - Sample profilometric scan covering a 40mm travel span**

The data was corrected for any underlying sample tilt and curvature by the software produced by Veeco Inc.

Surface roughness is a product of disorganized film growth, and may be a result of water content and/or dissolved oxygen present in the propylene carbonate loading bath, as the experiments were not conducted in an inert atmosphere. Any water present while loading will lead to the decomposition of the film as described by Schopf and Koßmehl [79], and the resultant film will be rough and porous, while dissolved gasses may result in bubbles on the surface producing porosity.

### **2.2.3 Spectral Analysis – UV-Vis Spectrophotometry**

The sample films prepared on FTO and ITO substrates were used for spectral analysis. UV-Vis absorption was performed on a Cary 4000 spectrophotometer by transmission of a scanned monochromatic beam. The scan rate was set at 1 nm/s and scanned over a range of 800-300 nm with a resolution of 0.1 nm. The absorption spectra of the samples were subtracted from that of the blank substrate in order to show only the absorptive properties of the film. It was found that the FTO samples sourced from Solaronix SA were deposited on a borosilicate glass which severely limited the analysis of the UV portion of the absorption spectrum as the substrate interfered heavily. The ITO substrates from Delta Technologies were composed of Corning Eagle 2000 glass and had less absorption in the near UV region. All of the data presented in this thesis are subtracted from their respective baselines and exist as absolute absorption.

### **2.2.4 Morphological Analysis – Scanning Electron Microscopy**

Scanning Electron Microscopy (SEM) was used to examine the polymer loading on TGP-H-030 as well as to confirm the presence of TiO<sub>2</sub> in PBT-TiO<sub>2</sub> films by energy-dispersive x-ray

spectroscopy (EDX). Initially, film thickness measurements to gauge the uniformity of distribution for polymeric coatings was measured by SEM assaying, although such a measurement is wrought with bias as it depends where the controller selects nucleated sites on the surface of the carbon fibres. The images selected for this analysis exhibit a variety of film morphologies, and those presented represent typical structures found under the specified loading conditions. The fibres were viewed at a variety of magnifications and also at a variety of angles. Freeze-fractured samples, dipped in liquid nitrogen then cleaved by striking the sample, were used to examine a profile view of in-plane loading and device architecture. This was accomplished with the use of a 90<sup>0</sup> SEM stub, upon which there is a ridge allowing for the samples to be mounted in a position such that in plane viewing of the fractured edge was head on.

EDX was used to characterize the elements present in the film deposited on the surface of several samples. Three polymerized areas for each loaded film were analyzed for the presence of sulphur (representative of the polymeric centres) as well as titanium (indicating the presence of titania inclusion). These results confirmed the presence of TiO<sub>2</sub> in the composite polymers, but a quantification of the relative amounts of titanium and sulphur was not possible to discern due to the variable penetration depth of the x-ray beam with differing film thicknesses and porosity. However, the samples were analyzed using inductively coupled plasma mass spectroscopy (ICP-MS) to quantify TiO<sub>2</sub> inclusion instead.

### **2.2.5 Nanoparticulate Inclusion Analysis – Inductively Coupled Plasma Mass Spectroscopy**

Inductively Coupled Plasma Mass Spectroscopy (ICP-MS) was conducted on samples from an assortment of geometric areas of polymer loaded TGP-H-030. The prepared samples had

1/8" holes punched from them, and either one, two, or three sample circles were dissolved in hot 18M H<sub>2</sub>SO<sub>4</sub> for a duration of one week. The dissolved, titanium ion loaded sulfuric acid was diluted in 18 MΩ H<sub>2</sub>O to a volume of one litre, mixed well, and compared with a calibration curve of set amounts of dissolved TiO<sub>2</sub> in similarly diluted 18M H<sub>2</sub>SO<sub>4</sub>. The results were measured on an ELAN 6000 inductively coupled plasma-mass spectrometry system at UBC under the guidance of Robin Stoodley, and conducted in a double-blind manner to ensure that there was no bias in analysis.

#### **2.2.6 Through-Plane Conductivity Analysis – Sandwiched Conductivity Cell**

Initially the analysis of the electrodeposited films called for the use of a four point probe method to measure the conductivity of the deposits with varied thicknesses. Problems arose however, as the underlying carbon substrate was more conductive than our applied films, and the four point probe would pierce the film and simply measure the resistance of the underlying carbon support. This problem was tackled by design of a compressed average resistance measurement as a means to find out the relative resistance of the applied films in relation to a given contact area (for through plane measurements). The setup is shown in Figure 21.

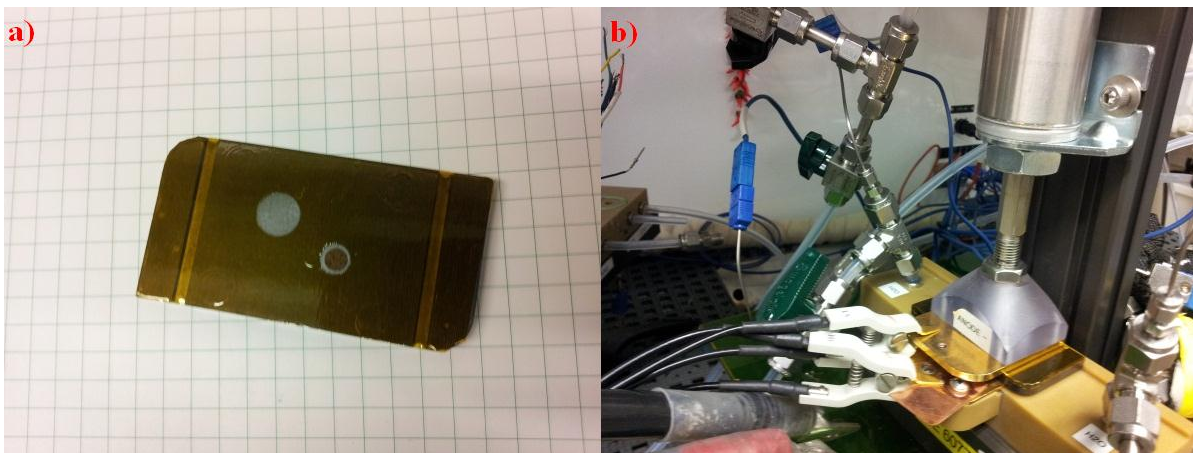


**Figure 21 - Photographs of conductivity cell equipment, including: a) Kapton masked graphite plate with composite coated 1/8" TGP-H-030 sample placed for measurement, b) Graphite plate compressed between gold-coated contacts**

The conductivity cell was adapted from existing fuel cell hardware using an architecture consisting of two parallel graphite plates which are set against one another and compressed using air to a pressure of 120 psi. Gold-coated copper connectors allow for contacts to the graphite plates. One of the graphite plates was covered with a layer of Kapton (an insulating polyimide sheet) which had a small hole cut in order to have a contact for sample placement. Initially, a 1/8" circle of TGP-H-030 was used to measure the blank conductivity of the TGP-H-030. Samples of the as-prepared films were then tested subsequently. Conductivity measurements were conducted through the use of a GW Instek LCR-819 LCR meter connected to the electrical contacts. Scans of 100 kHz down to 1 Hz in logarithmic steps were done to ensure no sensitivity in resistive measurement due to applied AC frequency.

## **2.3 Film Testing Procedures**

There were a variety of preparation techniques used to ensure that electrochemical testing was conducted in a reproducible manner. The preparation of electrodes, membrane assemblies, and substrates is detailed in the subsections below.

### **2.3.1 Spray Loading of Electrodes**

Spray loading is a typical technique employed by the PEM fuel cell research community in order to create a reproducible dispersed particle loading on a substrate. This technique is valuable as it is scalable and requires little energy to achieve a variety of deposition conditions. The deposition begins with a powdered slurry of nanoparticulate metals or carbon-supported metal catalyst mixed with Nafion ionomer and aliphatic alcohols to form a suspension. This suspension is sonicated for no less than 90 minutes, with intermittent stirring to further disperse the solution. This well mixed solution is referred to as a catalyst ink. The catalyst ink composition can be varied through the ratio of Nafion ionomer to dispersed particles that when dry form a random polymer and nanoparticle network.

The substrate to be sprayed is placed upon an aluminum sheet atop a hot plate set to 115°C. This temperature is set so that when the sprayed catalyst ink hits the pre-heated substrate it evaporates and leaves behind the Nafion and metal deposition. The purity of the RuO<sub>2</sub> and platinum powders were 99.9%. A mask is applied to limit the sprayed area to a desired shape. The ink is deposited in the canister of a standard automotive spray gun, and the air pressure and flow rate of the solution are adjusted in order to supply a flow rate such that when sprayed complete evaporation occurs almost immediately. Spraying is conducted in a serpentine like fashion and after 5 passes the aluminum plate stage is rotated 90 degrees. This rotation is conducted after every 5 spray passes in order to avoid any edge effects of the

serpentine spray path on the final loadings. Intermittently, the substrate is weighed and the total catalyst weight noted until the set loading goal is achieved.

### **2.3.2 Membrane Preparation and Conditioning**

Nafion 117 manufactured by DuPont Inc. was used exclusively in this study since it is a robust and relatively well understood proton exchange membrane. The membrane is shipped in a state which needs several treatments to activate and purify the sulfonate sites in the membrane. First, the membrane is cut into strips and boiled for one hour in 3% H<sub>2</sub>O<sub>2</sub> solution. The membrane is removed and further boiled in 18 MΩ D.I. water to remove the dissolved ions, and then boiled again in 0.5M H<sub>2</sub>SO<sub>4</sub> to protonate the sulfonic groups of the membrane. Each boiling occurs for a period of one hour, and then the membranes are left to cool, or re-boiled in D.I. water or the required storage electrolyte as needed. In this study membranes were stored in D.I. water or 0.5mM H<sub>2</sub>SO<sub>4</sub> for electrode assembly, with membranes punched from the bulk treated membrane strips as needed.

### **2.3.3 Membrane Electrode Assembly**

For photoelectrochemical testing, the prepared films on Toray carbon fibre paper (TGP-H-030) were prepared in several different ways in an evolving effort to reduce variability in our testing procedure. Initially samples were cut into 2 cm<sup>2</sup> circles and sandwiched in a membrane electrode assembly as shown in Figure 22 below. The cell was composed of niobium current collectors, a 1.5 mgcm<sup>-2</sup> spray loaded RuO<sub>2</sub> on TGP-H-060 anode, separated from the cathode by a Nafion 117 ion exchange membrane. Seals were used to prevent leakage.

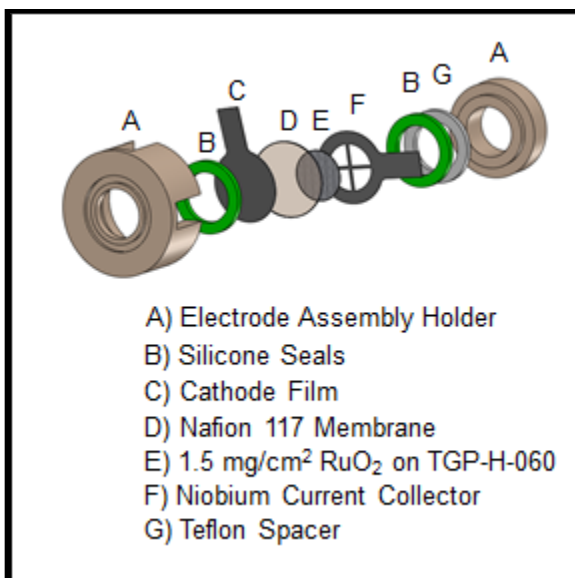


**Figure 22 - Schematic of membrane electrode assembly (MEA)**

Further iterations of the electrical connections to the sample were sought as it was found that there was a variation in resistance for similarly loaded samples on account of lining up of the 2 cm<sup>2</sup> carbon fibre cathode cut-out with the niobium current collector. This variation was due to an umbral loading effect seen in higher loadings of polymer film, which resulted in a small deposition of polymer into the electrical connection edge of the CFP. A solution to correct for this for the baseline measurements was that the samples were cut into 2 cm<sup>2</sup> circles with a tab that extends off one side for electrical connection.

This configuration ensured a direct connection for multistat control and DAQ measurement, but also resulted in a slow leak from the system as electrolyte would wick out of the cell from the porous carbon tab. This leak did not account for a large volume loss for the cell (approximately 5% of the initial cathode reactor volume per hour), but a more permanent solution was sought to allow for proper cell sealing. The carbon tab was also very fragile,

and connection to multiple shielded wires and alligator clips meant assembly was limited to one or two measurement configurations due to tab degradation.

The next trial for electrical connection was to extend the size of the cathode cut-out to 3/4" to allow for a greater contact between the carbon and niobium current collector. With this larger cutout a 800 grit sandpaper could be used to gently remove any excess surface loading from the contact edge before MEA assembly without fear of damaging the active surface.

The active area of the cell was still restricted to 2cm<sup>2</sup> by sandwiching the sample restricting contact with the electrolyte to a 2cm<sup>2</sup> area, with the use of a die-cut Kapton cover to seal the TGP-H-030 to the niobium electrode. Problems arose in lining up the Kapton cover with the niobium electrode and carbon cutout, so a hinge jig was built to align all the elements before closing it to provide for a repeatable electrode assembly manufacturing procedure. This jig can be seen below in Figure 23, with placement of the MEA elements:



**Figure 23 - MEA hinge jig schematic**

### 2.3.4 Cell and Instrumentation Setup

The membrane electrode assembly was joined to an optical cell which has a 1" x 1" x 1/8" quartz plate as an opening parallel to the photoactive surface. This assembly was held together with a clamp to a jacketed glass anode reservoir. The jacketed anode reactor allowed for temperature control, and was typically set to 20<sup>0</sup>C in order to keep the cell cool and at approximately constant temperature while under solar irradiation. The catholyte solution was also cooled during recirculation, and detailed in Section 2.5. The assembled photoreactor is shown in Figure 24 below:

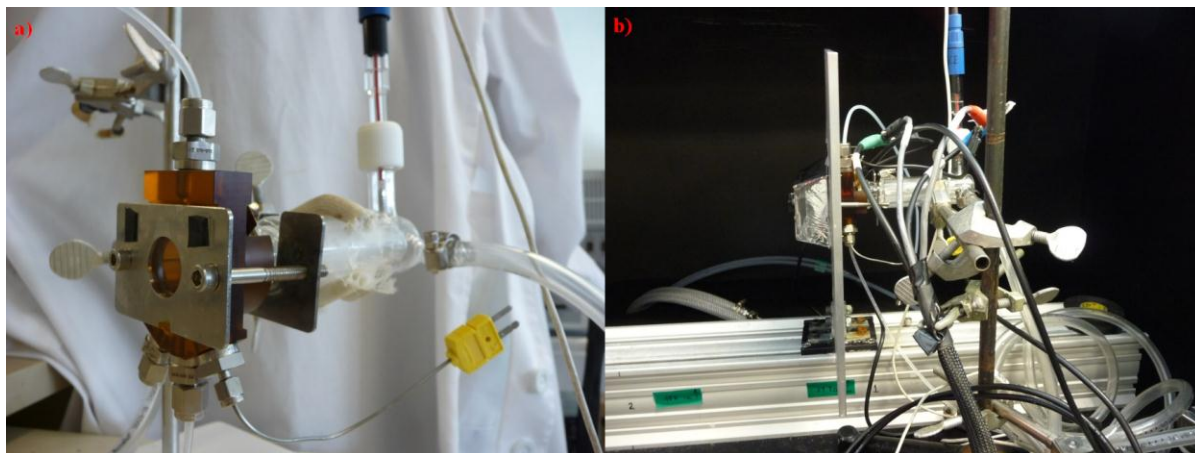


**Figure 24 - Photograph of a) assembled reactor and optical cell, b) assembled reactor mounted in beam path with electrical connections**

In order to measure the electrode potentials versus the redox scale, a reference electrode was placed in the anode compartment. Either a saturated calomel (SCE) or mercury sulfate (MSE) double junction reference electrodes were chosen, but MSE was preferred as it has good compatibility with the sulfuric acid electrolyte. As shown in the assembled reactor

schematic below in Figure 25, there is a series of electrical connections in order to control the cell potential and measure the electrode potentials versus the redox scale. The cell performance was measured using 2 channels of a National Instruments NI-PXI-6221 DAQ system, with the anode and cathode voltage independently measured with respect to the SCE at 3000Hz and then filtered to 5Hz. The cell was controlled using a Solartron 1470E model multistat in a 2 electrode galvanostatic configuration, with the WE and RE2 leads connected to the cathode, and the RE1 and CE leads connected to the anode.

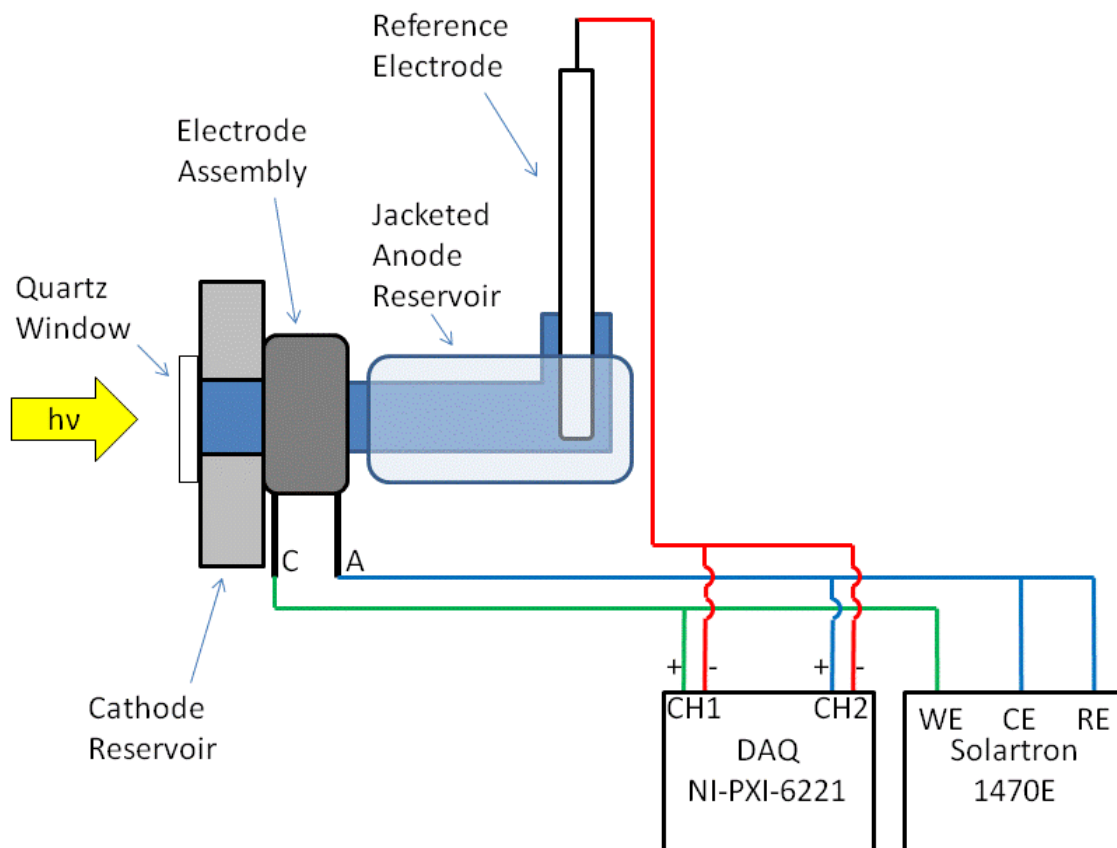


Figure 25 - Schematic of electrical connection and control of the photoelectrochemical cell

The films were tested under galvanostatic operation at different current densities. Each galvanostatic operation was held until an equilibrium potential was reached. The ‘equilibrium’ potential was defined as exhibiting a typical change in  $\Delta E_{\text{cell}}$  of less than 2-3 mV over the span of a minute. Once equilibrium had been reached, the substrate was exposed to the solar source and the shutter was held open until an equilibrium potential had again been reached. Typical cell responses with light activation are shown in Figure 26.

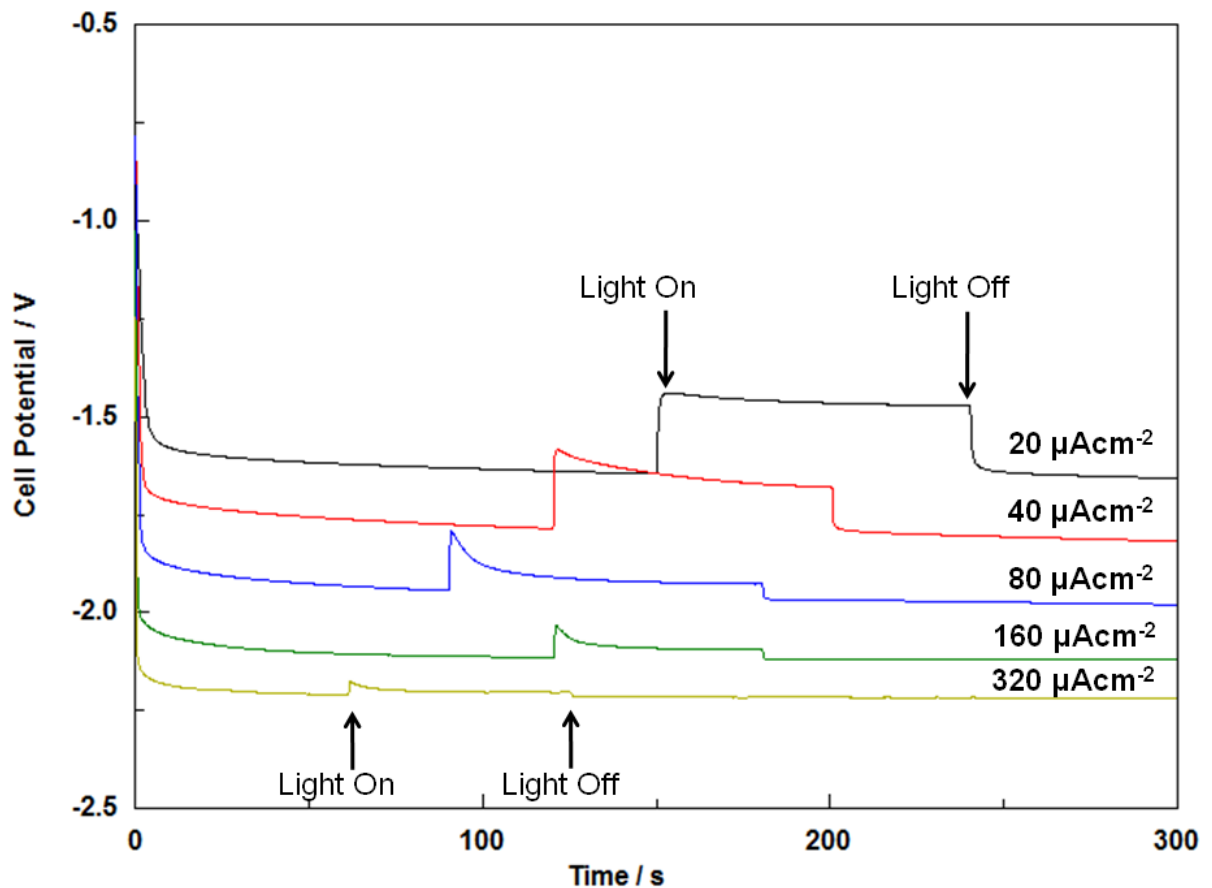


Figure 26 - Electrochemical cell response with illumination for galvanostatic electrolysis runs at different current densities.

For smaller current densities, the time needed to reach this equilibrium potential was typically very long, over an hour. Subsequent experiments conducted at higher current

densities once the cell had been in operation appeared to reach equilibrium more quickly. It was seen that the cathodic electrode achieved a set potential very quickly, and it was the anodic electrode that needed significantly more time to reach an equilibrium potential. The experiments were carried out in a step-wise fashion, and typically the current density was increased in the following order, expressed in  $\mu\text{A}/\text{cm}^2$ ; 10, 20, 40, 80, 120, 160, 200, 240, 320, 640, 960, 1280. Several repetitions of selected current densities (typically 160, 960, 240) were done immediately following the step-wise series in order to check the repeatability of the measurements. These repetitions highlighted two influencing factors in the deviation of experimental results. The repeated measurements were often very similar to the original measurements, with less than approximately a 5-10 mV variation in performance. However, there were some difficulties that arose from this stepwise experimental progression. The first difficulty arises since titania is sensitive to reductive potentials and will dissolve if held at a potential less than -0.502 V vs. NHE as detailed in Appendix K. In conducting the experiments in a step-wise galvanostatic manner, there exists a chance for the cathode potential to be pushed into a potential region in which the titania nanoparticles could be dissolved from the film and enter the solute as titania ions. If this occurs, there would be a deviation in the repeated measurements due to a change in film morphology as well as a possible increase in solution conductivity due to the titanium ions presence. Indication of the dissolution of the titania from the film after exposure to high negative potential will be discussed in the experimental results section of this dissertation. The second difficulty of the step-wise galvanostatic experimental procedure was that Nafion membranes seem to exhibit conditioning, and typically showed an improvement in performance with extended use. It is for this reason a fresh membrane was used for each sample tested, and a deviation from the

galvanostatic operating times was unchanged from run to run in order to minimize this membrane aging effect. For these two reasons it was unusual for samples to be tested for multiple conditions or iterations and a fresh sample was used for every test unless otherwise indicated. Obviously for samples that did not reach breakdown cathodic potentials, the films were used as trials for additional experimental inquiry (such as higher solar intensity tests, step-wise potentiostatic EIS analysis, etc.) in order to limit the number of new samples being generated.

Some galvanostatic trials were conducted with an additional reference electrode in the cathode compartment (as accessed through an optional side port in the optical cell) and the variance between the potential measured at each separate reference electrode varied by less than 2-3 mV. It was for this reason decided that a single reference electrode was sufficient for measuring the potential of the electrodes in the system.

For some experiments, the cell setup was put in 3-electrode format in order to directly control the potential of the cathode. The WE and RE2 leads were left connected to the cathode, and the CE lead connected to the anode. The MSE was connected to the RE1 lead, and the DAQ system was not used. The cyclic voltammetry (CV) and potentiostatic EIS experiments were conducted in this configuration.

CV plots of an inactive region of the redox spectrum in our system were used to examine the capacitive double layer of the prepared films. CV sweeps were performed at several slow scan rates (1, 2, 5, 10 mV/s) and the resultant plots were analyzed to determine the specific charge in the CV sweep as shown in Figure 27.

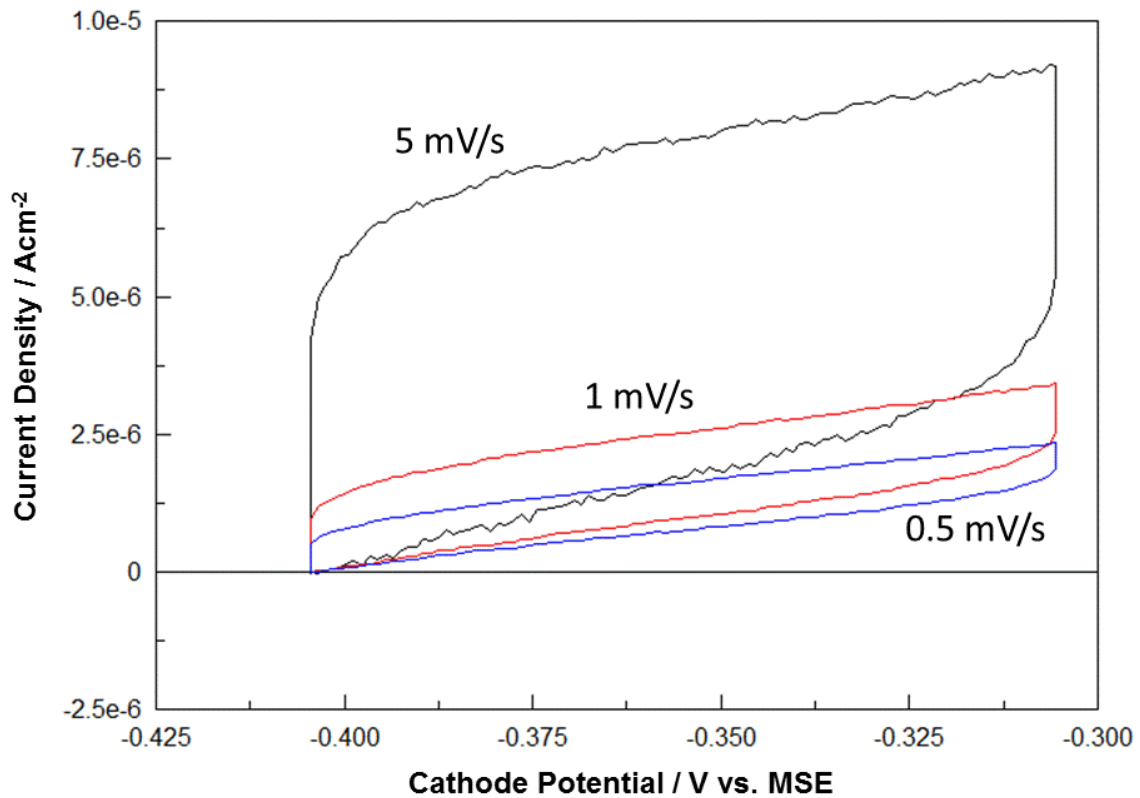


Figure 27 - Example CV sweep rate variation for capacitive double layer calculation

The double layer capacitance is calculated by dividing the specific charge as found from the integration of the area in the CV sweep divided by the voltage window (0.1V), and plotted versus sweep rate. When the double layer capacitance is plotted versus sweep rate for various CV's, the y-intercept corresponds to a sweep rate of 0 mV/s, and this value is the rest  $C_{dl}$ .

### 2.3.5 Photoelectrochemical Experiment Control Systems

As mentioned previously, a NI-PXI-6221 DAQ system along with a Solartron 1470E model multistat were used to control the electrical aspects of the system. Another integral part of the system allowing for measurements at constant temperature was a Thermo DC10-K10

heater chiller. The chiller was attached to the jacketed anodic compartment of the cell by a series of silicone and PTFE tubing. The electrochemical system also incorporated a dewar of catholyte that was situated in the basin of the chiller unit to keep the temperature constant and consistent with the anode. This setup is shown in Figure 28.

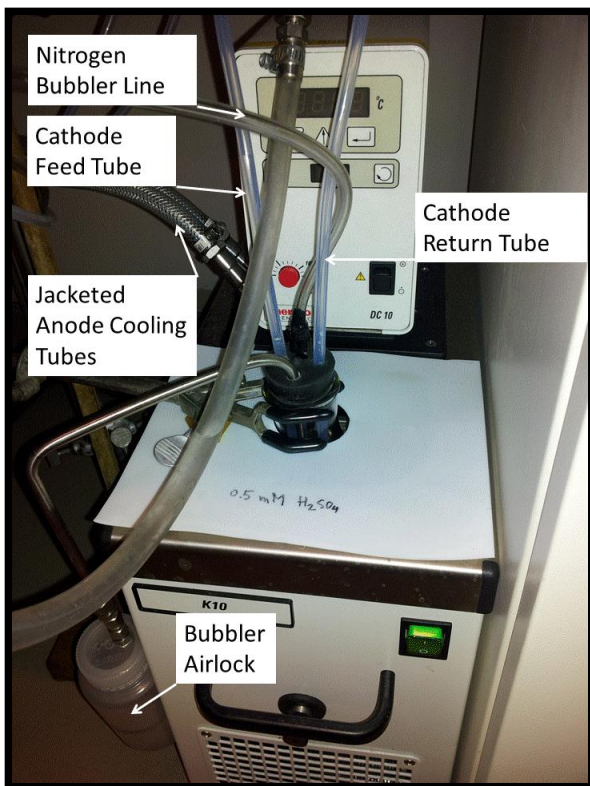


**Figure 28 - Photograph of chiller unit and catholyte dewar setup**

The catholyte was circulated through the cathode compartment with the use of a Masterflex 7518-00 peristaltic pump, shown in the Figure 29.

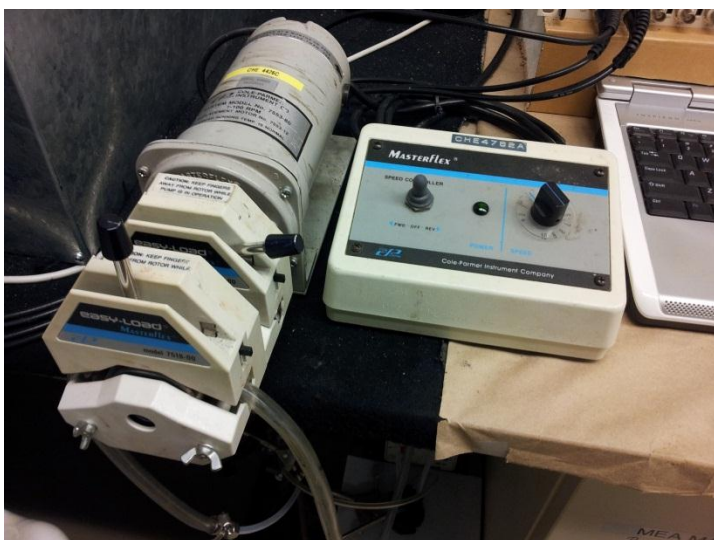


**Figure 29 - Photograph of peristaltic pump setup**

The peristaltic pump flowrate calibration (shown in Appendix T.1) was done by measuring the amount of collected electrolyte in a volumetric flask after a known amount of time.

The catholyte flow rate was set to 1 mL/min, a flow rate that did not perturb the electrode-membrane interface, but still allowed for large bubble ( $H_2$ ) removal from the cathode compartment. The flow rate also served to mix the catholyte solution.

A nitrogen purge was also installed in the catholyte dewar in order to remove any oxygen from the cathode stream. Care was taken to clear any air bubbles from the lines as well as from the corners of the cathode compartment of the reactor. Once all the air was purged from the system, nitrogen was bubbled through the catholyte for a period of one hour. Since oxygen is an electron scavenger, it is important that the catholyte be well purged.

The reactor set up was enclosed inside a darkened steel box, designed to allow for the output from the solar simulator to enter from one side. The inside of the box was coated with a high temperature matte black BBQ paint to prevent errant reflections within the experimental environment. The reactor set up was shielded from the bulk of the beam by an aluminum

plate and shutter system, held orthogonal to the solar simulator beam output using an optical rail. Figure 30 shows the solar simulator and optical control setup.

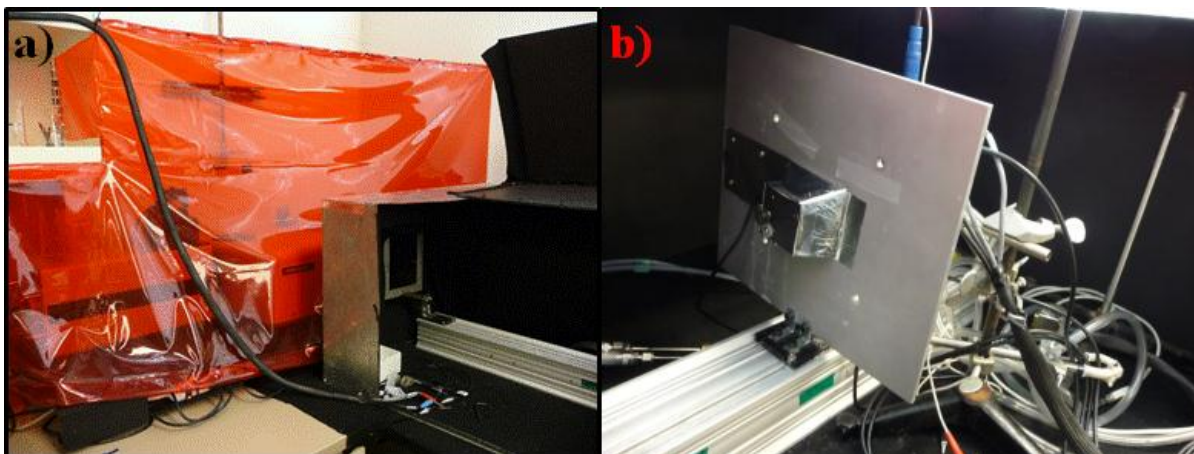


**Figure 30 - Photograph of a) Sciencetech solar simulator with optical rail orthogonal to beam output, and b) optical control (shutter and aluminum plate) mounted on optical rail**

The shutter was computer controlled, allowing for precise control of the timing of light exposure and replication of similarly irradiated samples. The shutter system was sourced from Picard Industries, and was USB connected to a computer running a Labview script for control.

### **2.3.6 Error Analysis of Experimental Data**

The recorded data was analyzed after repeating several replicate samples (2-3) in order to ensure reproducibility. The reproducibility of same sample measurement is described in Section 2.3.4 and deviates by less than approximately a 5-10 mV after reaching an equilibrium potential that deviated by less than 2-3 mV/minute. Deviation in replicate experiments is discussed in the individual chapter results sections, but in an inspection of the variability of repeated samples in Chapter 5 it was found that the pooled standard deviation

in repeated samples was  $\pm 25$  mV ( $n=78$  measurements). Individual analysis of statistical congruence is done to determine if differences in data are statistically significant, and the results are found in Appendix U, and further discussed in the results text. The statistical analysis conducted was a pooled difference of two sample means, with the above standard distribution used as the pooled standard distribution.

### **2.3.7 Solar Simulator Calibration**

The solar simulator in our setup was a Sciencetech Inc. SS1kW solar simulator. This model of solar simulator was chosen, as it is more efficient than other solar simulator models because it employs a fully reflective design to produce a coherent beam from a 1kW Xenon lamp. At the simulator output the beam is filtered down to the AM1.5G spectrum by passing the beam through a filter.

The beam intensity is measured at several distances from the filter using a Fieldmax II laser power meter, coupled with a PM10 full spectrum (150nm-11000nm) broadband sensor. A calibration curve was developed for measured full-spectrum intensities in relation to position from the beam output, and is shown in Appendix T.2.

Standardized intensities were set according to equivalent powers of one, two, and three sun intensities, at  $0.1 \text{ W/cm}^2$ ,  $0.2 \text{ W/cm}^2$ , and  $0.3 \text{ W/cm}^2$  respectively. These standard intensities were set according to the IEC-904-3 Standard for solar irradiation.

The uniformity of the beam is reported by the manufacturer as constant within 10% over the selected field, an 8" diameter spot at a length of 36" from the beam output. The stability is reported to be  $\pm 1\%$  after a warm-up period of 30 minutes. This warm up was done at the same time as nitrogen purging of the electrolyte solution to streamline the testing protocol.

### 2.3.8 Reference Electrode Calibration

Reference electrode calibration was done periodically to ensure no drift from expected reference electrode potential. A jacketed glass cell was filled with 0.5M H<sub>2</sub>SO<sub>4</sub> and the reference electrode was cleaned with D.I. water and wiped dry. The electrode was immersed in the sulfuric acid and connected to a platinum flag electrode via a hand-held voltammeter. A bubbler was placed in the solution and hydrogen gas was bubbled on the face of the platinum flag electrode until the potential difference between the reference electrode and the platinum electrode was stable. Typically for the K<sub>2</sub>SO<sub>4</sub> saturated MSE a value of 0.705 V vs. SHE was reported, and for the KCl saturated SCE, a value of 0.241 V vs. SHE. Individual measurements reported in the body of this work with respect to the corrected potentials were done according to the true value of the MSE or SCE, measured immediately prior to the experiment.

### 2.3.9 Platinization of Titania

For some of the experiments in Chapter 3 platinum incorporation into the composite films was required. Platinization of the titania was chosen as a route for platinum incorporation, and was accomplished by UV degradation of hexachloroplatinic acid onto the surface of P25 nanoparticles. This experiment was performed in a quartz beaker in 18 MΩ D.I. water with an amount of H<sub>2</sub>PtCl<sub>6</sub> added as calculated to have a final 10 wt.% on the titania surface (assuming complete reaction and deposition). The H<sub>2</sub>PtCl<sub>6</sub> had a purity of ≥37.50% Pt basis (ACS grade) with alkalies and other metals ≤0.05%. The stirred beaker was set under a low pressure 11W collumnated mercury lamp for a period of one week and over the course of the reaction the solution colour changed from an orange white to a bluish white. The solution was then dried in an oven at 60<sup>0</sup>C for approximately 24 hours until the platinized titania was

fully desiccated. As discussed in Chapter 3 the presence of platinum was confirmed by EDX but not further quantified, as the results indicated device performance did not benefit from platinum incorporation by this method.

## **Chapter 3: Phase 1 – Benchmarking of Photocathode Function**

As outlined in the introduction to this dissertation, solar assisted electrolysis is usually accomplished at the photoanode due to the ability of titania based devices to oxidize water. What has received little investigation, however, is the exploration into light assisted electrolysis using a photocathode. With the majority of attention focused on the anodic process, alternatives to typical cathodic elements should follow. This is especially true when anode research has been optimized, and needs to be mated with an equivalently designed photocathode. At the time of this publication, one of the most common cathode elements is platinum, prized for its chemical robustness and catalytic performance for the hydrogen generation reaction. Work has been conducted on catalyst coated silicon electrodes for use as photocathodic electrodes, and details the fundamental issues of ensuring hydrogen generation to prevent charge recombination [53].

As previously mentioned, there are several potential advantages for using a composite conducting polymer as the photoactive component on the cathode side. These advantages include no oxidative degradation of the polymer, and potentially at cathodic potentials inherent electrocatalytic performance that could allow for platinum to be replaced. The groundwork for investigation of utilizing composites of conductive polymer with titania inclusions is investigated in this chapter, and the results show that these materials can indeed be employed to reduce the amount of energy needed to drive the water splitting reaction from the cathode side.

### **3.1 Introduction**

The direction of this chapter is outlined as follows: Films to be deposited were produced by the procedure outlined in Chapter 2.1.2. This procedure was chosen as the device presented

in the study detailing the polymerization procedure showed an extremely high  $V_{oc}$  of  $\sim 2V$  (albeit with a small short circuit currents density of  $5 \mu A/cm^2$ ). It was hoped that this high  $V_{oc}$  would result in large energy savings for solar-assisted water splitting.

The films were first characterized to analyze their morphology on CFP. Sequential analysis of the surface structure using SEM, AFM and profilometry were followed by destructive testing to measure titania content of the films using ICP-MS. Spectral data of the films was measured for samples loaded on FTO coated slides, and measured using absorptive UV-Vis spectroscopy.

The analysis of photoelectrochemical cathode operation of a p-n junctioned tunnelling surface for a PEM electrolysis device was accomplished using the setup described in Chapter 2.3.4. Samples of PBT coated TGP-H-030 as well as titania included films were compared to baseline blank substrates and platinum spray-loaded electrodes. Recent developments in solid state photoelectric cells have investigated cheap and easy methods to process polymers in conjunction with titania to more effectively separate and trap photoexcited charge in mesoporous coated devices [80]. These polymers also have a complimentary bandgap to  $TiO_2$ , and with selection of regioregular monomer precursors have shown that through galvanostatic growth they form very organized dipole moments in a nucleated film structure which lends to the creation of a high voltage generating device [73].

Junctioned p-n semiconducting devices can be run in reverse bias operation, as tunneling photodiodes, and in a titania based system hydrogen generation would occur at the photoactive surface [81]. As noted in Appendix H-3, reverse junction cells can have higher carrier mobility due to the electrostatic potential between dissimilar materials. One drawback of reverse bias operation is the photoactive surface is limited by stability of the

titania in an acidic environment. Also photoreactors typically use indium tin oxide (ITO) or fluorine doped tin oxide (FTO) as a transparent conductive oxide substrate and these substrate materials also have limited stability under cathodic polarization. The standard reduction potential for these oxide films is near to the potential at which hydrogen is generated. For this reason a typical fuel cell material, TGP-H-030, was chosen to act as a stable substrate. With a careful selection of the electrochemical operating window and working solution pH a balance between these limiting material constraints can be achieved. The pH set for this series of tests was 3, chosen as an intermediate value between high hydrogen ion concentration and optimum conduction band edge position for redox operation. If the conduction band edge is below the potential at which hydrogen is formed, the reaction cannot proceed photoelectrochemically. An example of the conduction band position variance with pH is shown in Figure 133. This pH remained unchanged as it was essential to have some constants to provide baseline analysis. Alteration of pH is a facile method to further examine the performance of photoelectrochemical devices, and is highlighted in the recommendations for further work.

Using the photoactive surface as a photocathode has an additional attraction as conductive polymer composites have recently been shown to exhibit catalytic properties for hydrogen generation. This catalytic effect is reported to be a mating of a localized bonding site for a hydronium ion coupled with the extended  $\pi$  bond of the conductive polymer to facilitate the hydrogen reduction reaction. It may be possible to utilize incorporated titania in a conductive polymer matrix in a similar manner – as the localized hydronium ion bonding site. If these composites prove to be active and stable they may act as a replacement for platinum catalyst at the cathode, which would lead to a significant reduction of cost.

A hybrid variety of films incorporating platinum and TiO<sub>2</sub> loading were also tested, although due to known polymer degradation mechanisms with platinum incorporation [82] as well as providing metallic sites for charge recombination, this film loading was expected to have limited performance. The experiments were also conducted at low acid concentration and low temperature to ensure the stability of materials.

The hypothesis of this study is that TiO<sub>2</sub> incorporation will increase performance with an increase in charge separation due to included p-n junctions in the bulk of the material, as well as improving catalysis by TiO<sub>2</sub> surface site presence. The benefit of using titania is that it is a cheap and non-toxic material, although there are problems since the wide bandgap only allows for 5% of the solar spectrum to be absorbed, as well as recombination of photoexcited carriers owing to the fast photoexcitation rate versus the slow chemical reaction rate disparity [83]. This disparity is caused by photonic activation and recombination happening in the nanosecond regime versus chemical reaction rates occurring at the microsecond rate and even slower rates.

The results in this chapter have been presented at the 217<sup>th</sup> ECS Meeting held in Vancouver, British Columbia, Canada, and appear in the Transactions journal associated with the meeting [84].

As a summary of the direction of this chapter the electrochemical and photonic performance of several photoactive films were be investigated comparing:

- Blank and baseline platinum loadings
- Plain PBT versus nanoincluded PBT-titania films
- Effect of inclusion of platinum augmented nanoparticles

Select studies are also shown in this section highlighting surface bound titania films as a comparison to our composite films. These tests have been limited to a simple analysis of only one spray loaded titania electrode, yet results highlight the advantage of our prepared photoactive surface.

### **3.2 Experimental**

A composite film can be formed in many ways, and the formation procedure can severely affect the device properties. Tunneling architectures are sensitive on the 10-100 nm scale, and the abovementioned catalytic effect requires even finer control of interfacial architecture. Otsuka et al. [80] found that TiO<sub>2</sub> mesoporous layers coated with polythiophene through a photodeposition process yielded lackluster results when compared to chemical deposition of the same polymer. Even though the pores were more fully coated with polymer, they showed that structural control of the titania-polymer interface was crucial and dependant on the fabrication technique. Beck et al. [85] showed that composite films of nanoparticles can be formed through in-situ electropolymerization and their composite inclusion can be simply controlled by the degree of mixing without affecting the nanoparticulate features. This technique is employed in this study.

In this work a nanoparticulate loaded conductive polymer-titania dispersed p-n junctioned reverse bias photocatalytic surface was investigated for hydrogen generation. The following aspects of the system were investigated: Performance of the conductive polymer (polybithiophene) as a catalyst for H<sub>2</sub> production either with or without nanoparticulate titania inclusion, effect of inclusion of nanoparticulate features on the overall photocatalytic performance of the device under AM1.5G 0.1Wcm<sup>-2</sup> operation, and finally, evaluation of the performance of a carbon based material as a replacement substrate option to ITO/FTO in

terms of stability under cathodic polarization and compatibility with the created composite films. Platinized titania as prepared by the method described in Chapter 2, and Degussa P25 were selected for nanoparticulate inclusion for the composite samples tested.

The films were deposited on the substrates at a current density of  $0.5 \text{ mAcm}^{-2}$  for 646 seconds and 1292 seconds, which should correspond to PBT loading thicknesses of approximately  $0.5 \text{ }\mu\text{m}$  and  $1.0 \text{ }\mu\text{m}$ , respectively as determined from the results by Leguenza et al. [73]. The treatment of the films follows the procedure outlined in Chapter 2.1.2 without modification. This includes the step of soaking in  $0.5\text{mM H}_2\text{SO}_4$  (pH 3) electrolyte prior to electrochemical testing.

### **3.3 Characterization Results**

The samples of deposited conductive polymer and polymer composites were analyzed according to the procedures outlined in Sections 2.2.

#### **3.3.1 SEM/EDX**

Initial SEM tests were conducted at NRC – IFCI under the guidance of Mark Robertson and Sick Ying. Initial efforts to analyze the surfaces of the samples were hampered by the limitations of the equipment. The SEM used for imaging was a Hitachi S3500N SEM with an Oxford X-Max  $50\text{mm}^2$  SSD detector used for EDX work. Resolution of several microns was possible, but good sub-micrometric resolution ( $<1000 \text{ }\mu\text{m}$ ) was impossible due to an inability to focus the beam further. Some of the resolution problems may be attributed to the fact that we chose to not gold coat our samples, but this also allowed inspection of the unperturbed surface. SEM was used to examine the polymer loading on TGP-H-030 as well as to confirm the presence of  $\text{TiO}_2$  in the PBT- $\text{TiO}_2$  films by energy-dispersive x-ray

spectroscopy (EDX). An SEM image of blank TGP-H-030 is shown below in Figure 31 to serve as a baseline for analysis.

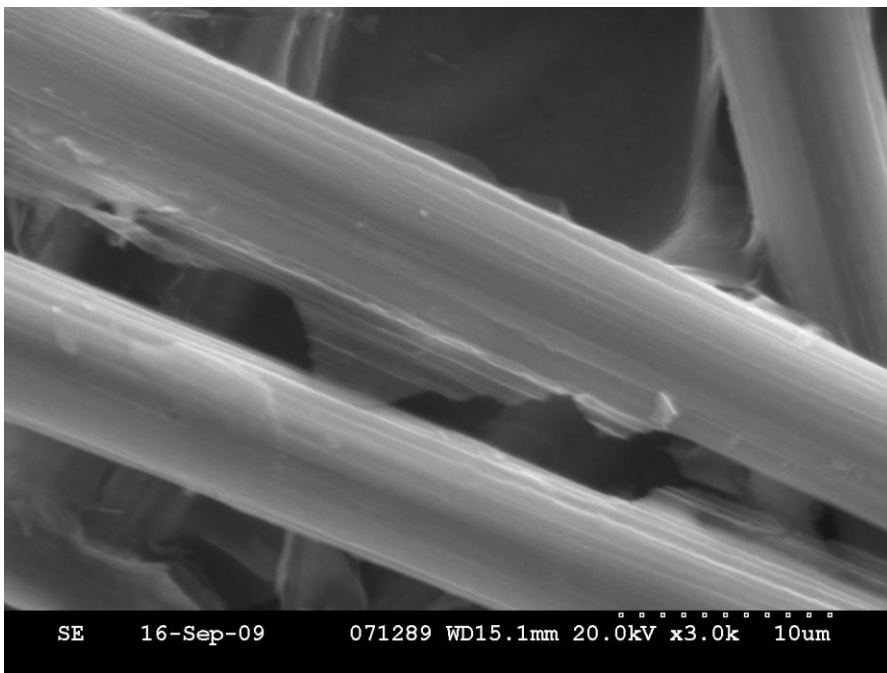


**Figure 31 - Morphology of blank TGP-H-030 measured at 3,000X magnification**

It can be seen from the above image that the TGP-H-030 is composed of fibres of approximately 8-10  $\mu\text{m}$  in diameter. This is in agreement with the data set forth in the article by Lysenko. [86]. As can be seen in Figures 32 and 33, the 1292s loadings of PBT on TGP-H-030 are non-uniformly distributed on the surface of the carbon fibres. In Figure 32 the loading is sparse. In Figure 33 the loading has a bulky crust on a large section of the fibre. There exists patches of polymer typical of both figures, sparse or lumped together, on both samples examined. This degree in disparity in the nucleation and growth of the films is likely a product of localized differences in energy levels with preferential loading occurring at edges, intersections, and dislocations accounting for the ‘preferential’ growth.

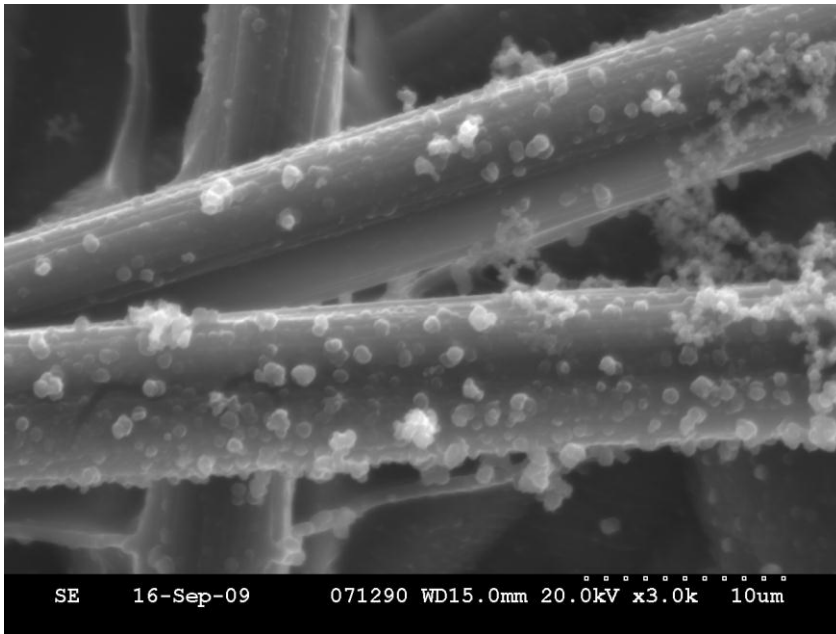


**Figure 32 - Morphology of 1292s PBT loaded TGP-H-030 measured at 3,000X magnification – Site A**

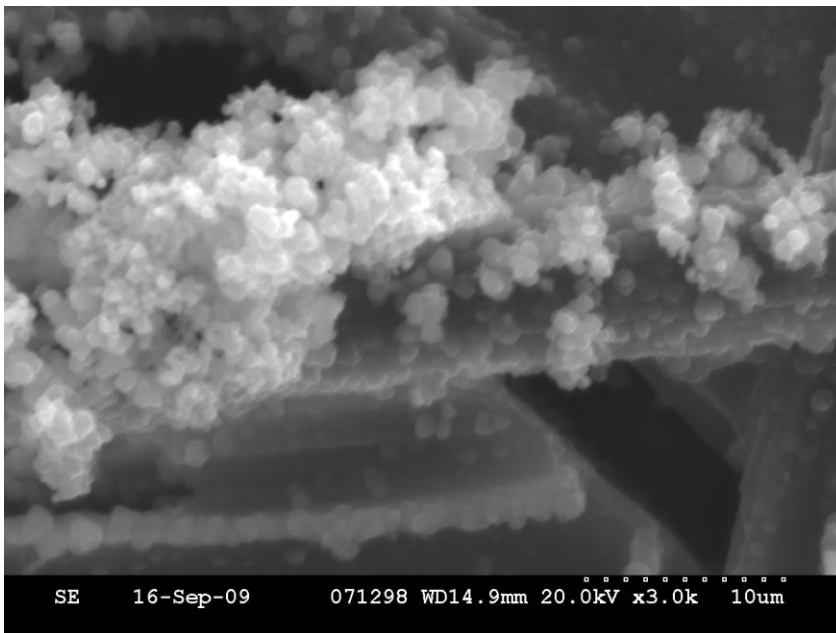


**Figure 33 - Morphology of 1292s PBT loaded TGP-H-030 measured at 3,000X magnification – Site B**

EDX was used to characterize the elements present in the films deposited on the surface of several samples. These results can be seen in Table 1 for the 10kX magnification, with the

number of samples measured indicated. This magnification for EDX was chosen to encompass the beam focal path and was focused so that bare patches of the substrate were not included in the analysis.

Sample	Percent Average Elemental Content								n
	C	±	S	±	Ti	±	Pt	±	
PBT	87.4	1.1	12.9	1.2	0.0	0.0	-0.3	0.1	6.0
PBT-TiO <sub>2</sub>	83.8	2.9	13.8	2.1	2.7	1.0	-0.3	0.4	6.0
PBT-TiO <sub>2</sub> :Pt	83.5	8.2	11.6	4.2	4.6	4.1	0.4	0.0	3.0

**Table 1 - EDX Results for 1292s loadings of PBT and PBT composite films**

Three polymerized areas for each loaded film were analyzed for the presence of sulphur as well as titanium. As expected, films formed in the stock PBT solution showed an elemental composition of sulphur with the remaining composition being carbon. These measurements should serve to be a basis for composition, but it is unknown if parts of the substrate are being detected by the scan. If the beam cross section is focused on a sample that has partial loading it may indicate a lower elemental concentration as a result. This may be one source of error in the above measurements. The samples formed in the PBT-TiO<sub>2</sub> solution showed an elemental composition of sulphur and titanium with the remaining composition being carbon. Similarly, samples of PBT-TiO<sub>2</sub>:Pt showed the presence of sulphur, titanium, and platinum with the remaining composition being carbon. These results confirm the presence of TiO<sub>2</sub> in the composite polymers. The polymer composites coated on TGP-H-030 are shown in the following Figures below, with PBT-TiO<sub>2</sub> samples shown in Figure 34 and with PBT-TiO<sub>2</sub>:Pt in Figure 35.

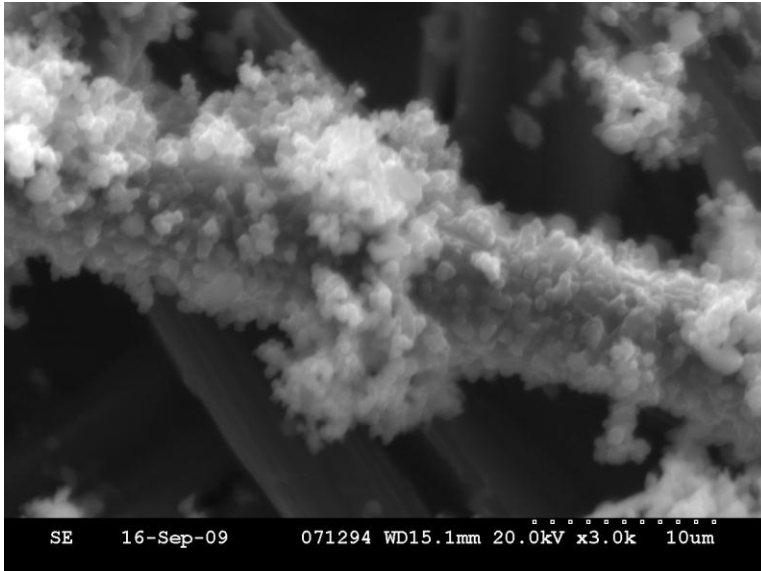


**Figure 34 - Morphology of 1292s PBT-TiO<sub>2</sub> loaded TGP-H-030 measured at 3,000X magnification**

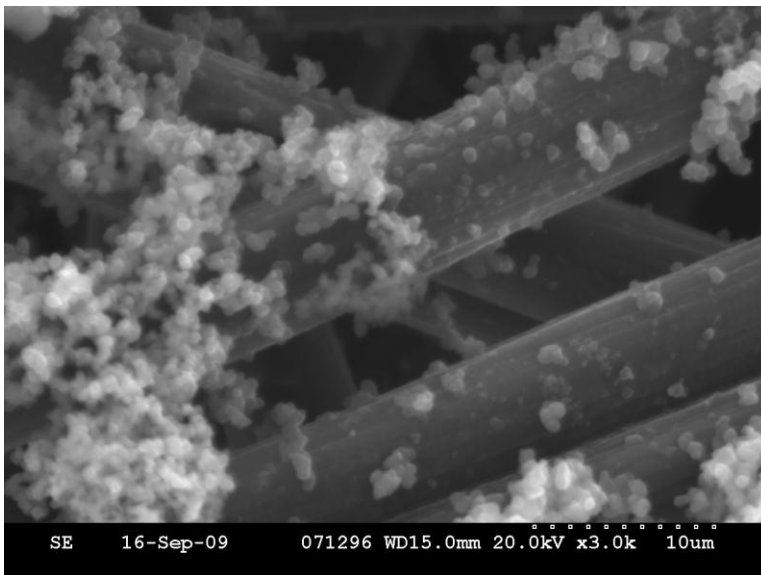


**Figure 35 - Morphology of 1292s PBT-TiO<sub>2</sub>:Pt loaded TGP-H-030 measured at 3,000X magnification**

As can be seen from the above SEM images there is little notable difference in the morphology of the deposited composite films at these SEM resolutions.

Quantification of the relative amounts of incorporated nanoparticle was impossible to discern as we had no set standards to compare the loadings to, so the samples were analyzed using ICP-MS to quantify the TiO<sub>2</sub> inclusion in terms of typical catalyst loading standards (mg/cm<sup>2</sup>).

### **3.3.2 AFM**

Atomic Force Microscopy was conducted on samples of varying deposition time in order to ensure that the surface morphology of the samples remained consistent, independent of deposition time. With PBT film growth following a nucleation and growth mechanism it was expected that the film will be deposited at a constant rate with constant galvanostatic loading density. As previously outlined in Chapter 2, these experiments were conducted on an Asylum Scanning Probe Microscope with an ORCA module. It was hoped that the ORCA module would be able to discern spatially resolved current measurements in the deposited film to identify between the nanoparticulate and polymeric nodes, but the surface roughness coupled with the softness of the sample limited our results to purely physical measurements. The samples were measured several times with a variety of scan areas (1x1, 2x2, 5x5, and 20x20 μm<sup>2</sup>). It is difficult to compare the roughness of the film surface from a large scale perspective, as there is no way of knowing if the slide is sitting precisely flat on the AFM stage so tilt correction is not possible and would require a reference depth to the substrate surface. Even a small deviation in the angle of the substrate could allow for a large film-height variation in the magnitude of the larger scans, resulting in elevated roughness measurements, so the AFM data is limited to analysis on a sub-micrometer scale to limit this effect. It may be possible to scratch the surface to expose the underlying substrate in order to estimate the surface tilt, but this technique was not employed.

Upon examination of the  $1 \mu\text{m}^2$  scan areas for both PBT and PBT-TiO<sub>2</sub>, it was found that the sample roughness on a nano-scale was  $28 \pm 14$  nm and differed by less than 15 nm either between PBT and PBT-TiO<sub>2</sub> samples of the same loading time, or between PBT samples of differing loading times. These results were very similar to the RMS results (26.2 nm) published by Innocenti et al. [87]. From this we can conclude that the film build up either with or without TiO<sub>2</sub> leads to similar nano-surface roughness morphology at all loading conditions after the initial surface nucleation. Since the incorporated titania nanoparticles have a similar size ( $\sim 25$  nm) to the nucleated polymer grains it is not possible to validate if the individual features measured are the polymer grains or nanoparticulates.

Examination of the surface of the films with the AFM showed individual polymer grains as grown through the galvanostatic polymer deposition. It can be seen in Figure 36 that the surface has distributed clusters of PBT with diameters ranging between 50 to 150 nm. A similar distribution can also be seen in the samples of PBT-TiO<sub>2</sub> composite films and the grain sizes are of similar size. Analysis of grain distribution could be used to measure the degree of uniformity of polymer crystal size, but such analysis was not conducted due to time constraints. Most of the grain sizes found were smaller than that found by Innocenti et al. [87]. Their reported grain size was found to be 400 nm and although in our samples a number of nucleated grains of this size are present on the surface they are surrounded by smaller grains. The distribution of these polymer grain sizes films are in agreement with O'Neil and Semenikhin [88] where thicker polymer films formed have low molecular weight fractions (smaller grains) deposited alongside the formation of a large number of highly crystalline nuclei, forming an amorphous grain periphery. The distribution of PBT grain size growth will be further discussed in the UV-Vis absorption portion of the next section, as the

PBT chain length (and nucleated grain size) is directly proportional to the absorbance peak sharpness.

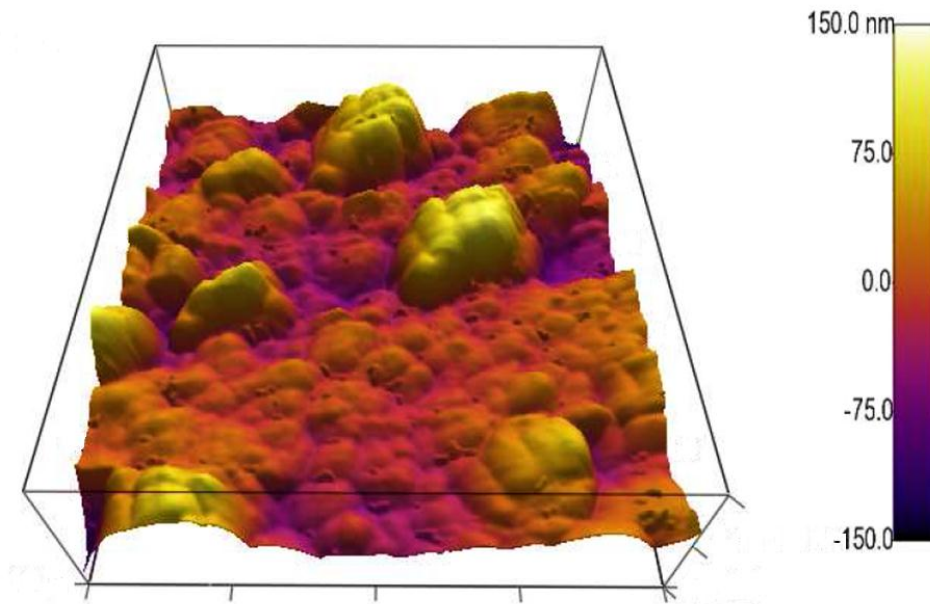


**Figure 36 - 2x2  $\mu\text{m}^2$  AFM image of the surface of PBT-TiO<sub>2</sub> film deposited on FTO**

### **3.3.3 Profilometry**

The film thicknesses were measured using a Dektak150 profilometer with the travel length set to 50 mm in order to fully traverse the breadth of the 25 mm x 25 mm deposited film. This was done to ensure that the height of the film was measured at both sides of the sample in order to correct for any unevenness or tilt of the underlying substrate. The samples were measured at three points across the film and the averages can be seen in Table 2, with an associated deposition weight for comparison. Weights of deposited films were estimated based on the density of PBT and PBT composites.

Sample	Loading Time	Thickness / $\mu\text{m}$	Weight / $\mu\text{gcm}^{-2}$
<b>PBT</b>	323 s	$0.465 \pm 0.060$	$69.7 \pm 9.0$
	646 s	$5.948 \pm 1.404$	$892.2 \pm 210.7$
	1292 s	$19.889 \pm 2.452$	$2983.2 \pm 367.8$
<b>PBT-TiO<sub>2</sub></b>	323 s	$0.701 \pm 0.051$	$105.2 \pm 7.7$
	646 s	$9.961 \pm 0.911$	$1494.1 \pm 136.6$
	1292 s	$21.235 \pm 2.337$	$3185.2 \pm 350.6$
<b>PBT-TiO<sub>2</sub>:Pt</b>	30 s	$0.109 \pm 0.021$	$16.3 \pm 3.1$
	60 s	$0.169 \pm 0.029$	$25.3 \pm 4.3$
	90 s	$0.251 \pm 0.030$	$37.7 \pm 4.5$
	323 s	$0.410 \pm 0.081$	$61.6 \pm 12.1$

**Table 2 - Profilometry measured film thickness comparison of PBT, PBT-TiO<sub>2</sub>, and PBT-TiO<sub>2</sub>:Pt.**

The projected loading thicknesses of 0.5  $\mu\text{m}$  (646 s) and 1.0  $\mu\text{m}$  (1292 s) were estimated from the data reported by Leguenza et al. [73] but when the loadings were complete, the total polymerization current and the profilometry results indicated a much thicker film deposition. Using an approximation as reported by Kraljić et al. [89] to estimate the film thickness, the calculated thickness (d) can be given by:

$$d = \frac{QM_w}{zFA\rho} \quad \text{Eq. 16}$$

where Q is the charge transferred in coulombs (C),  $M_w$  is the molecular weight of polybithiophene (166.27 g/mol), z is the number of electrons/bithiophene unit (2.3 [90]), F is the Faraday's constant (96,500 C/mol), A is the area of the electrode (6.25  $\text{cm}^2$ ), and  $\rho$  is the density of polybithiophene (1.5  $\text{g/cm}^3$  [91]). Druy and Seymour [92] reported that the

passage of  $35 \text{ mC/cm}^2$  yields a film thickness of  $4000 \text{ \AA}$  which results in a ratio of  $11.4 \text{ nm/mC}$ , which is in agreement with the Kraljić et al. thickness calculation. This calculation does not however take into account the porosity and counter-ion volume of the prepared film. It is assumed that since the polybithiophene loadings were conducted in an identical manner that these properties should be relatively constant between film loadings.

When comparing the film loading charge thickness to the actual film thickness differences were found. The estimated thickness as calculated due to charge transfer is  $803 \text{ nanometers}$  for  $323\text{s}$ ,  $1.605 \text{ microns}$  for  $646\text{s}$  and  $3.211 \text{ microns}$  for  $1292\text{s}$  loadings, respectively. This is  $300\%$  larger than the results presented by Leguenza et al. [73]. These larger measured thicknesses, assuming  $100\%$  loading charge transfer, would indicate the porosity of the film accounts for a large degree of their measured thickness.

When the profilometry results are further analyzed it can be seen that the roughness of the surface is very high – and is reflected in the large standard deviation in the thickness measurements. This surface roughness is a product of disorganized nucleation and film growth and/or may be a result of water content or dissolved oxygen present in the propylene carbonate loading bath, as the experiments were not conducted in an inert atmosphere. Any water present while loading will lead to the decomposition of the film as described by Schopf and Koßmehl [79], and the resultant film will be rough and porous thus potentially accounting for the large degree of porosity of the loaded films. Dissolved oxygen while loading could result in oxidative degradation of the films.

A large degree of porosity is not optimum for an optical device due to reflective and diffractive effects, but also not necessarily a bad feature for an electrode active surface due to

better transport properties. This optical scattering may also be a source of uncertainty in the UV-Vis absorption measurements.

From the measured thicknesses, as seen in Table 2, it can also be seen that film thickness for PBT-TiO<sub>2</sub> samples is thicker than their PBT counterparts, but this increase in thickness is not linear with increasing deposition time. This non-linear effect will be further explained in the ICP-MS section (Section 3.3.5) but is likely on account of the particulate settling out of solution during longer loading times.

### **3.3.4 UV-Vis**

The sample films prepared on FTO substrates were used for spectral analysis. UV-Vis absorption was performed on a Cary 4000 spectrophotometer. The absorption spectra of the samples were subtracted from that of the blank substrate in order to show only the absorptive properties of the film. Unfortunately the FTO slides supplied by Solaronix used borosilicate glass (no alternatives were available at the time of analysis) and absorbed a large portion of the ultraviolet spectrum, allowing for comparison of visible range absorbance only. As TiO<sub>2</sub> is absorptive up to approximately 400nm (UV light) [83], it was not possible to confirm the associated UV absorption peak in our samples. The absorption of the blank substrate is shown in Figure 37.

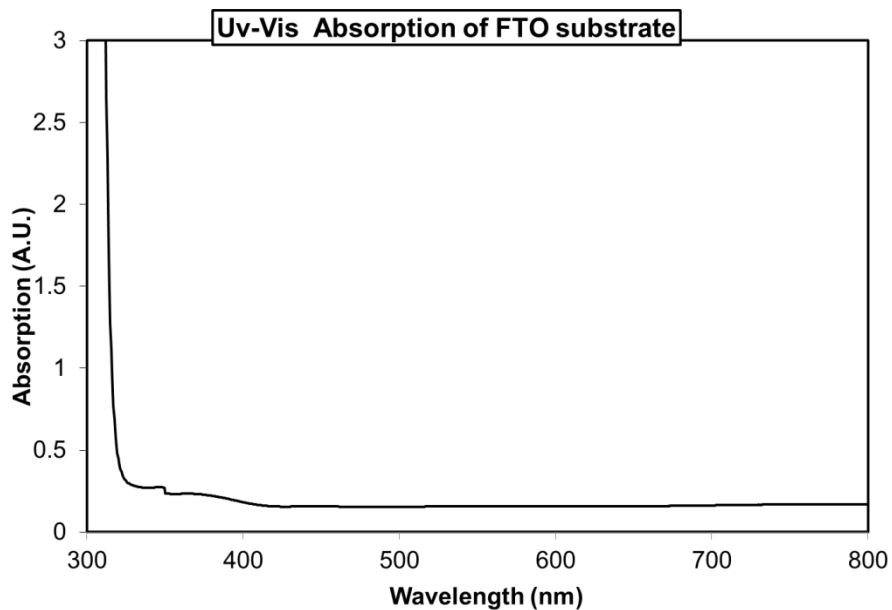


**Figure 37 - UV-Vis Absorption of blank FTO substrate**

The peak location for all of the prepared polymer films was approximately 480 nm, shown in Figures 38 and 39. The peak at 480 nm has been attributed to a  $\pi$ - $\pi^*$  transition of the aromatic rings of the polymer by Druy and Seymour [92]. The broad peak width is also representative of the distributed grain sizes as seen in the AFM results.

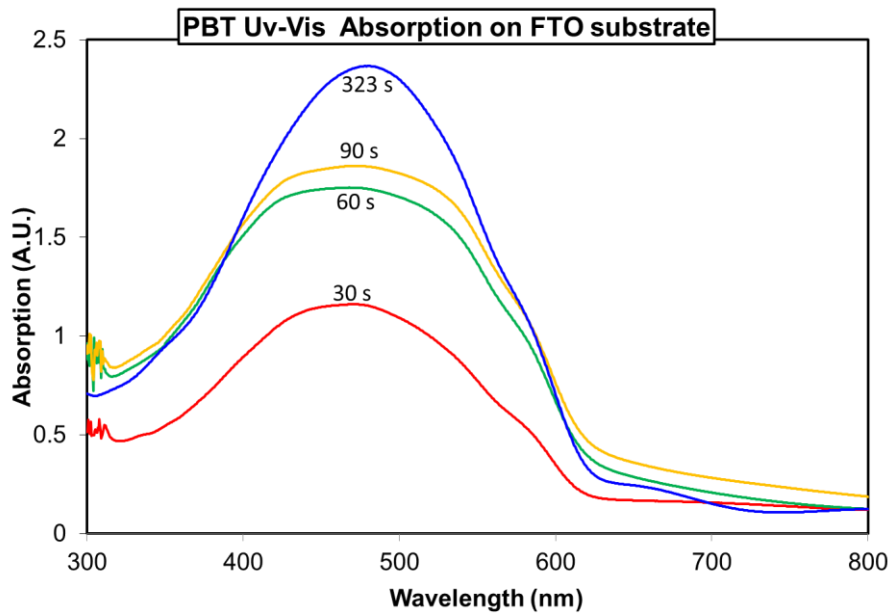


Figure 38 - PBT UV-Vis Absorption of FTO substrate

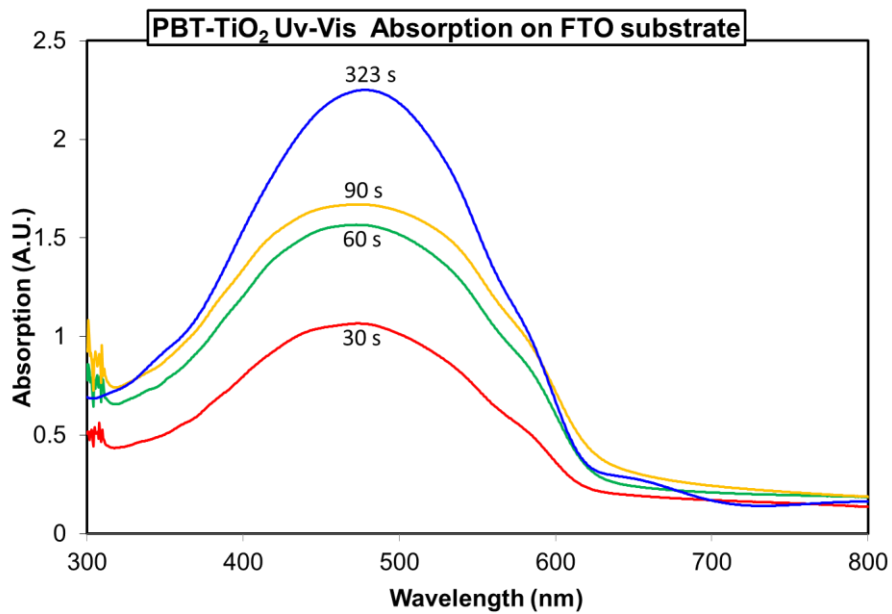
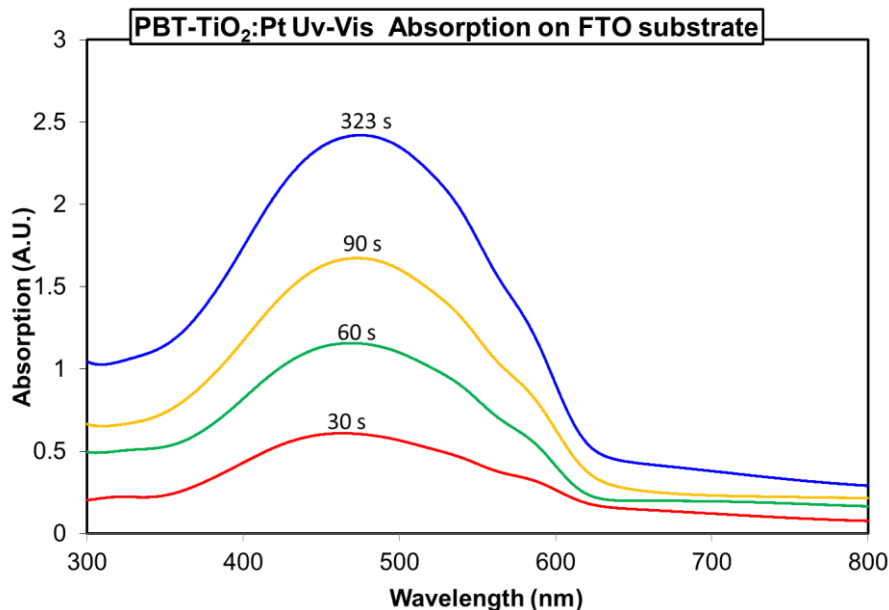


Figure 39 - PBT-TiO<sub>2</sub> UV-Vis Absorption on FTO Substrate

It can be seen from the absorption results in Figure 39 above, that regardless of the galvanostatic loading times there was a decrease in the visible absorption spectra of the

applied films with TiO<sub>2</sub> inclusion. This decrease in absorption is due to the inclusion of nanoparticles into the films, which are non-absorptive in the visible spectrum, and not a result of a thinner film thickness as was shown in the previous section as measured by profilometry. A similar result was found in the analysis of absorption spectra of poly(3-hexylthiophene)-TiO<sub>2</sub> composites by Muktha et al. [93].

With the inclusion of titania nanoparticles there is a shift in the peak wavelength for the lower loaded samples (30s, 60s, 90s) from 471 nm to 474 nm. This peak frequency shift is measured as a 3 nm difference, with the titania included samples red shifted, and thus having a slightly lower band gap for titania included polymer composites. When the 323s films were analyzed, it was seen that the shift in this peak disappeared, with the average peak position between the included and plain PBT films differing by less than 1 nm, and had a value of 478 nm. This change in peak position could indicate that there is an uneven loading in terms of stratification of the prepared sample due to the mixing issues such as settling of nanoparticles. The analysis of the included nanoparticles in the composite films is further examined using ICP-MS.



**Figure 40 - PBT-TiO<sub>2</sub>:Pt UV-Vis Absorption on FTO Substrate**

For the films with platinum deposited titania the absorption spectrum is shown above in Figure 40. The samples of platinized-titania included PBT have a lower absorption than the P25 titania included samples. This decrease may be due to several factors, but it is likely due to the decreased film thickness of similarly loaded films, as shown from the profilometry results. For the highest loading sample (323s), the peak position is similar to the other two loading conditions; located at 478nm. There is a shift in the absorption peak position of the lower loaded samples, and the increase in peak position with increased loading is also seen in these films. The peak position relative to baseline PBT is lower, at 469nm, which would indicate an overall increase in band gap of the TiO<sub>2</sub>:Pt included polymer composite. These peak position values may be within experimental error, and will be further analyzed in the next chapter (Section 4.3.3), in which higher loading of titania are investigated.

### 3.3.5 ICP-MS

ICP-MS was conducted on samples from an assortment of geometric areas of polymer loaded TGP-H-030. The samples were dissolved in 100°C 18M H<sub>2</sub>SO<sub>4</sub> for a duration of one week. The dissolved titanium content was diluted in 18 MΩ H<sub>2</sub>O and compared with a calibration curve of set amounts of dissolved TiO<sub>2</sub> in similarly diluted 18M H<sub>2</sub>SO<sub>4</sub>. The plot of the calibration curve for titanium (isotope 49) versus diluted titania ion content is shown in Appendix T-3.

The results were measured on an ELAN 6000 inductively coupled plasma-mass spectrometry system, and the amount of included titania in the composite films can be seen in Figure 41:

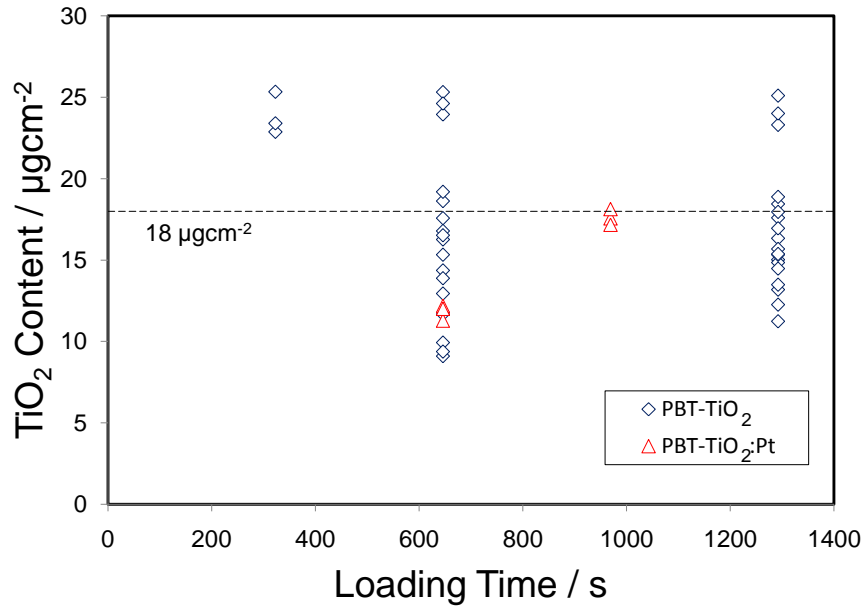


**Figure 41 - Titania content as determined by ICP-MS of various loading times for composite films of PBT-TiO<sub>2</sub> and PBT-TiO<sub>2</sub>:Pt films loaded on TGP-H-030. Line is added for illustrative purposes and indicates the average loading.**

The particulate loading of the films did not follow the expected increasing linear trend of increasing titania content with increased loading time, as with thicker films one would assume to find a larger titania inclusion. This result however does agree with the work of Beck and Dahlhaus [85] who found that the degree of incorporation of the nanoparticle content is directly proportional to the degree of mixing while the polymer is being loaded, albeit for a differing polymer composite system. Since our system was sonicated prior to loading, and not during loading, we should expect to find a decreasing nanoparticulate content with extended loading, as the nanoparticulates settled out of suspension from the unperturbed loading solution during polymerization. Although the variation in the data seems large, at these low nanoparticle loadings the incorporation of titania will vary with the film deposition method and this may also account for the variability in the results. Our recent findings regarding more highly nanoparticle included films also agree with the work of Beck and Dahlhaus and will be discussed in the following chapter, but for the current discussion the particle inclusion of all the prepared composite films was found to be approximately  $18 \pm 5 \mu\text{gcm}^{-2}$  on average.

### **3.4 Photoelectrochemical Results**

The films prepared on TGP-H-030 were assembled in the photoelectrochemical cell and tested under galvanostatic operation at different current densities. It was observed that the anodic operation of the counter electrode was stable and unchanged with current density from film to film (for the cathode), as expected since the anode was not changed. This observation was made by measuring the anode potential versus the reference electrode. The results reported for cathodic polarization and reaction to illumination for different films are not differently affected by the anode. The average anode potentials are shown for each of the

composite and baseline PBT systems as shown in Figure 42, simply to show the variation (see error bars) in measurements between runs.

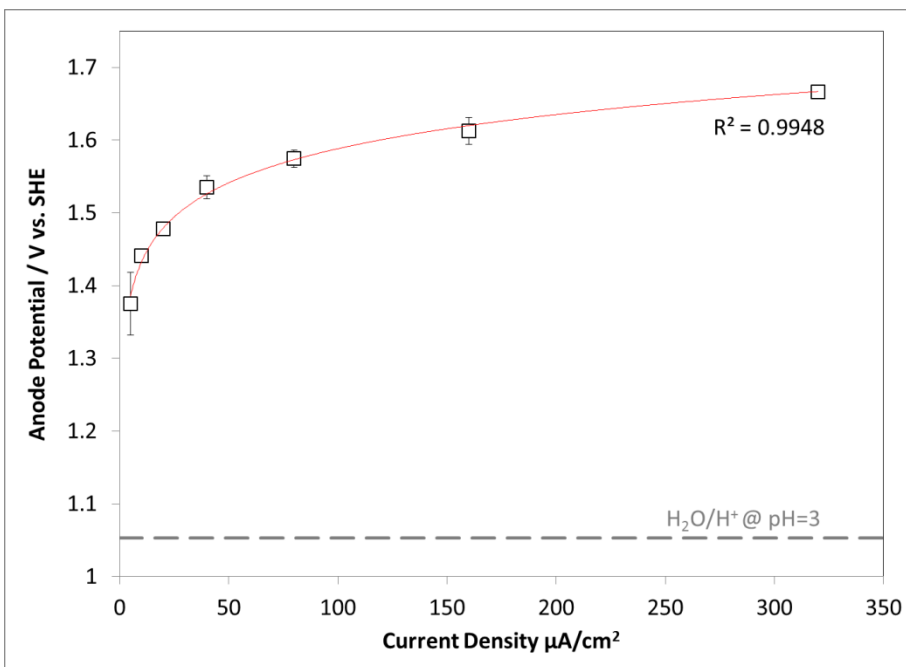


**Figure 42 - Average Anode Potential for Electrolysis. Logarithmic trendline added to indicate Tafel correspondence.**

It can be seen that when a logarithmic trendline is fit to the anode data, the regression matches the data very well.

In terms of a benchmark for comparison to analyze the performance of our system, several references were chosen to reflect real-world operating conditions. The first benchmark chosen was that of the redox potential for hydrogen generation as a function of pH, which acts as a reference point for the photonic activity of the surface. When the reaction proceeds at a potential which is less than the thermodynamically calculated redox potential, the energy supplied by the irradiated film provides the potential difference needed to facilitate the reaction. From the potential difference of the illuminated vs. dark reactions we can also

calculate the energy collected and can gauge the total overall incoming photonic conversion efficiency (IPCE). The second benchmark chosen was that of a bare TGP-H-030 substrate, to reflect the worst case scenario of a non-catalyzed reaction. The third benchmark chosen reflects a best case scenario, a very high loaded platinum black catalyst spray loaded with 15% Nafion monomer on TGP-H-030. Other amounts of platinum are plotted for comparison, with the results also tested at several different operating temperatures.

### 3.4.1 Standard Cathode Function – Platinum and Blank TGP-H-030

As described above, real world baselines for electrolysis catalysts are compared with the blank substrate in order to establish some baseline values. Variation of  $\text{mgcm}^{-2}$  Pt spray loaded on TGP-H-030 are shown below in Figure 43, as well as for a  $0 \text{ mgcm}^{-2}$  baseline (Blank TGP-H-030):

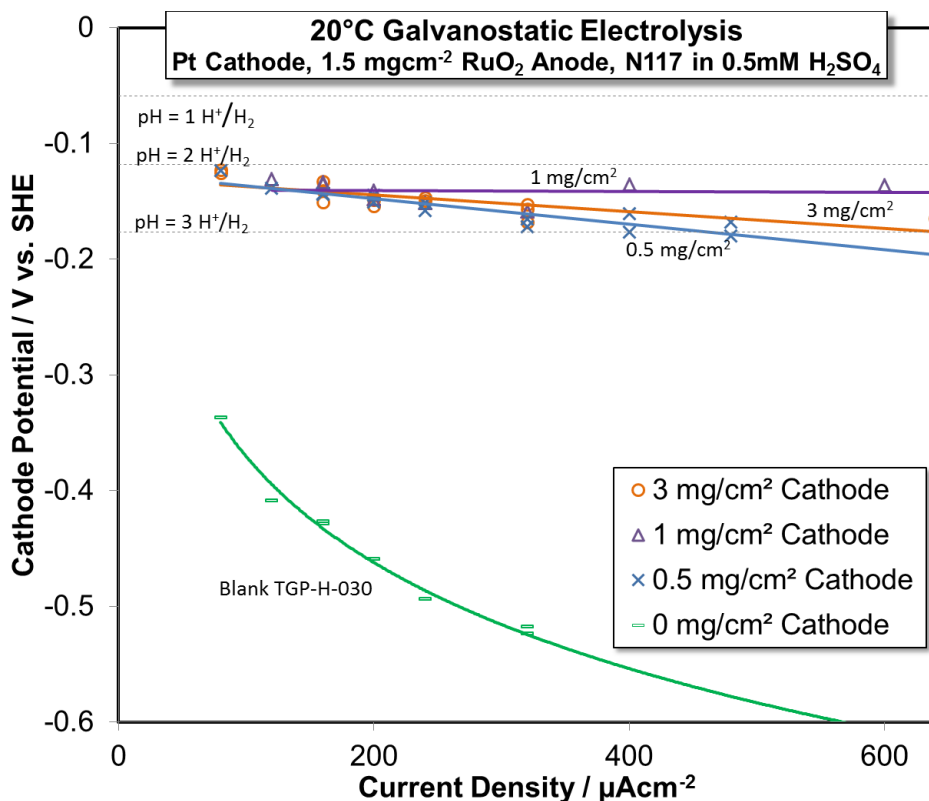
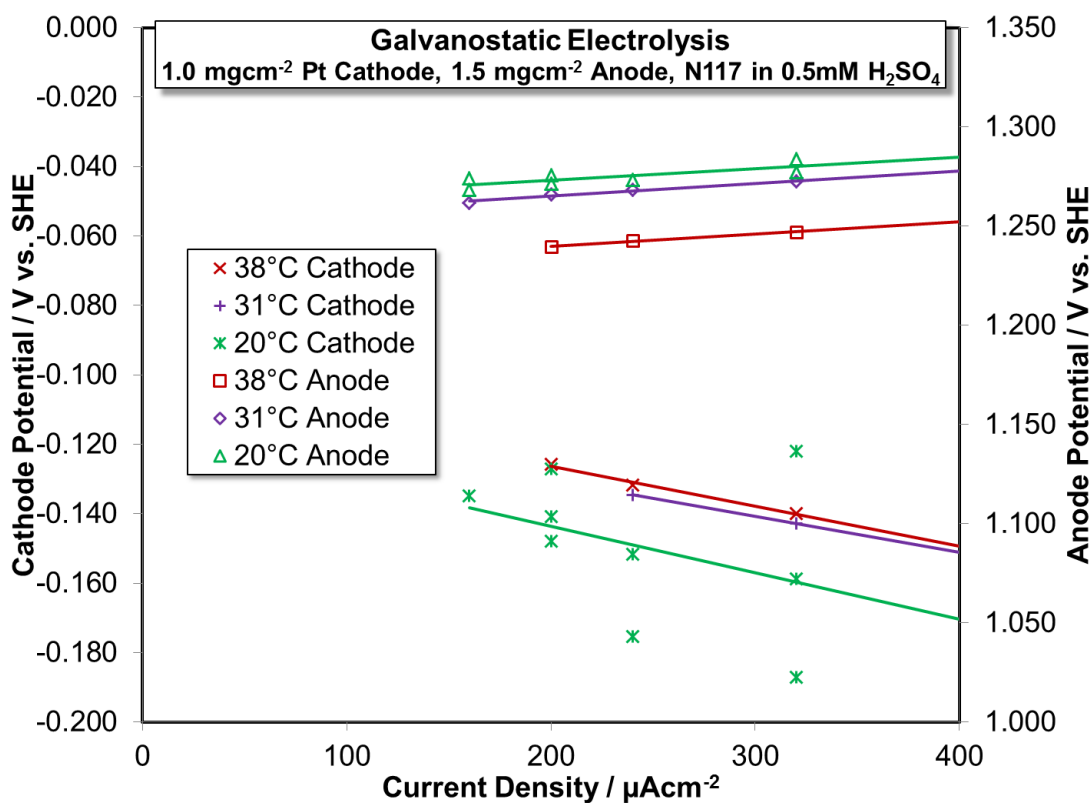


Figure 43 - Baseline and Platinum Cathode Performance. **Logarithmic trendlines added to indicate Tafel correspondence.**

It can be seen that for our system there exists an optimum loading of platinum spray loaded on to the substrates. Since the depositions were made with platinum black and not carbon supported platinum it is thought that the accumulation of Nafion binder may be responsible for the decrease in performance that we see at higher loadings. It seems that the optimum performance was found when a loading of  $1 \text{ mg/cm}^2$  was used as the catalyst with 15 w.t.% Nafion binder, although more repetitions of this experiment would need to be conducted to confirm this result experimentally as the results had a large variance.

In order to check the validity of our measurements, we also ran the same experiments at higher temperatures. It can be seen from the following plot (Figure 44) that the results presented above are confirmed by improvements with higher temperature measurements, as performance increases with increased temperature as expected. As the temperature increases as does the activity of the catalyst, and this is shown by a reduction of overpotential losses at each electrode.



**Figure 44 - Spray deposited platinum (1.0 mg/cm<sup>2</sup>) electrolysis results with temperature variation. Logarithmic trendlines added to indicate Tafel correspondence.**

It was also found that there was a transient behaviour of the cathode performance at low current densities. Cathodic potential data for lower current densities drifted and did not allow for steady state galvanostatic measurement. This suggests another cathodic function regarding electron transfer, most notably pseudocapacitive hydrogen adsorption, otherwise known as hydrogen underpotential deposition. This deposition would transfer electrons to surface adsorbed hydrogen, flooding the surface with an adsorbed hydrogen species at potentials greater than 0 vs. SHE. This is typical for a platinum surface, and these peaks can be seen from a typical cyclic voltammogram [94] as occurring at 0.1 and 0.23V vs. SHE as shown in Figure 45:

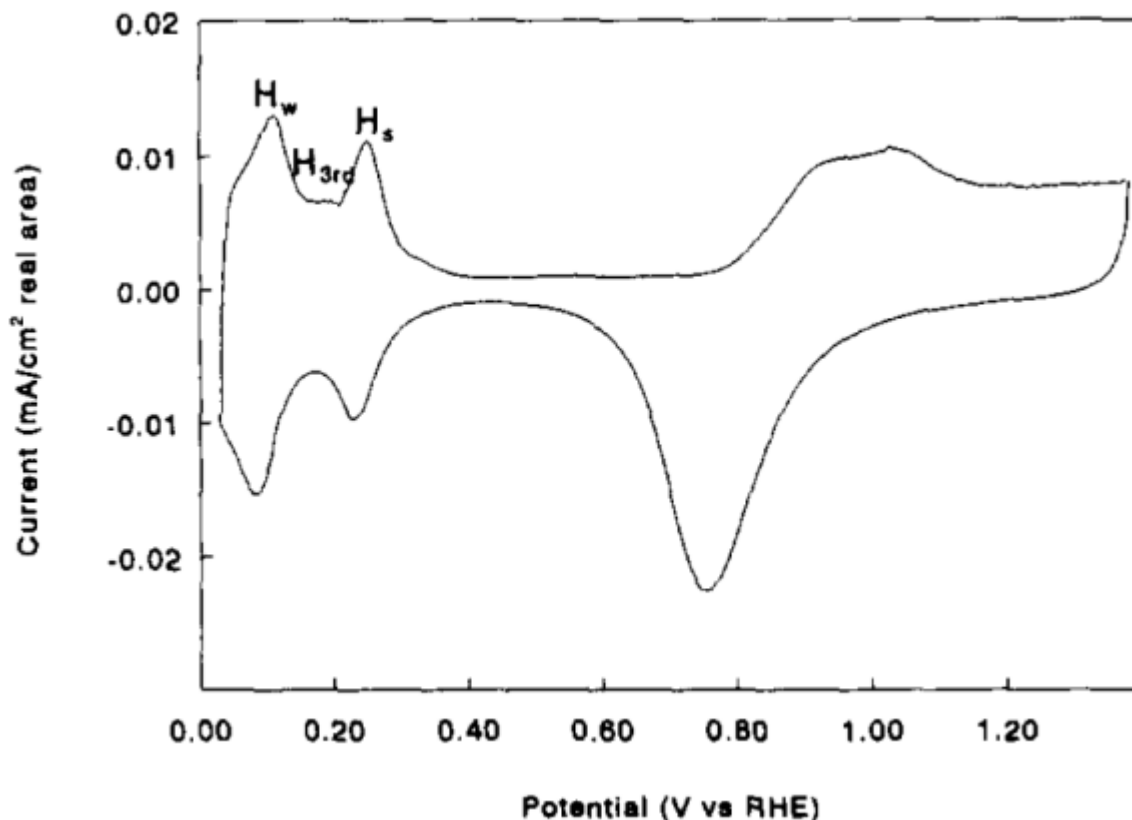


Figure 45 - Cyclic voltammogram of platinumized platinum in 0.5M H<sub>2</sub>SO<sub>4</sub>,  $\nu = 10\text{mV/s}$ . [91] Reprinted with permission from *Electrochimica Acta*.

### 3.4.2 PBT Cathode Function

The 646 s and 1292 s loadings of PBT were tested at 20°C under dark and illuminated conditions. The results can be seen in Figure 46. For the 646 s loading it appears that the PBT sample performs poorly, and is comparable to the performance of the blank TGP-H-030 substrate in the dark within experimental error. The error bars presented represent the standard deviation of the measured data points. It appears that the PBT sample is a poor catalyst substrate for the hydrogen generation reaction. When the loading of PBT is increased to 1292 s however, the performance of the electrode increases as well. This performance increase is statistically significant and detailed in Appendix U-1. This increase

in performance indicates that there is a catalytic effect of the base PBT film. A comparison of the overall electrochemically active area would need to be determined, as a thicker film can perform better simply due to an increase in effective nanostructural surface area. Determination of an active surface is difficult to estimate in a mixed phase system with partial surface coverage such as ours, due to preferential areas of catalysis. Therefore the device performance was left as measured by geometric device area. Upon illumination both thicknesses of the PBT films had significant performance increases, and as expected the potential difference between the illuminated and dark current is greatest at lower current densities and decreases until a saturation limit is reached. This saturation limit is akin to the short circuit current density of solid state devices. It is interesting to note that both the 646 and 1292 s films had the same potential difference decrease regardless of the larger film deposition for the 1292 s sample. This result is likely caused by the random loading in the porous TGP-H-030 substrate. Since the photonic beam path arrives from only one direction it will not activate film loaded in the internal pores and/or on the backside of the TGP-H-030 carbon fibres. Therefore increased loading should be placed where it can be contacted by the beam. This may require a different substrate and/or film loading approach.

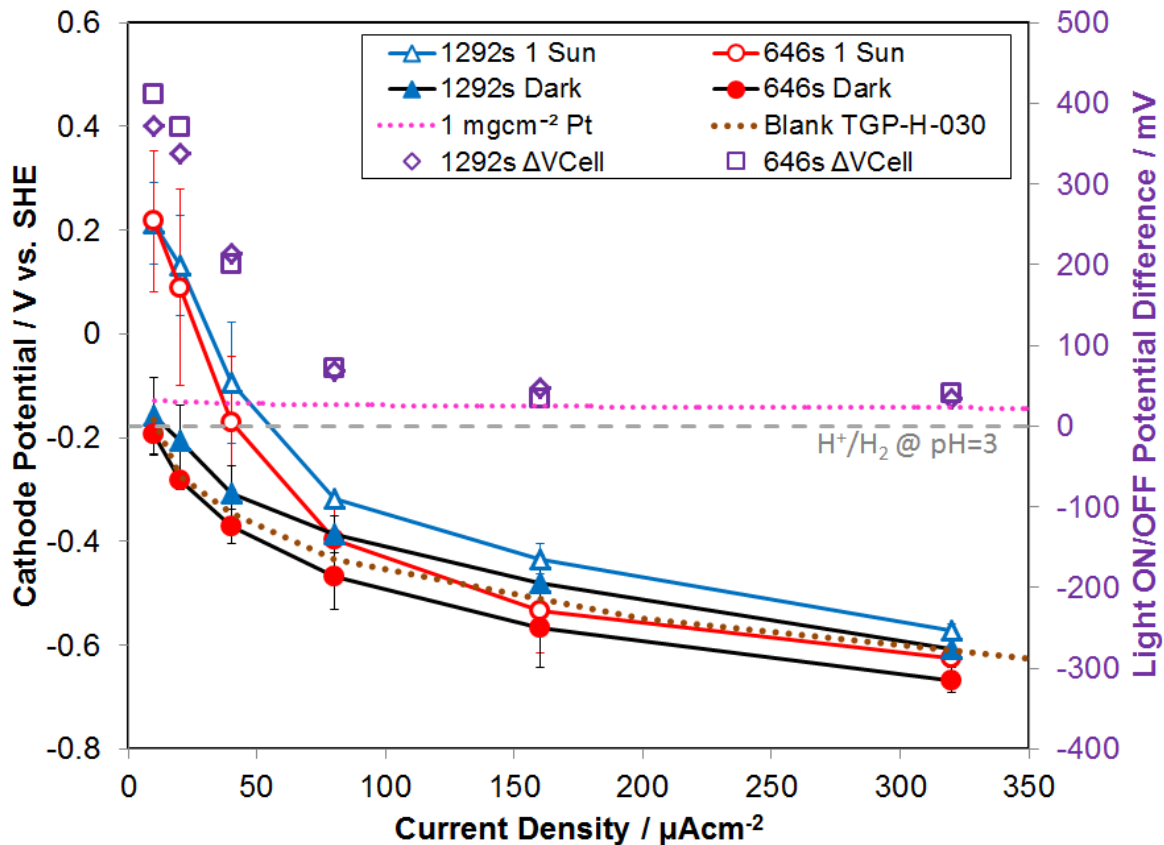


Figure 46 - Cathode polarization and light on/off potential difference for 646 s and 1292 s loadings of PBT films coated on TGP-H-030. Benchmark plots indicated with lines added for illustrative purposes.

### 3.4.3 PBT-TiO<sub>2</sub> Cathode Function

Figure 47 shows the better performing 1292 s loadings of PBT compared with a similar 1292 s loading of PBT-TiO<sub>2</sub> for testing at 20°C in dark and illuminated conditions.

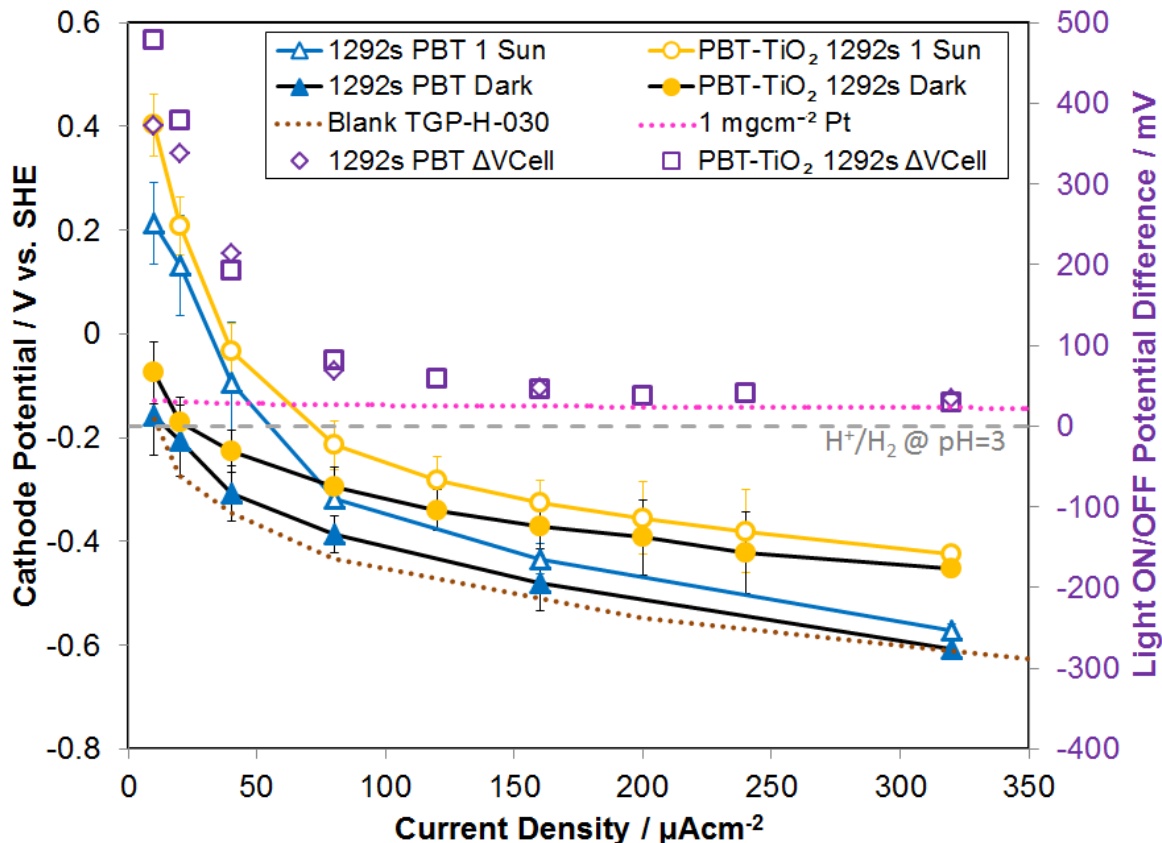


Figure 47 - Cathode polarization and light on/off potential difference for 1292 s loadings of PBT and PBT-TiO<sub>2</sub> films coated on TGP-H-030. Benchmark plots are indicated with lines added for illustrative purposes.

It can be seen that a PBT-TiO<sub>2</sub> composite performs far better than solely a PBT based film, but is still far less electrocatalytically active than the not optimized 1 mg/cm<sup>2</sup> Pt loading at higher current densities. A statistical analysis of the PBT vs. PBT-TiO<sub>2</sub> films is detailed in Appendix U-2, and the error bars presented represent the standard deviation of the measured data points. The similar deposition thickness/weight and roughness of the polymeric film for PBT and PBT-TiO<sub>2</sub> suggest the electrochemical performance improvement is due to a synergistic effect between the TiO<sub>2</sub> inclusions in the PBT film, as the film is not significantly altered with the exception of nanoparticle incorporation. The films performed similarly

under illumination, and the sharp drop off in illuminated performance can again be attributed to the poor substrate architecture. The PBT-TiO<sub>2</sub> films did show a larger illuminated versus dark potential difference at low current densities, attributed to the inclusion of the larger bandgap nanoparticle inclusions. More work is discussed in the following chapter (Chapter 4) regarding the variation in surface coverage and thickness of the deposited films.

Additional studies on more suitably electrochemically connected substrates are also examined in Chapter 5.

The light driven cathodic current at potentials more positive to the H<sub>2</sub>O/H<sub>2</sub> redox potential was shown, similar to the results for catalyzed silicon photocathodes detailed by Bookbinder et al. [53]. Hydrogen gas formation was evident on the surface of the cathode after the series of tests had been completed. The mechanisms of bubble formation and coalescence in this system are unknown, but the presence of the bubbles on the surface is a clear indication that the device is functioning as intended.

As discussed in the previous chapter (Chapter 2) there is a variation in our measured cell resistance with different ways of electrically connecting the samples to the power source, and with physical assembly of the membrane electrode assembly. There also exists a natural variation in resistance of the deposited films, as the deposition is random and represents an average measured value across the entire electrode area. These sources of resistance are difficult to separate. The variation in cell resistance and performance was investigated for the best performing baseline PBT-TiO<sub>2</sub> film, a 1292s loading. As shown in Figure 48, there is a significant performance variance in terms of photonic harvesting when the cell resistance changed.

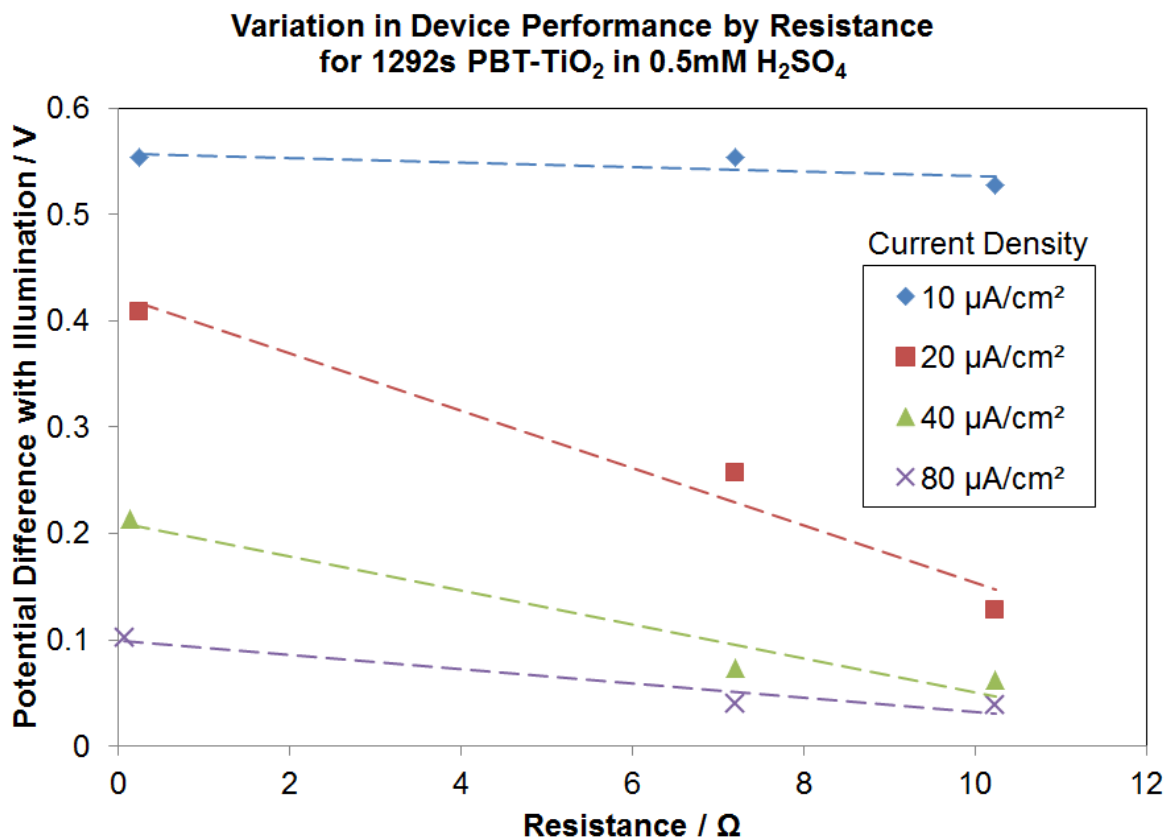


Figure 48 - Variation in photoresponse of 1292s loaded PBT-TiO<sub>2</sub> with a variation in cell resistance.

Lines are added for illustrative purposes.

This variation in performance with cell resistance was discussed in terms of ITO surfaces in Chapter 2 with respect to the work of Denhoff and Drolet [77]. Care must be taken when comparing samples of differing resistances, although effects of titania inclusion and sample thickness on resistance will affect this property. This variation will be discussed in more detail in the next chapter, although methods for improving this resistance are simple and include: increased conductivity of the composite films, and reduced film thickness. The electrochemical results presented in this chapter represent the baseline samples (both composite and base polymer) that had the best performance (and corresponding lowest

resistances). In terms of any  $iR$  correction of these results, even with high cell resistances of up to  $10\ \Omega$  the correction would be small for the currents measured. At  $1\ \text{mA}/\text{cm}^2$  a  $10\ \Omega$   $iR$  correction would only amount to  $10\ \text{mV}/\text{cm}^2$ .

For another comparison of electrochemical performance with and without illumination, a sample of spray loaded  $\text{TiO}_2$  with Nafion was tested in order to get a perspective into the performance of a spray loaded titania based PEM electrolytic cell. The electrodes were made by creating a spray mask to narrow the spray loading of a 20% w/w Nafion ionomer - P25 ink to  $2\ \text{cm}^2$  circles on TGP-H-030. This spray was applied in the manner outlined in Chapter 2, and deposited to a loading of  $2\ \text{mg}/\text{cm}^2$ .

First, the cell was set up as before, but with a platinum mesh cathode, a Nafion 117 separator, and the spray loaded Nafion- $\text{TiO}_2$  electrode as the anode. This would serve to mimic the configuration of the Fujishima and Honda cell, albeit in our electrochemical cell and with an SPE at our electrolyte separator. The results are shown in Figure 49 with error bars presented that represent the standard deviation of the measured data points.

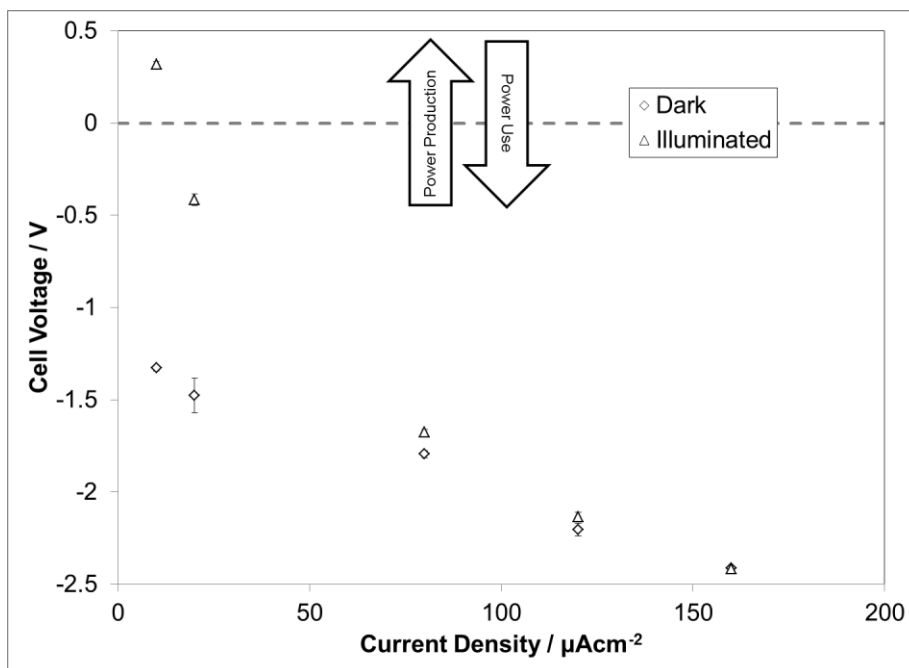


**Figure 49 - Dark and illuminated cell performance of a spray loaded Nafion-TiO<sub>2</sub> on TGP-H-030 anode with Pt mesh cathode, separated by N117 in 0.5 mM H<sub>2</sub>SO<sub>4</sub>.**

It can be seen from the above plot that at the lowest current density (10  $\mu\text{A}/\text{cm}^2$ ) the cell not only provides direct water splitting, but the cell has an excess of power, as shown by its positive cell voltage. By using an interpolation between the 10 and 20  $\mu\text{A}/\text{cm}^2$  values we can determine that under solar irradiance with no bias (cell voltage of 0V) the cell would run at a steady state of  $\sim 14 \mu\text{A}/\text{cm}^2$ . The change in potential with solar adsorption with increased current density for this P25/Nafion film is shown in Figure 50. The corresponding potential difference between the illuminated and non-illuminated cell is 1.393 V at the current density of 14  $\mu\text{A}/\text{cm}^2$ . This is a potential difference that would correspond to the redox potential difference of 1.229 V as well as accommodating an overpotential of 164 mV. The rapid decrease in solar energy harvest is likely on account of the applied film structure. With spray deposition of titania and Nafion it is expected that there will be some conductivity losses by

using Nafion ionomer as a binder. This is illustrated in the rapidly descending cell potential as shown in the non illuminated cell (Figure 49), with an overall cell voltage of less than -2 V at a current density of 100  $\mu\text{A}/\text{cm}^2$ . This overpotential is not a product of the cathode overpotential, as it is comprised of a highly catalytic platinum wire mesh and thus the losses originate at the anode. Obviously if more work is to be done on this type of system, optimization of titania particulate size and shape, as well as ionomer content should be examined.

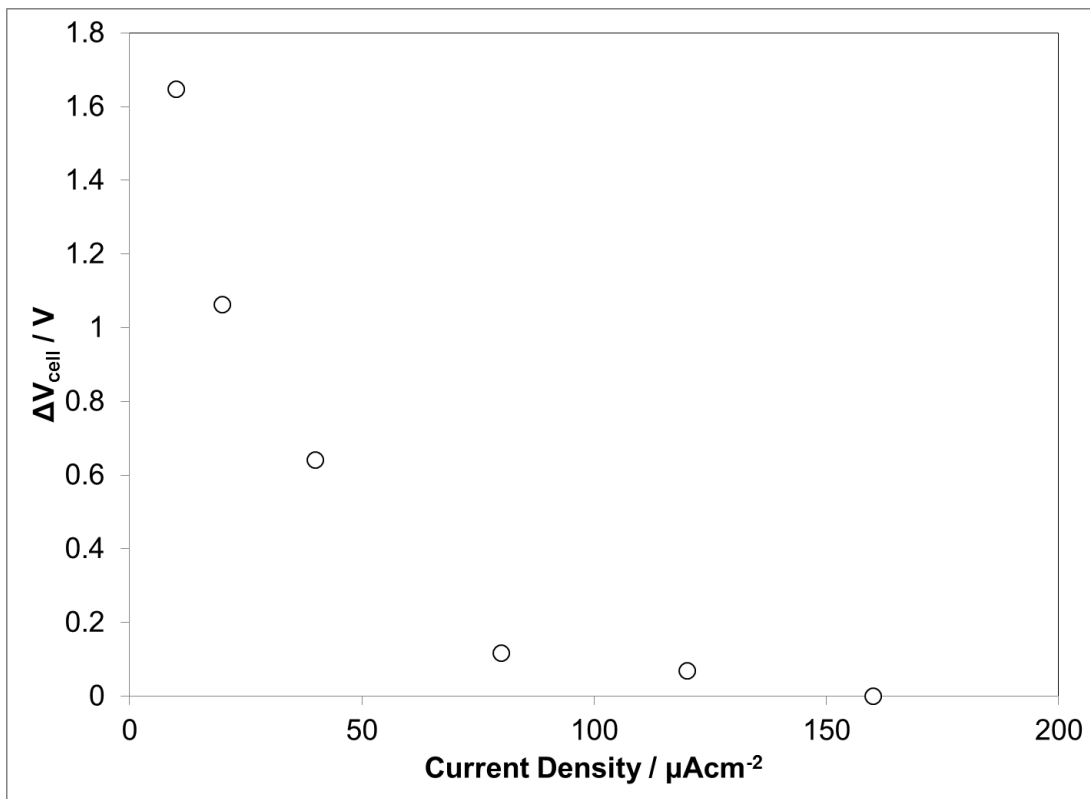


**Figure 50 – Cell potential change with solar irradiation for a spray loaded Nafion-TiO<sub>2</sub> on TGP-H-030 anode with Pt mesh cathode, separated by N117 in 0.5 mM H<sub>2</sub>SO<sub>4</sub>.**

The spray loaded Nafion-TiO<sub>2</sub> electrode was also tested as a photocathode with no PBT. It was expected that the cell would perform very poorly, and as shown previously the conductivity of the films severely limited the performance. The cell was set up with the spray loaded Nafion-TiO<sub>2</sub> electrode as the cathode, a Nafion 117 separator, and a standard 1.5 mg/cm<sup>2</sup> spray loaded RuO<sub>2</sub> on CFP as the anode. This would serve to mimic the configuration of our junctioned PBT-TiO<sub>2</sub> cell, albeit without the PBT ‘p-type’ component in the junction. The results are as shown in Figure 51.

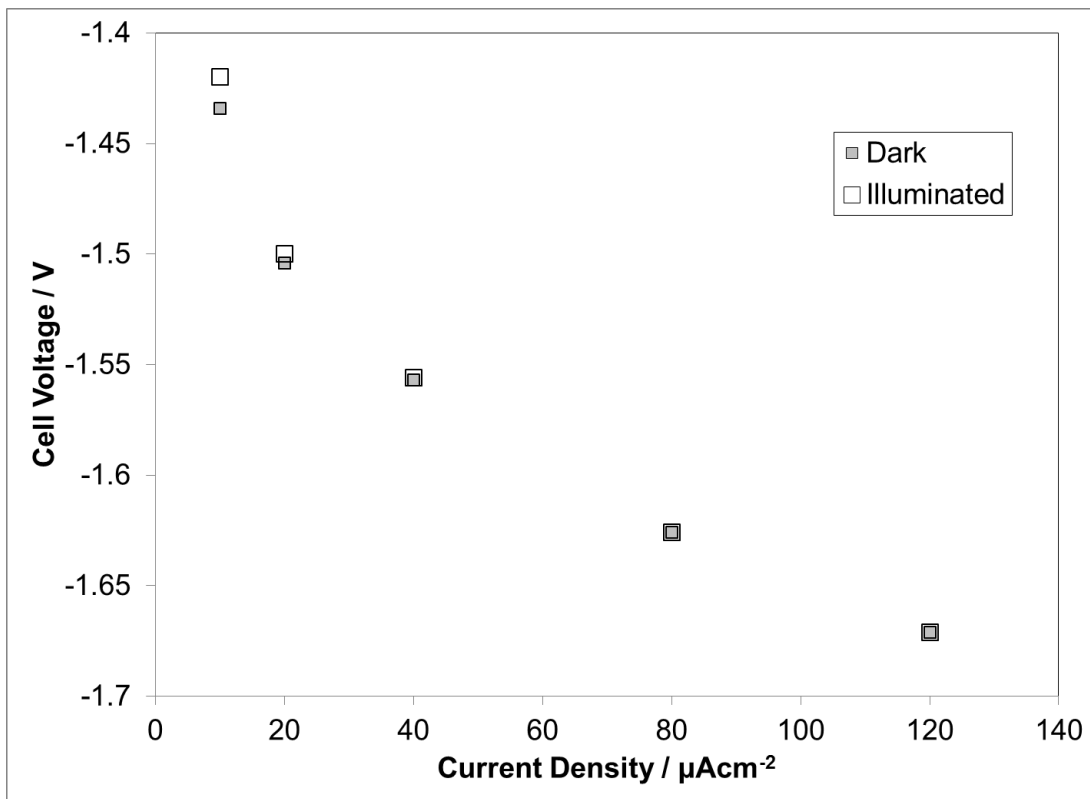


**Figure 51 - Dark and illuminated performance of a spray loaded Nafion-TiO<sub>2</sub> cathode on TGP-H-030 with a 1.5 mg/cm<sup>2</sup> RuO<sub>2</sub> anode separated by N117 in 0.5 mM H<sub>2</sub>SO<sub>4</sub>.**

As can be seen there is little to no solar response in using the spray loaded titania films as a n-type element on the cathode side. Additionally, the potential of the cathode at  $120 \text{ uA/cm}^2$  was approaching the dissolution potential for titania ( $-0.502 \text{ V vs. NHE}$ ). It is for both of these reasons that titania is considered unsuitable as a cathode catalyst for hydrogen generation on its own. Considering the performance of the anode side photoelectrode, i.e. the photoanode, (and the large anodic overpotential from the spray loaded titania there) titania is shown to be of little use in particulate form without the junction with PBT.

#### **3.4.4 PBT-TiO<sub>2</sub>:Pt Cathode Function**

Figure 52 shows the 1292 s loadings of PBT-TiO<sub>2</sub> compared with a similar 1292 s loading of platinized PBT-TiO<sub>2</sub> and tested at 20°C in dark and illuminated conditions. It was hypothesized that the addition of a typical hydrogen evolution catalyst such as platinum in the film would lead to better performance.

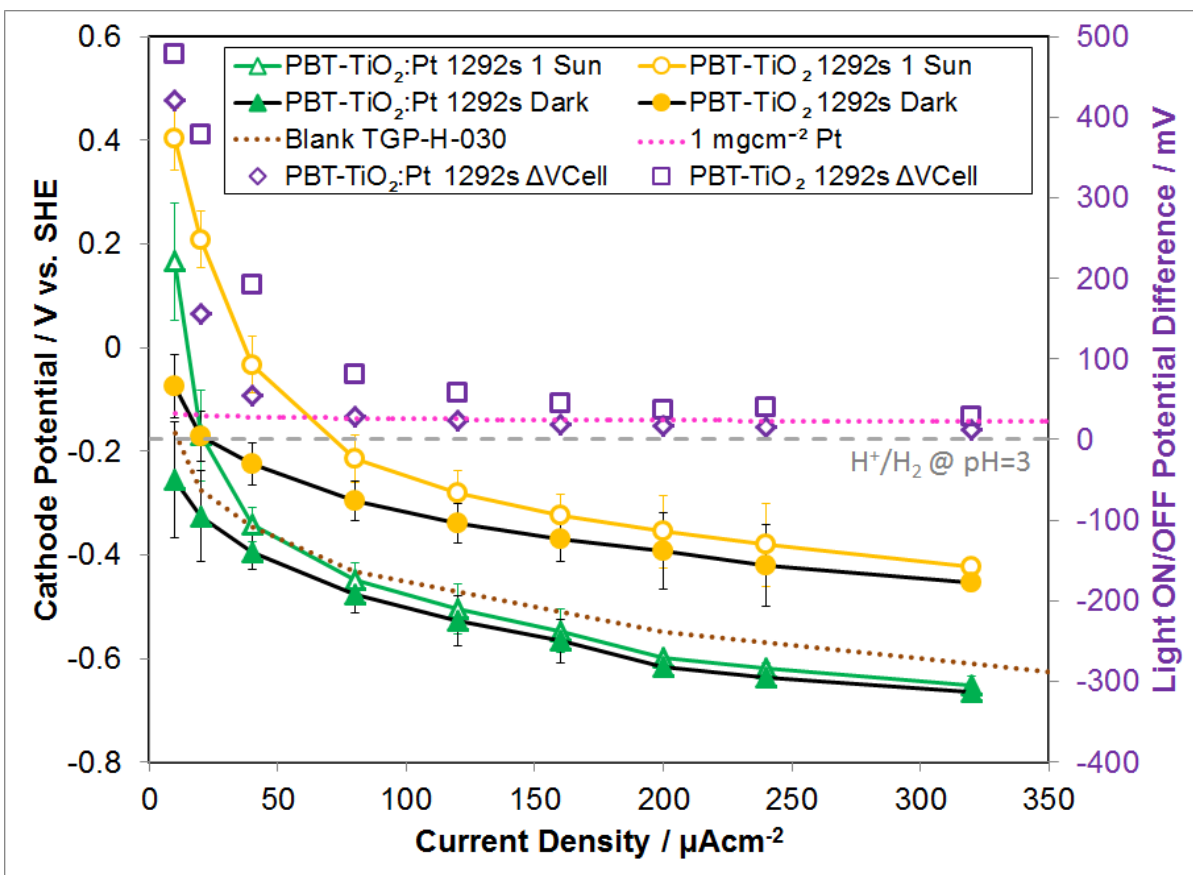


Figure 52 - Cathode polarization and light on/off potential difference for 1292 s loadings of PBT-TiO<sub>2</sub> and PBT-TiO<sub>2</sub>:Pt films coated on TGP-H-030. Benchmark plots indicated with lines added for illustrative purposes.

It can be seen that the inclusion of platinumized TiO<sub>2</sub> in the PBT films has an unexpected detrimental effect on the performance. A statistical analysis of the PBT-TiO<sub>2</sub> vs. PBT-TiO<sub>2</sub>:Pt films is detailed in Appendix U-3, and the error bars presented represent the standard deviation of the measured data points. Given the difference in particle size distribution, crystallinity, and phase composition of the included titania nanoparticles it is not necessarily a fair comparison as to the effect of platinum inclusion in these films. The P25 TiO<sub>2</sub> catalyst included in the PBT-TiO<sub>2</sub> films is known to be a highly active particulate photocatalyst, while the in-house prepared platinumized TiO<sub>2</sub> catalyst has not been fully characterized and may

have a different phase distribution (anatase/rutile). This phase distribution change may result in a less photoactive titania particle, and P25 is known to be highly photocatalytic due in part to the highly disorganized crystallinity. This result illustrates that even a small change in the nature of the included particles can have a dramatic effect on the composite film properties. It can be seen from Figure 52 that the photonic effect of the platinized TiO<sub>2</sub> drops off quickly, and this quenching of the photoactivity has yet to be explained. One possible explanation as discussed in Chapter 1 is that with the inclusion of Pt in polythiophene films the platinum acts as a catalyst for breakdown of the polymer, resulting in diminished performance. Another explanation is that the platinum sites interfere with the p-n junctioning of the polymer and titania nanoparticles, reducing separation of electron – hole pairs or providing enhanced recombination.

### **3.5 Conclusions**

Films loaded with TiO<sub>2</sub> nanoparticles were successfully developed through a repeatable *in-situ* loading of TiO<sub>2</sub> in PBT films by electropolymerization in propylene carbonate.

The PBT films alone were not conclusively shown to act as a catalyst for hydrogen generation, as there is some speculation as to the overall active electrochemical area available with increased film deposition. Further experiments to compare the electroactive surface area available are needed to clarify this result, and will be discussed in the following chapter.

The PBT-TiO<sub>2</sub> films were found to act as a better catalyst for hydrogen generation than PBT alone, and titania inclusion was found to potentially have a synergistic effect with PBT resulting in improved performance. Further work looks at the variation in surface coverage, film thickness, and TiO<sub>2</sub> content to fully examine this phenomenon and is discussed in Chapter 4.

The prepared films were used for photovoltaic assisted water splitting and reduced the energy needed to drive the cathode hydrogen reduction reaction up to a current density of about 75  $\mu\text{Acm}^{-2}$  for the 1292s PBT-TiO<sub>2</sub> film. When the IPCE was compared, it was found that the films had a peak performance at 240  $\mu\text{Acm}^{-2}$  which amounted to only 0.01% absorption efficiency. Although organic based reverse bias photovoltaic devices have typically exhibited low IPCE, it was deduced from observing no apparent increase in saturation of the photonic performance with increased film loading that the TGP-H-030 substrate was likely limiting efficiency the most, as its bulk porosity is not photon accessible. To address this issue, films were deposited on more dense sub-microarchitectural substrates, and these results are shown in Chapter 5.

## Chapter 4: Phase 2 – Tunable Inclusion Parameters

### 4.1 Introduction

The market price of platinum is a limiting factor in the adoption of fuel cell and conventional electrolytic devices due to its high cost and finite availability. Platinum is used in many chemical industries due to its unmatched nobility and its superior catalytic properties. The catalytic characteristics of platinum for electrochemical applications have been attributed to its well balanced volcano plot energy profile, with good attraction of reactants, efficient charge transfer, and swift release of products [95]. Platinum is well known as the premier cathodic catalyst in membrane based electrolytic devices. However, experiments have shown that composites of metal alloys with intermixed semiconductors have performed more efficiently due to intra-band electron coupling [96]. Close proximity of complimentary electronic states has also been shown to act as a hydrogen reduction catalyst, with composite mixes of polymeric catalysts with a Gore-Tex/ Poly-3,4-ethylenedioxythiophene(PEDOT)/ Polyethylene-glycol(PEG) system designed so that the reactant hydronium ion is drawn towards the surface with the PEG allowing effective charge transfer from the conductive polymer [97]. These results show good evidence that further research into the electrocatalytic effects of cheap, easy to process composites should be further examined as a replacement to platinum in hydrogen production systems.

As mentioned in Chapter 1, a suitable cathode for electrolysis in acidic media could be a composite of conductive polymer and  $\text{TiO}_2$ . This combination mimics the dual functionality of the PEDOT/PEG system with  $\text{TiO}_2$  providing good wettability to attract  $\text{H}_3\text{O}^+$  ions, and the conductive polymer providing an electronic conduit to the catalysis sites. This PBT- $\text{TiO}_2$  composite material has shown preliminary results indicated promising catalytic properties in

both dark and illuminated conditions as seen in Chapter 3. In keeping with our previous chapter, polybithiophene (PBT) was chosen as the conductive polymer matrix for our testing, as it has similar Head-Tail coupling symmetries to PEDOT, with predominantly to exclusively  $\alpha$ - $\alpha'$  coupled polymers respectively, ensuring good charge transfer properties [98],[99]. Using a variation in polymer/titania content and interfacial design variants the performance in a PEM electrolysis cell was examined. Films were loaded onto both flat substrates, similar to those reported for PEDOT-PEG 2-D films [97], and also porous carbon substrates (TGP-H-030), widely used in PEM fuel cell systems as the current best material for cheap 3-D area substrates. Different loadings of platinum black sprayed on TGP-H-030 using a Nafion binder, as well as blank TGP-H-030 substrates served as 3-D baselines for our system, and were detailed in Chapter 3. As the 2-D baselines for our system, E-beam deposited Pt on a flat 316SS metal substrate as well as blank 316SS substrates were used for comparison.

The films were placed in one of two configurations. The first configuration involved placing the film directly against the Nafion membrane, in an effort to ensure intimate triple phase contact. The second configuration, as studied in Chapter 3, facing the film to the open solution for direct irradiation. In our cell configuration this film placement allows for photonic bombardment, but should result in worse electrochemical performance, as triple phase contact is limited, especially in dilute acid concentrations.

In this chapter, the films facing the open solution were also examined in terms of their solar performance. Further examination into the effects of increased nanoparticulate inclusions was investigated and compared for various film thicknesses. These results were compared with similar variation in films loaded in the manner examined in Chapter 3.

As a summary, the variation in film examination in this chapter is split into the following divisions:

- 3-D vs. 2-D film loading variation
- Films facing the N117 membrane vs. films facing the solution/beam path
- Variation in composition and thickness altered by initial loading conditions
  - Sol w/w% titania and mixing intensity.

The observations of changes in performance were achieved through analysis of polarization data, high-frequency electronic impedance spectroscopy, and ex-situ resistance measurements. In addition, further characterization using profilometry, ICP-MS, and UV-Vis spectroscopy was conducted.

## **4.2 Experimental**

Low (0.1% w/w) and high (1% w/w) concentrations of  $\text{TiO}_2$  in the baseline loading sol were coupled with low intensity mixed (not-stirred) and high intensity mixed (sonicated) loading procedures. The  $\text{TiO}_2$  content in the loaded film was altered by changing the wt.% of  $\text{TiO}_2$  in the loading sol as well as by variation in stirring intensity of loading bath (by sonication) as described by Beck et al. [85]. Increasing the  $\text{TiO}_2$  content and increasing the energetics of stirring were shown to increase the  $\text{TiO}_2$  content in the loaded film. The films were loaded in a Teflon loading cell after sonicating the mixture for 60 minutes. Films were loaded immediately after their initial sol sonication for the non-stirred samples to ensure complete nanoparticle suspension. The nanoparticle content loaded into the films was determined empirically by ICP-MS after set loading amounts.

The details of the testing equipment, membrane assembly hardware and film loading protocol can be found in Chapter 2. Several testing variables were kept constant, with the flowrate of

recirculated catholyte set at 1 mL/min, the temperature set at 20<sup>0</sup>C, and the anode catalyst composition set at 1.5 mg/cm<sup>2</sup> RuO<sub>2</sub> on TGP-H-060.

### **4.3 Characterization Results**

The characterization techniques employed in this section are detailed in Chapter 2. The samples were characterized by profilometry to determine their thickness with loading time, ICP-MS to measure the included titania per loading time, UV-Vis to determine their spectral absorption with increasing loading time, SEM to analyze their surface morphology, and finally an ex-situ resistance measurement to estimate how the film conductivity changed with titania inclusion and film thickness.

#### **4.3.1 Profilometry**

For ease of film thickness characterization, films were deposited onto indium tin oxide (ITO) coated microscope slides (8-10 Ω/□) obtained from Delta Technologies (Stillwater, MN, USA). The slides were cleaned with a mild detergent and 18 MΩ de-ionized water rinses followed by a thorough rinse in isopropanol and dried. The films were deposited on to the middle area (625 mm<sup>2</sup>) of a 75 mm x 25 mm slide to allow for comparison of deposited film thicknesses. The profilometry results are presented below in Figure 53:

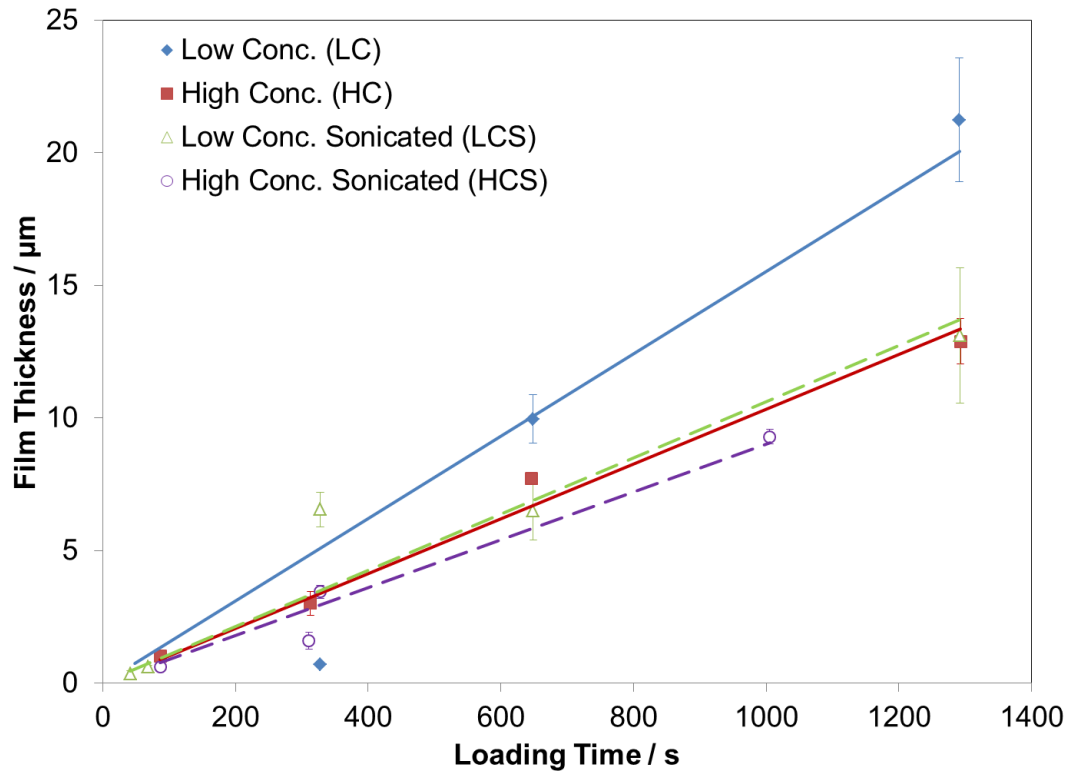


**Figure 53 - Variation of loaded film thickness by loading method and loading time. Lines are added for illustrative purposes.**

As can be seen from the above plot that as expected the film thickness increases with loading time for all of the film loading methods. When comparing the low concentration versus high concentration sols it can be seen that the higher concentration loading sols load more slowly. This can be attributed to the passage of charge needed to polarize the included nanoparticles. With an increase in nanoparticle sol concentration there should be an increase in composite included particles, but the particles in solution will not be of the same potential as that of the surface. The particles in solution will not have the same potential as the electrode, so when they are embedded into the composite, charge must be passed to polarize the included surface. Therefore, an increase of charge passage (i.e., imposed current) is needed to

polarize the electrode inclusions as they are loaded, as well as for polymerizing the film. When comparing the sonicated versus non-sonicated samples it can be seen that there is again a decrease in loading for the higher-included (sonicated) samples.

### 4.3.2 ICP-MS

The films were loaded on a masked 2.0 cm<sup>2</sup> circular area of TGP-H-030 carbon fibre paper and 1/8" diameter circles were punched from random areas of the deposited film. The punched samples were then dissolved in hot 18 M H<sub>2</sub>SO<sub>4</sub>. The dissolved titanium content was diluted in 18 MΩ H<sub>2</sub>O and analyzed with ICP-MS. The ICP-MS results are presented below in Figure 54:

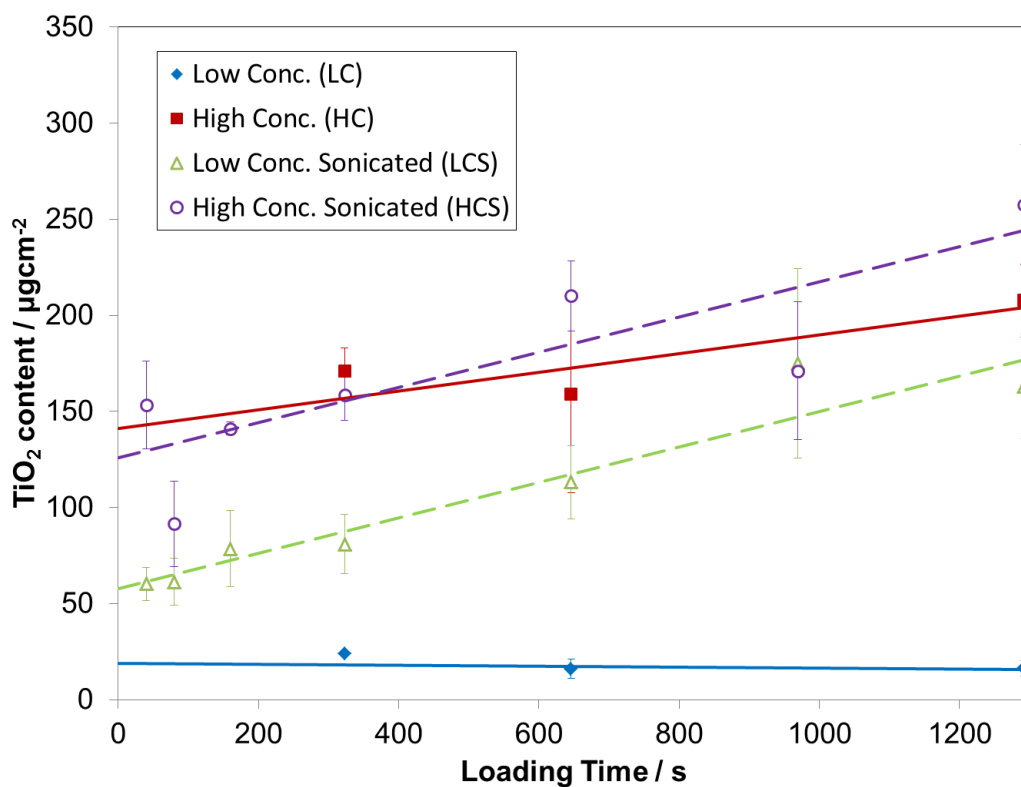


Figure 54 - Variation of titania content by loading method with increasing loading time. Lines are added for illustrative purposes.

As seen in the plot above, with an increase in sol concentration as well as with an increase in mixing intensity there is indeed an increase in nanoparticle inclusion in the deposited films. The included samples of the baseline loadings show little change with loading time, indicating that there is a change in the distribution of included particles, with particles loaded initially but then less loaded as the polymerization continues. This is explained by the fact that immediately prior to loading the solution was sonicated, but as loading proceeds there is a settling of the nanoparticles. This settling would reduce the kinetic energy of the particles, reducing the amount loaded into the polymer film. This same trend can be seen in the high concentration loaded film, although there is still a small increase at higher loading times, likely due to the increased concentration.

For both of the sonicated film loadings it can be seen that there is a direct correlation to the amount of nanoparticles loaded with the stirring intensity. This is seen as the slope of both the sonicated loading plots is equivalent. There is an increase in particulate loading with the higher mixing intensity.

Overall, this variation in sol concentration with mixing intensity and loading time shows that there is enough distribution in the loading procedure in order to tailor the films for differing titania inclusion. What is also noted is this variation may be a result of possible maldistribution in the film loadings, and this is confirmed by UV-Vis spectroscopy.

### **4.3.3 UV-Vis**

Samples prepared for UV-Vis absorption were analyzed for the high concentration non-sonicated and high concentration sonicated loading methods. The samples were again prepared on the ITO substrates acquired from Delta Technologies Ltd., sourced to overcome the limitations of the glass slides obtained from Solaronix S.A. Once again, a blank sample

was run as the baseline absorption case and for the deposited films absorption is reported as measured from this blank. The UV-Vis scan for the blank ITO slide is shown in Figure 55.

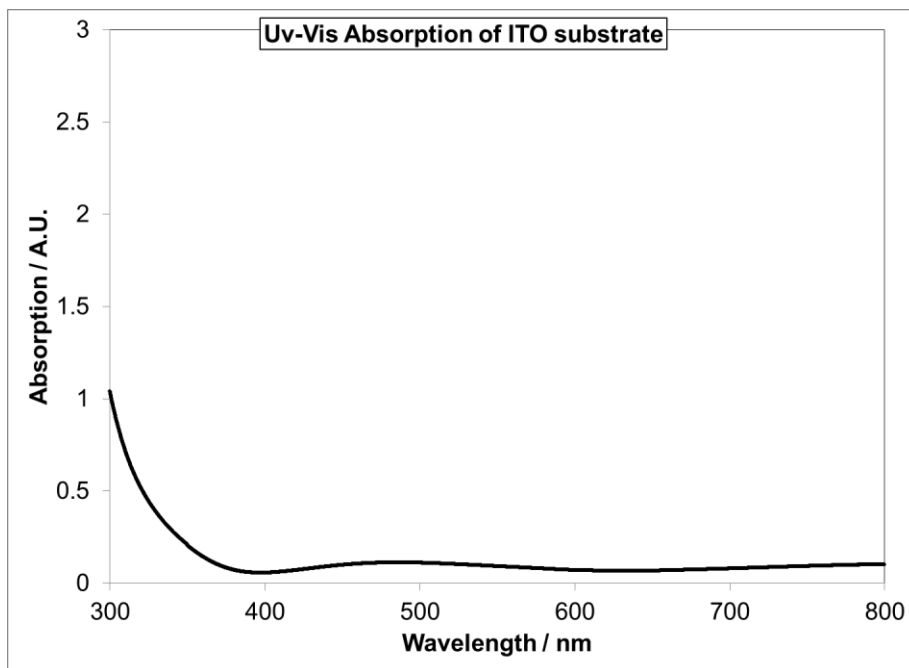


**Figure 55 - UV-Vis Absorption of blank ITO substrate**

The absorption spectrum for the high concentration loading sol is shown in Figure 56, and can be compared to the baseline UV-Vis analysis of PBT and PBT-TiO<sub>2</sub> samples shown in Chapter 3 (Figure 38 and Figure 39, respectively).

From the plots it can be seen that with the higher concentration loading a distinct peak in the ~300nm region, as well as the main peak at ~480nm are present. This peak at 300-350 nm is indicative of titania inclusion in the films. When the film loading increases, it appears that this peak is gradually red-shifted (as seen with the peak at ~350 in the 60s sample in Figure 56), indicative of a change in the composition of the deposited films with time. Although we know the peak position of titania, it is difficult to de-convolute the two absorption spectra in

terms of their absolute amounts, especially if the absorption peak of the polymer shifts with nanoparticle inclusion. At the highest loading time the smaller titania peak is completely enveloped by the more pronounced polymer peak.

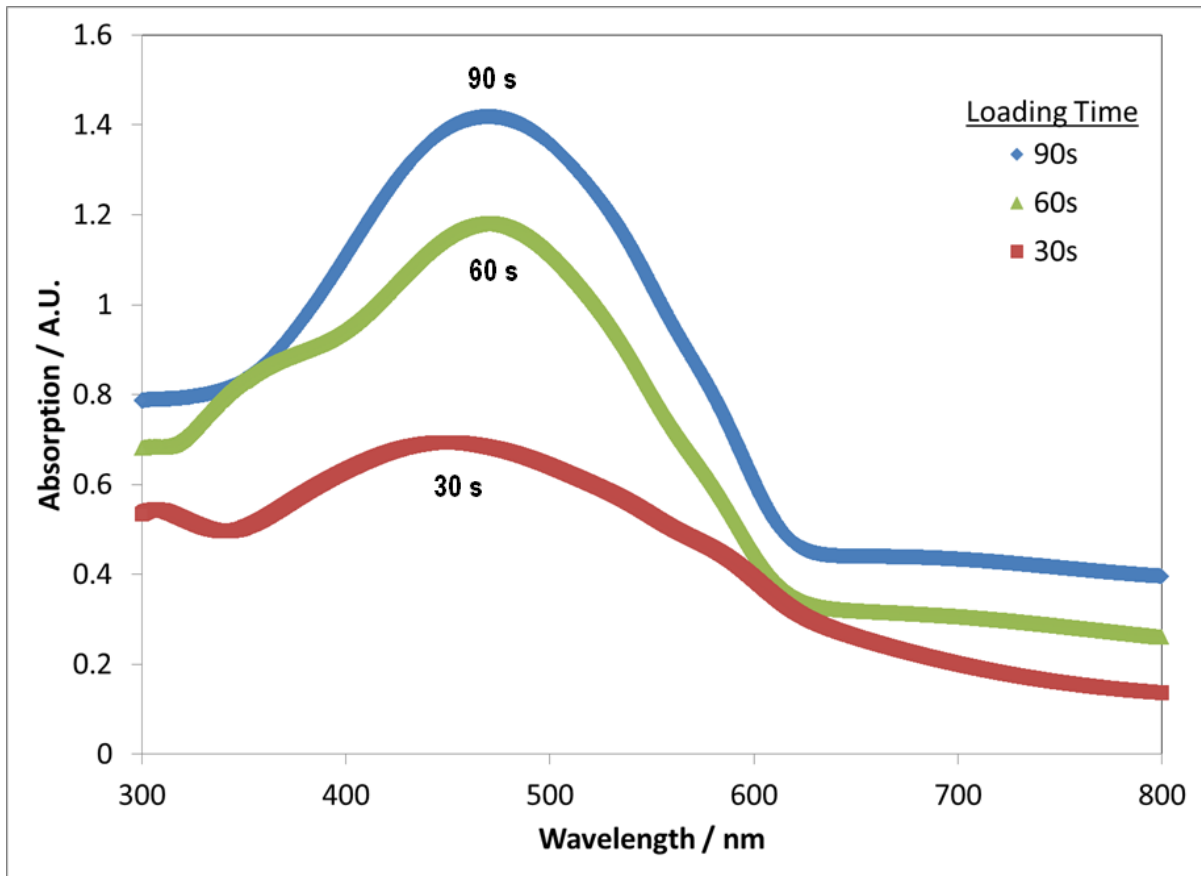


Figure 56 - High concentration sol PBT-TiO<sub>2</sub> UV-Vis absorption on ITO substrate

The absorption spectrum of the high-concentrated sonicated loading sol is shown in Figure 57.

It can be seen from comparing Figure 56 and Figure 57 that while there does also seem to be a red-shift of the titania inclusion in the high concentration sonicated samples with increased loading time, the peak is still most pronounced at the highest loading tested. This result

indicates that with the mixed samples (sonicated) the distribution of the nanoparticle inclusion is independent of loading time as there is no settling of the suspension with loading. Results from ICP-MS analysis as examined in Section 4.3.2 confirm this trend.

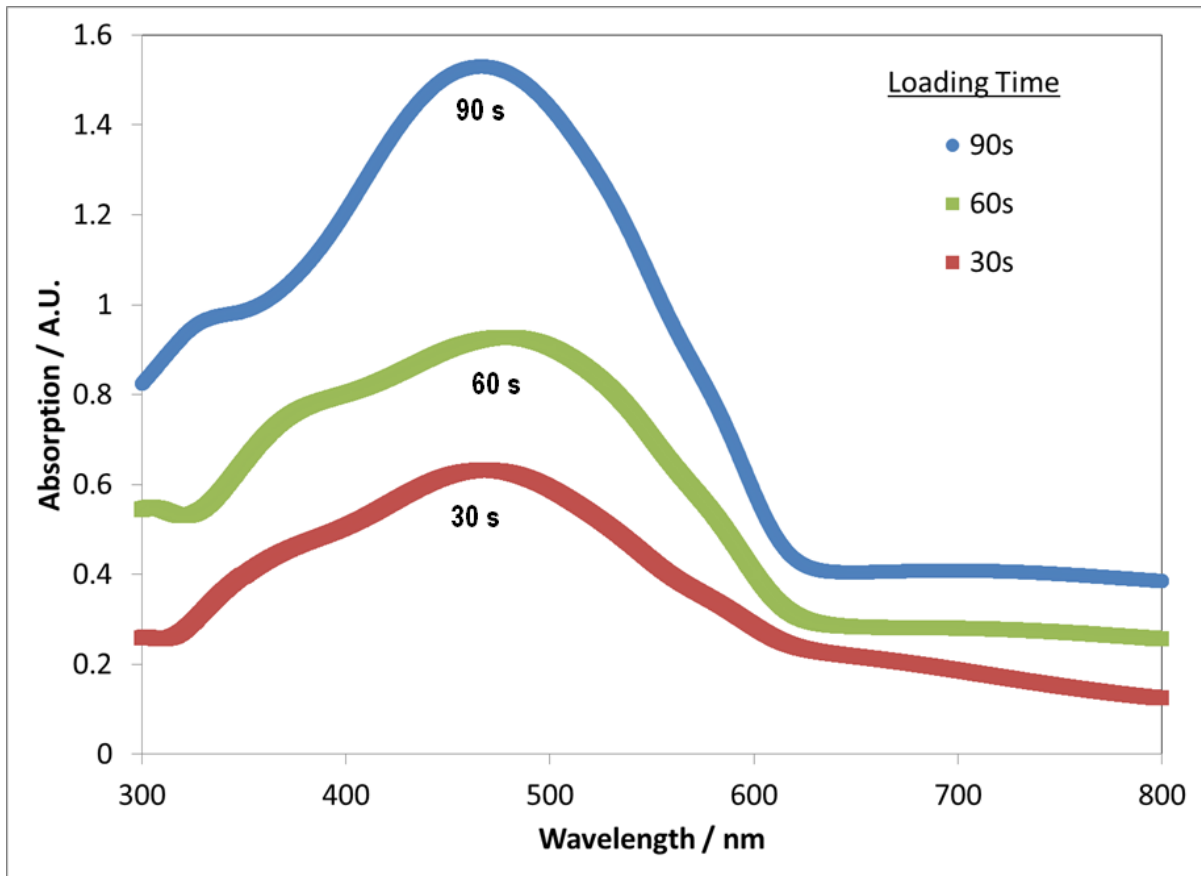


Figure 57 - Sonicated high concentration sol PBT-TiO<sub>2</sub> UV-Vis absorption on ITO substrate

One consideration regarding the spectral response with included nanoparticulate doping is the effect of clustering. With higher loadings of TiO<sub>2</sub> in thin organic films it is possible for regions of high concentration of titania to agglomerate and form larger domains. These larger domains should show up as a distinct spectral absorption peak, and this was seen most pronounced in the sonicated high concentration samples. The doping effects and peak

position shifts demonstrated by titania addition in Chapter 3 were not immediately present in the higher concentration TiO<sub>2</sub> included films, although they may be present but just not apparent due to convolution from the titania agglomerate spectral absorption.

Another possible source of error in this measurement is the effect of beam scatter by embedded nanoparticles. Beam scatter in absorption is more prevalent in higher nanoincluded samples and would report a higher absorption than is actually present.

Unfortunately without additional spectroscopic techniques, this scatter is difficult to quantify.

#### **4.3.4 SEM**

Efforts were made to enhance the SEM analysis to try to discern specific regions in the polymer composite. With questions regarding the through-plane distribution of nanoparticulate inclusions, the samples were dipped in liquid nitrogen and freeze-fractured by cleaving the frozen sample against a sharp aluminum block. It was hoped that by cleaving the samples and looking at the cross-sectional profile, regions of polymer versus titania could be separated. After several discussions with Derrick Horne, the SEM expert at the bioimaging lab at UBC, it was determined that with the analysis of backscattered electron emission versus secondary ion emission it may be possible to map out different electron dense or rich regions of the sample. After several attempts at identifying titania nanoparticles in the composite films it was decided that there was little difference between the nanoparticles and artifacts of the scan itself at the extreme focal length needed to identify the P25 particles. Therefore analysis of the cross-sectional films are of morphological importance only. EDX at the resolutions needed to determine individual nanoparticles (diameter 25nm) was too coarse to be performed conclusively as well.

Shown in Figure 58.a is the cross-sectional morphology of a 1  $\mu\text{m}$  high concentrated sol formed PBT-TiO<sub>2</sub> film magnified at 500X. This magnification was chosen to illustrate the overall coverage of the fibres. From the micrograph it can be seen that there is a random nucleation of the polymer composite on all sides of the carbon fiber substrate. The sample was mounted so that the composite loaded side is to the left, and there does appear to be a preferential loading on this open side of the sample.

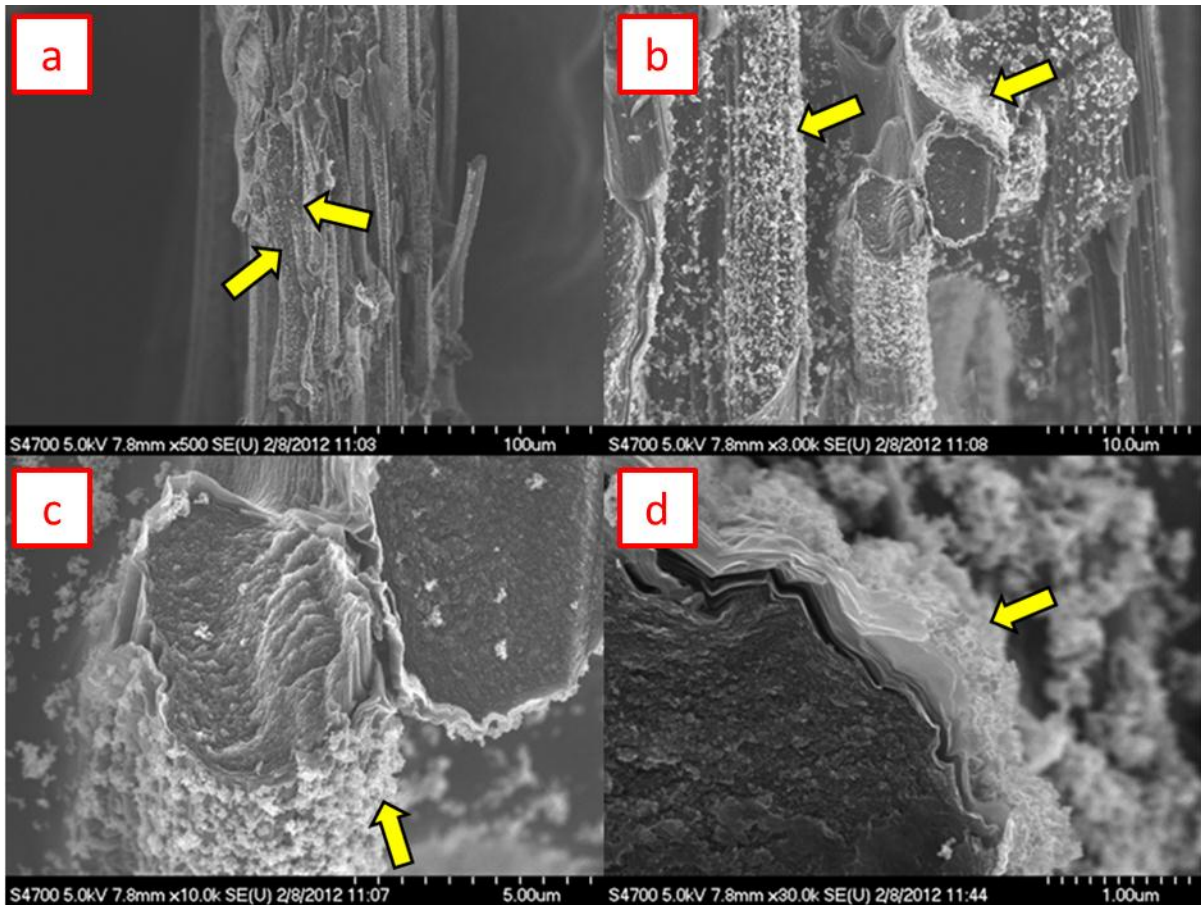


Figure 58 - Cross-sectional morphology of 1  $\mu\text{m}$  high concentration sonicated sol PBT-TiO<sub>2</sub> loaded TGP-H-030 measured at a) 500X, b) 3,000X, c) 10,000X, and d) 30,000X. Arrows highlight areas of composite deposition.

The random nucleated loading of the sample is more apparent in Figure 58.b. It can also be seen at this magnification that there are areas of bare carbon fibre substrate. This was deduced by examining the surface structure of the apparent bare fibres and comparing them to the bare micrographs as seen in Chapter 3.

The next micrograph shown in Figure 58.c is an even closer examination of the same sample area, viewed at 10,000X magnification. At this magnification it is possible to discern that when fractured there are some composite particles dislodged and these can be seen resting on the end of the carbon fiber. It was noted that the composite film had a very brittle structure, so that it would be expected that mechanical agitation would dislodge particles from the carbon fiber surface.

The final micrograph shown in Figure 58.d is a 30,000X magnification of the edge of a fractured carbon fibre. At the resolution of this micrograph it can be seen that with the fracture there is a delamination of the carbon fiber itself. Also, the film thickness of the deposited film seems to vary between 0.5-0.1  $\mu\text{m}$ . This is an expected result, as the distributed film structure will be deposited at random on the porous carbon network resulting in a film thickness less than the 1  $\mu\text{m}$  found for a flat surface. The 1  $\mu\text{m}$  deposited thickness measurement is for a flat plate and will be less on a distributed 3-D substrate.

In general, since the morphology of the polymer film is formed with a disordered nucleation and growth of polymeric nodes it is difficult to determine what is polymer and what is titania. The following micrograph is an image of one of the thicker 10  $\mu\text{m}$  films, once again from the sonicated high concentration loading sol. The image below (Figure 59.a) is again displayed at 500X magnification, in order to provide perspective on the distribution of loading.

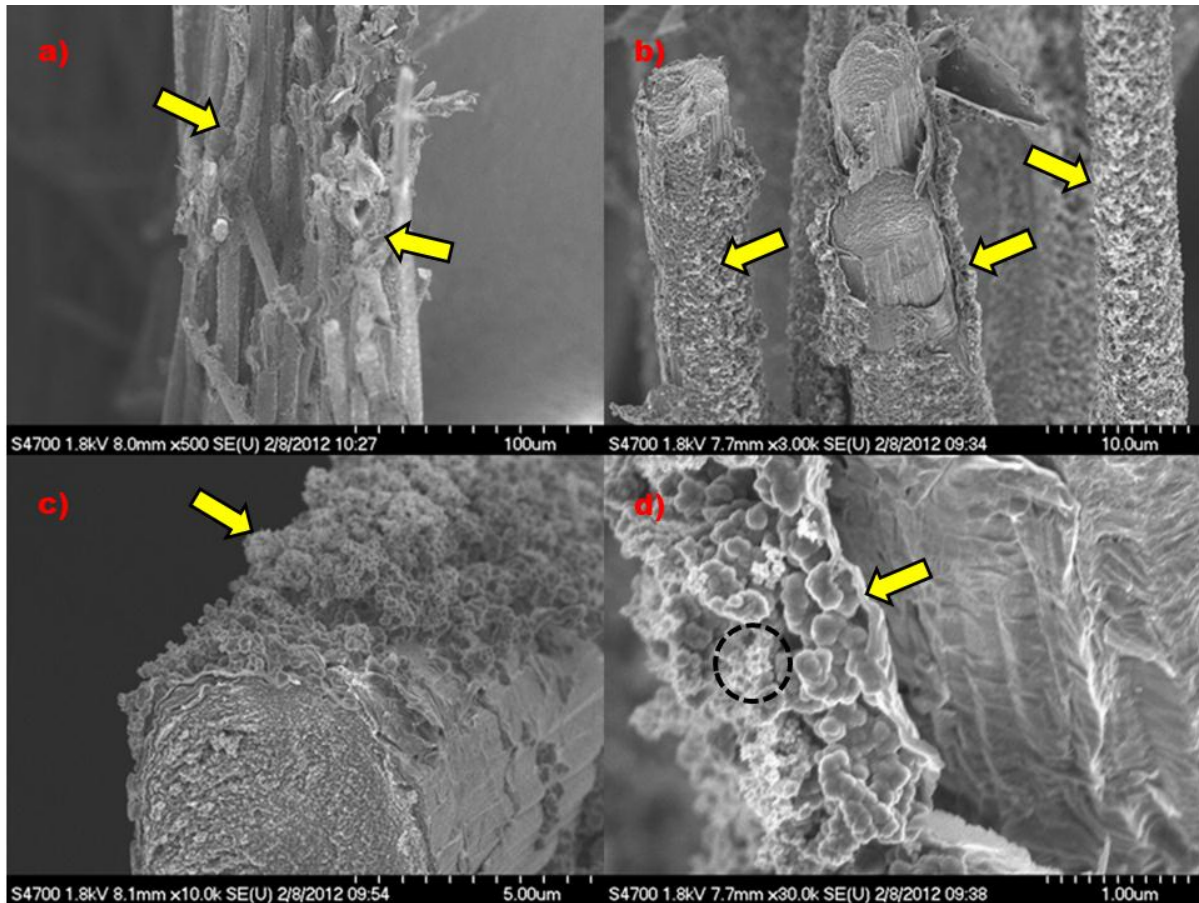


**Figure 59 - Cross-sectional morphology of 10  $\mu\text{m}$  high concentration sonicated sol PBT-TiO<sub>2</sub> loaded TGP-H-030 measured at a) 500X, b) 3,000X, c) 10,000X, and d) 30,000X. Arrows highlight areas of composite inclusion, dashed circle highlights area of titania concentration.**

It can be seen from the above figure that while there is a random nucleation of film with once again preferential composite loading on the ‘front’ side, there are also patches of high nucleation and growth at intersections. This preferred loading at positions of intersection was also seen in the lower loaded film thicknesses and likely forms some of the first nucleation sites due to lowered surface energy at edge sites.

Figure 59.b shows a 3,000X magnification of the image in Figure 59.a. With this micrograph it is apparent that the shell cladding of the polymeric layer is more complete compared to the lower loaded film, although there are still gaps in the polymer composite film.

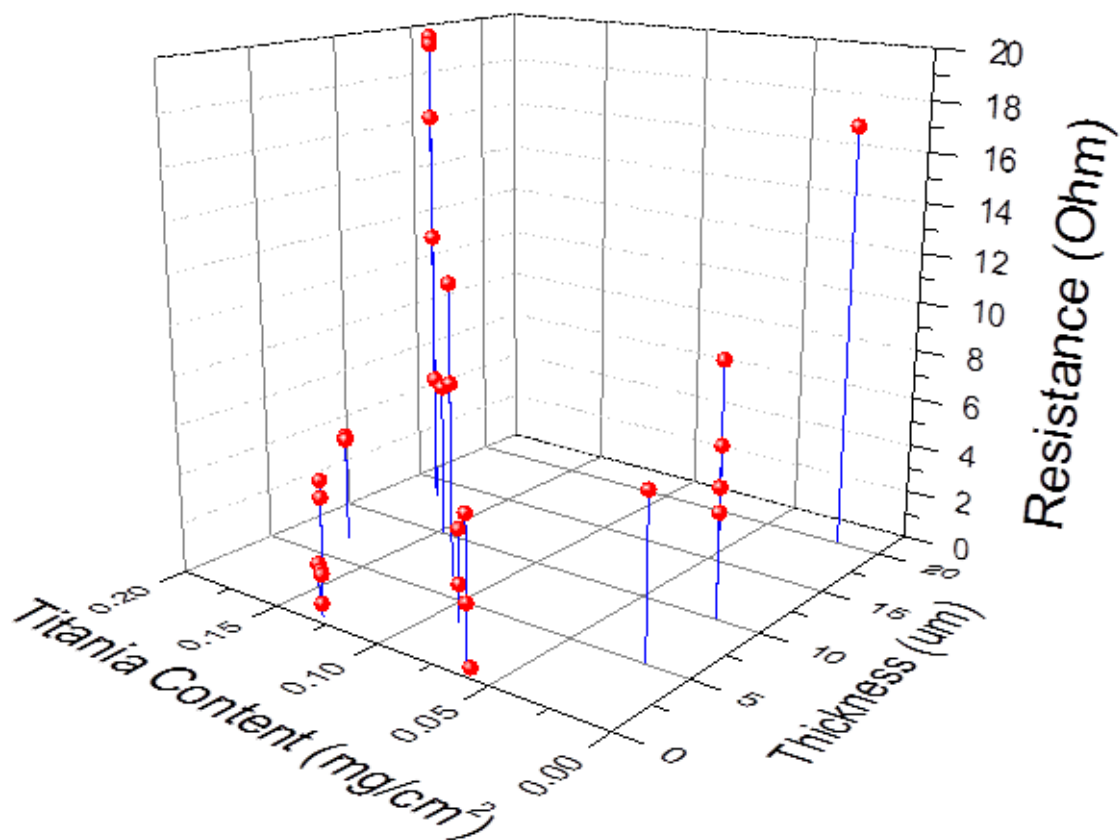
Again, an image taken at 10,000X magnification shows the polymer film coating at a single cross-sectioned fibre (Figure 59.c). From this magnification it is possible to estimate the film thickness of the distributed composite to be approximately 2—4  $\mu\text{m}$  thick. It also appears that there is a larger variation in film thickness, with some seemingly bare patches and some patches larger than 4  $\mu\text{m}$ , although a statistical representation was impossible to discern due to fibre intersection.

Figure 59.d shows a magnification of the 10  $\mu\text{m}$  thick film, sonicated high concentration sol sample magnified at 30,000X. From the above image the shell peeling away from the carbon fiber core does appear to have distinct morphological regions. Near the center of the image are the circular shaped polymer grains, but slightly to their left (highlighted by the dashed circle) is a cluster of small particulates. There are several areas similar to that in the circle distributed throughout the sample. Without verification by elemental analysis it is not possible to confirm that these represent the structure of included titania, although this small grain structure is peculiar and approximately the same size as the P25 nanoparticles. This elemental analysis was not done as it was not within resolution limits of the SEM EDX unit. Even with a finer elemental analysis technique there are fundamental problems with attempting to discern particulate inclusions in these composite films. With the distributed nucleation and growth structure the composite will always break along the grain boundary of the nucleated crystal grains. If the nanoparticles are being incorporated within grains such a fracture would not show the inclusion as it would separate at the disconnect between grains.

Even with a technique such as ion milling or entombed cleaving the resultant sample would have either a melt, smudge from tooling, or other surface modification that would prevent seeing inside of the polymeric grains. It may be possible to examine the inside of the grains using TEM, although such techniques are time consuming and still may not represent the as-prepared composite film as sample preparation for TEM also involves destructive manipulation.

#### **4.3.5 Ex-Situ Resistance**

As discussed in Chapter 2, an ex-situ resistance measurement technique was developed in order to measure the relative resistance of small samples of deposited polymer film on TGP-H-030. Samples of loaded film were punched into 1/8" diameter circles and compressed between the graphite plates. Resistance measurements were taken with an LCR meter and are shown in Figure 60.



**Figure 60 - Variation in ex-situ resistance for PBT-TiO<sub>2</sub> loaded TGP-H-030**

As expected it can be seen that there are two general trends. The first is that with an increase in titania content of the film (as previously measured using ICP-MS) there is generally an increase in electric resistance. This is expected since with a disruption in the regular polymeric structure of the conductive polymer there is a decrease in the long range ‘hopping’ of electronic charges. The second trend seen is that there is an increase in resistance of the samples with an increase in film thickness. This is also expected as the charges must travel through a thicker film, thus increasing the resistance.

It should be noted that there is some variation in the data as represented by the multiple data points at some of the film thickness/titania combinations. This variation in resistance is

normal of course, as it was shown in Figure 53 and Figure 54 that there exists a variation in both film thickness as well as titania inclusion over the tested area as well as from sample to sample.

#### **4.4 Photoelectrochemical Results**

The films loaded on the TGP-H-030 and 316SS substrates were investigated under galvanostatic operation at different current densities in a lightproof enclosure at 20°C with N<sub>2</sub> purged H<sub>2</sub>SO<sub>4</sub> electrolyte. The anodic potential of the counter electrode was stable and constant for different film samples, thus potential variations observed originated at the cathodic electrode, as shown in Chapter 3.

Initially, a parametric analysis was planned to compare equivalent film thicknesses and titania inclusion. By using the two characterization techniques of profilometry and ICP-MS, a plot can be formed correlating film thickness and titania content per loading method, and can be seen in Figure 61. The resultant film thickness and titania loading ranges under investigation were 1 μm to 10 μm, and approximately 0.02 mgcm<sup>-2</sup> to 0.25 mgcm<sup>-2</sup>, respectively. The film thicknesses presented are for 2-D depositions as measured using profilometry and the equivalent conditions are used for the 3-D deposition loadings, but would result in thinner coatings as discussed in Section 4.3.4. The variation in the data is discussed in 4.3.2 and 4.3.1 and the error bars represent the standard deviation of the data points.

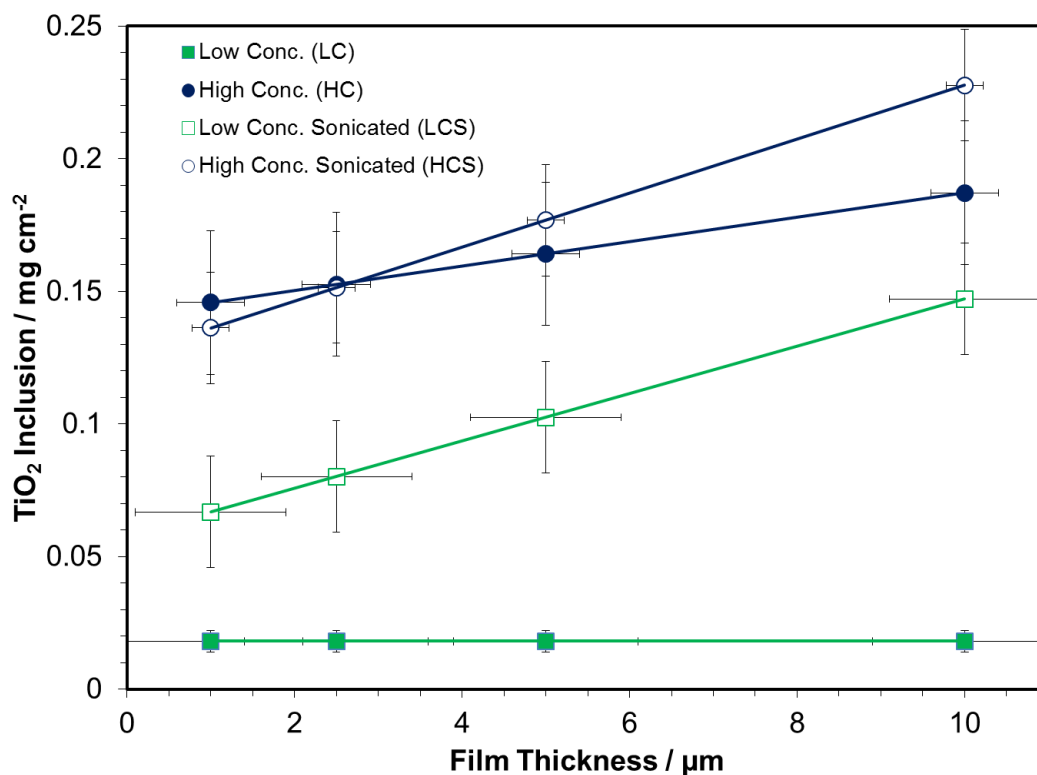


**Figure 61 - Variation of loaded film thickness with titania inclusion, sorted by loading method. Lines are added for illustrative purposes.**

For some of the comparisons between parameters, the experimental study was limited, as a full variation in parameters would encompass too many experiments. Therefore select experiments were chosen to illustrate potentially significant differences in the data. These samples had identical loadings, so a paired statistical analysis was performed to confirm or deny their statistical relevance.

#### **4.4.1 Dark Performance**

For electrochemical measurements, the films prepared on Toray carbon fibre paper (TGP-H-030) were cut into 2 cm<sup>2</sup> circles and sandwiched in the MEA holder as described in Chapter 2. Films were also prepared on photoetched 316 stainless steel substrates (316SS),

perforated with 2208 holes per square inch to provide a 20% open area, and masked to expose only the middle 2 cm<sup>2</sup> circular area for film loading for the 2-D samples. The pooled standard deviation in repeated samples was  $\pm 25$  mV (n=78 measurements), but error bars were excluded from the electrochemical plots as to not convolute the curves. The operation of the loaded films in acidic media is depicted in Figure 62 and Figure 63 with the catalyst films facing in and facing out, respectively.

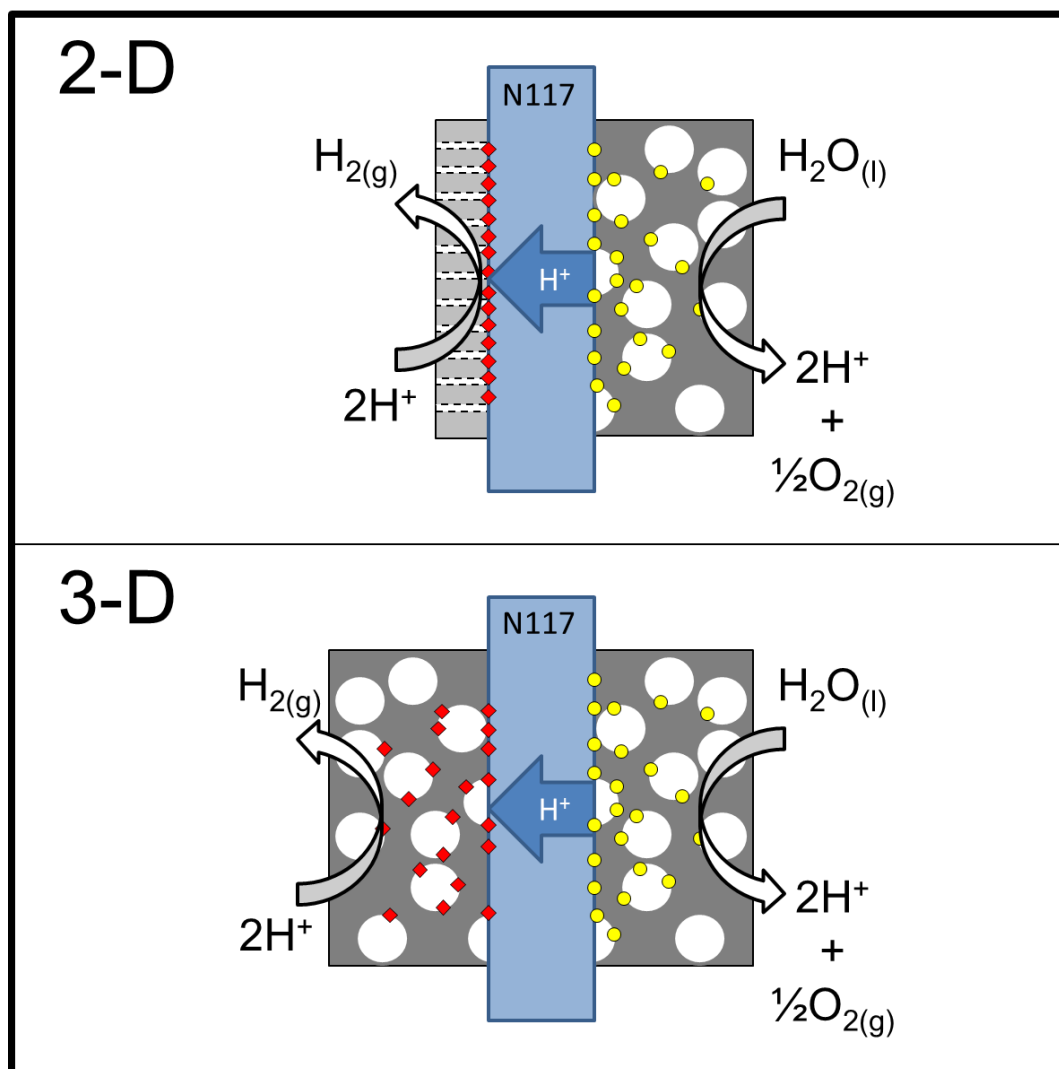


Figure 62 - Schematic of electrolysis using a 2-dimensional 316-SS substrate and a 3-dimensional TGP-H-030 substrate with the film facing the N117 membrane. Cathodic composite catalyst sites are denoted with red diamonds, while RuO<sub>2</sub> anode catalyst sites are denoted as yellow circles.

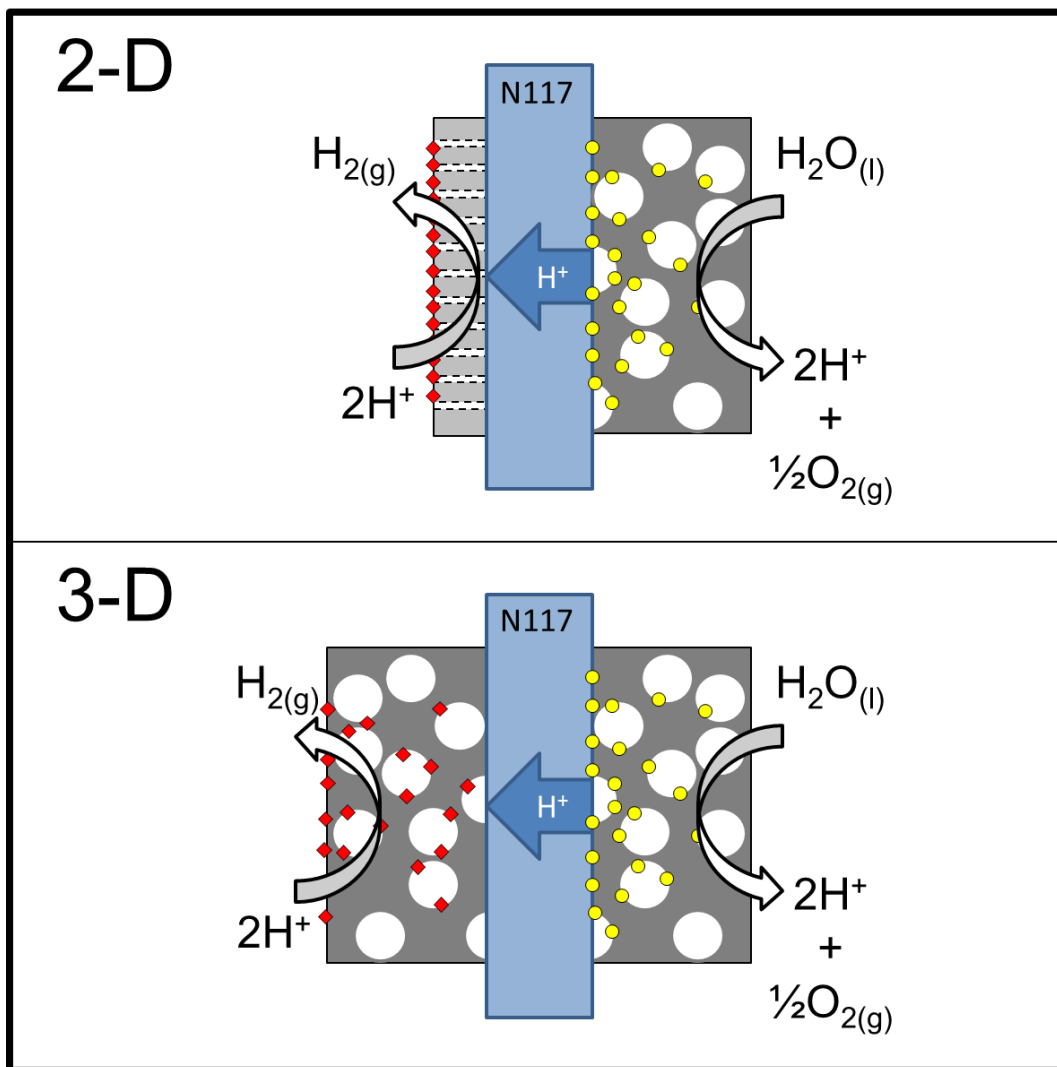


Figure 63 - Schematic of electrolysis using a 2-dimensional 316-SS substrate and a 3-dimensional TGP-H-030 substrate with the film facing away from the N117 membrane. Cathodic composite catalyst sites are denoted with red diamonds, while RuO<sub>2</sub> anode catalyst sites are denoted as yellow circles.

#### 4.4.1.1 3-D (CFP Loadings)

The 3-D distributed loadings were first analyzed for 1 and 10 μm film thicknesses. The films facing the membrane were first analyzed with respect to a variation in film thickness and titania content controlled by the deposition technique and loading sol titania concentration.

#### 4.4.1.1.1 3-D Films Facing In Electrochemical Results

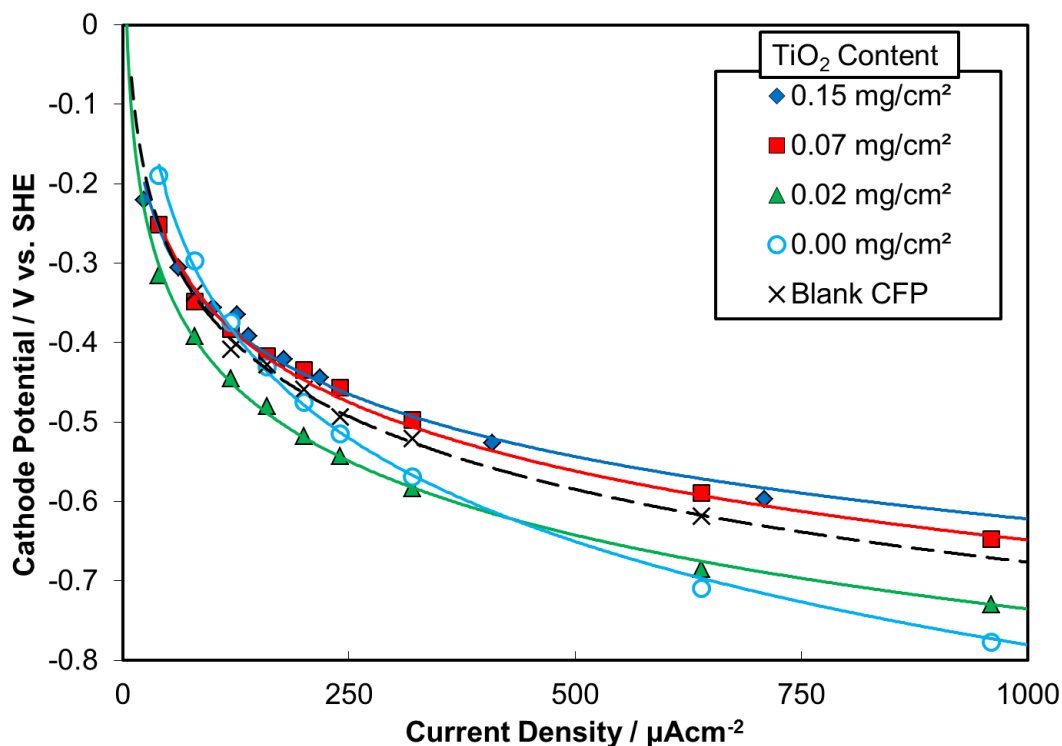


Figure 64 - Cathodic potential (dark performance) of 1 $\mu\text{m}$  thick PBT-TiO<sub>2</sub> films for increasing TiO<sub>2</sub> content facing the N117 membrane in 0.5 mM H<sub>2</sub>SO<sub>4</sub>. Data at 1280  $\mu\text{A cm}^{-2}$  not shown but included in logarithmic curve fit.

When PBT is deposited on the surface of carbon fibre paper the overpotential of the system increases, as seen from the 0.00 mg/cm<sup>2</sup> result in Figure 64. The PBT, which under cathodic polarization is in its reduced state, has a conductivity four orders of magnitude less than that of TGP-H-030 (specific values measured by other research groups are detailed in Appendix M) so that the electronic resistance at the surface results in worse performance. With the addition of TiO<sub>2</sub> to an equivalent thickness of film there is an improvement in the overpotential losses of the system, even though with the substitution of titania for PBT the conductivity of the film should be even less. TiO<sub>2</sub> is three orders of magnitude less

conductive than PBT [100]. This improvement in performance indicates that for very thin films with minimal through plane conductivity losses, the addition of TiO<sub>2</sub> to PBT acts as a catalyst for hydrogen generation as there is enhanced activity despite a reduced surface conductivity. Unfortunately the conductivity of the applied films are not able to be measured directly *ex-situ*. The requirement for the electrodeposition process is that the underlying substrate is conductive and probing methods typically perturb and destroy the fragile film structure and simply give a measurement of the substrate conductivity. Despite not being able to perform a direct conductivity measurement for the films, the ex-situ bulk conductivity measurements do show an increase in resistance (which include the film) of the samples with increasing titania content.

In order to further evaluate the films loaded on TGP-H-030, the solution conductivity was adjusted by changing the pH of the electrolyte for two of the samples. With the concentration of the electrolyte changed to 1M there should be a shift in the entire system potential by  $0.059 \times \Delta\text{pH}$ . This adjustment was made to check the catalytic activity of the films in a higher density proton environment. For the solar tested samples this pH was not used, as the shift in the conductive band edge would deactivate the solar effect, as shown in Figure 133. A variation in working solution pH is recommended in Section 6.2.3.4 for potential further examination.

The polarization curves were broken down further in order to analyze their core electrochemical performance parameters, exchange current density and Tafel slope. Since the electron transfer mechanism of this process is unknown, we are unable to formally detail this process as a 'Tafel' parameterization; however this analysis is used to qualitatively analyze the loss mechanisms of the polarization curves, hence the use of the logarithmic

trendlines. Pseudo-Tafel slope and pseudo-exchange current density represent empirical correlations derived using a similar breakdown to the equations in Section 1.3.4.2. The breakdown of the logarithmic and intercept analysis was done with data that had an overpotential of between ~100 mV-400 mV, and  $R^2$  values of the fit with experimental data were typically  $0.98 \pm 0.01$  indicating little to no error in the regressed fit. These results are shown below in Figure 65.

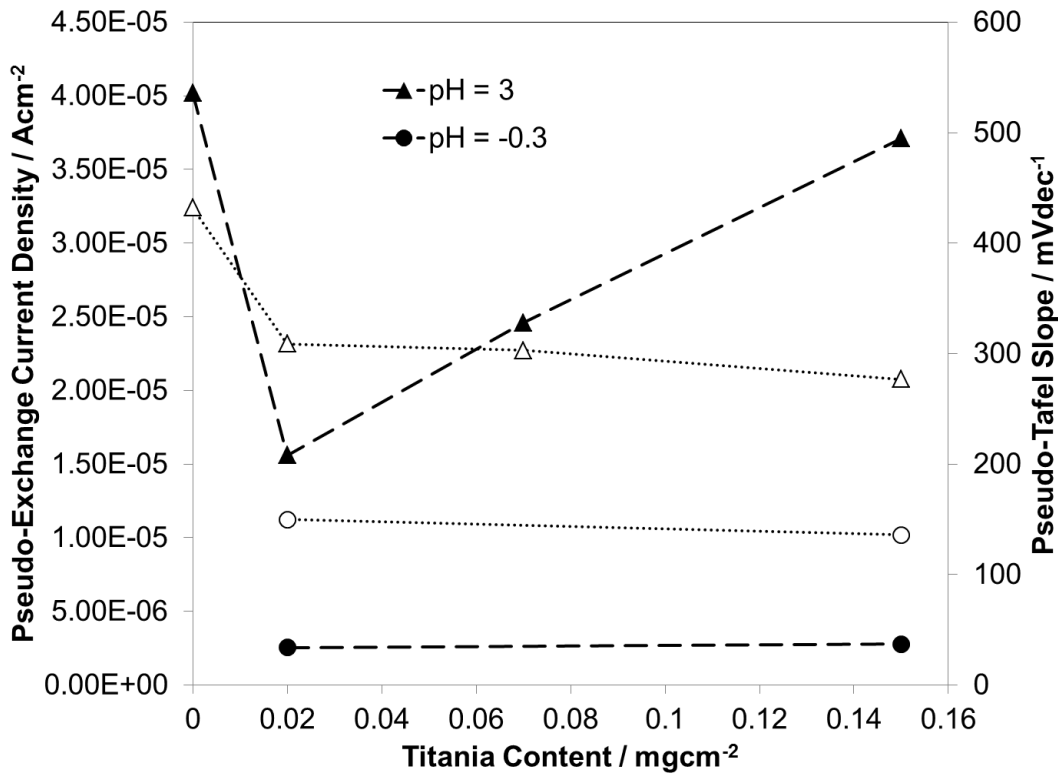


**Figure 65 - Variation of pseudo-exchange current density and pseudo-Tafel slope with titania inclusion for 1  $\mu\text{m}$  films loaded on CFP when placed facing the N117 membrane. Filled symbols represent pseudo-exchange current density and open symbols represent pseudo-Tafel slope with lines added for illustrative purposes.**

The pseudo-exchange current density of the 1 μm thick films exhibits a sharp decrease upon initial addition of titania. It is unknown as to why there is this initial decrease, although if the crystal structure of the polymer is disturbed, perhaps this increase in resistance could account for an increase in electronic charge transfer resistance. After the initial titania addition, the pseudo-exchange current density then increases as the titania content increases for the films tested in pH 3 H<sub>2</sub>SO<sub>4</sub>. This shows good correlation for the synergistic effect described at the beginning of this section and in Chapters 1 and 3. The films tested in pH -0.3 acid did not show this increase in pseudo-exchange current density with increased titania content. A possible explanation for this trend in inherent catalytic performance (directly related to pseudo-exchange current density) is that if the titania enhanced the catalytic activity as suggested through a synergistic drawing in of hydronium ion then the enhancement would be decreased at higher hydronium ion concentration. This would be because at this higher acid concentration, the ions would be drawn closer to the surface naturally by the decreased Helmholtz/Gouy-Chapman layer thickness. The validity of this assumption will be discussed with the specific capacitance of the films measured, and will be examined in Section 4.4.1.2. Upon examination of the pseudo-Tafel slope for these 1 μm thick films it is noted that upon addition of titania there is an immediate decrease in the pseudo-Tafel slope, which accounts for the better performance of the titania included films. This decrease in pseudo-Tafel slope does not change much with further addition of titania at pH 3. This would indicate that for these levels of titania in a thin film there is not a significant loss mechanism for electron transfer resistance through the films, despite the dry ex-situ results showing an increase in electronic resistance losses. A possible explanation for this result would be an increase in hydrogen ion transfer (to electronically connected catalytic sites) with an increase in TiO<sub>2</sub>,

offsetting the increasing electronic resistance. The results for pH -0.3 tested samples show that there is also no noticeable difference in pseudo-Tafel slope with titania inclusion for this film thickness, however there is a large decrease in pseudo-Tafel slope with the increase in hydrogen ion concentration when compared to the more dilute electrolyte. This result is expected, and supports the postulate that although there is an increase in electronic resistance of the films, it is offset by an increase in ionic mobility. For the 1  $\mu\text{m}$  films, it can be seen that there is a statistical significance between the 0.02 and 0.15  $\text{mg}/\text{cm}^3$  titania loadings, detailed in Appendix U-4.

When thicker 10  $\mu\text{m}$  films were prepared on TGP-H-030 and tested in the electrochemical cell the same pseudo-exchange current density performance decrease from simple PBT films is present over that of bare TGP-H-030. This can be seen from the plot in Figure 66. The performance increase of  $\text{TiO}_2$  in the thicker samples increases similarly to those of the thin films, up to a point at which it is hypothesized that the combined film thickness and titania content result in a deactivation of the surface through insulative losses. Unfortunately at these thicker deposition amounts the films do not perform better than a bare carbon fiber substrate, and much worse than any of the platinized loadings. The similarities in performance for these films do not show statistical significance however, as detailed in Appendix U-4, due to the variability in the loadings being greater than the electrochemical performance difference.

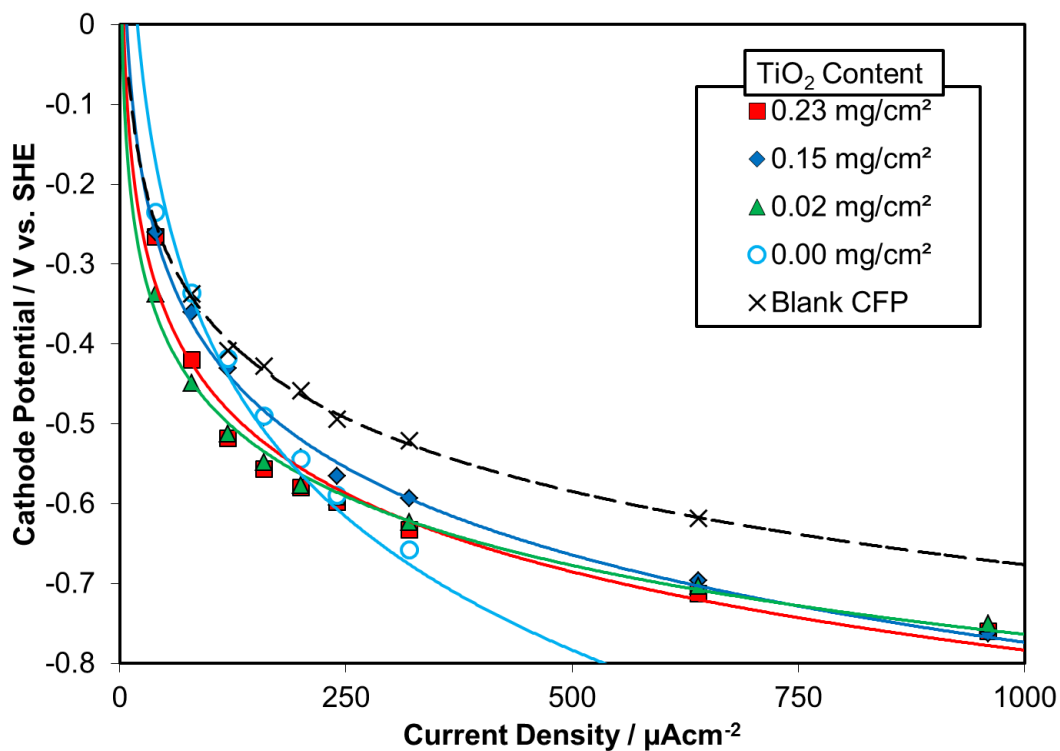


**Figure 66 - Cathodic potential (dark performance) of 10 $\mu\text{m}$  thick PBT-TiO<sub>2</sub> films for increasing TiO<sub>2</sub> content facing the N117 membrane in 0.5 mM H<sub>2</sub>SO<sub>4</sub>. Data at 1280  $\mu\text{A cm}^{-2}$  not shown but included in logarithmic curve fit.**

The films were analyzed once again in accordance to a separation of their polarization data into pseudo-exchange current density and pseudo-Tafel slope for further analysis, with similar regressed accuracy. The results are shown in Figure 67:

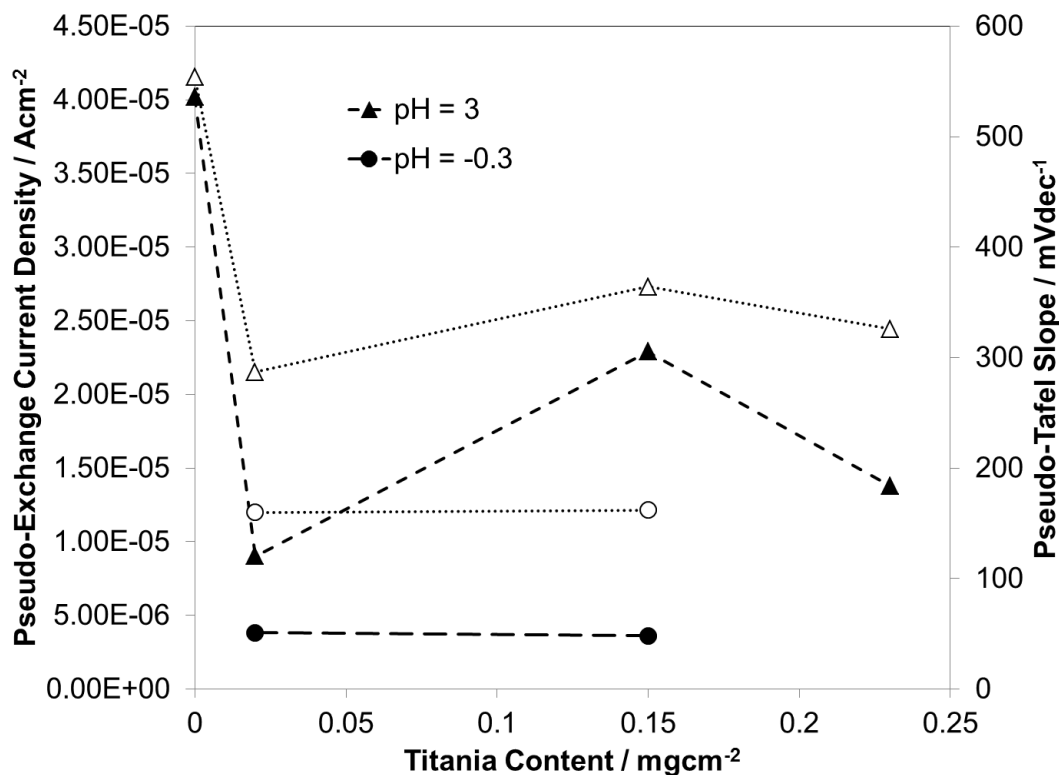


**Figure 67 - Variation of pseudo-exchange current density and pseudo-Tafel slope with titania inclusion for 10 µm films loaded on CFP when placed facing the N117 membrane. Filled symbols represent pseudo-exchange current density and open symbols represent pseudo-Tafel slope with lines added for illustrative purposes.**

The pseudo-exchange current density of the 10 µm thick films exhibits a sharp decrease upon initial addition of titania, similar to the 1 µm thick films. There also is an increase with titania inclusion, but a peak is seen in the medium concentration sample at 0.15 mg/cm<sup>2</sup>. The cause of this peak is unknown, but given the degree of uncertainty in the titania content with the higher loaded samples it is possible that this peak is artificial, and due to variation in true titania content of the medium and high concentration samples. Another possibility as mentioned previously is a deactivation through increased resistance. Once again, there is no change in pseudo-exchange current density with an increase in titania content for the high

concentration acid samples, but the pseudo-exchange current density is once again less than that of the pH 3 tested samples.

The pseudo-Tafel slope for the thicker films also follows the same trends as the 1  $\mu\text{m}$  samples. There is a large decrease in pseudo-Tafel slope upon initial titania inclusion, and potentially a small increase with titania content, although once again the highest concentration sample shows a slight decrease from the  $0.15 \text{ mg/cm}^2$  loading. For the samples tested in higher concentration acid there is again a decrease in the pseudo-Tafel slope, which remains constant with titania inclusion. A highly resistive film could be deactivating the catalyst surface at areas that are too heavily covered.

Comparing the 1  $\mu\text{m}$  samples to 10  $\mu\text{m}$  samples it is found that at pH 3 there is a lower pseudo-exchange current density for the thicker films. There is also a slightly higher pseudo-Tafel slope, likely on account of an increase in film thickness adding to increase in resistance of the films. For the pH -0.3 tests there is a slightly higher pseudo-Tafel slope and pseudo-exchange current density for the thicker films. Statistically there is a difference in performance for the low loading films, but for the higher loadings the film performance could not be shown to have a significant performance difference. This statistical analysis can be seen in Appendix U-5.

#### **4.4.1.1.2 3-D Films Facing Out Electrochemical Results**

The film facing out samples include in addition to 1  $\mu\text{m}$  and 10  $\mu\text{m}$  film thicknesses, 5  $\mu\text{m}$  and 20  $\mu\text{m}$ , as the solar aspect of this project is highlighted by increased samples for solar testing. All the sample testing was conducted at pH 3 (as required by conduction band position), and the 20  $\mu\text{m}$  sample of  $0.02 \text{ mg/cm}^2$  was comprised of the 1292s loading found to be the best performing in Chapter 3. The dark electrochemical performance of additional

titania included 1  $\mu\text{m}$  films is shown below, in Figure 68. Subsequent plots for 5  $\mu\text{m}$ , 10  $\mu\text{m}$ , and 20  $\mu\text{m}$  films follow in Figures 69-71, and some of the higher current density data was removed as the values fell off to very low potentials. It should be noted that while the fitted exponential curves were plotted to guide the eye, the pseudo-Tafel slope and pseudo-exchange current density do not reflect the plotted curve. As previously discussed, for these parameter estimates data from the middle section of the dataset were chosen to minimize the regressed error. This was necessary, as for higher current measurements the potential is such that titania would be degraded/degrading at that point, so those data points were excluded.

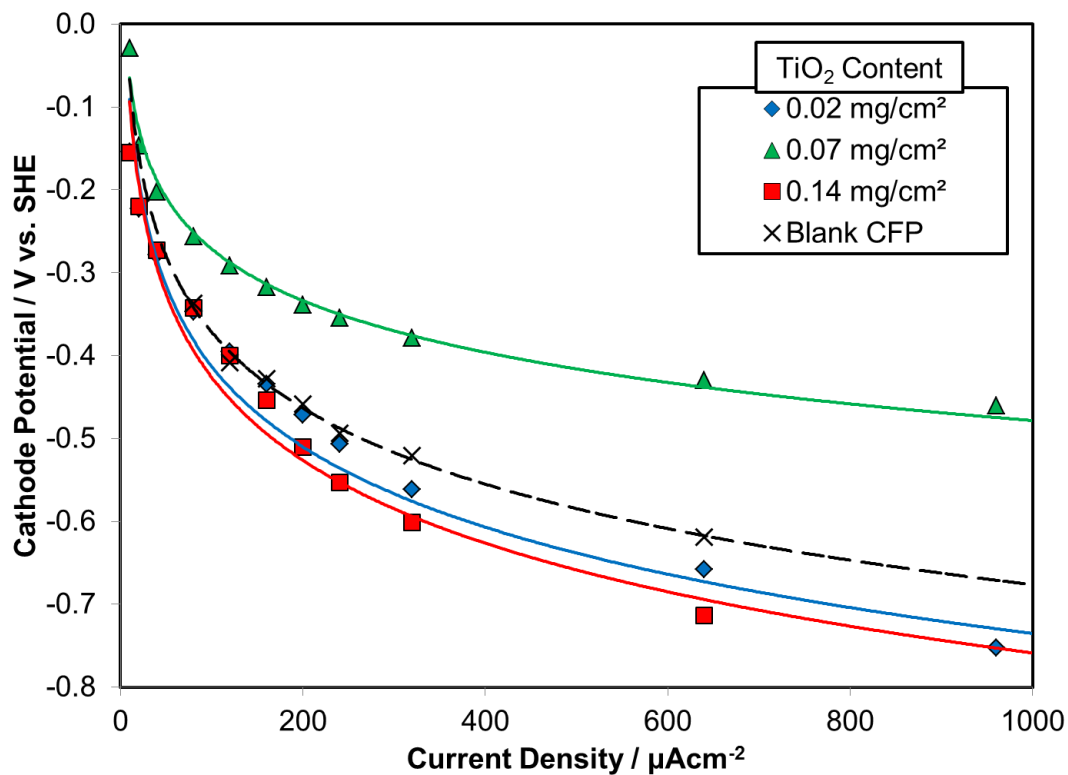
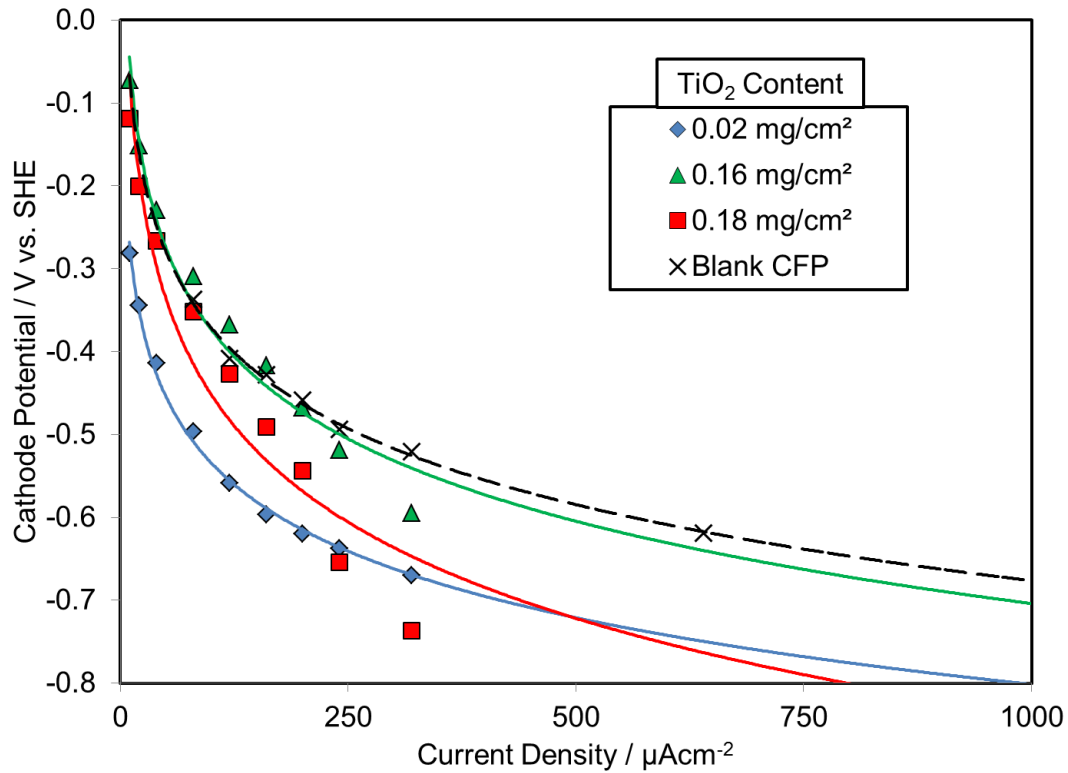
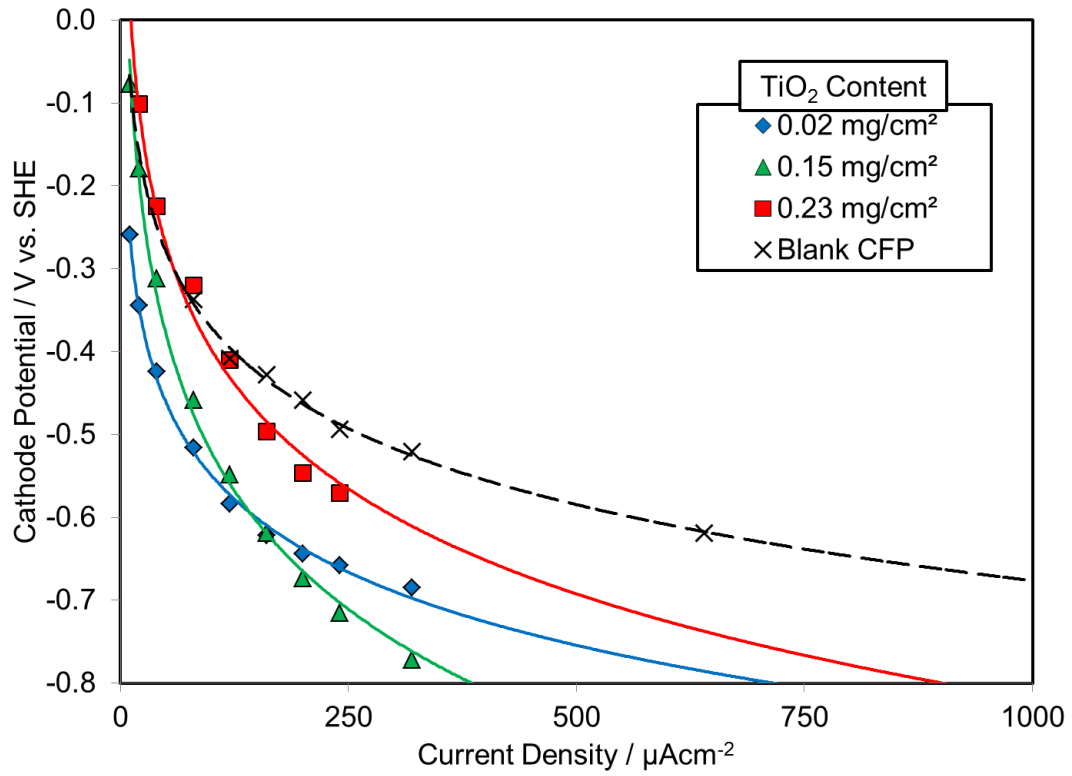


Figure 68 - Cathodic potential (dark performance) of 1  $\mu\text{m}$  thick PBT-TiO<sub>2</sub> films for increasing TiO<sub>2</sub> content facing away from the N117 membrane in 0.5 mM H<sub>2</sub>SO<sub>4</sub>. Data at 1280  $\mu\text{A cm}^{-2}$  not shown but included in logarithmic curve fit.



**Figure 69 - Cathodic potential (dark performance) of 5  $\mu\text{m}$  thick PBT-TiO<sub>2</sub> films for increasing TiO<sub>2</sub> content facing away from the N117 membrane in 0.5 mM H<sub>2</sub>SO<sub>4</sub>. Higher current density data not shown due to titania degradation issues, and not included in logarithmic curve fit.**



**Figure 70 - Cathodic potential (dark performance) of 10  $\mu\text{m}$  thick PBT-TiO<sub>2</sub> films for increasing TiO<sub>2</sub> content facing away from the N117 membrane in 0.5 mM H<sub>2</sub>SO<sub>4</sub>. Higher current density data not shown due to titania degradation issues and not included in logarithmic curve fit.**

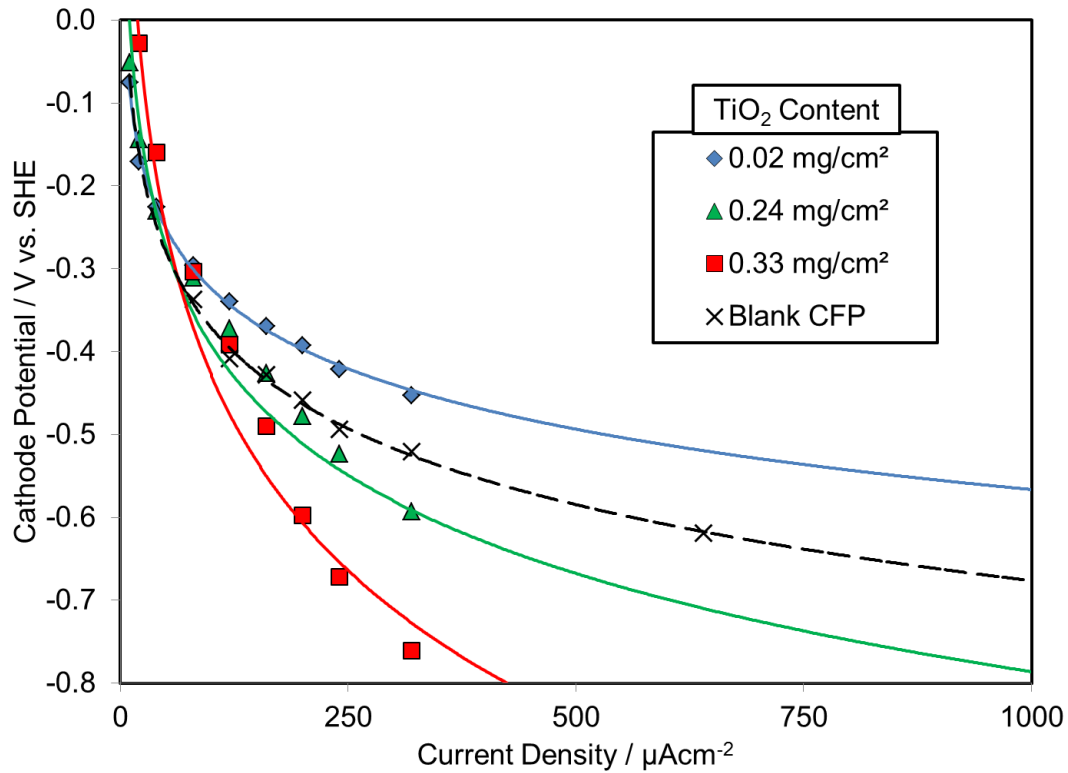


**Figure 71 - Cathodic potential (dark performance) of 20 μm thick PBT-TiO<sub>2</sub> films for increasing TiO<sub>2</sub> content facing away from the N117 membrane in 0.5 mM H<sub>2</sub>SO<sub>4</sub>. Higher current density data not shown due to titania degradation issues.**

Once again, the polarization curves of all of these testing parameters are analyzed in order to compare their relative pseudo-exchange current densities and pseudo-Tafel slopes. The exchange current densities of the 3-D facing out samples is shown in Figure 72.

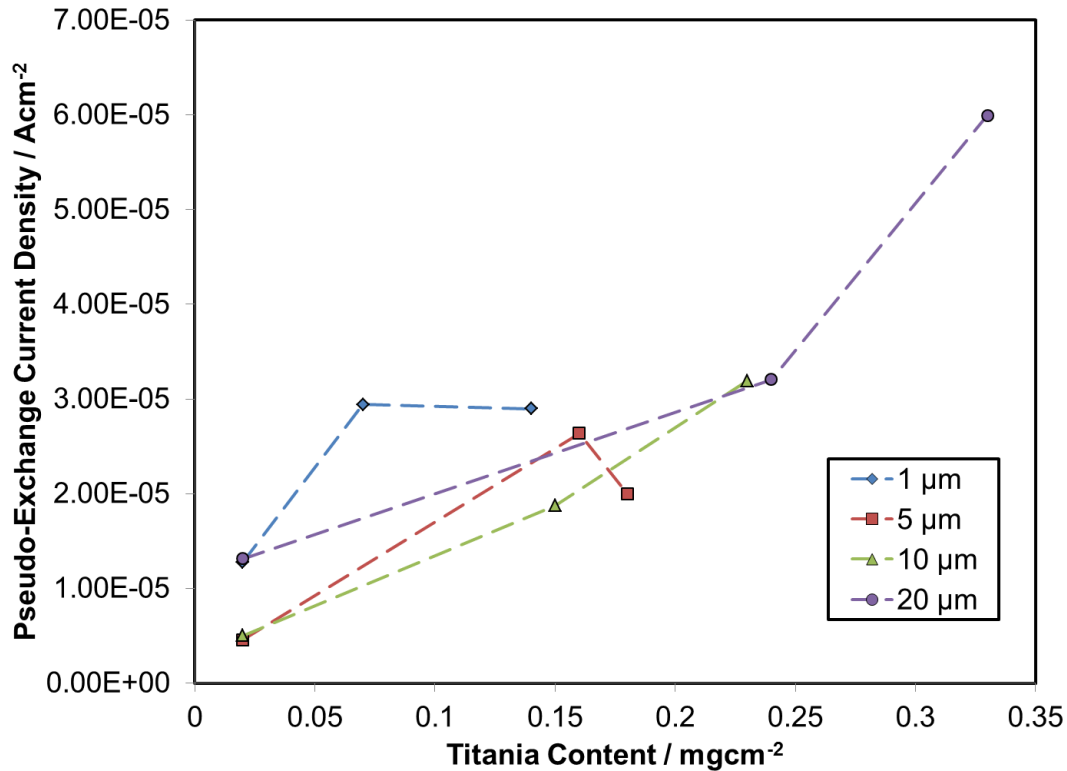


**Figure 72 - Variation of pseudo-exchange current density with titania inclusion for films loaded on TGP-H-030 substrates when placed facing away from the N117 membrane in 0.5mM H<sub>2</sub>SO<sub>4</sub>. Lines are shown for illustrative purposes.**

As can be seen from the above plot, there is a strong influence of pseudo-exchange current density with titania inclusion with an increase in pseudo-exchange current density with included titania. Statistically, the significance of these results are presented in Appendix U-6, with 1um samples showing a statistical difference, while the 10um samples do not. When analyzing the effect of film thickness variation with equivalent titania content, the results are all statistically significant, and this result is shown in Appendix U-7. Upon analysis of the difference in pseudo-exchange current density with film thickness there is a decrease from 1um to 5um, but also seen is an increase in pseudo-exchange current density from 10um to 20um film thickness. Once again, the variation in confidence in titania loading would limit

our ability to estimate if the trend indeed has a maxima for high and low loading concentrations, but it appears that the pseudo-exchange current density is much more dependent on titania content than on film thickness, which is more apparent in the thinner samples. Given the degree of error (standard deviation) in the dataset is  $\pm 25$  mV, and shown by the error bars in the electrochemical performance of the baseline films (Figure 46, Figure 47), more work should be done to investigate the variance in this data. Recommendations are made in Chapter 6.2.3 regarding improvements of this analysis.

When comparing the results of the 1 $\mu$ m and 10 $\mu$ m films facing out to the facing in samples, the following conclusions can be drawn, and the statistical analysis is shown in Appendix U-8. For the 1 $\mu$ m samples, there is a decrease in the pseudo-exchange current density from the facing in samples to the facing out samples. This is attributed to the majority of the distributed loading being farther away from the membrane. This illustrates that the catalytic properties of the film can be better enhanced by providing improved triple phase contact throughout the film. This result was shown to be statistically significant, as shown by the 1 $\mu$ m analysis in Appendix U-8. For the 10 $\mu$ m samples, the pseudo-exchange current density is nearly equal for facing in vs. facing out positioning, but do not show statistical significance for the higher loaded films. As seen from the SEM photos for the higher loaded 10 $\mu$ m films, there was a large degree of interconnection in the composite loading which may serve as a conduit for triple phase connectivity. In Chapter 1 it was discussed that titania is included in some membrane technologies as a filler to provide an additional hydronium ion conduit, and this may be acting to enhance the pseudo-exchange current density of the heavily loaded 10 $\mu$ m film. While the statistical analysis shows that the results were not statistically differing, this hypothesis is supported by the results of the 20 $\mu$ m films, in which the pseudo-

exchange current density is nearly an order of magnitude higher than the lower loaded films. Another explanation is that at higher loadings, composite films are distributed on all sides of the CFP, resulting in membrane-composite interaction even when facing out. The pseudo-Tafel slope of the titania included 3-D films facing away from the membrane are shown in Figure 73.

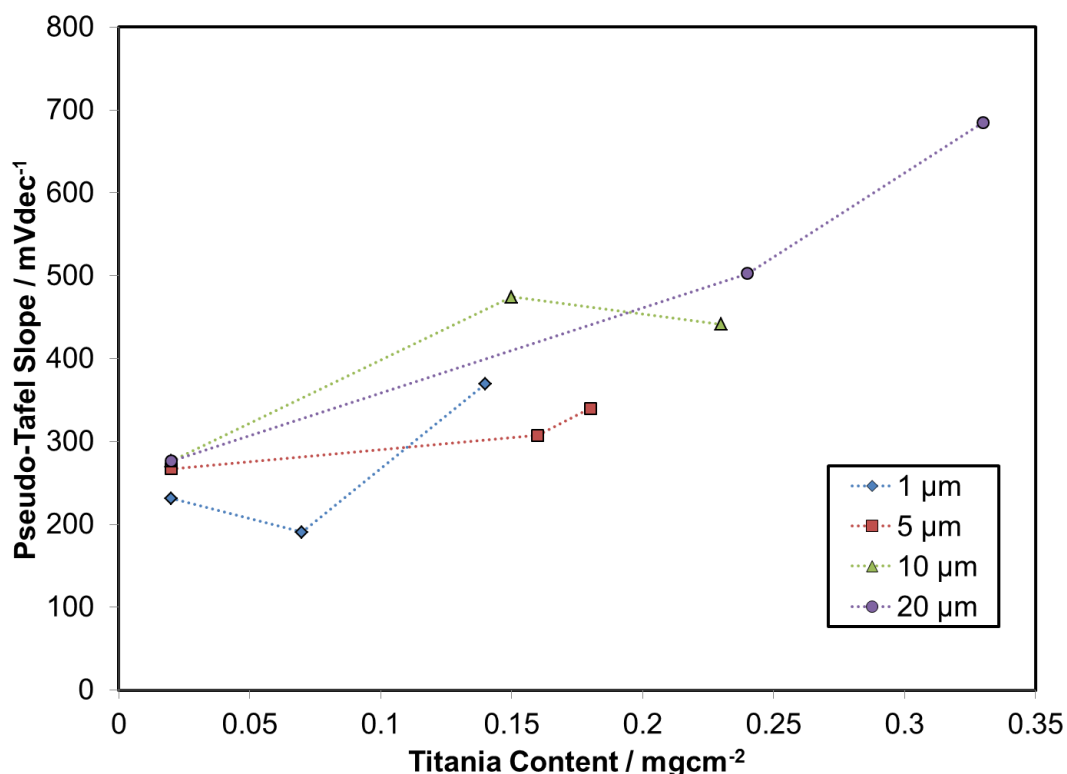


**Figure 73 - Variation of pseudo-Tafel slope with titania inclusion for films loaded on TGP-H-030 substrates when placed facing away from the N117 membrane in 0.5M H<sub>2</sub>SO<sub>4</sub>. Lines are shown for illustrative purposes.**

From the above plot it can be seen that there is a strong increase in the pseudo-Tafel slope with titania inclusion for all thicknesses of films. Also, there is an increase in pseudo-Tafel slope with an increase in film thickness, as expected for an insulating material.

In comparison for facing in versus facing out results, for 1  $\mu\text{m}$  films the pseudo-Tafel slopes are approximately equal. This is likely due to the random dispersed loading of the lower loaded films, so facing in versus facing out would have little effect. For the 10  $\mu\text{m}$  films there is a pronounced increase of 100-200 mV/dec for the facing out samples. Once again, this is likely due to an increase in ionic transfer resistance to the catalyst sites when the films are not placed against the membrane, next to the triple phase interface.

In conclusion, for 3-D samples, it was found that there was an increase in pseudo-Tafel slope and pseudo-exchange current density for higher titania included films. The pseudo-exchange current density was slightly higher for films facing the membrane, but this may be within experimental error. The pseudo-Tafel slope was decreased by placing the films facing the membrane, enhancing the triple phase connectivity.

#### **4.4.1.2 2-D (316 SS Loadings)**

The 2-D distributed loadings were analyzed for 1 and 10  $\mu\text{m}$  film thicknesses. The films facing the membrane were analyzed with respect to variation in film thickness and titania content, again controlled by the deposition technique and loading sol titania concentration. Analysis of the films facing out follow the facing in analysis below.

##### **4.4.1.2.1 2-D Films Facing In Electrochemical Results**

For a 2-D analysis the 1  $\mu\text{m}$  samples were loaded on a photoetched, uniformly perforated 316 stainless steel substrate with 20% open pore area, as depicted in Chapter 2. The films were placed adjacent to the N117 membrane as shown in Figure 62, and the pores allowed for release of generated hydrogen. For comparison to a baseline, a bare perforated stainless steel substrate was used as the non-catalyzed blank and a perforated platinized stainless steel substrate was used for the catalyzed sample. A 100nm platinum film was deposited over a

50nm chromium adhesion layer, both by e-beam evaporation. The films were tested using only the 1M H<sub>2</sub>SO<sub>4</sub> electrolyte to ensure best catalytic performance (reduction of pseudo-Tafel slope).

For the 1 μm film loaded on the 2-D surface it can be seen that at all TiO<sub>2</sub> concentrations the film performs more poorly than the bare SS substrate, as shown in Figure 74. This is due to the complete coverage and hence insulation of the 2-D substrate by the composite film, as opposed to the distributed system that is found with the carbon fibre paper. The random nucleation and growth of the film on the carbon fibres in the 3-D sample is distributed across the sample, while the 2-D film samples completely cover the metal surface. The distribution of fibres and film deposit in the 3-D case should provide better ion transport and electronic conduction than the 2-D case. Another interesting feature of the 2-D substrate electrochemical results is the apparent mass transfer losses occurring at approximately 300 μA/cm<sup>2</sup> for the coated 2-D samples, as shown by the tailing off in performance. This mass transfer loss was not seen in the blank and platinized samples on the stainless steel substrate or for the 3-D CFP samples. This further confirms the hypothesis of deactivation of the film coated on the stainless steel surface closest to the N117 membrane, as the hydrogen ion diffusion through the substrate to the other side of the electrode would restrict the performance of the then-activated stainless steel surface in contact with the open solution.

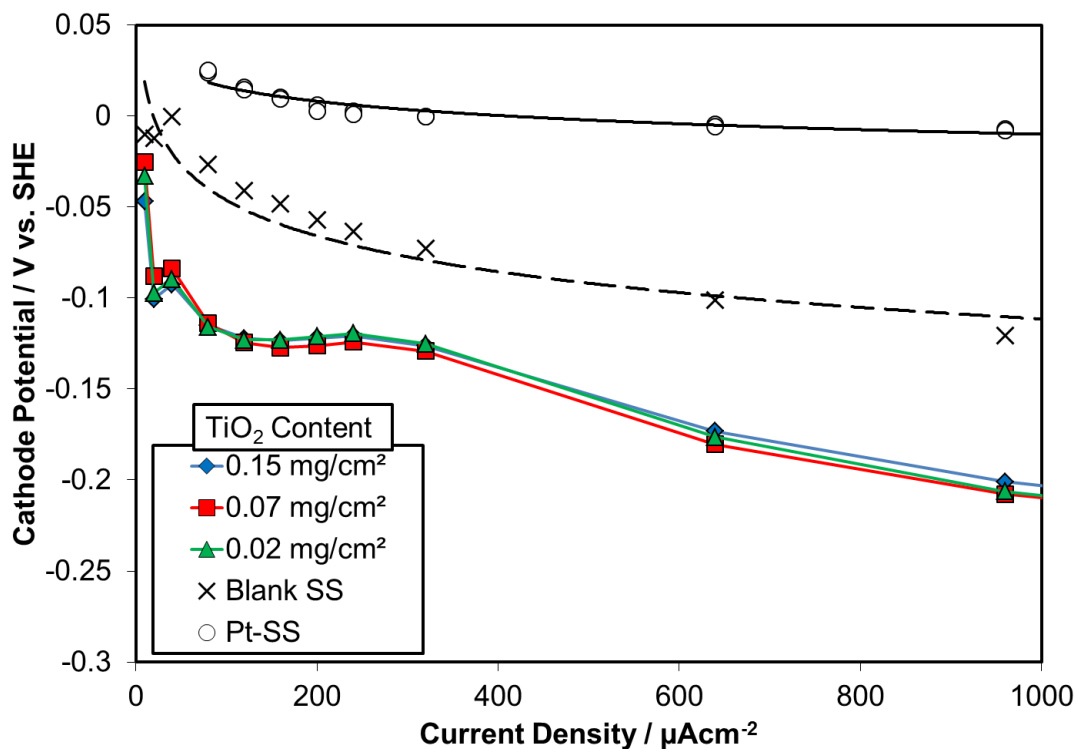


**Figure 74 - Cathodic potential (dark performance) of 1 $\mu\text{m}$  thick 2-D PBT-TiO<sub>2</sub> films for increasing TiO<sub>2</sub> content facing the N117 membrane in 1M H<sub>2</sub>SO<sub>4</sub>. Lines are added for illustrative purposes.**

Results for the 10  $\mu\text{m}$  samples shown in Figure 75 further seem to support the trend of a decrease in activation with increasing film thickness, yet the differences are less pronounced than in the 3-D samples. This may be because the 1 $\mu\text{m}$  thick film might be blocking the surface even at the lower film thickness. Once again the effect of increasing the TiO<sub>2</sub> content only results in a limited increase in performance before the inclusions further detrimentally affect electronic charge transfer. Statistically, the 2-D facing in samples are equivalent both with respect to increases in film thickness and titania content. These statistical analyses are found in Appendices U-9 and U-10, respectively.

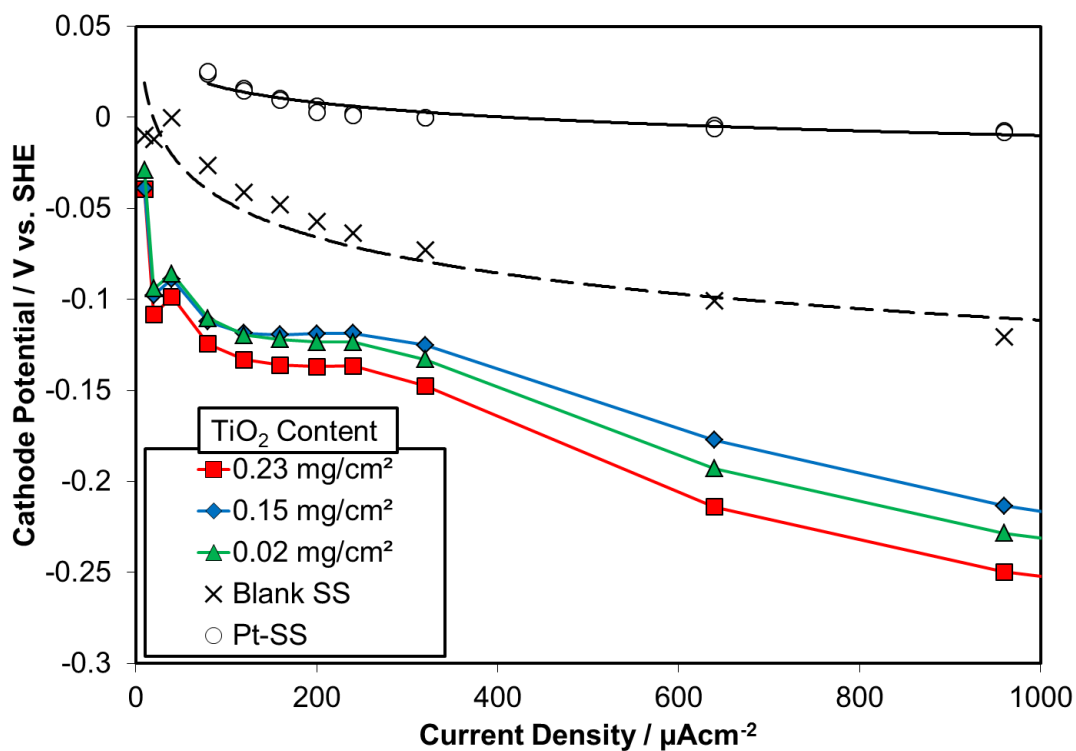


**Figure 75 - Cathodic potential (dark performance) of 10  $\mu\text{m}$  thick 2-D PBT-TiO<sub>2</sub> films for increasing TiO<sub>2</sub> content facing the N117 membrane in 1M H<sub>2</sub>SO<sub>4</sub>. Lines are added for illustrative purposes.**

Further analysis is once again accomplished using a breakdown of the polarization curves (before the apparent mass transfer effect occurs) into the substituent pseudo-exchange current density and pseudo-Tafel slopes as shown in Figure 76.

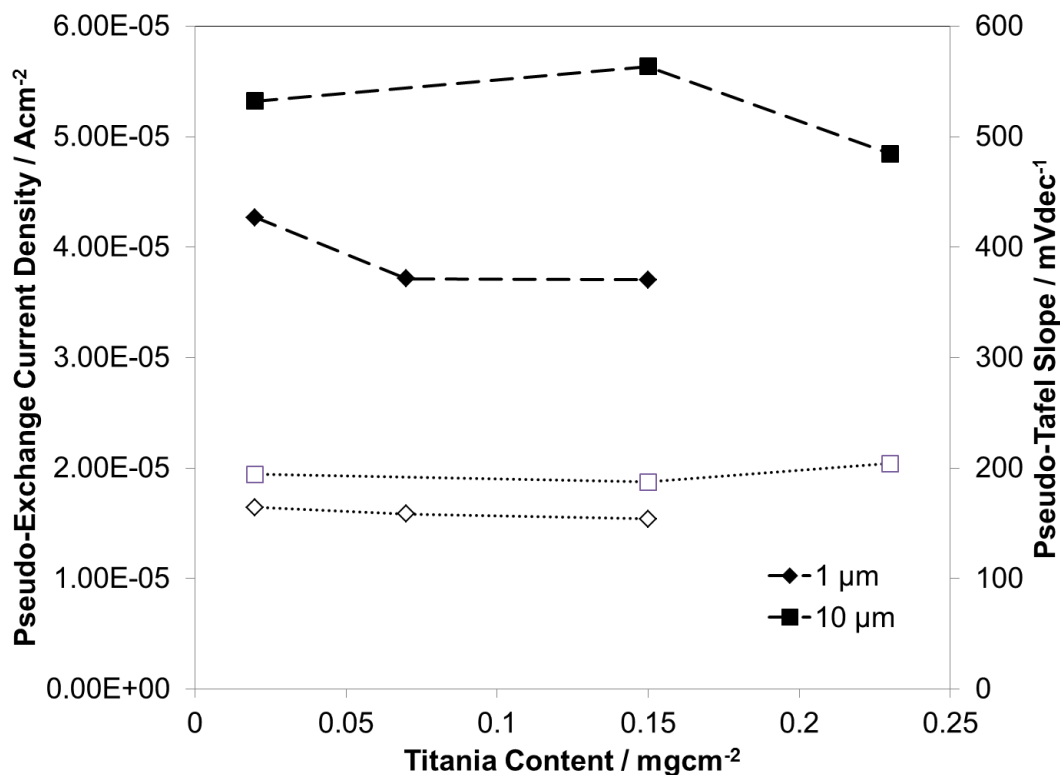


**Figure 76 - Variation of pseudo-exchange current density and pseudo-Tafel slope with titania inclusion for 1 and 10 μm films loaded on 316SS perforated substrates when placed facing the N117 membrane in 1M H<sub>2</sub>SO<sub>4</sub>. Filled symbols represent pseudo-exchange current density and open symbols represent pseudo-Tafel slope with lines added for illustrative purposes.**

As can be seen in the above plot, there is little variation with titania increase, as also seen with the 1M H<sub>2</sub>SO<sub>4</sub> samples of 3-D samples facing the membrane. However, when compared with the 3-D films, the 2-D pseudo-exchange current density is an order of magnitude higher for both the 1 μm and 10 μm film loadings. This is likely a result of having the catalytic surface pressed directly against the membrane, which results in more active sites. This result further emphasizes the benefit of having an intimate triple phase contact.

With regard to the pseudo-Tafel slope, the thicker film has a higher pseudo-Tafel slope, although only slightly. In comparison to the 3-D film variant, the 2-D films showed approximately equal pseudo-Tafel slope for both the 1um and 10um samples. This is to be expected, as both electrodes are pressed against the N117 membrane, and would have the same catalytic area in triple-phase contact.

#### 4.4.1.2.2 2-D Films Facing Out Electrochemical Results

It was expected that from the early onset of mass transfer limitations for the 2-D facing in film, the results of the 2-D films facing out would be poor. The results of the polarization curves for 2-D films facing out samples are shown in Figure 77:

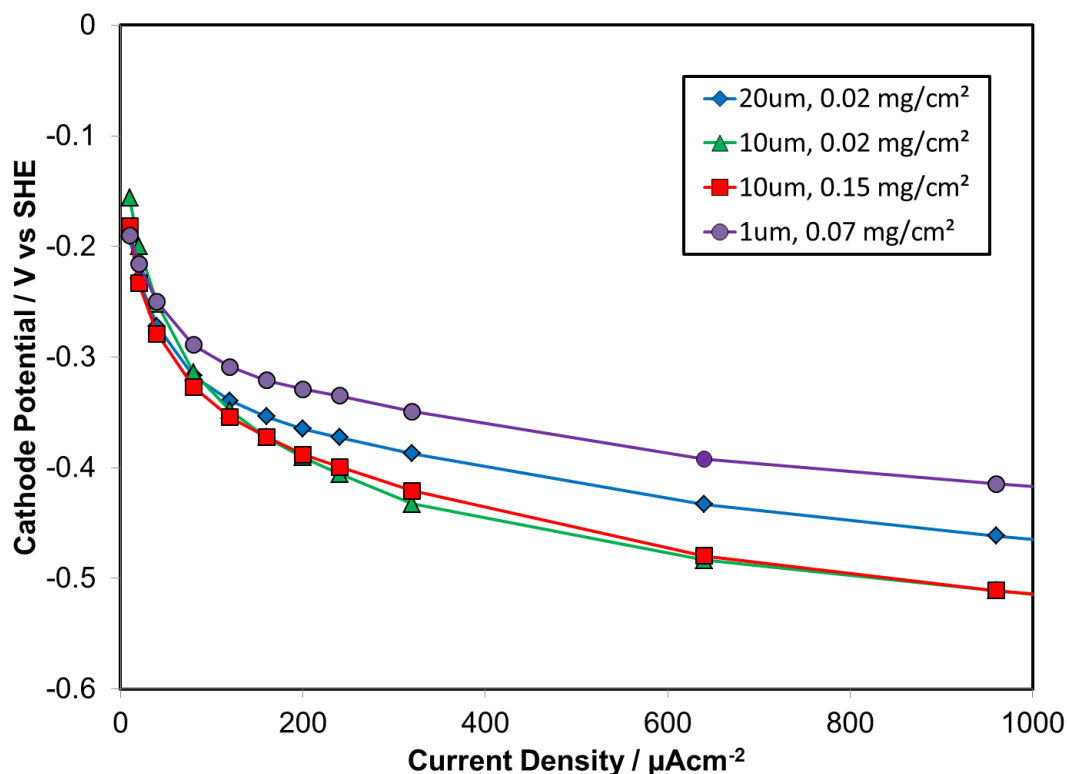
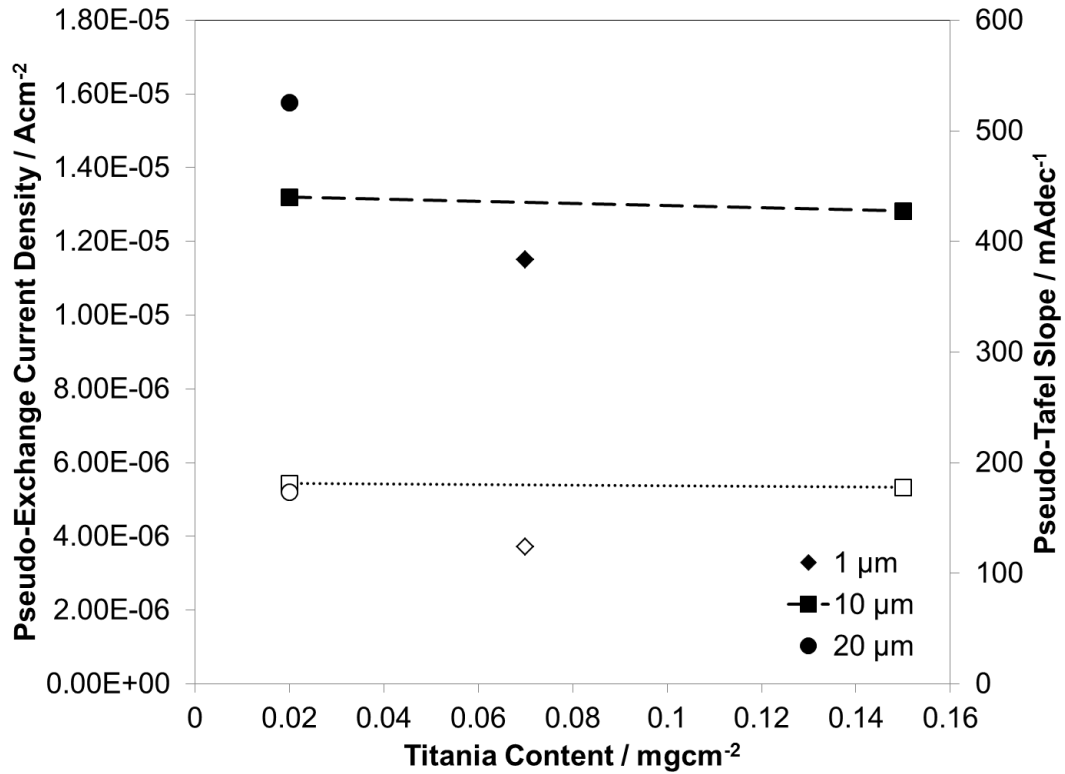


Figure 77 - Cathodic potential of various thicknesses of PBT-TiO<sub>2</sub> films with differing TiO<sub>2</sub> content loaded on 316SS perforated substrates when placed facing away from the N117 membrane in 0.5 mM H<sub>2</sub>SO<sub>4</sub>. Data at 1280  $\mu\text{A}/\text{cm}^2$  not shown but included in logarithmic curve fit.

From the polarization curve data it appears that there is a decrease in film performance with titania inclusion and a non-linear variation in performance with film thickness. The polarization results were again broken down into pseudo-exchange current density and pseudo-Tafel slope data for further analysis as shown in Figure 78.



**Figure 78 - Variation of pseudo-exchange current density and pseudo-Tafel slope with titania inclusion for 1, 10, and 20 μm films loaded on 316SS substrates when placed facing away from the N117 membrane in 0.5 mM H<sub>2</sub>SO<sub>4</sub>. Filled symbols represent pseudo-exchange current density and open symbols represent pseudo-Tafel slope with lines added for illustrative purposes.**

As can be seen in the above plot, there is an increase in pseudo-exchange current density with increased film thickness. With the selected data there is little to compare regarding an increase with increasing titania concentration, but for the 10um film thickness no increase

can be seen. In comparison of the above data with 3-D distributed films facing out, there is a 3x decrease in the pseudo-exchange current density, showing that the catalytic performance of the films in a 2-D configuration perform worse than their distributed counterparts. In comparison with the 2-D films facing the membrane there is also a significant decrease in pseudo-exchange current density, and this is analyzed in Appendix U-11. In spite of an increase in solution pH (as was previously shown to increase the exchange current density of the previous 3-D samples) there was a decrease in pseudo-exchange current density from 2-D films facing in by an order of magnitude. This further supports the decrease in performance with a disconnected triple phase interface. In comparison to the equivalent 3-D films facing in, there is also a decrease in performance (as measured by the pseudo-exchange current density), with a 3x decrease in film performance for the 1 $\mu$ m samples and approximately equivalent performance for the 10 $\mu$ m samples. The decrease of performance for the thicker film can be accounted for by the bipartite film distribution with the 2-D samples. Since the film heavily covers one side of the metal substrate, the bare metal face can act as a reactive surface in comparison to a highly blocked thick film 2-D loading. This results in the reaction occurring at the less catalytic steel surface, with resistive losses deactivating the catalytic composite outer surface.

In regard to the pseudo-Tafel slope, there is an increase from 1 $\mu$ m to 10 $\mu$ m, but little change from 10 to 20 $\mu$ m. This lack of increase in pseudo-Tafel slope from the 10 to 20  $\mu$ m films could again be a result of the reaction ordinate changing upon the thicker film coverage deactivating the composite surface. This would mean that once the reaction was not being catalyzed by the thick film, an increasing film thickness would have little further effect. When compared with the 2-D films facing towards the membrane, the pseudo-Tafel slopes

are approximately equivalent despite the weaker acid concentration of the facing out samples. As shown there is a significant increase in pseudo-Tafel slope (nearly double) with more dilute acid (Figures 65,67), indicating an improvement in facing the films outwards compared with those facing towards the membrane. This improvement is a bit misleading, as the performance increase is not from the catalyst, but from the enhanced contact from the bare substrate, leading to another catalytic path for the reaction to occur. For a comparison with the 3-D samples, the pseudo-Tafel slope is less than all of the samples tested, but once again, this is likely a measure of the bare substrate performance enhanced with good triple phase contact.

In conclusion it was deduced that when applied in a 2-D distribution on a metallic substrate the composite films have high catalytic activity when pressed against the membrane, but suffer from a very large pseudo-Tafel slope which causes a preference for the reaction to proceed on the uncatalyzed uncoated side of the substrate. Although performance of these films did not act as expected, they did show an enhancement in catalytic performance when triple phase contact is preserved.

Overall, it can also be concluded that the optimum film composition and direction would be a film with high titania content, while keeping the films as thin as possible and as close to the membrane as possible in order to minimize the pseudo-Tafel slope which unfortunately increases with titania inclusion. This increase in pseudo-Tafel slope is most noticeable in the thicker film variants, as the composite film rife with dislocations seems to have difficulty in through plane charge passage. Investigation into the connection of the catalytic film with proximity to the membrane through a reduction in 3-D substrate options as well as addition of Nafion ionomer percolated into the 3-D network will be investigated in Chapter 5.

## 4.4.2 Illuminated Performance

The films tested for electrochemical performance in 0.5 mM H<sub>2</sub>SO<sub>4</sub> were again tested with AM1.5G 0.1 W/cm<sup>2</sup> artificial sunlight in order to measure their photoelectrochemical performance. Since the setup of the cell only allowed for insolation from one direction, the experiments were limited to films facing away from the membrane, even though the dark electrochemical studies clearly favored the films facing towards the membrane.

### 4.4.2.1 3-D PBT-TiO<sub>2</sub> Photocathode Function

As mentioned with the dark electrochemical performance studies, the parametric film thickness analysis was expanded upon to include 5um films and 20um films for greater breadth of data. Rather than re-plotting the electrochemical light and dark cathode performances, the polarization curves were subtracted and the difference plotted to express the energy savings as a function of increasing current, according to Eq. 17:

$$E_{hv} = E_{Light} - E_{Dark} \quad \text{Eq. 17}$$

The results for the 20 μm 3-D films are shown in Figure 79, and the 0.02 mg/cm<sup>2</sup> represents the baseline titania loading as shown in Chapter 3, from Figure 47.

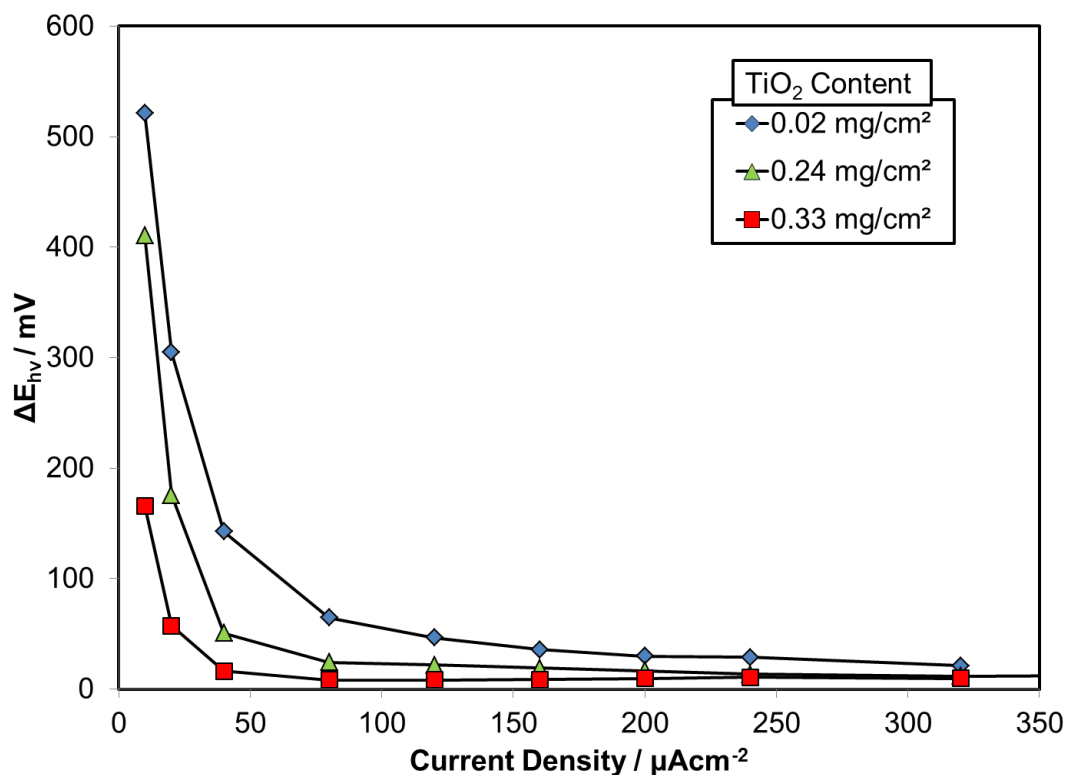


**Figure 79 - Energy harvested for 20  $\mu\text{m}$  PBT-TiO<sub>2</sub> films with differing TiO<sub>2</sub> content. Films loaded on TGP-H-030 substrate, tested against 1.5 mg/cm<sup>2</sup> RuO<sub>2</sub> on TGP-H-030, N117 membrane separator, in 0.5 mM H<sub>2</sub>SO<sub>4</sub> recirculated at 1 mL/s at 20°C. Lines are added for illustrative purposes.**

It can be seen from the plot above that with an increase in titania in the 20 $\mu\text{m}$  films there is a decrease in energy collection. This is likely a result of increased charge recombination with increased loading from the included titania particles forming dislocation trap states in the composite. It was hypothesized that the formed junctions would enhance charge separation, but this would only occur if the separated charge was then transferred to the hydrogen ion. With an increase in particles included in the film, the particle-polymer interface density increase would result in enhanced photogenerated electron-hole pairs. The increase in dislocations in the polymer composite would also enhance recombination from photogenerated hole and electron encounters. It appears from the above data that the latter

event dominates, as there is reduced performance with increasing titania. Also, 10  $\mu\text{m}$  films were tested and the results are shown in Figure 80.

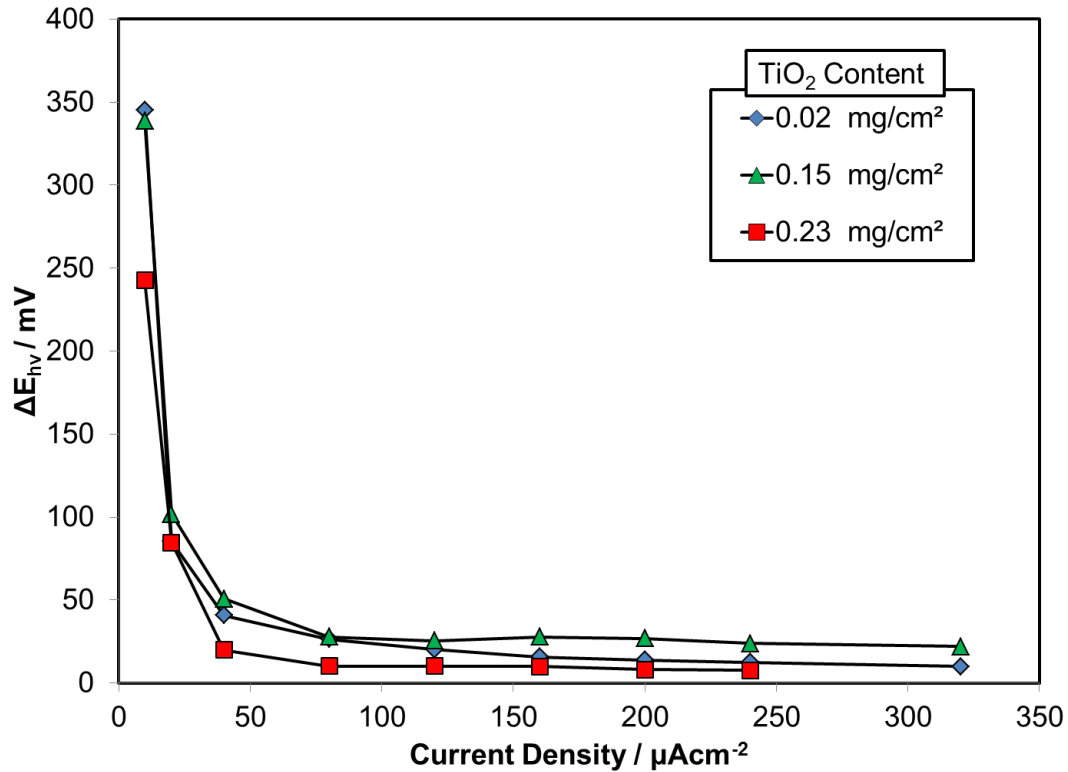
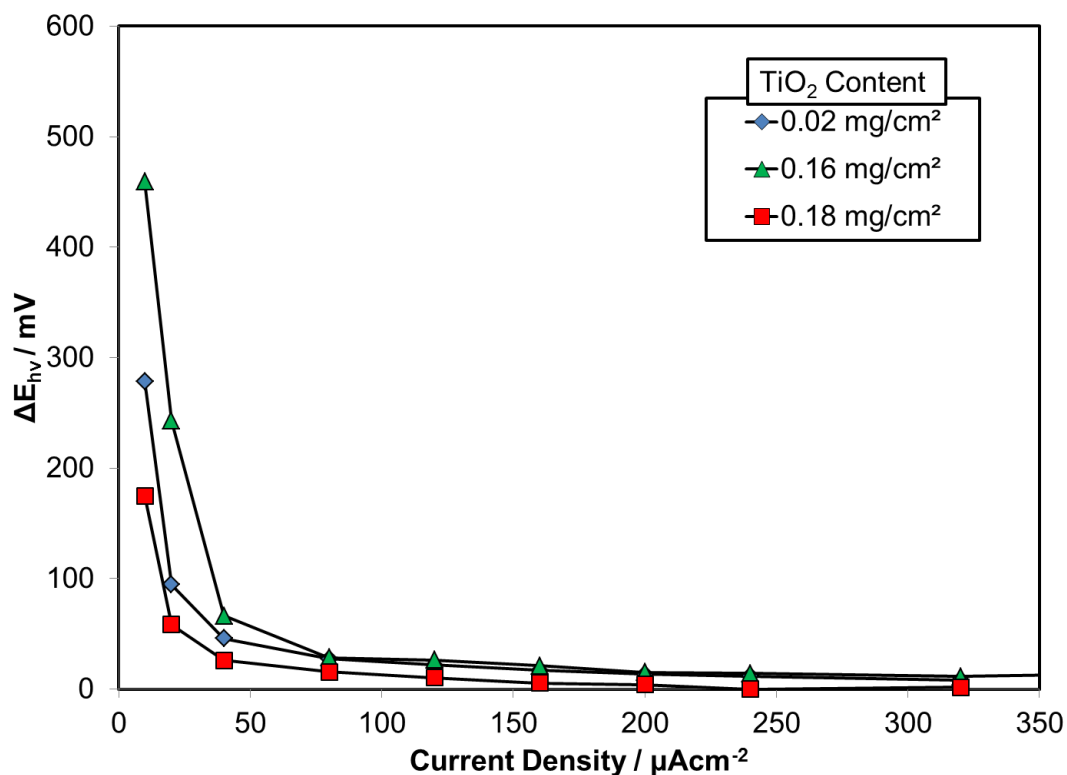


Figure 80 - Energy harvested for 10  $\mu\text{m}$  PBT- $\text{TiO}_2$  films with differing  $\text{TiO}_2$  content. Films loaded on TGP-H-030 substrate, tested against 1.5  $\text{mg/cm}^2$   $\text{RuO}_2$  on TGP-H-030, N117 membrane separator, in 0.5 mM  $\text{H}_2\text{SO}_4$  recirculated at 1 mL/s at 20°C. Lines are added for illustrative purposes.

It can be seen in Figure 80 that again there is a decrease in solar energy harvested with an increase in titania content. This is likely due to poor optimization of the film thickness, with unused photons not being absorbed with the thinner films that would be absorbed by the thicker films. Recombinant issues from increased titania inclusion also apply.



**Figure 81 - Energy harvested for 5  $\mu\text{m}$  PBT-TiO<sub>2</sub> films with differing TiO<sub>2</sub> content. Films loaded on TGP-H-030 substrate, tested against 1.5 mg/cm<sup>2</sup> RuO<sub>2</sub> on TGP-H-030, N117 membrane separator, in 0.5 mM H<sub>2</sub>SO<sub>4</sub> recirculated at 1 mL/s at 20°C. Lines are added for illustrative purposes.**

Results are shown for the 5 $\mu\text{m}$  films in Figure 81. There is a shift in the trend of decreasing performance with increasing titania content. Surprisingly, the mid-concentration samples performed better than the low and high concentration samples, although this variability may also be due to experimental error. As shown in Chapter 3, there is a large variability in solar performance with cell resistance. However, an explanation for this result may also be due to an optimal titania concentration allowing for an enhancement of the photogenerated charges separation without a large film thickness that would allow for enhanced charge recombination. Apart from the mid concentration samples the 5 $\mu\text{m}$  films again decreased in photonic harvest, again due to their smaller thickness for absorption.

Results for 1  $\mu\text{m}$  films are shown in Figure 82.

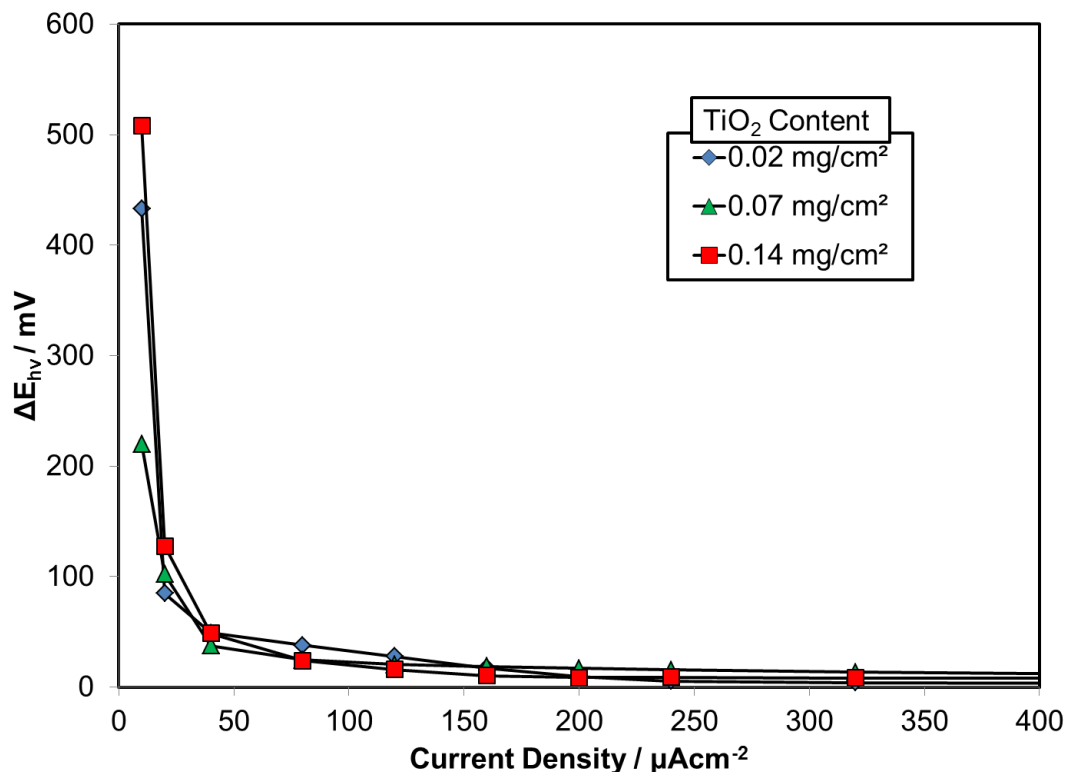


Figure 82 - Energy harvested for 1  $\mu\text{m}$  PBT-TiO<sub>2</sub> films with differing TiO<sub>2</sub> content. Films loaded on TGP-H-030 substrate, tested against 1.5 mg/cm<sup>2</sup> RuO<sub>2</sub> on TGP-H-030, N117 membrane separator, in 0.5 mM H<sub>2</sub>SO<sub>4</sub> recirculated at 1 mL/s at 20°C. Lines are added for illustrative purposes.

Again there is a shift in the trend of decreasing performance with increasing titania content, although less at this film thickness. For this film thickness there appears to be a decrease in performance from low to mid concentration, but then the high concentration sample outperforms both the other inclusion concentrations. It appears that at these thin film coverages the initial low current performance is enhanced, likely as a result of direct utilization of photogenerated charges. Upon comparison with the 20 $\mu\text{m}$  samples however, the 1 $\mu\text{m}$  sample performance falls off far more quickly. This result again points to an

underutilization of the incoming photons for the thinner films, and the diminished performance at higher current densities shows that the photoelectrochemical enhancement cannot be sustained with such thin films due to lack of film thickness for photon absorption. Overall, examination of the specific resistances of the tested films may yield more insight into these variations from the thicker film trend of decreased performance with titania inclusion, and this will be discussed in Section 5.4.3.1. It was noted in Chapter 3 that the solar performance has a direct correlation to cell resistance. This is a difficult comparison for different film thicknesses with differing inclusions, as it was shown in section 5.3.5 that the inherent resistance increases with an increase in titania and film thickness. Therefore, a balance between inclusion to enhance charge separation and increased electronic resistance (charge carrier mobility and lifetimes) is required. Performance variability due to film composition is increased with the possibility of clustering of the nanoparticulate inclusions as postulated in the UV-Vis and SEM characterization.

It was shown that there is an enhancement in spectral absorption of the films with increased titania in the UV range, which should result in an increase in energy harvested. This was not seen to be the case with the higher concentration films, where there was a reduction in performance with more energy harvested. While this result was attributed to an increase in recombination due to trap states caused by particle inclusion, it may also indicate that an increase in the UV spectrum may not lead to better performance. This postulate brings to light the possibility that UV light may not be the only part of the spectrum required for efficient cell performance, i.e., the titania does not need to be photostimulated for an enhancement in performance. If this is indeed true, photostimulation through the Nafion membrane (which would normally absorb the UV spectrum) could be possible for

photoactivation of our applied films. A recommendation of a more thorough examination of this configuration is discussed in Chapter 6.

#### 4.4.2.2 2-D PBT-TiO<sub>2</sub> Photocathode Function

The 2-D film loadings were tested and the results are shown in Figure 83. Once again, only a select few tests were run due to the poor electrochemical performance of the facing out stainless steel samples. Facing in samples which had better electrochemical properties were unable to be also confirmed experimentally due to the electrode configuration and light direction.

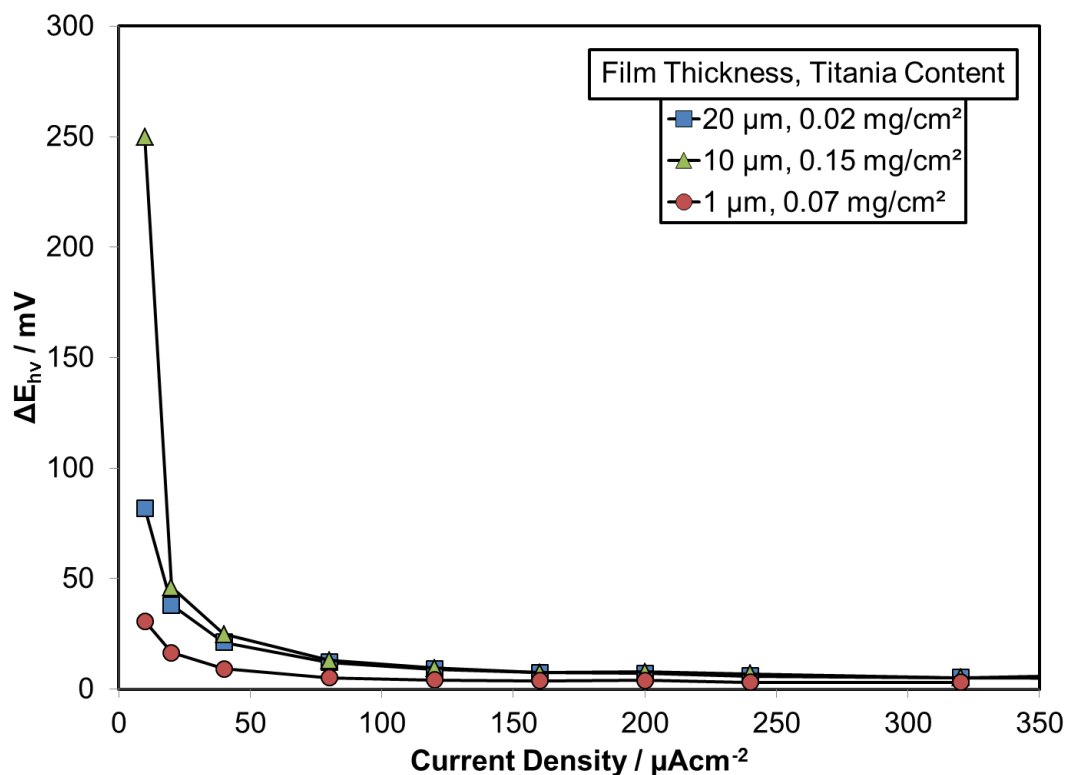


Figure 83 - Energy harvested for 1, 10, and 20  $\mu\text{m}$  PBT-TiO<sub>2</sub> films with differing TiO<sub>2</sub> content. Films loaded on 316SS perforated substrate, tested against 1.5  $\text{mg/cm}^2$  RuO<sub>2</sub> on TGP-H-030, N117 membrane separator, in 0.5 mM H<sub>2</sub>SO<sub>4</sub> recirculated at 1 mL/s at 20°C. Lines are added for illustrative purposes.

For the 2-D loadings it appears that there is very poor performance as compared to the 3-D samples. The 2-D loading sample with the highest titania content performed best. The extremely poor performance was re-evaluated with a change in the stainless steel substrate. It was realized that the underlying metal substrate could be affecting charge transfer by having a different substrate-composite material junction (316SS vs. carbon), so a thin layer of carbon was applied to the substrates before coating. The carbon was applied by ‘coloring’ the surface of the substrate with a graphite carbon rod until a uniform grey coating covered the middle 2 cm<sup>2</sup> active area. The graphitized substrate films results are shown in Figure 84.

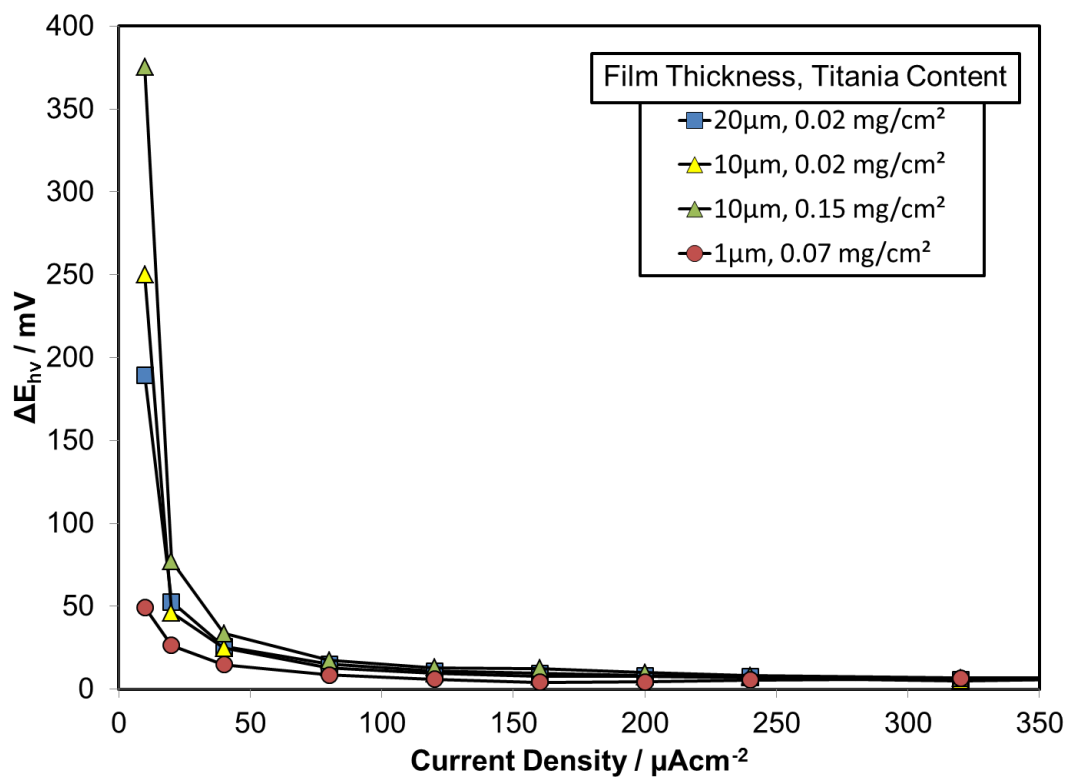


Figure 84 - Energy harvested for 1, 10, and 20  $\mu\text{m}$  PBT-TiO<sub>2</sub> films with differing TiO<sub>2</sub> content. Films loaded on graphitized 316SS perforated substrate, tested against 1.5  $\text{mg/cm}^2$  RuO<sub>2</sub> on TGP-H-030, N117 membrane separator, in 0.5 mM H<sub>2</sub>SO<sub>4</sub> recirculated at 1 mL/s at 20°C. Lines are added for illustrative purposes.

From the plots above it can be seen that there is an increase in performance across the board when compared to the non-graphitized samples. The high concentration 10um film performed best, followed by the lower concentration 10um film. With the 20um as well as the 1 um films performing worse than the mid-thickness films it again illustrates that there is a balance between resistance, charge separation and extinction, and photonic absorption that needs to be considered for an optimal device design. Overall, none of the 2-D films performed as well as their 3-D counterparts, showing there is a significant benefit for a distributed loading structure.

#### **4.4.3 EIS Analysis**

In Appendix O several EIS models had been proposed by researchers to analyze PBT and PBT-TiO<sub>2</sub> systems. It was decided that for simplicity the EIS analysis would be limited to a measurement of the overall resistance of the system. The resistance measurements were taken from the high frequency intercept (or an extrapolation thereof) with the real axis in the Nyquist plot.

##### **4.4.3.1 Cell Resistance**

The electrical resistance of the EIS profiles measured at open circuit for the 3-D films facing out is shown below, in Figure 85:

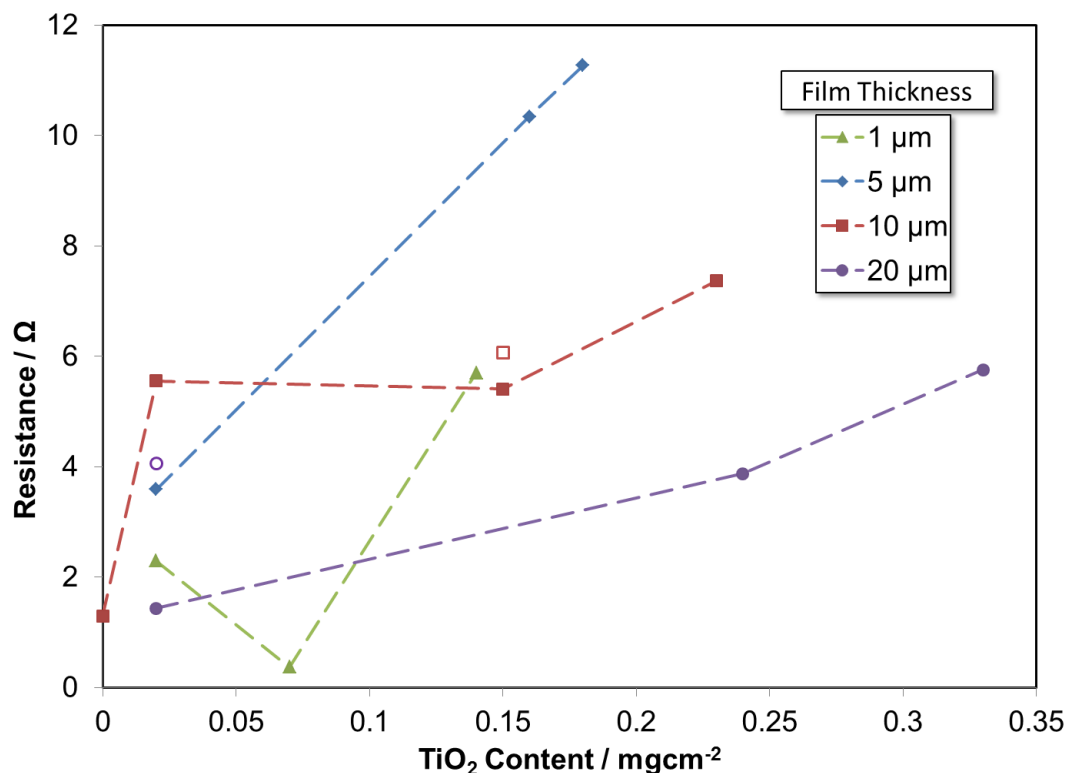


**Figure 85 - Cell resistance of PBT-TiO<sub>2</sub> samples loaded on TGP-H-030 in 0.5 mM H<sub>2</sub>SO<sub>4</sub> facing away from the membrane. Filled symbols denote 3-D samples, and open symbols denote 2-D samples. Lines are added for illustrative purposes.**

It can be seen that overall with titania inclusion there is an increase in cell resistance, for both the 3-D and 2-D samples, which agrees with the results shown from the ex-situ measurements (Figure 60).

What did not follow the expected trend is correlation of resistance with film thickness, although there was a large variability, as was seen with the *in situ* resistance measurement data. From the 3-D 0.02 mg/cm<sup>2</sup> film measurements, there was an average of 3.3Ω standard deviation. Even with this variation in error, several points stand out, most notably the 0.02 mg/cm<sup>2</sup> 10um film and the 0.07 mg/cm<sup>2</sup>, 1um film. For the low concentration (0.02 mg/cm<sup>2</sup>) 10 um film the electrochemical results did not stand out as behaving like an outlier, however

the solar performance was lower than the expected trend seen in the 20um samples. With the increased resistance of that sample it should be expected that the solar performance should be lower, in line with the measured value. For the mid-concentration 1um sample (0.02 mg/cm<sup>2</sup>), the dark electrochemical performance had a higher pseudo-exchange current density and lower pseudo-Tafel slope than the expected trend. In terms of solar performance however, it was much lower than the other samples and did not perform better in spite of the extremely low cell resistance. One possible explanation for this is that since the cell was already performing very well electrochemically, the enhancement from solar irradiation was less. This result could show that the connection between electrochemical performance and solar energy harvest is directly proportional to the overpotential of the unstimulated film. Considering a limited number of runs were conducted for each film thickness and concentration, more evidence would be needed to prove this correlation.

#### **4.4.3.2 Capacitive Double Layer**

With the EIS results limited to resistance analysis, another method was employed to examine the capacitive double layer. Using very slow cyclic voltammetry scans in a non-reactive portion of the potential diagram (0.3-0.4V vs. SHE) the capacitive double layer can be calculated by extrapolating the specific charge measured under the CV sweep to a 0 mV s<sup>-1</sup> scan rate, as discussed in Appendix P. When these values are plotted for the carbon fibre substrate samples it can be seen that there is an increase of the C<sub>dl</sub> with an increase in TiO<sub>2</sub> content, with an increase in applied film thickness, as well as with an increase in solution conductivity. This relationship is shown in Figure 86.

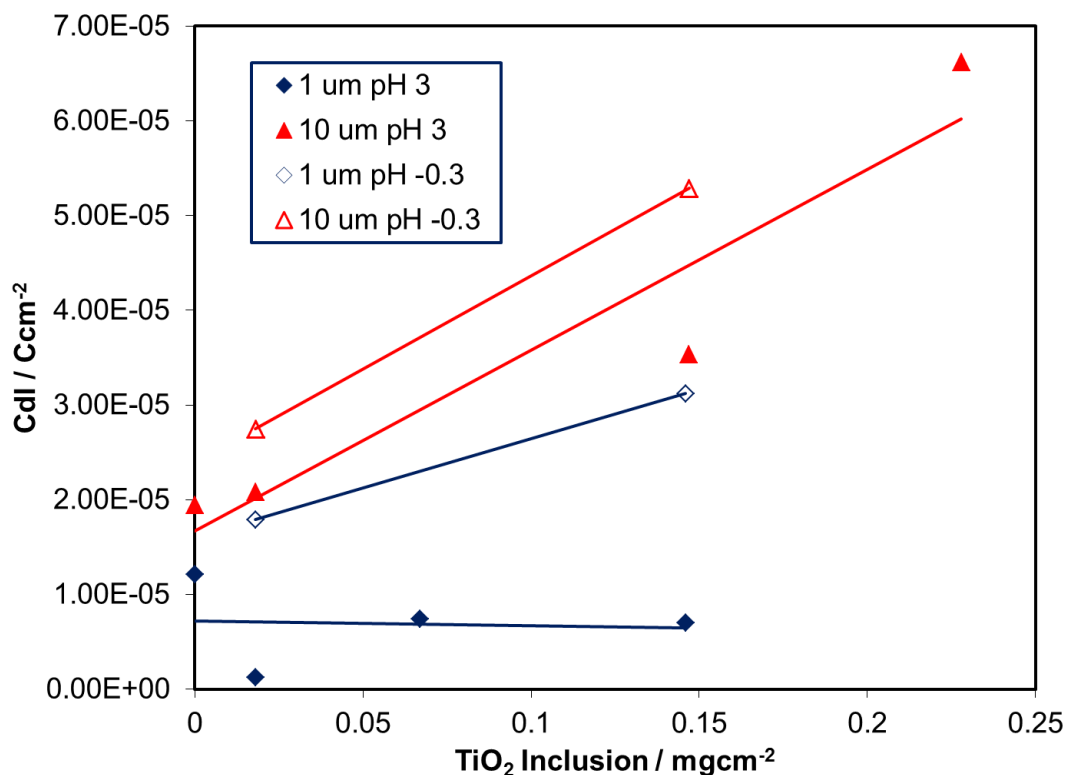


**Figure 86 - Measured capacitive double layer of PBT-TiO<sub>2</sub> films loaded on TGP-H-030 facing the N117 membrane, in 0.5 mM and 1M H<sub>2</sub>SO<sub>4</sub> recirculated at 1 mL/s at 20°C. Lines are added for illustrative purposes.**

An increase in the C<sub>dl</sub> for equivalent thickness samples would indicate more free surface electrons present and at a given surface area, a larger charge would mean smaller Gouy-Chapman layer thickness, enhancing charge transfer. This could serve as an explanation for the enhancement in catalytic performance (*i*<sub>0</sub>) of high titania loaded films.

#### 4.5 Conclusions

It was shown that PBT forms an insulating layer on a substrate and by itself does not perform well as a hydrogen generation catalyst. The addition of TiO<sub>2</sub> in the film and increasing the loading improves the overpotential losses and catalyzes the reaction for thin distributed films loaded on a 3-D carbon fibre paper system. With thicker films, the insulative properties of

the composite prevent effective charge transfer and hinder the reaction. Increasing TiO<sub>2</sub> content in the thicker films also increases the performance as seen in the thinner loadings, until film thickness combined with increased titania content further result in a deactivation of the surface through insulative losses. By analyzing the capacitive data it was determined that a high concentration acid reduced the effects of enhancement by titania inclusion and increased ion transport in the system. It was also concluded that thinner films were indeed much more active than larger thicknesses of films.

For compact 2-D films, it was found that even the thinnest applied films performed worse than the blank stainless steel substrate. It was found that these applied films formed a solid insulated blocking layer, likely facilitating an activation of the bare backside of the substrate which then exhibited poor performance and mass transfer characterized losses at higher current densities. This was also shown by the electrochemical enhancement of the 2-D facing out studies. Although poor performing, the films also exhibited the same increase in performance with an increase in TiO<sub>2</sub> content until the performance decreased due to a deactivation by further insulative losses.

Comparing 2-D and 3-D substrates, the 3-D substrates had lower overpotential losses than the 2-D substrates in spite of the pseudo-exchange current density being significantly higher for the 2-D films pressed against the membrane. Overall, it can also be concluded that the optimum film composition and direction would be a film with high titania content as close to the membrane as possible in order to minimize the overpotential contribution. This increase in overpotential is most noticeable in the thicker film variants, and with an increase in titania content.

In terms of solar performance, in spite of an increase in photonic absorption in the UV region the films did not perform as well as those with a minimum amount of titania. This increase in absorption coupled with a decrease in performance indicates the included films may have increased recombination problems (due to an increase in trap site dislocations), leading to poorer performance. Obviously a balance must be struck between a film thickness that maximizes the amount of light absorbed, while mediating the catalytic activity at the surface and recombinatory processes within the films.

## Chapter 5: Phase 3 – Tunable Substrate Parameters

### 5.1 Introduction

In Chapter 4 it was illustrated that there was an increase in electrochemical performance of the catalytic composites films when placed facing the N117 membrane. With the current testing architecture however, this film placement prevented photonic interaction as the irradiation originated from the direction facing the open solution. In theory, extension of the triple phase of other electrolytic systems can be accomplished by an increase in solute concentration, but this is not an option in this system due to constraints of the conduction band position of our semiconducting materials with respect to acid concentration. If the conduction band position is not at a potential that is lower than 0 vs NHE (plus additional overpotential losses), the redox reaction would not proceed with photonic stimulation. This is illustrated by T.Bak in Figure 133.

There are two obvious solutions to this problem without changing the solution concentration or film direction; a decrease of the substrate thickness to move the applied outward-facing films closer to the N117 interface, and/or incorporation of Nafion ionomer into the existing substrate to move the membrane interface closer to the applied films. Due to the complexities of manufacturing, characterizing, and testing new, thinner substrate architectures the latter option (Nafion ionomer) was chosen as a method to examine interconnectivity of the Nafion membrane with the applied films. Nafion ionomer is typically used to bond catalytic particles to the TGP-H-030 electrodes, as described in Chapter 2. Where with spray loading, the substrate is kept at an elevated temperature in order to instantaneously evaporate away the carrier alcohol. For this application a different method was chosen to impregnate the substrate with Nafion. Leguenza et al. [73] noted that

when drying at temperatures higher than 60<sup>0</sup>C there was a loss of performance of their solid state devices. Since the temperature of the substrates for spray loading would be higher than this set point, the spray loading procedure was abandoned in favor of a lower temperature drop cast method. The drop cast method is further described in subsection 5.2.

In an effort to examine the connectivity of the extension of the triple phase interfacial layer, composite films were also loaded onto bi-layer devices. These loadings involved placing two samples of TGP-H-030 into the loading cell and polymerizing composite on the surface as if it was a single separate substrate. The substrate was then divided upon processing, and selective loadings of Nafion ionomer were drop cast onto either none, one, or both pieces of electrode. This was done to examine the effect of continuity of the Nafion ionomer within a layer of the cathode with absolute discretion as to where the ionomer loading ended up. This setup was essential, as trials for incorporating selective ionomer loadings onto either the front face or back face through selective Nafion doping of a single layer sample failed. The selective doping samples failed as there was significant bleed through due to the open structure of the carbon fibre paper, not allowing for Nafion to be coated onto or into a single specific region.

## **5.2 Experimental**

Variation in Nafion interconnect architecture is separated into two main categories; incorporation of Nafion ionomer into TGP-H-030 substrates, and a bi-layer loading of Nafion ionomer on two co-deposited TGP-H-030 layers.

Incorporation of Nafion into the TGP-H-030 substrates was done after the films had been loaded onto the substrate and dried to remove the propylene carbonate. Efforts were made to load films onto TGP-H-030 pre-loaded with ionomer, but upon inspection and testing of the

pre-loaded substrate it appears that the ionomer inclusion interfered with the conductive polymer composite loading. This interference resulted in little to no composite polymer coating even at the conditions usually used for thick films. It is unknown as to why the ionomer coating prevented composite film deposition.

As mentioned previously, a drop-cast method was chosen to inundate the photoactive-film loaded substrates with Nafion. This method was chosen as it could be done at a low temperature without thermally conditioning the loaded photoactive film. The drop-cast solution was a 50/50 mix by weight of 5% Nafion in aliphatic alcohols with isopropyl alcohol resulting in a 2.5% w/w Nafion ionomer solution. 200  $\mu\text{L}$  of the solution was then added to the middle of the TGP-H-030 samples drop wise with the substrate laying horizontally on a Teflon sheet. Immediately after the substrate had soaked up the dropping solution, the substrate was placed in a drying rack and dried at 60<sup>0</sup>C for 30 minutes. After drying, the Nafion doped films were soaked in 0.5 mM H<sub>2</sub>SO<sub>4</sub> for 24 hrs before testing. Due to the encapsulating nature of the Nafion ionomer it was suspected that there would be an optimum coating of the TGP-H-030 fibers, so an analysis of the electrochemical performance of blank TGP-H-030 samples with various drop castings was conducted. Once an optimum Nafion coating had been established, as above, incorporation of Nafion into the co-deposited TGP-H-030 substrates was also done after the composite films had been loaded onto the substrates and dried to remove the propylene carbonate.

The nature of the composite films in this chapter have been previously characterized and discussed in Chapters 3 and 4, therefore limited testing was needed to further describe the loaded films. Nafion interconnectivity and any augmentations to the TGP-H-030 substrates

from the drop casting procedure were analyzed using SEM to check for morphological changes.

The details of the testing equipment, membrane assembly hardware and film loading protocol can be found in Chapter 2. Several testing variables were kept constant, with the flowrate of recirculated catholyte set at 1 mL/min, temperature set at 20<sup>0</sup>C, and anode catalyst composition set at 1.5 mg/cm<sup>2</sup> RuO<sub>2</sub> on TGP-H-060.

### **5.3 Characterization Results**

The characterization results were limited to analysis of the Nafion loading of the CFP samples as previous chapters dealt extensively with composite film analysis.

#### **5.3.1 MPL Layer Variation – Nafion Addition**

Since the drop casting method has not been used extensively by our group before, preliminary investigation as to the amount of Nafion loaded per number of drop casting times was investigated. The mass of 3cm x 3cm carbon fibre samples were weighed and successive amounts of Nafion added as described above. The dried samples were weighed, and their bare weights subtracted from the loaded weights to yield the total amount of Nafion loaded per applications of the drop cast ionomer. A plot of the resultant amount of Nafion loaded per times drop cast is shown in Figure 87.

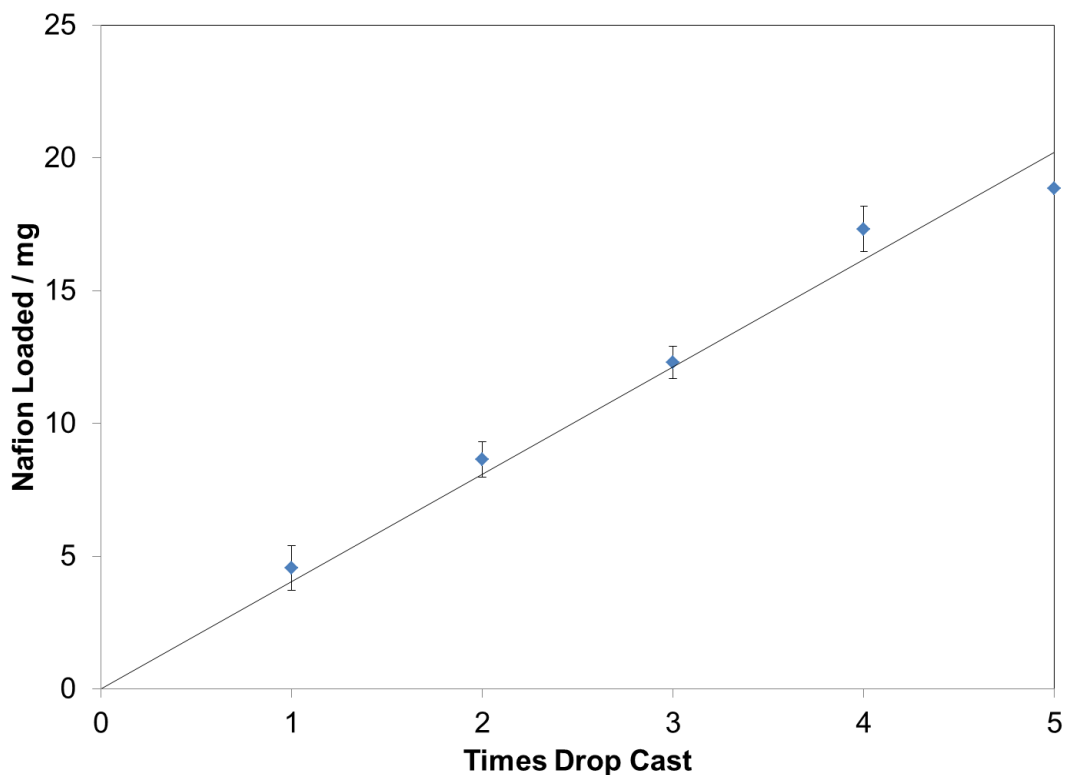


**Figure 87 - Amount of Nafion ionomer added per times drop cast for bare TGP-H-030 substrates. Fitted line is added for illustrative purposes.**

It can be seen that there is a linear dependence on the amount of Nafion loaded per number of times drop cast, providing confidence in the regularity of the loading procedure.

Although a regular amount of Nafion can be loaded by using this method, it is unknown as to the effect of the Nafion coating on electrochemical performance. An excess in Nafion coverage can block the surface of the electrode and restrict reactants from escaping, reducing the overall triple phase interfacial area. Therefore, an electrochemical investigation as to the optimum amount of Nafion was explored. These results can be found in Section 5.4.1.2.

The next examination of the Nafion doped substrates was the characterization of the Nafion coating using SEM.

### **5.3.2 SEM**

As discussed in the previous chapters, the SEM analysis of this dissertation is limited to a morphological overview of the applied films. Two sets of films were analyzed in this section, Nafion doped TGP-H-030 and Nafion doped 20um PBT-TiO<sub>2</sub> loaded baseline film. The Nafion coated samples can be compared with the SEM image of the bare substrate as found in Chapter 3 (Figure 31).

#### **5.3.2.1 Nafion Coated TGP-H-030**

The first samples examined were the Nafion coated TGP-H-030 substrates. These substrates were prepared by two applications of the drop-cast polymer application as described above. The first two images for analysis are Figure 88.a and Figure 88.b. Arrows indicate example areas of Nafion ionomer inclusion. These areas of Nafion inclusion were deduced by morphological means as compared with the previous SEM images of undoped TGP-H-030. These images represent a 500X magnification of through plane and in-plane Nafion distribution on the substrate, respectively.

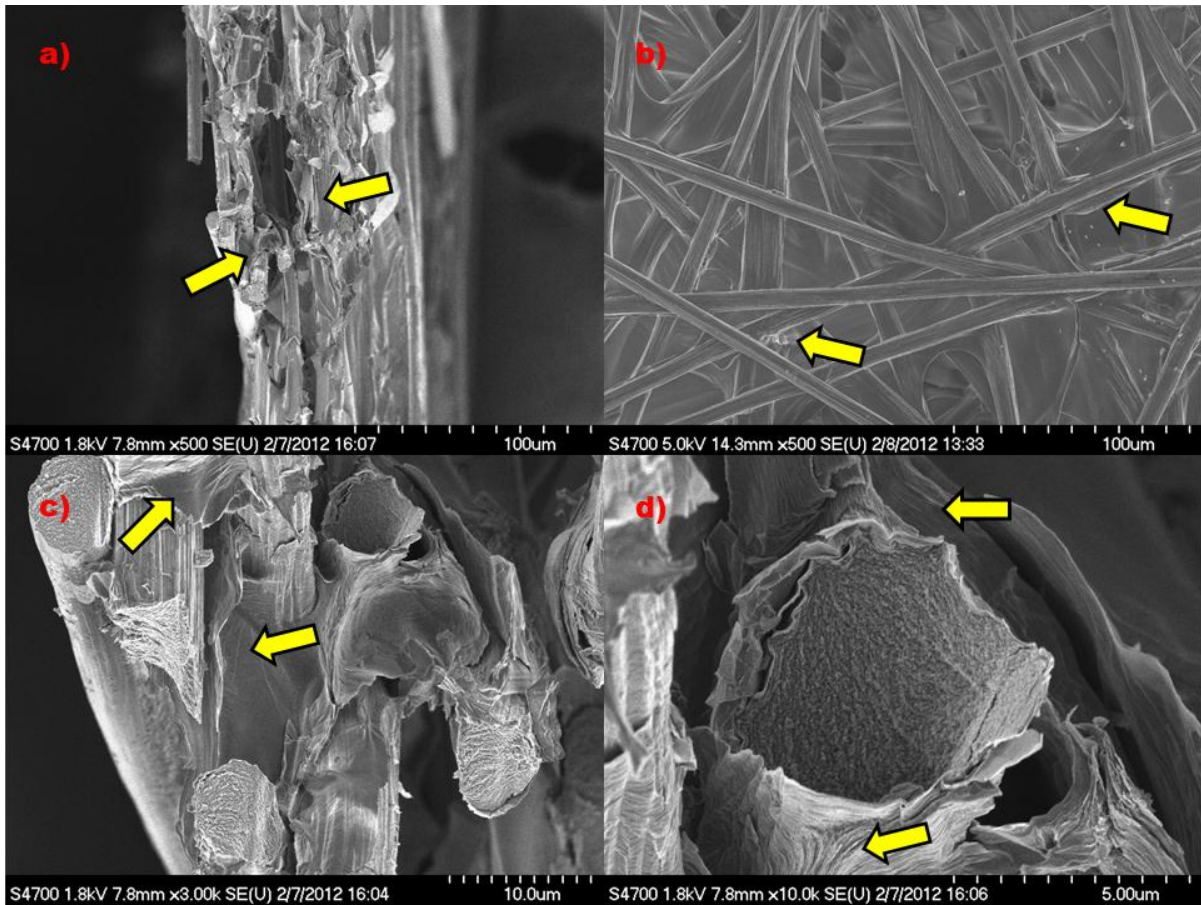


**Figure 88 - Morphology of Nafion-coated TGP-H-030 measured for a) cross-sectional sample at 500X magnification, b) planar sample at 500X magnification, c) cross-sectional sample at 3,000X, and d) cross-sectional sample at 10,000X. Arrows highlight areas of Nafion inclusion.**

As can be seen in the above images, the Nafion layer covers random areas of the fiber network and is more concentrated at junctions between the fibers. At these junctions there is a webbing that spans the fibers, enveloping the corners in Nafion polymer. It was determined that this webbing had Nafion coverage as it was lumpy and not smooth as seen in Figure 31. Since it was seen that there is an increase in composite loading at these fiber intersections in Chapter 4, this may be a problem with encapsulation of loaded photoactive polymer with this doping strategy. A closer examination of the fibres is shown in Figure

88.c, at a magnification of 3000X. In the SEM it appears that there is indeed a preference of Nafion loading at the fibre junctions, and the outer facing surface of the surface carbon fibre on the far left has minimal loading. Distribution of the Nafion ionomer is shown again on the surface of an individual carbon fibre in Figure 88.d at a 10,000X magnification. In the final micrograph it appears that there is a lamellar structure of the Nafion coating. The lamellar structure would be formed by a solvent front moving as the ionomer solution dries. This graduated coating shows that there is a fairly uneven distribution of Nafion on the microscale level and is not optimum as a coating method. Standard coating of microporous layers on fuel cell substrates employ high temperature evaporation of the spray loaded catalyst, that typically do not have such lamellar structure due to rapid evaporation.

#### **5.3.2.2 Nafion Coated 20 $\mu\text{m}$ PBT-TiO<sub>2</sub> TGP-H-030**

Baseline 20 $\mu\text{m}$  PBT-TiO<sub>2</sub> films were loaded with Nafion as described by the drop-casting process described in the previous section. A 500X magnification of the sample is shown in Figure 89.a:

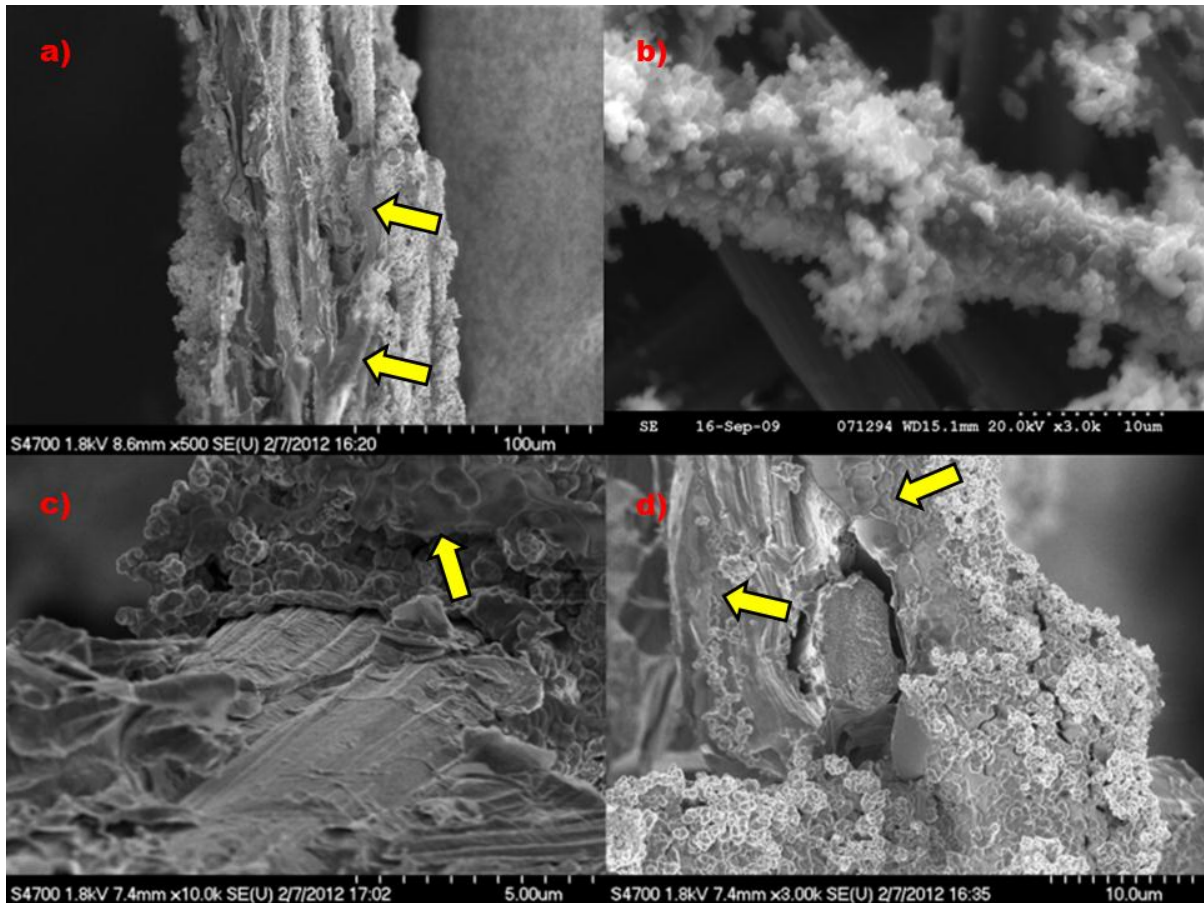


**Figure 89 - Morphology of PBT-TiO<sub>2</sub> loaded, Nafion-coated TGP-H-030 measured for a cross-sectional sample at a) 500X c) 10,000X, and d) 3,000X magnification. A reproduction of Figure 35 is shown in section b) for comparison with the Nafion loaded sample d) below. Arrows highlight areas of Nafion inclusion.**

As can be seen in the above micrograph, there is a high degree of coverage of the carbon fibre substrate by the two polymer film moieties. It appears that there are 2 distinct morphologies, the smooth lamellar structure of the Nafion and the granular structure of the composite film. A closer examination of the polymeric coverage is shown in Figure 89.d, at a 3,000X magnification and can be compared with the non-Nafion doped equivalent from Figure 35 in Figure 89.b. When a comparison is made to the plot of non-Nafion treated

composite loading (and other loadings in Chapter 3 and Chapter 4), it appears that there are areas of the composite morphology that are covered by the Nafion. These areas have a morphology that appears to be smoothed over, with an underlying structure that resembles the nucleation and growth of the pristine composite film. A further example of this partial coating of the composite films is shown in Figure 89.c at 30,000X magnification. Again at this magnification, regions of composite film seem to have areas of coverage by a Nafion layer.

## **5.4 Photoelectrochemical Results**

The electrochemical performance of Nafion doped blank TGP-H-030 and Nafion doped, composite loaded film variants were tested under galvanostatic operation at different current densities in a lightproof enclosure at 20°C with N<sub>2</sub> purged 0.5 mM H<sub>2</sub>SO<sub>4</sub> electrolyte. The anodic potential of the counter electrode was again stable and constant for different film samples, with variation in cell potential observed originating at the cathodic electrode, as detailed in Chapter 3.

### **5.4.1 Dark Performance**

The dark catalytic performance of the Nafion doped blank samples, Nafion doped, composite coated samples, and Nafion doped, bi-layered coated samples were tested as outlined in Chapter 2.

#### **5.4.1.1 Blank Nafion Coated CFP**

As mentioned in section 5.3, there should be a balance between Nafion interconnectivity, enhancing proton transfer in low concentration acid solutions, with a reduction in electrode surface area with increased coverage by ionomer. The optimization of these two parameters for our electrode configuration is shown by measuring the electrochemical performance of

sequentially greater loadings of drop cast Nafion coverage. The cathodic potential of the Nafion doped TGP-H-030 films as a function of current density is shown in Figure 90:

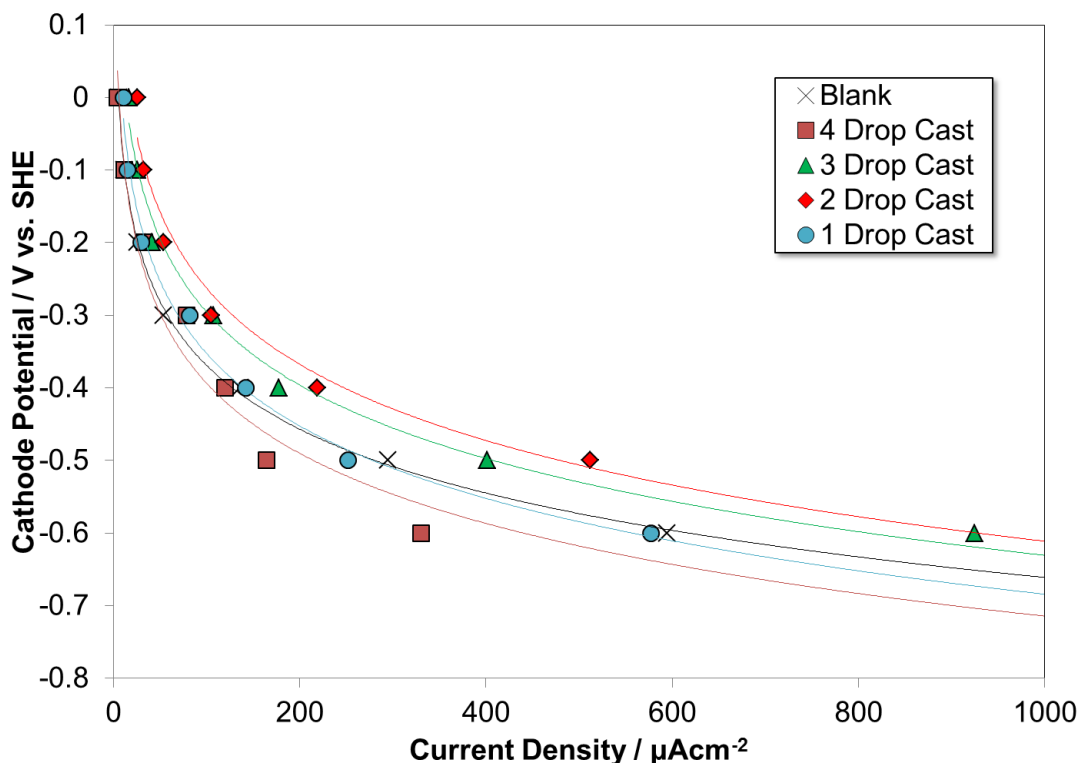


**Figure 90 - Cathodic potential of Nafion doped blank TGP-H-030 substrates. Logarithmic curve fit used to demonstrate Tafel correlation.**

It can be seen that with Nafion addition to the TGP-H-030 there is an increase in electrochemical performance with 1 and 2 times Nafion ionomer drop casting, but then a decrease in performance with further loading. The analysis of the Tafel-type performance parameters of the above films is shown in the following table, Table 3:

Sample	Pseudo- $i_0$		Pseudo-Tafel Slope
	Drop Cast	A/cm <sup>2</sup>	mV/dec
Blank CFP	0	2.51E-05	289
Nafion Loaded	1	2.81E-05	323
	2	4.31E-05	305
	3	3.65E-05	304
	4	3.28E-05	421

**Table 3 – Pseudo-exchange current density and pseudo-Tafel slope of blank and Nafion loaded TGP-H-030 substrates**

From the data in the above table it can be seen that there is a peak in pseudo-exchange current density for the Nafion doped substrates that had undergone 2 loadings of ionomer coating. Upon examination of the pseudo-Tafel slope, there is a slight increase upon initial Nafion addition, however it is not until the 4<sup>th</sup> loading where the pseudo-Tafel slope becomes very high. The variance as measured from multiple blank testing is on the order of  $3 \times 10^{-6}$  A/cm<sup>2</sup> for pseudo-exchange current density and 20 mV/dec for the psuedo-Tafel Slope. It was decided that since the electrochemical performance of the blank samples peaked upon 2 loadings of Nafion doping, the composite loaded film samples should also be loaded with similar amounts of Nafion impregnation. The results do not indicate a statistically conclusive difference in performance, but served as a basis for Nafion addition to the PBT-TiO<sub>2</sub> samples.

#### **5.4.1.2 Nafion Coated CFP Baseline Samples**

A varied selection of composite loadings on TGP-H-030 were chosen for comparison to Nafion doped samples. This varied selection was chosen to illustrate that regardless of composition of composite loading there was a uniform performance difference with Nafion

doping. The Nafion doping was held constant at approximately  $1.0 \text{ mg/cm}^2$  (2 drop cast loadings).

The Nafion doped composite film electrochemical results are shown in Figure 91 below:

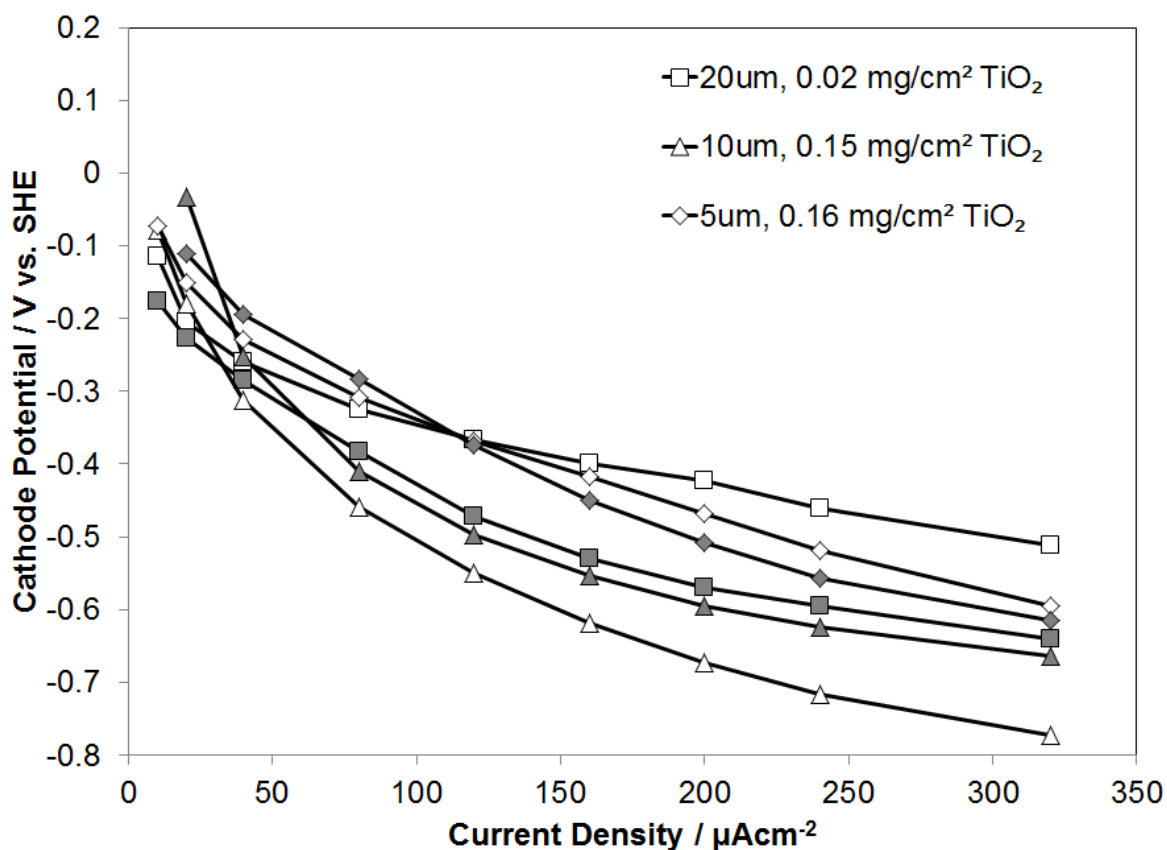


Figure 91 - Cathodic potential of Nafion doped PBT-TiO<sub>2</sub> (filled symbol) composite films compared to non-doped (open symbol) samples loaded on TGP-H-030 substrates tested against  $1.5 \text{ mg/cm}^2$  RuO<sub>2</sub> on TGP-H-030, with N117 membrane separator, in  $0.5 \text{ mM H}_2\text{SO}_4$  recirculated at  $1 \text{ mL/s}$  at  $20^\circ\text{C}$ . Lines are added for illustrative purposes.

As seen above, the results do not show a distinct trend. Analysis of the electrochemical results again involved determining the pseudo-Tafel slope and pseudo-exchange current density, and comparing these results with the same films without Nafion doping as presented

in Chapter 4. The results can be seen in Table 4, with the change in pseudo-exchange current density and pseudo-Tafel slope between Nafion doped and pristine composite films represented by the  $\Delta$ pseudo-exchange current density and  $\Delta$ pseudo-Tafel slope columns:

Sample thickness [ $\mu\text{m}$ ], $\text{TiO}_2$ content [ $\text{mg}/\text{cm}^2$ ]	Pseudo- $i_0$	$\Delta$ Pseudo- $i_0$	Pseudo-Tafel Slope	$\Delta$ Pseudo-Tafel Slope	$R_{\text{ohmic}}$
	$\text{A}/\text{cm}^2$	$\text{A}/\text{cm}^2$	$\text{mV}/\text{dec}$	$\text{mV}/\text{dec}$	$\Omega$
20, 0.02	1.37E-05	104%	324	117%	2.3
10, 0.15	2.58E-05	138%	462	97%	3.7
5, 0.16	5.22E-05	198%	562	183%	1.8

**Table 4 – Pseudo-exchange current density and pseudo-Tafel slope of 1  $\text{mg}/\text{cm}^2$  Nafion doped, PBT- $\text{TiO}_2$  films loaded on TGP-H-030 substrates and in comparison with equivalent undoped PBT- $\text{TiO}_2$  films**

It can be seen from the above data there is an increase in pseudo-exchange current density with the largest change for the thinnest film loading tested. As discussed in Chapter 4 this is likely due to the composite loading for the less loaded samples being sparsely distributed, where the higher loaded samples have more complete coverage. With Nafion addition to heavily composite loaded films it was seen that there was some coverage of the catalytic film surface by the ionomer, resulting in a possible deactivation of the catalytic activity by encapsulation in Nafion. For higher titania loaded thick films this encapsulation would also occur. For the less Nafion encapsulated samples (sparsely covered, 5  $\mu\text{m}$ , 0.16  $\text{mg}/\text{cm}^2$   $\text{TiO}_2$  sample), the deactivation would be less (provided there was not a selective deposition of ionomer onto composite sites), and the interconnectivity would further enhance the catalytic performance. In terms of pseudo-Tafel slope there did not appear to be any benefit from Nafion doping of the samples. This result was further scrutinized in the bi-layer analysis of Nafion loading (Section 5.4.1.3)

### 5.4.1.3 Bi-layered Nafion Coated CFP Baseline Samples

The bi-layered sample analysis of Nafion distribution was carried out on the best performing baseline 20 $\mu\text{m}$  thick film. The composite PBT-TiO<sub>2</sub> film was loaded onto either one or two substrates compressed in the deposition cell, keeping careful attention to the order and direction of the deposited film. For the single substrate sample, Nafion deposition was applied to the back side of the CFP. For the bi-layer samples, the Nafion was deposited onto the substrates such that there was a variation in loading with: the inner substrate, the outer substrate, both substrates, or neither substrate. These films were analyzed alongside the undoped baseline sample reported in Chapter 3 (CFP one layer), and are shown in Figure 92.

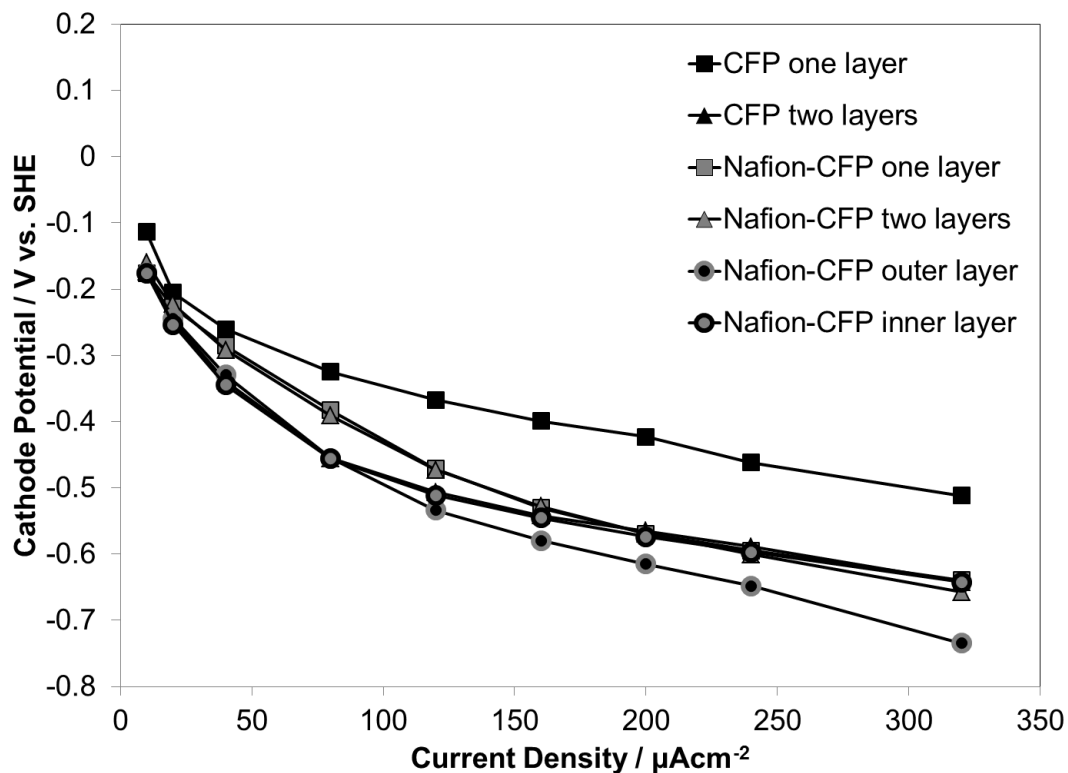


Figure 92 - Cathodic potential of bi-layer Nafion doped 20  $\mu\text{m}$ , 0.02  $\text{mg}/\text{cm}^2$  titania loaded, PBT-TiO<sub>2</sub> composite films on TGP-H-030 substrates tested against 1.5  $\text{mg}/\text{cm}^2$  RuO<sub>2</sub> on TGP-H-030, with N117 membrane separator, in 0.5 mM H<sub>2</sub>SO<sub>4</sub> recirculated at 1 mL/s at 20°C. Lines are added for illustrative purposes.

It can be seen that with addition of Nafion to the bi-layer loaded films there is an overall decrease in performance with Nafion addition. Also there is a decrease in performance with the division of film loading onto bi-layered substrates. As expected, the worst performing film is for the bi-layer with the inner substrate having no Nafion but the outer substrate having Nafion doping. This sample was expected to perform the worst, as it included two CFP layers and a blocking Nafion layer without any direct interconnect to the N117 membrane.

A further breakdown of the cathodic electrochemical performance into the pseudo-exchange current density and pseudo-Tafel slope is shown in Table 5. The cell resistances as measured by EIS are included to aid the discussion in performance, and to show that the resistance corrections are small.

Sample	Pseudo- $i_0$	Pseudo-Tafel Slope	$R_{ohmic}$
	A/cm <sup>2</sup>	mV/dec	$\Omega$
Single Layer	1.31E-05	277	1.4
Single Layer Coated	1.37E-05	324	2.3
Double Layer	1.11E-05	314	3.6
Double Layer Coated	2.23E-05	410	2.8
Inside Layer Coated	1.08E-05	314	7.2
Outside Layer Coated	1.24E-05	365	5.2

**Table 5 – Pseudo-exchange current density and Pseudo-Tafel slope of bi-layer 1.0 mg/cm<sup>2</sup> Nafion doped 20  $\mu$ m, 0.02 mg/cm<sup>2</sup> titania loaded, PBT-TiO<sub>2</sub> composite films on TGP-H-030 substrates**

As discussed previously for the analysis of one layer CFP samples coated in Nafion, there is only a small increase in pseudo-exchange current density and pseudo-Tafel slope of the highly loaded composite samples. The decrease in performance is attributed mostly to the

increase in pseudo-Tafel slope, as the Nafion coating could serve to block the active sites for catalysis.

When the film deposition is coated onto the bi-layered TGP-H-030 substrates it can be seen that there is a slight decrease in pseudo-exchange current density and an increase in pseudo-Tafel slope from the single layered samples. This decrease in performance is expected, as the distribution of film is farther away from the N117 membrane with the thicker dual CFP electrode. With addition of the Nafion ionomer into the dual layer structure there is a large increase in pseudo-exchange current density, showing that for thicker substrates the extension of Nafion linkage helps to increase catalysis. This was also seen for the lower loadings of PBT-TiO<sub>2</sub> on single layered substrates with Nafion linkage. However there is also a large increase in pseudo-Tafel slope with Nafion inclusion.

When comparing the single layer coating on bi-layered electrodes the inner layer coated sample performs similarly to the non-coated sample in spite of having a cell resistance double that of the uncoated bi-layer device. For the outer layer coated device there does not appear to be any gains in pseudo-exchange current density, but again the pseudo-Tafel slope increases and as a result the film structure. These results shows that for an increase in pseudo-exchange current density, the Nafion ionomer must extend fully through the carbon fibre substrate but such gains overall are offset by higher pseudo-Tafel slopes.

#### **5.4.2 Illuminated Performance**

The films were again tested in AM1.5G 0.1 W/cm<sup>2</sup> artificial sunlight in order to measure their photoelectrochemical performance. These results are divided into two sections: i) single layer Nafion doped samples, and ii) bi-layer Nafion doped samples.

### 5.4.2.1 Nafion Coated CFP Baseline Samples

The dark and light polarization curves were subtracted and the difference plotted to express the energy savings with a variation in increasing current. The results for the single substrate Nafion doped films (filled symbols) are shown below in Figure 93, and can be compared to the results for non-Nafion doped samples from Chapters 3 and 4 (open symbols).

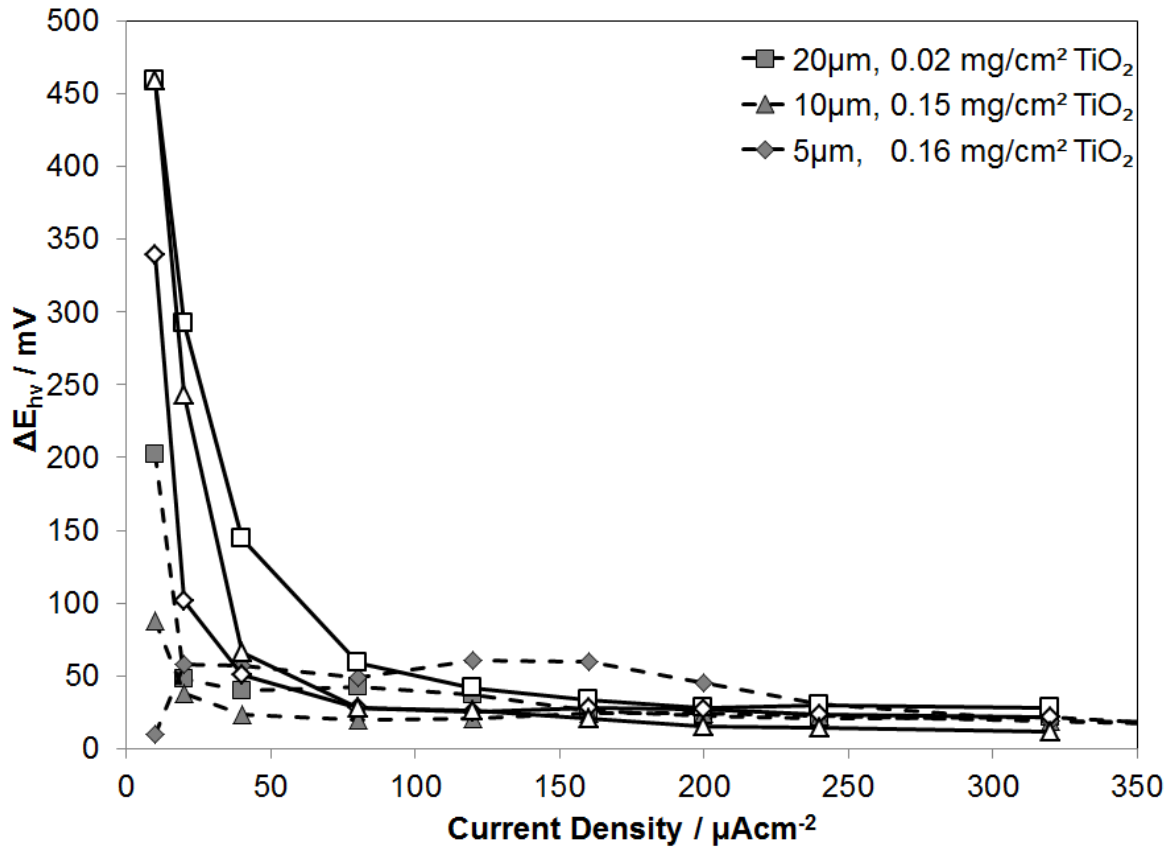


Figure 93 - Energy harvested from 1  $mg/cm^2$  Nafion doped PBT- $TiO_2$  (filled symbols) composite films with differing film thickness and  $TiO_2$  content compared to non-doped (open symbol) samples loaded on TGP-H-030 tested against 1.5  $mg/cm^2$   $RuO_2$  on TGP-H-030, with N117 membrane separator, in 0.5 mM  $H_2SO_4$  recirculated at 1 mL/s at 20°C. Lines are added for illustrative purposes.

There are two trends to note upon inspection of the Nafion doped solar data. The most striking feature of the Nafion addition to the single layer CFP films is that there is a severe deactivation of the photoelectrochemical gains from those seen in previous chapters. There may be two different possible explanations for this, both on account of Nafion coverage of the active photocatalytic surface. The first possible reason for deactivation is the blocking of the active surface, reducing the enhancement of the photonic promotion by not allowing products to be released from the catalytic sites. Since protons can be transported to the catalytic surface, but the product gas ( $H_2$ ) would have trouble escaping, this could be a reason for deactivation of the composite films with Nafion addition. Another explanation for the deactivation lies in the electronic density of the Nafion polymer itself. As mentioned in Chapter 1 and the Appendices, the grafted sulfonic sites in the Nafion polymer act as acidic centres, and this 'superacid' film structure may serve to alter the surface potential of the films in the proximity of the Nafion. The working fluid was chosen at a pH of 3 to allow for promotion of electrons to the conduction band of the PBT-TiO<sub>2</sub> composite film, however, if there is a shift through coverage by an acidic structure at the surface of the film, the potential at that point may be such that the conduction band is shifted to a position where the redox reaction cannot proceed. Another possible explanation is the absorption of higher energy light (UV) by the Nafion, reducing photostimulation. Although these results do not serve to enhance our device performance, they may be an indicator that device enhancement is possible by tailoring of active surfaces is possible by doping with regions of 'superbasic' structure at the cathode to pin the potential, provided there is still a 'superacid' component for proton transfer.

Although there is a severe decrease in the photocatalytic performance of the Nafion doped films, the addition of Nafion is not without its merits. Considering the resistance values are not as high as the poorly performing, high resistance samples shown for the baseline analysis in Figure 48, (although the samples were only tested once) it gives one confidence that this effect is due to Nafion and not simply due to variability. Upon closer examination of the photo-response of the doped films it can be seen that there is a different shape to the collected energy curve, most notably for the 5um film loading. After the initial deactivation of the low-current ( $< 50 \mu\text{A}/\text{cm}^2$ ) region there is an increase in the film performance up to about  $225 \mu\text{Acm}^{-2}$ , potentially due to the enhanced triple phase connectivity. This effect is why the Nafion addition was chosen for study, to possibly enhance the ionic transfer and extend the solar performance into higher current densities. It is postulated that perhaps with a more dichotomous lamellar structure (with layers of segregated photoactive composite separated but in close proximity to a Nafion conduit) this effect can be promoted without deactivation with surface coverage as seen by the drop-wise addition of the Nafion ionomer.

#### **5.4.2.2 Bi-layered Nafion Coated CFP Baseline Samples**

The results for the bi-layer substrate Nafion doped films are shown below in Figure 94, and the baseline result from Chapter 3 (CFP one layer) included for reference.

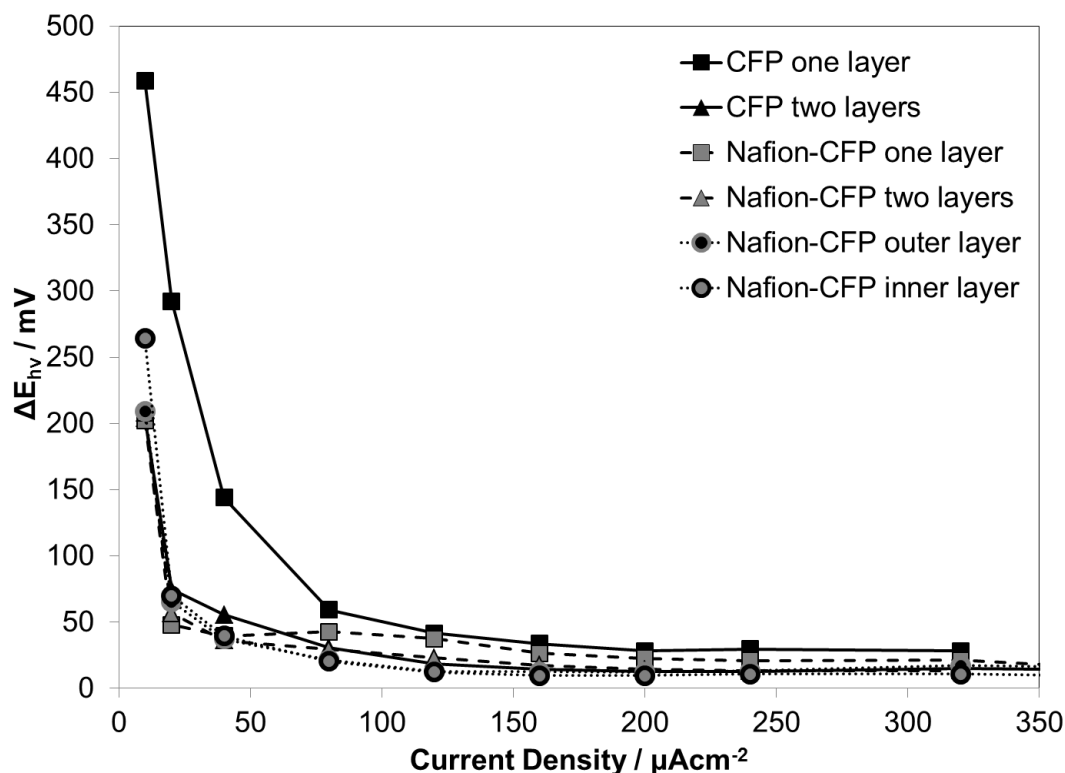


**Figure 94 - Energy harvested from single and bi-layer TGP-H-030 20  $\mu\text{m}$ , 0.02  $\text{mg}/\text{cm}^2$   $\text{TiO}_2$  baseline PBT- $\text{TiO}_2$  films with selective Nafion doping. Films are tested against 1.5  $\text{mg}/\text{cm}^2$   $\text{RuO}_2$  on TGP-H-030, with N117 membrane separator, in 0.5 mM  $\text{H}_2\text{SO}_4$  recirculated at 1 mL/s at 20°C. Lines are added for illustrative purposes.**

From the above plot the deactivation of the solar performance in the Nafion doped and bi-layered structures is seen. Again there is a small hump in performance for both the single and double layer TGP-H-030 fully loaded Nafion-CFP samples, which would be indicative of enhanced triple phase connectivity. The single layer Nafion doped sample performed better than the double layer on account of the photoactive surface being closer to the membrane. This result leads to the conclusion that a reduction of distance from the membrane would also enhance the photoelectrochemical performance.

The bi-partial Nafion loadings (either on only the inner layer, or only the outer layer) did not exhibit the enhanced performance hump. It is suspected that with division of the Nafion loading, and with the substrate thickness being too large the result is that the Nafion doping is too far away from the outer active surface to enhance the photoelectrochemical performance. Perhaps with thinner substrates this bi-partial approach could function as intended. For the Nafion-CFP outer layer the proximity of ionomer is there, but the connectivity to the N117 membrane is missing, resulting in no improvement in performance.

## **5.5 Conclusions**

It was shown that for blank TGP-H-030 substrates doped with drop cast Nafion ionomer there is an increase in electrochemical performance as the Nafion permeates the substrate. This performance increase continues with increased loading until there is an eventual decrease due to too much Nafion coverage, which would encapsulate the active surface and prevent product gas release. It was found that for our particular drop casting method the optimum Nafion coverage of bare TGP-H-030 substrates was 2 times drop cast ( $1 \text{ mg/cm}^2$ ), with drying between layers.

Electrochemical results showed that when this Nafion drop cast technique was used on various loadings of PBT-TiO<sub>2</sub> composite films, there was an increase in pseudo exchange current density, most notably for the lower loaded film thicknesses. This increase in exchange current density is attributed to better connectivity of the triple phase interface. This result was confirmed with the bi-layer selective addition of Nafion, where the largest increase was seen for films that were fully loaded with Nafion on the extended substrate architecture (double layer TGP-H-030).

There was mixed performance in regard to the pseudo-Tafel slope for single TGP-H-030 samples. Analysis of the bi-layer treated samples showed that there was an increase in pseudo-Tafel slope upon addition of Nafion to the films. The pseudo-Tafel slope increase was considered to result from blockage of the active surface. Coverage of the composite film was shown in the SEM micrographs.

Although a large positive effect on the photocatalytic performance of the Nafion doped films was expected, it was seen that there is instead a significant deactivation of the films. This deactivation was due to the blocked surface coverage as discussed in the dark electrochemical results, due to a shifting of the conduction band potential to an inactive position, or by absorption of UV light by the Nafion layer. This result, although negative does suggest that surface doping of acidic or basic sites may provide a new strategy for photoelectrode development.

Although deactivating, one positive element about Nafion doping of the photoactive films is there was an apparent enhancement in the middle to higher current regions of the testing range. This result was shown by a change in the photonic response from a largely exponential decrease in performance with increasing current density for undoped samples to a performance that has a small hump enhancing the middle current range for the doped samples. Although limited repetitions were performed, this phenomena was seen in both the single-layer and bi-layered Nafion doped structures, confirming the effect. This result suggests that with better control of Nafion placement, such as with a dichotomous lamellar structure that does not block the active surface an enhancement in photoelectrochemical performance is possible.

## Chapter 6: Conclusions and Recommendations

### 6.1 Conclusions

It was demonstrated that although semiconducting elements are typically used as photoanodic electrodes, composite films of conductive polymer with nanoparticulate inclusions also have benefits for hydrogen generation on the cathodic side of the half-cell. Since the majority of research has focused on the photoanode, this has allowed for opportunity to develop new approaches for the cathode, which has been relatively under-examined and which does not operate in an oxidative environment. Results were similar to photocathodic results found by Bookbinder et al. [53], where electrode potentials significantly more positive than the electrochemical  $H^+/H_2$  potential occurred. This result showed that photocathode driven hydrogen production is possible and could have significant benefit using these composite materials.

With regard to cathodic performance, two aspects were considered; i) catalytic electrochemical performance as well as ii) photonic energy harvest. Unfortunately, these two aspects proved to be conversely proportional to one another.

For strictly electrochemical performance it was found there was a strong influence with the three variables tested – film thickness, titania content, and proximity to the Nafion membrane. The optimum structure tested for electrochemical performance was with the thinnest films, to avoid high through plane resistance losses of the composite films. With increased titania inclusion this increased resistance in thicker films, but for the thinnest films it was seen that with increased inclusion there was increased performance.

It was also shown that electrochemical performance was improved when the films were pressed against the N117 membrane. Limitations on the conductive band position of the

materials tested required a weak concentration (0.5 mM, pH 3) of acid for solar activation, so ionic conductivity to sites farther from the membrane was limited. An augmentation of triple phase connectivity through a Nafion drop casting method was also examined. Improvement of connectivity resulted in an increase in inherent catalytic activity for films that were placed further from the membrane for films that were sparsely populated. Unfortunately, this increase in performance was offset by an increase in the pseudo-Tafel slope. The slope based decrease in performance is especially pronounced in the higher polymer composite loaded films, indicating that this loading technique could be covering some of the composite deposition. Covering of the composite with Nafion would still allow for proton conduction, but would not allow for gas escape, effectively deactivating the surface. This assertion was confirmed with SEM micrographs. Alternate loading of Nafion either by spray loading or pre-loading were not possible due to manufacturing constraints (high temperature and Nafion incompatibility with the polymer loading sol, respectively), so recommendations based on reduction of carbon substrate thickness without Nafion loading are suggested in Section 6.2.2.

External quantum efficiency as a measure of photonic performance indicated there were also strong influence with film thickness, titania content, and Nafion interconnectivity, albeit differing from the electrochemical performance results. With an increase in film thickness on a 3-D substrate, there is an increase in solar energy collection, especially when the current density is increased. Despite an increase in spectral absorption, with an increase in titania content there was a decrease in photonic performance. This is likely due to increased recombination due to increased interfacial (PBT-TiO<sub>2</sub>) inclusion, but no fluorescent studies were employed to confirm this conclusion due to the lack of high speed photonic testing

equipment needed to measure fluorescent emission. The results of Nafion doping showed a photo responsive deactivation of the films (potentially in part to UV absorption by the Nafion layer), although there was an apparent enhancement in the middle to higher current regions of the testing range.

## **6.2 Recommendations**

The recommendations section of this dissertation is split into several sections, outlining suggestions for research direction, system upgrades, and further device architectural considerations. The sections recommended for investigation are outlined as follows; reactor and testing apparatus upgrades, alternative sample preparation, and additional electrochemical testing protocol.

### **6.2.1 Reactor and Testing Apparatus Upgrades**

During the course of our study there have been several augmentations to the equipment used for device preparation and testing. However, using the experience garnered from our experimental studies there are a number of further improvements that could be implemented to improve the performance, reliability, and functionality of our devices.

One such improvement is the use of a microcell array. In the course of investigating solid state devices for comparison to our setup, i.e., benchmarking, it was noted that most of the devices reported active areas of less than  $1 \text{ cm}^2$ . Benchmarks in the range of active areas similar to our device architecture ( $2 \text{ cm}^2$ ) and larger were not found. It was also discussed in Chapter 3 that there was a large variation in device performance with resistance that did not follow ohm's law, which was a result of non-uniform electric fields that would alter solid state device performance. For this reason, the performance of the devices outlined in Appendix Q may have an over-inflated performance value when compared to a scaled-up

version of their designs. For some of the solid state device fabrication techniques scale up is difficult, if not possible at all. Vapor deposition, e-beam fabrication, and organic spin coating techniques all have inherent device production difficulties which arise when scale-up is attempted.

While it is beneficial that the results of this dissertation showed an operational scale-up of device area ( $2 \text{ cm}^2$ ) to better represent an actual device, there is merit to conducting and reporting research that could serve as a 'best in class', even with a miniscule device active area. Smaller scale research can also have less variation in sample composition and performance, as we found with our larger scale research that variation in composition resulted in a larger variation in performance.

The approach of analyzing variability of device loading with microcell performance improvements can be accomplished with a change in sample substrate architecture. If the underlying carbon fiber substrate was divided into sections with individual electronic contacts, then an array deposition could be examined. There are several alternative substrates to accomplish this, and with a division of a larger variable loading of catalyst with individual microcells it would allow for a much faster screening against a common counter electrode.

#### **6.2.1.1 Acid Dosing and pH Measurement**

It can be noted that with several of the baseline platinum loaded TGP-H-030 studies, the steady-state cathode potentials have an apparent position just slightly less than that of the redox potential. This could be the result of several factors, but the most likely reasons are miscalibration of the reference electrode, or variation in solution pH. Since the reference electrode was checked periodically and did not vary by more than 5 mV, it is suspected that

this variation is a result of a shift in solution pH on the cathode side. In electrolytic processes that employ a common electrolyte bath there should be no pH variation. However, in our membrane separator based system, there may be a shift in the pH of the two electrolyte compartments through proton pumping effects.

In our current cathode compartment there are unused 1/8" Swagelok ports that previously housed a second reference electrode used to confirm measurements of the primary reference electrode. These electrode ports could be retrofitted to incorporate a direct pH monitor, or alternatively the pH sensor could be added to the catholyte dewer to measure the bulk catholyte pH. These two values should be the same, so only one sensor would need to be incorporated. This system enhancement can be further developed with the addition of an acid titrant into the catholyte dewer. This would allow for *in situ* acid concentration variation of the catholyte, with the possibility to vary the concentration as a function of time at a set current density. This addition would further allow for rapid scans of performance variation with acid concentration without sample perturbation. One specific example of such an experiment would be to fix a specific current density and scan the pH to measure the reaction of the device performance with conduction band position variation.

#### **6.2.1.2 Gas Capture and Analysis**

Another addition to the testing equipment would be an upgrade to the gas handling system. As described in Chapter 2, the catholyte system is bubbled with nitrogen and a water trap is employed to form a hermetic seal to prevent oxygen access. Product hydrogen gas is captured within this stream when the catholyte is returned to the dewer through a series of PTFE tubing and carried away in the nitrogen stream. If this exit nitrogen stream were to be coupled with a GC/MS system then the relative amounts of nitrogen and hydrogen gas, as

well as water vapour, could be analyzed. This would allow a further improvement to the experimental results, as it would then be possible to confirm the mass balances of generated species with electrochemical data.

### **6.2.1.3 Optical Upgrades**

Currently the reactor setup allows for testing under dark/light conditions with “one solar intensity” set by the distance of the reactor from the solar simulator beam output. Changing to a new intensity means moving the reactor, which can disrupt sensitive electrical connections. An alternative to moving the reactor could be through the use of filters. Since the solar simulator has space for an additional filter along with the current AM1.5G filter, several spectral intensities could be tested without any cell movement. A selection of filters are available from the manufacturer (Sciencetech Inc.) with graduations of 10% to allow for a multitude of full spectrum filtering options. There are also bandpass filters available if certain wavelengths are desired to be selectively filtered out. This could be used to test the electrode films without assembling the full reactor setup for through membrane spectral testing where the membrane filters out some of the spectrum.

### **6.2.2 Alternative Sample Preparation**

Sample preparation in this thesis was chosen to mimic the loading procedures as outlined by Leguenza et al., outlined in Chapter 2. However, several variations of this procedure should be considered in order to further examine the variability in composite composition and deposition techniques. Several variations in the loading procedure and the reasoning for why their investigation is important are described below.

### **6.2.2.1 Microfibre Carbon Supports and Decal Architecture**

As described in Chapter 4, there were two approaches presented for better triple phase interconnectivity. As a conclusion to that chapter and as a recommendation for future work, it was surmised that a thinner carbon structure should be tested to reduce the distance from the membrane to the active surface in a dilute acid environment. Considering that the TGP-H-030 CFP was the thinnest CFP in that product line, alternative forms of thin carbon substrates are recommended for testing. One possible substrate choice is an electrospun polymer that is then graphitized, such as that under development by the research group of F. Ko at UBC [101]. These substrates are currently under investigation as a replacement to ITO in solar cells by the research efforts of P. Servati. They could serve well as a replacement underlying carbon substrate, as their thickness can be controlled by deposition time and can vary between 5-50  $\mu\text{m}$  and conductivity can be tuned by the degree of carbonization. Another interesting alternative to carbon fiber deposition would be to deposit the films directly on the membrane similar to catalyst coated membranes (CCM) in the fuel cell industry. Preliminary experiments of deposition onto commercial CCMs resulted in significant distortion of the membrane assembly due to swelling from the chemicals in the plating bath. An alternative to depositing composite films on the membrane directly is to load the polymer composite on a surface that could then be dissolved. With the substrate dissolved, the detached film can then be transferred onto a membrane and then hot pressed for adhesion. Experiments are currently underway to further investigate this technique, although preliminary results indicate that the morphology of the films is seriously altered with the hot pressing procedure.

Additionally, preliminary experiments were conducted to investigate through-membrane irradiation of the samples. It is possible to mate the research presented in this dissertation to complimentary photoanode development to set-up a stand-alone device. Considering that the conductive polymer composites represent mid-bandgap semiconductors, an ideal pairing would be with higher bandgap monolithic photoanodes such as  $\text{WO}_3$  and  $\text{TiO}_2$ . With high energy absorption cutting out the polymer damaging UV irradiation, a membrane based device could then utilize the visible transparency of the Nafion to transmit the appropriate photonic irradiation to the photocathode. A limited study of this through-membrane irradiation approach is shown in Appendix V, where a through membrane irradiation was conducted with films facing in on the cathode side. This initial work serves as a basis to recommended future work, as it showed promise as a successful strategy for layered spectral division with enhanced catalysis.

#### **6.2.2.2 Pulse Current Density Deposition**

All of the depositions were carried out at a galvanostatic current of  $0.5 \text{ mA/cm}^2$ .

Unfortunately it seemed that with this deposition rate held constant, films at lower loading times had sparse loading on select areas of the carbon fibre substrate rather than an overall thinner loading over the entire sample surface. By using a pulse deposition technique to ‘shock’ the system into spontaneous nucleation of a larger number of sites it is hypothesized that a more complete thinner surface coverage could be achieved. This would of course alter the thickness and nanoparticle incorporation of the applied films, thus an entire spectrum of characterization tests would need to be repeated.

### **6.2.2.3 Different Conductive Polymer/Nanoparticle Combinations**

Work began on studying the polymer composite films for the anodic reactions, or for a direct solar water splitting reaction, but the oxidizing degradation of PBT in an aqueous environment did not allow for direct anodic use (for decomposition mechanism see Figure 134). If a suitably stable polymer could be found to operate on the anode side it could be paired to form a direct solar driven polymeric device. Several limitations on the working electrolyte of the system were also in place due to the conduction band edges of the chosen materials. If an electron donating/withdrawing side group is substituted onto a side branch of the thiophene molecule it could be possible to shift the position of the conduction band [102]. Care must be taken however to ensure that side reactions do not take place with any substituent side moiety when the cell is running. A substitution of the nanoparticulate inclusion is also possible. Although Degussa's P25 titania (25 nm spherical nanoparticles) remains one of the premier choices for inclusion due to its inert nature, non-toxicity, and inexpensive cost, it is possible to perhaps consider different titania particle shapes. This approach has shown improved device performance increases in solid state systems as discussed in Appendix G.2 for tetrapod shaped CdS nanoparticles versus rod shaped particles. Alternative particulate inclusions should also be considered, focusing on cheap, earth abundant oxides such as  $\text{Fe}_2\text{O}_3$ .

### **6.2.2.4 Temperature and Supporting Electrolyte Variation**

Another film loading consideration is a variation in electrolyte composition and temperature. All of the films loaded in this dissertation were polymerized at room temperature in propylene carbonate. Since the freezing point of many organic solvents is lower than  $0^\circ\text{C}$  it is possible to fabricate the device films in a sub-zero temperature regime. This lower

temperature device film fabrication could lead to a better crystalline structure, enhancing the electronic charge transport in the films. Changes in temperature can also be used for post-treatment annealing procedures that could be performed to tune or form the deposited films. The supporting organic electrolyte and also plays a role in the final device film structure, as the size of the organic molecules and supporting anion dopant help to determine pore sizes in the final polymer film [103]. Considering ionic transport properties were found to have a large role in device performance, an alteration in the supporting organic electrolyte could be used to form devices with a better pore distribution. Pore size variation should be studied in order to enhance device performance.

#### **6.2.2.5 Selective Titania Surface Loading and Enhanced Particulate Connection**

The final and perhaps most prominent recommendation for sample preparation comes from the analysis of the difference in solar versus electrochemical results. It was shown that there was an enhancement in electrocatalytic performance with titania inclusion, but the improvement was most prominent when the film was thinnest. It was also noted that titania inclusion in the thicker films resulted in deactivation of solar energy harvest. It is therefore recommended that a bi-layer approach to titania loading be conducted. This bi-layer structure would reduce internal recombination sites, but still allow for surface catalysis and enhance charge separation to occur. There are also facile methods for surface deposition of titania with conductive polymers through UV polymerization using the oxidizing power of the nanoparticles themselves [104]. If a set composite thickness and composition could coat a surface and photocatalyzed this may result in a more even and complete layered composite loading.

An enhancement of selective layering can also be achieved with increased electronic coupling to the nanoparticulate inclusion. Currently the inclusion is embedded in the conductive polymer matrix and no polymer ligand linkage is binding the particles to the conductive polymer. It has been illustrated that solid state device performance can be enhanced by several orders of magnitude by using an acidic end group on the polymer (such as pentathiophene phosphonic acid) to bind together the titania and polymer components [105]. For the device electrolyte, care must be taken to ensure that competing acid effects do not result in a preferential detachment of particles from the polymer surface. Therefore, the end groups of the polymeric species must be stronger than those in solution. Polymeric monomers with phosphonic end groups would likely be the best choice, although they do not currently exist commercially.

### **6.2.3 Additional Photoelectrochemical Testing Protocol**

In this dissertation, an engineering approach was taken in order to test a fully fabricated device and vary parameters to check overall operating efficiency. Therefore most recommendations in this section revolve around the concept of basic electrochemical studies to further identify and dissect the core parameters in an *ex-situ* manner. Additional recommendations involving the current set-up but with differing working solution and photonic conditions follows, as well as recommendations for alternative substrate development and lifetime testing.

#### **6.2.3.1 Rotating Disc Electrode (RDE) Experiments**

In our experimental setup it was found that there were considerable ionic transfer effects with respect to device performance. In order to further examine these effects it would be beneficial to alter the ionic transfer properties without significantly altering the film

structure. A facile way of doing this would be to deposit the films on the tip of an RDE and alter the rotation rate. Of course with this alteration in experimental setup there must be a change in the direction that the solar flux is entering the cell, as RDE units typically operate in a vertical manner. This could be simply be accomplished using a 45<sup>0</sup> mirror below the cell to reflect the beam through a quartz bottomed reactor vessel with the RDE mounted above it.

### **6.2.3.2 Single Surface Energy Studies**

In order to further investigate the thin film properties of our deposited composite films, an analysis of thin films should be conducted. It was found in our first attempts with conductive AFM (Chapter 3) that electronic resolution of the through plane resistance was not able to be seen due to film surface roughness, film thickness variability, and variation in AFM tip contact. If thin layers of film, decorated with known amounts of titania were to be tested mapping of the surface energy with performance could be further determined. This technique could be used in conjunction with the above recommended microcell array testing to increase the breadth of data from a fully assembled device as well.

### **6.2.3.3 Electrochemical Impedance Spectroscopy**

As discussed in Appendix O, there exist many models for electronic circuit de-convolution of porous composite films. These models show promise in determining additional film properties, although only simplistic models were used for evaluating the described RC values in this dissertation. If a more rigorous modeling study was done, as well as a breakdown to simpler design structures (thin monolayer films, no membrane) then this technique could prove very valuable for a better understanding of the mechanisms by which the device is

operating. This is especially true for potentiostatic measurements of dark versus multiple solar intensity irradiations, and how the energetics of the system changes with insolation.

#### **6.2.3.4 Solar, pH and Temperature Variation**

Also discussed in Chapter 1, there is a major benefit to multiple solar intensity irradiation as a diagnostic tool as well as to reduce the active area of a finished device using a concentrator design. Due to the time constraints and the amount of variables already presented in this dissertation there were only limited higher intensity sun studies done for select experiments. Some of these results are shown in Appendix W, and show additional performance with increased solar intensity. Further experiments run at multiple solar intensities (in conjunction with the solar filter recommendations in Section 6.2.1) could serve to broaden the understanding of the underlying concepts.

A change in pH of the electrochemical system was addressed in Section 6.2.1. Additional solar testing of a variation with pH is recommended to determine optimum electrolyte properties such as conductivity and hydrogen ion concentration.

In Chapter 1 it was illustrated that optimum electrolytic cell performance is achieved with high temperature operation. Our system was tested primarily at 20<sup>0</sup>C, simply to avoid any strong temperature gradients that can be found in poorly insulated devices. It is known however, that the conductivity of organic polymers operates conversely to that of metals; i.e., as the temperature increases, so does conductivity. Therefore there could be a major benefit for the operation of these devices at higher temperatures in light of this conductivity increase. With current solid state silicon solar cell technology, device performance also decreases with temperature, so with higher temperature device structures, such as those that use concentrators, these organic polymer devices could have an advantage.

#### **6.2.3.5 Lifetime/Degradation**

The final recommendation is for studies to analyze the lifetime of created devices. Current devices have been operated for up to 2 hours at a time, far too short to comment on any degradation mechanisms. Also, there may be different degradation pathways with different spectral regions of light. Higher energy light has more damaging ionizing power, and is more likely to cause free radical generation. Therefore, a separation of UV and visible light lifetime studies is suggested.

## References

- [1] J. Conti and P. Holtberg, "International Energy Outlook 2011 - DOE/EIA-0484," 2011.
- [2] M. A. K. Lodhi, "Helio-hydro and Helio-thermal Production of Hydrogen," *International Journal of Hydrogen Energy*, vol. 29, p. 1099, 2004.
- [3] M. Grätzel, "Photovoltaic and Photoelectrochemical Conversion of Solar Energy.," *Philosophical Transactions. Series A, Mathematical, Physical, and Engineering Sciences*, vol. 365, no. 1853, p. 993, 2007.
- [4] J. Bolton, "Solar Photoproduction of Hydrogen: A Review," *Solar Energy*, vol. 57, no. 1, p. 37, 1996.
- [5] J. Biddle, D. Peterson, and T. Fujita, "Solar Photochemical Process Engineering for Production of Fuels and Chemicals," *International Journal of Hydrogen Energy*, vol. 10, no. 10, p. 633, 1985.
- [6] V. Flexer and N. Mano, "From Dynamic Measurements of Photosynthesis in a Living Plant to Sunlight Transformation into Electricity," *Analytical Chemistry*, vol. 82, no. 4, p. 1444, 2010.
- [7] A. Jenkins, "Soaking up the Sun," *Nature*, vol. 1, p. 1, 2007.
- [8] M. Grätzel, "Photoelectrochemical Cells," *Nature*, vol. 414, no. 6861, p. 338, 2001.
- [9] S. E. Shaheen, D. S. Ginley, and G. E. Jabbour, "Organic-Based Photovoltaics : Toward Low-Cost Power Generation," *MRS Bulletin*, vol. 30, p. 10, 2005.
- [10] D. Ginley, M. Green, and R. Collins, "Solar Energy Conversion Toward 1 Terawatt," *MRS Bulletin*, vol. 33, p. 355, 2008.
- [11] J. R. Durrant and S. A. Haque, "Solar Cells: A Solid Compromise," *Nature Materials*, vol. 2, no. 6, p. 362, 2003.
- [12] T. Kodama, "High-temperature Solar Chemistry for Converting Solar Heat to Chemical Fuels," *Progress in Energy and Combustion Science*, vol. 29, no. 6, p. 567, 2003.
- [13] D. Graf, N. Monnerie, M. Roeb, M. Schmitz, and C. Sattler, "Economic Comparison of Solar Hydrogen Generation by means of Thermochemical Cycles and Electrolysis," *International Journal of Hydrogen Energy*, vol. 33, no. 17, p. 4511, 2008.
- [14] D. N. Lapedes, *Encyclopedia of Energy*. New York: McGraw-Hill Inc., 1976, p. 622.

- [15] J. W. Tester and E. M. Drake, *Sustainable Energy: Choosing Among Options*. Cambridge, Massachusetts: MIT Press, 2005, p. 846.
- [16] J. A. Turner, "A Realizable Renewable Energy Future," *Science*, vol. 285, no. 5428, p. 687, 1999.
- [17] M. Zach, C. Hagglund, D. Chakarov, and B. Kasemo, "Nanoscience and Nanotechnology for Advanced Energy Systems," *Current Opinion in Solid State and Materials Science*, vol. 10, no. 3-4, p. 132, 2006.
- [18] H. Huang, W. K. Zhang, and X. P. Gan, "Improved Electrochemical Storage of Lithium into Multi-walled Carbon Nanotubes by Light Irradiation," *Materials Chemistry and Physics*, vol. 104, no. 2-3, p. 271, 2007.
- [19] B. E. Conway and W. G. Pell, "Double-layer and Pseudocapacitance Types of Electrochemical Capacitors and their Applications to the Development of Hybrid Devices," *Journal of Solid State Electrochemistry*, vol. 7, no. 9, p. 637, 2003.
- [20] T. N. Murakami, N. Kawashima, and T. Miyasaka, "A High-voltage Dye-sensitized Photocapacitor of a Three-electrode System.," *Chemical communications*, no. 26, p. 3346, 2005.
- [21] I. Rousar, M. Rudolf, P. Lukasek, L. Kavan, N. Papageorgiou, and M. Grätzel, "Optimization of Parameters of an Electrochemical Photovoltaic Regenerative Solar Cell," *Solar Energy Materials and Solar Cells*, vol. 43, no. 3, p. 249, 1996.
- [22] T. Nomiya, H. Takeuchi, K. Kawazoe, Y. Horie, and T. Miyazaki, "Photoexcited-Charge Transfer and Energy-Storage Reaction of Photorechargeable TiO<sub>2</sub>/Carbon Fibers Composite Electrodes," *Japanese Journal of Applied Physics*, vol. 44, no. 7, p. 5219, 2005.
- [23] X. Zou, "Photo-rechargeable battery with TiO<sub>2</sub>/carbon fiber electrodes prepared by laser deposition," *Solar Energy Materials and Solar Cells*, vol. 62, no. 1-2, p. 133, 2000.
- [24] T. E. Mallouk, "The Emerging Technology of Solar Fuels," *The Journal of Physical Chemistry Letters*, vol. 1, no. 18, p. 2738, 2010.
- [25] B. Ewan and R. Allen, "A Figure of Merit Assessment of the Routes to Hydrogen Production," *International Journal of Hydrogen Energy*, vol. 30, no. 8, p. 809, 2005.
- [26] P. W. T. B. Lu and S. B. Srinivasan, "Advances in Water Electrolysis Technology with Emphasis on use of the Solid Polymer Electrolyte," *Journal of Applied Electrochemistry*, vol. 9, no. 3, p. 269, 1979.

- [27] A. J. Appleby and G. Crepy, "Advanced Electrolysis in Alkaline Solution," in *Proceedings of the Symposium on Electrode Materials and Processes for Energy Conversion and Storage (A79-11776 02-25)*, 1977, p. 382.
- [28] M. J. Braun, "Description of Processes for Producing Hydrogen by Advanced Electrolysis," in *Proceedings of the Symposium on Electrode Materials and Processes for Energy Conversion and Storage (A79-11776 02-25)*, 1977, p. 375.
- [29] S. A. Grigor'ev, V. I. Poremsky, and V. N. Fateev, "Pure hydrogen production by PEM electrolysis for hydrogen energy," *International Journal of Hydrogen Energy*, vol. 31, no. 2, pp. 171-175, 2006.
- [30] A. Marshall, B. Borresen, G. Hagen, M. Tsyarkin, and R. Tunold, "Hydrogen Production by Advanced Proton Exchange Membrane (PEM) Water Electrolysers—Reduced Energy Consumption by Improved Electrocatalysis," *Energy*, vol. 32, no. 4, p. 431, 2007.
- [31] M. H. Miles, "Effect of Temperature on Electrode Kinetic Parameters for Hydrogen and Oxygen Evolution Reactions on Nickel Electrodes in Alkaline Solutions," *Journal of the Electrochemical Society*, vol. 123, no. 3, p. 332, 1976.
- [32] C. A. Linkous, H. R. Anderson, R. W. Kopitzke, and G. L. Nelson, "Development of New Proton Exchange Membrane Electrolytes for Water Electrolysis at Higher Temperatures," *International Journal of Hydrogen Energy*, vol. 23, no. 7, p. 525, 1998.
- [33] R. L. LeRoy, "Hydrogen Production by the Electrolysis of Water," *Journal of the Electrochemical Society*, vol. 130, no. 11, p. 2158, 2006.
- [34] R. L. LeRoy and C. T. Bowen, "The Thermodynamics of Aqueous Water Electrolysis," *Journal of the Electrochemical Society*, vol. 127, no. 9, p. 1954, 1980.
- [35] H. R. Anderson, R. W. Kopitzke, and C. A. Linkous, "Development of New Proton Exchange Membrane Electrolytes for Water Electrolysis at Higher Temperatures," *International Journal of Hydrogen Energy*, vol. 23, no. 7, p. 525, 1998.
- [36] A. Fujishima and K. Honda, "Electrochemical Photolysis of Water at a Semiconductor Electrode," *Nature*, vol. 238, no. 5358, p. 37, 1972.
- [37] E. Selli, G. L. Chiarello, E. Quartarone, P. Mustarelli, I. Rossetti, and L. Forni, "A Photocatalytic Water Splitting Device for Separate Hydrogen and Oxygen Evolution.," *Chemical communications*, no. 47, p. 5022, 2007.
- [38] A. Fujishima, X. Zhang, and D. Tryk, "TiO<sub>2</sub> Photocatalysis and Related Surface Phenomena," *Surface Science Reports*, vol. 63, no. 12, p. 515, Dec. 2008.

- [39] E. Smotkin, A. J. Bard, A. Campion, M. A. Fox, T. Mallouk, S. E. Webber, and J. M. White, "Bipolar  $\text{TiO}_2/\text{Pt}$  Semiconductor Photoelectrodes and Multielectrode Arrays for Unassisted Photolytic Water Splitting," *Journal of Physical Chemistry*, vol. 90, no. 19, p. 4604, 1986.
- [40] A. Fujishima, X. Zhang, and D. Tryk, "Heterogeneous Photocatalysis: From Water Photolysis to Applications in Environmental Cleanup," *International Journal of Hydrogen Energy*, vol. 32, no. 14, p. 2664, 2007.
- [41] S. Licht, "Efficient Solar Generation of Hydrogen Fuel – A Fundamental Analysis," *Electrochemistry Communications*, vol. 4, no. 10, p. 790, 2002.
- [42] M. Radecka, "TiO<sub>2</sub> for photoelectrolytic decomposition of water," *Proceedings of Symposium D on Thin Film and Nano-Structured Materials for Photovoltaics, of the E-MRS 2003 Spring Conference*, vol. 451-452, pp. 98-104, 2004.
- [43] V. M. Aroutiounian, V. M. Arakelyan, and G. E. Shahnazaryan, "Metal Oxide Photoelectrodes for Hydrogen Generation using Solar Radiation-driven Water Splitting," *Solar Hydrogen*, vol. 78, no. 5, p. 581, 2005.
- [44] O. Khaselev and J. A. Turner, "A Monolithic Photovoltaic-photoelectrochemical Device for Hydrogen Production via Water Splitting," *Science*, vol. 280, no. 5362, p. 425, 1998.
- [45] O. Khaselev and J. A. Turner, "Electrochemical Stability of in Aqueous Electrolytes Toward Photoelectrochemical Water Splitting," *Journal of the Electrochemical Society*, vol. 145, no. 10, p. 3335, 2005.
- [46] O. Khaselev, A. Bansal, and J. A. Turner, "High-efficiency Integrated Multijunction Photovoltaic/electrolysis Systems for Hydrogen Production," *International Journal of Hydrogen Energy*, vol. 26, no. 2, p. 127, 2001.
- [47] S. Licht, B. Wang, and S. Mukerji, "Efficient Solar Water Splitting , Exemplified by RuO<sub>2</sub>-Catalyzed AlGaAs/Si Photoelectrolysis," *Journal of Physical Chemistry B*, vol. 104, p. 8920, 2000.
- [48] N. G. Dhere and A. H. Jahagirdar, "Photoelectrochemical Water Splitting for Hydrogen Production using combination of CIGS2 Solar Cell and RuO<sub>2</sub> Photocatalyst," *Thin Solid Films*, vol. 480, p. 462, 2005.
- [49] G. Milczarek, A. Kasuya, S. Mamykin, T. Arai, K. Shinoda, and K. Tohji, "Optimization of a Two-compartment Photoelectrochemical Cell for Solar Hydrogen Production," *International Journal of Hydrogen Energy*, vol. 28, no. 9, p. 919, 2003.

- [50] N. Kelly and T. Gibson, "Design and Characterization of a Robust Photoelectrochemical Device to Generate Hydrogen using Solar Water Splitting," *International Journal of Hydrogen Energy*, vol. 31, no. 12, p. 1658, 2006.
- [51] P. R. Mishra, P. K. Shukla, A. K. Singh, and O. N. Srivastava, "Investigation and Optimization of Nanostructured TiO<sub>2</sub> Photoelectrode in regard to Hydrogen Production through Photoelectrochemical Process," *International Journal of Hydrogen Energy*, vol. 28, no. 10, p. 1089, 2003.
- [52] H. Morisaki, T. Watanabe, M. Iwase, and K. Yazawa, "Photoelectrolysis of Water with TiO<sub>2</sub>-covered Solar-cell Electrodes," *Applied Physics Letters*, vol. 29, no. 6, p. 338, 1976.
- [53] D. C. Bookbinder, J. A. Bruce, R. N. Dominey, N. S. Lewis, and M. S. Wrighton, "Synthesis and Characterization of a Photosensitive Interface for Hydrogen Generation: Chemically Modified p-type Semiconducting Silicon Photocathodes," *Proceedings of the National Academy of Sciences of the United States of America*, vol. 77, no. 11, p. 6280, 1980.
- [54] B. D. Alexander, P. J. Kulesza, I. Rutkowska, R. Solarska, and J. Augustynski, "Metal Oxide Photoanodes for Solar Hydrogen Production," *Journal of Materials Chemistry*, vol. 18, no. 20, p. 2298, 2008.
- [55] W. B. Ingler Jr and S. U. M. Khan, "A Self-driven Tandem Photoelectrochemical Cell for Water Splitting," *Electrochemical and Solid-State Letters*, vol. 9, no. 4, p. 144, 2006.
- [56] E. L. Miller, B. Marsen, D. Paluselli, and R. Rocheleau, "Optimization of Hybrid Photoelectrodes for Solar Water-Splitting," *Electrochemical and Solid-State Letters*, vol. 8, p. A247, 2005.
- [57] E. L. Miller, N. Gaillard, J. Kaneshiro, A. Deangelis, and R. Garland, "Progress in New Semiconductor Materials Classes for Solar Photoelectrolysis," *International Journal of Energy Research*, no. 2009, p. 1215, 2010.
- [58] T. Bak, J. Nowotny, M. Rekas, and C. C. Sorrell, "Photo-electrochemical Hydrogen Generation from Water using Solar Energy. Materials-related Aspects," *International Journal of Hydrogen Energy*, vol. 27, no. 10, p. 991, 2002.
- [59] S. Y. Ryu, J. Choi, W. Balcerski, T. K. Lee, and M. R. Hoffmann, "Photocatalytic Production of H<sub>2</sub> on Nanocomposite Catalysts," *Industrial & Engineering Chemistry Research*, vol. 46, no. 23, p. 7476, 2007.
- [60] W. J. Youngblood, S.-H. A. Lee, K. Maeda, and T. E. Mallouk, "Visible Light Water Splitting using Dye-sensitized Oxide Semiconductors," *Accounts of Chemical Research*, vol. 42, no. 12, p. 1966, 2009.

- [61] T. Bak, J. Nowotny, M. Rekas, and C. C. Sorrell, "Photo-electrochemical Properties of the TiO<sub>2</sub>-Pt System in Aqueous Solutions," *International Journal of Hydrogen Energy*, vol. 27, p. 19, 2002.
- [62] M. Ni, M. Leung, D. Leung, and K. Sumathy, "A Review and Recent Developments in Photocatalytic Water-splitting using TiO<sub>2</sub> for Hydrogen Production," *Renewable and Sustainable Energy Reviews*, vol. 11, no. 3, p. 401, 2007.
- [63] A. Kudo, "Recent Progress in the Development of Visible Light-driven Powdered Photocatalysts for Water Splitting," *International Journal of Hydrogen Energy*, vol. 32, no. 14, p. 2673, 2007.
- [64] A. Kudo and Y. Miseki, "Heterogeneous Photocatalyst Materials for Water Splitting," *Chemical Society Reviews*, vol. 38, no. 1, p. 253, 2009.
- [65] K. Vinodgopal, S. Hotchandani, and P. V. Kamat, "Electrochemically Assisted Photocatalysis: Titania Particulate Film Electrodes for Photocatalytic Degradation of 4-chlorophenol," *The Journal of Physical Chemistry*, vol. 97, no. 35, p. 9040, 1993.
- [66] P. K. Shukla, R. K. Karn, A. K. Singh, and O. N. Srivastava, "Studies on PV Assisted PEC Solar Cells for Hydrogen Production through Photoelectrolysis of Water," *International Journal of Hydrogen Energy*, vol. 27, no. 2, p. 135, 2002.
- [67] S. Khare, "Photoassisted Hydrogen Generation by Integrated Electroactive SPE Membrane System," *International Journal of Hydrogen Energy*, vol. 25, no. 4, p. 327, 2000.
- [68] A. Yildiz, A. Sobczynski, A. J. Bard, A. Campion, M. A. Fox, T. E. Mallouk, S. E. Webber, and J. M. White, "Sensitized Polypyrrole-coated Semiconducting Powders as Materials in Photosystems for Hydrogen Generation," *Langmuir*, vol. 5, no. 1, p. 148, 1989.
- [69] N. Hebestreit, "Physical and Electrochemical Characterization of Nanocomposites formed from Polythiophene and Titaniumdioxide," *Electrochimica Acta*, vol. 48, no. 13, p. 1779, 2003.
- [70] Z. Han, J. Zhang, X. Yang, H. Zhu, and W. Cao, "Synthesis and Photoelectric Property of Poly(3-octylthiophene)/Titanium Dioxide Nano-composite Material," *Journal of Materials Science: Materials in Electronics*, vol. 21, no. 6, p. 554, 2009.
- [71] T. Ishwara, D. D. C. Bradley, J. Nelson, P. Ravirajan, I. Vanseveren, T. Cleij, D. Vanderzande, L. Lutsen, S. Tierney, M. Heeney, and I. McCulloch, "Influence of Polymer Ionization Potential on the Open-circuit Voltage of Hybrid Polymer/TiO<sub>2</sub> Solar Cells," *Applied Physics Letters*, vol. 92, no. 5, p. 053308, 2008.

- [72] K. Kajihara, K. Tanaka, K. Hirao, and N. Soga, "Photovoltaic Effect in Titanium Dioxide/Polythiophene Cell," *Japanese Journal of Applied Physics*, vol. 36, p. 5537, 1997.
- [73] E. L. Leguenza, R. L. Patyk, R. M. Q. Mello, L. Micaroni, M. Koehler, and I. a. Hümmelgen, "High Open-circuit Voltage Single-layer Polybithiophene-based Photovoltaic Devices," *Journal of Solid State Electrochemistry*, vol. 11, no. 5, p. 577, 2006.
- [74] R. L. Patyk, B. S. Lomba, A. F. Nogueira, C. a. Furtado, A. P. Santos, R. M. Q. Mello, L. Micaroni, and I. a. Hümmelgen, "Carbon Nanotube–polybithiophene Photovoltaic Devices with High Open-circuit Voltage," *Physica Status Solidi – Rapid Research Letters*, vol. 1, no. 1, p. R43, 2007.
- [75] A. J. Bard and L. R. Faulkner, *Electrochemical Methods: Fundamentals and Applications, 2nd Edition*. New York: John Wiley & Sons Inc., 2001, p. 856.
- [76] O. Osmanbas, A. Koca, M. Kandaz, and F. Karaca, "Electrocatalytic Activity of Phthalocyanines Bearing Thiophenes for Hydrogen Production from Water," *International Journal of Hydrogen Energy*, vol. 33, no. 13, p. 3281, 2008.
- [77] M. W. Denhoff and N. Drolet, "The Effect of the Front Contact Sheet Resistance on Solar Cell Performance," *Solar Energy Materials and Solar Cells*, vol. 93, no. 9, p. 1499, 2009.
- [78] M. Ilieva, S. Ivanov, and V. Tsakova, "Electrochemical Synthesis and Characterization of TiO<sub>2</sub>-polyaniline Composite Layers," *Journal of Applied Electrochemistry*, vol. 38, no. 1, p. 63, 2007.
- [79] G. Schopf and G. Koßmehl, *Polythiophenes: Electrically Conductive Polymers*,. Berlin: Springer, 1997.
- [80] Y. Otsuka, Y. Okamoto, H. Y. Akiyama, K. Umekita, Y. Tachibana, and S. Kuwabata, "Photoinduced Formation of Polythiophene/TiO<sub>2</sub> Nanohybrid Heterojunction Films for Solar Cell Applications," *Journal of Physical Chemistry C*, vol. 112, no. 12, p. 4767, 2008.
- [81] M. Antoniadou and P. Lianos, "Photoelectrochemical Oxidation of Organic Substances over Nanocrystalline Titania: Optimization of the Photoelectrochemical Cell," *Catalysis Today*, vol. 144, no. 1-2, p. 166, 2009.
- [82] M. T. Giacomini, M. Balasubramanian, S. Khalid, J. McBreen, and E. A. Ticianellia, "Characterization of the Activity of Palladium-Modified Polythiophene Electrodes for the Hydrogen Oxidation and Oxygen Reduction Reactions," *Journal of The Electrochemical Society*, vol. 150, no. 5, p. A588, 2003.

- [83] A. L. Linsebigler, G. Lu, and J. T. Yates Jr, "Photocatalysis on TiO<sub>2</sub> Surfaces: Principles, Mechanisms, and Selected Results," *Chemical Reviews*, vol. 95, no. 3, p. 735, 1995.
- [84] D. R. Bruce and D. P. Wilkinson, "Conductive Polymer-Titania Photocathode Development for Hydrogen Production," *ECS Transactions*, vol. 28, no. 26, p. 119, 2010.
- [85] F. Beck and M. Dahlhaus, "Anodic Formation of Polypyrrole/Tungsten Trioxide Composites," *Journal of Applied Electrochemistry*, vol. 23, p. 781, 1993.
- [86] V. A. Lysenko, "Carbon Fibre Porous Conducting Substrates for Hydrogen Energetics," *Fibre Chemistry*, vol. 41, no. 2, p. 133, 2009.
- [87] M. Innocenti, F. Loglio, L. Pigani, R. Seeber, F. Terzi, and R. Udisti, "In-situ Atomic Force Microscopy in the Study of Electrogeneration of Polybithiophene on Pt Electrode," *Electrochimica Acta*, vol. 50, no. 7-8, p. 1497, 2005.
- [88] K. D. O'Neil and O. a. Semenikhin, "AFM Phase Imaging of Electropolymerized Polybithiophene Films at Different Stages of Their Growth," *Journal of Physical Chemistry C*, vol. 111, no. 40, p. 14823, 2007.
- [89] M. Kraljic, "Inhibition of Steel Corrosion by Polyaniline Coatings," *Corrosion Science*, vol. 45, no. 1, p. 181, 2003.
- [90] V. S. Bagotsky, *Fundamentals of Electrochemistry 2nd Ed.* Hoboken: John Wiley & Sons Inc., 2006.
- [91] K. G. Jung, J. W. Schultze, K. S. Robinson, and H. Schmiedel, "Low Energy Ion Implantation in Polybithiophene: Microstructuring and Microanalysis," *Fresenius' Journal of Analytical Chemistry*, vol. 353, no. 3-4, p. 282, 1995.
- [92] M. A. Druy and R. J. Seymour, "Poly(2,2' - Bithiophene) : An Electrochromic Conducting Polymer," *Le Journal de Physique Colloques*, vol. 44, no. 3, p. 595, 1983.
- [93] B. Muktha, D. Mahanta, S. Patil, and G. Madras, "Synthesis and Photocatalytic Activity of Poly(3-hexylthiophene)/TiO<sub>2</sub> Composites," *Journal of Solid State Chemistry*, vol. 180, no. 10, p. 2986, 2007.
- [94] Frelink T., Visscher W., and van Veen J.A.R., "The Third Anodic Hydrogen Peak on Platinum: Subsurface H<sub>2</sub> Adsorption," *Electrochimica Acta*, vol. 40, no. 5, p. 5, 1995.
- [95] V. Tripkovic, M. E. Bjo, G. Karlberg, J. Rossmeisl, T. Bligaard, H. Jo, and J. K. Nørskov, "Modeling the Electrochemical Hydrogen Oxidation and Evolution Reactions on the Basis of Density Functional Theory Calculations," *Journal of Physical Chemistry C*, vol. 114, p. 18182, 2010.

- [96] P. Paunović, I. Radev, A. T. Dimitrov, O. Popovski, E. Lefterova, E. Slavcheva, and S. H. Jordanov, "New Nano-structured and Interactive Supported Composite Electrocatalysts for Hydrogen Evolution with Partially Replaced Platinum Loading," *International Journal of Hydrogen Energy*, vol. 34, no. 7, p. 2866, 2009.
- [97] B. Winther-Jensen, K. Fraser, C. Ong, M. Forsyth, and D. R. MacFarlane, "Conducting Polymer Composite Materials for Hydrogen Generation," *Advanced Materials*, vol. 22, no. 15, p. 1727, 2010.
- [98] G. G. Min, S.-J. Choi, S. B. Kim, and S.-M. Park, "Electrochemistry of Conductive Polymers 44: A Comparative Study on Electrochemically Polymerized Polythiophenes from Thiophene, Bithiophene, and Terthiophene," *Synthetic Metals*, vol. 159, no. 19-20, p. 2108, 2009.
- [99] R. D. McCullough, "The Chemistry of Conducting Polythiophenes," *Advanced Materials*, vol. 10, no. 2, p. 93, 1998.
- [100] H. Tang, K. Prasad, R. Sanjinés, and F. Lévy, "TiO<sub>2</sub> Anatase Thin Films as Gas Sensors," *Sensors and Actuators B: Chemical*, vol. 26, no. 1-3, p. 71, 1995.
- [101] J. Ritchie, J. Mertens, H. Yanga, P. Servati, and F. K. Ko, "Electrospun Composite Nanofiber Transparent Conductor Layer for Solar Cells," *MRS Proceedings*, vol. 1323, no. 3, p. 48, 2011.
- [102] C. Cutler, "Effect of Electron Withdrawing or Donating Substituents on the Photovoltaic Performance of Polythiophenes," *Synthetic Metals*, vol. 128, no. 1, p. 35, 2002.
- [103] A. Malinauskas, J. Malinauskiene, and A. Ramanavičius, "Conducting Polymer-based Nanostructured Materials: Electrochemical Aspects," *Nanotechnology*, vol. 16, no. 10, p. R51, 2005.
- [104] C. L. Huisman, A. Huijser, H. Donker, J. Schoonman, and A. Goossens, "UV Polymerization of Oligothiophenes and their Application in Nanostructured Heterojunction Solar Cells," *Macromolecules*, vol. 37, no. 15, p. 5557, 2004.
- [105] D. J. Milliron, A. P. Alivisatos, C. Pitois, C. Edder, and J. M. J. Fréchet, "Electroactive Surfactant Designed to Mediate Electron Transfer Between CdSe Nanocrystals and Organic Semiconductors," *Advanced Materials*, vol. 15, no. 1, p. 58, 2003.
- [106] J. E. Funk, "Thermochemical Hydrogen Production: Past and Present," *International Journal of Hydrogen Energy*, vol. 26, no. 3, p. 185, 2001.
- [107] S. Licht, "Solar Water Splitting To Generate Hydrogen Fuel : Photothermal Electrochemical Analysis," *Journal of Physical Chemistry B*, vol. 107, p. 4253, 2003.

- [108] S. Baykara, "Hydrogen Production by Direct Solar Thermal Decomposition of Water, Possibilities for Improvement of Process Efficiency," *International Journal of Hydrogen Energy*, vol. 29, no. 14, p. 1451, 2004.
- [109] S. Baykara, "Experimental Solar Water Thermolysis," *International Journal of Hydrogen Energy*, vol. 29, no. 14, p. 1459, 2004.
- [110] C. Perkins and A. W. Weimer, "Likely Near-term Solar-thermal Water Splitting Technologies," *International Journal of Hydrogen Energy*, vol. 29, no. 15, p. 1587, 2004.
- [111] T. Nakamura, "Hydrogen Production from Water Utilizing Solar Heat at High Temperatures," *Solar Energy*, vol. 19, no. 5, p. 467, 1977.
- [112] T. Kodama, Y. Nakamuro, and T. Mizuno, "A Two-Step Thermochemical Water Splitting by Iron-Oxide on Stabilized Zirconia," *Journal of Solar Energy Engineering*, vol. 128, no. 1, p. 3, 2006.
- [113] B. Bischoff, C. Forsberg, L. K. Mansur, and L. Trowbridge, "Nuclear Thermochemical Production of Hydrogen with a Lower-temperature Iodine-Westinghouse-Ispra Sulphur Process," in *Nuclear Production of Hydrogen*, OECD, 2004, p. 159.
- [114] "Blackbody Radiation: Electromagnetic Energy," *Encyclopædia Britannica Online*, 2012. [Online]. Available: <http://www.britannica.com/EBchecked/media/1374/Ele>.
- [115] T. Verbiest, "Magnetic-dipole Nonlinearities in Chiral Materials," *Journal of Photochemistry and Photobiology A: Chemistry*, vol. 145, no. 1-2, p. 113, 2001.
- [116] P. Zeeman, "The Effect of Magnetisation on the Nature of Light Emitted by a Substance," *Nature*, vol. 55, no. 1424, p. 347, 1897.
- [117] G. Mie, "Contributions to the Optics of Turbid Media, Particularly of Colloidal Metal Solutions," *Annalen der Physik*, vol. 23, no. 3, p. 377, 1908.
- [118] M.-L. Kuo, D. J. Poxson, Y. S. Kim, F. W. Mont, J. K. Kim, E. F. Schubert, and S.-Y. Lin, "Realization of a Near-perfect Antireflection Coating for Silicon Solar Energy Utilization," *Optics letters*, vol. 33, no. 21, p. 2527, 2008.
- [119] J. Joannopoulos, P. Villeneuve, and S. Fan, "Photonic Crystals: Putting a New Twist on Light," *Nature*, vol. 386, p. 143, 1997.
- [120] J. W. Bae, S. W. Lee, and G. Y. Yeom, "Doped-Fluorine on Electrical and Optical Properties of Tin Oxide Films Grown by Ozone-Assisted Thermal CVD," *Journal of The Electrochemical Society*, vol. 154, no. 1, p. D34, 2007.

- [121] A. E. Rakhshani, Y. Makdisi, and H. A. Ramazaniyan, "Electronic and Optical Properties of Fluorine-doped Tin Oxide Films," *Journal of Applied Physics*, vol. 83, no. 2, p. 1049, 1998.
- [122] G. M. Hale and M. R. Querry, "Optical Constants of Water in the 200-nm to 200-microm Wavelength Region.," *Applied optics*, vol. 12, no. 3, p. 555, 1973.
- [123] H. R. Zelsmann, "Temperature Dependence of the Optical Constants for Liquid H<sub>2</sub>O and D<sub>2</sub>O in the Far IR Region," *Journal of Molecular Structure*, vol. 350, p. 95, 1995.
- [124] S. H. de Almeida and Y. Kawano, "Ultraviolet-visible Spectra Membrane of Nafion," *European Polymer Journal*, vol. 33, no. 8, p. 1307, 1997.
- [125] Z. Liang, "FT-IR Study of the Microstructure of Nafion Membrane," *Journal of Membrane Science*, vol. 233, no. 1-2, p. 39, 2004.
- [126] M. D. Curtis, A. M. Y. Koren, and J. W. Kampf, "Effects of  $\pi$ -Stacking on the Absorption and Emission of Light by Conjugated Polymers and Oligomers," *MRS Proceedings*, vol. 598, p. BB10.8, 1999.
- [127] A. Bock, A. Topeters, and C. Kryschi, "A Spectroscopic Study of the Growth and Redox Processes of Electrodeposited Polybithiophene Films," *Synthetic Metals*, vol. 75, no. 2, p. 133, 1995.
- [128] P. A. Christensen, A. Hamnett, A. R. Hillman, M. J. Swann, and S. J. Higgins, "An In-situ Fourier-transform Infrared Study of the Electroreduction of Polybithiophene," *Journal of the Chemical Society, Faraday Transactions*, vol. 89, no. 6, p. 921, 1993.
- [129] P. Kumar, "Nanocrystalline TiO<sub>2</sub> studied by Optical, FTIR and X-ray Photoelectron Spectroscopy: Correlation to Presence of Surface States," *Thin Solid Films*, vol. 358, no. 1-2, p. 122, 2000.
- [130] T. Ohno, K. Sarukawa, K. Tokieda, and M. Matsumura, "Morphology of a TiO<sub>2</sub> Photocatalyst (Degussa P-25) Consisting of Anatase and Rutile Crystalline Phases," *Journal of Catalysis*, vol. 203, no. 1, p. 82, 2001.
- [131] M. Ivanda, S. Musić, M. Gotić, A. Turković, A. M. Tonejc, and O. Gamulin, "The Effects of Crystal Size on the Raman Spectra of Nanophase TiO<sub>2</sub>," *Journal of Molecular Structure*, vol. 480-481, no. 1999, p. 641, 1999.
- [132] H. J. Moller, *Semiconductors for Solar Cells*. Artech House Publishers, 1993, p. 356.
- [133] A. Hangleiter and R. Häcker, "Enhancement of Band-to-band Auger Recombination by Electron-hole Correlations," *Physical Review Letters*, vol. 65, no. 2, p. 215, 1990.

- [134] V. M. Fthenakis, H. C. Kim, and E. Alsema, "Emissions from Photovoltaic Life Cycles.," *Environmental Science & Technology*, vol. 42, no. 6, p. 2168, 2008.
- [135] E. Kintisch, "Light-splitting Trick Squeezes More Electricity out of Sun's Rays," *Science*, vol. 317, no. 5838, p. 583, 2007.
- [136] H. Hoppe and N. S. Sariciftci, "Organic Solar Cells: An Overview," *Journal of Materials Research*, vol. 19, no. 7, p. 1924, 2004.
- [137] R. Valaski, C. Canestraro, L. Micaroni, R. Mello, and L. Roman, "Organic Photovoltaic Devices Based on Polythiophene Films Electrodeposited on FTO Substrates," *Solar Energy Materials and Solar Cells*, vol. 91, no. 8, p. 684, 2007.
- [138] C. W. Tang, "Two-layer organic photovoltaic cell," *Applied Physics Letters*, vol. 48, no. 2, p. 183, 1986.
- [139] R. A. J. Janssen, J. C. Hummelen, and N. S. Sariciftci, "Polymer – Fullerene Bulk Heterojunction Solar Cells," *MRS Bulletin*, vol. 30, no. January, p. 33, 2005.
- [140] G. Barbarella, M. Melucci, and G. Sotgiu, "The Versatile Thiophene: An Overview of Recent Research on Thiophene-Based Materials," *Advanced Materials*, vol. 17, no. 13, p. 1581, 2005.
- [141] E. Arici, H. Hoppe, F. Schäffler, D. Meissner, M. A. Malik, and N. S. Sariciftci, "Hybrid Solar Cells Based on Inorganic Nanoclusters and Conjugated Polymers," *Thin Solid Films*, vol. 451-452, p. 612, 2004.
- [142] D. J. Milliron, I. Gur, and A. P. Alivisatos, "Hybrid Organic – Nanocrystal Solar Cells," *MRS Bulletin*, vol. 30, p. 41, 2005.
- [143] G. G. Wallace, C. O. Too, D. L. Officer, and C. Dastoor, "Photoelectrochemical Cells Based on Inherently Conducting Polymers," *MRS Bulletin*, vol. 30, no. January, p. 46, 2005.
- [144] C. J. Brabec, J. A. Hauch, P. Schilinsky, and C. Waldauf, "Production Aspects of Organic Photovoltaics and Commercialization of Devices," *MRS Bulletin*, vol. 30, p. 50, 2005.
- [145] B. A. Gregg and M. C. Hanna, "Comparing Organic to Inorganic Photovoltaic Cells: Theory, Experiment, and Simulation," *Journal of Applied Physics*, vol. 93, no. 6, p. 3605, 2003.
- [146] R. J. Kline, M. D. McGehee, E. N. Kadnikova, J. Liu, and J. M. J. Fréchet, "Controlling the Field-Effect Mobility of Regioregular Polythiophene by Changing the Molecular Weight," *Advanced Materials*, vol. 15, no. 18, p. 1519, 2003.

- [147] H. Bässler, "Charge Transport in Disordered Organic Photoconductors a Monte Carlo Simulation Study," *Physica Status Solidi B*, vol. 175, no. 1, p. 15, 1993.
- [148] H. Meng, D. F. Perepichka, and F. Wudl, "Facile Solid-State Synthesis of Highly Conducting Poly(ethylenedioxythiophene)," *Angewandte Chemie International Edition*, vol. 42, no. 6, p. 589, 2003.
- [149] S. R. Forrest, "The Limits to Organic Photovoltaic Cell Efficiency," *MRS Bulletin*, vol. 30, p. 28, 2005.
- [150] L. Shen, W. Guo, Z. Zhong, G. Zhu, C. Tao, Z. Liu, J. Zhou, and W. Chen, "Water-soluble Poly(3,4-ethylenedioxythiophene)/Nano-crystalline TiO<sub>2</sub> Heterojunction Solar Cells," *Microelectronics Journal*, vol. 39, no. 12, p. 1683, 2008.
- [151] Y.-M. Chang, W.-F. Su, and L. Wang, "Photoactive Polythiophene:Titania Hybrids with Excellent Miscibility for Use in Polymer Photovoltaic Cells," *Macromolecular Rapid Communications*, vol. 29, no. 15, p. 1303, 2008.
- [152] R. Senadeera, N. Fukuri, Y. Saito, T. Kitamura, Y. Wada, and S. Yanagida, "Volatile Solvent-free Solid-state Polymer-sensitized TiO<sub>2</sub> Solar cells with Poly(3,4-ethylenedioxythiophene) as a Hole-Transporting Medium.," *Chemical Communications*, no. 17, p. 2259, 2005.
- [153] K. M. Coakley, Y. Liu, C. Goh, and M. D. McGehee, "Ordered Organic-inorganic Bulk Heterojunction Photovoltaic Cells," *MRS Bulletin*, vol. 30, p. 37, 2005.
- [154] M. Wang and X. Wang, "P3HT/TiO<sub>2</sub> Bulk-heterojunction Solar Cell Sensitized by a Perylene Derivative," *Solar Energy Materials and Solar Cells*, vol. 91, no. 19, p. 1782, 2007.
- [155] D. Gebeyehu, "Hybrid Solar Cells Based on Dye-sensitized Nanoporous TiO<sub>2</sub> Electrodes and Conjugated Polymers as Hole Transport Materials," *Synthetic Metals*, vol. 125, no. 3, p. 279, 2001.
- [156] E. Becquerel, "Recherches sur les Effets de la Radiation Chimique de la Lumière Solaire, au moyen des Courants Électriques.," *Comptes Rendus de l'Académie des Sciences*, vol. 9, p. 145, 1839.
- [157] L. Sicot, C. Fiorini, A. Lorin, J. Nunzi, P. Raimond, and C. Sentein, "Dye Sensitized Polythiophene Solar Cells," *Synthetic Metals*, vol. 102, no. 1-3, p. 991, 1999.
- [158] P. Brown, K. Takechi, and P. V. Kamat, "Single-Walled Carbon Nanotube Scaffolds for Dye-Sensitized Solar Cells," *Journal of Physical Chemistry C*, vol. 112, no. 12, p. 4776, 2008.

- [159] G. Mor, O. Varghese, M. Paulose, K. Shankar, and C. Grimes, "A Review on Highly Ordered, Vertically Oriented TiO<sub>2</sub> Nanotube Arrays: Fabrication, Material Properties, and Solar Energy Applications," *Solar Energy Materials and Solar Cells*, vol. 90, no. 14, p. 2011, 2006.
- [160] A. Nattestad, A. J. Mozer, M. K. R. Fischer, Y.-B. Cheng, A. Mishra, P. Bäuerle, and U. Bach, "Highly Efficient Photocathodes for Dye-sensitized Tandem Solar Cells.," *Nature Materials*, vol. 9, no. 1, p. 31, 2010.
- [161] K. Shankar, G. K. Mor, H. E. Prakasam, O. K. Varghese, and C. A. Grimes, "Self-assembled Hybrid Polymer-TiO<sub>2</sub> Nanotube Array Heterojunction Solar Cells.," *Langmuir*, vol. 23, no. 24, p. 12445, 2007.
- [162] M. Grätzel, "Dye-sensitized Solid-state Heterojunction Solar Cells," *MRS Bulletin*, vol. 30, p. 23, 2005.
- [163] X. Wang, L. Zhi, and K. Müllen, "Transparent, Conductive Graphene Electrodes for Dye-sensitized Solar Cells.," *Nano letters*, vol. 8, no. 1, p. 323, 2008.
- [164] P. A. M. Dirac, "The Quantum Theory of the Emission and Absorption of Radiation," *Proceedings of the Royal Society of London. Series A, Containing Papers of a Mathematical and Physical Character*, vol. 114, no. 767, p. 243, 1927.
- [165] A. Amtout, "Calculation of the Line Shape of One-phonon Replicas in Polar Semiconductors having Direct Forbidden Band Gaps," *Physical Review B*, vol. 52, no. 19, p. 13955, 1995.
- [166] R. F. Oulton, V. J. Sorger, D. a. Genov, D. F. P. Pile, and X. Zhang, "A Hybrid Plasmonic Waveguide for Subwavelength Confinement and Long-range Propagation," *Nature Photonics*, vol. 2, no. 8, p. 496, 2008.
- [167] Y. Han, G. Wu, H. Chen, and M. Wang, "Preparation and Optoelectronic Properties of a Novel Poly ( N-vinylcarbazole ) with Covalently Bonded Titanium Dioxide," *Applied Polymer Science*, vol. 109, no. 2, p. 882, 2008.
- [168] P. Würfel, A. S. Brown, T. E. Humphrey, and M. A. Green, "Particle Conservation in the Hot-carrier Solar Cell," *Progress in Photovoltaics: Research and Applications*, vol. 13, no. 4, p. 277, 2005.
- [169] R. E. Hummel, *Electronic Properties of Materials*, 3rd ed. New York: Springer, 2005, p. 438.
- [170] K. S. Raja, V. K. Mahajan, and M. Misra, "Determination of Photo Conversion Efficiency of Nanotubular Titanium Oxide Photo-electrochemical Cell for Solar Hydrogen Generation," *Journal of Power Sources*, vol. 159, no. 2, p. 1258, 2006.

- [171] L. Esaki, "New Phenomenon in Narrow Germanium p-n Junctions," *Physical Review*, vol. 109, no. 2, p. 603, 1958.
- [172] R. Asahi, T. Morikawa, T. Ohwaki, K. Aoki, and Y. Taga, "Visible-light Photocatalysis in Nitrogen-doped Titanium Oxides.," *Science (New York, N.Y.)*, vol. 293, no. 5528, p. 269, 2001.
- [173] O. Diwald, T. L. Thompson, T. Zubkov, E. G. Goralski, S. D. Walck, and J. T. J. Yates, "Photochemical Activity of Nitrogen-doped Rutile TiO<sub>2</sub> (110) in Visible Light.," *Journal of Physical Chemistry B*, vol. 35, no. 30, p. 6004, 2004.
- [174] V. Gombac, L. Derogatis, A. Gasparotto, G. Vicario, T. Montini, D. Barreca, G. Balducci, P. Fornasiero, E. Tondello, and M. Graziani, "TiO<sub>2</sub> Nanopowders Doped with Boron and Nitrogen for Photocatalytic Applications," *Chemical Physics*, vol. 339, no. 1-3, p. 111, 2007.
- [175] J. Graciani, L. J. Alvarez, J. A. Rodriguez, and J. F. Sanz, "N Doping of Rutile TiO<sub>2</sub> (110) Surface. A Theoretical DFT Study," *Journal of Physical Chemistry C*, vol. 112, no. 7, p. 2624, 2008.
- [176] H.-J. Her, W.-H. Baek, H. H. Lee, C. J. Kang, and Y.-S. Kim, "Influence of Titania Thin Film Morphology on the Photovoltaic Action of Hybrid Titania-P3HT Solar Cell," *Journal of Physics: Conference Series*, vol. 100, no. 8, p. 82020, 2008.
- [177] P. Balaya, "Size Effects and Nanostructured Materials for Energy Applications," *Energy & Environmental Science*, vol. 1, no. 6, p. 645, 2008.
- [178] P. V. Kamat, "Meeting the Clean Energy Demand: Nanostructure Architectures for Solar Energy Conversion," *Journal of Physical Chemistry C*, vol. 111, no. 7, p. 2834, 2007.
- [179] P. V. Kamat, "Quantum Dot Solar Cells. Semiconductor Nanocrystals as Light Harvesters," *Journal of Physical Chemistry C*, vol. 112, p. 18737, 2008.
- [180] R. Gangopadhyay and A. De, "Conducting Polymer Nanocomposites: A Brief Overview," *Chemistry of Materials*, vol. 12, no. 3, p. 608, 2000.
- [181] H. Liang and X. Li, "Environmental Visible-induced Photocatalytic Reactivity of Polymer-sensitized Titania Nanotube Films," *Applied Catalysis B*, vol. 86, p. 8, 2009.
- [182] N. D. Ce, M. Bellec, M. Leclerc, and G. Durocher, "Conformational and Spectroscopic Analysis of Selected 2,2'-Bithiophene Derivatives," *Spectroscopy*, vol. 5639, no. 96, p. 776, 1997.

- [183] K. G. Jung, J. W. Schultze, K. S. Robinson, and H. Schmiedel, "Low Energy Ion Implantation in Polybithiophene: Microstructuring and Microanalysis," *Fresenius' Journal of Analytical Chemistry*, vol. 353, no. 3-4, p. 282, 1995.
- [184] T. Rajh, O. G. Poluektov, and M. C. Thurnauer, "Charge Separation in Titanium Oxide Nanocrystalline Semiconductors Revealed by Magnetic Resonance," *Chemical Physics*, pp. 1-34, 2003.
- [185] B. Abrams and J. Wilcoxon, "Nanosize Semiconductors for Photooxidation," *Critical Reviews in Solid State and Material Sciences*, vol. 30, no. 3, p. 153, 2005.
- [186] G. Li and K. Gray, "The Solid–solid Interface: Explaining the High and Unique Photocatalytic Reactivity of TiO<sub>2</sub>-based Nanocomposite Materials," *Chemical Physics*, vol. 339, no. 1-3, p. 173, 2007.
- [187] G. Li, L. Chen, M. E. Graham, and K. a. Gray, "A Comparison of Mixed Phase Titania Photocatalysts Prepared by Physical and Chemical Methods: The Importance of the Solid–solid Interface," *Journal of Molecular Catalysis A: Chemical*, vol. 275, no. 1-2, p. 30, 2007.
- [188] M. Benmami, K. Chhor, and A. Kanaev, "High Photocatalytic Activity of Monolayer Nanocoatings prepared from Non-crystalline Titanium Oxide Sol Nanoparticles," *Chemical Physics Letters*, vol. 422, no. 4-6, p. 552, 2006.
- [189] M. A. Green, "Multiple Band and Impurity Photovoltaic Solar Cells: General Theory and Comparison to Tandem Cells," *Progress in Photovoltaics: Research and Applications*, vol. 9, no. 2, p. 137, 2001.
- [190] A. Watanabe and A. Kasuya, "Effect of Atmospheres on the Open-circuit Photovoltage of Nanoporous TiO<sub>2</sub>/poly(3-hexylthiophene) Heterojunction Solar Cell," *Thin Solid Films*, vol. 483, no. 1-2, p. 358, 2005.
- [191] A. Riss, T. Berger, H. Grothe, J. Bernardi, O. Diwald, and E. Knözinger, "Chemical Control of Photoexcited States in Titanate Nanostructures," *Nano Letters*, vol. 7, no. 2, p. 433, 2007.
- [192] C. S. Kim, S. S. Lee, E. D. Gomez, J. B. Kim, and Y.-L. Loo, "Transient Photovoltaic Behavior of Air-stable, Inverted Organic Solar Cells with Solution-processed Electron Transport Layer," *Applied Physics Letters*, vol. 94, no. 11, p. 113302, 2009.
- [193] A. Saeki, S. Seki, Y. Koizumi, T. Sunagawa, K. Ushida, and S. Tagawa, "Increase in the Mobility of Photogenerated Positive Charge Carriers in Polythiophene," *The Journal of Physical Chemistry B*, vol. 109, no. 20, p. 10015, 2005.
- [194] A. Burquel, V. Lemaire, D. Beljonne, R. Lazzaroni, and J. Cornil, "Pathways for Photoinduced Charge Separation and Recombination at Donor-acceptor

Heterojunctions: The Case of Oligophenylenevinylene-perylene Bisimide Complexes.,” *The Journal of Physical Chemistry A*, vol. 110, no. 10, p. 3447, 2006.

- [195] A. Kahn, N. Koch, and W. Gao, “Electronic Structure and Electrical Properties of Interfaces between Metals and  $\pi$ -Conjugated Molecular Films,” *Journal of Polymer Science Part B: Polymer Physics*, vol. 41, no. 21, p. 2529, 2003.
- [196] A. Takshi, M. Mohammadi, and J. Madden, “Study the Effect of Distribution of Density of States on the Depletion Width of Organic Schottky Contacts,” *Solid-State Electronics*, vol. 52, no. 11, p. 1717, 2008.
- [197] K. H. Yoo, K. S. Kang, Y. Chen, K. J. Han, and J. Kim, “The TiO<sub>2</sub> Nanoparticle Effect on the Performance of a Conducting Polymer Schottky Diode.,” *Nanotechnology*, vol. 19, no. 50, p. 505202, 2008.
- [198] T. Lemma and T. Yohannes, “Poly(3-methylthiophene-co-3-octylthiophene) Based Solid-state Photoelectrochemical Device,” *Journal of the Brazilian Chemical Society*, vol. 18, no. 4, p. 818, 2007.
- [199] W. U. Huynh, J. J. Dittmer, W. C. Libby, G. L. Whiting, and A. P. Alivisatos, “Controlling the Morphology of Nanocrystal–Polymer Composites for Solar Cells,” *Advanced Functional Materials*, vol. 13, no. 1, p. 73, 2003.
- [200] K. S. Leschkies, A. G. Jacobs, D. J. Norris, and E. S. Aydil, “Nanowire-quantum-dot Solar Cells and the Influence of Nanowire Length on the Charge Collection Efficiency,” *Applied Physics Letters*, vol. 95, no. 19, p. 193103, 2009.
- [201] N. Greenham, X. Peng, and A. Alivisatos, “Charge Separation and Transport in Conjugated-polymer/Semiconductor-nanocrystal Composites Studied by Photoluminescence Quenching and Photoconductivity.,” *Physical Review B*, vol. 54, no. 24, p. 17628, 1996.
- [202] D. Ginger, “Charge Transport in Semiconductor Nanocrystals,” *Synthetic Metals*, vol. 124, no. 1, p. 117, 2001.
- [203] B. C. Sih and M. O. Wolf, “Metal Nanoparticle-conjugated Polymer Nanocomposites.,” *Chemical Communications*, vol. 27, p. 3375, 2005.
- [204] A. Yamakata, T. Ishibashi, and H. Onishi, “Kinetics of the Photocatalytic Water-splitting Reaction on TiO<sub>2</sub> and Pt/TiO<sub>2</sub> Studied by Time-resolved Infrared Absorption Spectroscopy,” *Journal of Molecular Catalysis A: Chemical*, vol. 199, no. 1-2, p. 85, 2003.
- [205] A. J. Nozik, “Quantum Dot Solar Cells,” *Physica E*, vol. 14, no. 1-2, p. 115, 2002.

- [206] A. L. Stroyuk, A. I. Kryukov, S. Y. Kuchmii, and V. D. Pokhodenko, "Quantum Size Effects in Semiconductor Photocatalysis," *Theoretical and Experimental Chemistry*, vol. 41, no. 4, p. 207, 2005.
- [207] K. Rajeshwar, N. R. de Tacconi, and C. R. Chenthamarakshan, "Semiconductor-Based Composite Materials: Preparation, Properties, and Performance," *Chemistry of Materials*, vol. 13, no. 9, p. 2765, 2001.
- [208] N. Serpone, D. Lawless, and R. Khairutdinov, "Size Effects on the Photophysical Properties of Colloidal Anatase TiO<sub>2</sub> Particles: Size Quantization versus Direct Transitions in This Indirect Semiconductor?," *The Journal of Physical Chemistry*, vol. 99, no. 45, p. 16646, 1995.
- [209] C. Aprile, A. Corma, and H. Garcia, "Enhancement of the Photocatalytic Activity of TiO<sub>2</sub> through Spatial Structuring and Particle Size Control: From Subnanometric to Submillimetric Length Scale.," *Physical Chemistry Chemical Physics*, vol. 10, no. 6, p. 769, 2008.
- [210] A. Mihi, F. J. López-Alcaraz, and H. Míguez, "Full Spectrum Enhancement of the Light Harvesting Efficiency of Dye Sensitized Solar Cells by Including Colloidal Photonic Crystal Multilayers," *Applied Physics Letters*, vol. 88, no. 19, p. 193110, 2006.
- [211] J. E. Wijnhoven, "Preparation of Photonic Crystals Made of Air Spheres in Titania," *Science*, vol. 281, no. 5378, p. 802, 1998.
- [212] M. Fu, Y. Zhu, R. Tan, and G. Shi, "Aligned Polythiophene Micro- and Nanotubules," *Advanced Materials*, vol. 13, no. 24, p. 1874, 2001.
- [213] T. Ha, "How Nanocrystals Lost Their Blink," *Nature*, vol. 459, no. June, p. 3, 2009.
- [214] F. Barbir, "PEM Electrolysis for Production of Hydrogen from Renewable Energy Sources," *Solar Hydrogen*, vol. 78, no. 5, p. 661, 2005.
- [215] B. Drolet, "The Euro-Quebec Hydro-hydrogen Pilot Project," *International Journal of Hydrogen Energy*, vol. 21, no. 4, p. 305, 1996.
- [216] C. A. Schug, "Operational Characteristics of High-pressure, High-efficiency Water-hydrogen-electrolysis," *International Journal of Hydrogen Energy*, vol. 23, no. 12, p. 1113, 1998.
- [217] M. Kato, S. Maezawa, K. Sato, and K. Oguro, "Polymer-electrolyte Water Electrolysis," *Applied Energy*, vol. 59, no. 4, p. 261, 1998.

- [218] K. Uosaki and H. Kita, "Photoelectrochemical Characteristics of Semiconductor-Metal/SPE/Metal Cells," *Journal of the Electrochemical Society*, vol. 130, no. 11, p. 2179, 2006.
- [219] Y. A. Dobrovolsky, P. Jannasch, B. Lafitte, N. M. Belomoina, A. L. Rusanov, and D. Y. Likhachev, "Achievements in the Field of Proton-conductive Porion Electrolyte Membranes," *Russian Journal of Electrochemistry*, vol. 43, no. 5, p. 489, 2007.
- [220] A. Herring, "Inorganic-Polymer Composite Membranes for Proton Exchange Membrane Fuel Cells," *Polymer Reviews*, vol. 46, no. 3, p. 245, 2006.
- [221] L. Wang, D. M. Xing, Y. H. Liu, Y. H. Cai, Z.-G. Shao, Y. F. Zhai, H. X. Zhong, B. L. Yi, and H. M. Zhang, "Pt/SiO<sub>2</sub> Catalyst as an Addition to Nafion/PTFE Self-humidifying Composite Membrane," *Journal of Power Sources*, vol. 161, no. 1, p. 61, 2006.
- [222] A. Sacca, A. Carbone, E. Passalacqua, A. Depifanio, S. Licoccia, E. Traversa, E. Sala, F. Traini, and R. Ornelas, "Nafion-TiO<sub>2</sub> Hybrid Membranes for Medium Temperature Polymer Electrolyte Fuel Cells (PEFCs)," *Journal of Power Sources*, vol. 152, p. 16, 2005.
- [223] M. Eikerling, A. A. Kornyshev, A. M. Kuznetsov, J. Ulstrup, and S. Walbran, "Mechanisms of Proton Conductance in Polymer Electrolyte Membranes," *Journal of Physical Chemistry B*, vol. 105, p. 3646, 2001.
- [224] B. Pivovar, "An Overview of Electro-osmosis in Fuel Cell Polymer Electrolytes," *Polymer*, vol. 47, no. 11, p. 4194, 2006.
- [225] J. J. Fontanella, C. A. Edmondson, M. C. Wintersgill, Y. Wu, and S. G. Greenbaum, "High-Pressure Electrical Conductivity and NMR Studies in Variable Equivalent Weight Nafion Membranes," *Macromolecules*, vol. 29, no. 14, p. 4944, 1996.
- [226] L. A. Zook and J. Leddy, "Density and Solubility of Nafion: Recast, Annealed, and Commercial Films," *Analytical Chemistry*, vol. 68, no. 21, p. 3793, 1996.
- [227] M. Kelly, G. Fafilek, J. Besenhard, H. Kronberger, and G. Nauer, "Contaminant Absorption and Conductivity in Polymer Electrolyte Membranes," *Journal of Power Sources*, vol. 145, no. 2, p. 249, 2005.
- [228] A. J. Nozik and R. Memming, "Physical Chemistry of Semiconductor-liquid Interfaces," *Journal of Physical Chemistry*, vol. 100, p. 13061, 1996.
- [229] D. R. Lide, *CRC Handbook of Chemistry and Physics: A Ready-reference Book of Chemical and Physical Data*, vol. 89, no. 2003. CRC Press, 2004, p. 20.

- [230] A. W. Bott, "Electrochemistry of Semiconductors," *Current Separations*, vol. 17, no. 3, p. 87, 1998.
- [231] T. Preo and N. Kallay, "Point of Zero Charge and Surface Charge Density of TiO<sub>2</sub> in Aqueous Electrolyte Solution as Obtained by Potentiometric Mass Titration," *Croatica Chemica Acta*, vol. 79, no. 1, p. 95, 2006.
- [232] J. C. Yu, Z.-T. Jiang, H.-Y. Liu, and J. Yu, "Influence of Solvation Interactions on the Zeta Potential of Titania Powders.," *Journal of Colloid and Interface Science*, vol. 262, no. 1, p. 97, 2003.
- [233] T. Bak, J. Nowotny, M. Rekas, and C. . Sorrell, "Photo-electrochemical Hydrogen Generation from Water using Solar Energy. Materials-related Aspects," *International Journal of Hydrogen Energy*, vol. 27, no. 10, p. 991, 2002.
- [234] A. Barnard, Z. Saponjic, D. Tiede, T. Rajh, and L. Curtiss, "Multi-scale Modeling of Titanium Dioxide: Controlling Shape with Surface Chemistry," *Reviews on Advanced Materials Science*, vol. 10, p. 21, 2005.
- [235] H. Harada, T. Fuchigami, and T. Nonaka, "Degradation and its Prevention, and the Deactivation and Reactivation of Electroactive Polythiophene Films during Oxidation/Reduction Cycles," *Journal of Electroanalytical Chemistry and Interfacial Electrochemistry*, vol. 303, no. 1-2, p. 139, 1991.
- [236] M. M. Lohrengel and O. Genz, "Mechanism of the Redox Process of Conducting Polymers," *Ionics*, vol. 1, no. 4, p. 304, 1995.
- [237] V. E. Kazarinov, M. D. Levi, A. M. Skundin, and M. A. Vorotyntsev, "Phenomenological Description of Dark Redox Reactions at Electrodes Covered with Conducting Polymer Films: Part I. Mechanism and Kinetics of Ferrocene Oxidation at Polythiophene," *Journal of Electroanalytical Chemistry and Interfacial Electrochemistry*, vol. 271, no. 1-2, p. 193, 1989.
- [238] I. Mukoyama, K. Aoki, and J. Chen, "Electrochemical Dissolution of Polythiophene Films," *Journal of Electroanalytical Chemistry*, vol. 531, no. 2, p. 133, 2002.
- [239] M. F. Suarez-Herrera and J. M. Feliu, "Electrochemical Properties of Thin Films of Polythiophene Polymerized on Basal Plane Platinum Electrodes in Nonaqueous Media," *Journal of Physical Chemistry B*, vol. 113, no. 7, p. 1899, 2009.
- [240] U. Rammelt, N. Hebestreit, A. Fikus, and W. Plieth, "Investigation of polybithiophene/n-TiO<sub>2</sub> bilayers by electrochemical impedance spectroscopy and photoelectrochemistry," *Electrochimica Acta*, vol. 46, no. 15, p. 2363, 2001.

- [241] N. S. Lewis, "Progress in Understanding Electron-Transfer Reactions at Semiconductor/Liquid Interfaces," *The Journal of Physical Chemistry B*, vol. 102, no. 25, p. 4843, 1998.
- [242] C. Wagner, "Theoretical Analysis of the Current Density Distribution in Electrolytic Cells," *Journal of The Electrochemical Society*, vol. 98, no. 3, p. 116, 1951.
- [243] H. E. Unalan, D. Wei, K. Suzuki, S. Dalal, P. Hiralal, H. Matsumoto, S. Imaizumi, M. Minagawa, A. Tanioka, A. J. Flewitt, W. I. Milne, and G. a. J. Amaratunga, "Photoelectrochemical Cell using Dye Sensitized Zinc Oxide Nanowires Grown on Carbon Fibers," *Applied Physics Letters*, vol. 93, no. 13, p. 133116, 2008.
- [244] E. V. Ovsyannikova, O. N. Efimov, A. P. Moravsky, R. O. Loutfy, E. P. Krinichnaya, and N. M. Alpatova, "Electrochemical Properties of Thin-layered Composites formed by Carbon Nanotubes and Polybithiophene," *Russian Journal of Electrochemistry*, vol. 41, no. 4, p. 439, 2005.
- [245] S. D. Yim, G. G. Park, Y. J. Sohn, W. Y. Lee, Y. G. Yoon, T. H. Yang, S. Um, S. P. Yu, and C. S. Kim, "Optimization of PtIr electrocatalyst for PEM URFC," *International Journal of Hydrogen Energy*, vol. 30, p. 1345, 2005.
- [246] M. Metikos-Hukovic and A. Jukic, "Correlation of Electronic Structure and Catalytic Activity of Zr-Ni Amorphous Alloys for the Hydrogen Evolution Reaction," *Electrochimica Acta*, vol. 45, no. 25-26, p. 4159, 2000.
- [247] H. Ma, C. Liu, J. Liao, Y. Su, X. Xue, and W. Xing, "Study of Ruthenium Oxide Catalyst for Electrocatalytic Performance in Oxygen Evolution," *Journal of Molecular Catalysis A: Chemical*, vol. 247, no. 1-2, p. 7, 2006.
- [248] A. Marshall, B. Borresen, G. Hagen, M. Tsympkin, and R. Tunold, "Electrochemical Characterisation of  $\text{Ir}_x\text{Sn}_{1-x}\text{O}_2$  Powders as Oxygen Evolution Electrocatalysts," *Electrochimica Acta*, vol. 51, no. 15, p. 3161, 2006.
- [249] S. A. Grigor'ev, M. M. Khaliullin, N. V. Kuleshov, and V. N. Fateev, "Electrolysis of Water in a System with a Solid Polymer Electrolyte at Elevated Pressure," *Russian Journal of Electrochemistry*, vol. 37, no. 8, p. 819, 2001.
- [250] S. A. Grigor'ev, P. Millet, and V. N. Fateev, "Evaluation of Carbon-supported Pt and Pd Nanoparticles for the Hydrogen Evolution Reaction in PEM Water Electrolysers," *Journal of Power Sources*, vol. 177, p. 281, 2008.
- [251] A. Wolz, S. Zils, M. Michel, and C. Roth, "Structured Multilayered Electrodes of Proton/Electron Conducting Polymer for Polymer Electrolyte Membrane Fuel Cells Assembled by Spray Coating," vol. 195, p. 8162, 2010.

- [252] M. T. Giacomini, E. A. Ticianelli, J. McBreen, and M. Balasubramanian, "Oxygen Reduction on Supported Platinum/Polythiophene Electrocatalysts," *Journal of The Electrochemical Society*, vol. 148, no. 4, p. A323, 2001.
- [253] S. Y. Reece, J. A. Hamel, K. Sung, T. D. Jarvi, A. J. Esswein, J. J. H. Pijpers, and D. G. Nocera, "Wireless Solar Water Splitting using Silicon-based Semiconductors and Earth-abundant Catalysts.," *Science*, vol. 334, no. 6056, p. 645, 2011.
- [254] E. Rasten, G. Hagen, and R. Tunold, "Electrocatalysis in Water Electrolysis with Solid Polymer Electrolyte," *Electrochimica Acta*, vol. 48, no. 25-26, p. 3945, 2003.
- [255] M. W. Kanan and D. G. Nocera, "In-situ Formation of an Oxygen-evolving Catalyst in Neutral Water containing Phosphate and  $\text{Co}^{2+}$ ," *Science*, vol. 321, no. 5892, p. 1072, 2008.
- [256] M. Calatayud and C. Minot, "Effect of Relaxation on Structure and Reactivity of Anatase (100) and (001) Surfaces," *Surface Science*, vol. 552, no. 1-3, p. 169, 2004.
- [257] J. C. R. Reis, "Thermodynamic Analysis of the Symmetry Factor and the Transfer Coefficient in Electrode Kinetics," *Journal of the Electrochemical Society*, vol. 144, p. 2404, 2005.
- [258] M. M. Jaksic, "Hypo-hyper-d-electronic Interactive Nature of Interionic Synergism in Catalysis and Electrocatalysis for Hydrogen Reactions," *International Journal of Hydrogen Energy*, vol. 26, no. 6, p. 559, 2001.
- [259] M. M. Jaksic, "Volcano Plots along the Periodic Table, their Causes and Consequences on Electrocatalysis for Hydrogen Electrode Reactions," *Journal of New Materials for Electrochemical Systems*, vol. 3, p. 153, 2000.
- [260] P. Gomez-Romero, "Hybrid Organic-Inorganic Materials—In Search of Synergic Activity," *Advanced Materials*, vol. 13, no. 3, p. 163, 2001.
- [261] A. J. Bard, H. D. Abruna, C. E. Chidsey, L. R. Faulkner, S. W. Feldberg, K. Itaya, M. Majda, O. Melroy, and R. W. Murray, "The Electrode/Electrolyte Interface - A Status Report," *The Journal of Physical Chemistry*, vol. 97, no. 28, p. 7147, 1993.
- [262] R. A. Marcus, "On the Theory of Electron-Transfer Reactions. VI. Unified Treatment for Homogeneous and Electrode Reactions," *The Journal of Chemical Physics*, vol. 43, no. 2, p. 679, 1965.
- [263] C. Creutz, B. S. Brunschwig, and N. Sutin, "Interfacial Charge-transfer Absorption: Semiclassical Treatment," *The Journal of Physical Chemistry B*, vol. 109, no. 20, p. 10251, 2005.

- [264] D. W. Small, D. V. Matyushov, and G. a Voth, "The Theory of Electron Transfer Reactions: What May be Missing?," *Journal of the American Chemical Society*, vol. 125, no. 24, p. 7470, 2003.
- [265] T. P. Pearsall, "Electrical Conduction in TiO<sub>2</sub>," *Journal of Physics D: Applied Physics*, vol. 3, no. 12, p. 1837, 1970.
- [266] M. D. Earle, "The Electrical Conductivity of Titanium Dioxide," *Physical Review*, vol. 61, no. 1-2, p. 56, 1942.
- [267] G. R. Hutchison, M. A. Ratner, and T. J. Marks, "Hopping Transport in Conductive Heterocyclic Oligomers: Reorganization Energies and Substituent Effects.," *Journal of the American Chemical Society*, vol. 127, no. 7, p. 2339, 2005.
- [268] W. M. Sears, "The Effect of Humidity on the Electrical Conductivity of Mesoporous Polythiophene," *Sensors and Actuators B: Chemical*, vol. 130, no. 2, p. 661, 2008.
- [269] W. C. D. Whetham, "The Electrical Conductivity of Dilute Solutions of Sulphuric Acid," *Proceedings of the Royal Society A: Mathematical, Physical and Engineering Sciences*, vol. 76, no. 513, p. 577, 1905.
- [270] H. E. Darling, "Conductivity of Sulfuric Acid Solutions," *Journal of Chemical & Engineering Data*, vol. 9, no. 3, p. 421, 1964.
- [271] B. K. Joshi and N. D. Kandpal, "Volumetric and Transport Properties of Aqueous Sulphuric Acid," *Physics and Chemistry of Liquids*, vol. 45, no. 4, p. 463, 2007.
- [272] N. Papageorgiou, M. Grätzel, and P. P. Infelta, "On the Relevance of Mass Transport in Thin Layer Nanocrystalline Photoelectrochemical Solar Cells," *Solar Energy Materials and Solar Cells*, vol. 44, no. 4, p. 405, 1996.
- [273] Y. Lin, Y. T. Ma, L. Yang, X. R. Xiao, X. W. Zhou, and X. P. Li, "Computer Simulations of Light Scattering and Mass Transport of Dye-sensitized Nanocrystalline Solar Cells," *Journal of Electroanalytical Chemistry*, vol. 588, p. 51, 2006.
- [274] Y. Tanaka, S. Uchinashi, Y. Saihara, K. Kikuchi, T. Okaya, and Z. Ogumi, "Dissolution of Hydrogen and the Ratio of the Dissolved Hydrogen Content to the Produced Hydrogen in Electrolyzed Water using SPE Water Electrolyzer," *Electrochimica Acta*, vol. 48, no. 27, p. 4013, 2003.
- [275] M. Dolata, P. Kedzierzawski, and J. Augustynski, "Comparative Impedance Spectroscopy Study of Rutile and Anatase TiO<sub>2</sub> Film Electrodes," *Electrochimica Acta*, vol. 41, no. 7-8, p. 1287, 1996.
- [276] F. Fabregat-Santiago, G. Garcia-Belmonte, J. Bisquert, P. Bogdanoff, and A. Zaban, "Mott-Schottky Analysis of Nanoporous Semiconductor Electrodes in Dielectric State

Deposited on SnO<sub>2</sub> Conducting Substrates,” *Journal of the Electrochemical Society*, vol. 150, no. 6, p. E293, 2003.

- [277] B. W. Johnson, D. C. Read, P. Christensen, A. Hamnett, and R. D. Armstrong, “Impedance Characteristics of Conducting Polythiophene Films,” *Journal of Electroanalytical Chemistry*, vol. 364, no. 1-2, p. 103, 1994.
- [278] A. A. Diagne, M. Fall, M. Guène, M. M. Dieng, F. Deflorian, S. Rossi, P. Bonora, and C. D. Volpe, “Electrochemical Impedance Spectroscopy of Polybithiophene Films in an Aqueous LiClO<sub>4</sub> Solution,” *Comptes Rendus Chimie*, vol. 10, no. 6, p. 558, 2007.
- [279] G. Láng and G. Inzelt, “An Advanced Model of the Impedance of Polymer Film Electrodes,” *Electrochimica Acta*, vol. 44, no. 12, p. 2037, 1999.
- [280] G. S. Popkirov, E. Barsoukov, and R. N. Schindler, “Investigation of Conducting Polymer Electrodes by Impedance Spectroscopy during Electropolymerization under Galvanostatic Conditions,” *Journal of Electroanalytical Chemistry*, vol. 425, no. 1-2, p. 209, 1997.
- [281] G. S. Popkirov and E. Barsoukov, “In-situ Impedance Measurements During Oxidation and Reduction of Conducting Polymers: Significance of the Capacitive Currents,” *Journal of Electroanalytical Chemistry*, vol. 383, no. 1-2, p. 155, 1995.
- [282] L. Li, J.-F. Drillet, R. Dittmeyer, and K. Jüttner, “Formation and Characterization of PEDOT-modified Nafion 117 Membranes,” *Journal of Solid State Electrochemistry*, vol. 10, no. 9, p. 708, 2006.
- [283] O. Aksimentyeva, O. Konopelnyk, I. Bolesta, I. Karbovnyk, D. Poliovyi, and A. I. Popov, “Charge Transport in Electrically Responsive Polymer Layers,” *Journal of Physics: Conference Series*, vol. 93, p. 12042, 2007.
- [284] R. de Levie, “On Porous Electrodes in Electrolyte Solutions,” *Electrochimica Acta*, vol. 8, no. 10, p. 751, 1963.
- [285] S. A. Sarac, B. Schulz, A. Gencturk, and H. D. Gilsing, “Potential Dependence of Electrochemical Impedance of Nanoscale Modified Carbon Fibre Surface,” *Surface Engineering*, vol. 24, no. 5, p. 358, 2008.
- [286] S. Biniak, “The Electrochemical Behaviour of Carbon Fibre Electrodes in Various Electrolytes. Double-layer Capacitance,” *Carbon*, vol. 33, no. 9, p. 1255, 1995.
- [287] J.-N. Nian and H. Teng, “Influence of the Semiconducting Properties of a Current Collector on the Electric Double Layer Formation on Porous Carbon,” *The Journal of Physical Chemistry B*, vol. 109, no. 20, p. 10279, 2005.

- [288] R. Sharma, A. Rastogi, and S. Desu, "Manganese Oxide Embedded Polypyrrole Nanocomposites for Electrochemical Supercapacitor," *Electrochimica Acta*, vol. 53, no. 26, p. 7690, 2008.
- [289] Q. Wang, C.-S. Cha, J. Lu, and L. Zhuang, "The Electrochemistry of Solid/Water Interfaces Involved in PEM-H<sub>2</sub>O Reactors: Part I. The Pt/Water Interfaces," *Physical Chemistry Chemical Physics*, vol. 11, no. 4, p. 679, 2009.
- [290] H. D. Yoo, J. H. Jang, B. H. Ka, C. K. Rhee, and S. M. Oh, "Impedance Analysis for Hydrogen Adsorption Pseudocapacitance and Electrochemically Active Surface Area of Pt Electrode.," *Langmuir*, vol. 25, no. 19, p. 11947, 2009.
- [291] J. Wang, J. Polleux, T. Brezesinski, S. Tolbert, and B. Dunn, "The Pseudocapacitance Behaviors of TiO<sub>2</sub> (Anatase) Nanoparticles," *ECS Transactions*, vol. 11, no. 31, p. 101, 2008.
- [292] W. U. Huynh, J. J. Dittmer, and A. P. Alivisatos, "Hybrid Nanorod-polymer Solar Cells," *Science*, vol. 295, no. 5564, p. 2425, 2002.
- [293] G. Wang, C. Hua, Z. Hong, S. Yaochun, Y. Chunwei, L. Zuhong, W. Guangmin, and Y. Weiyi, "Current-voltage Characteristics of TiO<sub>2</sub>/PPy Complex Films," *Physics Letters A*, vol. 237, no. 3, p. 165, 1998.
- [294] M. Lira-Cantu, K. Norrman, J. Andreasen, N. Casan-Pastor, and F. C. Krebs, "Semiconductor Oxides as Electron Acceptors in Hybrid Organic-Inorganic Solar Cells," *ECS Transactions*, vol. 3, no. 22, p. 1, 2007.
- [295] Z. Liu, W. Guo, D. Fu, and W. Chen, "p-n Heterojunction Diodes made by Assembly of ITO/Nano-crystalline TiO<sub>2</sub>/Polyaniline/ITO," *Synthetic Metals*, vol. 156, no. 5-6, p. 414, 2006.
- [296] H. Neugebauer, S. Günes, and S. Sariciftci, "Solid State Dye Sensitized Solar Cells Using Poly(3-hexylthiophene) as Hole Transport Material," *ECS Transactions*, vol. 2, no. 12, p. 145, 2007.
- [297] M. Y. A. Rahman, M. M. Salleh, I. A. Talib, and M. Yahaya, "Light Intensity and Temperature Dependence on Performance of a Photoelectrochemical Cells of ITO/TiO<sub>2</sub>/PVC-LiClO<sub>4</sub>/Graphite," *Ionics*, vol. 13, no. 4, p. 241, 2007.
- [298] L. Roberson, M. A. Poggi, J. P. Kowalik, G. P. Smestad, L. A. Bottomley, and L. M. Tolbert, "Correlation of Morphology and Device Performance in Inorganic-organic TiO<sub>2</sub>-polythiophene Hybrid Solid-state Solar Cells," *Coordination Chemistry Reviews*, vol. 248, no. 13-14, p. 1491, 2004.
- [299] A. Sergawie, T. Yohannes, and T. Solomon, "A Comparative Study on Liquid-state Photoelectrochemical Cells based on Poly(3-hexylthiophene) and a Composite Film of

Poly(3-hexylthiophene) and Nanocrystalline Titanium Dioxide,” *Synthetic Metals*, vol. 157, no. 2-3, p. 75, 2007.

- [300] K. Takahashi, Y. Takano, T. Yamaguchi, J.-ichi Nakamura, C. Yokoe, and K. Murata, “Porphyrin Dye-sensitization of Polythiophene in a Conjugated Polymer/TiO<sub>2</sub> p-n Hetero-junction Solar Cell,” *Synthetic Metals*, vol. 155, no. 1, p. 51, 2005.
- [301] Y. Zhu, S. Xu, L. Jiang, K. Pan, and Y. Dan, “Synthesis and Characterization of Polythiophene/Titanium Dioxide Composites,” *Reactive and Functional Polymers*, vol. 68, no. 10, p. 1492, 2008.
- [302] Y. Hao, M. Yang, C. Yu, S. Cai, M. Liu, L. Fan, and Y. Li, “Photoelectrochemical Studies on Acid-doped Polyaniline as Sensitizer for TiO<sub>2</sub> Nanoporous Film,” *Solar Energy Materials and Solar Cells*, vol. 56, no. 1, p. 75, 1998.
- [303] F. Cecchet, C. Bignozzi, F. Paolucci, and M. Marcaccio, “Electrochemical and Electrochromic Investigation of Poly-bithiophene Films on a Mesoporous TiO<sub>2</sub> Surface,” *Synthetic Metals*, vol. 156, no. 1, p. 27, 2006.

## Appendix A - Helio-thermal Hydrolysis

If the focused thermal energy of a large arrays of mirrors reaches temperatures upwards of 4700K [106] (4330K [12]), then the water that is pumped to the target is instantaneously dissociated and forms a mixture of steam, hydrogen and oxygen gas. A complete thermodynamic description of this process is detailed by Licht [107] and illustrated in Figure 95 by Kodama [12] below:

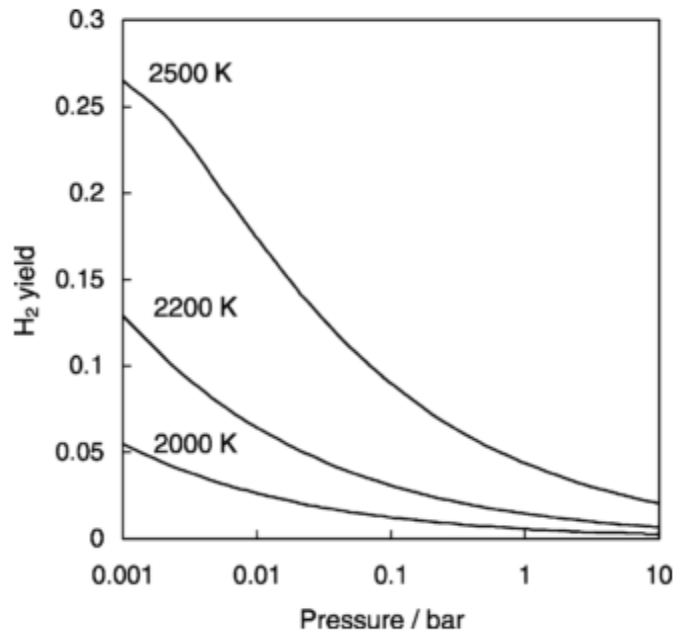


**Figure 95 - Equilibrium H<sub>2</sub> yields for direct thermal splitting as a function of temperature and pressure.**

[12] Reprinted with permission from *Progress in Energy and Combustion Science*.

A review of different schemes for direct solar water splitting which includes a combination of steam turbine electric generation or/as well as with possible additional electrolysis step was examined by Baykara [108].

In terms of thermodynamic efficiency as well as production costs it was found that a system of direct solar thermal dissociation of water with gas separation at reactor conditions coupled

with high-temperature electrolysis appeared to be the ultimate option. There are examples of pilot plants of this type, the first being a 2kW furnace at Odeillo, France, constructed in 1981, another 2kW installation in Minnesota, USA, a 3.2 kW installation in Rheovot, Israel, and a 1kW installation constructed in Montreal [109]. Currently the problems associated with this technology involve the maintenance and upkeep of the reactor, as the intense heats have an energy that degrades most man-made materials; especially in such a reducing ( $H_2$  present) and oxidizing ( $O_2$  present) environment. A thermodynamic evaluation of some of these materials can be found for temperatures up to 3000K [110] along with a discussion as to likely near-terms solutions through materials development. Another problem with these systems is the co-generation of hydrogen and oxygen needs a separation step after generation, and this gas separation can be costly. In the pilot scale systems this separation step was omitted due to this cost limitation. The efficiency of these plants was 1% or lower, and depended strongly on the success of quenching the product stream.

## Appendix B - Metal-oxide Particle Thermochemical Cycles

The first metal oxide redox pair to be investigated was by Nakamura [111], as shown below in Figure 96.

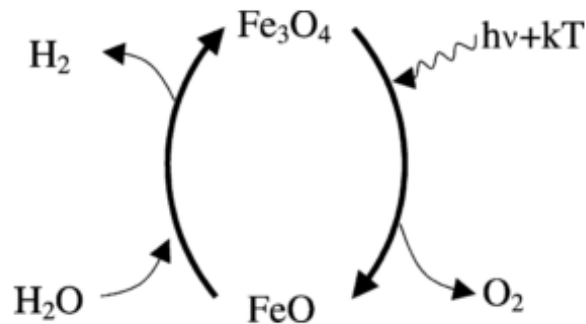


Figure 96 - Solar thermochemical water-splitting cycle using the redox pair  $\text{Fe}_3\text{O}_4/\text{FeO}$ . [111] Reprinted with permission from Solar Energy.

A comparison of other of oxide pairs is given in Figure 97 by Kodama [12]. These oxide pairs can also be used for higher hydrocarbon fuel reforming.

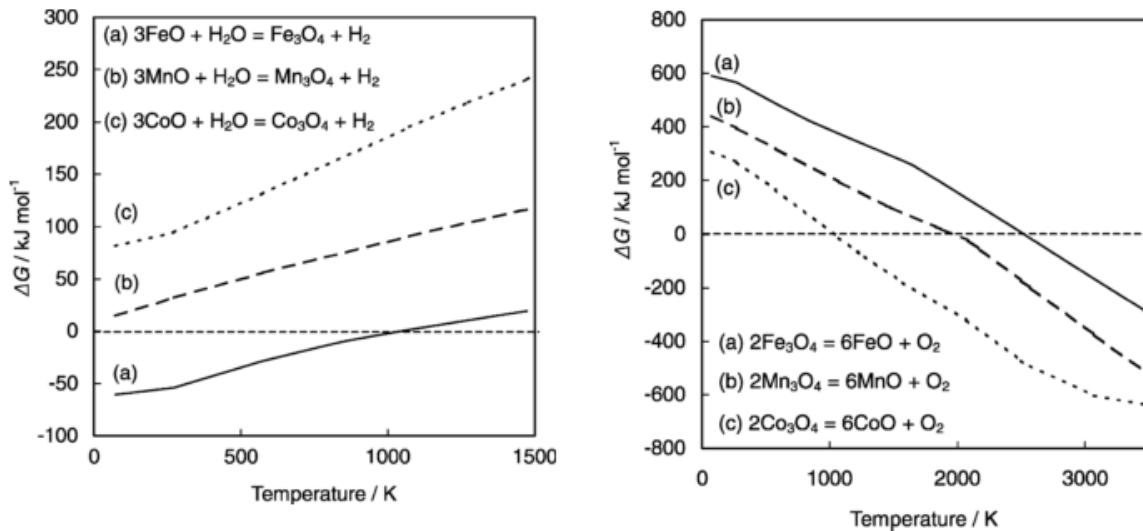
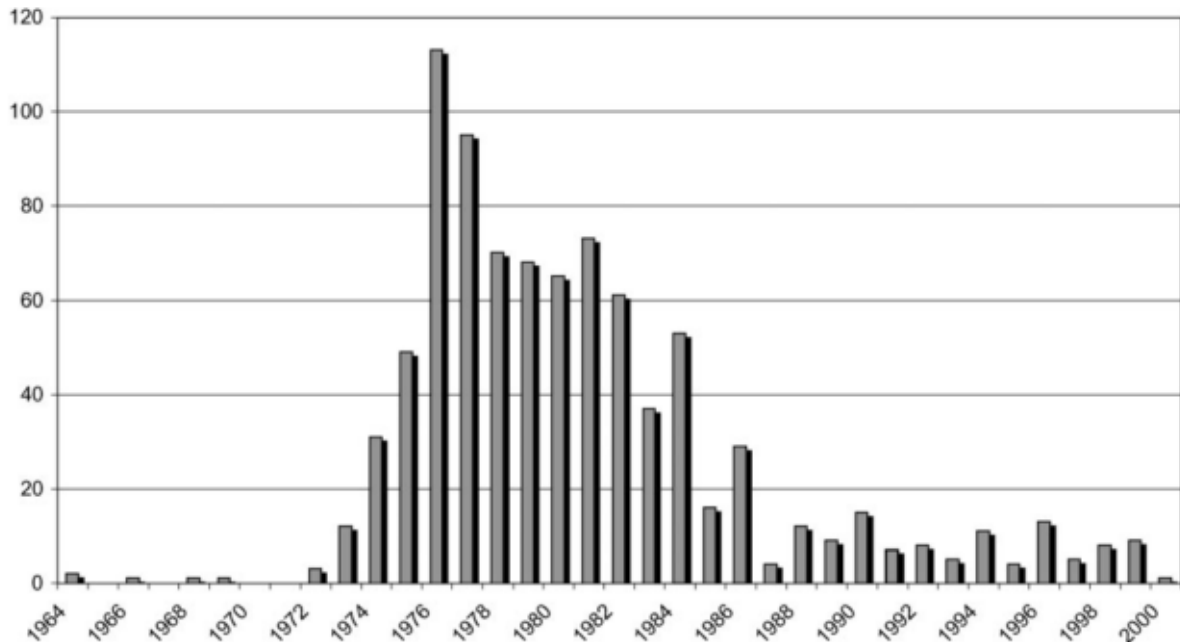


Figure 97 - Variation of  $\Delta G^0$  for the thermal decomposition of metal oxide and reduced metal oxide pairs as a function of temperature at 1 bar. [12] Reprinted with permission from Progress in Energy and Combustion Science.

The metal powders act as a catalyst sponge in a system that incorporates gases flowing across them for conversion. These systems have an overall efficiency of 40%, and although not presently operating as power plants (or pilots) to this author's knowledge, research efforts are under way for alloys of the above materials in search of more favourable redox energetics and stability [112]. The inefficiency in these systems is due to irreversibility if the quenching of the product is not accomplished, as a vapor of the metal oxide can form and would then need to be re-oxidized. The advantage of these systems is that the temperature to drive the reaction forward is far less than that required for dissociating water directly, putting less stress on the rest of the system. Perkins and Weimer discuss some materials degradation issues with these systems but conclude that SiC with a protective SiO<sub>2</sub> coating could work, but this has yet to be experimentally validated [110]. Research of other thermochemical cycles for hydrogen production was at a peak in 1977, and today there is an overall total of over 800 papers dealing with different aspects of individual chemical cycles. A breakdown of the publications can be seen below in Figure 98, and further information can be found in the article by Funk [106].



**Figure 98 - Number of thermochemical publications by year [106] Reprinted with permission from the International Journal of Hydrogen Energy.**

Overall the thermal hydrogen processes have a similar operation to the redox cycles by which heat provided by solar or nuclear sources is used for sulfuric acid decomposition. Most critically acclaimed of the reviewed cycles was the Ispra process which had an estimated efficiency of 47% thermal energy capture to hydrogen production, and hydrogen fuel could be produced for an estimated 44-48 yen/Nm<sup>3</sup> [106]. A breakdown of the sulfur family of thermochemical cycles is detailed by Bischoff et al. including two generations of the Ispra process [113]. At the time, solar sources of power for this process were cited as having critical intrinsic difficulties; small size and discontinuity.

## Appendix C - Properties of Light

### C.1 Solar Emission and Optical Attenuation of Terrestrial Insolation

The source of light in our study is chosen to mimic the spectrum that we get terrestrially from our sun. Photons originate from electromagnetic emissions activated through nuclear reactions that stimulate the photosphere. These emissions occur due to electronic transitions in the different molecules of the photosphere of the sun. These molecules are not stationary; they are bouncing around at random as governed by the entropic movement of the internal kinetic energy of the sun. This movement translates to twisting, turning, and deflection in all directions while interacting with each one other, and so the resultant electronic transition for the emission of the light beams also has a complex polarization. That polarization is described by the position of the orthonormal electric and magnetic field of the generated electromagnetic waves. Although the emission is travelling in a straight line, the polarization is a complex function representative of how the original emissive molecule was moving through space. The emissive power of the light is governed by the blackbody radiation at this temperature, as given by:

$$W = \sigma_{sb} T^4 \quad \text{Eq. 18}$$

where  $W$  is the radiant energy emitted,  $\sigma_{sb}$  is a constant, set at  $0.136 \text{ cal}\cdot\text{m}^{-2}\cdot\text{s}^{-1}\cdot\text{K}^{-4}$ , and  $T$  is absolute temperature. The spectral emission dependence on temperature is shown in Figure 99 [114]:

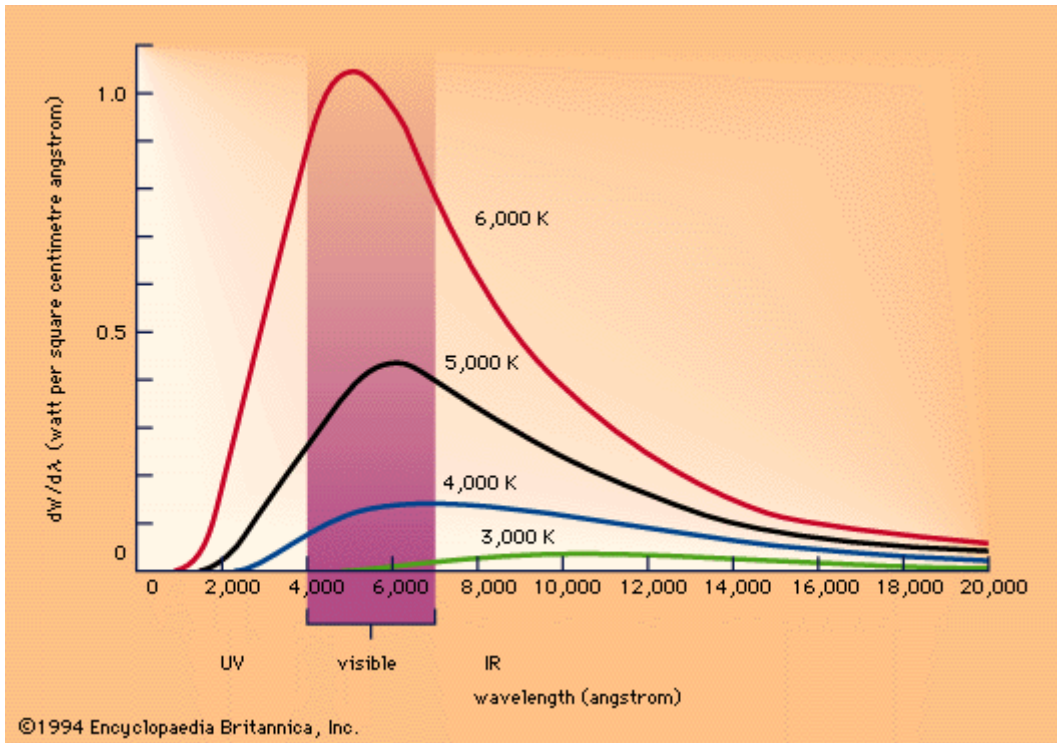


**Figure 99 - Electromagnetic energy  $dW$  emitted per unit area and per second into a wavelength interval,  $d\lambda =$ one angstrom, by a blackbody at various temperatures between 3,000 and 6,000 K as a function of wavelength. [114] Reprinted with permission from Encyclopedia Britannica Online.**

and can be broken down to Planck's radiation law (Eq. 19) to account for the 'ultraviolet catastrophe' to:

$$dW = \frac{8\pi ch\lambda^{-5}d\lambda}{e^{hc/\lambda kT} - 1} \quad \text{Eq. 19}$$

where  $c$  is the speed of light,  $h$  is Planck's constant,  $\lambda$  is the wavelength,  $k$  is the Boltzmann constant, and  $T$  is absolute temperature.

The light wave travels through free space, also known as the void. It is suitably named as no matter there exists. The wave travels at the speed of light through free space, which has a permittivity of  $\epsilon_0 = 8.854 \times 10^{-12} \text{ C}^2\text{N}^2\text{m}$  and relates the electric field to the electric displacement by Eq. 20:

$$D = \epsilon_0 E + P \quad \text{Eq. 20}$$

where D is the electric displacement, E is the electric field, and P is the bound polarization of charges in the dielectric.

## C.2 Maxwell Equations and Electromagnetic Wave Movement

Electromagnetic waves travelling through space have a wave form. As mentioned above, even though they are polarized in a specific way, they have an alternating electromagnetic wave function. The propagation of this electromagnetic function is described by the Maxwell Equations [115]:

$$\nabla \times E = -\frac{1}{c} \frac{\partial B}{\partial t} \quad \text{Eq. 21}$$

$$\nabla \times B = \frac{1}{c} \frac{\partial D}{\partial t} + \frac{4\pi}{c} J \quad \text{Eq. 22}$$

$$\nabla \cdot D = 4\pi \rho_q \quad \text{Eq. 23}$$

$$\nabla \cdot B = 0 \quad \text{Eq. 24}$$

where J and  $\rho_q$  are the current and charge densities, E the electric field, D the electric displacement, H the magnetic field and B the magnetic induction.

These equations govern the movement of electromagnetic waves in an idealized system. For our considerations these assumptions are adequate.

## C.3 Refraction

Light passing through the void goes on to encounter the earth's atmosphere. If this light ray interacts at a direct 90° angle, its direction is unperturbed. If the wave encounters this new distribution of electronic states (a change in the dielectric of the propagation media due to matter) at an angle, there is a deflection proportional to the difference in the speed of light.

This difference is given in relation to the speed of light in a vacuum, having a standard value of 1, and designated as  $n$ . This is known as Snell's Law, and graphically it is represented as:

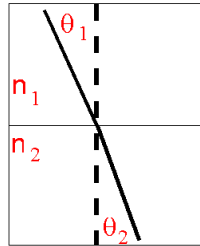


**Figure 100 - Snell's Law**

Snell's Law is equated:

$$n_{r1} \sin \theta_1 = n_{r2} \sin \theta_2 \quad \text{Eq. 25}$$

where  $n_{r1}$  and  $n_{r2}$  are indices of refraction and  $\theta_1$  and  $\theta_2$  are the angle of incidence and angle of refraction, respectively.

With refraction, there is also some consideration as to if a strong magnetic field is present while photonic diffraction occurs. Light waves can be split into finer graduations as defined by Zeeman [116] under the influence of a strong magnetic field. This effect will not be extensively considered in our analysis; although may hold some virtue when dealing with polarizing fields in materials that incorporate strong magnetic elements or that have formations of strong dipole interaction.

#### **C.4 Reflection**

If the light beam encounters a surface that is bound by a network of chemical bonds, the surface exerts a coherent deflection of the source from that surface. This deflection is caused by electromagnetic stimulation of the surface which emits a secondary wave function that is seen as the reflected wave. This coherent emission is a product of plane contact of an electromagnetic wave, and is known as Huygens' construction.

Special attention should also be placed on the effect of particles by which their size is close to that of the size of the incoming light wavelength. First reported by Mie, particle sizes of one third to one quarter the size of the incoming wavelength of light will scatter light with different polarizations, and have increased reflection producing more turbid solutions [117]. For solid state devices, considerable research efforts have been put forth to reduce the amount of reflection from planar devices. Kuo et al. have reported a nearly perfect seven layer optical coating that has a reflectivity of only 3.79% for incident angles of 0-60 degrees in the visible spectrum (400-1600nm) [118]. The device structure is shown below.

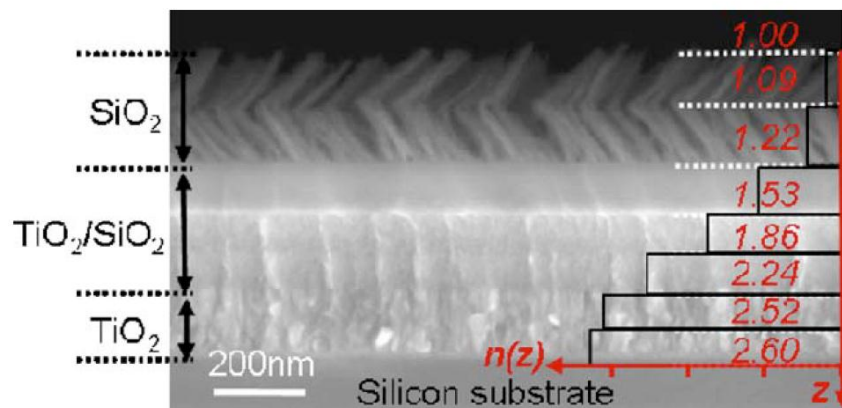


Figure 101 - Example visible spectrum anti-reflective coating diagram. [118] Reprinted with permission from Optics Letters.

Although for our studies we do not investigate the effect of reflectivity of our device and augmentation to it, it is satisfying to know that solutions are available for this loss mechanism.

### C.5 Absorption

With the interaction of an electromagnetic beam with matter, there exists a damping of the EM beam as described by the Beer-Lambert Law. The absorption is equated by:

$$A = \log\left(\frac{I_0}{I}\right) \quad \text{Eq. 26}$$

where  $I_0$  is the power of incoming monochromatic light and  $I$  is the power of the transmitted light. This relationship can be further broken down in a solute by the equation:

$$A = \varepsilon_a bc \quad \text{Eq. 27}$$

where  $\varepsilon_a$  is the molar absorptivity,  $b$  is the path length, and  $c$  is the concentration of the compound in solution.

In solids, the damping is specific to the frequency of the rotation and vibration of the bonds of the absorbing material. New studies in the design and fabrication of photonic crystals for the ordered transmission of photons along directed conduits in materials are actively being pursued [119], but will not be discussed in this work.

In the situation where the photonic rays from the sun are passing through the atmosphere to our device, the AM spectrum is used. The AM spectrum is a deviation from the standard blackbody radiation as detailed in Figure 99 that includes the significant absorptive peaks of major atmospheric constituents. We have chosen to express our baseline using a particular spectrum, the AM1.5G, which accounts for the apparent increase in photonic energy as applied through the diffuse (non-direct) refraction of additional light beams, as well as considering as an average the angle by which the sun would hit our device. There is an easy correlation to express the numerical value of the AM spectrum, as it represents the fraction of an object's shadow to that of the object's length. The AM1.5G spectrum shown below in Figure 102 [58], and represents a power density of  $100 \text{ mW/cm}^2$  at 1 sun intensity:

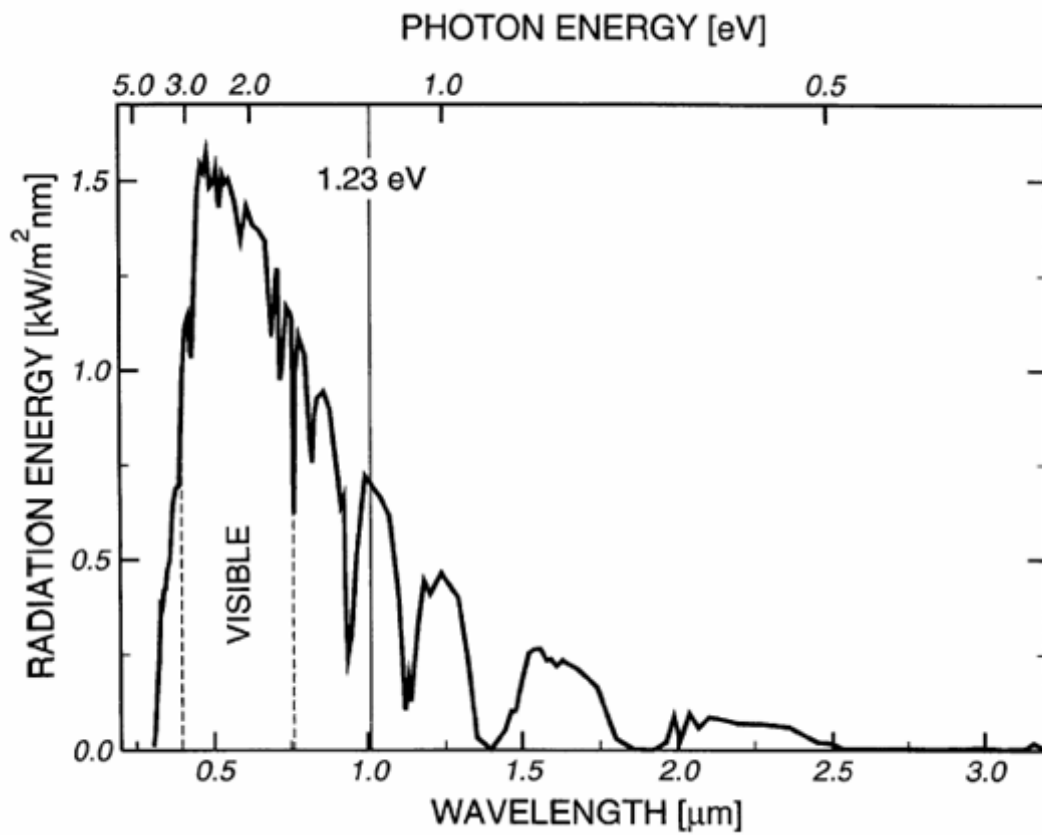


Figure 102 - AM1.5G full absorption spectrum. [58] Reprinted with permission from the International Journal of Hydrogen Energy.

Absorption spectra of additional materials and solutions employed in this study are detailed in Appendix D.

## Appendix D - Absorption Spectra

### D.1 Absorption Spectra of FTO/ITO

With standard photonic devices, typically ITO is used as an optically transparent conductive oxide. The absorption spectra of the glass is due to inclusions of Cr, B and Ti (among other trace elements) that are in the SiO<sub>2</sub> melt. The ITO/FTO is mainly visible light transparent, and has strong absorption in the infrared and ultraviolet. As can be seen below in , there is much variability with fabrication of TCO substrates, as in the cited study, the flow rate of doping for FTO was varied and produced some variation in the visible transmittance spectra [120].

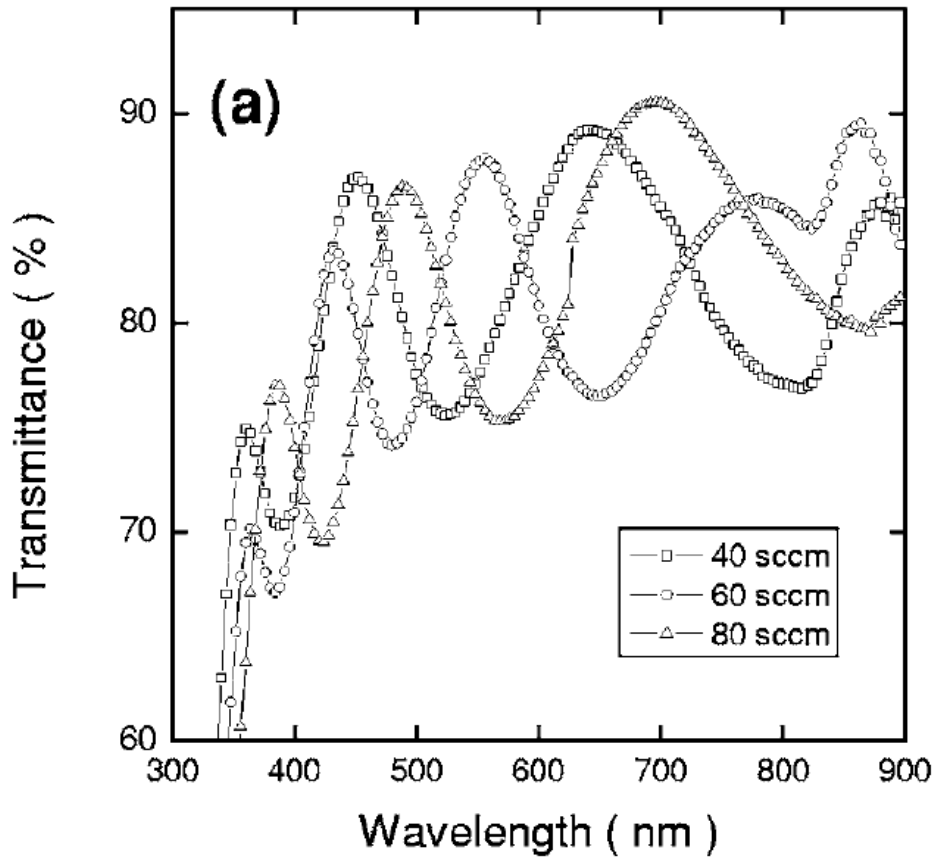


Figure 103 - Transmission spectrum variability in FTO substrates with a variation in Fluorine doping rate. [120] Reprinted with permission from the Journal of the Electrochemical Society.

The degree of doping also has a strong influence on the electronic properties of the TCO, as shown by Rakhshani et al., with variation spanning several orders of magnitude for resistivity and electron mobility [121]:

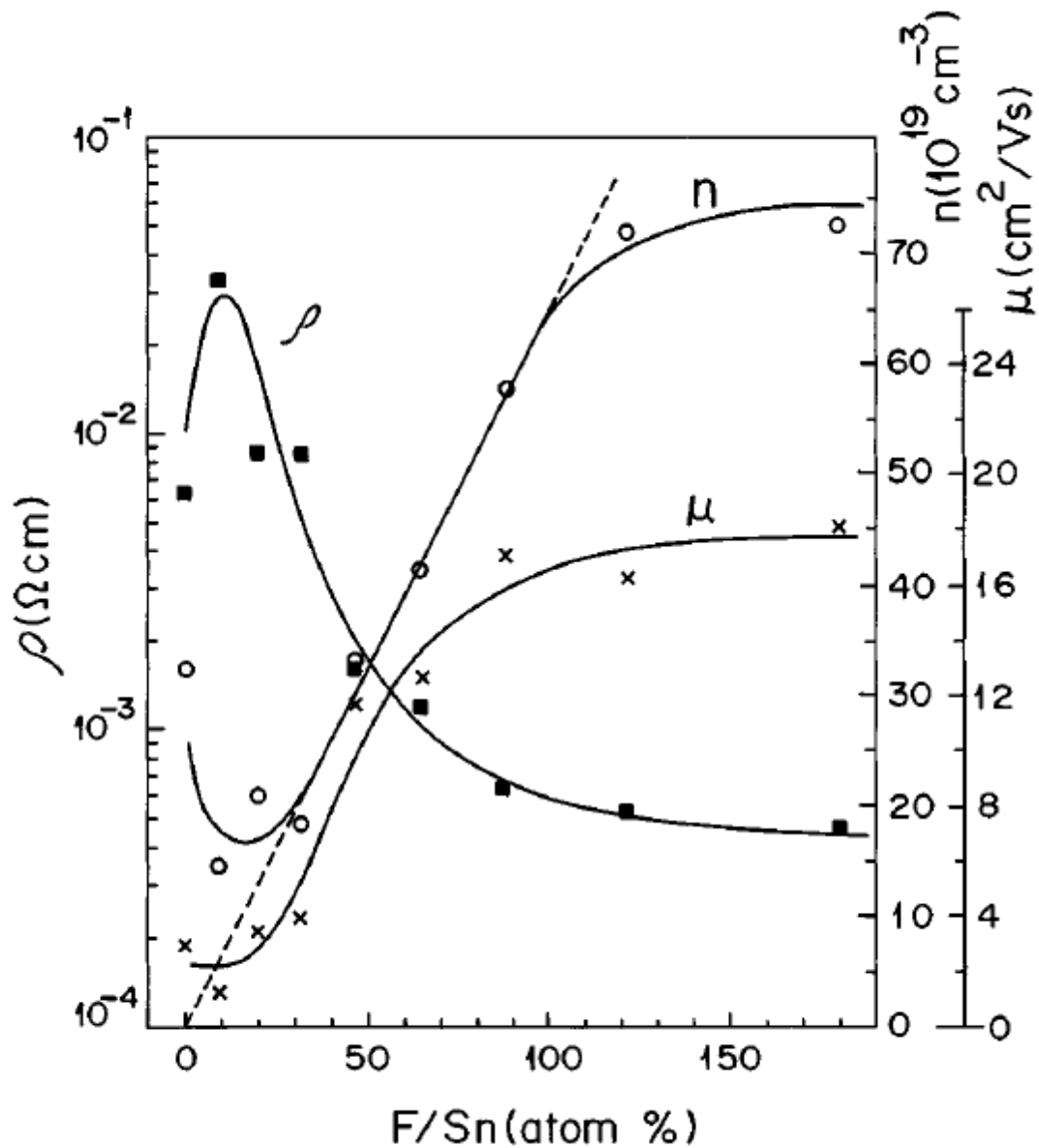


Figure 104 - Variation in optoelectronic properties of FTO films with a modulation in Fluorine doping.

[121] Reprinted with permission from the Journal of Applied Physics.

The optimum films reported by these authors indicated that a 1.1  $\mu\text{m}$  film can have 85% visible light transmittance with a resistance of  $2 \Omega/\square$ .

## D.2 Absorption Spectra of Water/ Sulfuric Acid

In our particular system we will be working with an aqueous acidic electrolyte. This electrolyte also contains absorptive frequencies, but these mainly lie in the IR spectrum. Hale and Querry have examined a large range of absorption (200nm – 200  $\mu\text{m}$ ) and the results are tabulated and plotted in terms of  $n$  and  $k$  values and compared to several other period publications to ensure validity [122]. The IR absorbance is shown below in a more recent publication and depicts the absorption variation with temperature, as shown in Figure 105 below [123]:

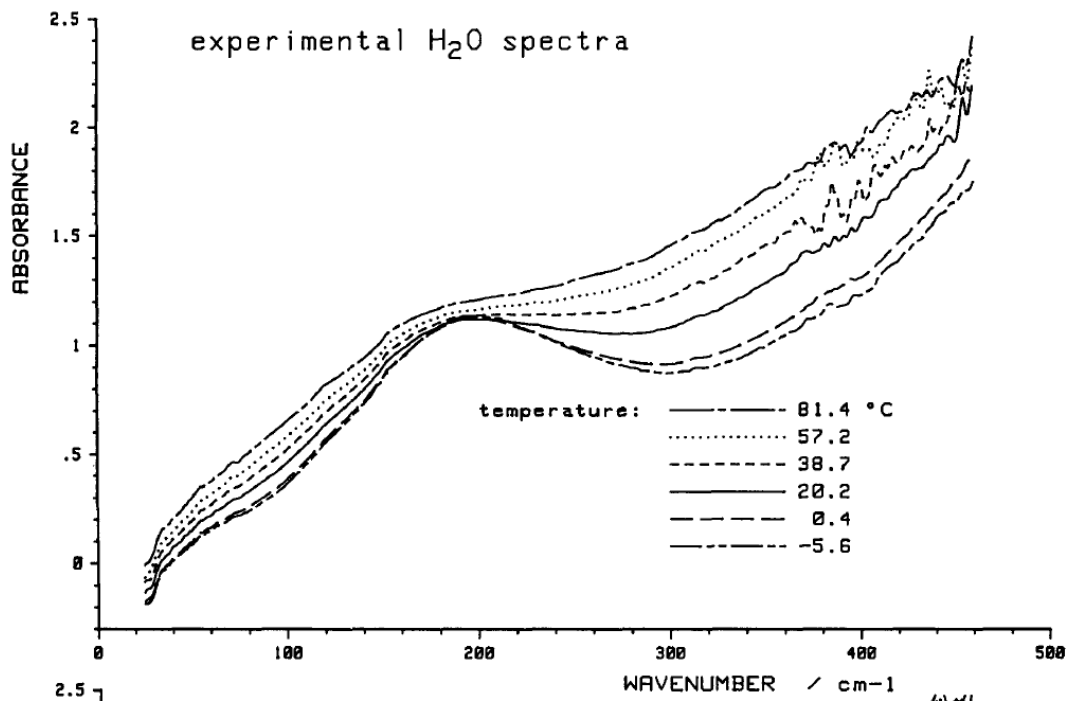


Figure 105 - IR absorption spectrum of H<sub>2</sub>O [123] Reprinted with permission from the Journal of Molecular Structure.

### D.3 Absorption of Nafion

Along with the aqueous electrolyte, if a solid polymer is used and light is transmitted through it, the specific absorption must also be considered. This absorption is detailed by de Almeida and Kawano and is shown below in Figure 106 [124]. It has been shown that higher energy (>UV) light damages the backbone of these polymers and increases UV absorption with exposure. Visible light is transmitted and transmission increases in a hydrated environment.

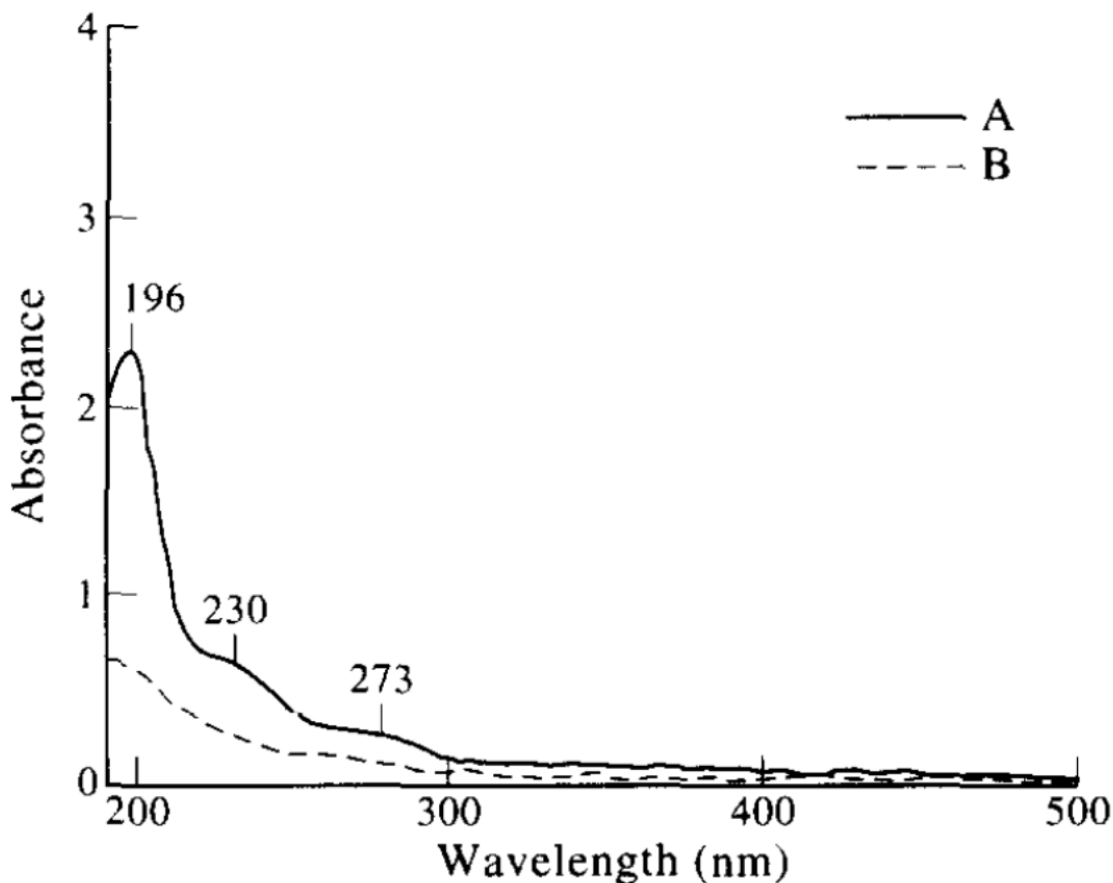


Figure 106 - UV-Vis absorption of Nafion 117 membrane a) as received and b) hydrated. [124] Reprinted with permission from European Polymer Journal.

In Figure 107, line 2 represents the IR transmission spectra for Nafion 115 from Liang et al. and shows absorption in the far IR spectrum [125]:

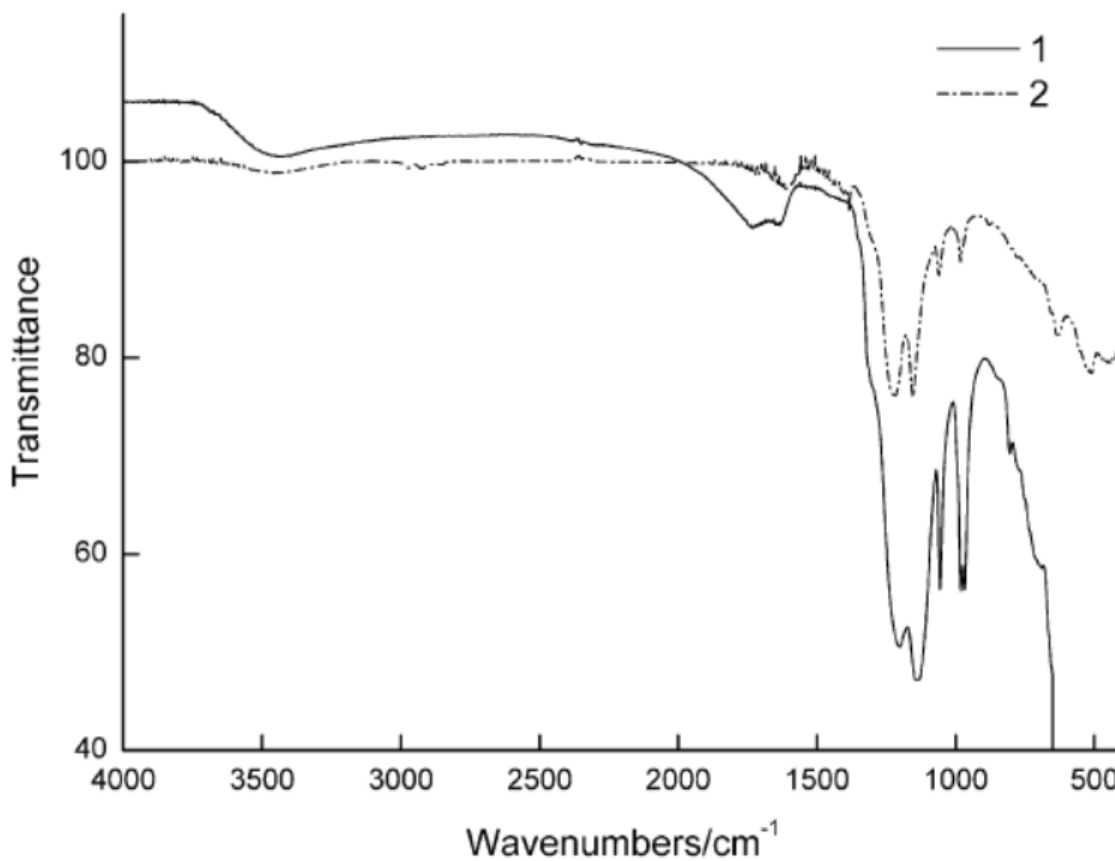


Figure 107 - IR absorption of Nafion 115 membrane (Line 2) [125] Reprinted with permission from the Journal of Membrane Science.

#### D.4 Absorption Spectra of Conductive Polymers

As mentioned in the introduction, conductive polymers can be tailored to match the incoming photonic spectra. This tailoring is used to match the incoming spectrum to a specific order of decreasing incoming photonic energy. It is altered by specific properties that help or hinder the torsion and stretching or bonded components, as well as the packing of the underlying crystal structure.

Alkyl-substituted polymers tend to crystallize in  $\pi$ -stacked structures, whereas unsubstituted, planar conjugated molecules tend to crystallize in a "herringbone" pattern [126].  $\pi$ -Stacking, favored by crystallization of sidechains, induces planarity in the conjugated backbone, and is

a form of aggregation that leads to exciton splitting. The exciton splitting and appearance of "fine structure" on the  $\pi$ - $\pi^*$  absorption peaks is similar to the Zeeman effect previously discussed and may have some relation to the localized magnetic field of the  $\pi$  stack. The polymer under investigation in our study is polybithiophene. The electrodeposition of the polymer and characteristic absorption spectra has been reported before in its reduced state by Bock et al. [127]. It is also shown that there is a linear dependence between film thickness and absorption, shown in Figure 108. The broad absorption spectrum is attributed to the superposition of  $\pi$ - $\pi^*$  absorption peaks from a distributed length of polymeric crystalline centres, with the peak associated with the mean effective conjugation length.

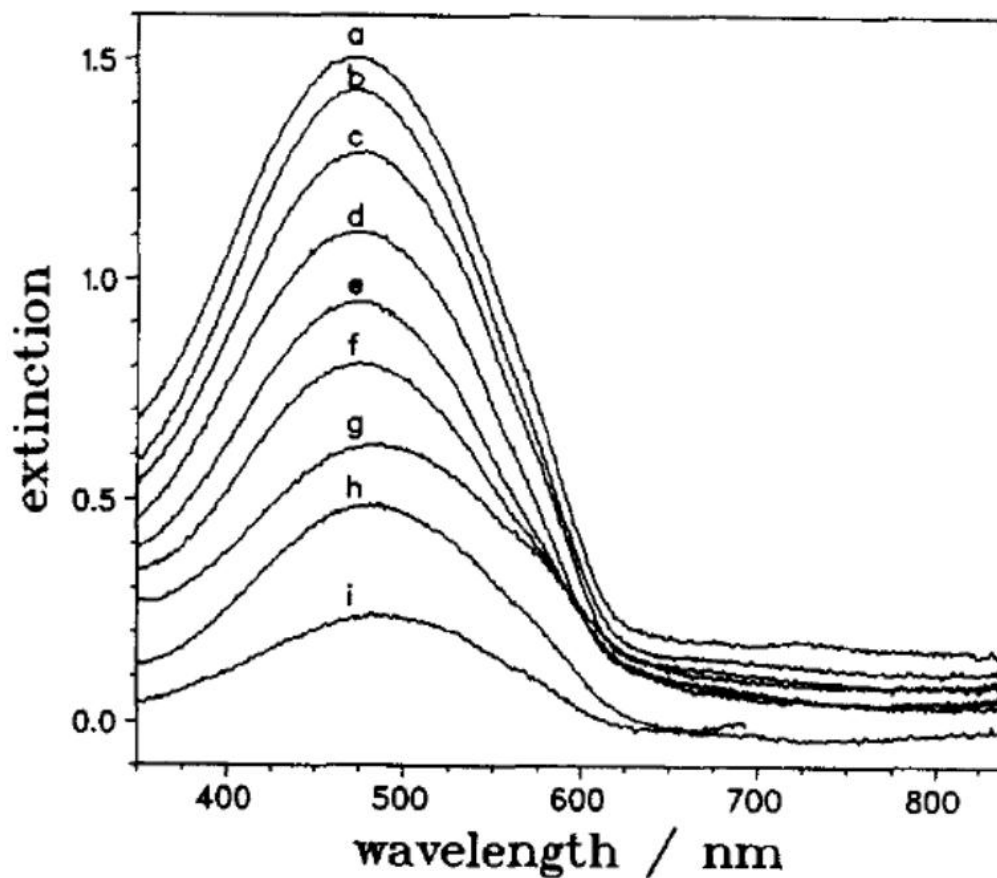


Figure 108 - Absorption spectra of undoped polybithiophene films with various thicknesses: a)150, b)136, c)128, d) 110, e) 98, f) 72, g) 62, h) 50, i) 17 nm. [127] Reprinted with permission from Synthetic Metals.

For polybithiophene in its oxidized state there is a strong absorbance of the polaronic band at 750 nm upon oxidation, coupled with the presence of a free carrier tail (dication charged species) at 900 nm [102]. This is characteristic of conducting polymers in their oxidised conducting state. The spectra of these materials in their fully reduced state (as seen above in Figure 108) shows that the absorbance of the 750 nm polaronic band had decreased relative to the absorbance of the 450 nm band.

FTIR studies have also been carried out of PBT in order to examine the charge transport functionality of p and n doped films [128]. It was reported that the intensities of selected vibrational bands are strongly enhanced by the motion of electronic charge carriers, and a simple model involving carrier-carrier interactions (whose magnitude increases linearly with carrier density) was employed to explain the data.

#### **D.5 Absorption Spectra of TiO<sub>2</sub>/Composite Films**

In the build-up of photonic devices, the creation of absorptive composites have also been investigated and published. These devices have different effects on the mobility and separation of excited charge carriers in relation to their pure constituents, and will be further discussed with regard to excitation and doping of the electronic band structure. As such, the photospectra of TiO<sub>2</sub> can be influenced by morphology and phase as well, and can be seen in the spectra reported by Kumar [129]:

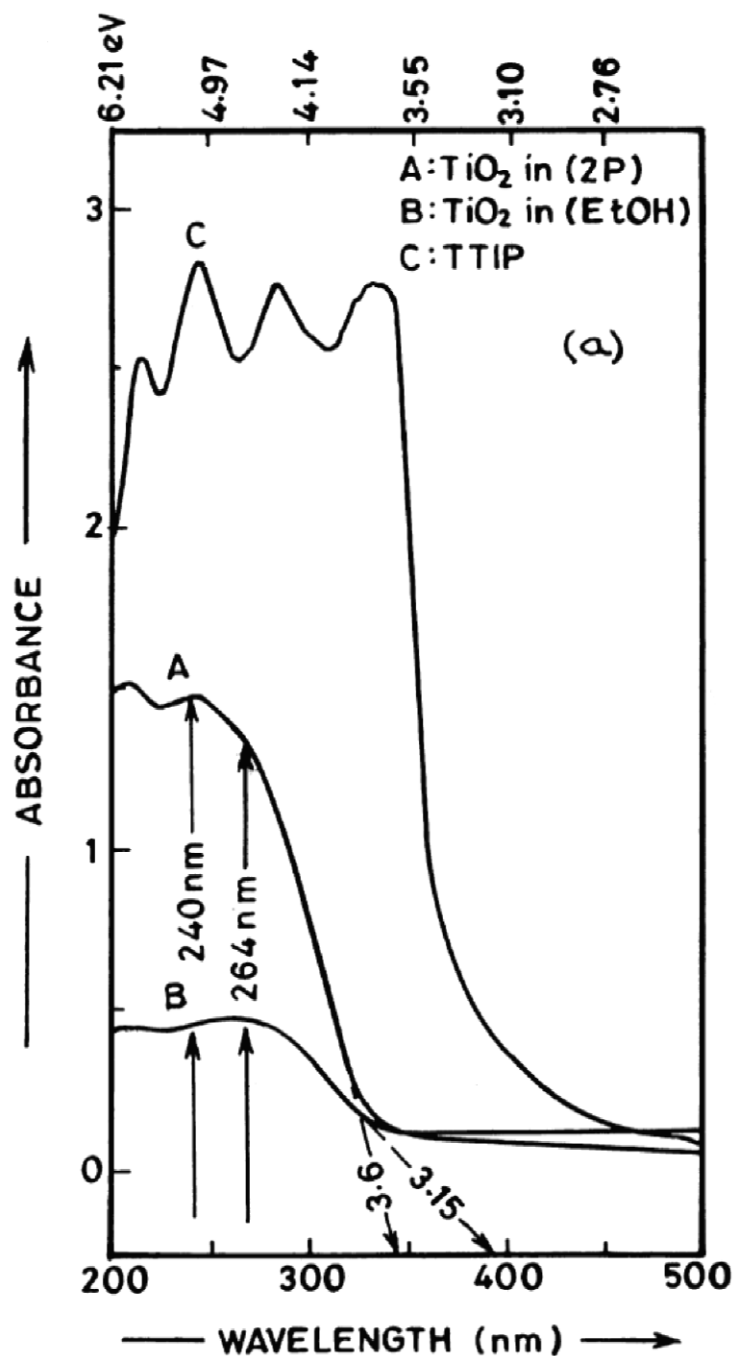
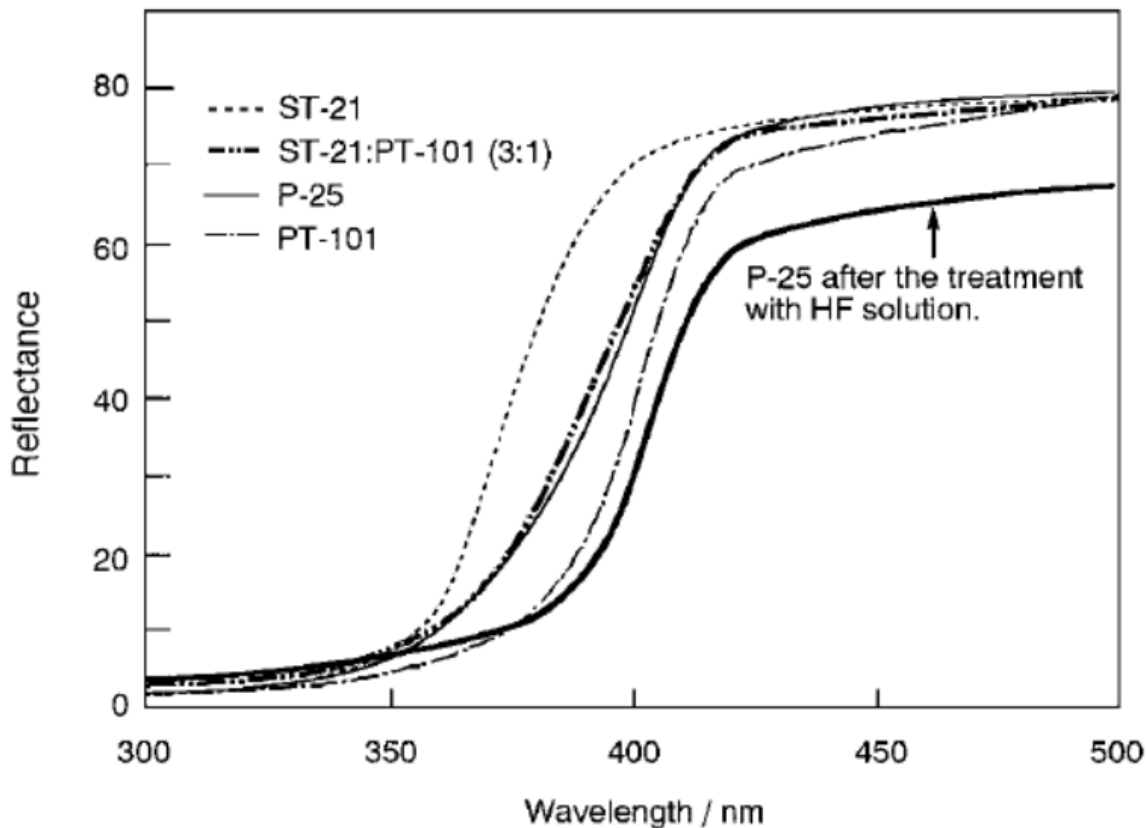


Figure 109 - UV-Vis Absorption spectrum of TiO<sub>2</sub>. [129] Reprinted with permission from Thin Solid Films.

The absorption spectrum of the two curves above have been shifted due to quantum size effects of the deposited titania film. In our study, we employ Degussa P25, a commercial

titania particulate, as our TiO<sub>2</sub> source and its diffuse reflectance spectra (converse to absorption spectra) is as follows as compared to pure anatase and rutile powders[130]:



**Figure 110 - Diffuse reflectance spectra of pure anatase powder (ST-21), pure rutile powder (PT-101), a mixture of pure anatase and rutile powders (3:1), and P-25. [130] Reprinted with permission from the Journal of Catalysis.**

The particle size of nanophase titania also affects the IR and Raman spectra and is discussed in the article by Ivanda et al. [131]. It is pertinent to acknowledge the existence of these effects, although since we will not be altering our titania particles from the standard P25 morphology, we will not be needing to further consider such analysis.

## Appendix E - Type I Solar Cells

The first generations of solar cells were made of single crystal and multicrystalline silicon, respectively, grown into large boules and then sliced into wafers for further device processing. The costs of the purification of the raw materials, as well as the relatively large amount of raw materials needed resulted in a large cost for these bulky panels, approximately \$3.50 to \$4.00 per Watt [132]. The primary source of silicon is  $\text{SiO}_2$  conventionally reduced by carbothermic reduction which yields impure silicon with 1 to 2% impurities. The silicon is then converted into volatile compounds for further purification with the final product being a highly pure polycrystalline rod. This purified silicon is then grown into single and tri-crystal morphologies using the Czochralski process, and is then sliced into wafers. Typically the concentrations of lattice defects are in the range of  $10^{17} - 10^{18} \text{ cm}^{-3}$ . This silicon is typically used for electronic devices and the waste recycled for solar devices, resulting in far larger defect concentrations. Use of light beam induced current techniques to determine internal spectral response has shown that light generated current is reduced for dislocation densities above  $10^5 \text{ cm}^{-3}$  [132]. This examination of material defect requirements has led to the use of recycled silicon from the consumer electronics industry, leading to a reduction of costs. Under the constraint of low production costs it is difficult to retain the quality of the crystal structure - the lattice defects depend on many factors but the most important source of efficiency reduction due to defects is the loss of charge carriers by recombination. Recombination is due to two mechanisms: band-band recombination and crystal defect recombination, with the shortest lifetime usually dominating the total recombination. The basic principles of recombination will be discussed further in the

following chapter. The upper limit for the total electron hole pair lifetime in a crystal is mainly determined by the direct band-band recombination. Radiative recombination or the excitation of a second free electron or hole (Auger recombination) releases the energy by photonic or phononic emission respectively. Hangleiter and Hacker [133] have shown Auger recombination is enhanced with an increase in the density of holes in the vicinity of electrons, and is strongly affected by the crystalline structure of the material and the degree of doping [132].

The reduction in historical costs of these devices is mostly attributed to economies of scale. The efficiency of these panels is also far from ideal, between 10 and 20%. Because of the limited range of the silicon panels (with bandgaps of approximately 1.12 eV), light of higher energy is effectively wasted, and this waste is turned into heat in the device. Heat build-up in silicon based systems is a major problem, as an increase in temperature of the cell results in further reducing their efficiency[132].

The current cost of silicon crystal substrate based solar cells of \$4/W is still too high for a global rollout, as the DOE has benchmarked a target of \$0.33/W [132]. Research into low-cost amorphous silicon has opened up a completely new research field during the last decade and will be further discussed in the Appendix F.

## **Appendix F - Type II Solar Cells**

Over the last decade, there has been considerable effort in advancing thin film, “second-generation” technologies that can be manufactured at significantly reduced cost. The cost savings come from fabrication using techniques such as sputtering, physical vapor deposition, and plasma-enhanced chemical vapor deposition. Steady progress has been made in laboratory efficiencies, as can be seen in Figure 3 for devices based on CdS/CdTe, Cu(In,Ga)Se<sub>2</sub> (CIGS), and multijunction a-Si/a-SiGe [9].

### **F.1 CIGS and CdS/CdTe Cells**

Efficiencies for these devices range between 16-18%. Polycrystalline devices of CdTe and CIGS mated with wide bandgap materials such as CdS can be formed using various deposition techniques [132]. Among this group of photovoltaic technologies, thin-film cadmium telluride (CdTe) photovoltaics emit the least amount of harmful air emissions as they requires the least amount of energy during module production. The emissions from different PV technologies are very small in comparison to the emissions from conventional energy technologies that PV could displace [134]. The economics of production are sensitive to the manufacturing techniques used. Costs can be reduced by manufacturing these devices using cheap substrate options, but care must be taken as the deposition of semiconductors on foreign substrates usually results in films with properties which can differ substantially from their single crystal behavior due to large numbers of grain boundaries and other lattice effects.

## **F.2 Multijunction a-Si/a-SiGe Cells**

Multijunction cells based on a-Si/a-SiGe have been the most successful second-generation technology to date due to their relatively low fabrication costs. Several companies are manufacturing a-Si/a-SiGe modules using roll-to-roll processing on flexible stainless steel and other substrates that allow high-speed production as well as easy integration into roofing materials. [9].

## **Appendix G - Type III Solar Cells**

A third generation of solar cell design types began *circa* 2000, wherein the focus of research was split into two categories, based on the economics of materials and production methods.

Type IIIa solar cells are characterized by ultra-high efficiency designs that incorporate stringent material purities and crystal-matched lattice inorganic devices. These type IIIa cells include two junction and three junction monolithic cells.

### **G.1 Type IIIa Solar Cells**

In standard p-n junction devices the incident light energy is underutilized. Improvement of the efficiency of a solar cell can be achieved by using materials with different bandgap energies which match the solar spectrum better. This concept is realized in hetero junction devices where typically the material with the larger bandgap is on the top. Photons with energy less than bandgap energy pass through the top semiconductor and are absorbed by smaller bandgap semiconductors below. However, an inherent problem is that both the crystals have structural changes across the junction with interfaces formed between the semiconducting layers. Interfaces can be efficient recombination centers where trap levels are formed. The changing band structure can also result in band spikes where minority carriers (holes or electrons) are repelled and accumulate at the interface, resulting in additional recombination. Care must be taken to avoid hetero junctions with high crystal lattice mismatch. Monolithic tandem solar cells made from InGaP/GaAs have achieved efficiencies more than 30% as reported by Friedman et al. in 1994 [132].

These novel approaches to solar power conversion have a very high cost in order to achieve the levels of precision needed for optimum device operation. It is only through high purity materials and precisely ordered device design that concepts such as hot carriers, multiple

electron–hole pair creation, and thermophotonic operation are allowed. These new techniques have theoretical maximum efficiencies well in excess of the 31% target for single p-n junction devices due to their enhanced carrier generation mechanisms. Examples of the mechanisms for these devices have been demonstrated in fundamental experimental setups, but practical working devices have yet to be achieved. These devices owe their increase in efficiency to optical congruency and accurate matching of the incoming photonic radiation. Devices can be combined with optical coatings that manipulate light [135], in some cases dividing high energy and low energy photons using mirrors to redirect the incoming solar energy. These devices push the limits of precise device manufacturing, and will be limited to lab scale devices and space based application for the near future. Lab scale state of the art solar cells have most recently been able to harvest 42.8% of the incoming energy from the sun as demonstrated by the Barnett group at the University of Delaware [135]. Apart from the apparent unapproachable costs of purification of these precise crystals as well as the costs associated with doping with exotic rare earths, and device manufacturing, these devices suffer from three other well defined environmental problems; (i) oxidative breakdown in the presence of air, (ii) degeneration of the devices in the presence of water vapor, and (iii) toxicity of the materials in use when not properly disposed. The oxidative and water vapour breakdown of these devices occurs due to oxygen and water permeability through the sealing in these devices. These chemicals permeate the cell and react with the metals inside, creating oxides that destroy the device structures.

## **G.2 Type IIIb Solar Cells**

Type IIIb solar cells are characterized by moderate device efficiency (15-20%) but at very low costs. To achieve this will require inexpensive materials for the active components as

well as the packaging, low-temperature atmospheric processing, and high fabrication throughput [9]. Type IIIb solar cells can be loosely divided into two groups; (i) Organic thin film, bulk heterojunction and composite cells which rely on solid state buildup of organic layers, or (ii) Redox-coupled dye cells which include a chemical mediator for charge transfer.

### **G.2.1 Organic Thin Film, Bulk Heterojunction, and Composite Cells**

First-generation organic photovoltaic solar cells were single layer organic films between two metal electrodes of different work function. The power conversion efficiency reported was generally poor in the range of  $10^{-3}$  to  $10^{-2}\%$ . Orders of magnitude improvement to 2.7% was achieved by changing one of the metal layers to metal oxide enhancing the Schottky barrier effect (MIS)[136]. The open circuit voltage in organic photovoltaic devices is strongly dependent on the electronic features of the active layer and on interface phenomena [137].

Bilayer heterojunction devices achieved 1% power conversion efficiency was achieved using phthalocyanine and perylene derivatives between a transparent conducting oxide and metal electrode [138]. Tang was first to make an organic thin film photovoltaic device structured as positive electrode/donor/acceptor/negative electrode [138]. The development of three layered structures followed. Highly increased photoconductivities were eventually achieved with addition of  $C_{60}$  structures into the blend. This addition led to the development of polymer fullerene bilayer heterojunction and bulk heterojunction devices [136]. Bulk heterojunction cells are organic–organic composites in which donor and acceptor species are intimately mixed. Among the most successful bulk heterojunction devices to date are those with conjugated polymers such as poly(3-hexylthiophene) as the donor and a fullerene derivative as the acceptor [9]. These devices are further described by Janssen et al. [139].

Bulk heterojunctions can have a wide variety of opto-electronic properties, and can be simply

controlled by the formation of a variety of crystallographic morphologies (lamellar, spherical, cylindrical) [140]. With the addition of buckminster fullerene blended with hole conducting materials charge transport does not improve in the dark but leads to a large increase in photo conductivities under illumination as a result of photoinduced charge transfer sometimes termed “photodoping” [136]. Composites have also been made to include inorganic dopants in organic solar devices. Organic–inorganic composites combine a light-absorbing conjugated polymer as the donor and hole transporter with a nanostructured, large-bandgap inorganic semiconductor such as  $\text{TiO}_2$ ,  $\text{ZnO}$ , or  $\text{CdS}$  as the acceptor and electron transporter. These work similarly to the bulk heterojunctions [9]. Composites can also be made with blended nanoparticle inclusions. In this case, both components can efficiently absorb light, and the bandgap of the nanocrystals can be tuned by growing them to different sizes [140]. This is a distinct advantage as it allows for complete spectral tuning of the nanoparticle included films. A new composite of near-IR bandgap with an environmentally friendly, well established photovoltaic energy conversion material has recently been discussed, using copper indium disulfide (CIS) nanocrystals blended in photovoltaic cells [141]. Currently organic-inorganic composite morphology is determined by that of the nanostructured oxide that is usually grown in a self-organizing manner on the electrode [9]. Recent progress in this area is discussed in the article by Milliron et al. [142], with conversion efficiencies ranging between 1.5 to 4% achieved for bulk hetero junction polymer fullerene devices, organic molecular devices and organic-inorganic hybrid devices [136]. Four consecutive steps convert light into electric current in organic photovoltaics. Absorption of a photon forms the excited state, an electron-hole pair [136]. In order for free carriers to be generated, the electron-hole pair must be dissociated. This can happen in the presence of high

electric fields, at interfaces between two materials that have a mismatch in their energetic levels (band offset), or at defect sites in the material. In the case of dissociation at the interface between two materials, an exciton created in either material can diffuse to the interface, leading to either electron transfer from the donor material to the acceptor material or hole transfer from the acceptor to the donor [9]. The separated charge is transported to the anode and cathode to supply DC load. The current generated corresponds to the fraction of photons absorbed, the fraction of electron hole pairs dissociated, and finally the fraction of separated charges that reached the electrode [136]. The exciton can only diffuse through the material across a few tens of nanometers before it disassociates or recombines in 3 main processes; recombination to produce a photon, recombination to phonon generation, or the production of a free electron and hole pair. Charge dissociation typically occurs at interfaces, although some debate remains as to whether it predominantly happens later at the electrode/polymer interface (rectifying behavior) or at the polymer solution interface [143]. Thin-film devices are mostly field drift dominated [136] and this mechanism of charge transfer will be further discussed in Appendix H-7. External Quantum efficiency values exceeding 70% over a large spectral range indicate that transport limitations have been overcome in these devices [144].

As a result of the excitonic nature of the photoexcitations in organic semiconductors, the operational mechanisms of organic photovoltaics are different from those of conventional photovoltaics, as discussed above. These differences are further described in detail by Gregg et al. [145]. Charge transport in organic semiconductors is determined by the intermolecular overlap of the frontier (outer shell) orbitals of adjacent molecules [9]. This coupling is very weak compared with the interatomic coupling of conventional inorganic semiconductors.

Furthermore, the arrangement of molecules in organic semiconductors is disordered and more resembles an amorphous material than a crystalline lattice. As a result, the conventional band transport description of charge transport cannot be used for organic semiconductors and instead charge transport is based on carrier hopping between crystalline centres in the material. Charge hopping is a temperature activated process that results in an increase in carrier mobility with increasing temperature, in contrast to the decreasing temperature dependence of the carrier mobility in conventional semiconductors [9]. This is a distinct advantage of organic solar power devices, as it allows for the underused IR portion of the spectrum to improve device performance. Most of the organic semiconductors have an optical bandgap around 2 electron volts which is considerably higher than that of silicon and thus limits the harvesting of the solar spectrum to a great extent [136]. It has also been found that carrier mobilities in organic semiconductors follow an exponential dependence on the square root of the electric field [9], and Kline et al. reported that the charge mobility is directly related to the polymer molecular weight [146]. This could be used as an advantage in bias assisted solar devices. Temperature and field dependence for polymer organic semiconductors has been successfully modeled by Bäessler [147] and is further described in Appendix H-7.

Organic photovoltaics have the advantage of facile device preparation using high-throughput, low temperature approaches that employ a variety of well-established printing techniques and roll-to-roll processes. Such low-temperature and therefore low-energy consuming techniques require less capital investment than fabrication techniques for Si-based or other inorganic grown crystal devices [9]. A new approach to device formation has also been shown where a solid-state catalyst free polymerization of highly conductive PEDOT can also be achieved

just by storing a precursor (2,5-dibromo-3,4-ethylenedioxythiophene) for a prolonged time in air or by heating it to a temperature between 60-120<sup>0</sup>C [148]. Such advances in low energy preparation of devices is essential to economic feasibility of solar devices. Further device structures are being researched, with production of polymer nanoparticles by mini-emulsion routes allowing 3-D matrices of cast polymer blends [136]. In addition to roll to roll production, the possibility of using flexible plastic substrates in an easily scalable, high-speed printing process can reduce the balance-of-system costs for organic photovoltaics to make them competitive with high temperature deposition of inorganic thin-film technologies [9]. Ambient temperature processing allows for a large increase in production throughput. Typically, 30cm Si wafer production will average 88,000 m<sup>2</sup> per year for one plant. Using a printing machine for organic device production, this output can be completed in 1-10 hours [144]. From the decrease in material related and production related costs, if efficiencies are comparable or even slightly lower than existing technologies, there may be compelling cost arguments favouring organic photovoltaics.

A key issue faced by the organic electronics community is the stability of the organic materials. It is encouraging that organic light-emitting displays are demonstrating acceptable lifetimes under high injection currents. Device degradation pathways stem largely from changes in morphology, loss of interfacial adhesion, and interdiffusion of components, as opposed to strictly chemical decomposition [9]. Loss mechanisms due to enhanced recombination and poor charge carrier transport can also be caused by mixing that is too intimate, resulting in mean free paths that are too small [136]. Diode imperfections and material impurities also account for the loss mechanisms in organic based devices [144].

Care must also be considered as to the degree of oxidation or doping the devices exhibit. While in the oxidized state, the electronic conductivity of the polymer is highest, but exciton generation and transmission is greatly hindered. Optimized photoelectrochemical efficiency is obtained when excitons can be generated (high resistance) and transported, but efficient electron transfer to an electrolyte depends on maintaining a low electrical resistance. It has been shown that optimal PEC performance is obtained when the polymer is predominantly reduced [143]. With this balance the optimization of devices seems to be fairly rudimentary, with trial and error used to determine individual device performance dependence on film thickness, even in simple thin film devices. The current-voltage response for of a FTO/polythiophene/Al device is shown below in Figure 111 for dark conditions and under monochromatic illumination ( $\lambda = 620 \text{ nm}$ ,  $1 \text{ W/m}^2$ ) through the FTO. Photovoltaic device characterization is based on the following parameters: short-circuit current density ( $J_{sc}$ ), open-circuit voltage ( $V_{oc}$ ) and the fill factor (FF). These comparative measures are further described in Chapter 1.

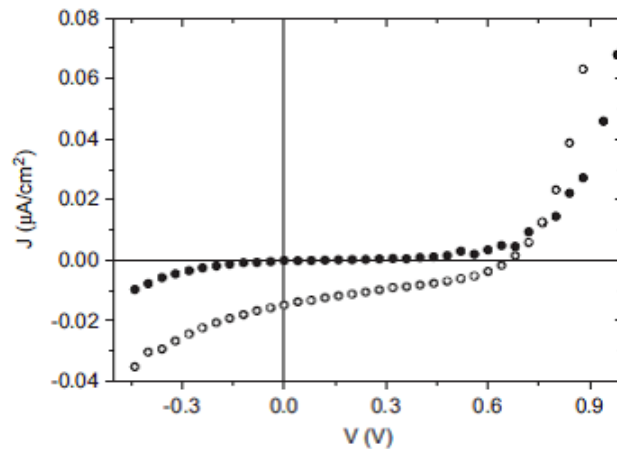


**Figure 111 - Current-voltage response for of a FTO/polythiophene/Al device for dark conditions and under monochromatic illumination ( $\lambda = 620 \text{ nm}$ ,  $1 \text{ W/m}^2$ ) through the FTO. [137] Reprinted with permission from Solar Energy Materials and Solar Cells.**

These thin film devices presented a FF of 35% and a power conversion efficiency ( $\eta_e$ ) of 0.02% with an average  $V_{oc}$  of 700mV [137]. These monolayer organic photovoltaic devices are very efficient with high  $V_{oc}$  values, comparable with the values reached by blends and multilayer devices. More recently open circuit voltages of up to 2 V have been demonstrated by FTO/polythiophene/Al devices. This high-voltage is attributed to a high degree of dipole polarization in the films [73]. More work on device structure must be done however, as the power efficiency is very low, resulting from the planar device design. Devices in which small molecule organic semiconductors are deposited sequentially form stacked multilayer devices. Recent research has approached the reduction of the series resistance of the layers, and has led to increased efficiencies. This technology has the added benefit of increased spectral absorption as well, which trade off current for voltage and possess higher theoretical efficiencies. These devices are further discussed by Forrest [149].

As mentioned above, care must also be taken in energy level matching of junctions. A water-soluble single film PEDOT over  $TiO_2$  on ITO was created to form a rectifying heterojunction device, with a gold back contact. The device showed a  $V_{oc}$  of 0.39V,  $I_{sc}$  of  $54.9 \mu A/cm^2$  and a FF of 0.429, with an energy conversion of 0.03% [150]. This device exhibited poor performance likely due to its layered design, as the PEDOT/Au contact is nearly ohmic due to the matching of the HOMO and Au work function levels.

Contact between the layers of heterojunction devices can also be tuned. Colloidal nanorods of CdSe or  $TiO_2$  are utilized with tail-to-tail poly(3-hexylthiophene), and the CdSe based devices showed a conversion efficiency of 1.7%. End-functionalization of the polythiophene can lead to a better dispersion of the CdSe rods and enhanced performance. Solubilizing groups on polythiophene in  $TiO_2$  composite devices also lead to enhanced performance

[151]. Introduction of a hydroxyl moiety onto the sidechain of the conductive polymer results in formation of colloids preventing the aggregation of TiO<sub>2</sub> and also allows for improved device performance by forming strong nanoparticles polymer interface. These devices show approximately 3.4 fold and 2.4 fold higher short-circuit current density and IPCE, respectively [151]. Carboxylic end groups to enhance covalent bonding between polymer-titania have also been shown with an increase in IPCE from 10% to 15% [152].

The acceptor domain size can be tuned to optimize dissociation and electron transport, with colloidal nano crystals of different shapes and sizes used to improve charge transport and thus energy conversion [136]. Long nanorods and branched nano crystals have given the best results [142]. CdTe tetrapods have been synthesized with 200 nm long “arms”, sufficient in length to span the thickness of a blend film and conduct charges to the electrode without a single hopping step [142]. Reducing the number of hopping events improves transport efficiency [142]. Surface roughness in devices plays a large part in their efficiency. The minimum roughness correlates with the minimum photoluminescent efficiency, the maximum charge transfer, and the maximum external quantum efficiency of associated photovoltaic cells. The film roughness creates inhomogeneity in the electric field and can be caused by agglomeration of nanoparticulate inclusion. This aggregation also decreases charge collection through scattering and reduces the interfacial area [142]. More on the critical optimization of the organic–inorganic interface is discussed by Coakley et al. [153].

There have also been developments in dye sensitizing the nanoparticles in composite organic solar cells, which dramatically increase the layer absorption as well as decreasing the photoluminescence, indicating more efficient separation of electrons and holes. For these devices, Wang and Wang show an open circuit voltage of 0.43 V and a short-circuit current

density of  $256.7 \mu\text{A}/\text{cm}^2$  [154] and Gebeyehu reported an open circuit voltage of 0.65V and a short-circuit current density of  $450 \mu\text{A}/\text{cm}^2$  [155]. A further device structure employing dye sensitization is discussed in the following subsection.

### G.2.2 Redox-coupled Dye cells

Organic-inorganic devices have also been prepared using a redox couple to shuttle charge between photoexcited electrodes. Light-driven redox reactions were first studied by Becquerel [156] where solutions containing a metal halide salt were illuminated and produced a current between two platinum electrodes. Vogel expanded upon this study, incorporating dye sensitization of the halide semiconductor [143]. The addition of a dye allows for spread of absorption into the red spectral range (sensitization) [157]. Current research is conducted on dye-sensitized nanostructured oxide devices, colloquially known as “Grätzel Cells”. These cells are named after a chief researcher in this field [120], who developed a scheme for the tandem utilization of semiconducting elements. One such device structure is shown below in Figure 112 [3]:

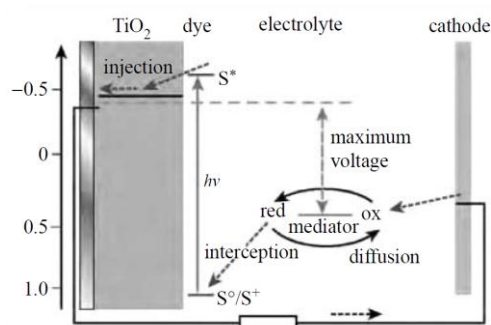


**Figure 112 - Energy level diagram of Grätzel cell. [3] Reprinted with permission from Philosophical Transactions of the Royal Society A.**

These cells use an organic dye to absorb light and rapidly inject electrons into a monolithic nanostructured oxide such as anatase TiO<sub>2</sub>. The hole is scavenged by a redox couple, such as iodide/triiodide, in solution, or by a solid-state organic semiconductor or ionic medium [30].

Introduction of organic hole conductors as a replacement for the liquid electrolyte and by exchange of electron conducting acceptor materials with inorganic nanocrystals means electrochemical and organic photovoltaic research is merging together. [136] The development of these devices are in their infancy, and are reviewed by Wallace et al. [143]. Nanoparticulate mesoporous TiO<sub>2</sub> films provides a surface area for dye chemisorption over a thousand times that of an equivalent flat electrode. This increase in interfacial area, combined with more efficient electron-hole transport, affords an incident photon-to-current conversion efficiency (IPCE) of more than 80%, a 600-fold improvement in photoelectrochemical efficiency compared with a single-crystal electrode [143]. Single walled carbon nanotubes (SWCNT) have been added into the mesoscopic titania in order to improve the charge transfer. No net power conversion improvement was seen, but an increase in IPCE represented an improvement to charge separation. This phenomena was explained by a 30% higher photocurrent (better electron transfer), coupled with a decrease in the open circuit voltage due to the shift in apparent Fermi level of the SWCNT doped to a more positive potential [158]. A thorough review in the fabrication processes and tuneability of titania nanotube arrays has been completed by Mor et al. [159].

The dye morphology can also influence charge separation by controlling the length of the interfacial separation between the charge carriers. This allows the charge recombination mean free path to be tailored allowing for several orders of magnitude decrease in recombination [160]. This allows dye sensitized hole injection into p-type semiconductors to proceed at quantum yields of almost unity. Highly efficient photo cathodic p-type dye sensitized solar cells (DSC's) can be mated with conventional n-type dye sensitized solar cells to form tandem-DSC's. These tandem devices show an efficiency of 2.42% with an

open circuit voltage of 1.08V. Limitations in this device stem from the common absorption spectra of the photo anode and photo cathode [160]. With dye incorporated organic devices, a limitation also exists that the dye must be miscible with the spin coated polymer solvent. For example, phenol blue was limited to 10 w/w% while a tailored dye, PR3072 (1,3bis(dicyanovinyl)-2-(4-dibutylaminobenzylidene)indane), could be absorbed to 50/50 w/w%. More details can be found in [157] regarding the dye structure and solvency limitations.

As mentioned above, polymeric sensitizers have also been investigated as a replacement to the dye structures, as well as advances in titania nanotube arrays in order to improve charge transfer in the devices. These devices reportedly achieved a  $V_{OC}$  ranging from 0.7 to 0.76V with photocurrents up to  $6.5 \text{ mA/cm}^2$ . Maximum IPCEs of 53% and 25% were shown for these polymeric liquid junctioned cells and solid state devices, respectively [161], showing that further increases in IPCE can be made to mirror the performance of dye based devices. To date, solid-state approaches have not been as effective, but progress is being made in understanding the nature of the redox behavior of the organic hole transport. The interface between polymer and semiconductor is less uniform and complete than with a self-assembling dye structure, and this may lead to the decrease in performance. Further discussion on the improvements sought by polymeric hole conductors is reviewed by Grätzel [162].

The overall efficiency of the Grätzel photoelectrochemical cell is still limited by the rate of charge transfer from the photoactivated dye to the redox couple in the electrolyte [143]. This may be increased by increasing redox species concentration, and improving redox species transport through non-static flow regimes in cells.

As a final note regarding new directions in solar cell development, the concept of using transparent, conductive graphene films as window electrodes in solar cells works well, even in a non-optimized state. The advantages of graphene include cheap and abundant carbon resources and simple fabrication procedures. The unique properties of graphene films includes good transparency in both the visible and near-infrared regions, an ultrasmooth surface with tunable wettability, excellent conductivity, high chemical and thermal stabilities, and flexibility for transfer between alternative substrates [163]. This will certainly affect the next generation of solar devices for all approaches.

## **Appendix H - Semiconductor Properties**

### **H.1 Excitation**

When electromagnetic waves interact with a structure (matter) there is a transfer of energy.

One of the first people to describe electronic transfer and the mathematical formalism regarding it was Paul Dirac in his proceedings to the Royal Society of London [164]. The polarization of light impinging on our devices is random and thus an ordered description of polarization of crystal states will not be considered, although this has recently been shown to have possible non-linear harmonic effects on the absorption of the light due to chiral structured dipoles as discussed by Verbeist et al. [115]. These effects will not be considered in the discussion in this dissertation.

Electromagnetic waves interact with molecules or groups of molecules organized in a degree of crystalline state. The result is a conversion of energy with photonic radiation transferred to electrons in the matter, displacing them from their natural ground state. If this energy overcomes the work function of a single molecule, the electron is released and forms a plasma – a conjoined separation of ions and electrons. If this energy overcomes the work function of a crystal, there is a promotion of the electron into a higher energy band of orbitals, and the ion is held in place by other bonds in the crystal structure. These excited electron/matter phases can be described by functions expressing the phononic resonance of electrons moving about the surface of a material or through a plasma. Incoherent states (deviations from a regular crystal structure) and along defects and grain boundaries primarily act as localized energy states for reflection and recombination. These phonons have a waveform and radiative direction, but this theory (plasmonics) is beyond the scope of this thesis, and even the simplified physical description of one phonon assisted photonic

excitation is exceedingly complicated [165]. For further reading, new directions in this field regarding waveguides for confinement and long range propagation of these stimulations have been discussed by Oulton et al. [166].

In terms of the physical promotion of electrons in a material, Albert Einstein won the Nobel prize for the discovery of the quantization of the photoelectric effect. The kinetic energy of a liberated electron is equated:

$$E_k = hf - \phi \quad \text{Eq. 28}$$

where  $h$  is Planck's constant,  $f$  is the frequency of the incident photon, and  $\phi$  is the work function of the material.

The work function of the materials used in this study can be calculated from their absorption spectra, which have been shown above for the materials in our study, and the energies without emission are equated by their absorptive band gap,  $E_{bg}$ :

$$E_{bg} = hc/\lambda \quad \text{Eq. 29}$$

Electronic promotion differs in different bulk material, and if the material is junctioned or under an externally applied field. These variations are described in the following subsections.

## **H.2 Electronic Promotion in a Bulk Material**

In a semiconductor, if the electromagnetic stimulation does not free the electron above other semi-filled orbitals, the electron is said to be promoted to the semi-filled conduction band. If the band gap energy is exactly met a spin-transition-free transmission of the electron takes place. If the energy level is higher than the band gap (but not sufficiently high enough to ionize the surface) then the electron relaxes into the conduction band in a series of phononic emissions of lower energy electromagnetic waves. These wave emissions are described by

Auger. The spatial transition of electrons is aided with phononic movement in an indirect bandgap semiconductor, where the density of state (DOS) diagrams of the associated valence and conduction bands do not lie in the same physical quadrants.

Semiconductors are classified by their inherent propensity to attract and have high mobilities for either holes or electrons. Such designations are tailored in inorganic devices through doping, which will be further discussed in the next subsection. If the material has an excess of electrons, it is known as an n-type semiconductor, and the majority charge carriers in this material are electrons. Conversely, a p-type semiconductor has a deficiency of electrons and holes represent the major charge carriers in these materials. Conductive polymers are generally electron acceptors, and are used as a p-type material. In other words, in an n-type material, the Fermi level is closer to the bottom of the conduction band, whereas in a p-type material, it is closer to the top of the valence band [167].

In organic materials the photogeneration of electrons and holes are generated in a coupled state known as an exciton. These excitons need to be separated through the use of an external electric field or at a material junction to produce a separated electron and hole. Excited electrons, when provided with a circuit by which they can return to their ground state, produce a current which can be described by a generalized Planck Law [168], an integration of Eq. 19:

$$j(\hbar\omega) = \int_{E_{bg}}^{\infty} \frac{\Omega}{4\pi^3 \hbar^3 c^2} \cdot \frac{(\hbar\omega)^2}{\exp\left(\frac{\hbar\omega - \mu_{eh}}{kT}\right) - 1} d(\hbar\omega) \quad \text{Eq. 30}$$

where  $\Omega$  is the solid angle of absorbed solar radiation,  $E_G$  is the bandgap of the material,  $\hbar$  is the reduced Planck constant,  $\omega$  is the angular frequency ( $\omega=2\pi f$ ), and  $\mu_{eh}$  is the chemical potential of the electron-hole pair. The absorptivity is assumed to be 1 for  $\hbar\omega \geq E_G$ .

This expression serves to integrate all photonic energy higher than that of the semiconductor bandgap and equate it to a current density with chemical potential equal to the Fermi energy of the conduction band minus the Fermi level of the valence band.

### H.3 Electronic Promotion in Junctions and Under Bias

The promotion of electrons and holes in a real material is not as simple as the above description, due to junctions of dissimilar materials and applied electric fields. Different junctions and polarizations are surmised below, as explained with respect to the work function of the junctioned material. At each junction there must be an equation of the Fermi level of the materials, and thus band bending occurs to facilitate this equalization.

If an n-type semiconductor is junctioned with a metal which has a work function less than that of the semiconductor (ie.  $\phi_M < \phi_S$ ) an ohmic contact is formed. In an ohmic contact the valence and conduction bands are bent and polarization occurs as shown in the following diagram [169]:

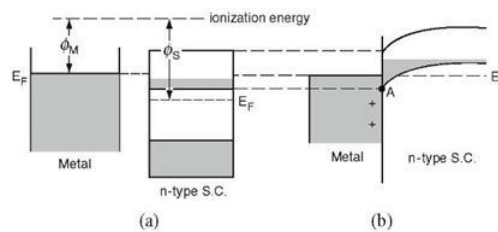


**Figure 113 - Energy diagram for an n-type semiconductor-metal ohmic junction a) before and b) after contact. [169] Reprinted with permission from Springer.**

A different situation exists when a metal of high work function is used. If a n-type semiconductor is junctioned with a metal which has a work function greater than that of the semiconductor (ie.  $\phi_M > \phi_S$ ) a rectifying contact is formed [169]:

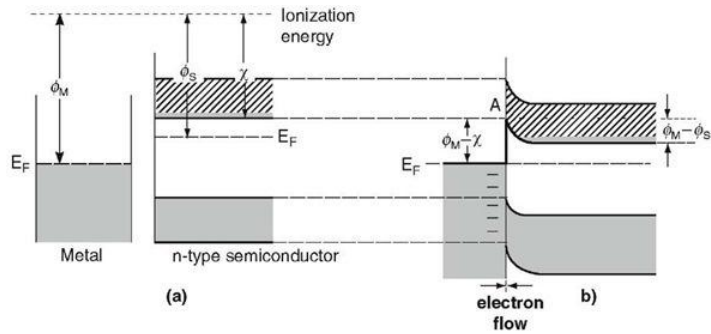


**Figure 114 - Energy diagram for an n-type semiconductor-metal rectifying junction a) before and b) after contact. [169] Reprinted with permission from Springer.**

When this junction is subject to an externally applied electric field, the following band diagram occurs under a) reverse bias and b) forward bias [169]:

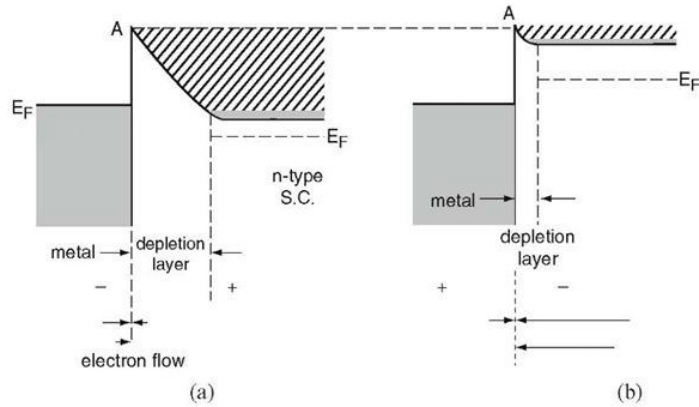


**Figure 115 - Energy diagram for band bending of an n-type semiconductor-metal rectifying junction under a) reverse bias and b) forward bias. [169] Reprinted with permission from Springer.**

For a p-type semiconductor, the converse band bending applies, and for an ohmic junction,  $\phi_M < \phi_S$  [169]:

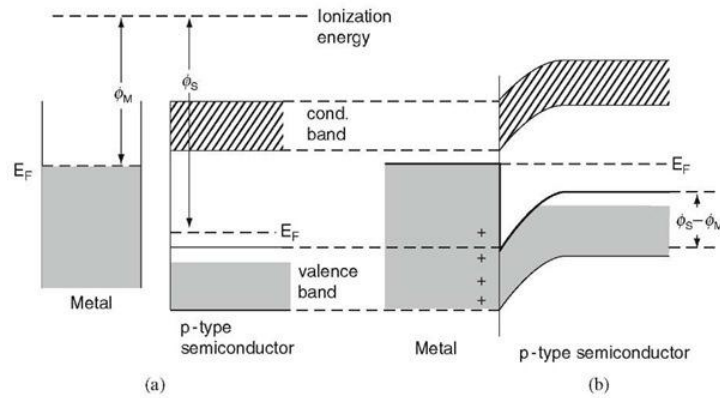


**Figure 116 - Energy diagram for a p-type semiconductor-metal rectifying junction a) before and b) after contact. [169] Reprinted with permission from Springer.**

Once again, a rectifying junction is made when the metal has a work function greater than that of the p-type semiconductor ( $\phi_M > \phi_S$ ), and under a) no bias, b) reverse bias and c) forward bias, the band profile is:

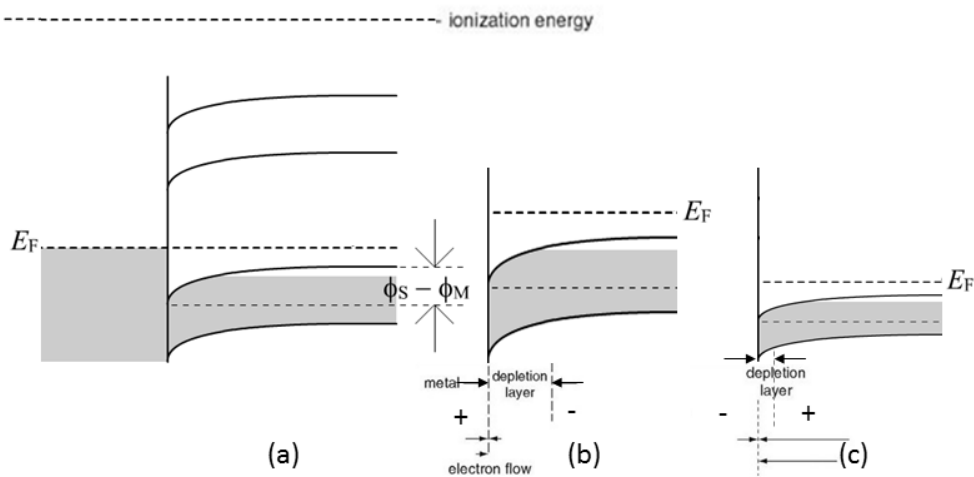


**Figure 117 - Energy diagram for band bending of an p-type semiconductor-metal rectifying junction under a) no bias, b) reverse bias and c) forward bias. [169] Reprinted with permission from Springer.**

When an external load is connected (such as in the short-circuit condition), band bending is not changed by illumination, and this was demonstrated for monolithic  $\text{TiO}_2$  by K. Raja et al. [170].

When the junction between two semiconductors occurs, the connection is known as a diode. The unbiased, forward, and reverse bias band profiles are shown below in Figure 118. The equilibrium state and bias of a p-n junction can control the direction of flow in a material.

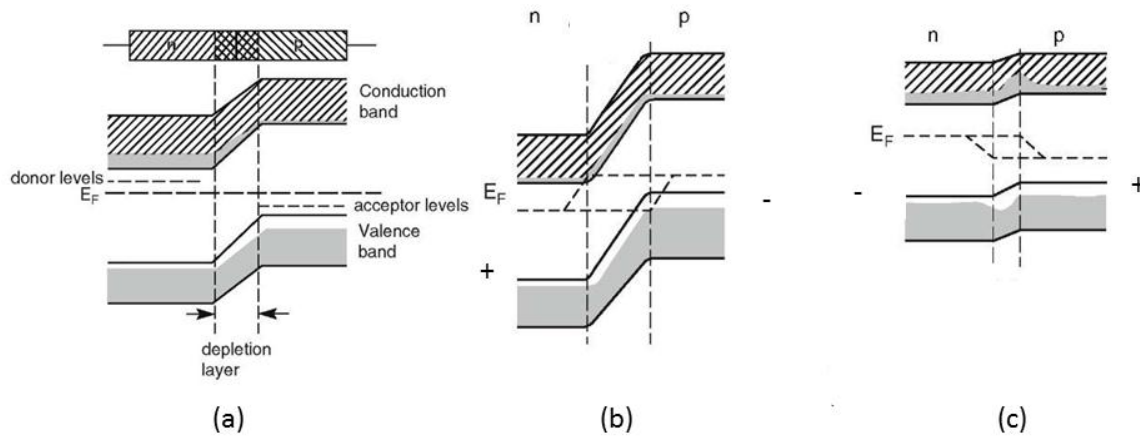


**Figure 118 - Energy diagram for a diode for a) unbiased, b) reverse bias, and c) forward bias operation. [169] Reprinted with permission from Springer.**

Diodes can be used to control the flow of current in a material. A special situation occurs when the band energies of the diode line up in such a way that there is a filling of the conduction band of one of the semiconductor by a spillover of charge from the valence band of the other semiconductor. This is known as a zener diode, and the band energy diagrams under potential are shown in the following diagram:

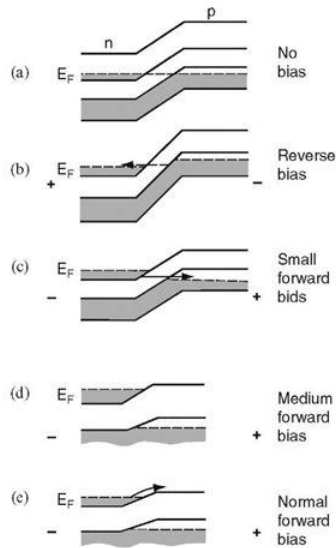


**Figure 119 - Band energy diagram for a Zener diode under a) no bias, b) reverse bias, c) small forward bias, d) medium forward bias, and e) normal forward bias. [169] Reprinted with permission from Springer.**

This property was first described by Esaki in thin films of p-n junctioned germanium, which exhibited more conduction in the reverse direction than the forward direction [171]. The device relies on a generation of a very strong electric field at the junction of the materials, and the electrons were said to be carried by the internal field emission; the tunneling driven by the p-n junction.

#### **H.4 Valence and Conduction Band Theory**

The valence and conduction band of the semiconductors are determined by the relative density of electronic states in these materials. There can be modification of the position of the bands through the use of doping, or deposition of other states within the material.

Organic photovoltaics and organic light harvesting devices are low bandgap polymers meaning they have the ability to harvest a larger portion of the solar spectrum. Organics semiconductors are classified into several subgroups depending on the core chain monomer that carries the delocalized  $\pi$  orbital. Each class has benefits and drawbacks. The fabrication

roots of these polymers also change the electronic properties as well, as the bonding and groups of specific side-chains alter their performance. They can significantly affect the performance, as partially described in defining their absorptive functionality, and while this may seem like a drawback, it allows us to further tailor the properties of these materials. Luminescence of these films can also have multiple bands and can lead to a higher generation of electrons. This effect will not be considered for the study but remains an important characteristic for further investigation.

For PBT-TiO<sub>2</sub> bilayer devices, Kajihara et al. have reported the following energy diagram [72]:

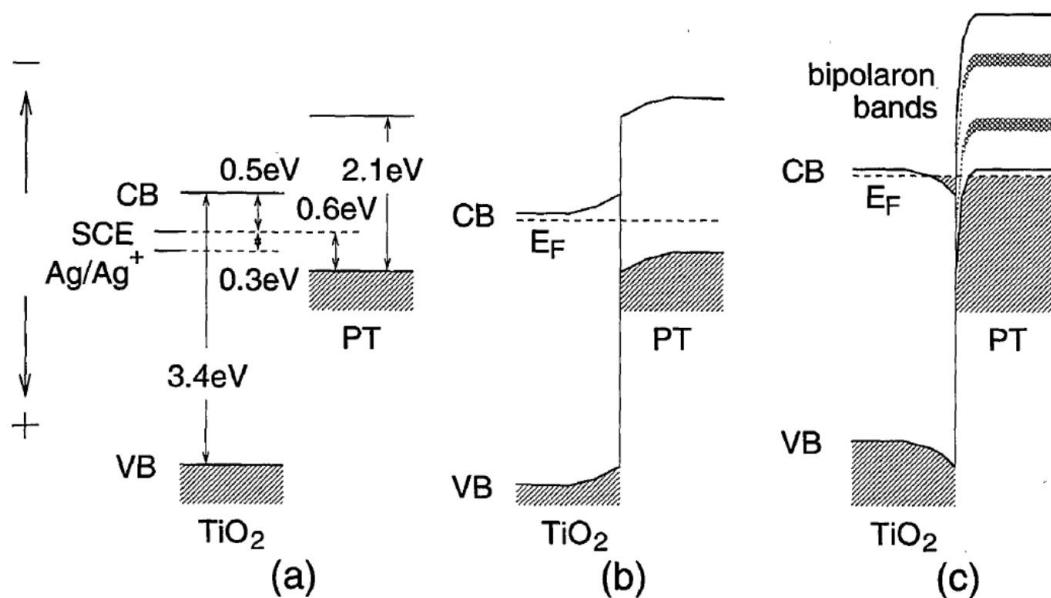


**Figure 120 - Band energy diagrams of TiO<sub>2</sub>/PT junction a) before forming junction, and when the Fermi levels lie b) above and c) below the valence band of the PT layer. [72] Reprinted with permission from the Japanese Journal of Applied Physics.**

The energetics of other polythiophene moieties coupled to TiO<sub>2</sub> are given by Otsuka et al. [80]:

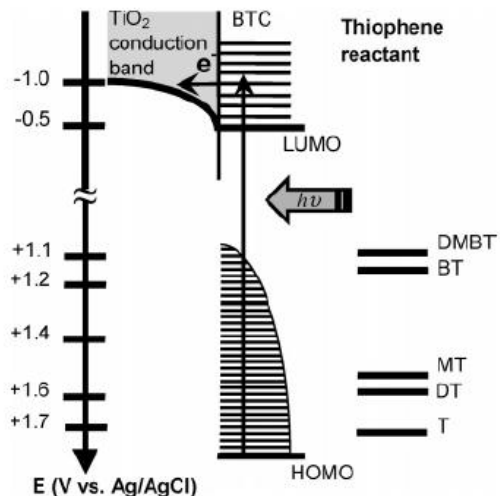
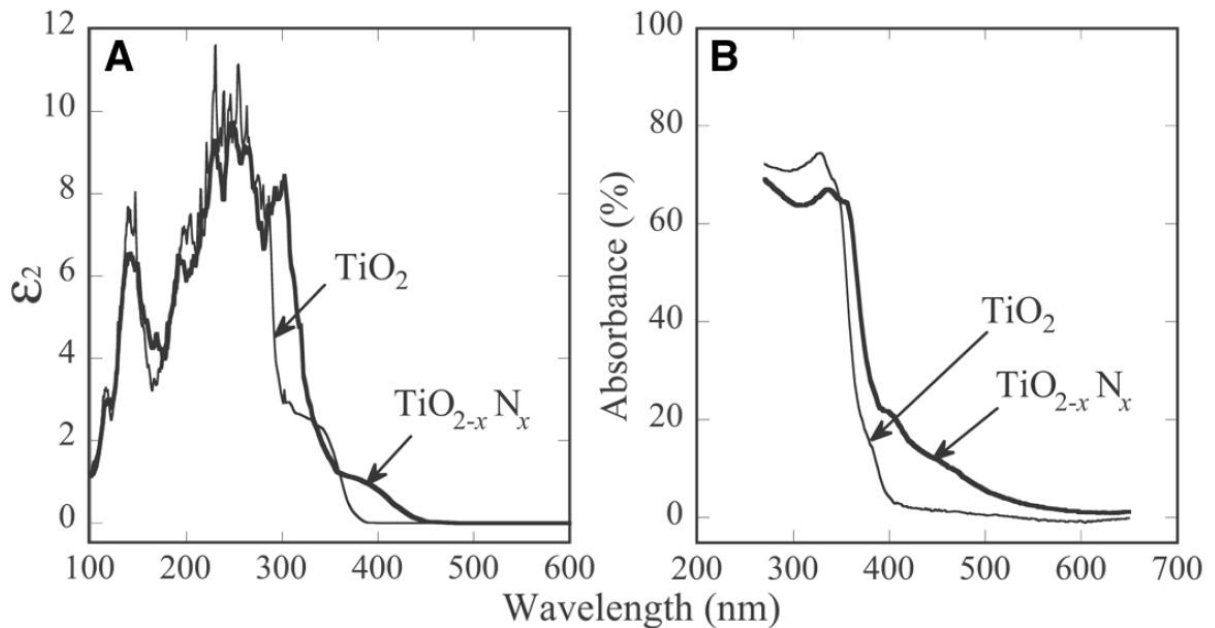


Figure 121 - Band energy diagram for different moieties of polythiophene [80] Reprinted with permission from the Journal of Physical Chemistry C.

## H.5 Doping and Solid Solutions

Modification and tuning of the bandgap can serve to enhance or reduce the energy taken to promote electrons to a conducting state. Modification of the conduction band is accomplished by modifying the more electron rich material in the solid solution (cationic replacement). The converse can be said regarding the doping of valence bands through replacement of the dominant valence band in the DOS diagram with that of a higher or lower energy variant. As an example, titania films doped with nitrogen to enrich the valence band shows increased visible light absorption as shown by Asahi et al. (expressed both A: theoretically, and B: experimentally) [172]:



**Figure 122 - a) Theoretical and b) experimental validation of nitrogen doping shift in absorption spectra for  $\text{TiO}_2$  [172] Reprinted with permission from Science.**

The nitrogen doping by another author was found to be effective in reducing the threshold photon energy for photochemistry from 3.0 eV to 2.4 eV, which is a shift of 0.6 eV into the visible spectral region [173]. Gombac et al. found similar results for B doping of  $\text{TiO}_2$  [174], and a DFT explanation by Graciani et al. can be consulted for further information [175].

Electronic states are also in part controlled by the domain sizes of the material. As discussed previously, crystalline electromagnetic wave progression depends on the regular propagation of the energized states. If there is a multitude of grain boundaries to pass through, there will be an increase in the scattering within the material. This property can also be a disadvantage, especially when dealing with excitonic based devices as defect sites can increase the recombination of separated charges [176].

If the domain sizes in a bulk material are much smaller than the frequency of light absorbed, the material will be regarded as being an irregular lattice and can be treated as a

metamaterial. This is because included interfaces will form space charge layers adjacent to the grain boundaries, and the space charges at interfaces will form accumulation or depletion situations as discussed above. If the spacing of the interfaces is less than the effective width of the space charge layers, these layers overlap and the sample is charged throughout [177]. With nanoincluded composites, the inclusions can serve to shift the Fermi energy level of the material. Such a shift has been described by Kamat in recent reviews of nanostructured architectures for solar energy conversion [178],[179]. In a mixture of  $\text{TiO}_2$  and Au nanoparticles, when the semiconductor and metal nanoparticles are in contact, the photogenerated electrons are distributed between  $\text{TiO}_2$  and Au nanoparticles (Fermi level of Au = +0.45V versus NHE). Upon photonic stimulation, the transfer of electrons from the excited  $\text{TiO}_2$  into Au continues until the two systems attain equilibration with electron accumulation increasing the Fermi level of Au to a more negative potential. The negative shift in the Fermi level is an indication of better charge separation and more reductive power for the composite system. The shift in the Fermi level of the composite as a result of charge equilibration between semiconductor and metal nanoparticles is illustrated below in Figure 123 [178]:

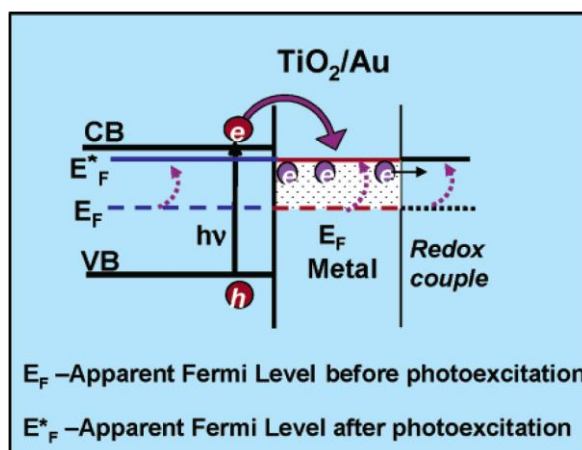


**Figure 123 - Shift in Fermi level of composite semiconductor system with metal nanoparticle inclusion.**

[178] Reprinted with permission from the Journal of Physical Chemistry C.

In terms of organic semiconductors, different pi-conjugated organics groups (PPy, PT, PANi) give rise to different electronic states. These states can further be tailored by changing the size of domain and the geometry of these electronic organics. A brief review of PPy and PANi composites was compiled by Gangopadhyay et al. [180]. The side-chains of polythiophene can also influence the photocatalytic activity significantly in an order from high to low as poly3-methylthiophene  $\approx$  polythiophene > polythiophenecarboxylic acid > poly3-hexylthiophene [181]. Cutler et al. [102] found that for polybithiophene, copolymers with different side groups attached to the polybithiophene backbone produced distinct reduction peaks attributed with two distinct regions of the polymers that are observed with one broad oxidation response. The two reduction peaks were associated with expulsion of anions from the two discrete parts of the polymer or the first response may be anion expulsion with the latter cation incorporation to balance negative charge. Similar responses are reported for the copolymer containing cyanostyryl thiophene unit and nitrostyryl thiophene with potentials slightly more positive due to the presence of the electron withdrawing groups on the substituents. The presence of electron donating groups, e.g.

(dimethylaminostyrylthiophene) resulted in polymer oxidation occurring at less positive potentials. Tailoring of this kind is no doubt useful for the matching of spectral intensities in films, and that still contain discrete redox states. Geometrically, the  $S_1-T_n$  energy gap decreases as the dihedral angle between thiophene rings increases, as observed for unsubstituted bithiophene [182]. This shows that aspects of charge transfer can be controlled dependent on spatial organization of components.

Low energy ion implantation is also possible for solid solution surface doping of organic films. Jung [183] found that the composition of the modified layer is dependent on the implanted species: N causes doping, while O has a sputtering effect. The modified layer does not penetrate beyond ~20nm and acts as an electronic and ionic barrier as shown by cyclic voltammetry and electron transfer reactions. This could be an advantage as it can be patterned, and could act as a rectifying layer as explained above. We have not incorporated this technique in our study, as depositions on 3-D surfaces would prevent ion-implantation techniques from being employed on interior surfaces.

## **H.6 Dislocations and Trap Site Effects**

With the inclusion of these additional states in a material, there is formation of dislocations and trap states from the inclusions and is inevitable. In mixed phase P25, several trap states have been found including lattice electron trapping sites, surface electron trapping sites, surface hole trapping sites, and interface trapping sites specific to Degussa P25 [184].

Longer range order in the crystals can serve to enhance charge transport through the crystal, but in the case of a clustered material or one with a large number of irregular substitutions, the band structure is replaced by a discrete density of states [185]. In Figure 124 below, the HOMO-LUMO transition energy is depicted with the presence of trap states [185]. Deep

trap states exist in bulk materials, but in small clusters will diffuse to the surface. If percolation of the deep trap is not allowed, it will facilitate a charge imbalance and thus a change in the DOS [185]. The additional formation of junctions and inclusions are not necessarily bad though, as with catalysis, many of these higher energy states can act as catalytic “hot spots” [186], [187] as seen in P25 and in non-crystalline TiO<sub>2</sub> layers [188]. In terms of semiconductor performance however, these trap sites can provide a location for exciton recombination for organic semiconductors as mentioned previously.

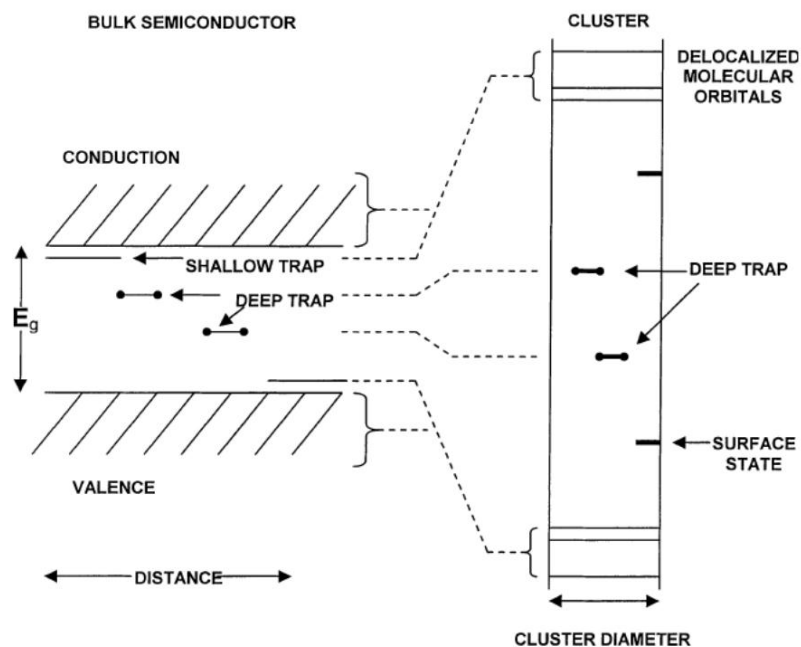


**Figure 124 - Schematic diagram correlating bulk crystal states with cluster states. [185] Reprinted with permission from Critical Reviews in Solid State and Material Sciences.**

There are new directions being pursued in the formation of trap based impurity photovoltaics which operate as lower bandgap solar cells in tandem with the original material bandgap. Studies have shown that there exists additional advantage to these types of devices, yet they are still in their infancy [189]. An equivalent circuit schematic of an impurity photovoltaic is shown below in Figure 125:

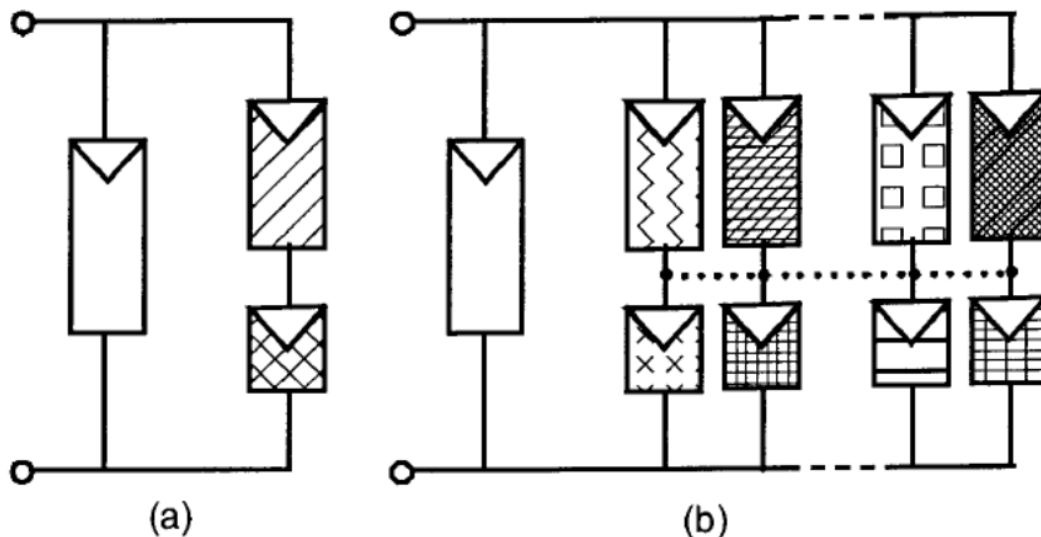


**Figure 125 - Equivalent circuit of an impurity photovoltaic cell with impurities located a) along a single plane, b) distributed through the bulk (dotted line shows the connection required to convert to the 3-band case). [189] Reprinted with permission from Progress in Photovoltaics: Research and Applications.**

Watanabe et al. suggested trapped electrons in the conduction band could decrease the diffusion potential at the TiO<sub>2</sub>/MEH-PPV heterojunction, reducing the exciton dissociation [190]. In bulk titania it was also reported that protonation of the [TiO<sub>6</sub>] octahedra suppresses radiative deactivation of trapped excitons [191]. Kim et al. attributed device performance increase in P3HT-TiO<sub>2</sub> cells to oxygen doping of the polymer [192], however, it may be due to the conversion of [TiO<sub>6</sub>] sites on the surface of the titania component. The authors noted that transient photoconductivity was observed that mirrors the increase and gradual saturation of J<sub>SC</sub>. When first illuminated, excited electrons first fill the shallow electron traps, thus photoconductivity increases with continuous illumination and is saturated when these traps are filled. An increase in the photoconductivity of titania reduces the serial resistance in the reported inverted organic solar cell [192].

## H.7 Junctions - Charge Separation and Mobility

Charge separation occurs due to the intrinsic mobilities of electrons and holes throughout a material. These conjugated sites are mediated by how well the electron-hole pairs can be separated and transferred. In terms of organic type devices, charge mobility occurs by more of a hopping mechanism. Of course with the crystal structure being distributed there are significant losses (in terms of the in phase conductivity of electrons or electronic waves), and the mobilities of organics are lower than their crystalline inorganic devices. Efforts are being made to create more regular polymeric films. Charge transfer in these organic films is also highly dependent on the magnetic dipole set up in the manufacturing of these materials [73]. For this reason electrochemical means of film production is desired as sets up this film in a regular manner as it is grown radially from the substrate. Mobility of charge carriers is also affected by inclusions of electron acceptors into conductive polymers. Saeki et al. found a two order of magnitude increase in polythiophene charge mobility with the addition of tetracyanoethylene [193]. In organic devices exciton diffusion range is quite limited, on the order of ~10 nm and thus a very fine dispersion between two components is required [194]. Burquel et al. go on to provide a very detailed examination of charge separation and transfer in terms of 1<sup>st</sup> principle models, which may be of use for designing pairs of donor-acceptor molecules based on the results of their research. Kahn et al. discussed mechanisms ranging from simple charge exchange, to Fermi level pinning by chemistry-induced states and metal surface modification by adsorbed molecules leading to substantial deviations from the ideal Schottky–Mott performance in OLED devices, which may be applied to junctions in solar cell technology [195]. The non-ideality of these junctions were attributed to the formation of interface dipole barriers, which was less present in random dipole oriented materials such as

PEDOT-PSS blends. In the case of electroformed PBT in our system, we know dipole coupling is strong, and therefore must be considered. A study of the distribution of DOS in rr-P3HT is in agreement with this result, as it was also found that with increased order of the organic semiconductor, the depletion layer is enhanced [196]. Kahn et al have described the dipole energetics of an organic system on a metal, as outlined in the following diagram [195]:

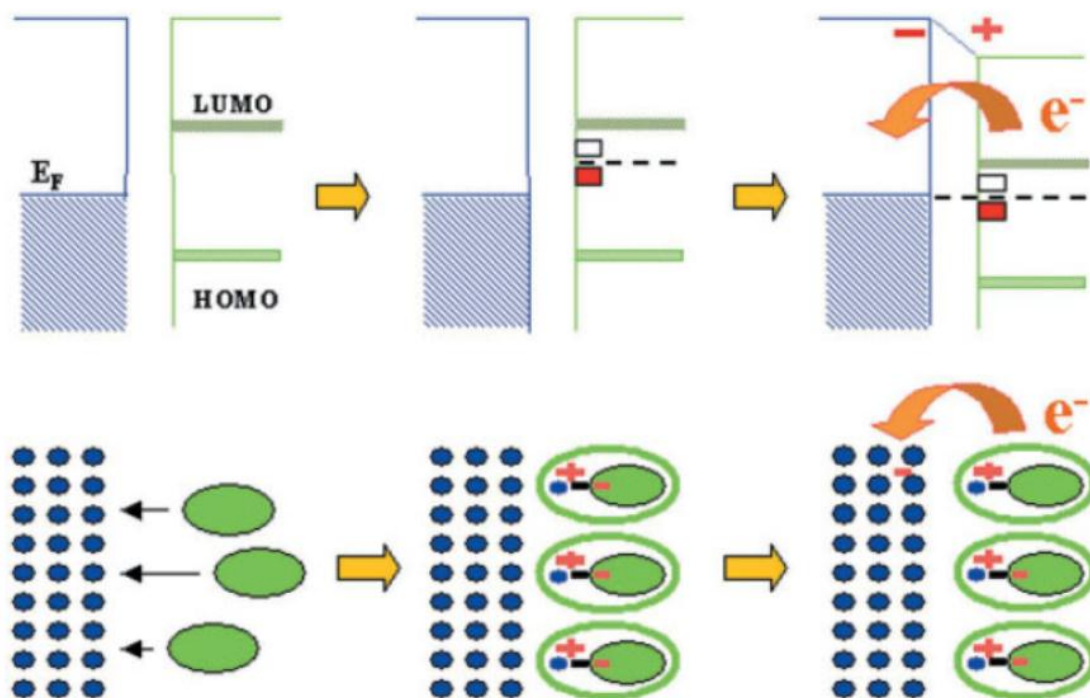


**Figure 126 - Mechanism of the formation of the dipole at the ALq3/Mg interface; separate materials (left), chemical reaction and formation of gap states that pin the Fermi level (middle), and electron transfer from an organometallic complex to the metal to establish thermodynamic equilibrium. [195]**

**Reprinted with permission from Polymer.**

Solid state devices have been formed by TiO<sub>2</sub> nanoparticles in a PEDOT:PSS matrix. The forward current increased nearly two orders of magnitude by doping approximately 1% of TiO<sub>2</sub> nanoparticles in PEDOT:PSS, and increasing the TiO<sub>2</sub> nanoparticles in the PEDOT:PSS matrix to 20%, the forward current was nearly four orders of magnitude higher with respect

to the pristine PEDOT:PSS Schottky diode [197]. The authors also concluded that the space-charge limited conduction (SCLC) is the major conduction mechanism as indicated by a linear relationship in a plot of  $\ln(J)$  versus  $\ln(V)$ . This conduction mechanism will be further discussed in Appendix M.

It has also been shown that for organic devices, performance is limited by exciton diffusion and separation. Improvement in conversion efficiency was shown by shining through the back side of the solar cell to create exciton generation closer to the charge separation interface. Exciton recombination was shown by plotting  $\log I_{sc}$  on  $\log I_i$  and a sublinear performance indicated the presence of surface states that act as recombination centers. Photovoltage dependence was shown to follow the usual semi trend on  $\log I_i$  expected for Schottky junction solar cells [198]. More on this is discussed in the comparative measures section of this dissertation.

For charge transfer in terms of junctioned energetic states, Fermi's golden rule applies; the translation of the EM wave (or transfer of energy levels) is directly proportional to the strength of the interaction between the two states squared. In terms of enhancement of catalytic processes, this will be further discussed in terms of semiconductor-liquid charge transfer in the electrochemical performance section of this document. In solid state, these junctions can be enhanced through the use of tighter binding end groups at differing material junctions. Milliron et al. have reported an electroactive surfactant (pentathiophene phosphonic acid) used to enhance transfer of electrons between CdSe nanoparticles and poly(2-methoxy-5-(2'-ethyl-hexyl-oxy)p-phenylenevinylene) (MEH-PPV) [105]. It is also seen that surfactants using in spin coated composite devices have an effect of reducing the quantum

efficiency of the devices unless the surfactant is removed [199]. This effect is shown below in Figure 127, where the surfactant is removed by heat treatment:

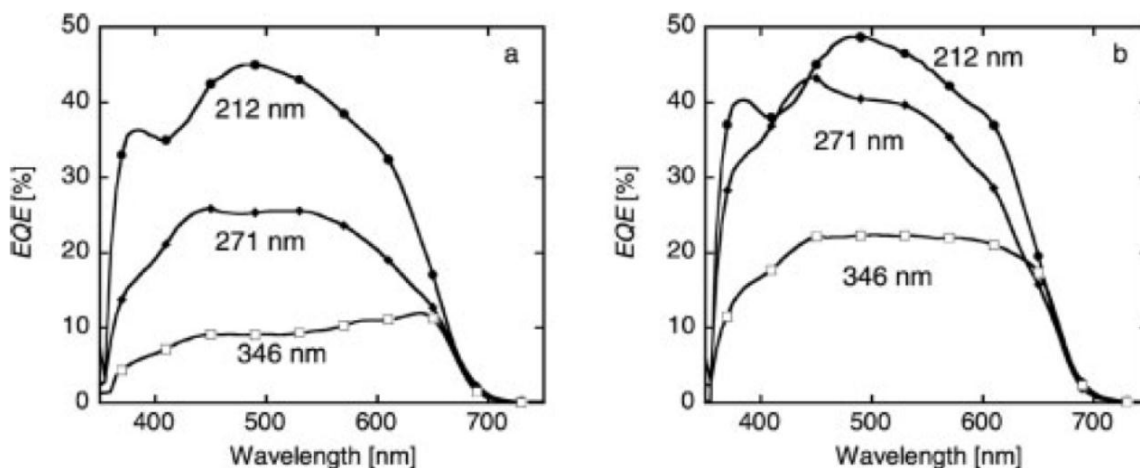


**Figure 127 - The EQE spectra of devices from 90 wt.% 7nm by 60 nm CdSe nanorods in P3HT of various thicknesses a) before and b) after 120<sup>0</sup>C heat treatment. [199] Reprinted with permission from Advanced Functional Materials.**

Particle shapes can have a large impact on device performance by providing for a conduit for current to flow as well as for an increase in charge separation. Leschkies et al. showed that a variation in nanowire length in composite quantum dot solar cells had a direct increase in charge collection efficiency [200]. Photoluminescent quenching was used by Greenham et al. and Ginger to study charge separation in conductive polymer-nanoparticle systems [201], [202]. It was found that the absorption spectra are simply the sum of the constituent parts of the composite films, with no evidence of any additional absorption peaks, yet quantum efficiency increased with nanoparticulate inclusion, as seen in Figure 128 below [201]:

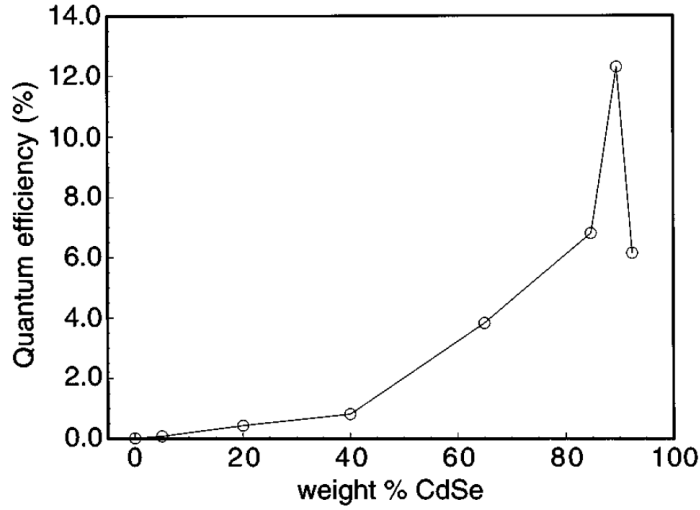


**Figure 128 - Quantum efficiency increase with an increase in nanoparticle inclusion for a CdSe composite solid state solar device. [201] Reprinted with permission from Physical Review B, Condensed Matter.**

3-D deposition of metal nanoparticles in conductive polymer composites has resulted in improved charge shuttling throughout the material [203]. When non-conjugated linkers connect the particles, electron tunneling is the predominant mechanism for electrical conductivity. When end groups link the particles with the conductive polymer matrix, the electrical conductivity ( $\sigma$ ) depends primarily on the charge carrier population ( $n_{pop}$ ), the electronic coupling term ( $\beta$ ) and the activation energy barrier ( $E_A$ ) to electron transfer according to the following formulae:

$$\sigma = \sigma_0 \exp[-\beta \delta_d] \exp\left[-\frac{E_A}{RT}\right] \quad \text{Eq. 31}$$

$$\sigma_0 = n_{pop} e \mu \quad \text{Eq. 32}$$

where  $\delta_d$  is the average inter-particle distance, R is the universal gas constant, T is the temperature, e is the elementary charge, and  $\mu$  is the mobility of the charge carriers. Further details on the difficulties in accurately assessing the mechanisms in charge transfer in these composites is detailed by Sih and Wolf [203].

Charge transfer across junctions are further complicated by absorbed species on the surface of the semiconductors. It was shown that when titania was exposed to O<sub>2</sub>, there was a withdrawal of electrons from a depletion layer at the surface, and when exposed to water the converse occurs [204]. This depletion layer will bend the energy levels at the surface of the semiconductor and will influence electron transfer. This will be discussed further in terms of electronic transfer from a semiconductor to a redox species further in the theory.

## **H.8 Quantum Efficiency and Quantum Effects**

Exciting work has been done in the isolation of materials in quantum domains to form nanodots, whose size in a dielectric tunes the bandgap using quantum confinement [205]. Quantum size effects were first discovered by Frohlich in 1937 in terms of spacing of electron energy levels [185]. Quantum confinement arises as when the particle size decreases to a comparable size to the de Broglie wavelength of the carriers or the excitonic Bohr radius spacial confinement occurs [185], [206]. In terms of the effective mass ( $m^*$ ) of the electronic charge carriers, the critical dimension for size quantization effects to appear occurs for when  $m^*/m_0 \sim 0.05$  ( $m_0$  = free electron mass), with the critical dimension being about 300 Å [207]. The small Bohr radius of TiO<sub>2</sub> ensures that the quantum confinement of P25 does not occur [208], although the large surface area to volume ratio allows for a rapid separation of charge carriers [185]. Examination of alternate structures such as filling zeolite pores with TiO<sub>2</sub> or fabrication of reverse-opal structure from nanospheres have also been examined, but as we are using randomly oriented particles in our study, these effects will not be considered [209], [210]. Photonic crystals have also been prepared with the converse of this concept, forming a TiO<sub>2</sub> opal, with air spheres prepared from titania through the dissolution or combustion of a polystyrene template [211].

Organic molecules have also been tuned in nanodomains, with polythiophene grown in alumina templates forming nanotubes with specific capacitances nearly an order of magnitude large than a flat film [212],[103].

Further advancements in graded nanoparticles have been investigated and they have found to suppress 'blinking' in which photoexcited charged nanoparticles would cease to emit light [213] – the result, if applied to solar cells, could mean 100% efficient quantum efficiency through the suppression of Auger transmission.

All of these developing properties enhance the quantum efficiency of the photoactive material, which is a measure of the % of incoming photons that generate an electron-hole pair. This is not the only metric by which to measure solar cell performance, and can be difficult to measure in a device due to recombinant events.

## **Appendix I - Electrolytic Options Mated with Non-Solar Renewable Energy Sources**

Options regarding hydrogen production have included many schemes. Relatively inexpensive hydrogen from hydropower and nuclear plants could be generated during off-peak hours. Large photovoltaic arrays in North Africa mated with hydrogen generation which could then be shipped or piped to Europe was proposed in 1987 by Justi [214]. Solar photovoltaic hydrogen was evaluated in 1989 by Ogden and Williams and they concluded that hydrogen produced from large PV power plants could be economically produced if the cost of photovoltaics could be brought to \$0.2 to \$0.4/W [214]. Production of hydrogen from hydropower in Canada by a Hydro-Quebec Hydro-Hydrogen Pilot Project considered the economics of producing hydrogen and shipping it to Northern Europe via tankers concluding with favorable economic and societal factors [215]. Obviously the economics of such systems shift from absurd to lucrative depending on many global factors ranging from raw material prices to the political situation. In any regard, a decrease in overall system costs is always favored.

Schug details a 100kW pilot electrolyzer that operates in the lower temperature window, and remarks upon operational problems solved over the 5000h of pilot plant life [216]. With respect to further examination of schemes for electrical control of green electrolysis, Barbir discusses a comparison of schemes for hydrogen generation using on and off grid alternatives [214]. Kato et al. further expand on this subject, with schemes for mating the energy generated from solar sources with electrolysis devices, some of which achieve over 95% power conversion from a solar source to the electrolyzer unit [217].

## Appendix J - PEM Systems Overview

The main manufacturers of PEM electrolyzers systems in the USA include Hamilton Sundstrand and Proton Energy Systems Inc.; in Germany Htec; in Russia include RRC “Kurchatov Institute”, STC “Luch” and SUP “Company MATYS”. The operating pressures operate on average at 28Bar and produce from 26-260 m<sup>3</sup>/h. Research and development of electrolyzers with PEM were provided in Norway under the Norwegian University of Science and Technology, in Spain with David Systems and Technology, and also in Japan under Matsushita Electric Works, Ltd. and Fuji Electric Co., Ltd.. The best reported performance has been achieved within the framework of the Japanese program WE-NET which focused on an electrolyzer with an area of 2500 cm<sup>2</sup>, with an operating voltage of 1.556V at 80 C and a current density of 1A/cm<sup>2</sup>. This unit operated with an efficiency of energy transformation of 95.1% [29].

In our proposed system design, a polymeric ion-permeable electrode has been incorporated to facilitate gas separation to provide for a pure product stream and to ensure no recombination of products. The first group to incorporate a solid polymer membrane for photoelectrochemical water splitting was Uosaki and Kita [218]. Uosaki and Kita found that electrolyte was required in their system but postulated that with an increase in light intensity or a decrease in charge carrier recombination that it may be conceivable to operate without any electrolyte at all.

Proton exchange membranes have been studied extensively for fuel cell research and have been modeled and improved upon through minor changes in their inherent structure. A fairly comprehensive overview of their underlying structure is presented by Dobrovolsky et al.

[219]. Composites have been made from these membranes too, in an effort to improve their mechanical stability and ionic conductivity [220], [221] – especially at higher temperatures. In fact,  $\text{TiO}_2$  has been incorporated into membranes and has been shown to act as a proton conductor [220], and used in composite Nafion- $\text{TiO}_2$  films [222]. In a system incorporating these membrane ionic transport pathways, care must be taken to ensure that triple phase contact, of electronic, ionic and solution(for mass transport) be preserved. Detailed analysis of the mechanism by which the proton conduction is transferred across PEM is discussed by Eikerling et al. [223], and an expression for proton mobility in the membrane is described. A more simplistic overview of the process is described by Pivovar et al. [224], and broken down into two main transport mechanisms; the Grotthuss and vehicle mechanisms. Further analysis is beyond the scope of this dissertation, but a basic understanding of the vehicle and Grotthuss mechanisms by which hydrogen ion movement is shown below:

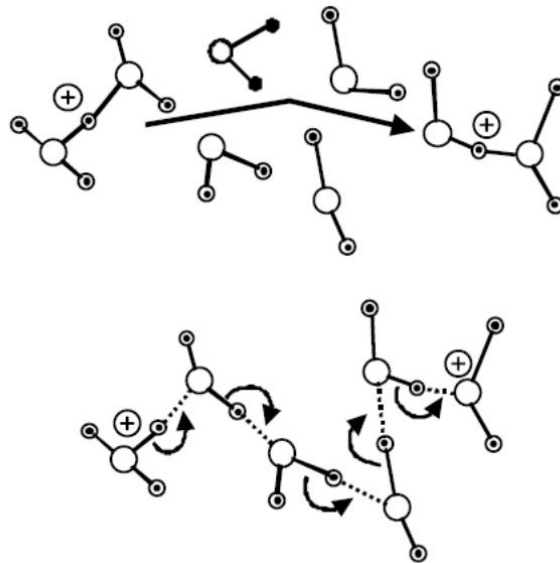


**Figure 129 - Schematic of proton transport mechanisms; the vehicle mechanism (top), the Grotthuss or hopping mechanism (bottom). [224] Reprinted with permission from Polymer.**

The conductivity of Nafion also changes with respect to hydration, and is summarized below [225]:

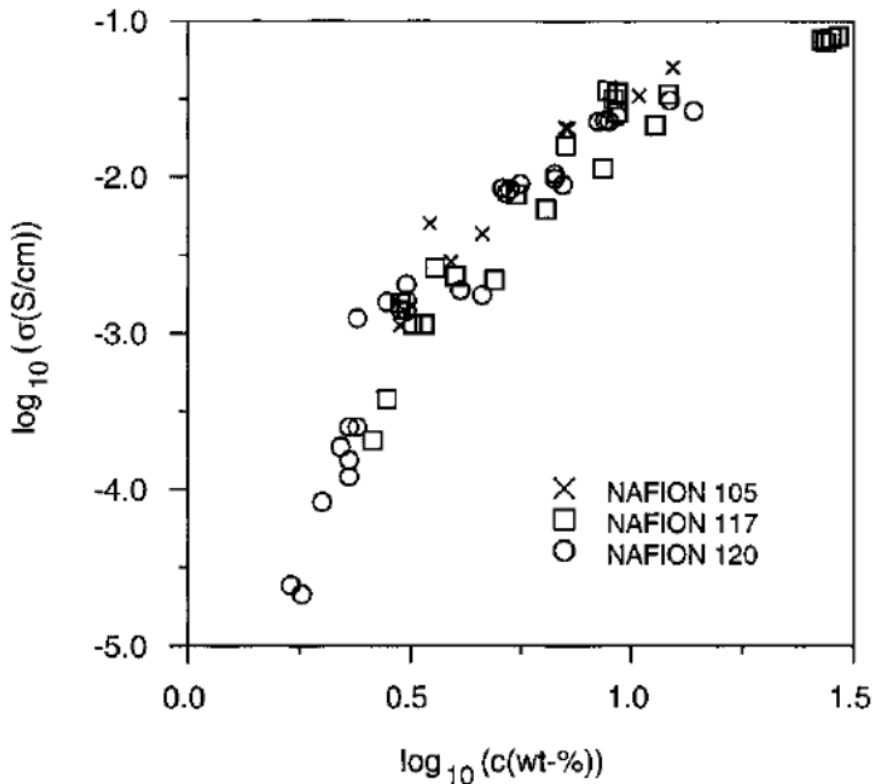


**Figure 130 - Electrical conductivity versus water content for various samples of Nafion. [225] Reprinted with permission from Macromolecules.**

It should also be noted that Nafion membranes have a large performance dependence on the processing and conditioning of the membrane [226]. It is imperative therefore to conduct all testing in a sequentially repeatable manner using pristine samples.

The biggest significance in polymeric electrolytes is that they are very high in sulfonic groups, allowing for efficient ion transport and high membrane proton concentration. The conductivity of a solution depends on hydrogen concentration but also shifts the propensity for an electron to be transferred to or from a semiconductor as discussed previously, allowing for the hydrogen generation reaction to take place. Therefore, there is a careful balance

between ion availability and mass transfer limitations, while not limiting the extension of the triple phase contact through the solution. The ionic conductivity of the membrane also has an integral role in the performance of PEM electrochemical cells. Much research has been done to improve the ionic conductivity of the membrane, and is proportional to the degree of sulfonation of polymeric states for which the Grotthuss mechanism can occur [35]. New polymeric species such as SPEEK have been researched for this purpose, and a correlation of the ionic conductivity and sulfonation are compared with that of the PEM used in our system, N117:

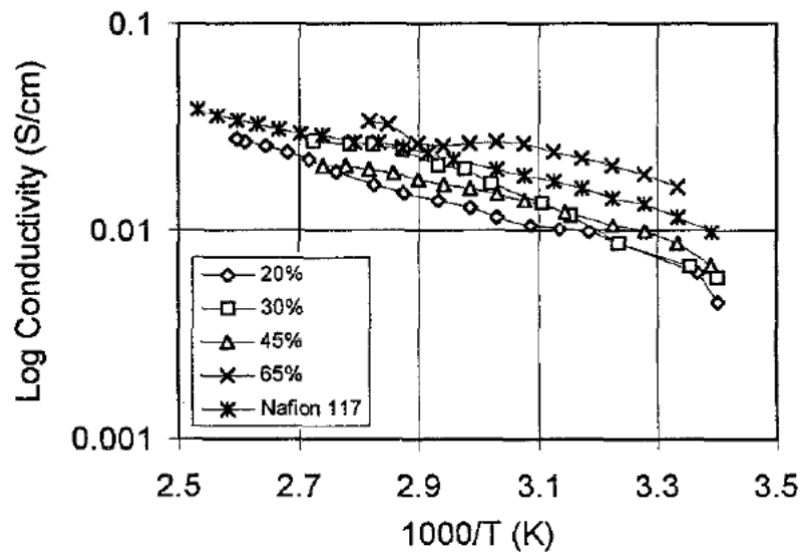


Figure 131 - SPEEK conductivity versus reciprocal temperature as compared to N117. [35] Reprinted with permission from the International Journal of Hydrogen Energy.

Contaminants or buffer solutions also play a role in electrochemical performance. While an improvement in solution conductivity can be expected with addition of a supporting electrolyte in a photoelectrochemical system, there can be a severe effect on the membrane conductivity as ions become preferentially locked into sulfonic sites. Kelly et al. reported the following ionic inclusion and membrane deactivation [227]:

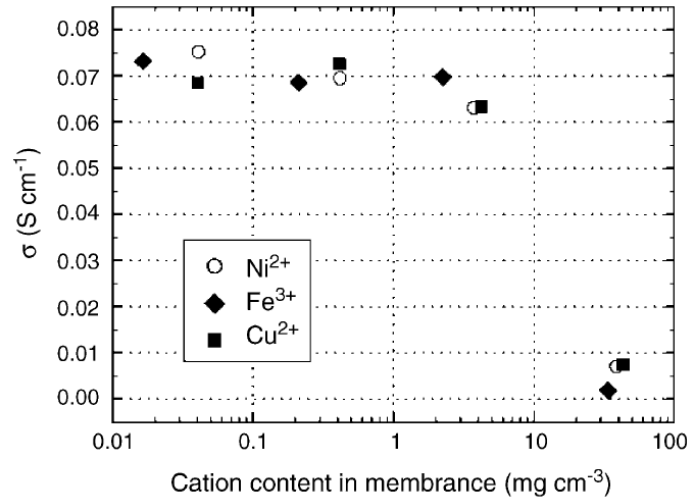


Figure 132 - Poisoning of Nafion membrane by increased concentration of contaminant ions. [227]

Reprinted with permission from the Journal of Power Sources.

## Appendix K - Electrochemical Basis for Electron Transfer and Equilibrium

Electronic promotion can be measured for a chemical reaction relating the electronic scale to the thermodynamics of the reaction. The redox scale has been developed for this matter.

The redox scale was defined to form a library of chemical reactions and their propensity to act as a reducing agent as compared to the energy needed to reduce hydrogen ions to H<sub>2</sub> (on a highly catalytic platinum surface) at a standard activity of 1. This potential is referred to as the normal hydrogen electrode (NHE).

On an absolute energy scale, the energy of a redox couple is given by:

$$E_{F,Redox} = \bar{\mu}_{e,Redox} \quad \text{Eq. 33}$$

$$E_{F,Redox} = E_{ref} - eU_{Redox} \quad \text{Eq. 34}$$

where  $U_{redox}$  is the redox potential vs NHE and  $E_{ref}$  is the energy of the reference electrode versus the vacuum level. The determination of  $E_{ref}$  has been subject of various calculations, with the value reported between 4.3 to 4.7 eV. An average value of  $E_{ref} = 4.5$  eV for NHE is usually used [228].

The standard reduction potentials of interest for components of our system are listed in Table 6 [229].

Reaction	E <sup>0</sup> / V vs. NHE
$O_2 + 4H^+ + 4e^- \leftrightarrow 2H_2O$	1.229
$2H^+ + 2e^- \leftrightarrow H_2$	0.000
$SnO_2 + 4H^+ + 2e^- \leftrightarrow Sn^{2+} + 2H_2O$	-0.094
$TiO_2 + 4H^+ + 2e^- \leftrightarrow Ti^{2+} + 2H_2O$	-0.502
$Sn^{2+} + 2e^- \leftrightarrow Sn$	-1.375
$Ti^{2+} + 2e^- \leftrightarrow Ti$	-1.630

**Table 6 - Standard reduction potentials. [225]**

For semiconducting compounds, additional considerations must be considered [230]. For electron transfer in solution, generally the point of zero charge (pzc) is what matters most, as it determines if the electron will be transferred to or from the material in question to the electrolyte. For P25 the pzc is at pH=6.3, as illustrated through various methods by Preo and Kallay [231], while an empirical expression for determining the zeta potential of P25 in solvents (through variation in  $\epsilon$ ) can be found by Yu et al. [232]. This transfer can be tailored by changing the pH of the solution; in essence changing the hydrogen ion density and free electron density in the solution. The position of the energy bands are imperative to the performance of the semiconductor system if the electrode is to operate as a hydrogen generation photocatalyst.

The variation in the conduction band edge is presented by Bak et al. [233]:

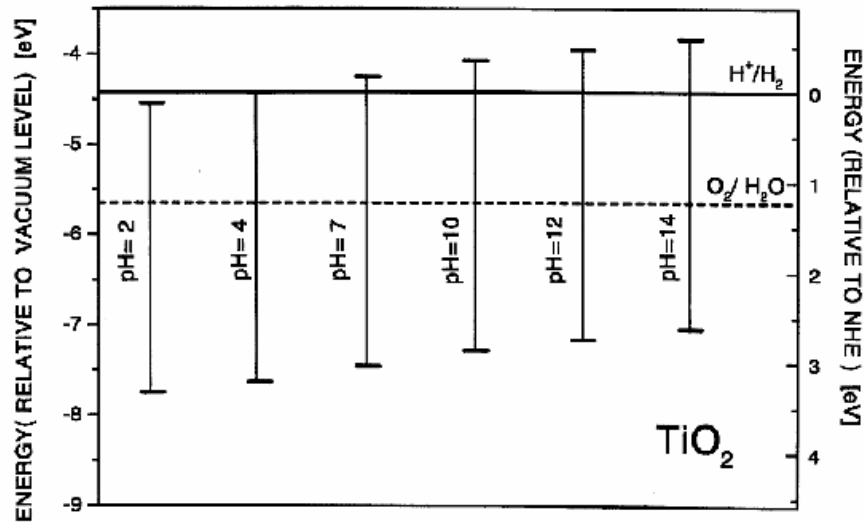


Figure 133 - Variation in titania conduction band edge with a variation in pH. [233] Reprinted with permission from the International Journal of Hydrogen Energy.

It can be seen that with photonic stimulation, the redox reaction would not proceed if the conduction band was at a potential lower than 0 vs NHE. This would occur at approximately pH = 4 and lower for bulk titania films (disregarding overpotential losses).

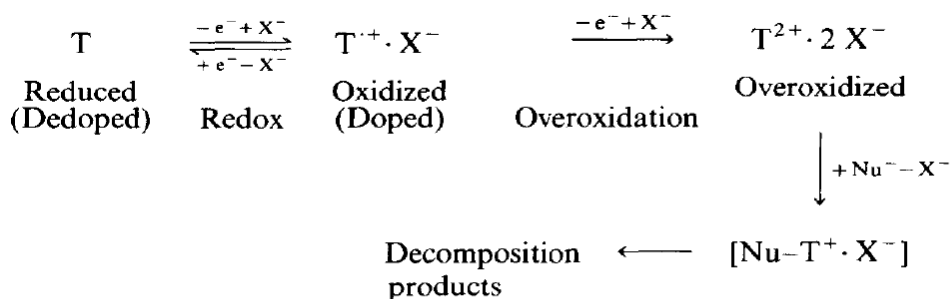
For nanoparticulate catalysts in use as a redox catalyst care must also be taken to ensure the phase stability. It has been shown for TiO<sub>2</sub> nanoparticles that phase stability is highly dependent on surface chemistry. Anatase nanoparticles have been shown to be stabilized by surface adsorbates containing a large fraction of hydrogen, whereas rutile nanoparticles are stabilized by surface adsorbates containing a large fraction of oxygen, and phase transitions can occur based on changing the surface energy. Evidence of such a phase transition is described whereas anatase nanotubes are found to unscroll and transform into rutile nanosheets when the pH of the solution is changed [234].

With organic materials electrochemically there exist additional situations for redox potential reactions, as the materials are very porous and they can absorb ions quasi-interstitially. It has

been shown that interstitial ion storage affects the conductivity of the materials, as well as the light absorption as seen in Appendix D. When used as a cathode, the PBT system de-dopes and becomes less conductive. This begins at 1.2V vs. SCE, and is reversible [235].

Extensive reviews of the mechanism by which conductive polymers proceed in redox processes are given by Lohrengel et al. [236] and Kazarinov et al. [237]. It is interesting to note that Kazarinov et al. showed that the equilibrium potential in the metal/polymer/electrolyte solution system is determined only by the chemical potentials of the components of the redox system in the bulk solution and does not depend on either the polymer nature or on the particular type of redox species in it. This is important as the level of doping should therefore not affect the redox potentials, only the electrical properties as stated above.

There also must be some consideration into the degradation of these materials, but this does not seem to be an issue for the organics in our system as we keep them fully reduced at negative potentials. Harada et al. reported that polythiophene films can be degraded and deactivated by repeated potential scans in electrolytic solutions including nucleophiles and bulky cations but these degradation pathways occurred at positive potentials [235]:



Scheme 1. Overoxidative degradation. T: Monomer unit of polymer; X<sup>-</sup>: supporting electrolyte anion; Nu<sup>-</sup>: nucleophile.

**Figure 134 - Oxidative degradation mechanism for polythiophene. [235] Reprinted with permission from the Journal of Electroanalytical Chemistry and Interfacial Electrochemistry.**

The dissolution and decomposition of overoxidized polythiophene is further described by Mukoyama [238].

As mentioned above Schottky contacts play a role in the charge separation of materials, and this can be seen in aqueous redox processes as well. The material that the polymer is deposited on has an underlying electronic nature, and affects the polymeric material as a junction is formed. A junction is also formed with the solution. Schematics of this junction are detailed in Figure 135 [230]. More regarding this junction is described by Bott [230] and for charge transfer redox states (polarons, bipolarons) by Suarez-Herrera and Feliu [239].

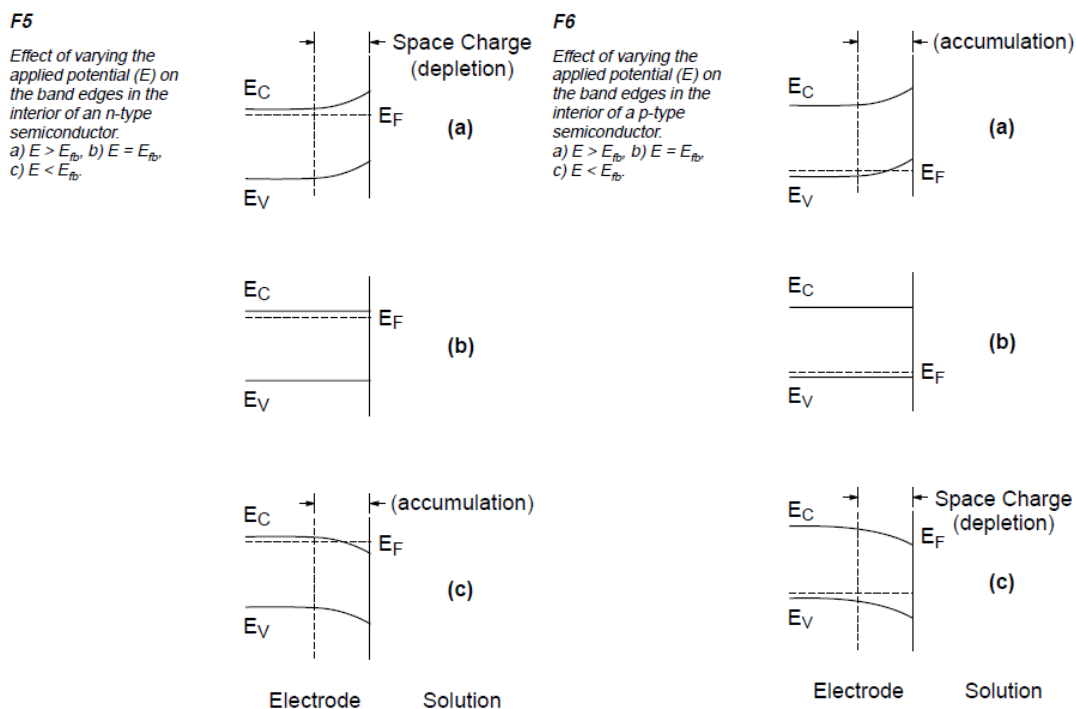


**Figure 135 - Solution polarization of semiconductor surfaces. [230] Reprinted with permission from Current.**

Rammelt et al. conducted a study of PBT coated on metal and coated on a  $\text{TiO}_2$  sublayer, and reported the following band energies under cathodic polarization [240]:

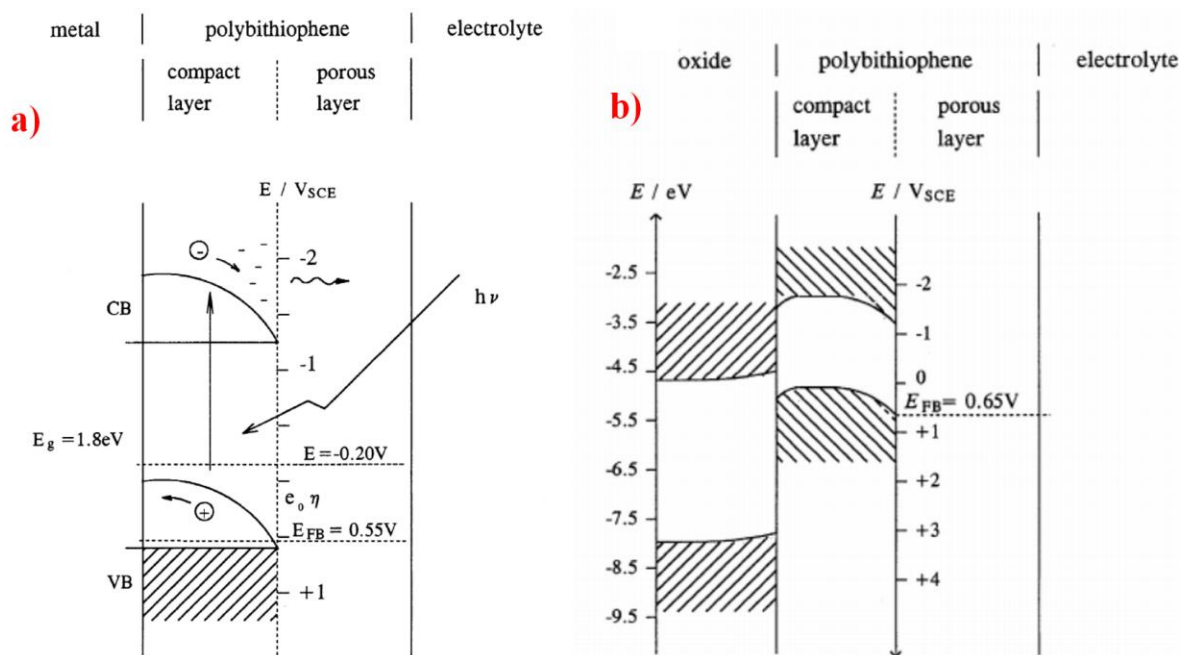


**Figure 136 - Band energy diagram of PBT on a) metal and b)  $\text{TiO}_2$ . [240] Reprinted with permission from *Electrochimica Acta*.**

A further analysis of electron-transfer reactions for redox-mediated systems has been compiled by Lewis [241]. In particular the report highlighted the possibility of enhanced charge utilization over single junction devices, where the charge separation was enhanced by redox mediated species.

For composite materials, the redox potential of the materials are more complex as dictated by a distribution of discrete states. This distribution has been detailed by Wagner [242]. As mentioned in the intro, if the composite contains different nanotube or ordered nanophase domains, the photovoltaic performance can be considerably altered [243]. The redox potential of the system however, is unchanged for thicker films (ie. complete surface coverage) when conductive polymers were grown on carbon substrates as compared to ITO substrates, as shown by Ovsyannikova et al. [244]. Considering we are unable to define discrete domains in our system, even though it is known they exist, our results will be

presented as a uniform material. Explanations will be given in the analysis of the results regarding the nanostructuring of our applied composite films and its effect on the bulk system.

## Appendix L - Activation Overpotential Losses

The cell voltage does not correspond to the theoretical equilibrium cell voltage,  $E_e$ , as there are losses in catalytic activation of the reaction. The catalytic activation losses can be divided into anodic and cathodic processes, with the majority of the research in the industry focused on anodic performance as it tends to be more cumbersome (4 electron coordination vs. 2 electron coordination).

The kinetic rate of an ideal 1st order reduction reaction can be expressed with the following equation:

$$r_c = k_c C_{Ox}(0, t) \quad \text{Eq. 35}$$

and expressed as a rate of applied current:

$$r_c = \frac{(-i_c)}{nF} \quad \text{Eq. 36}$$

Combining these two expressions relates the cathodic current density to kinetics:

$$i_c = -nFk_c C_{Ox}(0, t) \quad \text{Eq. 37}$$

And this kinetic relationship is governed by Arrhenius behaviour with respect to temperature according to:

$$k_c = A_c \exp \frac{-\Delta G_c^\ddagger}{RT} \quad \text{Eq. 38}$$

The activation energy of the reaction intermediate,  $\Delta G^\ddagger$ , is dependent on the potential of the electrode and this dependence can be illustrated by graphing the Gibbs free energy vs. the reaction coordinate. The potential difference between the reactants and products can be shifted with applied potential, and the resultant change in free energy is given by:

$$\Delta G = -n_{RDS}F(E - E^0) \quad \text{Eq. 39}$$

where  $n_{RDS}$  is the number of electrons transferred in the rate determining step of the reaction ordinate. The fraction of the total applied potential that is allocated to a half cell reaction depends on a parameter known as the symmetry factor,  $\beta$ , and when applied to the cathode yields the relationship:

$$\Delta G_c^\ddagger = \Delta G_0^\ddagger + n_{RDS}F\beta(E - E^0) \quad \text{Eq. 40}$$

The reaction rate can then be expressed:

$$k_c = \exp\left(\frac{-\Delta G_0^\ddagger}{RT}\right) \exp\left(\frac{-n_{RDS}F\beta(E - E^0)}{RT}\right) \quad \text{Eq. 41}$$

And the resultant current density relationship is:

$$i_c = -nFk_c^0 C_{Ox}(0, t) \exp\left(\frac{-\alpha_c F(E - E^0)}{RT}\right) \quad \text{Eq. 42}$$

Where

$$k_c^0 = A_c \exp\left(\frac{-\Delta G_0^\ddagger}{RT}\right) \quad \text{Eq. 43}$$

And

$$\alpha_c = n_{RDS}\beta \quad \text{Eq. 44}$$

The difference between the equilibrium potential and the measured potential is known as the activation overpotential, and is equated:

$$\eta = E - E^0 \quad \text{Eq. 45}$$

At the cathode, the majority of the research has focused on reduction or replacement of the expensive platinum catalyst while still minimizing the activation overpotential of the reaction. Catalyst loadings of platinum black in the range of 2-4 mg/cm<sup>2</sup> seem to be of optimum performance in a PEM electrolysis system as shown by Yim et al. [245]:

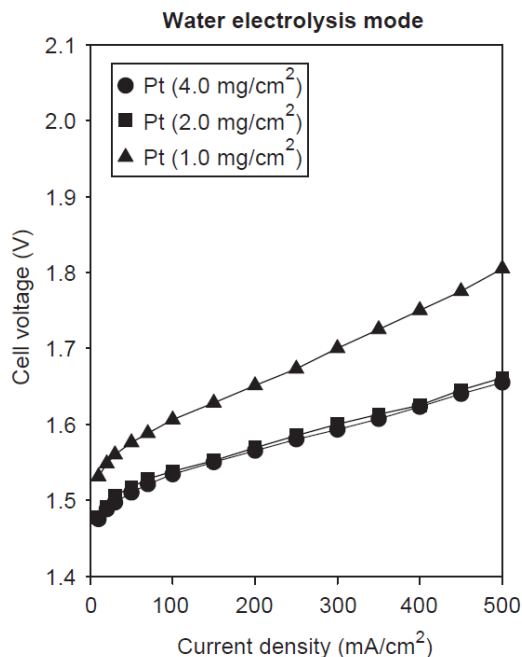


**Figure 137 - Variation in PEM electrolysis cell performance with platinum black cathode loading. [245]**

**Reprinted with permission from the International Journal of Hydrogen Energy.**

Replacement of platinum is being investigated by the alloying of metal groups in order to form co-ordinated complexes involving the d-band electron orbitals. In basic solution, glassy metals of Zn-Ni have shown promise due to 3d–4d hybridization and split band structure for the density of states of these alloys. With increasing Ni concentration, hybridization of 3d Ni and 4d Zr orbitals takes place and results in a rapid increase in the 3d Ni density of states at the Fermi level which had for a consequence a weaker bond between the alloy and hydrogen, causing a faster catalytic reaction [246]. A similar pursuit has been studied by Paunovic et al. where Co-TiO<sub>2</sub> on MWCNT have formed this same hyper-hypo d-shell coupling, and as shown below they have approached overpotential performance of Pt loadings on carbon black [96]:

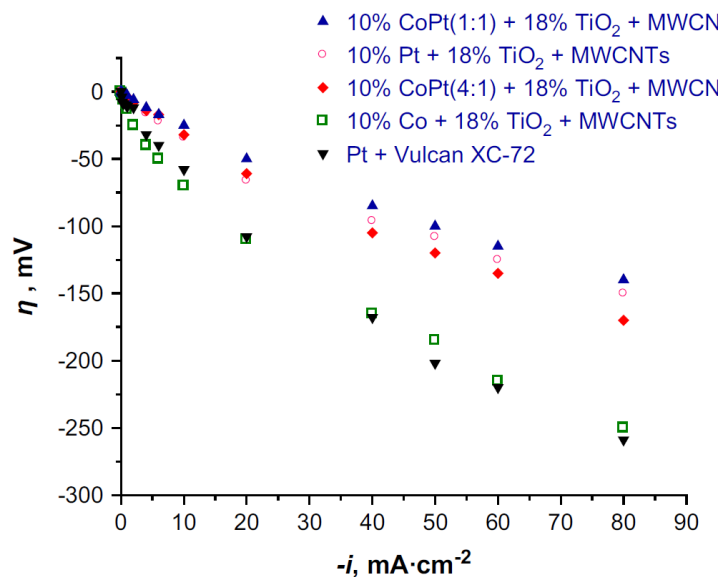


**Figure 138 - Comparison of cathodic overpotential for hydrogen production using Co and Pt doped TiO<sub>2</sub> on MWCNT. [96] Reprinted with permission from the International Journal of Hydrogen Energy.**

This orbital shell coupling has recently been extended to conductive polymeric systems in an acidic system to act as a hydrogen reduction catalyst, with composite mixes of polymeric catalysts with a Gore-Tex/Poly-3,4-ethylenedioxythiophene(PEDOT)/Polyethylene-glycol(PEG) system designed so that the reactant hydronium ion is drawn in with the PEG allowing effective charge transfer from the conductive polymer [97]. A cyclic voltammogram of this catalyst is compared to that of a sputtered platinum catalyst on a Gore-Tex membrane is compared in Figure 139:

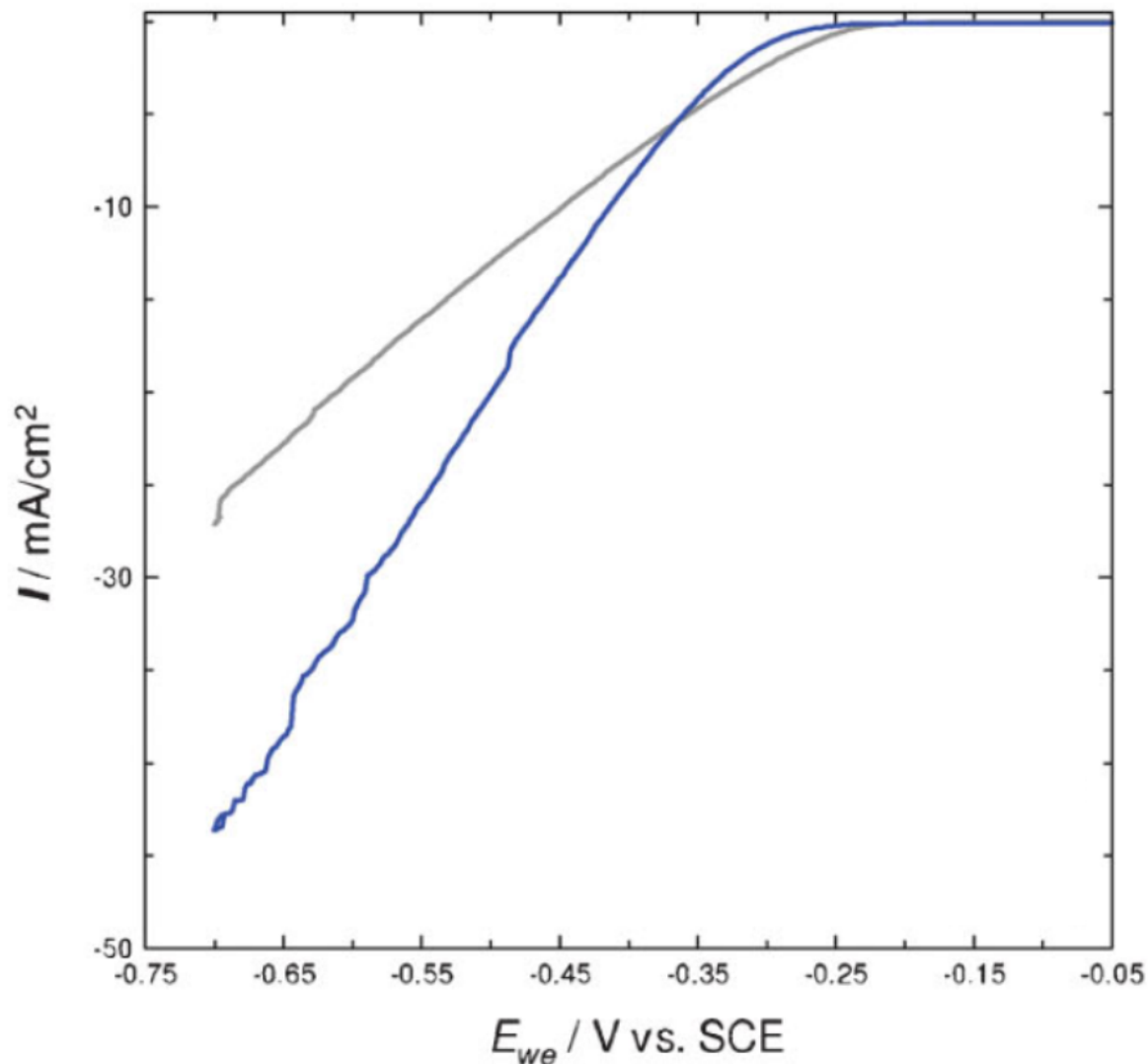


**Figure 139 - Cyclic voltammogram of Gore-Tex/Poly-3,4-ethylenedioxythiophene(PEDOT)/ Polyethylene-glycol(PEG) electrode (Blue line) versus Gore-Tex/Platinum electrode (Grey line) showing improved composite hydrogen catalysis. [97] Reprinted with permission from Advanced Materials.**

The heat treatment and conditioning of catalysts also plays an important role on the activity of the catalytic element. Ma et al. investigated the calcination temperature of a standard RuO<sub>2</sub> catalyst on SPE electrolysis performance and found that through heat treatment they could increase the conductivity and hence activity of the catalyst layer [247]. The drawback however was an increase in nucleated particle size, reducing the surface area to volume ratio – obviously there is a trade-off between activity and under-utilization of catalyst weight.

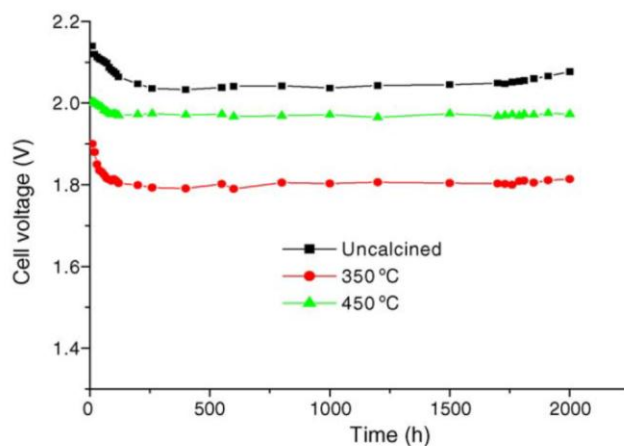


Figure 140 - Change of cell voltage with electrolysis time for heat treated  $\text{RuO}_2$  anodes at  $1100 \text{ mA cm}^{-2}$  in a SPE cell. [247] Reprinted with permission from the Journal of Molecular Catalysis A: Chemical.

Other efforts to effectively use catalyst involving incorporation of non-noble alloys with equivalent performance to bulk precious metal catalyst has been seen on the anodic electrode as well. One such example is an alloy of  $\text{Ir}_x\text{Sn}_{1-x}\text{O}_2$  powders which showed equivalent anodic performance with an increase up to 20% of Sn filler, up to a current density of  $1 \text{ A/cm}^2$  [248]:

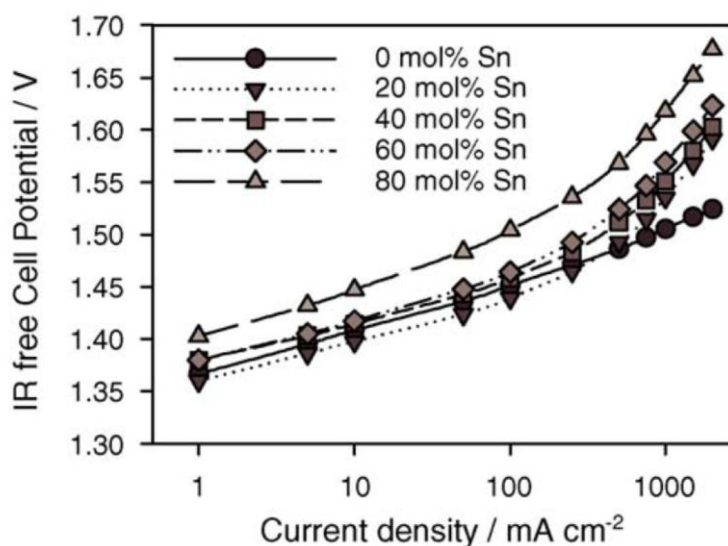
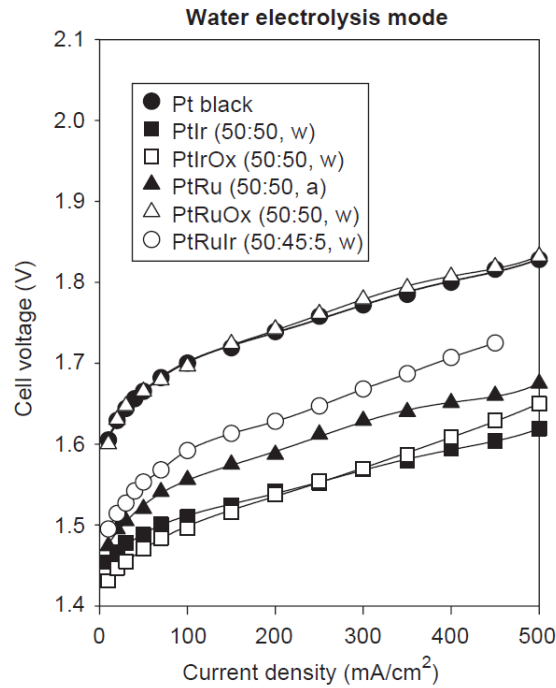


Figure 141 - Cell voltage of PEM electrolysis for a variation in Sn-filled  $\text{Ir}_x\text{Sn}_{1-x}\text{O}_2$  anodes. [248]

Reprinted with permission from Electrochimica Acta.

At the anode, composites of Ir, Ru, and Pt have been employed as catalyst, with performance reported by Kim et al. [245]. It was reported that the optimum anode loading for electrolysis increased with IrO<sub>x</sub> content. This is in strong agreement with the above anodic performance with Sn substituted IrO<sub>x</sub> powder which has better performance than that reported by Kim et al.



**Figure 142 - Cell voltage of PEM electrolysis for a variation in Pt-Ir-RuO<sub>x</sub> anodes. [245] Reprinted with permission of the International Journal of Hydrogen Energy.**

Advanced techniques are being developed to reduce the loading of noble metals on PEM electrolysis units from the present 4 mg/cm<sup>2</sup> to a desired goal of 0.18 mg/cm<sup>2</sup> on the anode and of 0.02 mg/cm<sup>2</sup> on the cathode [26]. Some measured values of exchange current densities reported by Grigoriev et al. [249] are shown in Table 7, below, with the corresponding Tafel slopes 0.06 V for the anode and 0.15–0.30 V, for the cathode:

$t, ^\circ\text{C}$	$P_{\text{excess}}, \text{MPa}$			
	0		2.5	
	anode	cathode	anode	cathode
30	$2.34 \times 10^{-7}$	$8.80 \times 10^{-4}$	$8.25 \times 10^{-7}$	$1.78 \times 10^{-2}$
60	$3.16 \times 10^{-7}$	$1.21 \times 10^{-2}$	$2.51 \times 10^{-6}$	$5.41 \times 10^{-1}$
90	$7.74 \times 10^{-7}$	$2.51 \times 10^{-2}$	$3.83 \times 10^{-6}$	$5.62 \times 10^{-1}$

**Table 7 - Values of exchange current densities ( $i_0$  in  $\text{A}/\text{cm}^2$  of  $S_{\text{vis}}$ ) at different pressures and temperatures for a  $20 \text{ cm}^2$  MF4-SK membrane electrode assembly. [249]**

On the cathode, platinum has typically been the catalyst of choice, but it is very expensive. The possibility of reducing noble metal content for hydrogen evolution in PEM water electrolysis cells has been examined by using carbon-supported nanoparticles (CSNs). Replacement of platinum by palladium has also been examined. Results show that Pd-CSNs have a lower electrochemical active surface than Pt-CSNs. Testing of Pt cathodes in PEM cells with CSNs metal loadings of  $0.7 \text{ mg}/\text{cm}^2$ , that is a three times lower than those usually found with metal-black loadings (typically ca.  $2 \text{ mg}/\text{cm}^2$ ) for water electrolysis using  $7 \text{ cm}^2$  single cells have demonstrated good performance, with conversion efficiencies of ca. 88% at  $1 \text{ A}/\text{cm}^2$ . Electrochemical performances measured with Pd catalysts are slightly lower than those obtained with Pt but still comparable, offering an alternative to Pt [250]. Pt has also been incorporated into PANI and SWCNT cathodes and the supported catalysts have been tested in fuel cell systems [251]. Recently, studies of composites of metal alloys with intermixed semiconductors have performed more efficiently [96] than Pt for hydrogen evolution due to intra-band electron coupling. Close proximity of complimentary electronic states has also been shown to act as a hydrogen reduction catalyst, with composite mixes of

polymeric catalysts with a Gore-Tex/ Poly-3,4-ethylenedioxythiophene(PEDOT)/ Polyethylene-glycol(PEG) system designed so that the reactant hydronium ion is drawn in with the PEG allowing effective charge transfer from the conductive polymer [97]. These results show good evidence that further research into the electrocatalytic effects of cheap, easy to process composites should be further examined as a replacement to platinum in hydrogen production systems.

A suitable cathode for electrolysis in acidic media could be a composite inclusion of conductive polymer and  $\text{TiO}_2$ . This combination mimics the dual functionality of the PEDOT/PEG system with  $\text{TiO}_2$  providing good wettability to attract  $\text{H}_3\text{O}^+$  ions, and the conductive polymer provides an electronic conduit to the catalysis sites.

Pd and Pt particles inserted into polythiophene films have also been studied with respect to their activity for hydrogen oxidation and oxygen reduction in acidic media for fuel cell applications and are discussed extensively by Giacomini et al. [252],[82]. At the anode, no activity for the hydrogen oxidation is seen for the polythiophene films in the absence of Pt or Pd. For the metal catalyzed polythiophene films, after initially good performance, the current for hydrogen oxidation decreases after successive potential scanning due to the lowering of the electrochemical activity of the polymer. A chemical reaction involving atomic adsorbed hydrogen on Pt or Pd and the carbon radical in the polaronic species may occur, leading to a breaking of the electronic resonance throughout the polymer chain, and causing a degradation of the electrical properties of the film [82]. Conductive polymer composites have yet to be used as HER elements in electrolysis systems to date, and it is not expected that the same degradation would occur in a reducing environment. In alkaline electrolytic solutions, sintered nickel electrodes, impregnated with non-stoichiometric amounts of cobalt

molybdate, have been investigated for hydrogen evolution from concentrated KOH solution. These electrodes show higher electrocatalytic activities than nickel and even platinized platinum. At 90°C and a current density of 400 mA/cm<sup>2</sup>, for example, the hydrogen overpotential on this electrode is about 50 mV less than platinized platinum at an equivalent current density [26]. Most recently Reece et al. have demonstrated a NiMoZn cathode catalyst operating in alkaline media for hydrogen generation, and this discovery will facilitate cheap catalysis as a replacement for platinum in the future [253].

On the anode in acidic media, Ru is superior to Ir as an O<sub>2</sub> electrocatalyst. The overpotential for oxygen evolution at 1 mA/cm<sup>2</sup> from 1 N H<sub>2</sub>SO<sub>4</sub> solution at 20°C is only ~ 210mV on Ru, while at the same current density, Pt and Ir show oxygen overpotentials of ~ 640 and ~360 mV, respectively [26]. Care must be taken with device operation, as it was observed that the ruthenium oxide film dissolves at potentials above 1.44 V and dissolution of iridium oxide film was found at potentials above 1.65 V [26]. The preparations of the catalysts are of critical performance, and were studied by Rasten et al. [254]. They varied the annealing temperature of Ir Oxides between 440-540°C and found a PEM electrolysis cell performed best based on an IrO<sub>2</sub> anode and a cathode with 10% Pt on Vulcan XC-72 (with a total noble metal loading of 2.4 mg/cm<sup>2</sup>). At a cell temperature of 80°C the cell voltage was 1.65 V at 1 A/cm<sup>2</sup> (10 kA/m<sup>2</sup>) with a hydrogen overpotential less than 150mV and a resultant anode overpotential of ~ 270mV [254]. In basic media, sintered nickel electrodes impregnated with nickel hydroxide, which are developed and broadly utilized in the battery industry, have been investigated for use as oxygen electrodes in KOH. These impregnated electrodes also show considerably higher catalytic activities for the oxygen evolution reaction than sintered or smooth nickel electrodes. According to the work of Gras and Pernot [26], the alloy 50 wt%

Ni-50 wt.% Fe, which exhibits high corrosion resistance in the strong alkaline environment, is better than the commercial Ni plates for the evolution of oxygen. The improvement in the electrocatalytic activity of this alloy is attributed to the in situ formation of a complex oxide film  $\text{Ni}_x\text{Fe}_y\text{O}_z\text{K}_t$ , which was identified using secondary ion mass spectroscopy (SIMS) [26]. Evaluation of Teflon bonded  $\text{NiCo}_2\text{O}_4$  electrodes for oxygen evolution in alkaline single cells showed that, at a current density of  $\sim 330 \text{ mA/cm}^2$ , a decrease of at least 150 mV in overpotential is achievable as compared with Ni electrodes. Unfortunately, the structural stability of Teflon-bonded electrodes is rather poor, particularly at temperatures above  $100^\circ\text{C}$  and at current densities over  $200 \text{ mA/cm}^2$  [26]. Considerations have been made to employ conductive polymers to bind ORR catalysts as highlighted by the work of Giacomini et al. [252], who found that polythiophene films loaded with dispersed Pt exhibited ORR catalysis with a Tafel slope close to  $120 \text{ mV/dec}$ , this corresponding to the expected value for the ORR, and similar to Pt catalysis. Yassar et al. electrodeposited Pd particles in polythiophene controlling the number, size, and three-dimensional distribution of the catalytic particles by the electrical conditions applied during the electrodeposition. They found that the Pd/polythiophene electrode is active for oxidative reduction of water and its activity varies with the metallic particle size, increasing with a decrease of the average size of the Pd particles. It was suggested that the oxygen reduction reaction proceeds under kinetic control with the electron transfer being the rate-limiting step [82]. These studies were not conducted under solar illumination of the electrode. A landmark  $\text{In}_x\text{Sn}_y\text{Co}_{2.1}\text{PK}_{0.8}$  oxygen evolution catalyst has also been found by Kanan and Nocera as published in Science in 2008 [255].

In terms of the activation losses in our system, the reaction rate is determined by the kinetics of what the rates of the individual steps of the reaction; adsorption, charge transfer, and desorption. The reaction rate can also be limited by the presence of available species to be adsorbed, but this occurs in the mass transfer limited region of the polarization curve.

In the kinetic activation term, the orbital theory dictates at what rate specific species will be drawn close to the surface of the electrode for charge transfer to take place. The desorption step is typically very quick, as the initial charged state no longer exists, and the force between two dissimilar charges in solution is far greater than that of an adsorbed gas or other phase.

For  $\text{TiO}_2$ , this higher activity has been described in detail and has been an active area of study for many years. Calatayud and Minot have described that on the (1 0 0) plane adsorption energy decreases with the degree of relaxation, while on the (0 0 1) plane the effect is the opposite [256]. This may be the source of the higher activity in highly distributed phases. A thermodynamic analysis of the charge transfer from the surface of an electrode has been detailed by Reis et al. [257], and dependence of the standard Gibbs energy of activation on the overpotential, temperature, and pressure were described. Of interest in our study is what happens when mixed phase materials are used with this orbital theory.

We are using P25 for our study, which has been exemplary in its activity – attributed to its mixed phase makeup of 75% anatase to 25% rutile crystal structure. There may be some correlation in this heightened activity and the thermodynamic phase stability of titania in nanocrystals, as at 14nm anatase is the preferential crystal state due to a balance in surface energy and stress of surface states, as it was noted before that the surface states are what determined the catalytic activity.

Research has been conducted for the hydrogen evolution reaction and a description of hyper d-shell orbital coupling has been described by Jaksic that explains this mixed phase material benefit in accordance to periodicity [258],[259]. This research has not been extensively studied in conductive polymer orbital theory, but there is some evidence that an extended  $\pi$ -bond with overlap to a d-shell orbital in nanoparticle inclusions may exhibit similar synergism [260].

The adsorption can be affected by the specific surface and energy levels of the material. The motion and the position of ions in a solution have also been shown to couple to interfacial electron transfer. As shown in the mass transfer section of this theory, it has been shown that that ion migration in the bulk electrolyte can have an effect on the potential available at the interface at high current or low supporting electrolyte concentration. By using microelectrodes, it has been shown that even at low currents migration effects can be significant. Outer-sphere reorganization needed to allow electron transfer to occur can be used to explain the ion motion at the molecular level, much like solvent motion [261].

Charge transfer from the surface occurs as a result of electrons dropping down from a higher state to a lower state (and conversely for holes to bubble-up from a lower state to a higher state). Marcus described this electron transfer in his famous theory as being homogenous for electrodes [262]. A thorough examination as to the mechanics of interfacial charge transfer has been approached by Creutz et al. [263], but this treatment is beyond the scope of this dissertation as the distribution of our energetic states are far from idealized. New postulations as to what may be missing from Marcus mediated charge transfer has been considered by Small et al. [264] but such considerations will not be incorporated in this study.

As detailed above, redox species in solution exhibit the standard heterogeneous rate constant,  $k^0$ . However, the reaction can proceed when the redox species are attached to an electrode surface or in the solution. Characteristics of electron transfer from an electrode to a solvated ion is not simple; parameters of electron transfer examined in light of Marcus theory including distance dependence (e.g., tunneling), reorganization energy, and a limiting rate constant at large driving force. Marcus theory predicts a current-voltage relationship that differs significantly from the Butler-Volmer relationship when the driving force,  $F(E-E_0)$ , becomes comparable to, or larger than, the reorganizational energy,  $\lambda$ . The implication of a large driving force is that the rate constant at an elevated  $E$  is significantly different from  $E^0$  [261]. Reorganizational energy is large in our system as dilute acid is used, so there may be deviation from the BV relationship, especially at high current densities [261].

The major outstanding issues involving electronic coupling is what drives electron delocalization. It is theorized that the type of bonds linking the molecular site to the electrode, as well as the coupling of the electrode potential to the redox species should be determinate electron position. The electrode potential (and hence the Fermi level) as it relates to the electronic levels of the linker bonds, should be important in determining the degree of electronic coupling through the linker. However, the evidence to date indicates very little potential dependence in the coupling [261]. This may be due to the shape of the linkage changing with applied potential.

## Appendix M - Ohmic Overpotential Losses

Ohmic losses stem from resistances in the electrolytic system that are contributions from electronic and ionic resistances in the membrane, electrolyte and electrode materials. An equation outlining the  $iR$  losses in the system is given by:

$$\eta_{iR} = i \sum_j R_j = i \sum_j \frac{\rho_j A_j}{L_j} \quad \text{Eq. 46}$$

where  $i$  is the current,  $R_j$  is the electronic/ionic resistance of component  $j$ ,  $\rho$  is the resistivity of component  $j$ ,  $A$  is the cross-sectional area of component  $j$ , and  $L$  is the thickness of component  $j$ .

There is a large range of electronic and ionic conductivities of the materials used in this study. An overview of the conductivities of carbon-fibre based materials is given by Lysenko and the physical properties are shown in Table 8 below:

Properties	TGP-H-030	TGP-H-060
Thickness, mm	0.11	0.19
Bulk density, g/cm <sup>3</sup>	0.40	0.44
Porosity, %	80	78
Surface roughness Ra, $\mu\text{m}$	8	8
Gas permeability, ml·mm/(cm <sup>2</sup> ·h·mm H <sub>2</sub> O)	2500	1900
Resistivity, m $\Omega$ ·m		
perpendicular to the plane	80	80
in the plane	–	5.8

**Table 8 - Physical properties of TGP-H carbon-fibre materials. [86]**

For semiconducting elements in a solid state device, the conductivity related to field effects associated with electron transfer must be considered. The emission of field-assisted electrons

across a potential barrier at a metal interface is known as the Schottky effect, while across barriers due to localized states is called Poole-Frenkel emission. Both effects give rise to essentially the same relationship between current and voltage, but this relationship changes with respect to the relative amount of injected electrons.

In the low-injection region (injected carrier density  $n_i \ll$  thermally generated carrier density  $n_t$ ) Ohm's law is utilized [265]:

$$J = n_t e \mu \frac{V}{w}. \quad \text{Eq. 47}$$

As  $n_i$  approaches  $n_t$ , conduction becomes less ohmic due to the spacecharge region built up at the injecting contact. When the field has increased sufficiently for the mean-free-path to be comparable with the thickness of the device, the Schottky model is used to describe the current flow in an ideal system. Invariably, there will be trapping states present in the device. The presence of trapping removes some of the injected carriers, reducing the efficiency of injection. This modification applies until all the traps are filled. Once all the traps are filled, space-charge-limited flow in a material with a Schottky barrier gives rise to the expression [265]:

$$J = J_0 \exp \frac{e(\beta V^{1/2} - \theta)}{kT} \quad \text{Eq. 48}$$

with

$$\beta = (e/4\pi\epsilon_1\epsilon_0 w)^{1/2} \quad \text{Eq. 49}$$

A third possibility for conduction relies on tunnelling effects. Tunnelling can occur between localized levels in a material, or from the cathode into the conduction band. Tunnelling has a weak temperature dependence, and expresses the following relation [265]:

$$J = J_0 \left( \frac{eEl}{\phi B} \right)^{1/2} \exp \left( \frac{\phi B}{eEl} \right) \quad \text{Eq. 50}$$

These device conductivity models, although useful, are based on a first principle approach to the conductivity of the semiconducting materials in our system. Measured variables are also useful in defining the conductivity of the base device materials. The conductivity of TiO<sub>2</sub> was first reported by Earle and the following figure was reported [266]:

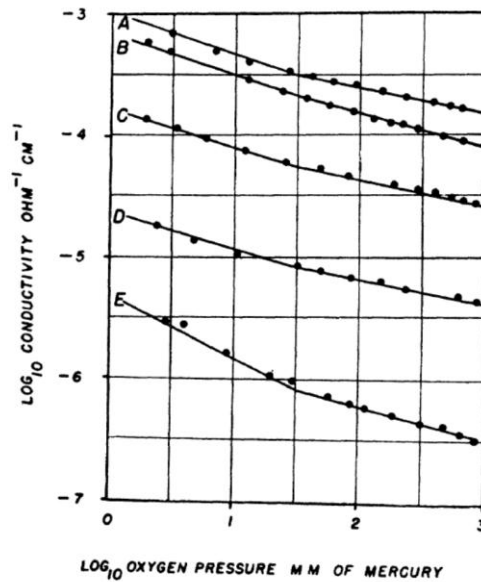


Figure 143 - Conductivity as a function of oxygen pressure for a) 968°C rutile, b) 820°C rutile, c) 861°C anatase, d) 755°C rutile, e) 626°C rutile. [262] Reprinted with permission of Physical Review.

Tang et al. and Pearsall followed up on this work with a more thorough study as to the mechanism of dc conductivity in titania [100],[265]. It was determined that the electron flow through titania thin films were rectified by the titanium contact, and that contact resistance

dominates in both thin films and single crystals. This implies that the electric field across the device is non-zero only over a small region about the metal-insulator interface[265].

For organic semiconductors, it has been previously discussed that the conduction mechanism occurs due to a ‘hopping’ of charge between crystalline centers. This hopping is governed by Marcus-Hush theory, and the hole hopping is represented by the following relationship:

$$k_{hole} = \left( \frac{\pi}{\lambda_E k_b T} \right)^{1/2} \frac{V^2}{\hbar} \exp \left( - \frac{\lambda_E}{4 k_b T} \right) \quad \text{Eq. 51}$$

where,  $\lambda_E$  is the reorganization energy due to geometric relaxation accompanying charge transfer, and V is the electronic coupling matrix element between the two species, dictated largely by orbital overlap [267]. These models assume carrier hopping between molecular sites, occurring with Gaussian distribution of energy states [9]. The hopping is associated with the drift mobility of holes by the Einstein relation:

$$\mu = \frac{e}{k_b T} D_c = \frac{e L^2 k_{hole}}{k_b T} \quad \text{Eq. 52}$$

where, e is the electronic charge,  $D_c$  is the diffusion coefficient of charge carriers, and L is the separation between sites [267].

Hutchison et al. have completed a thorough geometric study of the shape and energies associated with the transition of charged states, and electronic coupling between them [267].

It was noted that with a minimization of inter-ring torsional components it should lead to higher mobility, with a correlation between the number of monomer units and hole mobility as follows:

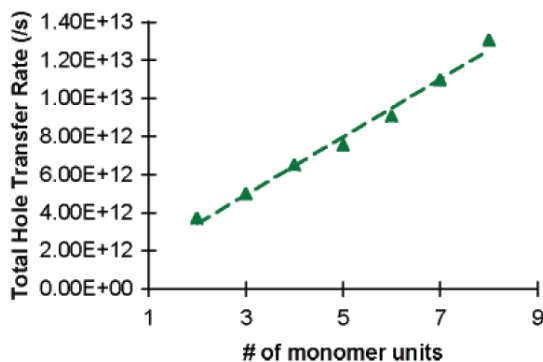


**Figure 144 - Correlation between the number of monomer units and hole mobility in conductive polymers. [267] Reprinted with permission from the Journal of the American Chemical Society.**

This correlation makes sense, as shown through DFT studies there is a distinct preference of longer oligomers for formation of  $\pi$ -stacked structures. The relationship between charge-transport and molecular packing have been coined “pitch and roll”, and are based on concepts of lateral and angular deviations from a rest state [140]. The control of charge transfer in constrained dimension devices also has an effect on charge transfer mobilities. Polymers infiltrated into nanoporous films have shown improved hole mobility of the organic semiconductor by aligning polymer chains along pore walls. More work is underway in ways to fabricate semiconducting films with optimally spaced straight pores to raise device efficiency [153]. As cast PBT at very low doping levels ( $< 11\%$ ), has been confirmed to exhibit polaron-hopping behaviour. The polarons are contained at areas of five to six monomer units, with a mobility of  $3.7 \times 10^{-6} \text{ m}^2\text{V}^{-1}\text{s}^{-1}$ , a diffusion coefficient of  $9 \times 10^{-8} \text{ m}^2\text{s}^{-1}$ , and a residence time of  $1.1 \times 10^{-13} \text{ s}$  [79].

It was further shown that with an increase in temperature there would also be an increase in conductivity, which is of merit especially in an uncooled solar harvesting device. The correlation is shown below for polysexithiophene below [267]:

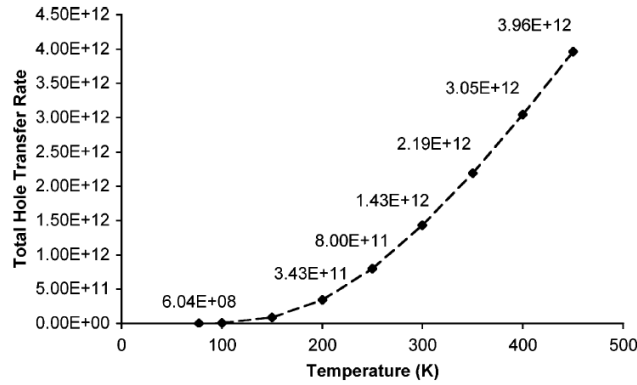


Figure 145 - Increase in hole transfer rate with an increase in temperature for conductive polymers. [267]

Reprinted with permission from the Journal of the American Chemical Society.

The humidification of polythiophene also affects the conductivity of the films, as reported by Sears [268], but as we operate in a saturated liquid environment, these effects will not be further considered.

The redox electrolyte also imparts a conductivity of solution that must be considered.

Whetham reported conductivity data for dilute solutions of sulfuric acid [269], and more recent results are as shown in Figure 146[270], [271]:

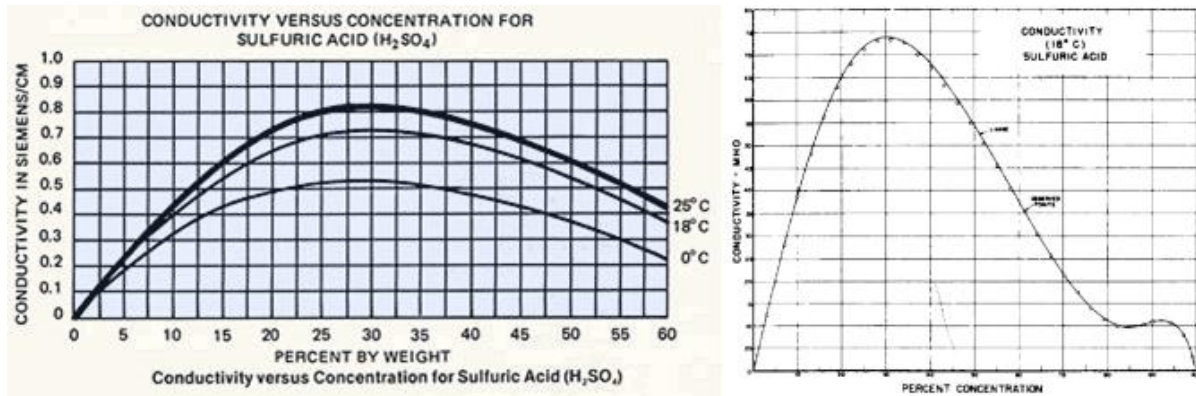


Figure 146 - Conductivity of sulfuric acid solutions. [270, 271] Reprinted with permission from the Journal of Chemical & Engineering Data, and Physics and Chemistry of Liquids.

An electrolyte exhibits conductivity due to the mobility of charged ions dissociated in solution. For a fully dissociated solution of ions in dilute concentration, the conductivity can be expressed by:

$$\kappa = F^2 \sum_j z_j^2 \mu_j C_j = \sum_j \lambda_j C_j \quad \text{Eq. 53}$$

where  $\kappa$  is the electrolyte conductivity,  $z_j$  is the charge number of ion  $j$ ,  $\mu_j$  is the mobility of ion  $j$ ,  $C_j$  is the concentration of ion  $j$ , and  $\lambda_j$  is the ionic molar conductivity of ion  $j$  for a summation of all ions in the solution.

## Appendix N - Mass Transport Overpotential Losses

The mass transfer losses of a system occur when presence of reactive elements are limiting the performance of a redox electrode. In consideration of the cathodic species for reduction, protons, this is an increasing problem in dilute acid solutions and can be expressed by the difference between the cathodic equilibrium potential based on the surface concentration ( $E_{c,s}$ ) and the bulk concentration ( $E_{c,b}$ ):

$$\eta_{Conc,c} = E_{c,s} - E_{c,b} \quad \text{Eq. 54}$$

which expanded is:

$$\eta_{Conc,c} = \left[ E^0 - \frac{RT}{nF} \sum_j s_{Red,j} \ln \left( \frac{C_{s,Red,j}}{C_{s,Ox,j}} \right) \right] - \left[ E^0 - \frac{RT}{nF} \sum_j s_{Ox,j} \ln \left( \frac{C_{s,Red,j}}{C_{s,Ox,j}} \right) \right] \quad \text{Eq. 55}$$

Since the electrolysis is conducted in a dilute aqueous acidic solution, it can be assumed at the limitation of mass transport is at the cathode, as the protons must travel between the anode compartment, through the membrane and percolate to the cathodic reaction sites. This reduces the above expression to:

$$\eta_{Conc,c} = -\frac{RT}{nF} s_{Red} \ln \left( \frac{C_{s,Red}}{C_{b,Red}} \right) \quad \text{Eq. 56}$$

Assuming one-dimensional Fickian diffusion to the electrode surface, the surface concentration is equated to the bulk by:

$$J_{Red} = -D_{Red} \frac{dC_{Red}}{dx} = D_{Red} \frac{(C_{s,Red} - C_{b,Red})}{\delta - 0} \quad \text{Eq. 57}$$

where  $J_{Red}$  is the flux of the protons,  $D_{Red}$  is the diffusion coefficient of the protons, and  $\delta$  is the length of the diffusion boundary layer.

Under mass transport control the current density is a function of the transport of ions to the surface of the electrode. This relationship is equated:

$$i = \frac{nF}{s} J \quad \text{Eq. 58}$$

Substituting for proton flux, we can find the limiting current density:

$$i_L = -\frac{nF}{s_{Red}} K_m C_{b,Red} \quad \text{Eq. 59}$$

with the mass transfer coefficient,  $K_m$  defined as:

$$K_m = \frac{D}{\delta} \quad \text{Eq. 60}$$

and the resultant overpotential due to mass transfer given by:

$$\eta_{conc,c} = -\frac{RT}{nF} s_{Red} \ln \left( 1 - \frac{i}{i_L} \right) \quad \text{Eq. 61}$$

Obviously this assumption of a simple first order Fickian diffusion model is a gross oversimplification of our system. Papageorgiou et al. have done a comprehensive model for mass transport in dye sensitized mesoporous solar cells and found that the concentration of the redox active species can be determined under steady state irradiation as a function of current density, location and direction of irradiation [272]. This model can be used to analyze the problem of transport and losses in a porous semiconductor material. A complimentary analysis has been completed by Lin et al. [273]. In using these models for a conductive polymeric matrix, additional considerations due to ionic absorption must be incorporated. Research into controlling the gas production from electrolysis cells has also been considered, and intensively studied by Tanaka et al. [274] by the effect of the linear velocity of water on the ratio of dissolved hydrogen. In their experiments the channel widths in the electrolyzer were altered to facilitate improved hydrogen gas removal.

## Appendix O - Extended EIS Analysis

For TiO<sub>2</sub>, EIS analysis in a 0.1M NaOH system with Pt counter electrode was conducted by Dolata et al. for anatase and rutile crystals [275]. Comments regarding the accuracy and dependence on the correct model used for analysis led to a more complicated model being developed for this simple system:

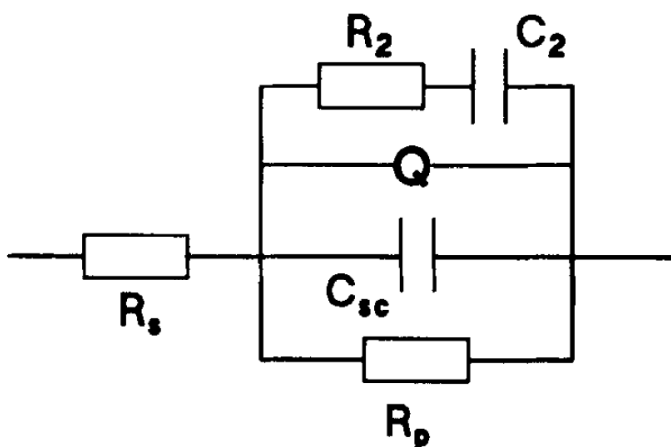


Figure 147 – Complex EIS model for TiO<sub>2</sub> in a 0.1M NaOH system with Pt counter electrode. [275]

Reprinted with permission of Electrochimica Acta.

In analyzing the EIS spectra, the space charge layer is represented in the high frequency region. The equivalent circuit in this region is determined by a series resistor  $R_s$ , and the space charge layer capacitance  $C_{sc}$ . A reasonable fit for this equivalent circuit was only obtained when  $C_{sc}$  was replaced by a constant phase element. The observed response due to small diameter pores is represented in the low frequency range, also described by a constant phase element. The frequency range of the spectrum between 1 Hz and 10Hz is the most difficult to interpret, and the  $R_2, C_2$  subcircuit has been employed to describe this region. It was modeled after a resonance observed on rutile single crystal characteristics with higher donor concentrations. Fabregat-Santiago analyzed a similar microporous TiO<sub>2</sub> system

deposited on ITO [276] but incorporated a junction of the solution to the underlying porous substrate.

For a conductive polymer, the surface behaves more or less like a capacitor, with charging and discharging modeled as a RC process with the redox capacity  $C$  and an ionic resistance  $R$  (of the film or electrolyte). The capacitive element often has pronounced dielectric losses and is thus modeled as a constant phase element (CPE). The polymer films have also been modeled as a battery, charging and discharging at an almost constant potential. In fact, the redox process is very complex [236].

The impedance of polythiophene film on an electrode was first described by Johnson et al. [277] and showed this simple relationship for an equivalent circuit:

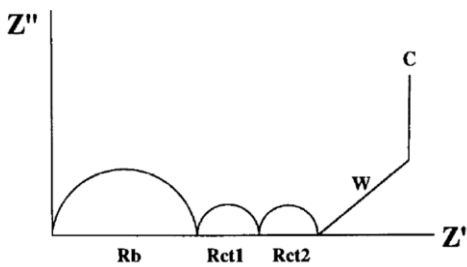


**Figure 148 - The equivalent circuit of impedance for a polythiophene film on an electrode. [277]**

Reprinted with permission from the Journal of the Electrochemical Society.

PBT film deposited on a Pt electrode was also modeled by Diagne et al. [278] and found a good fit using a combination of constant phase elements as shown in the equivalent circuit below:

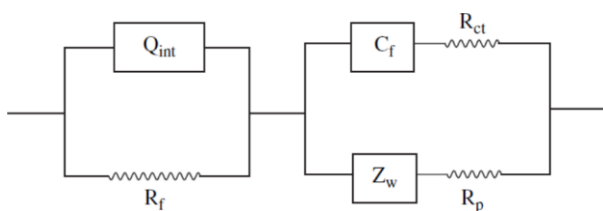


**Figure 149 – Equivalent circuit for PBT film deposited on a Pt electrode. [278] Reprinted with permission from Comptes Rendus Chimie.**

where ( $Q_{int}$ ) is the interfacial double-layer at the polymer electrolyte interface and  $R_f$  is the film resistance.  $C_f$  is the redox capacitance of the polymer itself, and is in series to the charge-transfer resistance ( $R_f$ ).  $R_p$  is the sum of resistances due to the electrolyte in the pores of the film and the 0.3 M  $LiClO_4$  solution.  $Z_w$  is attributed to diffusive capacitance (Warburg impedance). The resultant Nyquist Plot was:

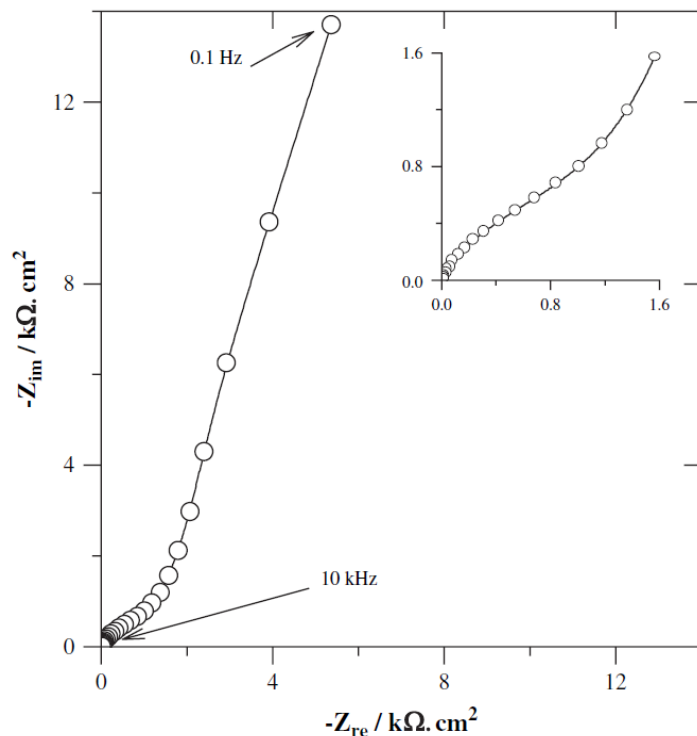


**Figure 150 - Nyquist plot for for PBT film deposited on a Pt electrode. [278] Reprinted with permission from Comptes Rendus Chimie.**

An even more extensive model based on 1<sup>st</sup> principles and incorporating Taylor series to further define the structure of a porous polymer network provided good results, but is far beyond the analysis provided for this dissertation [279]. Similar results are reported by the analysis of a PTh film under polymerization with in situ EIS analysis as shown by Popkurov et al. [280]. If these complex models were to be adopted for the inclusions of nanoparticles as well as including a SPE membrane it is estimated that the analysis would be a dissertation

upon itself. As it stands, Bard et al. have noted that the electrode-solution interface must include the atomic arrangement not only of the electrode surface but also the interaction of ions, solvent, and other neutral molecules in the solution [261]. EIS modeling hopes to provide clues as to the performance of this complex system. Such a detailed description has been labeled the “Holy Grail” of fundamental interfacial electrochemical studies, and may not be attainable [261].

U. Rammelt et al. defined the polymer as considered to be a two-layer system consisting of a more compact layer and a porous outer layer, which when coated on a  $\text{TiO}_2$  coated electrode functioned as a p-n junction [240]. Layers of porous polymer coated on PBT were reported to have the following EIS model:

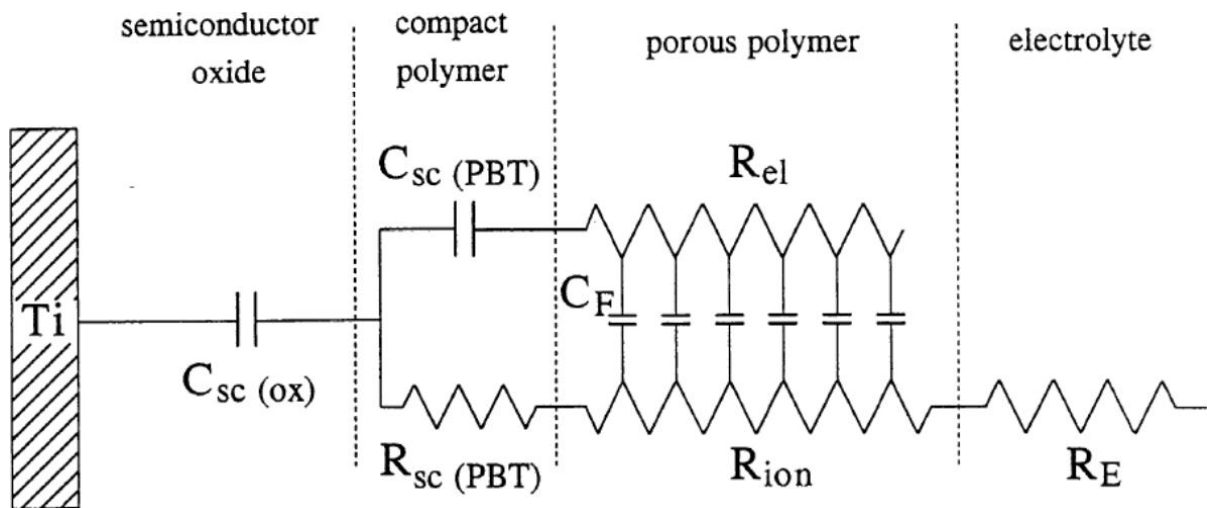


Figure 151 – Equivalent circuit for layers of porous PBT polymer coated on solid PBT deposited on a  $\text{TiO}_2$  electrode. [240] Reprinted with permission from *Electrochimica Acta*.

and the resultant Bode plot was:

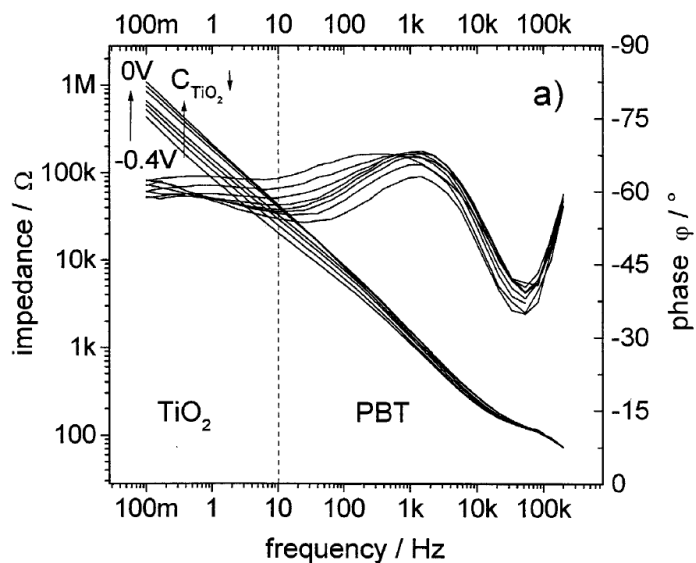


Figure 152 – Bode plot for layers of porous PBT polymer coated on solid PBT deposited on a  $\text{TiO}_2$  electrode. [240] Reprinted with permission from *Electrochimica Acta*.

For  $\text{TiO}_2$ -PT pressed composite electrodes, an equivalent circuit was presented by Hebestreit et al. [69]:

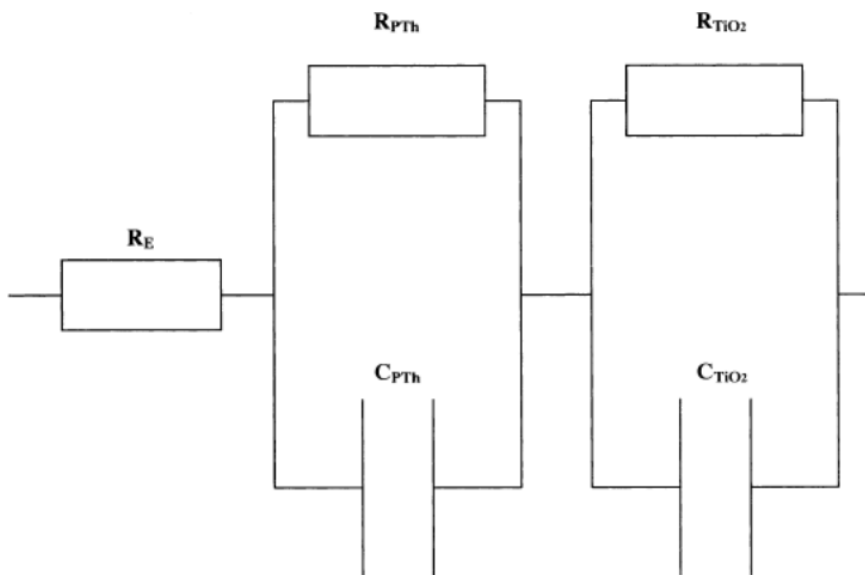
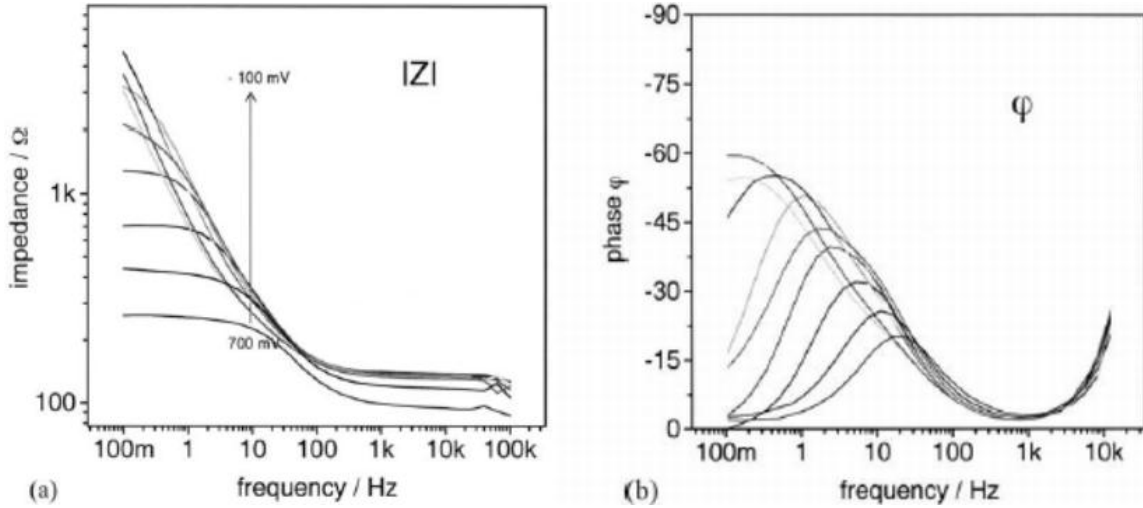


Figure 153 – Equivalent circuit for a  $\text{TiO}_2$ -PT pressed composite electrode. [69] Reprinted with permission from *Electrochimica Acta*

and the resultant Bode plots were:



**Figure 154 – Bode plots for a TiO<sub>2</sub>-PT pressed composite electrode. [69] Reprinted with permission from *Electrochimica Acta***

Similar to Rammelt et al., Hebestreit et al. considered the impedance of the TiO<sub>2</sub> core to be characterized between 1-10Hz, 1-100 Hz for PTh, and above 1kHz for the Electrolyte [69].

From the resultant space charge capacitance values at different applied potentials a Mott-Schottky plot the free carrier density of the material can determined. Popkirov and

Barsoukov found that for PBT the impedance spectra obtained during positive sweeps in the potential range 0.3-0.5 V cannot be approximated by such a RC circuit due to sluggish

oxidation and reduction kinetics for PBT [281]. The build-up of the capacitance of the

polymer layer is not completed during the 8.5 mVs<sup>-1</sup> positive sweep and continues to increase further during the reverse sweep. For this reason all EIS measurements should be conducted after a steady potential state has been held until stability has been reached.

EIS analysis has also been conducted for a deposition of PEDOT on N117, and the authors

found the most promising approach to be a one-dimensional cylindrical pore model derived

by DeLevie and Delahay. This model assumes a conductive free-standing membrane with the condition  $\sigma_e \gg \sigma_{ion}$  and the impedance function is shown below [282]:

$$Z_{por} = R^* \frac{th(\sqrt{j\omega R^* C^*})}{\sqrt{j\omega R^* C^*}} \quad \text{Eq. 62}$$

where  $R^*$  is the overall resistance of the ion-conducting phase (pore electrolyte) and  $C^*$  is the capacitance at the inner interface between the electron- and ion-conducting phases (pore wall). The associated Nyquist plot is shown below:

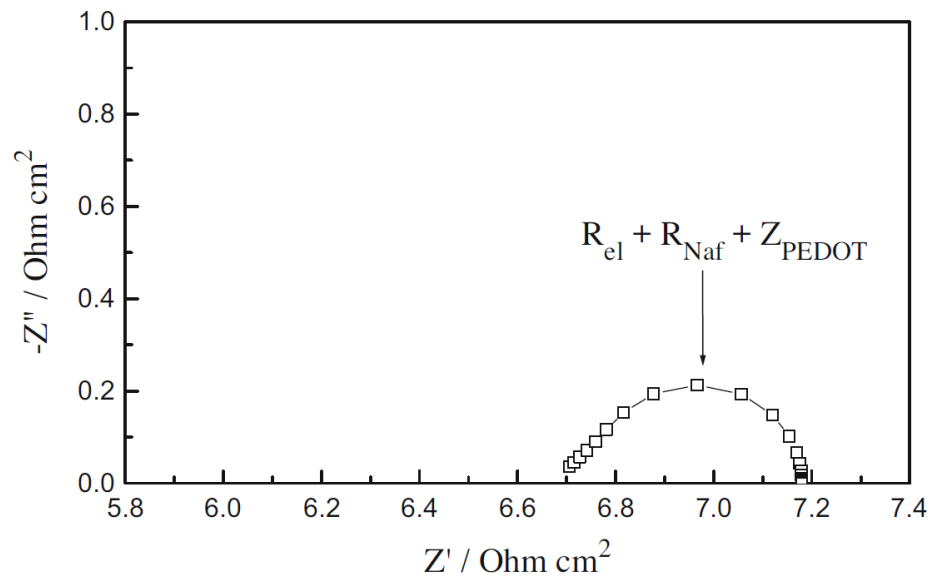


**Figure 155 – Nyquist plot for PEDOT on N117. [282] Reprinted with permission from the Journal of Solid State Electrochemistry.**

A similar porous model can be seen from the analysis of PANi on ITO by Aksimentyeva et al. [283]:

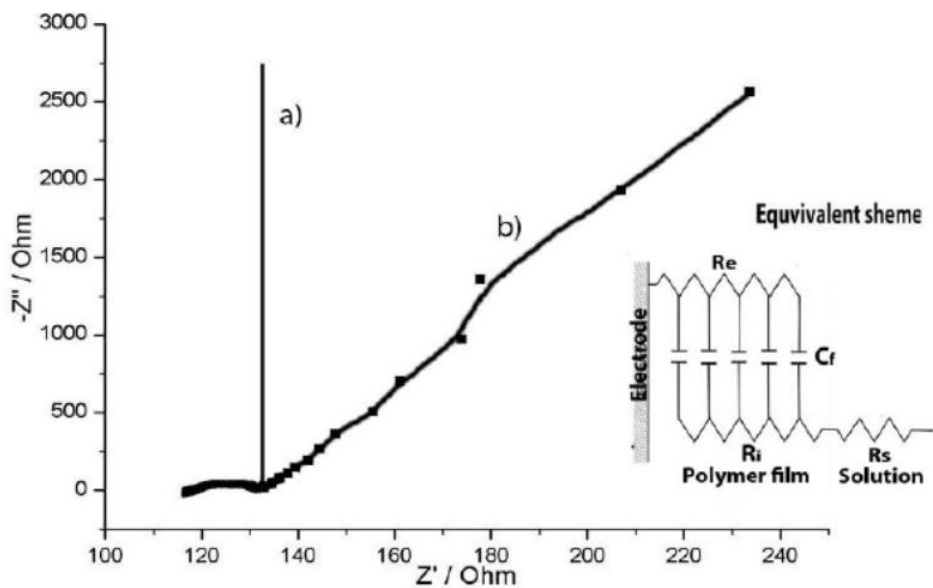


Figure 156 – Impedance analysis for porous PANi on ITO. [283] Reprinted with permission from the Journal of Physics: Conference Series.

Contributing to the complexity of a modeled analysis is the 3-d porous carbon network the films are deposited on. In terms of EIS measurements on porous electrodes, de Levie reported the following [284]:

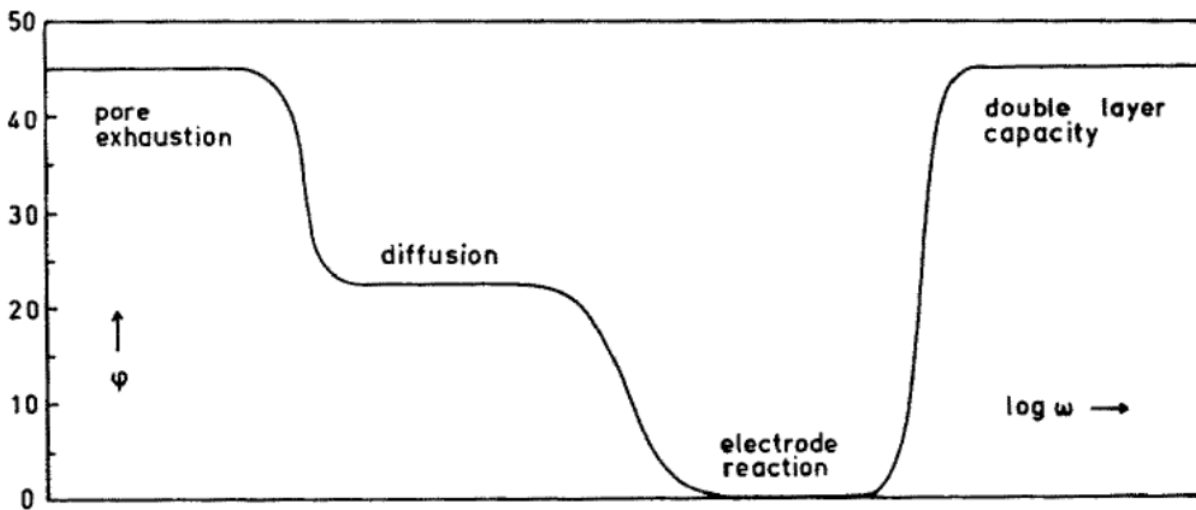
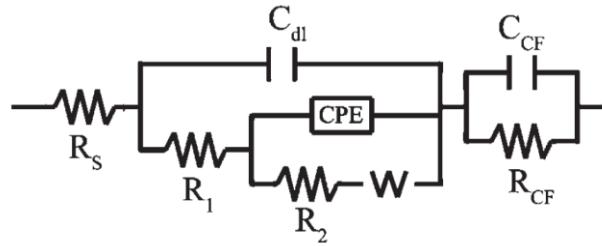


Figure 157 – Representation of EIS measurements on porous electrodes. [284] Reprinted with permission from Electrochimica Acta.

For polymer species deposited on a carbon fibre surface, Sarac et al. added an additional component to their model, a capacitor element  $C_{CF}$ , introduced in parallel with a charge transfer resistor  $R_{CF}$ . This additional model layer corresponded to the carbon fibre polymer coating, and with this additional component added the modeled results were in very good agreement to experimental data ( $\chi^2$  value  $< 0.0001$ ) [285]:



**Figure 158 – Equivalent circuit for a polymer deposited on a carbon fibre surface. [285] Reprinted with permission from Surface Engineering.**

The first loop is the bulk solution resistance of the polymer and the electrolyte  $R_s$ , the second loop is the parallel combination of the double layer capacitance  $C_{dl}$  and  $R_1$  (the resistance of the electrolyte). A series connection to  $R_1$  was made up using a Constant Phase Element (CPE) in parallel with  $R_2$  (the charge transfer resistance) and  $W$  (the Warburg impedance of the polymer).

It has been stated that EIS is a very good tool to analyze the decoupling of electronic from ionic charge transfer, and from this analysis the electron diffusion coefficient can be derived from the relation:

$$D_e = \frac{d^2}{R_e C_{low}} \quad \text{Eq. 63}$$

Where  $d$  is the film thickness,  $C_{low}$  is the capacitance at low frequency (which may be obtained from the inverse slope of a plot of imaginary impedance  $Z''$  versus reciprocal frequency,  $1/\omega$ , with  $\omega$  in  $\text{rad.s}^{-1}$ ), and  $R_e$  – electronic resistance [283].

## Appendix P - Capacitance

### P.1 Double-layer Capacitance

The double layer capacitance is described by the Gouy-Chapman region of electronic states adjacent to the electrode. For a carbon-fibre electrode, the double layer capacity and electrochemical activity depends not only on the surface area and pore structure, but also on the surface functionality (even when bare). There is a decrease in double-layer capacitance with increasing heat treatment temperature of carbon fibre electrodes, as illustrated by Biniak [286]. Structural changes in the carbon materials (e.g. graphitization) and changes in their surface chemical structure were cited as reasons for this change. The capacitive change with heat treatment is illustrated in the following chart:

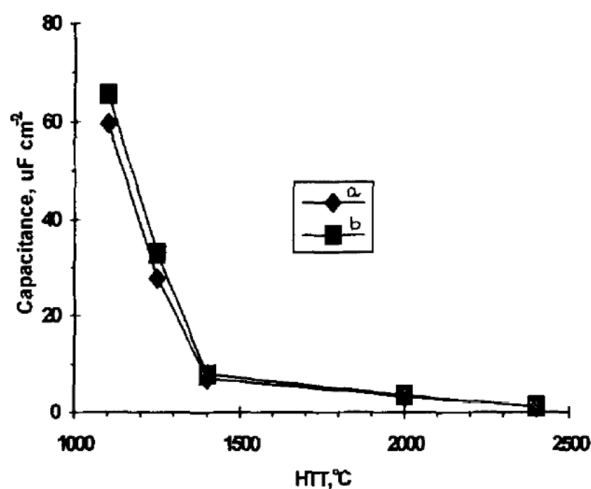
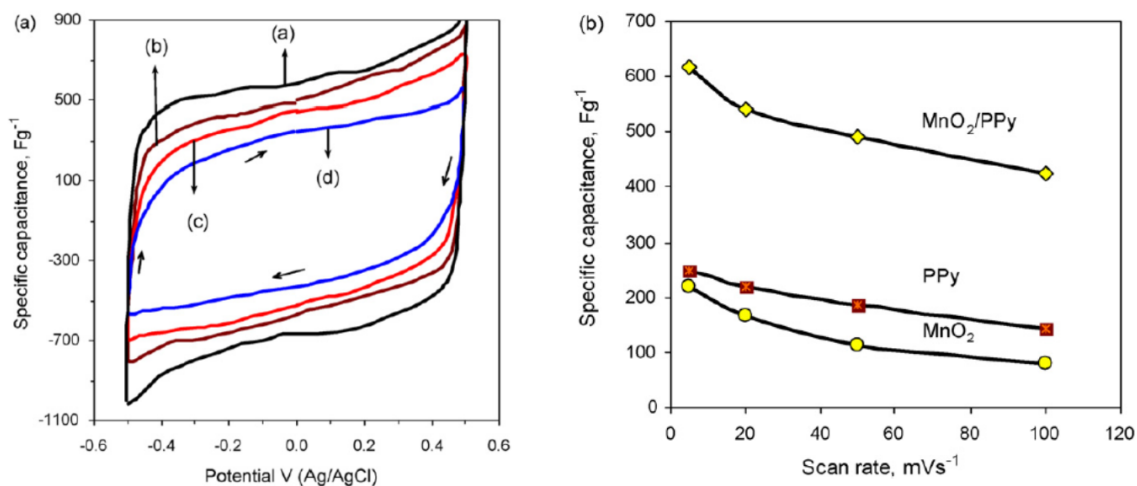


Figure 159 - Double-layer capacitance for carbon fibres in 0.1M LiClO<sub>4</sub>/acetonitrile solution as a function of their heat-treatment temperature for a) unmodified CF's, b) oxidized CF's. [286] Reprinted with permission from Carbon.

The capacity of a porous carbon electrode was first described mathematically by de Levie [284]. As discussed in Appendix O, the space charge resistance and capacitance can be determined from the EIS high frequency data [287], and the behaviour of carbon in contact with a semiconducting layer changes as a decreasing function of the space charge resistance

of the semiconducting layer. The maximum double layer capacitance would occur in the neighborhood of the flatband potential of the oxide, as with a deviation from flat band there would be an increased space charge layer, increasing the space charge resistance, and hence suppression of the Cdl. Recently, manganese oxides nanoparticle composites in a polypyrrole matrix have been studied as an electrochemical supercapacitor, utilizing this space charge effect [288]. The specific capacitance of the films was determined by cyclic voltammetry scans at different scan rates as shown below:



**Figure 160 - Scan rate dependence of MnO<sub>2</sub>/PPy composite electrode in 0.5 M Na<sub>2</sub>SO<sub>4</sub> at a) 5, b) 20, c) 50 and d) 100 mVs<sup>-1</sup>. Figure on the right shows the calculated specific capacitance of MnO<sub>2</sub>/PPy, MnO<sub>2</sub>, and PPY electrodes in 0.5 M Na<sub>2</sub>SO<sub>4</sub>. [287] Reprinted with permission from *Electrochimica Acta*.**

The thickness of this layer also has an effect on the adsorptive and charge transfer properties of the electrode. If the electrodes are porous, doped, covered with a polymer, the capacitive performance of the electrode is affected. This effect has been analyzed by Frumkin and the influence of the capacitive double layer is augmented by a correction to the exchange current density accounting for the effect of diffuse ionic charges due to the Cdl. The Gouy-Chapman-Stern model of electrostatics at the interface provides the distribution of mobile

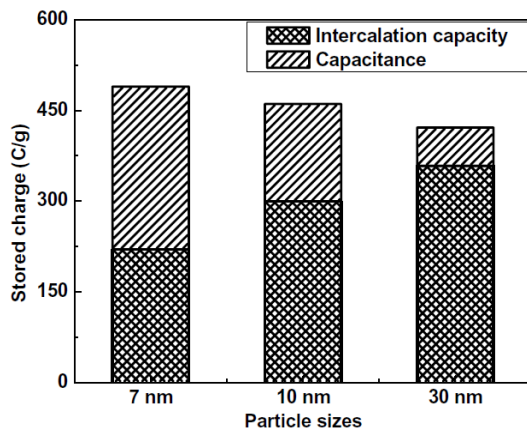
ions at the interface, while the Frumkin correction provides the incorporation of the resulting potential profile into a treatment of electrode kinetics [261].

There is also a dependence of  $C_{dl}$  on the conductivity of solution. It can be seen that operating a Pt electrode in a PEM cell in water versus in 0.5M  $H_2SO_4$  gives the capacitive double-layer parameters as functions of the deviation from pzc at the 'Pt/0.5M  $H_2SO_4$ ' interface, and the 'Pt/water' interface as detailed by Wang et al. [289].

## **P.2 Pseudocapacitance**

One final point regarding the nature by which the electrolysis reaction proceeds regards a process which is called pseudocapacitance. Pseudocapacitance is a process by which reduction of hydrogen ions is not accompanied by gas formation but rather by adsorbed uncharged surface hydrogen. The adsorbed hydrogen species will change the double layer capacitance of the material as well as to act as a source of sorbed hydrogen for reaction.

Pseudocapacitance of electrodes have been previously shown to occur for standard electrode materials such as platinum [290] on the cathode and  $Ir_xSn_{1-x}O_2$  on the anode [248]. On the anode, the adsorbed hydrogen operates in a slightly differing manner, and pseudocapacitance occurs primarily due to the lower electronegativity of Sn than Ir, indicating that the  $SnO_2$  will be less acidic than  $IrO_2$ . Differences in the acid–base properties may perturb the charging process as the  $SnO_2$  can act as a Brønsted base, accepting protons from the  $IrO_2$  sites. Proton exchange with the electrolyte gives rise to the pseudocapacitor behaviour of these oxides, and therefore if this process is altered by the presence of  $SnO_2$ , some irreversibility may occur [248]. Pseudocapacitive behaviour has also been found for  $TiO_2$  nanoparticles, and has been identified in capacitive energy storage systems as comparable, if not larger than interstitial intercalation of Li ions as the particle sizes decrease [291].

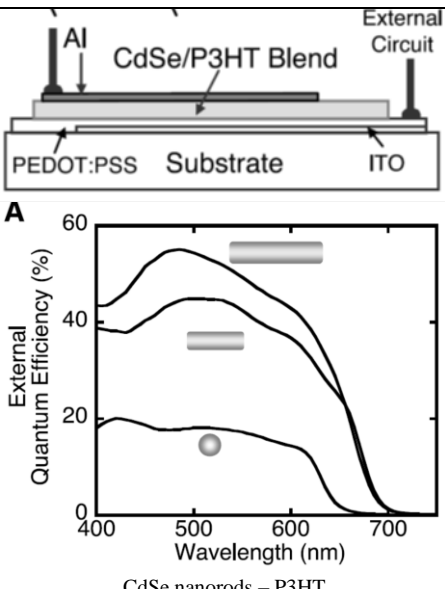


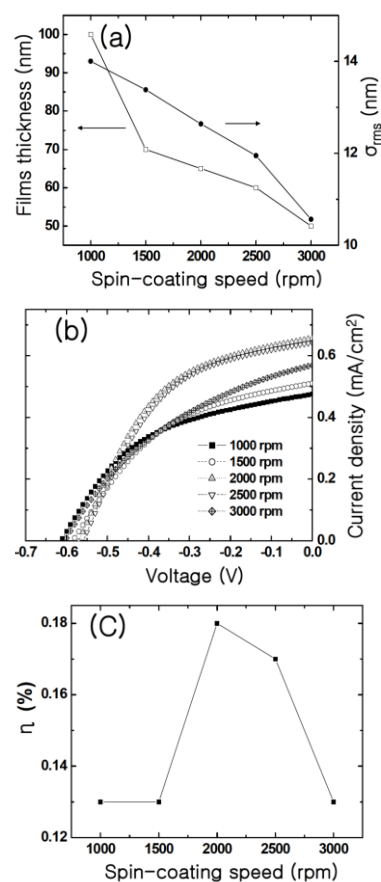
**Figure 161 - Intercalation and capacitive energy storage in titania nanoparticles. [291] Reprinted with permission from ECS Transactions.**

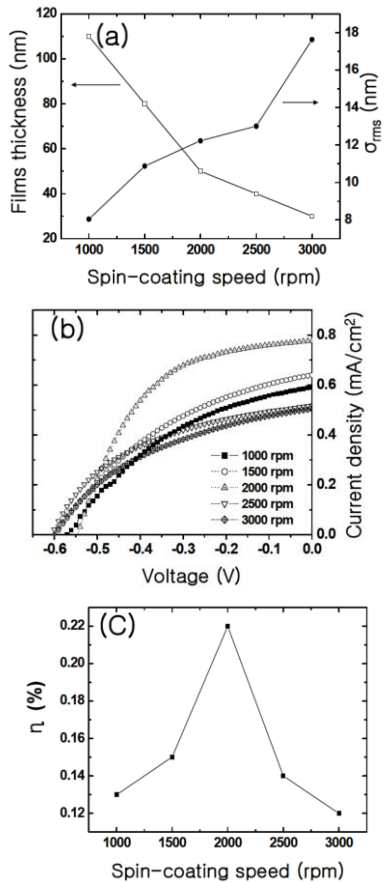
On platinum it was noted that impedance analysis can be used to separate hydrogen adsorption from H<sub>2</sub> evolution by frequency-dependence of the two processes. It was shown that hydrogen adsorption reaction is faster than H<sub>2</sub> evolution. There is a capacitive peak associated with the hydrogen adsorption and appears in the higher frequency region. The H<sub>2</sub> evolution reaction is characterized by a resistive tail that is relevant to the total capacitance (C<sub>dl</sub> + C<sub>p</sub>), and can be assessed simply from the area of the capacitive peak on imaginary capacitance plots or from the real part of the complex capacitance at the low frequency limit. It was noted that this method cannot be employed in the potential range where H<sub>2</sub> evolution is severe [290]. Pseudocapacitive behaviour is expected in our system, and will be described further when discussing the the experimental results.

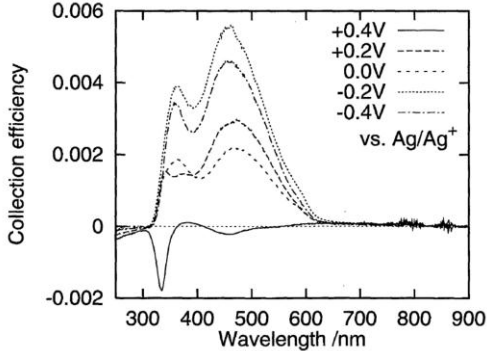
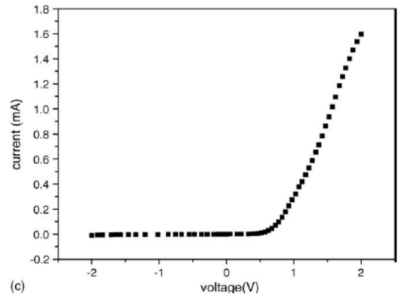
## Appendix Q - Photovoltaic Device Benchmarks

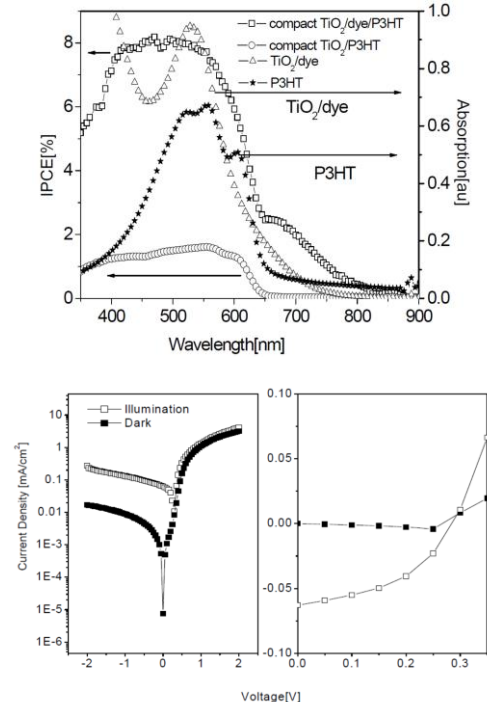
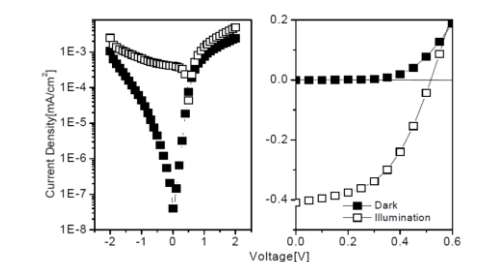
Images in table are reprinted with permission from appropriate references where applicable.

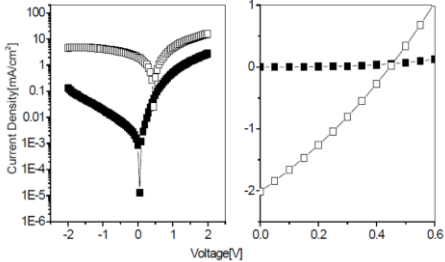
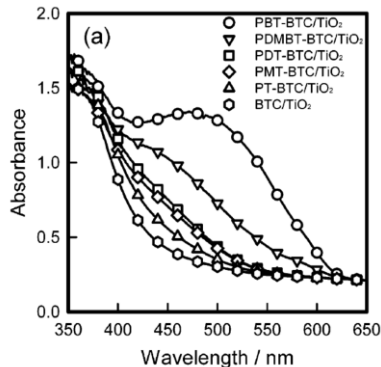
Section	Ref.	Device Type / Diagrams	Thickness (nm)	Length (mm)	Width (mm)	Q.E. (%)	F.F. (%)	V <sub>oc</sub> (V)	i <sub>sc</sub> (mAcm <sup>-2</sup> )	η <sub>cell</sub> (%)	P <sub>hv</sub> (mWcm <sup>-2</sup> )	Σλ (nm)
16	[292]	 <p>A schematic diagram of a photovoltaic device structure. It shows a cross-section with layers: Al (top), CdSe/P3HT Blend, PEDOT:PSS, Substrate, and ITO. An external circuit is connected between the Al and ITO layers. Below the schematic is a graph labeled 'A' showing External Quantum Efficiency (%) on the y-axis (0 to 60) versus Wavelength (nm) on the x-axis (400 to 700). The graph shows three curves representing different device configurations. The top curve peaks at approximately 55% efficiency around 500 nm. The middle curve peaks at approximately 45% efficiency around 500 nm. The bottom curve peaks at approximately 20% efficiency around 500 nm. A small grey circle is marked on the bottom curve at approximately 500 nm. The caption below the graph is 'CdSe nanorods - P3HT'.</p>	200	1.5	2	54	0.6	0.5	0.019	6.9	0.084	515
16	Ibid.	Ibid.	200	1.5	2	-	0.4	0.7	5.7	1.7	100	AM 1.5G
13	[293]	<p>TiO<sub>2</sub> - PPy Bilayer ITO-500nmTiO<sub>2</sub>-400nmPPy-Al</p>	900	5	5	-	-	-	0.002	-	diode study	-

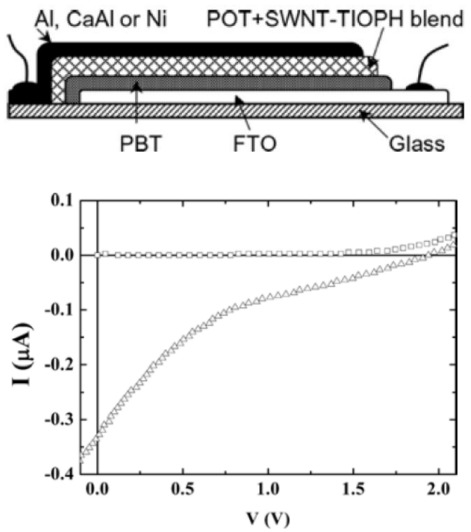
Section	Ref.	Device Type / Diagrams	Thickness (nm)	Length (mm)	Width (mm)	Q.E. (%)	F.F. (%)	$V_{oc}$ (V)	$i_{sc}$ (mA/cm <sup>2</sup> )	$\eta_{cell}$ (%)	$P_{hv}$ (mW/cm <sup>2</sup> )	$\Sigma\lambda$ (nm)
15	[176]	Rough TiO <sub>2</sub> -P3HT/TiO <sub>2</sub> composite-P3HT Trilayer ITO-TiO <sub>2</sub> -65nmTiO <sub>2</sub> /P3HT-80nmP3HT-Au  <p>(a) Film thickness (nm) and <math>\sigma_{rms}</math> (nm) vs Spin-coating speed (rpm). Film thickness decreases from ~95 nm at 1000 rpm to ~50 nm at 3000 rpm. <math>\sigma_{rms}</math> decreases from ~14 nm at 1000 rpm to ~10 nm at 3000 rpm.</p> <p>(b) Current density (mA/cm<sup>2</sup>) vs Voltage (V) for spin-coating speeds: 1000 rpm (squares), 1500 rpm (circles), 2000 rpm (triangles), 2500 rpm (inverted triangles), 3000 rpm (diamonds). Current density increases with voltage and is higher for higher spin-coating speeds.</p> <p>(c) <math>\eta</math> (%) vs Spin-coating speed (rpm). Efficiency peaks at 2000 rpm (~0.18) and is lowest at 1000 rpm and 3000 rpm (~0.13).</p>	-	-	-	-	0.48	0.56	0.657	0.18	100	AM 1.5G
15	Ibid.	TiO <sub>2</sub> -P3HT Bilayer ITO-TiO <sub>2</sub> -80nmP3HT-Au	-	-	-	-	-	0.52	0.277	0.06	100	AM 1.5G

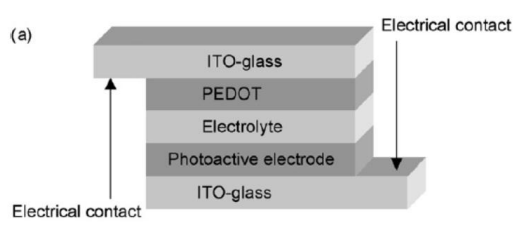
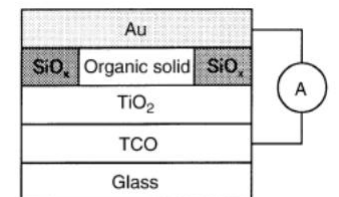
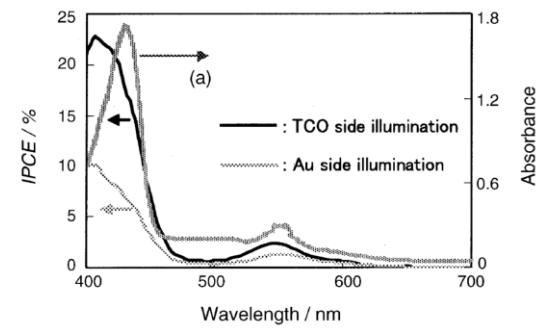
Section	Ref.	Device Type / Diagrams	Thickness (nm)	Length (mm)	Width (mm)	Q.E. (%)	F.F. (%)	V <sub>oc</sub> (V)	i <sub>sc</sub> (mA/cm <sup>2</sup> )	η <sub>cell</sub> (%)	P <sub>hv</sub> (mW/cm <sup>2</sup> )	Σλ (nm)
15	Ibid.	<p>Rough TiO<sub>2</sub>-P3HT Bilayer ITO-TiO<sub>2</sub>-50nmPEG/TiO<sub>2</sub>-80nmP3HT-Au</p>  <p>(a) Film thickness (nm) and <math>\sigma_{rms}</math> (nm) vs. Spin-coating speed (rpm). Film thickness decreases from ~110 nm at 1000 rpm to ~30 nm at 3000 rpm. <math>\sigma_{rms}</math> increases from ~8 nm at 1000 rpm to ~17 nm at 3000 rpm.</p> <p>(b) Current density (mA/cm<sup>2</sup>) vs. Voltage (V) for spin-coating speeds: 1000 rpm (squares), 1500 rpm (circles), 2000 rpm (triangles), 2500 rpm (inverted triangles), and 3000 rpm (diamonds). Current density increases with voltage and is highest for 1500 rpm.</p> <p>(c) Efficiency η (%) vs. Spin-coating speed (rpm). Efficiency peaks at ~0.22% at 2000 rpm.</p>	-	-	-	-	0.51	0.55	0.78	0.22	100	AM 1.5G
15	[72]	<p>TiO<sub>2</sub>-PBT Bilayer ITO-250nmTiO<sub>2</sub>-300nmPTh-Au</p>	-	10	10	-	0.37	0.278	0.078	0.008	100	AM 1.5G

Section	Ref.	Device Type / Diagrams	Thickness (nm)	Length (mm)	Width (mm)	Q.E. (%)	F.F. (%)	V <sub>oc</sub> (V)	i <sub>sc</sub> (mAcm <sup>-2</sup> )	η <sub>cell</sub> (%)	P <sub>hv</sub> (mWcm <sup>-2</sup> )	Σλ (nm)
15	Ibid.	 <p>Collection efficiency vs. Wavelength /nm for various bias voltages (+0.4V, +0.2V, 0.0V, -0.2V, -0.4V) vs. Ag/Ag<sup>+</sup>.</p>	-	10	10	-	-	-	-	-	150W Xe	-
18	[198]	<p>P3MT-co-3OCT-PEDOT Bilayer ITO-P3MTco3OT-POMOIE-PEDOT-ITO</p>	-	10	10	-	-	0.165	0.00021	-	100	-
14	[294]	<p>TiO<sub>2</sub>-MEHPPV Bilayer ITO-TiO<sub>2</sub>-450nm MEHPPV-Ag</p>	-	5.66	5.66	-	-	0.74	0.42	-	100	AM1.5G
12	[295]	<p>ITO-TiO<sub>2</sub>-PAni-ITO</p>  <p>current (mA) vs. voltage (V) for ITO-TiO<sub>2</sub>-PAni-ITO.</p>	-	-	-	-	-	-	-	-	diode study	-

Section	Ref.	Device Type / Diagrams	Thickness (nm)	Length (mm)	Width (mm)	Q.E. (%)	F.F. (%)	V <sub>oc</sub> (V)	i <sub>sc</sub> (mAcm <sup>-2</sup> )	η <sub>cell</sub> (%)	P <sub>hv</sub> (mWcm <sup>-2</sup> )	Σλ (nm)
15	[296]	<p>ITO-compactTiO<sub>2</sub>-porousTiO<sub>2</sub>-P3HT-Au</p>  <p>The figure contains three plots. The top plot shows IPCE [%] (left y-axis, 0 to 8) and Absorption [a.u.] (right y-axis, 0.0 to 1.0) versus Wavelength [nm] (x-axis, 400 to 900). Four data series are shown: compact TiO<sub>2</sub>/dye/P3HT (open squares), compact TiO<sub>2</sub>/P3HT (open circles), TiO<sub>2</sub>/dye (open triangles), and P3HT (filled stars). Arrows indicate the corresponding y-axis for each series. The bottom-left plot shows Current Density [mA/cm<sup>2</sup>] (logarithmic y-axis, 1E-6 to 10) versus Voltage [V] (x-axis, -2 to 2) for 'Illumination' (open squares) and 'Dark' (filled squares) conditions. The bottom-right plot shows Current Density [mA/cm<sup>2</sup>] (linear y-axis, -0.10 to 0.10) versus Voltage [V] (x-axis, 0.0 to 0.3) for 'Illumination' (open squares) and 'Dark' (filled squares) conditions.</p>	-	-	-	-	0.5	0.5	0.4	-	100	AM 1.5G
15	Ibid.	<p>ITO-porousTiO<sub>2</sub>-P3HT-Au</p>  <p>The figure contains two plots. The left plot shows Current Density [mA/cm<sup>2</sup>] (logarithmic y-axis, 1E-8 to 1E-3) versus Voltage [V] (x-axis, -2 to 2) for 'Dark' (filled squares) and 'Illumination' (open squares) conditions. The right plot shows Current Density [mA/cm<sup>2</sup>] (linear y-axis, -0.4 to 0.2) versus Voltage [V] (x-axis, 0.0 to 0.6) for 'Dark' (filled squares) and 'Illumination' (open squares) conditions.</p>	-	-	-	-	0.43	0.3	0.06	-	100	AM 1.5G

Section	Ref.	Device Type / Diagrams	Thickness (nm)	Length (mm)	Width (mm)	Q.E. (%)	F.F. (%)	V <sub>oc</sub> (V)	i <sub>sc</sub> (mAcm <sup>-2</sup> )	η <sub>cell</sub> (%)	P <sub>hv</sub> (mWcm <sup>-2</sup> )	Σλ (nm)
15	Ibid.	'ITO-compactTiO <sub>2</sub> -porousTiO <sub>2</sub> -RuDye-P3HT-Au 	-	-	-	-	0.3	0.45	2	-	100	AM 1.5G
15	[80]	Pth in TiO <sub>2</sub> monolith pores with carboxylate linker FTO-6-7μmTiO <sub>2</sub> mesopore-bithiophene-5-carboxylic acid 3,3'- dimethyl-2,2'-bithiophene-0.6 M dimethylpropylimidazolium iodide, 0.05 M iodine , 0.1 M lithium iodide, 0.5 M tert- butylpyridine in acetonitrile-Pt 	-	-	-	-	0.46	0.38	0.92	0.16	100	AM 1.5G

Section	Ref.	Device Type / Diagrams	Thickness (nm)	Length (mm)	Width (mm)	Q.E. (%)	F.F. (%)	$V_{oc}$ (V)	$i_{sc}$ ( $\text{mAcm}^{-2}$ )	$\eta_{cell}$ (%)	$P_{hv}$ ( $\text{mWcm}^{-2}$ )	$\Sigma\lambda$ (nm)
17	[74]	<p>CNT/P3OT Composite-PBT Bilayer</p> 	360	-	-	-	-	1.81	0.00032	1.48	1.55	AM 1.5G
14	[297]	<p>TiO<sub>2</sub>/PVC Bilayer</p> <p>ITO/TiO<sub>2</sub>/PVC-LiClO<sub>4</sub>/graphite</p>	-	-	-	-	-	0.18	0.00095	-	100	W- Halo gen
15	[298]	<p>TiO<sub>2</sub>-poly(3-undecyl-2,2-bithiophene) Bilayer</p> <p>ITO-TiO<sub>2</sub>-poly(3-undecyl-2,2-bithiophene)-C-Cu</p>	-	2	2	-	-	0.7	0.055	-	100	AM1. 5G

Section	Ref.	Device Type / Diagrams	Thickness (nm)	Length (mm)	Width (mm)	Q.E. (%)	F.F. (%)	V <sub>oc</sub> (V)	i <sub>sc</sub> (mAcm <sup>-2</sup> )	η <sub>cell</sub> (%)	P <sub>hv</sub> (mWcm <sup>-2</sup> )	Σλ (nm)
15	[299]	<p>Composite TiO<sub>2</sub>/P3HT-P3HT Bilayer</p> 	-	-	-	-	0.51	0.51	0.31	-	100	White
14	[300]	<p>TiO<sub>2</sub>-P3HT/Zn-TPP Composite Bilayer</p> 	-	-	-	-	0.48	0.5	1.11	0.26	100	AM 1.5G
15	Ibid.	<p>TiO<sub>2</sub>-P3HT Bilayer</p> 	-	-	-	-	0.31	0.24	0.34	0.025	100	AM 1.5G

Section	Ref.	Device Type / Diagrams	Thickness (nm)	Length (mm)	Width (mm)	Q.E. (%)	F.F. (%)	V <sub>oc</sub> (V)	i <sub>sc</sub> (mAcm <sup>-2</sup> )	η <sub>cell</sub> (%)	P <sub>hv</sub> (mWcm <sup>-2</sup> )	Σλ (nm)
15	[192]	<p>TiO<sub>2</sub>-P3HT/PCBM Composite Bilayer</p> <p>With TiO<sub>x</sub> in air</p> <p>J<sub>sc</sub> (mA/cm<sup>2</sup>)</p> <p>V<sub>oc</sub> (V)</p> <p>Efficiency (%)</p> <p>Illumination (min)</p>	-	0.8	0.8	-	0.49	0.38	9.13	1.74	-	AM 1.5G

## Appendix R - Photochemical Device Benchmarks

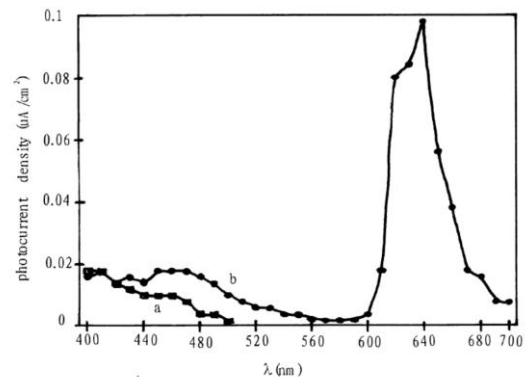
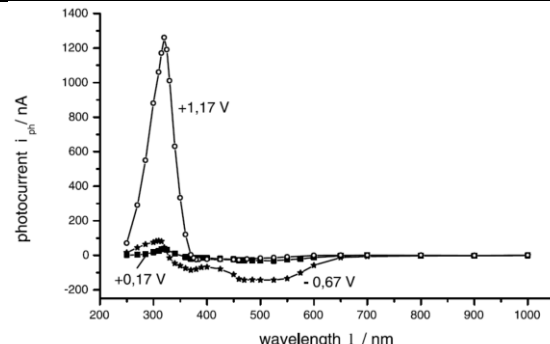
Images in table are reprinted with permission from appropriate references where applicable.

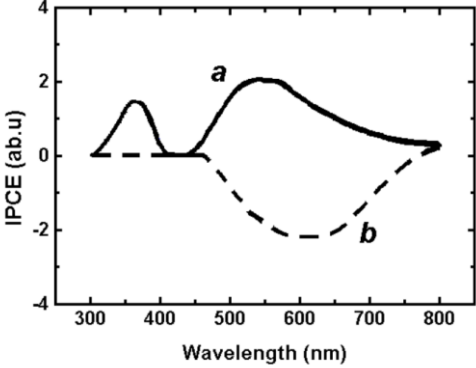
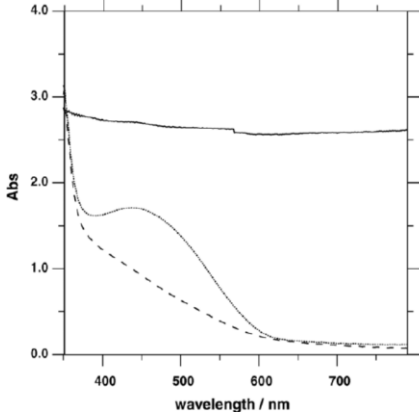
Section	Ref.	Device Type / Diagrams	Detail	Phv (mWcm-2)	$\Sigma\lambda$ (nm)
8	[181]	<p>TiO<sub>2</sub> nanotube-PTh Bilayer</p>	<p>(a) Original dye concentration <math>1.23 \times 10^{-4}</math> M</p>	120W Na	400-800
8	[93]	<p>TiO<sub>2</sub>-P3HT Composite</p> <p>Evaporated on Glass beaker filled with Orange G</p>	<p>Original dye concentration <math>10^{-4}</math> M</p>	125W Hg	~365

Section	Ref.	Device Type / Diagrams	Detail	Phv (mWcm-2)	$\Sigma\lambda$ (nm)
8	[301]	PT-TiO <sub>2</sub> Composite Evaporated on Glass filled with Methyl Orange	<p style="text-align: center;">Original dye concentration 40ppm</p> <p style="text-align: center;">Experimental time(min)</p>	20W	~253

## Appendix S - Photoelectrochemical Device Benchmarks

Images in table are reprinted with permission from appropriate references where applicable.

Section	Ref.	Device Type / Diagrams	Detail	Phv (mWcm-2)	$\Sigma\lambda$ (nm)
19	[302]	TiO <sub>2</sub> -PAni Bilayer ITO-TiO <sub>2</sub> -PAni   0.04M KHC <sub>8</sub> H <sub>4</sub> O <sub>4</sub> , 0.1M KI, 2 $\mu$ M I <sub>2</sub>  Pt	 <p>Fig. 6. Photocurrent action spectra of TiO<sub>2</sub> nanoporous film electrode (a) and the nanostructured TiO<sub>2</sub>/PAn film electrode (b) in pH = 4, 0.04 M KHC<sub>8</sub>H<sub>4</sub>O<sub>4</sub> buffer containing 0.1 M KI and 2 <math>\mu</math>M I<sub>2</sub>. Bias: -0.1 V (SCE).</p>	200W Xenon lamp	-
1	[69]	TiO <sub>2</sub> -Pth Core-Shell Pressed Composite "Island like"pressed on Pt   0.5M LiClO <sub>4</sub> in CH <sub>3</sub> CN   Pt	 <p>Fig. 10. Photocurrent (<math>i_{ph}</math>) spectra of 25 nm TiO<sub>2</sub> (P25) /polythiophene (PT) composites at different potentials (vs. NHE).</p>	1000 W Xenon lamp	-

Section	Ref.	Device Type / Diagrams	Detail	Phv (mWcm-2)	$\Sigma\lambda$ (nm)
19		<p style="text-align: center;">TiO<sub>2</sub>-Pani Composite-PATP Bilayer</p> <p style="text-align: center;">Au-PATP-Pani/TiO<sub>2</sub> 0.05 M K<sub>3</sub>Fe(CN)<sub>6</sub>/ K<sub>4</sub>Fe(CN)<sub>6</sub>   Pt</p>	 <p style="text-align: center;">Fig. 5. Photocurrent spectra of the TiO<sub>2</sub>/PANI/PATP film on a Au electrode at 0.7 V (a) and 0 V (b) in 0.05 M K<sub>3</sub>Fe(CN)<sub>6</sub> / K<sub>4</sub>Fe(CN)<sub>6</sub> aqueous solution.</p>	150W Xenon lamp	-
1	[303]	<p style="text-align: center;">Mesoporous TiO<sub>2</sub>-PBT Bilayer</p> <p style="text-align: center;">OTE/TiO<sub>2</sub>/PBT   0.1M LiClO<sub>4</sub> in Acetonitrile   Pt</p>	 <p style="text-align: center;">Fig. 6. Absorption UV-vis spectra recorded for the PBT/nanoporous TiO<sub>2</sub>/0.1 M LiClO<sub>4</sub> ACN solution. Applied potential: 0.0 V (dotted line), 1.0 V (dashed line) and -1.2 V (solid line). <i>T</i> = 298 K.</p>	Electro- chromic Response	-

## Appendix T - Calibration Curves

### T.1 Calibration Curve for Peristaltic Pump

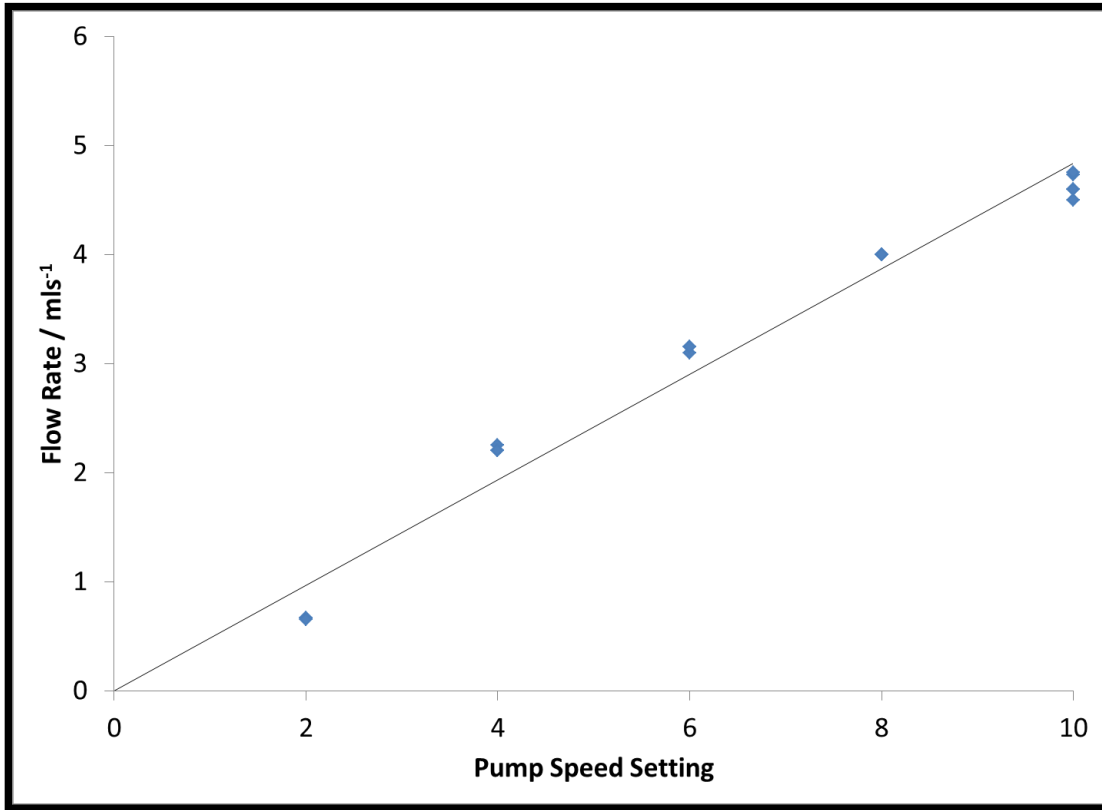


Figure 162 - Peristaltic pump flowrate calibration curve. Line is added for illustrative purposes.

## T.2 Calibration Curve for Solar Simulator Output

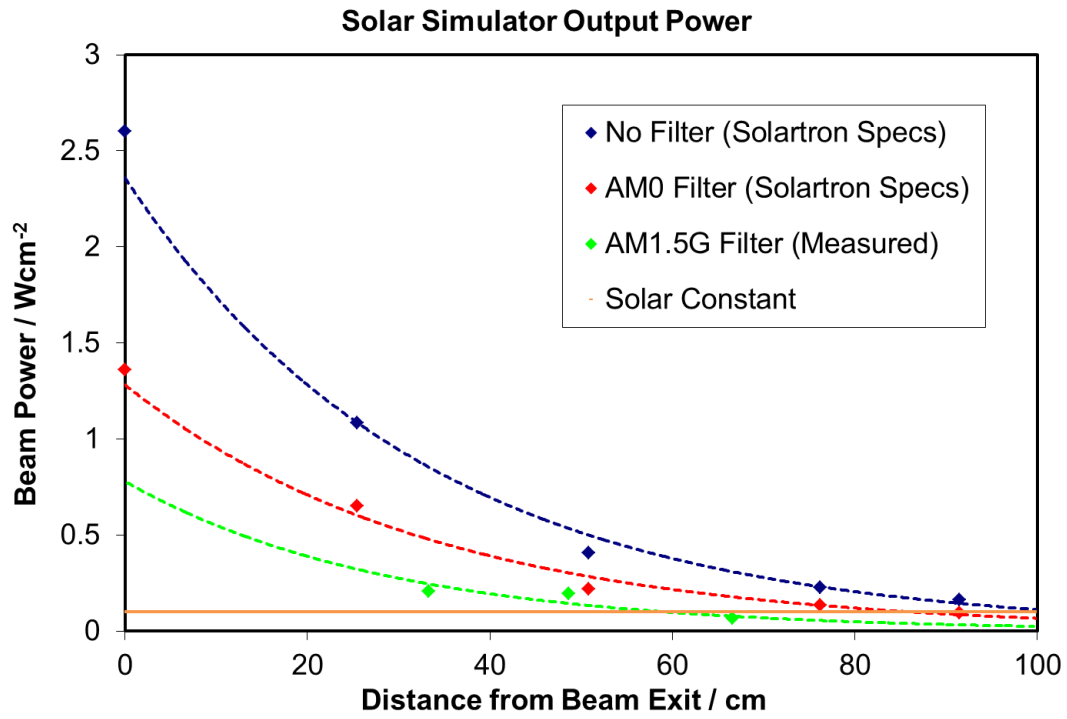


Figure 163 - Solar simulator calibration curve. Lines are added for illustrative purposes.

### T.3 Calibration Curve of ICP-MS

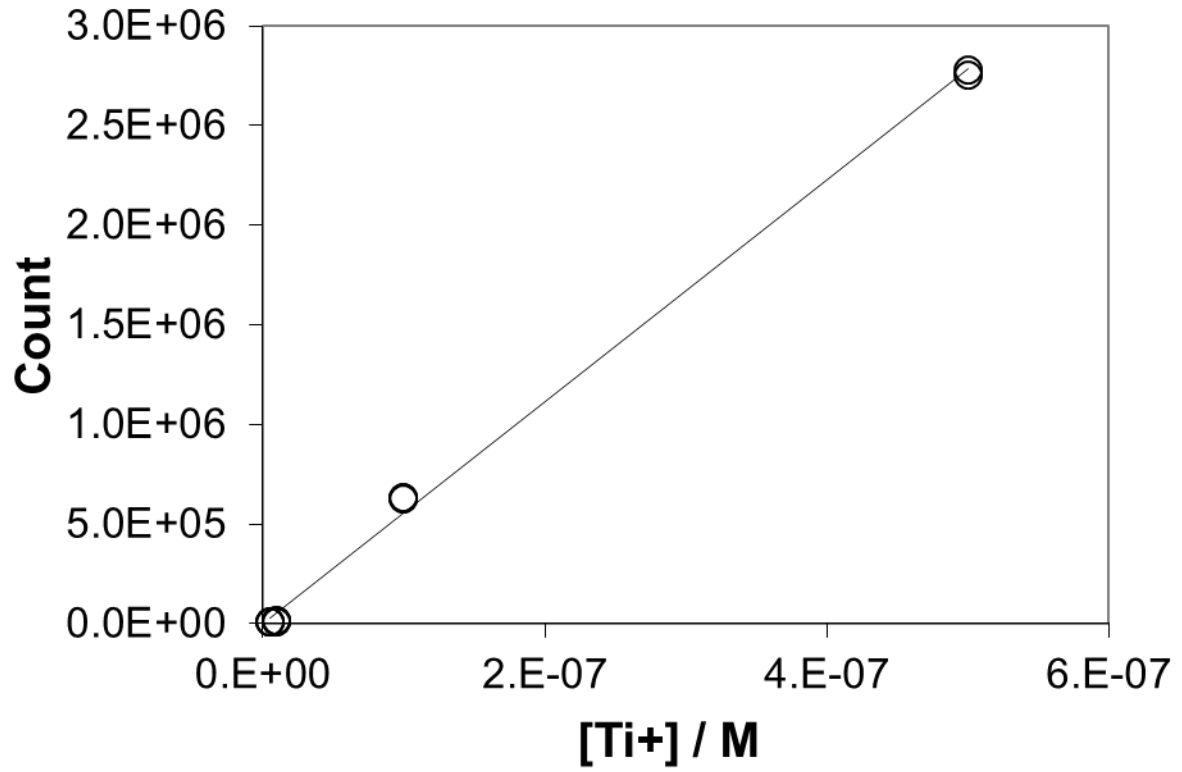


Figure 164 - Titanium Ion Calibration Curve for ICP-MS. Line is added for illustrative purposes.

## Appendix U - Paired Statistical Analysis

### U.1 PBT Film Thicknesses

Comparison: PBT film thicknesses

Data: 646s PBT

j [ $\mu\text{A}/\text{cm}^2$ ]	$E_{\text{dark}}$ vs SHE
10	-0.194
20	-0.281
40	-0.372
80	-0.467
160	-0.568
320	-0.667
Ave ( $\mu_1$ )	-0.425

Data: 1292s PBT

j [ $\mu\text{A}/\text{cm}^2$ ]	$E_{\text{dark}}$ vs SHE
10	-0.158
20	-0.206
40	-0.308
80	-0.386
160	-0.481
320	-0.606
Ave ( $\mu_2$ )	-0.358

j [ $\mu\text{A}/\text{cm}^2$ ]	$d_i$
10	-0.035
20	-0.075
40	-0.064
80	-0.080
160	-0.087
320	-0.061
Ave ( $\bar{d}$ )	-0.067

$(d_i - \bar{d})^2$	
0.00101	
0.00006	
0.00001	
0.00017	
0.00039	
0.00004	
Sum	0.00168

Assume populations are normally distributed and have equivalent variance.

Using a paired analysis:  $H_0: \mu_1 - \mu_2 = \mu_D = 0$

$H_1: \mu_1 - \mu_2 \neq 0$

using a 95% confidence interval,  $v = 5$ :

$$s = \sqrt{(\sum (d_i - \bar{d})^2 / (n - 1))} = 1.674\text{E-}02$$

$$SE = s / \sqrt{n} = 6.833\text{E-}03$$

$$t = [(x_1 - x_2) - D] / SE = -9.833\text{E+}00$$

$$P(t < -9.83318) = 1.853\text{E-}04$$

$$P\text{-value} = 3.706\text{E-}04$$

Since P-value is less than the significance level (0.05) we reject the null hypothesis.

Therefore there is a statistical difference in the two thicknesses of PBT

## U.2 1292s PBT vs. PBT-TiO<sub>2</sub>

Comparison: PBT vs. PBT/TiO<sub>2</sub> @ 1 thickness

Data: 1292s PBT

j [ $\mu\text{A}/\text{cm}^2$ ]	E <sub>dark</sub> vs SHE
10	-0.158
20	-0.206
40	-0.308
80	-0.386
160	-0.481
320	-0.606

Ave ( $\mu_1$ ) -0.358

Data: 1292s PBT-TiO<sub>2</sub>

j [ $\mu\text{A}/\text{cm}^2$ ]	E <sub>dark</sub> vs SHE
10	-0.075
20	-0.171
40	-0.226
80	-0.296
120	-0.340
160	-0.370
200	-0.392
240	-0.421
320	-0.453

Ave ( $\mu_2$ ) -0.246

j [ $\mu\text{A}/\text{cm}^2$ ]	d <sub>i</sub>
10	-0.083
20	-0.035
40	-0.082
80	-0.091
160	-0.111
320	-0.153

Ave ( $\bar{d}$ ) -0.093

(d <sub>i</sub> - $\bar{d}$ ) <sup>2</sup>
0.00486
0.01381
0.00499
0.00388
0.00177
0.00000

Sum 0.02929

Assume populations are normally distributed and have equivalent variance.

Using a paired analysis: H<sub>0</sub>:  $\mu_1 - \mu_2 = \mu_D = 0$

H<sub>1</sub>:  $\mu_1 - \mu_2 \neq 0$

using a 95% confidence interval,  $\nu = 5$ :

$$s = \sqrt{\frac{\sum (d_i - \bar{d})^2}{(n - 1)}} = 7.654\text{E-}02$$

$$SE = s / \sqrt{n} = 3.125\text{E-}02$$

$$t = \frac{(\bar{x}_1 - \bar{x}_2) - D}{SE} = 7.876\text{E+}00$$

$$P(t < 7.876) = 5.303\text{E-}04$$

$$P\text{-value (2 tailed)} = 1.061\text{E-}03$$

Since P-value is less than the significance level (0.05) we reject the null hypothesis.

Therefore there is a statistical difference between the PBT and PBT-TiO<sub>2</sub>

### U.3 1292s PBT-TiO<sub>2</sub> vs. PBT-TiO<sub>2</sub>:Pt

Comparison: PBT/TiO<sub>2</sub>:Pt vs. PBT/TiO<sub>2</sub> @ 1 thickness

Data: 1292s PBT-TiO<sub>2</sub>

j [ $\mu\text{A}/\text{cm}^2$ ]	E <sub>dark</sub> vs SHE
10	-0.075
20	-0.171
40	-0.226
80	-0.296
120	-0.340
160	-0.370
200	-0.392
240	-0.421
320	-0.453

Ave ( $\mu_1$ ) -0.305

Data: 1292s PBT-TiO<sub>2</sub>:Pt

j [ $\mu\text{A}/\text{cm}^2$ ]	E <sub>dark</sub> vs SHE
10	-0.255
20	-0.326
40	-0.395
80	-0.477
120	-0.528
160	-0.566
200	-0.616
240	-0.636
320	-0.665

Ave ( $\mu_2$ ) -0.496

j [ $\mu\text{A}/\text{cm}^2$ ]	d <sub>i</sub>
10	0.180
20	0.155
40	0.170
80	0.182
120	0.188
160	0.196
200	0.224
240	0.214
320	0.212

Ave ( $\bar{d}$ ) 0.191

(d <sub>i</sub> - $\bar{d}$ ) <sup>2</sup>
0.00026
0.00173
0.00072
0.00022
0.00007
0.00000
0.00075
0.00032
0.00025

Sum 0.00431

Assume populations are normally distributed and have equivalent variance.

Using a paired analysis: H<sub>0</sub>:  $\mu_1 - \mu_2 = \mu_D = 0$

H<sub>1</sub>:  $\mu_1 - \mu_2 \neq 0$

using a 95% confidence interval,  $\nu = 8$ :

$$s = \sqrt{\frac{\sum (d_i - \bar{d})^2}{(n - 1)}} = 2.321\text{E-}02$$

$$SE = s / \sqrt{n} = 7.736\text{E-}03$$

$$t = \frac{(\bar{x}_1 - \bar{x}_2) - D}{SE} = 2.472\text{E+}01$$

$$P(t < 24.72) = 7.664\text{E-}09$$

$$P\text{-value (2 tailed)} = 1.533\text{E-}08$$

Since P-value is less than the significance level (0.05) we reject the null hypothesis.

Therefore there is a statistical difference between the PBT-TiO<sub>2</sub> and PBT-TiO<sub>2</sub>:Pt

## U.4 Increased Titania Content by Film Thickness for 3-D Films Facing Out

Comparison: ( 3-D | pH3 | Thickness | F.O. constant) TiO<sub>2</sub> variation

Data: 1 μm 0.02 mg/cm<sup>2</sup> TiO<sub>2</sub>

j [μA/cm <sup>2</sup> ]	E <sub>dark</sub> vs SHE
10	-0.154
20	-0.222
40	-0.278
80	-0.347
120	-0.396
160	-0.435
200	-0.471
240	-0.507
320	-0.562
640	-0.658
960	-0.752
1280	-0.873

Ave (μ<sub>1</sub>) -0.375

Data: 1 μm 0.15 mg/cm<sup>2</sup> TiO<sub>2</sub>

j [μA/cm <sup>2</sup> ]	E <sub>dark</sub> vs SHE
10	-0.239
20	-0.359
40	-0.454
80	-0.551
120	-0.613
160	-0.649
200	-0.673
240	-0.695
320	-0.736

Ave (μ<sub>2</sub>) -0.552

j [μA/cm <sup>2</sup> ]	d <sub>i</sub>	(d <sub>i</sub> - $\bar{d}$ ) <sup>2</sup>
10	0.085	0.00852
20	0.137	0.00166
40	0.175	0.00000
80	0.204	0.00070
120	0.218	0.00161
160	0.214	0.00133
200	0.202	0.00060
240	0.188	0.00011
320	0.175	0.00001

Ave ( $\bar{d}$ ) 0.177 Sum 0.01455

Assume populations are normally distributed and have equivalent variance.

Using a paired analysis: H<sub>0</sub>: μ<sub>1</sub> - μ<sub>2</sub> = μ<sub>D</sub> = 0

H<sub>1</sub>: μ<sub>1</sub> - μ<sub>2</sub> ≠ 0

using a 95% confidence interval, v = 8:

$$s = \sqrt{[\sum(d_i - \bar{d})^2 / (n - 1)]} = 4.264E-02$$

$$SE = s / \sqrt{n} = 1.421E-02$$

$$t = [(x_1 - x_2) - D] / SE = 1.249E+01$$

$$P(t < 12.49) = 1.583E-06$$

$$P\text{-value (2 tailed)} = 3.167E-06$$

Since P-value is less than the significance level (0.05) we reject the null hypothesis.

Therefore there is a statistical difference in the two loadings at 1 μm

Data: 10 μm 0.02 mg/cm<sup>2</sup> TiO<sub>2</sub>

j [μA/cm <sup>2</sup> ]	E <sub>dark</sub> vs SHE
10	-0.155
20	-0.220
40	-0.273
80	-0.342
120	-0.400
160	-0.454
200	-0.511
240	-0.553
320	-0.601
640	-0.714
960	-0.818
Ave (μ <sub>1</sub> )	-0.390

Data: 10 μm 0.15 mg/cm<sup>2</sup> TiO<sub>2</sub>

j [μA/cm <sup>2</sup> ]	E <sub>dark</sub> vs SHE
10	-0.078
20	-0.179
40	-0.312
80	-0.458
120	-0.549
160	-0.619
200	-0.673
240	-0.716
320	-0.772
Ave (μ <sub>2</sub> )	-0.484

j [μA/cm <sup>2</sup> ]	d <sub>i</sub>	(d <sub>i</sub> - $\bar{d}$ ) <sup>2</sup>
10	-0.077	0.06495
20	-0.040	0.04751
40	0.039	0.01916
80	0.116	0.00377
120	0.149	0.00083
160	0.164	0.00017
200	0.162	0.00022
240	0.163	0.00022
320	0.171	0.00004
Ave ( $\bar{d}$ )	0.094	Sum 0.13687

Assume populations are normally distributed and have equivalent variance.

Using a paired analysis: H<sub>0</sub>: μ<sub>1</sub> - μ<sub>2</sub> = μ<sub>D</sub> = 0

H<sub>1</sub>: μ<sub>1</sub> - μ<sub>2</sub> ≠ 0

using a 95% confidence interval, v = 8:

$$s = \sqrt{(\sum(d_i - \bar{d})^2 / (n - 1))} = 1.308E-01$$

$$SE = s / \sqrt{n} = 4.360E-02$$

$$t = [(x_1 - x_2) - D] / SE = 2.157E+00$$

$$P(t < 2.157) = 6.311E-02$$

$$P\text{-value (2 tailed)} = 1.262E-01$$

Since P-value is greater than the significance level (0.05) we fail to reject the null hypothesis.

Therefore there is no statistical difference in the two loadings at 10 μm thickness

## U.5 Increased Film Thickness by Titania Content for 3-D Films Facing Out

Comparison: ( 3-D | pH3 | TiO<sub>2</sub> | F.O. constant) Thickness 1 μm vs. 10 μm

Data: 1 μm 0.02 mg/cm<sup>2</sup> TiO<sub>2</sub>

j [μA/cm <sup>2</sup> ]	E <sub>dark</sub> vs SHE
10	-0.154
20	-0.222
40	-0.278
80	-0.347
120	-0.396
160	-0.435
200	-0.471
240	-0.507
320	-0.562
640	-0.658
960	-0.752
1280	-0.873

Ave (μ1) -0.435

Data: 10 μm 0.02 mg/cm<sup>2</sup> TiO<sub>2</sub>

j [μA/cm <sup>2</sup> ]	E <sub>dark</sub> vs SHE
10	-0.155
20	-0.220
40	-0.273
80	-0.342
120	-0.400
160	-0.454
200	-0.511
240	-0.553
320	-0.601
640	-0.714
960	-0.818

Ave (μ2) -0.458

j [μA/cm <sup>2</sup> ]	d <sub>i</sub>	(d <sub>i</sub> -d̄) <sup>2</sup>
10	0.001	0.00050
20	-0.002	0.00067
40	-0.006	0.00085
80	-0.005	0.00083
120	0.004	0.00037
160	0.019	0.00002
200	0.040	0.00026
240	0.047	0.00053
320	0.040	0.00025
640	0.056	0.00103
960	0.066	0.00180

Ave (d̄) 0.024 Sum 0.00428

Assume populations are normally distributed and have equivalent variance.

Using a paired analysis: H<sub>0</sub>: μ<sub>1</sub> - μ<sub>2</sub> = μ<sub>D</sub> = 0

H<sub>1</sub>: μ<sub>1</sub> - μ<sub>2</sub> ≠ 0

using a 95% confidence interval, v = 10:

$$s = \sqrt{(\sum(d_i - \bar{d})^2 / (n - 1))} = 2.069E-02$$

$$SE = s / \sqrt{n} = 6.238E-03$$

$$t = [(x_1 - x_2) - D] / SE = 3.775E+00$$

$$P(t < 3.775) = 3.634E-03$$

$$P\text{-value (2 tailed)} = 7.269E-03$$

Since P-value is less than the significance level (0.05) we reject the null hypothesis.

Therefore there is a statistical difference in the two thicknesses at 0.02 mg/cm<sup>2</sup> TiO<sub>2</sub>

Data: 1 μm 0.15 mg/cm<sup>2</sup> TiO<sub>2</sub>

j [μA/cm <sup>2</sup> ]	E <sub>dark</sub> vs SHE
10	-0.239
20	-0.359
40	-0.454
80	-0.551
120	-0.613
160	-0.649
200	-0.673
240	-0.695
320	-0.736

Ave (μ<sub>1</sub>) -0.552

Data: 10 μm 0.15 mg/cm<sup>2</sup> TiO<sub>2</sub>

j [μA/cm <sup>2</sup> ]	E <sub>dark</sub> vs SHE
10	-0.078
20	-0.179
40	-0.312
80	-0.458
120	-0.549
160	-0.619
200	-0.673
240	-0.716
320	-0.772

Ave (μ<sub>2</sub>) -0.484

j [μA/cm <sup>2</sup> ]	d <sub>i</sub>	(d <sub>i</sub> -d̄) <sup>2</sup>
10	-0.161	0.03420
20	-0.180	0.04127
40	-0.142	0.02742
80	-0.093	0.01357
120	-0.065	0.00776
160	-0.030	0.00286
200	0.000	0.00055
240	0.021	0.00001
320	0.036	0.00015

Ave (d̄) -0.068 Sum 0.12779

Assume populations are normally distributed and have equivalent variance.

Using a paired analysis: H<sub>0</sub>: μ<sub>1</sub> - μ<sub>2</sub> = μ<sub>D</sub> = 0

H<sub>1</sub>: μ<sub>1</sub> - μ<sub>2</sub> ≠ 0

using a 95% confidence interval, v = 8:

$$s = \sqrt{(\sum(d_i - d)^2 / (n - 1))} = 1.264E-01$$

$$SE = s / \sqrt{n} = 4.213E-02$$

$$t = [(x_1 - x_2) - D] / SE = -1.618E+00$$

$$P(t < -1.618) = 1.444E-01$$

$$P\text{-value (2 tailed)} = 2.887E-01$$

Since P-value is greater than the significance level (0.05) we fail to reject the null hypothesis.

Therefore there is no statistical difference in the two thicknesses at 0.15 mg/cm<sup>2</sup> TiO<sub>2</sub>

## U.6 Increased Titania Content by Film Thickness for 3-D Films Facing Out

Comparison: ( 3-D | pH3 | Thickness | F.I. constant)  $\text{TiO}_2$  variation

Data:  $1 \mu\text{m}$   $0.02 \text{ mg/cm}^2 \text{ TiO}_2$

$j$ [ $\mu\text{A/cm}^2$ ]	$E_{\text{dark}}$ vs SHE
10	-0.185
20	-0.245
40	-0.315
80	-0.392
120	-0.445
160	-0.480
200	-0.518
240	-0.543
320	-0.584
640	-0.685
960	-0.730
1280	-0.767

Ave ( $\mu_1$ ) -0.491

Data:  $1 \mu\text{m}$   $0.15 \text{ mg/cm}^2 \text{ TiO}_2$

$j$ [ $\mu\text{A/cm}^2$ ]	$E_{\text{dark}}$ vs SHE
10	-0.151
20	-0.2
40	-0.221
80	-0.306
120	-0.356
160	-0.392
200	-0.421
240	-0.444
320	-0.3647
640	-0.526
960	-0.597
1280	-0.629

Ave ( $\mu_2$ ) -0.384

$j$ [ $\mu\text{A/cm}^2$ ]	$d_i$	$(d_i - \bar{d})^2$
10	-0.034	0.00530
20	-0.045	0.00382
40	-0.094	0.00016
80	-0.086	0.00043
120	-0.089	0.00032
160	-0.088	0.00035
200	-0.097	0.00010
240	-0.099	0.00006
320	-0.219	0.01266
640	-0.159	0.00273
960	-0.133	0.00069
1280	-0.138	0.00098

Ave ( $\bar{d}$ ) -0.107 Sum 0.02758

Assume populations are normally distributed and have equivalent variance.

Using a paired analysis:  $H_0: \mu_1 - \mu_2 = \mu_D = 0$

$H_1: \mu_1 - \mu_2 \neq 0$

using a 95% confidence interval,  $v = 11$ :

$$s = \sqrt{(\sum(d_i - \bar{d})^2 / (n - 1))} = 4.794\text{E-}02$$

$$SE = s / \sqrt{n} = 1.384\text{E-}02$$

$$t = [(x_1 - x_2) - D] / SE = -7.715\text{E+}00$$

$$P(t < -7.715) = 9.209\text{E-}06$$

$$P\text{-value (2 tailed)} = 1.842\text{E-}05$$

Since P-value is less than the significance level (0.05) we reject the null hypothesis.

Therefore there is a statistical difference in performance between the two titania concentrations at  $1 \mu\text{m}$  thickness.

Data: 10  $\mu\text{m}$  0.02  $\text{mg}/\text{cm}^2$   $\text{TiO}_2$

j [ $\mu\text{A}/\text{cm}^2$ ]	$E_{\text{dark}}$ vs SHE
10	-0.151
20	-0.230
40	-0.337
80	-0.449
120	-0.512
160	-0.549
200	-0.577
240	-0.591
320	-0.623
640	-0.703
960	-0.750
1280	-0.787

Ave ( $\mu_1$ ) -0.522

Data: 10  $\mu\text{m}$  0.15  $\text{mg}/\text{cm}^2$   $\text{TiO}_2$

j [ $\mu\text{A}/\text{cm}^2$ ]	$E_{\text{dark}}$ vs SHE
10	-0.089
20	-0.162
40	-0.26
80	-0.36
120	-0.431
160	-0.492
200	-0.542
240	-0.565
320	-0.593
640	-0.696
960	-0.763
1280	-0.806

Ave ( $\mu_2$ ) -0.480

j [ $\mu\text{A}/\text{cm}^2$ ]	$d_i$	$(d_i - \bar{d})^2$
10	-0.062	0.00200
20	-0.068	0.00150
40	-0.077	0.00089
80	-0.089	0.00032
120	-0.081	0.00065
160	-0.057	0.00253
200	-0.035	0.00515
240	-0.026	0.00652
320	-0.030	0.00589
640	-0.007	0.00996
960	0.013	0.01435
1280	0.019	0.01582

Ave ( $\bar{d}$ ) -0.042 Sum 0.06558

Assume populations are normally distributed and have equivalent variance.

Using a paired analysis:  $H_0: \mu_1 - \mu_2 = \mu_D = 0$

$H_1: \mu_1 - \mu_2 \neq 0$

using a 95% confidence interval,  $v = 11$ :

$$s = \sqrt{\frac{\sum (d_i - \bar{d})^2}{(n - 1)}} = 7.393\text{E-}02$$

$$SE = s / \sqrt{n} = 2.134\text{E-}02$$

$$t = \frac{(\bar{x}_1 - \bar{x}_2) - D}{SE} = -1.951\text{E+}00$$

$$P(t < -1.951) = 7.695\text{E-}02$$

$$P\text{-value (2 tailed)} = 1.539\text{E-}01$$

Since P-value is less than the significance level (0.05) we fail to reject the null hypothesis.

Therefore there is no statistical difference in performance for the two titania concentrations at 10  $\mu\text{m}$  thickness.

## U.7 Increased Film Thickness by Titania Content for 3-D Films Facing Out

Comparison: ( 3-D | pH3 | TiO<sub>2</sub> | F.I. constant) Thickness 1 μm vs. 10 μm

Data: 1 μm 0.02 mg/cm<sup>2</sup> TiO<sub>2</sub>

j [μA/cm <sup>2</sup> ]	E <sub>dark</sub> vs SHE
10	-0.185
20	-0.245
40	-0.315
80	-0.392
120	-0.445
160	-0.480
200	-0.518
240	-0.543
320	-0.584
640	-0.685
960	-0.730
1280	-0.767

Ave (μ1) -0.491

Data: 10 μm 0.02 mg/cm<sup>2</sup> TiO<sub>2</sub>

j [μA/cm <sup>2</sup> ]	E <sub>dark</sub> vs SHE
10	-0.151
20	-0.230
40	-0.337
80	-0.449
120	-0.512
160	-0.549
200	-0.577
240	-0.591
320	-0.623
640	-0.703
960	-0.750
1280	-0.787

Ave (μ2) -0.522

j [μA/cm <sup>2</sup> ]	d <sub>i</sub>	(d <sub>i</sub> -d̄) <sup>2</sup>
10	-0.034	0.00420
20	-0.015	0.00210
40	0.022	0.00008
80	0.057	0.00069
120	0.067	0.00132
160	0.069	0.00142
200	0.059	0.00079
240	0.048	0.00030
320	0.039	0.00007
640	0.018	0.00016
960	0.020	0.00012
1280	0.020	0.00012

Ave (d̄) 0.031 Sum 0.01136

Assume populations are normally distributed and have equivalent variance.

Using a paired analysis: H<sub>0</sub>: μ<sub>1</sub> - μ<sub>2</sub> = μ<sub>D</sub> = 0

H<sub>1</sub>: μ<sub>1</sub> - μ<sub>2</sub> ≠ 0

using a 95% confidence interval, v = 11:

$$s = \sqrt{(\sum(d_i - \bar{d})^2 / (n - 1))} = 3.077E-02$$

$$SE = s / \sqrt{n} = 8.883E-03$$

$$t = [(x_1 - x_2) - D] / SE = 3.468E+00$$

$$P(t < 3.468) = 5.256E-03$$

$$P\text{-value (2 tailed)} = 1.051E-02$$

Since P-value is less than the significance level (0.05) we reject the null hypothesis.

Therefore there is a statistical difference in the two thicknesses at 0.02 mg/cm<sup>2</sup> TiO<sub>2</sub>

Data: 1  $\mu\text{m}$  0.15  $\text{mg}/\text{cm}^2$   $\text{TiO}_2$

j [ $\mu\text{A}/\text{cm}^2$ ]	$E_{\text{dark}}$ vs SHE
10	-0.151
20	-0.2
40	-0.221
80	-0.306
120	-0.356
160	-0.392
200	-0.421
240	-0.444
320	-0.3647
640	-0.526
960	-0.597
1280	-0.629

Ave ( $\mu_1$ ) -0.384

Data: 10  $\mu\text{m}$  0.15  $\text{mg}/\text{cm}^2$   $\text{TiO}_2$

j [ $\mu\text{A}/\text{cm}^2$ ]	$E_{\text{dark}}$ vs SHE
10	-0.089
20	-0.162
40	-0.26
80	-0.36
120	-0.431
160	-0.492
200	-0.542
240	-0.565
320	-0.593
640	-0.696
960	-0.763
1280	-0.806

Ave ( $\mu_2$ ) -0.480

j [ $\mu\text{A}/\text{cm}^2$ ]	$d_i$
10	-0.062
20	-0.038
40	0.039
80	0.054
120	0.075
160	0.100
200	0.121
240	0.121
320	0.228
640	0.170
960	0.166
1280	0.177

Ave ( $\bar{d}$ ) 0.096

$(d_i - \bar{d})^2$
0.00861
0.00473
0.00007
0.00054
0.00195
0.00479
0.00813
0.00813
0.03900
0.01937
0.01828
0.02137

Sum 0.13499

Assume populations are normally distributed and have equivalent variance.

Using a paired analysis:  $H_0: \mu_1 - \mu_2 = \mu_D = 0$

$H_1: \mu_1 - \mu_2 \neq 0$

using a 95% confidence interval,  $v = 11$ :

$$s = \sqrt{\frac{\sum (d_i - \bar{d})^2}{(n - 1)}} = 1.061\text{E-}01$$

$$SE = s / \sqrt{n} = 3.062\text{E-}02$$

$$t = \frac{(\bar{x}_1 - \bar{x}_2) - D}{SE} = 3.134\text{E+}00$$

$$P(t < 3.134) = 9.517\text{E-}03$$

$$P\text{-value (2 tailed)} = 1.903\text{E-}02$$

Since P-value is less than the significance level (0.05) we reject the null hypothesis.

Therefore there is a statistical difference in the two thicknesses at 0.15  $\text{mg}/\text{cm}^2$   $\text{TiO}_2$

## U.8 Facing In vs. Facing Out 3-D performance

Comparison: ( 3-D | pH3 | TiO<sub>2</sub> ) Facing In vs. Facing Out

Data: F.O. 1 μm 0.02 mg/cm<sup>2</sup> TiO<sub>2</sub>

j [μA/cm <sup>2</sup> ]	E <sub>dark</sub> vs SHE
10	-0.154
20	-0.222
40	-0.278
80	-0.347
120	-0.396
160	-0.435
200	-0.471
240	-0.507
320	-0.562
640	-0.658
960	-0.752
1280	-0.873
Ave (μ1)	-0.471

Data: F.I. 1 μm 0.02 mg/cm<sup>2</sup> TiO<sub>2</sub>

j [μA/cm <sup>2</sup> ]	E <sub>dark</sub> vs SHE
10	-0.185
20	-0.245
40	-0.315
80	-0.392
120	-0.445
160	-0.480
200	-0.518
240	-0.543
320	-0.584
640	-0.685
960	-0.730
1280	-0.767
Ave (μ2)	-0.491

j [μA/cm <sup>2</sup> ]	di	(di- $\bar{d}$ ) <sup>2</sup>
10	0.031	0.00014
20	0.023	0.00001
40	0.037	0.00030
80	0.045	0.00063
120	0.049	0.00089
160	0.045	0.00066
200	0.047	0.00074
240	0.036	0.00028
320	0.022	0.00001
640	0.027	0.00006
960	-0.022	0.00174
1280	-0.106	0.01565
Ave ( $\bar{d}$ )	0.020	Sum 0.02110

Assume populations are normally distributed and have equivalent variance.

Using a paired analysis: H<sub>0</sub>: μ<sub>1</sub> - μ<sub>2</sub> = μ<sub>D</sub> = 0

H<sub>1</sub>: μ<sub>1</sub> - μ<sub>2</sub> ≠ 0

using a 95% confidence interval, v = 11:

$$s = \sqrt{(\sum(di - \bar{d})^2 / (n - 1))} = 4.194E-02$$

$$SE = s / \sqrt{n} = 1.211E-02$$

$$t = [(x_1 - x_2) - D] / SE = 1.613E+00$$

$$P(t < 1.6126) = 1.351E-01$$

$$P\text{-value (2 tailed)} = 2.702E-01$$

Since P-value is greater than the significance level (0.05) we fail to reject the null hypothesis.

Therefore there is no statistical difference in the two configurations (3-D vs. 2-D) 1 μm at 0.02 mg/cm<sup>2</sup> TiO<sub>2</sub>

Data: F.O. 1 μm 0.15 mg/cm<sup>2</sup> TiO<sub>2</sub>

j [μA/cm <sup>2</sup> ]	E <sub>dark</sub> vs SHE
10	-0.239
20	-0.359
40	-0.454
80	-0.551
120	-0.613
160	-0.649
200	-0.673
240	-0.695
320	-0.736
Ave (μ1)	-0.552

Data: F.I. 1 μm 0.15 mg/cm<sup>2</sup> TiO<sub>2</sub>

j [μA/cm <sup>2</sup> ]	E <sub>dark</sub> vs SHE
10	-0.151
20	-0.2
40	-0.221
80	-0.306
120	-0.356
160	-0.392
200	-0.421
240	-0.444
320	-0.365
640	-0.526
960	-0.597
1280	-0.629
Ave (μ2)	-0.317

j [μA/cm <sup>2</sup> ]	d <sub>i</sub>	(d <sub>i</sub> -d̄) <sup>2</sup>
10	-0.088	0.01155
20	-0.159	0.03190
40	-0.233	0.06359
80	-0.245	0.07008
120	-0.257	0.07659
160	-0.257	0.07630
200	-0.252	0.07388
240	-0.251	0.07307
320	-0.372	0.15291
Ave (d̄)	-0.235	Sum 0.62986

Assume populations are normally distributed and have equivalent variance.

Using a paired analysis: H<sub>0</sub>: μ<sub>1</sub> - μ<sub>2</sub> = μ<sub>D</sub> = 0

H<sub>1</sub>: μ<sub>1</sub> - μ<sub>2</sub> ≠ 0

using a 95% confidence interval, v = 8:

$$s = \sqrt{(\sum (d_i - \bar{d})^2) / (n - 1)} = 2.291E-01$$

$$SE = s / \sqrt{n} = 7.637E-02$$

$$t = [(x_1 - x_2) - D] / SE = -3.075E+00$$

$$P(t < -3.075) = 1.524E-02$$

$$P\text{-value (2 tailed)} = 3.047E-02$$

Since P-value is less than the significance level (0.05) we reject the null hypothesis.

Therefore there is a statistical difference in the two configurations (3-D vs. 2-D) 1 μm at 0.15 mg/cm<sup>2</sup> TiO<sub>2</sub>

Data: F.O. 10 μm 0.02 mg/cm<sup>2</sup> TiO<sub>2</sub>

j [μA/cm <sup>2</sup> ]	E <sub>dark</sub> vs SHE
10	-0.155
20	-0.220
40	-0.273
80	-0.342
120	-0.400
160	-0.454
200	-0.511
240	-0.553
320	-0.601
640	-0.714
960	-0.818

Ave (μ1) -0.458

Data: F.I. 10 μm 0.02 mg/cm<sup>2</sup> TiO<sub>2</sub>

j [μA/cm <sup>2</sup> ]	E <sub>dark</sub> vs SHE
10	-0.151
20	-0.23
40	-0.337
80	-0.449
120	-0.5122
160	-0.5485
200	-0.577
240	-0.591
320	-0.623
640	-0.703
960	-0.75
1280	-0.787

Ave (μ2) -0.497

j [μA/cm <sup>2</sup> ]	di	(di-d̄) <sup>2</sup>
10	-0.004	0.00055
20	0.010	0.00009
40	0.064	0.00202
80	0.107	0.00762
120	0.112	0.00858
160	0.094	0.00558
200	0.066	0.00218
240	0.038	0.00033
320	0.022	0.00001
640	-0.011	0.00091
960	-0.068	0.00769

Ave (d̄) 0.039 Sum 0.03555

Assume populations are normally distributed and have equivalent variance.

Using a paired analysis: H<sub>0</sub>: μ<sub>1</sub> - μ<sub>2</sub> = μ<sub>D</sub> = 0

H<sub>1</sub>: μ<sub>1</sub> - μ<sub>2</sub> ≠ 0

using a 95% confidence interval, v = 10:

$$s = \sqrt{(\sum(di - d)^2 / (n - 1))} = 5.962E-02$$

$$SE = s / \sqrt{n} = 1.798E-02$$

$$t = [(x_1 - x_2) - D] / SE = 1.034E+01$$

$$P(t < 10.338) = 1.172E-06$$

$$P\text{-value (2 tailed)} = 2.343E-06$$

Since P-value is less than the significance level (0.05) we reject the null hypothesis.

Therefore there is a statistical difference in the two configurations (3-D vs. 2-D) for 10 μm at 0.02 mg/cm<sup>2</sup> TiO<sub>2</sub>

Data: F.O. 10 μm 0.15 mg/cm<sup>2</sup> TiO<sub>2</sub>

j [μA/cm <sup>2</sup> ]	E <sub>dark</sub> vs SHE
10	-0.078
20	-0.179
40	-0.312
80	-0.458
120	-0.549
160	-0.619
200	-0.673
240	-0.716
320	-0.772

Ave (μ1) -0.484

Data: F.I. 10 μm 0.15 mg/cm<sup>2</sup> TiO<sub>2</sub>

j [μA/cm <sup>2</sup> ]	E <sub>dark</sub> vs SHE
10	-0.151
20	-0.23
40	-0.337
80	-0.449
120	-0.5122
160	-0.5485
200	-0.577
240	-0.591
320	-0.623
640	-0.703
960	-0.75
1280	-0.787

Ave (μ2) -0.447

j [μA/cm <sup>2</sup> ]	d <sub>i</sub>	(d <sub>i</sub> -d̄) <sup>2</sup>
10	0.073	0.00291
20	0.051	0.00096
40	0.025	0.00003
80	-0.009	0.00083
120	-0.036	0.00314
160	-0.070	0.00806
200	-0.096	0.01341
240	-0.125	0.02087
320	-0.149	0.02843

Ave (d̄) -0.037 Sum 0.07864

Assume populations are normally distributed and have equivalent variance.

Using a paired analysis: H<sub>0</sub>: μ<sub>1</sub> - μ<sub>2</sub> = μ<sub>D</sub> = 0

H<sub>1</sub>: μ<sub>1</sub> - μ<sub>2</sub> ≠ 0

using a 95% confidence interval, v = 8:

$$s = \sqrt{(\sum(d_i - d)^2 / (n - 1))} = 9.915E-02$$

$$SE = s / \sqrt{n} = 3.305E-02$$

$$t = [(x_1 - x_2) - D] / SE = 4.515E-01$$

$$P(t < 4.5147) = 6.636E-01$$

$$P\text{-value (2 tailed)} = 1.327E+00$$

Since P-value is greater than the significance level (0.05) we fail to reject the null hypothesis.

Therefore there is no statistical difference in the two configurations (3-D vs. 2-D) for 10 μm at 0.15 mg/cm<sup>2</sup> TiO<sub>2</sub>

## U.9 Increased Film Thickness by Titania Content for 2-D Films Facing In

Comparison: ( 2-D | pH-0.3 | TiO<sub>2</sub> | F.I. constant) Thickness 1 μm vs. 10 μm

Data: 1 μm 0.02 mg/cm<sup>2</sup> TiO<sub>2</sub>

j [μA/cm <sup>2</sup> ]	E <sub>dark</sub> vs SHE
10	-0.033
20	-0.097
40	-0.090
80	-0.116
120	-0.123
160	-0.123
200	-0.121
240	-0.119
320	-0.125
640	-0.176
960	-0.206
1280	-0.223

Ave (μ1) -0.129

Data: 10 μm 0.02 mg/cm<sup>2</sup> TiO<sub>2</sub>

j [μA/cm <sup>2</sup> ]	E <sub>dark</sub> vs SHE
10	-0.029
20	-0.094
40	-0.086
80	-0.110
120	-0.120
160	-0.122
200	-0.124
240	-0.124
320	-0.133
640	-0.193
960	-0.228
1280	-0.249

Ave (μ2) -0.134

j [μA/cm <sup>2</sup> ]	di	(di-d) <sup>2</sup>
10	-0.004	0.00008
20	-0.003	0.00006
40	-0.004	0.00007
80	-0.005	0.00011
120	-0.003	0.00007
160	-0.001	0.00004
200	0.002	0.00001
240	0.004	0.00000
320	0.008	0.00001
640	0.017	0.00014
960	0.022	0.00030
1280	0.026	0.00044

Ave (d) 0.005 Sum 0.00132

Assume populations are normally distributed and have equivalent variance.

Using a paired analysis: H<sub>0</sub>: μ<sub>1</sub> - μ<sub>2</sub> = μ<sub>D</sub> = 0

H<sub>1</sub>: μ<sub>1</sub> - μ<sub>2</sub> ≠ 0

using a 95% confidence interval, v = 11:

$$s = \sqrt{(\sum(di - d)^2 / (n - 1))} = 1.048E-02$$

$$SE = s / \sqrt{n} = 3.024E-03$$

$$t = [(x_1 - x_2) - D] / SE = 1.594E+00$$

$$P(t < 1.5937) = 1.393E-01$$

$$P\text{-value (2 tailed)} = 2.786E-01$$

Since P-value is greater than the significance level (0.05) we fail to reject the null hypothesis.

Therefore there is no statistical difference in performance from the two thicknesses at 0.02 mg/cm<sup>2</sup> TiO<sub>2</sub>

Data: 1  $\mu\text{m}$  0.15  $\text{mg}/\text{cm}^2$   $\text{TiO}_2$

j [ $\mu\text{A}/\text{cm}^2$ ]	$E_{\text{dark}}$ vs SHE
10	-0.047
20	-0.101
40	-0.092
80	-0.115
120	-0.122
160	-0.123
200	-0.122
240	-0.121
320	-0.126
640	-0.173
960	-0.201
1280	-0.218

Ave ( $\mu_1$ )                    -0.130

Data: 10  $\mu\text{m}$  0.15  $\text{mg}/\text{cm}^2$   $\text{TiO}_2$

j [ $\mu\text{A}/\text{cm}^2$ ]	$E_{\text{dark}}$ vs SHE
10	-0.039
20	-0.098
40	-0.089
80	-0.112
120	-0.119
160	-0.119
200	-0.119
240	-0.119
320	-0.125
640	-0.177
960	-0.214
1280	-0.238

Ave ( $\mu_2$ )                    -0.131

j [ $\mu\text{A}/\text{cm}^2$ ]	$d_i$	$(d_i - \bar{d})^2$
10	-0.008	0.00016
20	-0.003	0.00006
40	-0.004	0.00007
80	-0.003	0.00006
120	-0.004	0.00007
160	-0.004	0.00008
200	-0.003	0.00006
240	-0.002	0.00005
320	-0.001	0.00003
640	0.004	0.00000
960	0.013	0.00006
1280	0.020	0.00022

Ave ( $\bar{d}$ )                    0.000    Sum                    0.00092

Assume populations are normally distributed and have equivalent variance.

Using a paired analysis:       $H_0: \mu_1 - \mu_2 = \mu_D = 0$

$H_1: \mu_1 - \mu_2 \neq 0$

using a 95% confidence interval,  $v = 11$ :

$$s = \sqrt{(\sum(d_i - \bar{d})^2) / (n - 1)} = 8.740\text{E-}03$$

$$SE = s / \sqrt{n} = 2.523\text{E-}03$$

$$t = [(x_1 - x_2) - D] / SE = 1.697\text{E-}01$$

$$P(t < 0.1697) = 8.684\text{E-}01$$

$$P\text{-value (2 tailed)} = 1.737\text{E+}00$$

Since P-value is greater than the significance level (0.05) we fail to reject the null hypothesis.

Therefore there is no statistical difference in performance from the two thicknesses at 0.15  $\text{mg}/\text{cm}^2$   $\text{TiO}_2$

## U.10 Increased Titania Content by Film Thickness for 2-D Films Facing In

Comparison: ( 2-D | pH-0.3 | Thickness | F.I. constant) TiO<sub>2</sub> variation

Data: 1 μm 0.02 mg/cm<sup>2</sup> TiO<sub>2</sub>

j [μA/cm <sup>2</sup> ]	E <sub>dark</sub> vs SHE
10	-0.033
20	-0.097
40	-0.090
80	-0.116
120	-0.123
160	-0.123
200	-0.121
240	-0.119
320	-0.125
640	-0.176
960	-0.206
1280	-0.223

Ave (μ1) -0.129

Data: 1 μm 0.15 mg/cm<sup>2</sup> TiO<sub>2</sub>

j [μA/cm <sup>2</sup> ]	E <sub>dark</sub> vs SHE
10	-0.047
20	-0.101
40	-0.092
80	-0.115
120	-0.122
160	-0.123
200	-0.122
240	-0.121
320	-0.126
640	-0.173
960	-0.201
1280	-0.218

Ave (μ2) -0.130

j [μA/cm <sup>2</sup> ]	di	(di-d) <sup>2</sup>
10	0.014	0.00017
20	0.003	0.00001
40	0.003	0.00001
80	-0.001	0.00000
120	-0.001	0.00000
160	0.000	0.00000
200	0.001	0.00000
240	0.001	0.00000
320	0.001	0.00000
640	-0.003	0.00002
960	-0.005	0.00004
1280	-0.005	0.00003

Ave (d) 0.001 Sum 0.00027

Assume populations are normally distributed and have equivalent variance.

Using a paired analysis: H<sub>0</sub>: μ<sub>1</sub> - μ<sub>2</sub> = μ<sub>D</sub> = 0

H<sub>1</sub>: μ<sub>1</sub> - μ<sub>2</sub> ≠ 0

using a 95% confidence interval, v = 11:

$$s = \sqrt{(\sum(di - d)^2 / (n - 1))} = 4.728E-03$$

$$SE = s / \sqrt{n} = 1.365E-03$$

$$t = [(x_1 - x_2) - D] / SE = 5.100E-01$$

$$P(t < 0.51) = 6.201E-01$$

$$P\text{-value (2 tailed)} = 1.240E+00$$

Since P-value is greater than the significance level (0.05) we fail to reject the null hypothesis.

Therefore there is no statistical difference in performance from the two thicknesses at 0.02 mg/cm<sup>2</sup> TiO<sub>2</sub>

Data: 10  $\mu\text{m}$  0.02  $\text{mg}/\text{cm}^2$   $\text{TiO}_2$

j [ $\mu\text{A}/\text{cm}^2$ ]	$E_{\text{dark}}$ vs SHE
10	-0.029
20	-0.094
40	-0.086
80	-0.110
120	-0.120
160	-0.122
200	-0.124
240	-0.124
320	-0.133
640	-0.193
960	-0.228
1280	-0.249

Ave ( $\mu_1$ ) -0.134

Data: 10  $\mu\text{m}$  0.15  $\text{mg}/\text{cm}^2$   $\text{TiO}_2$

j [ $\mu\text{A}/\text{cm}^2$ ]	$E_{\text{dark}}$ vs SHE
10	-0.039
20	-0.098
40	-0.089
80	-0.112
120	-0.119
160	-0.119
200	-0.119
240	-0.119
320	-0.125
640	-0.177
960	-0.214
1280	-0.238

Ave ( $\mu_2$ ) -0.131

j [ $\mu\text{A}/\text{cm}^2$ ]	$d_i$	$(d_i - \bar{d})^2$
10	0.010	0.00009
20	0.004	0.00001
40	0.003	0.00001
80	0.002	0.00000
120	-0.001	0.00000
160	-0.003	0.00001
200	-0.005	0.00003
240	-0.005	0.00003
320	-0.008	0.00007
640	-0.016	0.00027
960	-0.015	0.00024
1280	-0.011	0.00014

Ave ( $\bar{d}$ ) -0.004 Sum 0.00091

Assume populations are normally distributed and have equivalent variance.

Using a paired analysis:  $H_0: \mu_1 - \mu_2 = \mu_D = 0$

$H_1: \mu_1 - \mu_2 \neq 0$

using a 95% confidence interval,  $v = 11$ :

$$s = \sqrt{\frac{(\sum(d_i - \bar{d})^2)}{(n - 1)}} = 8.723\text{E-}03$$

$$SE = s / \sqrt{n} = 2.518\text{E-}03$$

$$t = \frac{(\bar{x}_1 - \bar{x}_2) - D}{SE} = -1.468\text{E+}00$$

$$P(t < -1.468) = 1.702\text{E-}01$$

$$P\text{-value (2 tailed)} = 3.404\text{E-}01$$

Since P-value is greater than the significance level (0.05) we fail to reject the null hypothesis.

Therefore there is no statistical difference in performance from the two thicknesses at 0.15  $\text{mg}/\text{cm}^2$   $\text{TiO}_2$

## U.11 Facing In vs. Facing Out 2-D performance

Comparison: ( pH-0.3 | TiO<sub>2</sub> | F.I. constant) 2-D vs. 3-D

Data: 3-D 1 μm 0.02 mg/cm<sup>2</sup> TiO<sub>2</sub>

j [μA/cm <sup>2</sup> ]	E <sub>dark</sub> vs SHE
10	-0.071
20	-0.146
40	-0.145
80	-0.180
120	-0.201
160	-0.216
200	-0.229
240	-0.240
320	-0.258
640	-0.308
960	-0.343
1280	-0.371

Ave (μ1) -0.226

Data: 2-D 1 μm 0.02 mg/cm<sup>2</sup> TiO<sub>2</sub>

j [μA/cm <sup>2</sup> ]	E <sub>dark</sub> vs SHE
10	-0.033
20	-0.097
40	-0.090
80	-0.116
120	-0.123
160	-0.123
200	-0.121
240	-0.119
320	-0.125
640	-0.176
960	-0.206
1280	-0.223

Ave (μ2) -0.129

j [μA/cm <sup>2</sup> ]	di
10	-0.038
20	-0.049
40	-0.056
80	-0.064
120	-0.078
160	-0.093
200	-0.108
240	-0.121
320	-0.133
640	-0.131
960	-0.136
1280	-0.148

Ave (μD) -0.096

(di-d) <sup>2</sup>
0.00340
0.00225
0.00164
0.00101
0.00034
0.00001
0.00014
0.00059
0.00134
0.00123
0.00161
0.00265

Sum 0.01621

Assume populations are normally distributed and have equivalent variance.

Using a paired analysis: H<sub>0</sub>: μ<sub>1</sub> - μ<sub>2</sub> = μ<sub>D</sub> = 0

H<sub>1</sub>: μ<sub>1</sub> - μ<sub>2</sub> ≠ 0

using a 95% confidence interval, v = 11:

$$s = \sqrt{(\sum(di - d)^2 / (n - 1))} = 3.675E-02$$

$$SE = s / \sqrt{n} = 1.061E-02$$

$$t = [(x_1 - x_2) - D] / SE = -9.077E+00$$

$$P(t < -9.0765) = 1.010E-06$$

$$P\text{-value (2 tailed)} = 2.019E-06$$

Since P-value is less than the significance level (0.05) we reject the null hypothesis.

Therefore there is a statistical difference in the 3-D and 2-D loadings for 1 μm at 0.02 mg/cm<sup>2</sup> TiO<sub>2</sub>

Data: 3-D 1  $\mu\text{m}$  0.15  $\text{mg}/\text{cm}^2$   $\text{TiO}_2$

j [ $\mu\text{A}/\text{cm}^2$ ]	$E_{\text{dark}}$ vs SHE
10	-0.059
20	-0.121
40	-0.120
80	-0.149
120	-0.167
160	-0.178
200	-0.188
240	-0.195
320	-0.211
640	-0.264
960	-0.299
1280	-0.324

Ave ( $\mu_1$ ) -0.190

Data: 2-D 1  $\mu\text{m}$  0.15  $\text{mg}/\text{cm}^2$   $\text{TiO}_2$

j [ $\mu\text{A}/\text{cm}^2$ ]	$E_{\text{dark}}$ vs SHE
10	-0.047
20	-0.101
40	-0.092
80	-0.115
120	-0.122
160	-0.123
200	-0.122
240	-0.121
320	-0.126
640	-0.173
960	-0.201
1280	-0.218

Ave ( $\mu_2$ ) -0.130

j [ $\mu\text{A}/\text{cm}^2$ ]	$d_i$
10	-0.012
20	-0.020
40	-0.028
80	-0.034
120	-0.045
160	-0.055
200	-0.066
240	-0.075
320	-0.085
640	-0.091
960	-0.098
1280	-0.106

Ave ( $\mu_D$ ) -0.060

$(d_i - \bar{d})^2$
0.00710
0.00583
0.00471
0.00384
0.00265
0.00172
0.00092
0.00046
0.00013
0.00003
0.00000
0.00009

Sum 0.02750

Assume populations are normally distributed and have equivalent variance.

Using a paired analysis:  $H_0: \mu_1 - \mu_2 = \mu_D = 0$

$H_1: \mu_1 - \mu_2 \neq 0$

using a 95% confidence interval,  $v = 11$ :

$$s = \sqrt{(\sum(d_i - \bar{d})^2) / (n - 1)} = 4.787\text{E-}02$$

$$SE = s / \sqrt{n} = 1.382\text{E-}02$$

$$t = [(x_1 - x_2) - D] / SE = -4.307\text{E+}00$$

$$P(t < -4.3068) = 1.020\text{E-}03$$

$$P\text{-value (2 tailed)} = 2.039\text{E-}03$$

Since P-value is less than the significance level (0.05) we reject the null hypothesis.

Therefore there is a statistical difference in the 3-D and 2-D loadings for 1  $\mu\text{m}$  at 0.15  $\text{mg}/\text{cm}^2$   $\text{TiO}_2$

Data: 3-D 10 μm 0.02 mg/cm<sup>2</sup> TiO<sub>2</sub>

j [μA/cm <sup>2</sup> ]	E <sub>dark</sub> vs SHE
10	-0.053
20	-0.127
40	-0.127
80	-0.163
120	-0.185
160	-0.202
200	-0.215
240	-0.227
320	-0.247
640	-0.299
960	-0.337
1280	-0.368

Ave (μ1) -0.212

Data: 2-D 10 μm 0.02 mg/cm<sup>2</sup> TiO<sub>2</sub>

j [μA/cm <sup>2</sup> ]	E <sub>dark</sub> vs SHE
10	-0.029
20	-0.094
40	-0.086
80	-0.110
120	-0.120
160	-0.122
200	-0.124
240	-0.124
320	-0.133
640	-0.193
960	-0.228
1280	-0.249

Ave (μ2) -0.134

j [μA/cm <sup>2</sup> ]	d <sub>i</sub>
10	-0.024
20	-0.032
40	-0.041
80	-0.053
120	-0.065
160	-0.080
200	-0.092
240	-0.103
320	-0.114
640	-0.106
960	-0.109
1280	-0.119

Ave (μD) -0.078

(d <sub>i</sub> -d̄) <sup>2</sup>
0.00516
0.00408
0.00302
0.00188
0.00097
0.00028
0.00002
0.00005
0.00030
0.00010
0.00015
0.00053

Sum 0.01654

Assume populations are normally distributed and have equivalent variance.

Using a paired analysis: H<sub>0</sub>: μ<sub>1</sub> - μ<sub>2</sub> = μ<sub>D</sub> = 0

H<sub>1</sub>: μ<sub>1</sub> - μ<sub>2</sub> ≠ 0

using a 95% confidence interval, v = 11:

$$s = \sqrt{(\sum(d_i - \bar{d})^2 / (n - 1))} = 3.712E-02$$

$$SE = s / \sqrt{n} = 1.072E-02$$

$$t = [(x_1 - x_2) - D] / SE = -7.297E+00$$

$$P(t < -7.2969) = 9.518E-06$$

$$P\text{-value (2 tailed)} = 1.904E-05$$

Since P-value is less than the significance level (0.05) we reject the null hypothesis.

Therefore there is a statistical difference in the 3-D and 2-D loadings for 10 μm at 0.02 mg/cm<sup>2</sup> TiO<sub>2</sub>

Data: 3-D 10  $\mu\text{m}$  0.15  $\text{mg}/\text{cm}^2$   $\text{TiO}_2$

j [ $\mu\text{A}/\text{cm}^2$ ]	$E_{\text{dark}}$ vs SHE
10	-0.053
20	-0.134
40	-0.134
80	-0.172
120	-0.194
160	-0.211
200	-0.225
240	-0.236
320	-0.257
640	-0.311
960	-0.349
1280	-0.378

Ave ( $\mu_1$ ) -0.221

Data: 2-D 10  $\mu\text{m}$  0.15  $\text{mg}/\text{cm}^2$   $\text{TiO}_2$

j [ $\mu\text{A}/\text{cm}^2$ ]	$E_{\text{dark}}$ vs SHE
10	-0.039
20	-0.098
40	-0.089
80	-0.112
120	-0.119
160	-0.119
200	-0.119
240	-0.119
320	-0.125
640	-0.177
960	-0.214
1280	-0.238

Ave ( $\mu_2$ ) -0.131

j [ $\mu\text{A}/\text{cm}^2$ ]	$d_i$
10	-0.014
20	-0.036
40	-0.045
80	-0.060
120	-0.076
160	-0.092
200	-0.106
240	-0.118
320	-0.132
640	-0.134
960	-0.135
1280	-0.141

Ave ( $\mu_D$ ) -0.091

$(d_i - \bar{d})^2$
0.00674
0.00361
0.00258
0.00131
0.00042
0.00002
0.00009
0.00047
0.00125
0.00140
0.00152
0.00197

Sum 0.02136

Assume populations are normally distributed and have equivalent variance.

Using a paired analysis:  $H_0: \mu_1 - \mu_2 = \mu_D = 0$

$H_1: \mu_1 - \mu_2 \neq 0$

using a 95% confidence interval,  $v = 11$ :

$$s = \sqrt{\frac{\sum (d_i - \bar{d})^2}{(n - 1)}} = 4.219\text{E-}02$$

$$SE = s / \sqrt{n} = 1.218\text{E-}02$$

$$t = \frac{(\mu_1 - \mu_2) - D}{SE} = -7.447\text{E+}00$$

$$P(t < -7.4467) = 7.770\text{E-}06$$

$$P\text{-value (2 tailed)} = 1.554\text{E-}05$$

Since P-value is less than the significance level (0.05) we reject the null hypothesis.

Therefore there is a statistical difference in the 3-D and 2-D loadings for 10  $\mu\text{m}$  at 0.15  $\text{mg}/\text{cm}^2$   $\text{TiO}_2$

## Appendix V - Through Membrane Irradiation

A through membrane illumination was conducted for a 20  $\mu\text{m}$  PBT-TiO<sub>2</sub> baseline deposition (0.02  $\text{mgcm}^{-2}$  TiO<sub>2</sub>) on Nafion doped TGP-H-030 substrate deposited as detailed in Chapter 5. The sample was setup as outlined in Chapter 2, with a N117 separator and 1.5  $\text{mg/cm}^2$  RuO<sub>2</sub> on TGP-H-060 anode in 0.5 mM H<sub>2</sub>SO<sub>4</sub> at 20<sup>o</sup>C. The only difference between the film facing in and film facing out configuration is that the 1.5 $\text{mg/cm}^2$  anode was replaced by a platinum mesh to allow for solar penetration for the facing in sample in this study. This equivalent cathode deposition is compared to the ‘facing out’ sample results presented previously:

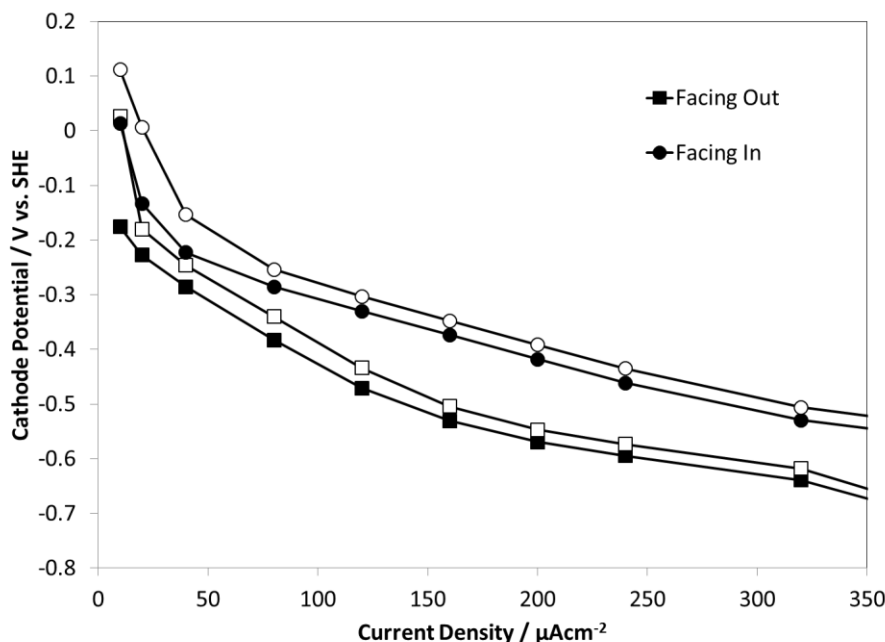
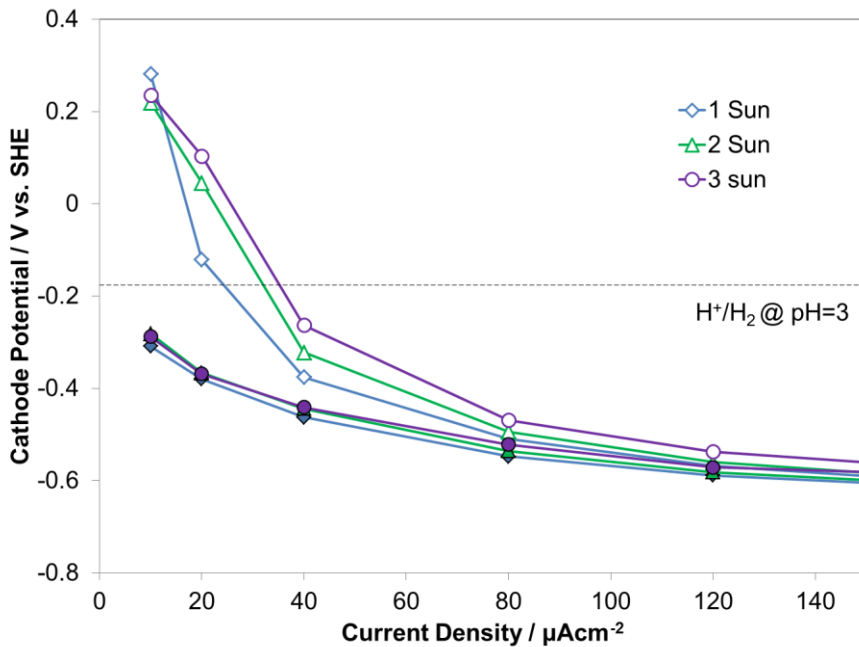


Figure 165 - Cathode polarization for 1292 s baseline loadings of PBT-TiO<sub>2</sub> films coated on Nafion doped TGP-H-030. Filled symbols represent dark performance while open symbols represent 1 Sun performance. Lines are added for illustrative purposes.

It can be seen from the above plot that as expected and previously shown in Chapter 4, the film facing in performs much better electrochemically, with enhanced triple phase connectivity. What was surprising to see however was that through membrane illumination resulted in nearly equivalent solar performance. Considering UV losses by beam passage through the membrane, as well as any shading by the platinum mesh, and reflection from the Nafion membrane this would indicate that the through membrane performance was actually better than the facing out equivalent. Since the platinum mesh has an open area of 65% this could represent nearly half of the total illumination. This result also indicated that UV stimulation is not necessarily needed for the photocatalytic reaction and the reaction can be driven by visible light alone. More work should be done in this area to characterize the losses as well as further investigate through membrane stimulation.

## Appendix W - Higher Intensity Sun Studies

Multiple sun testing was performed on a 3.33  $\mu\text{m}$  film thickness of PBT-TiO<sub>2</sub> with 0.09  $\text{mg}/\text{cm}^2$  TiO<sub>2</sub> loading. The sample was setup as outlined in Chapter 2, with a N117 separator and 1.5  $\text{mg}/\text{cm}^2$  RuO<sub>2</sub> on TGP-H-060 anode in 0.5 mM H<sub>2</sub>SO<sub>4</sub> at 20<sup>0</sup>C. The multiple sun result is shown below in Figure 166:



**Figure 166 - Cathode polarization for 3.33  $\mu\text{m}$  film thickness, 0.09  $\text{mgcm}^{-2}$  TiO<sub>2</sub> loading of PBT-TiO<sub>2</sub> coated on TGP-H-030. Filled symbols represent dark performance while open symbols represent varied solar performance. Lines are added for illustrative purposes.**

It can be seen from the above plot that there is an increase in solar performance with an increase in irradiation power. This result amounts to an increase in the Fill Factor of the above films, showing that the films could be optimized further in terms of film thickness. As mentioned in Chapter 5, there may be a significant advantage to operate these composite devices at higher temperatures as well. If a concentrator unit is used, these multi sun

improvements in performance could be coupled with improved performance from increased polymer conductivity as well.